AD NUMBER

AD460001

LIMITATION CHANGES

TO:

Approved for public release; distribution is unlimited.

FROM:

**Distribution authorized to U.S. Gov't. agencies and their contractors;
Administrative/Operational Use; DEC 1964. Other requests shall be referred to Naval Research Lab., Arlington, VA 22203.**

AUTHORITY

NRL ltr 25 Mar 1974

DISCLAIMER NOTICE

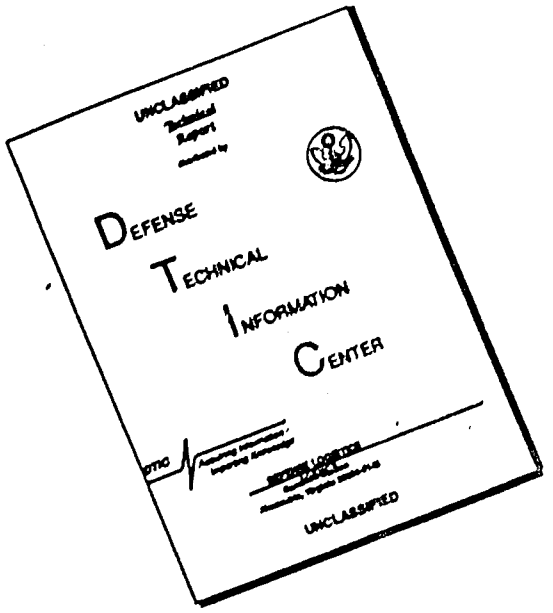

THIS DOCUMENT IS BEST QUALITY AVAILABLE. THE COPY FURNISHED TO DTIC CONTAINED A SIGNIFICANT NUMBER OF PAGES WHICH DO NOT REPRODUCE LEGIBLY.

Bulletin 34
Part 3
(of 5 Parts)

THE SHOCK AND VIBRATION BULLETIN

DECEMBER 1964

A Publication of
THE SHOCK AND VIBRATION
INFORMATION CENTER
U.S. Naval Research Laboratory, Washington, D.C.

Office of
The Director of Defense
Research and Engineering

Bulletin 34
Part 3
(of 5 Parts)

THE SHOCK AND VIBRATION BULLETIN

DECEMBER 1964

A Publication of
THE SHOCK AND VIBRATION
INFORMATION CENTER
U.S. Naval Research Laboratory, Washington, D.C.

The 34th Symposium on Shock, Vibration and Associated Environments was held in Pacific Grove, California on 13-15 October 1964. The Army was host.

Office of
The Director of Defense
Research and Engineering

CONTENTS

PART 3

Mechanical Impedance

NOTES ON THE DEVELOPMENT OF MECHANICAL IMPEDANCE 1
C. T. Molloy, Space Technology Laboratories

RECENT ADVANCES IN MECHANICAL IMPEDANCE INSTRUMENTATION AND APPLICATIONS 3
F. Schloss, David Taylor Model Basin

MECHANICAL IMPEDANCE OF SPACECRAFT STRUCTURES 15
C. C. Osgood, RCA-Astro Electronics Division

PRELIMINARY STUDY OF AN EXPERIMENTAL METHOD IN MULTIDIMENSIONAL MECHANICAL IMPEDANCE DETERMINATION 27
F. J. On, Goddard Space Flight Center

EFFECTS OF TECHNIQUE ON RELIABILITY OF MECHANICAL IMPEDANCE MEASUREMENT 37
G. M. Remmers and R. O. Belsheim, U.S. Naval Research Laboratory

RESONANCE FREQUENCY OF LARGE SOLID PROPELLANT ROCKET MOTOR DETERMINED BY MECHANICAL IMPEDANCE 59
L. G. Flippin, L. W. Gammell and G. S. Stibor, Thiokol Chemical Corporation

USE OF MECHANICAL IMPEDANCE IN DYNAMIC MEASUREMENT OF SOLID ROCKET MOTORS 75
R. E. Coleman, Rocketdyne

PREDICTING MAXIMUM RESPONSE OF A VIBRATION-EXCITED ELASTIC SUBSTRUCTURE 83
L. J. Pulgrano, Grumman Aircraft Engineering Corporation

DETERMINATION OF SYSTEM FIXED BASE NATURAL FREQUENCIES BY SHAKE TESTS 95
R. E. Kaplan and L. P. Petak, U.S. Naval Research Laboratory

EXPERIMENTAL PROGRAM TO DETERMINE DYNAMIC ENVIRONMENT OF LAUNCH VEHICLES 101
I. P. Vatz, Brown Engineering Company

SMALL DISPLACEMENT KINEMATIC ANALYSIS OF BAR LINKAGES 123
C. S. O'Hearne, Martin Company

A PRACTICAL METHOD FOR PREDICTING ACOUSTIC RADIATION OR SHOCK EXCURSIONS OF NAVY MACHINERY 129
R. A. Darby, U.S. Navy Marine Engineering Laboratory

A STEADY STATE RESPONSE ANALYSIS OF COMPLEX STRUCTURES USING IMPEDANCE COUPLING TECHNIQUES 139
M. J. Baruch and S. Telles, Republic Aviation Corporation

Shock and Vibration Isolation

INVESTIGATION OF A RATIONAL APPROACH TO SHOCK ISOLATOR DESIGN 157
R. A. Eubanks, IIT Research Institute

VIBRATION ISOLATION SYSTEMS FOR ELECTRONIC EQUIPMENT IN THE B-52 AIRPLANE LOW-LEVEL ENVIRONMENT 169
R. W. Spring, The Boeing Company

DESIGN AND DEVELOPMENT OF LOW-FREQUENCY VIBRATION ISOLATORS WHICH EXHIBIT LOW SHOCK AMPLIFICATION CHARACTERISTICS 177
S. Balan and L. J. Pulgrano, Grumman Aircraft Engineering Corporation

PROTECTING THE "EYES" OF THE OAO SATELLITE 185
J. T. Gwinn, Jr., Lord Manufacturing Company

DESIGN OF FOCALIZED SUSPENSION SYSTEMS 193
L. S. Pechter and H. Kamei, Autonetics Division of North American Aviation, Inc.

Shock

ELEMENTARY CONSIDERATIONS OF SHOCK SPECTRA 211
I. Vigness, U.S. Naval Research Laboratory

SPECTRAL CHARACTERISTICS OF SOME PRACTICAL VARIATIONS IN THE HALF-SINE AND SAW-TOOTH PULSES 223
E. H. Schell, Air Force Flight Dynamics Laboratory

USE OF SHOCK FOR LOW FREQUENCY VIBRATION TESTING 253
A. J. Villasenor and T. G. Butler, Goddard Space Flight Center

SPACECRAFT SHOCKS INDUCED BY ELECTRO-EXPLOSIVE DEVICES 259
D. A. Heydon and W. W. Aichroth, TRW Space Technology Laboratories

SIMULATION OF THE PYROTECHNIC SHOCK ENVIRONMENT 267
A. L. Ikola, Lockheed Missiles and Space Company

TEST TECHNIQUES FOR INCREASING THE ACCELERATION AND VELOCITY CAPABILITIES OF AN 18-INCH PNEUMATIC ACTUATOR 275
F. H. Mathews, Sandia Corporation

FIVE-MILLION POUND SHOCK TESTING FACILITY 291
R. M. Phelan, Cornell University and Lawrence Radiation Laboratory

SHOCK TESTING WITH EXPLOSIVE GASES 311
W. M. Sigmon, Jr., Sandia Corporation

HAND-HELD SHOCK TESTER WOX-6A 329
V. F. De Vost, J. E. Messner and G. Stathopoulos, U.S. Naval Ordnance Laboratory

DESIGN AND DEVELOPMENT OF A HYDRAULIC SHOCK TEST MACHINE PROGRAMMER 335
J. R. Russell, American Machine and Foundry Company

SHAPING SHOCK ACCELERATION WAVEFORMS FOR OPTIMUM ELECTRODYNAMIC SHAKER PERFORMANCE 345
W. R. Miller, LTV Ling Electronics Division

SHOCK TESTING WITH VIBRATION SYSTEMS 355
F. W. Young, Radiation, Inc.

HYGE SHOCK FACILITY IMPROVEMENTS 365
R. M. Stuart, Hughes Aircraft Co.

DISTRIBUTION 369

PAPERS APPEARING IN PART 1
Part 1 - Confidential
(Titles Unclassified)

PROGRESS IN THE NAVY'S WAR ON SHOCK
H. L. Rich, David Taylor Model Basin

FACTORS AFFECTING THE DEFINITION OF DESIGN AND TESTING CRITERIA FOR NAVAL SHOCK RESISTANT EQUIPMENT
P. B. Wishart, Naval Construction Research Establishment

ANALYTICAL METHODS FOR PREDICTION OF MECHANICAL SHOCK ENVIRONMENT FOR SHIPBOARD EQUIPMENT OF SUBMARINES SUBJECTED TO UNDERWATER EXPLOSIONS
M. Pakstys, Jr., General Dynamics/Electric Boat

GROWTH IN SHOCK AND VIBRATION ANALYSIS AND CORRESPONDING DESIGN IMPROVEMENTS
E. G. Fischer, C. R. Brown, and A. A. Parr, Westinghouse Electric Corporation

A GENERAL-PURPOSE NAVAL MOUNT
R. Hall, Naval Construction Research Establishment

AN APPROACH TO THE DESIGN OF A SHOCK/ANTI-VIBRATION MOUNT
T. A. Tugwood, Admiralty Surface Weapons Establishment

A MECHANICAL SHOCK DESIGN METHOD FOR SUBMARINE PRESSURE HULL ATTACHMENTS UNDER EXPLOSION ATTACK
E. W. Palmer, Underwater Explosions Research Division, DTMB

EVALUATION OF A MACHINERY INSTALLATION BY MECHANICAL IMPEDANCE METHODS
J. E. Smith, Portsmouth Naval Shipyard

A VIBRATION MONITORING SYSTEM USEFUL IN SUBMARINE SILENCING AND MAINTENANCE OF LOW NOISE EQUIPMENT
W. H. Ezell, General Dynamics/Electric Boat

THE DYNAMIC ENVIRONMENTS OF THE SHERIDAN/SHILLELAGH MISSILE SUBMARINE SYSTEM
H. M. Marshall, N. L. Haight and D. W. Parsons, Aeronutronic Division, Philco Corporation

IDENTIFICATION OF BATTLEFIELD VEHICLES BY SOUND AND VIBRATION TECHNIQUES
D. W. Rees, USA Tank-Automotive Center

REPETITIVE STRONG SHOCK GENERATION AND PROPOSED FLEXIBLE SHOCK-ABSORBER SYSTEM
C. V. David and E. A. Day, General Dynamics/General Atomic Division

THE DESIGN OF ELECTRONIC EQUIPMENT FOR DYNAMIC ENVIRONMENTS
R. H. Craig, General Electric Company Ltd.

ANALYSIS OF MISSILE RESPONSE TO HARD-TARGET IMPACT
M. B. Tate, Applied Physics Laboratory, JHU

THE TOW MISSILE LAUNCH ENVIRONMENT MEASUREMENT PROGRAM
A. D. MacLellan, Hughes Aircraft Company

HARD BASE EQUIPMENT—INSTALLATION DESIGN
B. R. Cocke, Martin Company

FIXTURES AND METHODS FOR OBTAINING THE FREE-FREE BREATHING AND BENDING MODES OF SOLID PROPELLANT ROCKET MOTORS
L. R. West, Hercules Powder Company

PAPERS APPEARING IN PART 2

Mathematical Analysis

PREDICTION OF LAUNCH VEHICLE TRANSONIC BUFFETING FROM WIND TUNNEL DATA
R. E. Bieber, Lockheed Missiles and Space Company

SPACECRAFT ADAPTER RESPONSE TO FLUCTUATING PRESSURE
G. A. Watts, Manned Spacecraft Center

SUBHARMONIC BEHAVIOR OF THIN-WALLED ELASTIC BEAM
W. K. Tso, Northrop Corporation

PREDICTION AND MEASUREMENT OF VIBRATION RESPONSE OF THE PEGASUS MICROMETEOROID MEASURING SATELLITE
C. E. Lifer and R. G. Mills, Marshall Space Flight Center

SPECTRA OF NONSTATIONARY RANDOM PROCESSES
G. P. Thrall, Measurement Analysis Corporation

RESPONSE OF MULTI-DEGREE-OF-FREEDOM SYSTEM TO RANDOM EXCITATION
R. C. Binder, University of Southern California

STRUCTURAL RESPONSE TO A VELOCITY-DEPENDENT STOCHASTIC EXCITATION
W. J. Stronge and C. K. Fisher, U.S. Naval Ordnance Test Station

VIBRATIONS OF A CANTILEVER BEAM CONSIDERING A NON-RIGID WALL SUPPORT
H. F. Cooper, Jr., Bell Telephone Laboratories, Inc.

Computers in Design

DIGITAL COMPUTER APPLICATION TO NONLINEAR VIBRATIONS
F. H. Collopy and R. Serbagi, AVCO Corporation

INTEGRATION OF A COMPUTER INTO THE DESIGN PROCESS
A. L. Head, Jr., and G. Harris, LTV Vought Aeronautics Division

DYNAMIC RESPONSE ANALYSIS OF COMPLEX MECHANICAL SYSTEMS
S. F. Mercurio and F. E. Niechniedowicz, Sperry Gyroscope Company

CONSIDERATIONS OF CAPTIVE FIRING VIBRATION ON NONOPERATING PROPULSION SYSTEM COMPONENTS
G. Sardella, Martin Company

A PRACTICAL APPLICATION OF A DIGITAL COMPUTER PROGRAM DURING THE DESIGN PHASE OF AN AEROSPACE STRUCTURE
B. T. Bata, Martin Company

STATIC AND DYNAMIC ANALYSIS BY A MATRIX FORCE METHOD
S. Kaufman and D. B. Hall, Martin Company

Design Techniques

SONIC AND ULTRASONIC VIBRATION SENSITIVITY OF X-BAND MICROWAVE COMPONENTS
R. Strike and G. G. Sundberg, General Dynamics/Pomona

DESIGNING ELECTRONIC EQUIPMENT FOR THE COMBINED RANDOM AND SINUSOIDAL VIBRATION ENVIRONMENT
A. W. Sinkinson, RCA

DESIGNING MECHANISMS FOR NONLINEAR DYNAMIC EFFECTS
H. F. Hunter, Lockheed-Georgia Company

PACKAGING ELECTRONICS FOR 250,000 G APPLICATIONS
D. W. Finger, Harry Diamond Laboratories

COMBINED ANALYTICAL AND EXPERIMENTAL APPROACH FOR DESIGNING AND EVALUATING STRUCTURAL SYSTEMS FOR VIBRATION ENVIRONMENTS
J. C. McClymonds and J. K. Gandung, Douglas Aircraft Company, Inc.

THOR 20-CYCLE LONGITUDINAL OSCILLATION STUDY
W. F. Davis, T. F. Lynch and T. R. Murray, Douglas Aircraft Company, Inc.

LOW FREQUENCY STRUCTURAL DYNAMICS OF THE SATURN VEHICLES
D. C. Christian, G. C. Marshall Space Flight Center

DESIGN AND TEST OF AN AIRJET ACOUSTIC NOISE GENERATOR TO REPRODUCE A MISSILE FLIGHT ENVIRONMENT
D. Richards, Applied Physics Laboratory

GRAPHICAL METHOD OF CALCULATING RMS VALUES FOR SHAPED RANDOM VIBRATION SPECTRA
H. Himelblau, North American Aviation, Inc.

DESIGN EVALUATION THROUGH VIBRATION TEST PROGRAM
D. A. Hausrath and J. R. Read, Autonetics, Division of North American Aviation, Inc.

DESIGNING FOR THE DYNAMIC ENVIRONMENT OF THE GEMINI INERTIAL PLATFORM
G. R. Grabow and J. E. Cottle, Honeywell Inc., Aeronautical Division

GUN FIRING ENVIRONMENT AND ITS RELATION TO STRUCTURAL AND EQUIPMENT INTEGRITY
J. E. Gross and R. Pittman, McDonnell Aircraft Corporation

REDUCTION OF NOISE AND VIBRATION IN MILITARY VEHICLES
J. W. Cameron, U.S. Army Tank-Automotive Center

DESIGNING FOR THE DYNAMIC ENVIRONMENT PRACTICAL DESIGN TECHNIQUES
J. G. Perri, Burns and Roe, Inc.

PAPERS APPEARING IN PART 4

Instrumentation

MEASUREMENT AND ANALYSIS OF ENVIRONMENTAL VIBRATION ON A SHIP DURING ANY OPERATION AND AT ANY SEA CONDITION
E. Buchmann, David Taylor Model Basin

SYSTEM TO CALIBRATE VIBRATION TRANSDUCERS AT LOW DISPLACEMENTS
J. R. Reed, Naval Boiler and Turbine Laboratory

USE OF RECIPROCITY CALIBRATED ACCELEROMETER STANDARDS FOR PERFORMING ROUTINE LABORATORY COMPARISON CALIBRATIONS
R. R. Bouche and L. C. Ensor, Endevco Corporation

NEW INSTRUMENT FOR ACCELEROMETER CALIBRATION
D. R. Workman, Lockheed Missiles and Space Company

DEVELOPMENT OF AN OMNIDIRECTIONAL ACCELEROMETER
L. E. Dunbar, Grumman Aircraft Engineering Corporation

USE OF MINIATURE FORCE TRANSDUCERS IN THE MEASUREMENT OF SHOCK AND VIBRATION ENVIRONMENTS
G. W. Painter, Lockheed-California Company

ACQUISITION, REDUCTION, AND ANALYSES OF TRANSIENT DATA
E. H. Copeland, T. E. Smart, and J. Arnold, Sandia Corporation

A TELEMETRY STANDARD FOR VIBRATION AND ACOUSTIC MEASUREMENTS
E. J. Kirchman and F. J. Holley, Goddard Space Flight Center

MEASURING LAUNCH-ABORT ENVIRONMENT
C. N. Golub, Pan American World Airways, Inc.

DYNAMIC RESPONSE OF A DIGITAL MAGNETIC FORCE-REBALANCE PENDULOUS ACCELEROMETER TO A VIBRATIONAL ENVIRONMENT
L. R. Beuder and R. C. Rountree, Nortronics Division of Northrop Corporation

MEASUREMENT OF RELATIVE DEFLECTIONS OF A GROUND MAPPING RADAR ANTENNA IN A VIBRATION ENVIRONMENT
E. F. Dyer, Westinghouse Electric Corp.

EXPERIMENTAL RESULTS OF THE APPLICATION OF SAMPLING TECHNIQUES TO VARIOUS TYPES OF FLIGHT DATA
J. Sudey, Jr., Martin Marietta Corp.

Environmental Data and Specifications

THE SHIPBOARD DYNAMIC ENVIRONMENT
H. B. Avery and W. L. Goodwin, Raytheon Company

A SUMMARY OF MODEL AND FULL-SCALE ACOUSTIC DATA FOR PREDICTION OF MISSILE LIFT-OFF NOISE ENVIRONMENT
D. A. Bond, Northrop Space Laboratories

PROBLEMS IN ADDING REALISM TO STANDARD SPECIFICATIONS
A. J. Silver, Litton Industries, Inc.

UTILIZING IN-FLIGHT VIBRATION DATA TO SPECIFY DESIGN AND TEST CRITERIA FOR EQUIPMENT MOUNTED IN JET AIRCRAFT
H. Katz and G. R. Waymon, McDonnell Aircraft Corp.

SOME RELIABILITY CONSIDERATIONS IN THE SPECIFICATION OF VIBRATION TEST REQUIREMENTS FOR NONRECOVERABLE COMPONENTS
C. V. Stahle, Martin Company

THE SPECIFICATION PROBLEM - PANEL SESSION

ROLLING CONTACT BEARING VIBRATION—THE STATE OF THE ART—
J. I. Schwartz and R. E. Gustafson, U.S. Navy Marine Engineering Laboratory

HUMAN RESPONSE TO RANDOM VIBRATIONS
F. Pradko, U.S. Army Tank-Automotive Center

MEASUREMENT, ANALYSIS AND INTERPRETATION OF F-5A 20MM GUNFIRE DYNAMIC ENVIRONMENT
R. F. Carmichael and D. Pelke, Norair Division, Northrop

Transportation Environments

ACQUISITION AND ANALYSIS OF ACCELERATION DATA FROM THE S. S. WOLVERINE STATE AND LONG-TERM PREDICTION OF SEAWAY INDUCED LOADS ON CARGO
F. C. Bailey and D. J. Fritch, Lessells and Associates

DEPARTMENT OF THE ARMY POSITION ON TRANSPORTATION ENVIRONMENT CRITERIA
R. Kennedy, US Army Transportation Engineering Agency

PROBLEMS ENCOUNTERED IN THE USE OF INSTRUMENTS FOR MEASURING DYNAMIC ENVIRONMENTS
L. J. Pursifull, US Army Transportation Engineering Agency

TRANSPORTATION ENVIRONMENTS
W. F. McCann, Lyon Aircraft Services

DYNAMIC TESTING OF MILITARY CONTAINERS VERSUS RELIABILITY
W. H. Myers and T. B. Gudis, Aeronautical Systems Division, USAF

IMPACT CONSIDERATIONS OF A NEW AIR DELIVERY SYSTEM
D. L. Griffin, Yuma Proving Ground

DESIGN OF A LIGHTWEIGHT PACKAGING SYSTEM TO SURVIVE DYNAMIC AND STATIC LOADS
K. D. Robertson, US Army Materials Research Agency

PAPERS APPEARING IN PART 5

Vibration Testing

PITFALLS IN RANDOM SIMULATION
W. C. Beecher, Lear Siegler Inc.

VIBRATION MEASUREMENTS
R. W. Mustain, Douglas Space Systems Center

FORCE-CONTROLLED VIBRATION TESTS: A STEP TOWARD THE PRACTICAL APPLICATION OF MECHANICAL IMPEDANCE
J. V. Otts, Sandia Corp.

SELECTION OF VIBRATION TEST LEVELS USING FATIGUE CRITERIA
L. W. Root, Collins Radio Company

ANALOG EXPERIMENTS COMPARE IMPROVED SWEEP RANDOM TEST WITH WIDE BAND RANDOM AND SWEEP SINE TESTS
G. Booth, MB Electronics and J. T. Broch, Bruel and Kjaer

SIMULATING MISSILE-FIRING ACOUSTICAL ENVIRONMENT BY MEANS OF EQUIVALENT MECHANICAL VIBRATION
J. H. Putukian, Raytheon Company

TEST CONTROL DEVICES—SNAP 10A VIBRATION TEST PROGRAM
E. L. Gardner and R. M. Oliva, Atomics International

TRANSMISSION OF VIBRATION TEST FORCES BY MEANS OF VISCOELASTIC LAYERS
A. J. Yorgiadis and S. Barrett, North American Aviation

FREE-FREE BENDING VIBRATION MEASUREMENTS OF THE OAO BOOST VEHICLE UTILIZING AIR BEARING SUPPORT
R. L. Turney, J. D. Jones and K. F. Koehl, General Dynamics/Astronautics

THE RESPONSE OF THE OGO SPACECRAFT STRUCTURE TO HIGH INTENSITY ACOUSTIC LOADING
P. J. Alfonsi, Goddard Space Flight Center

A LOW LEVEL VIBRATION TEST SYSTEM
R. C. Klinger and M. A. Kollodge, Honeywell Inc.

SYSTEM RESONANCE, A FUNCTION OF VIBRATION TEST PARAMETERS
A. M. Samborsky and C. J. Van Vliet, U.S. Navy Electronics Laboratory

A TEMPERATURE CONTROLLER FOR COMBINED TEMPERATURE-VIBRATION TESTS
R. E. Seely, U.S. Naval Research Laboratory

Damping

VIBRATION RESPONSE CHARACTERISTICS OF VISCOELASTIC-DAMPED STRUCTURES
J. E. Ruzicka, Barry Controls

MATERIAL DAMPING OF ALUMINUM BY A RESONANT-DWELL TECHNIQUE
N. Granick and J. E. Stern, Goddard Space Flight Center

EFFECT OF PRESSURE ENVIRONMENT ON THE DAMPING OF VIBRATING STRUCTURES
D. G. Stephens and M. A. Scavullo, Langley Research Center

DEVELOPMENT OF A HIGHLY DAMPED SUBMARINE MACHINERY FOUNDATION
E. V. Thomas, U.S. Navy Marine Engineering Laboratory

DESIGNING STRUCTURES FOR ACOUSTICAL AND VIBRATION ENVIRONMENTS
R. P. Thorn and G. E. Warnaka, Lord Manufacturing Company

Fixture Design

EQUALIZATION AND FIXTURE DESIGN
R. M. Mains, General Electric Co.

DEVELOPMENT OF A LAMINATED VIBRATION FIXTURE MATERIAL
R. L. Bergey, Burroughs Corporation

A REPORT ON THE DESIGN OF INTEGRATED HORIZONTAL AXIS VIBRATION FIXTURES
F. C. Tolleth, Autonetics

THE DESIGN OF LARGE VIBRATION FIXTURES FOR THE SATURN S-IV STAGE DESIGN DEVELOPMENT AND QUALIFICATION PROGRAM
L. G. Smith, Douglas Aircraft Company

SHAKER ATTACHMENTS FOR AEROSPACE GROUND EQUIPMENT IN PORTABLE CASES FOR VIBRATION TESTS
K. A. Jenicek, McDonnell Aircraft Corporation

DESIGN CRITERIA FOR VIBRATION FIXTURES
L. E. Lutz, Honeywell, Inc.

THE DESIGN AND UTILIZATION OF ENVIRONMENTAL TEST FIXTURES
W. S. Gorrell, Martin Company

DESIGNING TIGHT BOLTED JOINTS FOR VIBRATION ENVIRONMENT
O. J. Zamparo, MB Electronics

FIXTURE DESIGN - PANEL SESSION

Section 1
MECHANICAL IMPEDANCE

NOTES ON THE DEVELOPMENT OF MECHANICAL IMPEDANCE

C. T. Molloy - Chairman
Space Technology Laboratories

In view of the title of this session; namely, Mechanical Impedance, it seemed worthwhile to look back for a moment and to review very briefly a few of the milestones in the history of the subject.

The basic concept which underlies mechanical impedance; namely, the use of complex variables in the solution of oscillatory problems, was introduced by the French mathematician, Augustin Cauchy, whc was born in 1789 and died in 1857. It was 1885 when the English mathematical physicist, Oliver Heaviside, noted the utility of taking the ratio of the complex voltage to the complex current in electric circuits and, thus, formally defined electrical impedance. Nearly 30 years were to elapse before it was noted that a simiiar ratio to that which had proved so useful in electrical circuit theory, was also useful in acoustical and mechanical analyses. Thus, in 1914 A. G. Webster, an American and a professor at Clark University, in a classical paper on the theory of acoustic horns, formally introduced both acoustical and mechanical impedance. In the period following World War I, much use was made of this concept in the design of electromechanical transducers and transmission systems. For example, in 1923 A. E. Kennelly of Harvard published his book on electrical vibration instruments, in which will be found methods for measuring mec nical impedance, as well as many measurements of this quantity. One of the outstanding impedance successes of this period was the design of a mechanical phonograph by Maxfield and Harrison in 1926. By combining mechanical impedance, electrical analogs and electric filter theory they were able to design a phonograph that was substantially better than anything that had been built previously.

After World War II, a new type of problem came to the fore; namely, that of protecting equipment against shock and vibration. It was soon recognized that mechanical impedance played an important role in the analysis of this problem. Methods were devised for measurement of mechanical impedance of structures. However, only a limited amount of impedance data has been published. Perhaps this is due to the tediousness of point by point measurements. It appears, however, with the recent advent of automatic impedance measuring equipment, that it is reasonable to expect that a wealth of valuable information on the impedance of structures will soon become available.

We have come a long way but there is still much to do. In todays session you will hear discussions of some of the problems which are of concern to workers in the field of Mechanical Impedance.

* * *

RECENT ADVANCES IN MECHANICAL IMPEDANCE INSTRUMENTATION AND APPLICATIONS

Fred Schloss
David Taylor Model Basin
Washington, D.C.

An automatic impedance measurement system possessing a high degree of precision is described. Results of the "Round Robin" evaluation of the electronics of various mechanical impedance measurement systems and new developments of improved vibration generators for use in impedance measurements and of a miniature impedance head are presented. The impedance technique is applied to the evaluation of the dynamic properties of resilient mountings, couplings, damped structures, damping and viscoelastic material, as well as to a determination of the internal damping of materials as a function of vibratory stress, added water mass of propellers, and elastic moduli of heterogeneous materials such as Fiberglas.

AUTOMATIC IMPEDANCE MEASUREMENT SYSTEM

An automatic mechanical impedance measurement system of high precision was developed to comply with the condensed specifications given in Table 1. High phase accuracy, although not necessary for routine impedance measurement, is required to determine accurately the real component of the impedance, as will be discussed later in the applications of this technique. Precision may be obtained by careful design, paying particular attention to details without greatly increasing costs. The large dynamic range is necessary for routing measurements on structures where the ratio of maximum to minimum impedance may be as much as 150 db.

The measurement system meeting the specifications is shown in Fig. 1. This system is identical, except for the change in the intermediate frequency from 11 to 20.5 kc, to that shown in Fig. 23 of Ref. [1], where the principle of operation is discussed. The system was first conceived in 1958 and construction was begun under Navy contract in 1960. After the prototype had been built, approximately 30 modifications were made to the system to improve its performance. In the interim, other commercially available systems were developed and used, but—largely because of a lack of attention to detail or of inherent inaccuracies of the particular system—they do not meet the specifications given in Table 1, or even the specifications given by the manufacturers.

NOTE: References appear on page 14.

This present system has been used for many purposes other than impedance measurements, such as cross-correlation measurements, acoustic intensity measurements, transducer response curves, and determination of structural modal shapes.

"ROUND ROBIN" EVALUATION OF MECHANICAL IMPEDANCE MEASUREMENT SYSTEMS

To evaluate the state-of-the-art of impedance measurements, the U. S. Naval Research Laboratory in early 1963 enlisted various activities to participate in a "Round Robin" evaluation of three test structures. This evaluation of the transducer included the electronics; thereby, the transducer errors were not separated from the errors introduced by the electronics. Also, this test, due to the lack of background noise usually encountered in the field, probably does not strain the system sufficiently. Therefore, a separate electrical evaluation was initiated by the David Taylor Model Basin. Unfortunately, many activities declined to participate, mainly because of their complete trust in the electronics. Others commented, after conducting the three tests, that

TABLE 1
Condensed Specifications for
Automatic Impedance Measuring Apparatus

Property	Specification
Frequency Range	10 - 15,000 cps
Filtering	Filters tracking with audio oscillator, both channels, constant bandwidth of 5 cps or less. All filters to be temperature controlled.
Dynamic Range	80 db without switching and greater than 20 db signal/noise within the range. 140 db with switching.
Minimum Input	3×10^{6} volt
Phase Accuracy	± 0.25 degree 40 - 5,000 cps ± 1 degree 10 - 15,000 cps including high impedance preamplifiers and input attenuators.
Amplitude Accuracy	± 0.5 db
Noise Rejection	Amplitude and phase accuracy maintained for noise outside pass band which is 40 db above signal amplitude.
Noise and Hum	Less than 10×10^{-6} volt at input with capacitive source of 1000 pf and less than 3×10^{-7} volt at power frequency and harmonics.

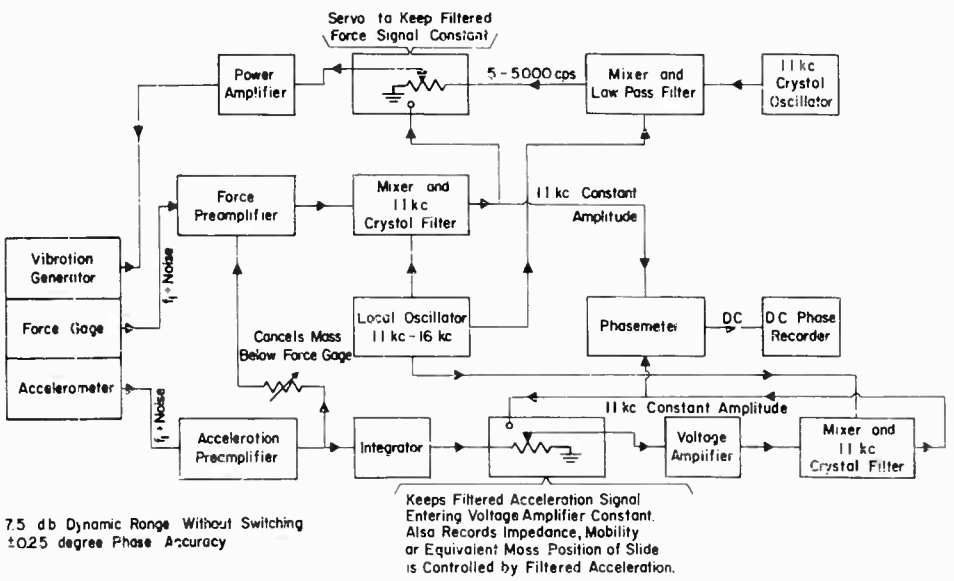

Fig. 1 - Automatic impedance, mobility or equivalent mass plotter (under construction)

this electrical evaluation helped them to realize the limitation of their equipment.

A sealed "black box" (Fig. 2) was constructed and evaluated by six activities using eight different systems, including all those presently available commercially. In test 1, pure sinusoidal signals were used; in tests 2 and 3, random and discrete frequency signals were added to one channel. Although tests 2 and 3 may appear to be quite severe, such conditions are not unusual in practice. The dynamic range of tests on the black box was less than 55 db, which is less than that of "live" structures. Results of the evaluations are presented in Table 2. Data taken by activity F1 were used as reference. The manual system with digital outputs was precisely adjusted for phase and amplitude for each measurement; it has a short-time accuracy of better than 0.2 db in amplitude and 0.1 degree in phase. This system is shown in Fig. 3.

Results of these three tests led to the following conclusions:

1. Four systems, including one automatic system, had a relatively high degree of accuracy and the results had a spread of less than 5 degrees and 1 db.

2. Surprisingly, the very expensive systems were inaccurate even in tests using pure signals of as much as 27 degrees and 4.4 db.

3. Maximum errors were 30 degrees and 23.5 db.

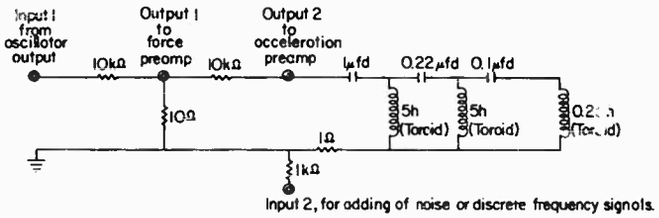

Test 1. Volt input 1 from 10—5,000cps plot amplitude ratio and phase between the two outputs.

Test 2. Repeat test 1 with 1 volt of random noise into input 2.

Test 3. Repeat test 1 with 5volts of a fixed frequency signal of 80cps into input 2.

Fig. 2 - "Black box" for electrical evaluation of mechanical impedance instrumentation

TABLE 2
Results of the "Round Robin" Evaluation of the Black Box

Activity	Type of System	Relative Cost	Max Error, Pure Signal		Max Error, with Noise	
			Phase (degree)	Amplitude (db)	Phase (degree)	Amplitude (db)
A	Heterodyne, automatic	Very high	- 25	- 4.4	- 19	- 23.5
B	Heterodyne, automatic	Very high	+ 27	+ 3.6	+ 30	+ 3.9
C	Homodyne, automatic	Very high	- 10	+ 1.1	+ 20	+ 1.0
D	Audio, automatic	Medium	+ 3.3	- 0.4	+ 6.2	- 0.6
E	Nulling, manual	Low	- 1.9	<0.2	- 2.0	< 0.3
F1	Heterodyne, automatic	High	+ 0.4	+ 0.5	+ 0.5	+ 0.5
F2	Heterodyne, manual	Medium	< 0.1	<0.2	< 0.1	< 0.2
F3	Nulling, manual	Low	+ 2.8	<0.2	+ 2.7	< 0.2

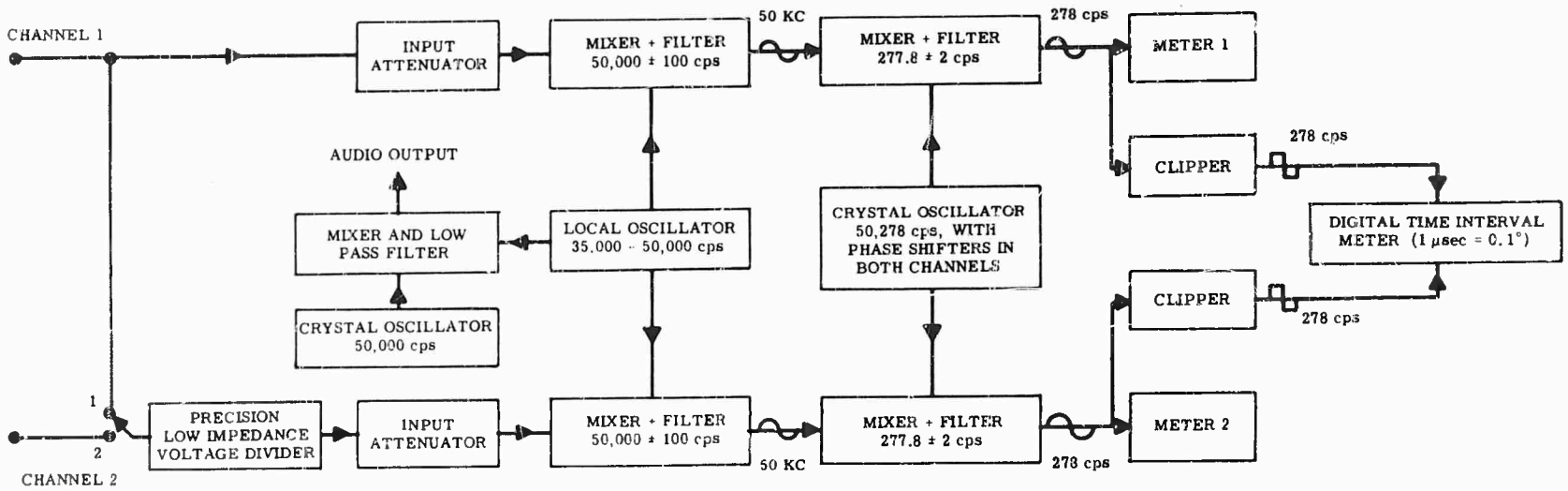

STEP 1: Insert larger of the two signals into Channel 1.

STEP 2: With switch in Position 2 and precision attenuator set at 0 attenuation, adjust input attenuators so that both meters read on scale and note reading of Meter 2.

STEP 3: With switch in Position 1 adjust precision attenuator only to obtain same reading as in Step 2 on Meter 2. Attenuator setting is indication of ratio of input signals. Adjust phase shifter for zero digital output.

STEP 4: Use same settings as in Step 2 and read phase from digital output.

Fig. 3 - Manual precision phase and ratio measuring system

It is felt that the inherent accuracy of Systems A, B, and C is greater than the results show and that, with minor modifications, the precision could be greatly improved. Other sources of phase errors, such as those introduced by changes of attenuation at the preamplifiers, were not evaluated by these tests.

NEW DEVELOPMENTS IN MECHANICAL IMPEDANCE INSTRUMENTATION

Vibration Generators

Whenever rotational impedance is low compared to lineal impedance, results are somewhat inconsistent when measurements are made with various types of impedance heads and vibration generators. The inconsistencies were wrongly attributed to a high degree of rotational or transverse sensitivity of the transducer; actually they are caused solely by changes of the rotational inertia of the transducer and driver system. This phenomenon was first observed when driving point impedance measurements were made on the end of a cantilever [1].

It is often a moot question as to which measurements are of value. For example, if a machine is to be mounted solidly to a structure, driving point impedance measurements made on the feet of the unmounted machine without the same rotational restraint as that of the structure are of little value. Similarly, if the machine is to be mounted on vibration isolators, the effects of the mounting plate must be taken into account.

To improve the measuring system, it became necessary to reduce its rotational inertia by decoupling the transducer and driver. One solution under development by the U.S. Navy Marine Engineering Laboratories involves the use of magnetic drivers and very light transducers. This solution, although best for very light structures, has the disadvantage of requiring critical alignment for the relatively low output magnetic drivers. Rather than using this approach, new electromagnetic drivers (needed also for rotational impedance measurements) were developed. Most of the mass of these drivers (Figs. 4, 5, and 6) is dynamically decoupled in all modes from the test structure above about 40 cps by having the relatively heavy annular magnet assembly supported by two rubber diaphragms. In addition, the annular arrangement and the rubber diaphragms provide a very low center of gravity of the assembly and also assure freedom from spurious effects such as rocking and high-frequency resonances in the suspension system. The added dynamic weight of the smaller vibration generator with a force output of 0.7 pound is less than 0.1 pound. The force output of the larger of the drivers is 5 pounds.

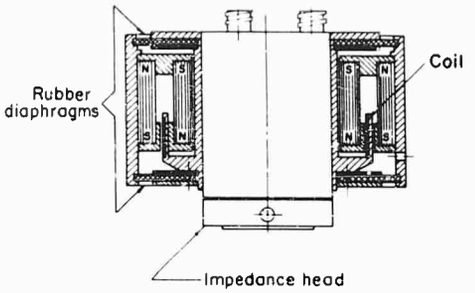

Fig. 4 - "Wrap-around" vibration generator

Fig. 5 - Electromagnetic driver

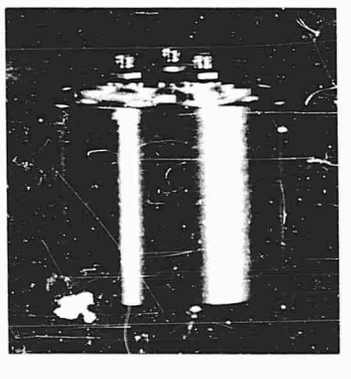

Fig. 6 - Electromagnetic driver

New Miniature Impedance Head

A miniature impedance head and driver was developed for measurements on very light structures, such as a 1/30-scale model of a submarine propeller (Fig. 7). With this head, 1/2 inch diameter and 1/2 inch long, an impedance equivalent to a weight of 0.0001 pound may be measured from 20 to 10,000 cps. The stiffness is 500,000 pounds per inch, which limits the maximum impedance that may be determined with this transducer. However, the stiffness of light structures is usually well below this value. The effective stiffness of the head may be increased to over 1,500,000 pounds per inch by reversing the specimen and driver attachment points, but the weight below the force gage is increased by a factor of six to 0.01 pound, thus increasing the minimum measurable impedance.

The miniature vibration generator weighing 0.2 pound has a force output of 0.15 pound.

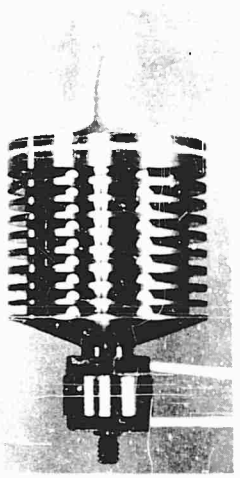

Fig. 7 - New miniature impedance head

Comments Regarding Effects of Attachments to Impedance Head On Impedance Measurements

It is hoped that the following discussion will clarify a common misconception in mechanical impedance measurements. The following question is often asked: Does the relatively heavy mass of the vibration generators directly attached to the impedance heads change the resonances and, therefore, should only relatively light shakers and impedance heads be used in order not to change the characteristics of the structure? The answer to the first part of this question is yes, the answer to the second part is no. This apparent paradox may be resolved by treating the problem in terms of impedances (the quantity measured) rather than in terms of resonances.

Fig. 8 - Spring-mass system

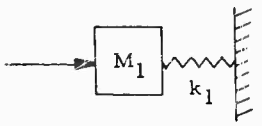

In the familiar spring-mass system (Fig. 8), resonance occurs at a frequency, $\omega_1 = (k_1/M_1)^{1/2}$, the same frequency at which a minimum occurs in the impedance. When an impedance head is attached to the mass, M_1, as shown in Fig. 9, M_a represents the mass below the force gage in the impedance head which includes the accelerometer mass (only frequencies below the resonant frequency of the accelerometer are considered here), k_2 represents the stiffness of the force gage (only frequencies below the standing wave frequencies in the force gage are considered), and M_2 represents the mass of the impedance head housing plus any other mass attached to it, such as rods and armatures of shakers or stators of reaction-type shakers. The two natural frequencies of this new system are different from the natural frequency of the system shown in Fig. 8. Yet the minimum in the impedance occurs at $\omega_2 = (k_1/M_1 + M_a)^{1/2}$, the same frequency as the natural frequency of the first system, except for the effect of M_a. Therefore, it is only M_a, the mass below the force gage, which changes the impedance measurements from the true impedance.

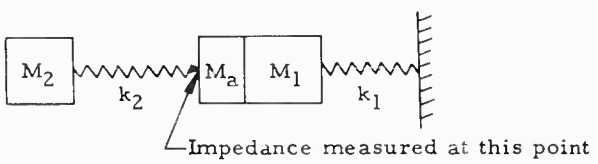

Fig. 9 - Spring-mass system with attached impedance head

The mass below the force gage may easily be subtracted electronically in the actual measurements by adding, 180 degrees out of phase (subtracting), a certain portion of the acceleration signal to the force signal, with adjustments being made when driving a zero impedance (no attachments to the specimen end of the impedance head). A 20-db cancellation is easily accomplished over the entire useful frequency

range of the impedance head, although much higher cancellations have been obtained by compensating electrically for the increase in response with frequency of the accelerometer.

If the motion transducer is attached to the wrong side of the force gage, the measured impedance will include the effect of the stiffness of the force gage, thus leading to large errors whenever the impedance of the specimen is of the same order of magnitude or higher than the impedance of the force gage, jk_2/ω.

In general, the masses M_1 and M_2 in Fig. 9 may be replaced by any two impedances for the true impedance to be affected in the measurements only by the mass below the force gage. This may be explained in another way by considering a transmissibility test on a mounting system. In the usual arrangement, a motion transducer is placed above and below the mount, and the transmissibility is the ratio of the two with the system placed on a shaker. If any other structure is placed between the shaker and the system under test, the transmissibility does not change if there is linearity in the system, although the magnitudes of the motions and total system resonances will change considerably.

In this discussion, it is assumed that the static load attached to the specimen does not exceed its elastic limit and that the contact area of the impedance head is sufficiently small to prevent stiffening of the specimen. Further, it is assumed that the rotational impedance is high compared to the axial driving point impedance. When the rotational impedance is low, such as at the end of a cantilever or at any unsymmetrical point on a structure, the total inertia of the impedance head and driver about the point of attachment affects the results. For example, the low-frequency stiffness of a cantilever of length b is $3EI/b^3$, where E is the Young's modulus and I the moment of inertia of the cantilever. If the end of the cantilever is restrained from rotating freely, such as by attaching a large inertia to its end, the low-frequency stiffness will approach the stiffness with axial restraint, or $12\ EI/b^3$. In this case the weight and, therefore, the inertia of the impedance head and attachments to shakers affect results due to changes in boundary conditions. To alleviate this problem, the new drivers (Figs. 4, 5, and 6) have been developed.

APPLICATIONS OF MECHANICAL IMPEDANCE TECHNIQUES

Dynamic Properties of Resilient Mountings

When considering the transmission of vibration through resilient mountings (or, more generally, through any isolator such as flexible shaft couplings), it is necessary to know certain characteristics as a function of frequency. Heretofore, the characteristic commonly named "transmissibility" was usually determined and reported. Transmissibility is the ratio of the blocked force on one end of the mounting to the force acting on the mass load (equal usually to the rated load) on the other end of the mounting; it is also equal to the ratio of the motion of the mass load at one end of the mounting to the applied motion at the other end. In either case, the transmissibility is a function of the mass load and, therefore, characterizes the system and not the mounting. It is difficult to make these transmissibility measurements under large rated loads—for Navy mountings up to 10,000 pounds—since these large loads cannot be regarded as lumped masses over the frequency range of interest, and the design of these loads affects the measurements.

A mounting may be represented as a mechanical black box with two accessible points. If the motion or force of each accessible point is restricted so that it can be described by a single space variable, then the mechanical behavior of the black box when connected to any system, including the conventional transmissibility, can be determined completely, provided three impedances measured at the two terminals of the box are known. It seemed most convenient to determine the following impedances:

1. Driving point impedance of end A with end B blocked.

2. Driving point impedance of end B with end A blocked (similar to condition 1 except for differences in plate weights).

3. Transfer impedance with one end blocked.

Except for wave effects, conditions 1 and 2 are impedances of a simple damped mass-spring system with the mass of the mounting plate,

compliance, and resistance of the resilient element. These driving point impedances are shown for an actual rubber mounting in Fig. 10. Wave effects at about 200 and 450 cps are masked in the impedance magnitude curve by the relatively large driving point impedance of the metal plates of the mount and they can only be detected from the more sensitive phase measurements.

Figure 11 shows the transfer impedance measurements under two different static loads. Essentially, this is a measure of the complex dynamic stiffness of the mounting, and with precision phase measurements the loss factor may be determined very easily over a wide range of frequencies [2]. The measuring apparatus is shown in Fig. 12, and the static load is applied by a Universal tension and compression testing machine. Mountings with rated loads up to 10,000 pounds have been evaluated up to 5000 cps by this technique. The acoustic decoupling properties of special coatings have also been evaluated by this method.

Dynamic Properties of
Damped Structures and Materials

A new technique was developed for measuring the loss factor of materials and systems continuously from 10 to 2000 cps or higher. By the use of this method [2], accuracy is increased with increased damping and, therefore, this method complements other methods that are usually used to determine damping properties at system resonances and are more accurate for low values of damping. High damping materials are playing a growing role in the defense effort.

By using essentially the same blocked transfer impedance technique described previously, the loss factor is equal in magnitude to the cotangent of the impedance phase angle or the ratio of the real to the imaginary component of the impedance, provided the frequency is low compared to the frequency of the first standing wave in the specimen. The loss factor is defined as $\omega R/k$, where R and k are the

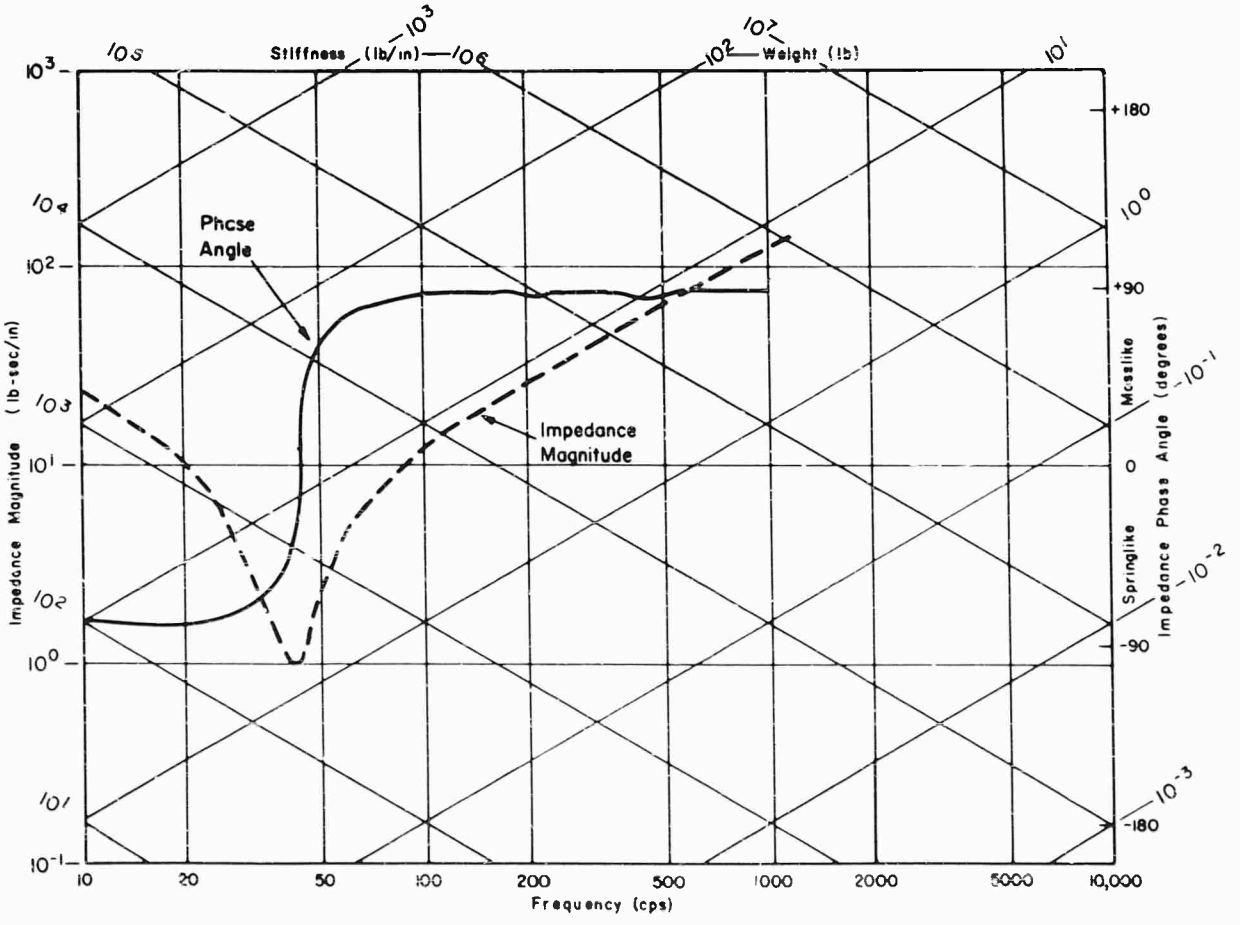

Fig. 10 - Driving point impedances for rubber mounting

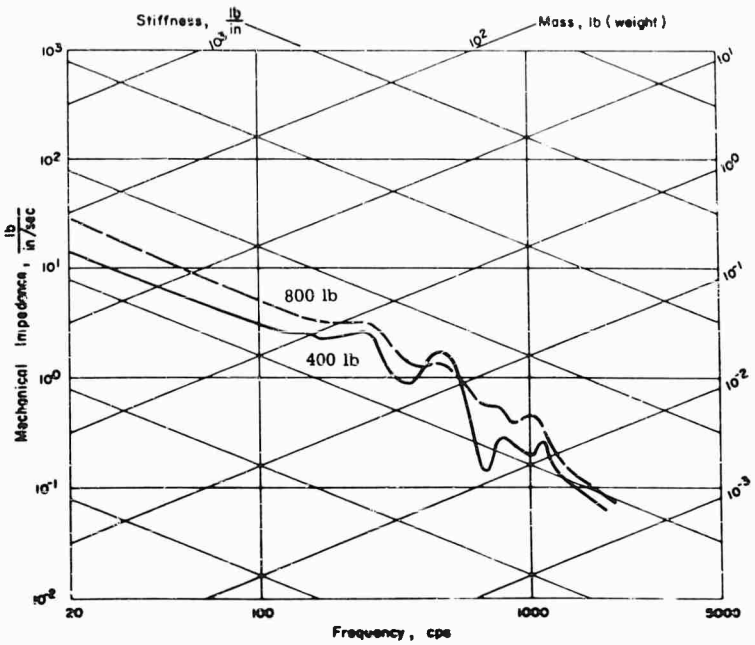

Fig. 11 - Transfer impedance of 6E900
(400- and 800-pound compression)

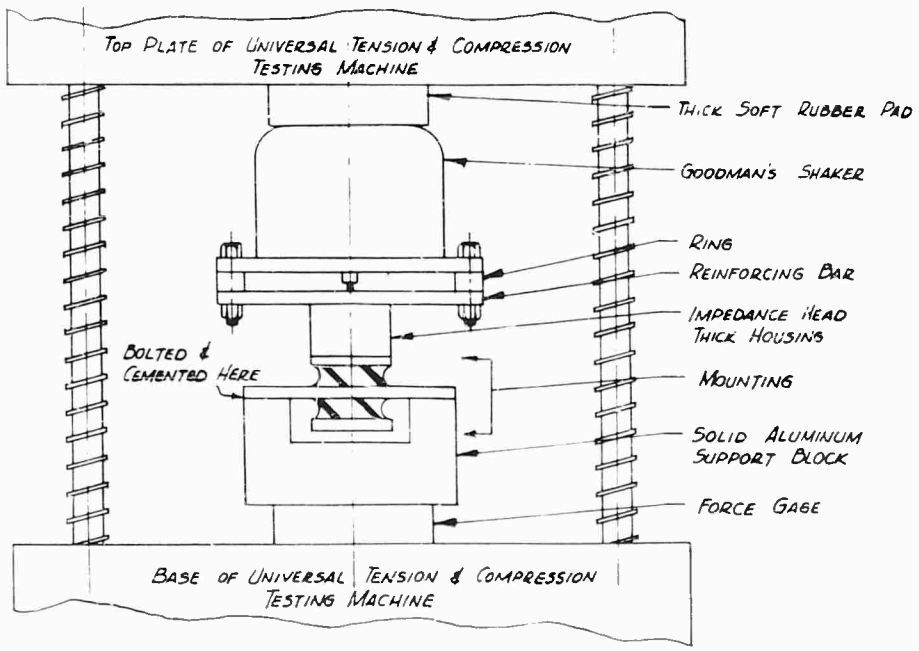

Fig. 12 - Mount transfer impedance measuring apparatus

resistance and stiffness of the system, respectively, and is equal to the reciprocal of the quality factor Q and 0.02 of the percentage of critical damping.

A high degree of phase precision is required in the instrumentation since, for example, a phase inaccuracy of 1 degree for a material having a loss factor of 0.1 is equivalent to a 17.5 percent error. The apparatus is shown in Fig. 13. A laminated beam blocked at the ends in the vertical direction and hinged to allow rotation is driven in the center. The transfer measurement is made between the force at the end and the motion in the center.

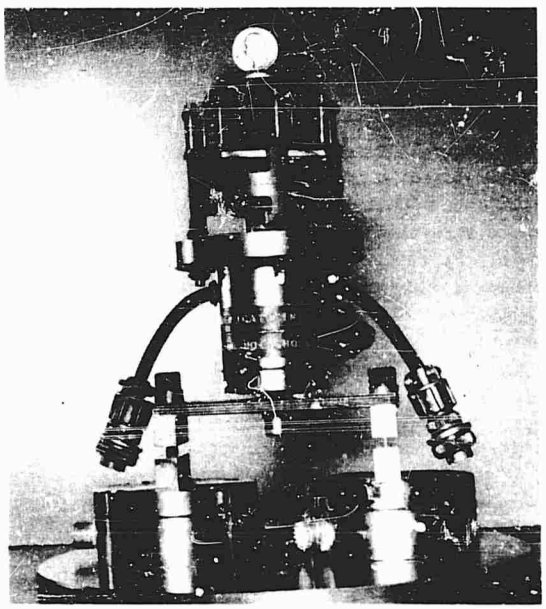

Fig. 13 - Apparatus for loss factor measurement

Dynamic Properties of Viscoelastic Materials

The blocked transfer technique can also be applied to plot loss factor continuously, and the real and imaginary moduli of viscoelastic materials such as solid fuels for missiles or mounting materials. The apparatus for the determination of Young's modulus is shown in Fig. 14. Sixty columns of viscoelastic material, 1/8 in. high and 1/32 in. in diameter, are bonded at each end to two plates, 1/2 in. in diameter. Since these materials have a low longitudinal bar velocity of sound, the height of the columns must be relatively short to increase the upper limit of the usable frequency range.

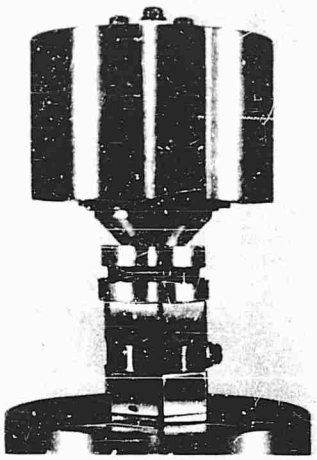

Fig. 14 - Apparatus for determination of Young's modulus

The diameter of each column must be small compared to the height to assure that the data are a true measure of Young's modulus. Many columns are used to provide mechanical stability and to prevent buckling. The apparatus may be inverted so that the columns are statically in tension, and the tension may be adjusted. Similarly, the bulk or shear properties may be evaluated by placing a thin layer of viscoelastic material either between two plates or between two concentric cylinders, respectively.

Fundamental Resonant Frequency of Propellers and Added Water Masses

Impedance techniques have been used to determine resonant frequencies of structures without loading the structure or changing the damping of the structure by placing the impedance head at a node; they have also been used conveniently for dynamic weighing.

Figure 15 shows the apparatus with which impedance measurements are made to determine the fundamental resonant frequency of full-scale submarine propeller models. The propeller is driven at its hub through a long rod to eliminate the need for waterproofing the transducer. The first antiresonant frequency (maximum in impedance) is measured in air and water. From these measurements, the added water mass at resonance and the resonance of full-scale propellers may be calculated even though the model propellers are made of a different material.

Viscous effects may also be determined by precision phase measurements. The heavy

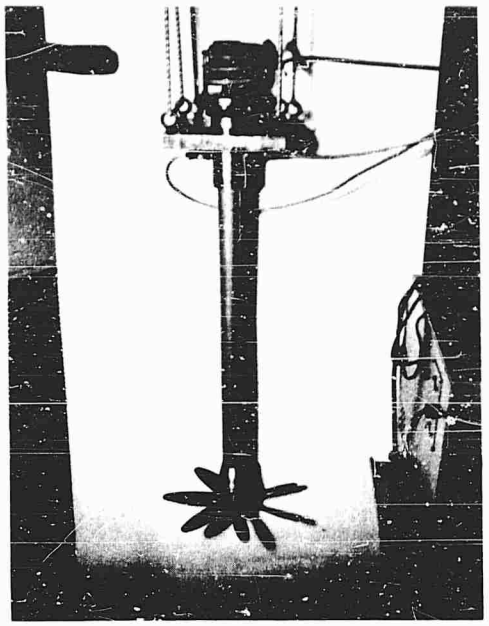

Fig. 15 - Impedance measuring apparatus for determination of fundamental frequency of submarine propellers

plate at the top of the impedance head above the force transducer is used to prevent rotation of the propeller in the water since the resonant frequencies of propellers are dependent on rotational restraint. This impedance measuring apparatus was also used as a convenient dynamic weighing device to obtain the added fluid mass of rigid bodies moving in fluids.

Measurement of Internal Damping Characteristics of Metals

In most of the theoretical impedance studies, linear behavior of structures is assumed, which was partially verified by measurements on submarines under relatively small vibratory stress levels. Yet it is known that under high stress levels, the internal damping of metals is not independent of the amplitude of vibration. Therefore, experiments were conducted to determine the internal damping characteristics of metals as a function of vibratory stress. Since there is very little internal damping in metals, no additional damping must be introduced by vibrating transducer cables and friction at the points of attachment. A double cantilever beam machined from one piece was driven in the middle through an impedance head at its first antiresonance (Fig. 16). The middle portion, a node at that frequency, was thickened to further reduce frictional effects. The damping properties may be calculated from the impedance magnitude or the shape of the impedance curve at the antiresonance. Results are shown in Fig. 17 for an aluminum, steel, and stainless steel bar as a function of the outer fiber stress.

Other Applications

A technique similar to that preceding, namely determining the impedance at a node, was used to obtain the Young's modulus of elasticity of heterogeneous materials such as Fiberglas in the various directions. With this

Fig. 16 - Apparatus for measuring internal damping characteristics of metals

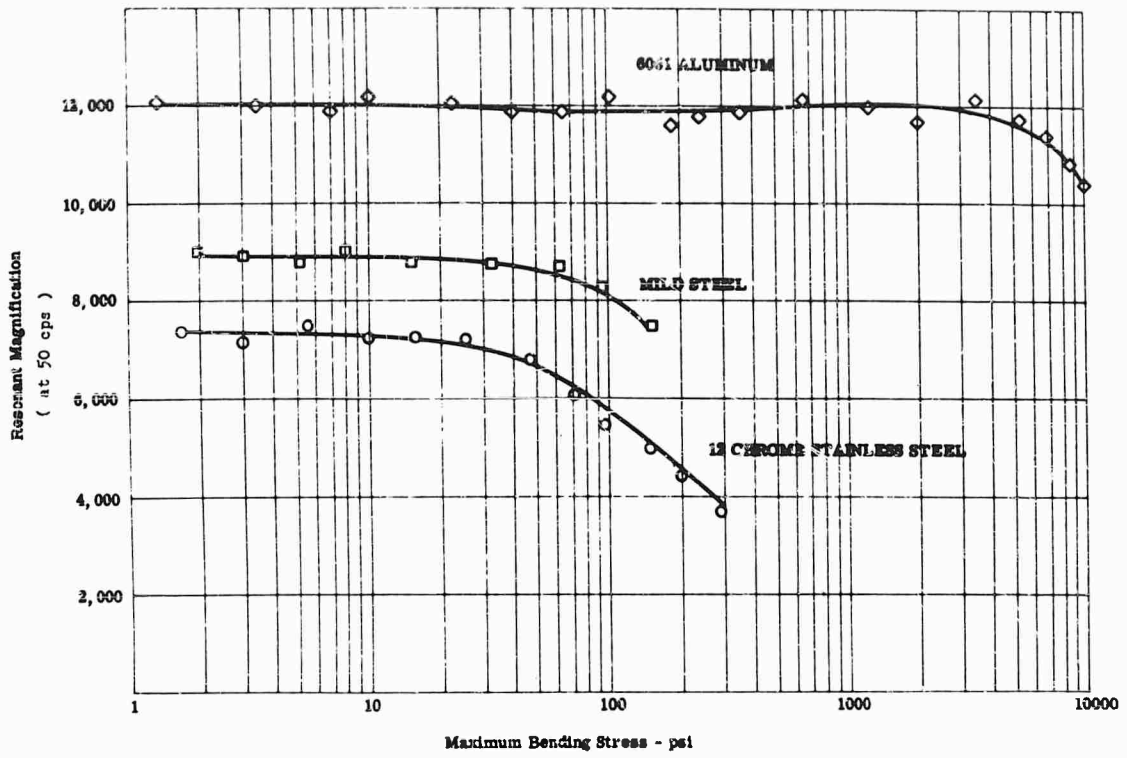

Fig. 17 - Resonant magnification of various materials vs stress levels

method, time and cost savings of over 80 percent were attained over more conventional static methods in which strain gages are employed.

The feasibility of using impedance techniques to quiet singing propellers is presently under study.

REFERENCES

1. F. Schloss, "Recent Advances in the Measurement of Structural Impedance," DTMB Report 1584 (Jan. 1963); SAE Paper 426B (Oct. 1961).

2. F. Schloss, "New Methods for Determining the Loss Factor of Materials and Systems," DTMB Report 1702 (April 1963).

* * *

MECHANICAL IMPEDANCE OF SPACECRAFT STRUCTURES*

C. C. Osgood
RCA-Astro Electronics Division
Princeton, New Jersey

The concept of mechanical impedance is discussed with reference to the response of a very non-rigid body to variable frequency force input. The transition of the action from that of a mass to that of a spring as a function of frequency is portrayed by plots of experimental data. The relationship of damping and frequency is also treated. Determination of the lowest natural frequency, and of the first few harmonics is explained.

Comparisons are formed of the responses of structures of the same material and mode of fabrication (riveted aluminum) but of different geometry, i.e., circular ribbed plates vs trusses in a cruciform configuration. A second comparison is made of structures of similar fabrication and geometry, ribbed plates, but of different size and total weight. The plots of driving point impedance are analyzed as to the significance of their general shape, number of loops, number and location of the crossings of the real axis, etc. A calculation scheme is established for the determination of effective loading as a function of frequency, the objective being to evaluate the capacity of a given vibration machine to provide a specified input force at a required frequency to a particular structure.

A description of the mechanical impedance test instrumentation and operation is given including a diagram of the test setup.

The conclusion is reached that the mechanical impedance test is, in general, a most illuminating means of examining the response of a spacecraft structure to variable frequency inputs; is, in particular, a most feasible method of determining the lowest natural frequency and is the only method of finding the effective loading as a function of frequency.

The response of any part of a vibrating system depends on mass, stiffness, and their respective distributions; on damping, and on input frequency. Changes in response due to changes in these parameters with frequency are described by the concept of mechanical impedance. The response may be defined in terms of displacement, velocity or acceleration, but a usual definition of mechanical impedance is the ratio of applied force to velocity, lb/in./sec or lb-sec/in.

The inverse of impedance is called "mobility" and is expressed mathematically by a reciprocal relationship. Some caution, however, is needed in applying the relationship, dependent on the type of connections among the elements: series, parallel or combinations. As a matter of preference, this discussion is based on impedance and is concerned chiefly with "driving point impedance" — the force and velocity being taken at the same (driving or excitation) point — as contrasted to "transfer impedance" — the force being taken at one point within the body and the velocity at another. The term "loading" is generally used to discuss the apparent change in weight of a vibrating body due to change in frequency.

*Extracted in part from "Spacecraft Structures," by Carl C. Osgood, copyrighted and to be published by Prentice-Hall, 1965.

A body exhibiting high impedance brings to mind massiveness, stiffness, and small motion; conversely, low impedance suggests lightness, springiness and large motion. Such qualitative statements are, however, apt to be misleading; the correct view may be formed only by consideration of the quantitative relationship with frequency. A resistive impedance implies that input energy is absorbed and dissipated as in a damper, whereas a reactive impedance indicates energy storage as in a spring. As the frequency with which the energy is impressed changes, there is a change of both magnitude and phase of the motion. The resistive and reactive components of impedance are complex functions of frequency and they tend to alternate in their dominance of the system response. It is this latter action which leads to the apparent change of weight, the system responding alternately as a mass or as a spring as the frequency is varied through the resonances and antiresonances. This type of response leads in turn to a great change in the degree of isolation for the components within the system and is, therefore, of importance to the structural designer.

FREQUENCY RELATIONSHIPS

A general expression for velocity impedance is found by forming the ratio of force to velocity, both defined at excitation or driving point. From $F = ma$ it can be shown that

$$F = \left[\frac{\left(1 - \frac{j\omega}{\omega_o Q}\right) m A_o}{1 - \frac{\omega^2}{\omega_o^2} + \frac{j\omega}{\omega_o Q}} \right] e^{j\omega t}, \qquad (1)$$

where

$$Q = \frac{\omega_o m}{c} = \frac{k_o}{\omega_o c}.$$

Integration of the acceleration

$$a_o = A_o e^{j\omega t} \qquad (2)$$

yields the velocity

$$V = \frac{A}{j\omega} e^{j\omega t} \qquad (3)$$

After some manipulation, the impedance Z becomes

$$Z = \frac{F}{V} = \omega m \frac{\frac{\omega}{\omega_o^3 Q}}{\left(1 - \frac{\omega^2}{\omega_o^2}\right)^2 - \frac{\omega^2}{\omega_o^2 Q}} + j\omega m \frac{1 - \frac{\omega^2}{\omega_o^2} + \frac{\omega^2}{\omega_o^2 Q}}{\left(1 - \frac{\omega^2}{\omega_o^2}\right)^2 - \frac{\omega^2}{\omega_o^2 Q}}. \qquad (4)$$

An examination of the effect on impedance of changing frequency indicates that at zero frequency, Eq. (4) reduces to zero, the mass offering no resistance to a steady velocity. At small frequencies

$$Z = j\omega m. \qquad (5)$$

Here the velocity acts directly on the mass, the spring being rigid. This reactive impedance is small enough that small velocity will produce relatively large motion. The velocity is proportional to impressed force, lagging it by $\pi/2$, and is inversely proportional to frequency. As frequency increases, the first term of Eq. (4) increases and the second term decreases, becoming zero just above resonance. The impedance at resonance may be approximated by setting $\omega = \omega_o$ and evaluating the first term, which yields

$$Z = m\omega_o Q = m^2\omega^2/c. \qquad (6)$$

This result is not surprising for, at resonance, all input energy is absorbed or dissipated by the damping; otherwise, the amplitude goes to infinity. The impedance is all resistive and equal to Q times the impedance value of the rigid spring. At resonance, the mass will dynamically load the system very sharply and the motion (displacement) of the driving point will tend to zero.

With further increase in frequency, both terms decrease; the second term goes through a temporary dominance, indicating a simple spring action with the mass nearly stationary and the motion leading the force. In a still higher range of frequency

$$Z = m\omega_o/Q = c, \qquad (7)$$

indicating a resistive type of impedance again with a motionless mass, the spring action being

zero and the system response typified by a damper. The difference in the conditions described by Eqs. (6) and (7) is that at resonance the macroscopic spring displacement is not zero; in fact, it is tending to infinity, being restrained by material damping. The mass tends to act as a rigid body on the spring. At the extremely high frequencies postulated for Eq. (7), the macroscopic spring displacement is zero and all input energy is dissipated by dilatational waves in the material. In the frequency range from zero to resonance, the system response is that of a damped mass, while for the range between the conditions of Eqs. (6) and (7) it is that of a damped spring.

Physical systems may be described adequately for the treatment of mechanical impedance by considering them as linear assemblies of elements with lumped constants. Only three types of elements are needed to describe completely a mechanical or structural system:

1. The "ideal spring" is defined as an element whose major characteristic is that the relative displacement between its ends is linearly proportional to the applied force, $F = kx$, where k is the stiffness. For a sinusoidal force, the displacement is in phase with the force

$$x = x_o e^{j\omega t}.$$

The relative velocity of the ends is the time derivative of x

$$V = \dot{x} = jx_o e^{j\omega t},$$

and the spring impedance is the F/V ratio, expressed finally as

$$Z_k = k/j\omega, \qquad (8)$$

an imaginary quantity dependent on the stiffness, k, and the frequency. For the spring, the velocity leads the applied force by 90 degrees.

2. The "ideal damper," or mechanical resistance, is an element such that the relative velocity between its end points is proportional to the applied force, $F = Vc$, where c is the damping constant. On application of a sinusoidal force,

$$V = F_o e^{j\omega t}/c = V_o e^{j\omega t}$$

and

$$Z_c = \frac{F}{V} = \frac{F_o e^{j\omega t}}{F_o e^{j\omega t}/c} = c; \qquad (9)$$

thus, the mechanical impedance of a resistance is exactly the value of its damping constant. The force and velocity vectors are in phase.

3. The impedance of the "ideal mass" is derived by assuming a system wherein one end of the mass is rigidly attached to an inertial reference and the other end is free to move. On application of a sinusoidal force, the acceleration becomes

$$\ddot{x} = F_o e^{j\omega t}/m,$$

and the velocity is

$$\dot{x} = -jV_o e^{j\omega t};$$

the ratio of force to velocity is then

$$Z_m = j\omega m. \qquad (10)$$

an imaginary quantity dependent on the magnitude of mass and frequency. The acceleration is in phase with the force, the velocity lags the force by 90 degrees, and the velocity is absolute, not relative as for the spring and damper. The general variation with frequency of the impedance of these elements is shown in Fig. 1.

Assembly of these elements into systems is made by various arrangements of series and parallel connections. The expressions for the impedance of a system depend on the particular

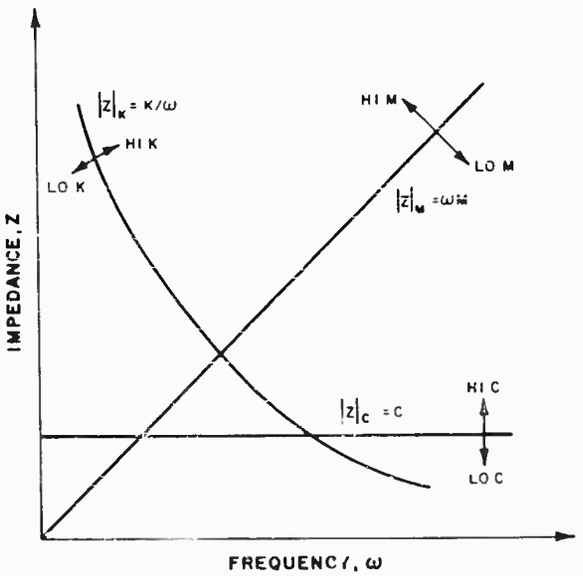

Fig. 1 - Impedance plots of ideal elements

combination of connections involved, and are typically for series connections,

$$Z = \frac{1/c - j(\omega/k - 1/m\omega)}{(1/c)^2 + (\omega/k - 1/m\omega)^2} , \qquad (11)$$

and for parallel connections,

$$Z = c + j(m\omega - k/\omega) . \qquad (12)$$

For a system where spring and damper are in parallel connection, and the mass in series with both

$$Z = \frac{m\omega\left\{m\omega c + j\left[c^2 - k/\omega(m\omega - k/\omega)\right]\right\}}{c^2 + (m\omega - k/\omega)^2} . \qquad (13)$$

Actual spacecraft structures (with their loads) exhibit extremely complex behavior under forced vibration, but in general, their response more nearly resembles that of a series or a combined system than that of a simple parallel one. The plotting of impedance in the complex plane, as in Figs. 2, 3 and 4, is of considerable help in interpreting the response of the structure. These plots are response loci, not root loci, despite the graphic resemblance. They exist only to the right of the imaginary axis, along the positive real axis, indicating that such damping as is present is positive and, thus, that the system is conservative. Further reading shows that, as expected, energy dissipation is by the real component only while energy storage is by both imaginary components. Resonances are shown by either of two conditions: (a) frequency at the crossings of the real axis, or (b) in the case of the circles and loops characteristic of series-connected elements, the mid-frequency of the maximum angular increment between frequency points (equal frequency increments being assumed). This latter condition obtains because the rate of change of the phase angle assumes maximum values in this frequency region and, at a resonance, the sign of the imaginary part of the impedance changes. For the ideal linear system with any degree of damping, the two points on the locus coincide.

A complete treatment of the impedance-frequency relationships must include consideration of the three different frequencies related to the resonance region of a system under forced vibration. With no damping, the natural frequency, $\omega_n = (k/m)^{1/2}$, is associated with the familiar open peak at $\omega_n/\omega = 1$ on the conventional plots of transmissibility vs frequency ratio. With significant damping, the natural frequency

$$\omega_{nd} = \left[k/m - (c/2m)^2\right]^{1/2} ,$$

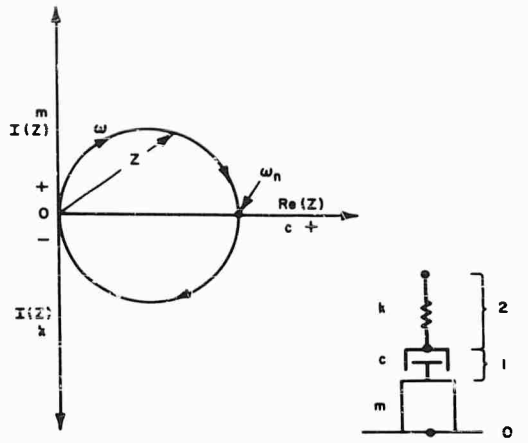

Fig. 2 - Impedance plots of series-connected elements

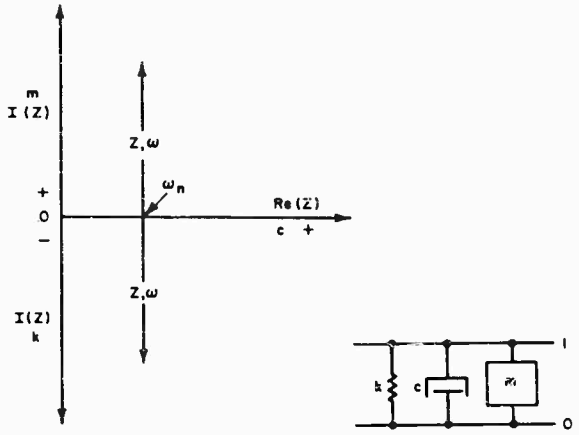

Fig. 3 - Impedance plots of parallel-connected elements

is the row of now closed, lower peaks at values of $\omega_n/\omega < 1$. Then there is the theoretical "frequency of maximum response amplitude," known as the "resonant" frequency, which is very close to ω_{nd} in value. The significant point here is that for systems with any degree of damping ($0 < c < c_c$), the change of phase angle occurs at the same frequency, which is the value of ω in $\omega_n/\omega = 1$, and not at the frequency of the transmissibility peak. Condition 2 above is also to be expanded to mean that the rate of change of impedance with frequency is zero at ω_{nd}, the damped natural frequency, i.e.,

$$[dZ/d\omega]_{\omega_{nd}} = 0 .$$

Although the rate of change of the phase angle is maximum in this region, the plot of ϕ vs ω

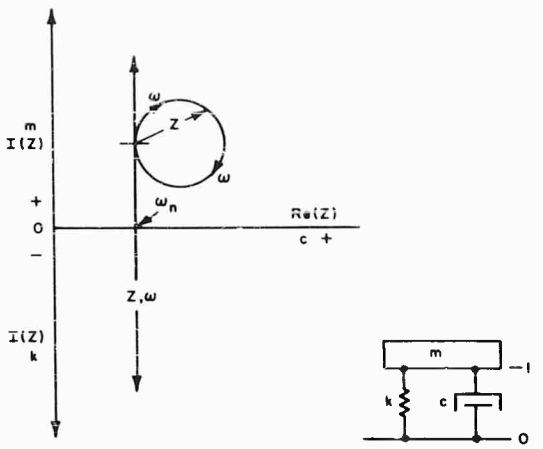

Fig. 4 - Impedance plots of series-parallel connected elements

for damped systems goes through the 90 degree point only at ω_n. The effect of increasing the damping is thus seen to be a reduction in transmissibility and in the natural frequency. The values $dZ/d\omega = 0$ and $d\alpha/d\omega = \max$, (α is the angle between the Z-vector and the real axis) occur coincidentally with the intersection of the locus and real axis only for ideal systems. The loci from many impedance tests show non-normal intersections with the real axis, thus condition 2 is not only the more accurate, but the basically correct manner of determining the popularly known "resonant" frequency, actually ω_{nd}.

As an example of impedance analysis and plotting, the Relay spacecraft (Fig. 5) is used. This structure was of four riveted aluminum trusses in a cruciform arrangement, with the components shear mounted as discrete loads. A plot of the data taken at the driving point, near the separation plane in this case, is shown in Fig. 6.

The major loop has a first crossing of the real axis at 102 cps; the sharpness of the resonance is indicated by the large angular increment of the Z-vector. The accuracy of the instrumentation was insufficient to provide any information on possible deviation of the maximum angular increment from coincidence with the real-axis crossing. In the absence of such information it may be assumed that the behavior is close to that of a series-connected system. Following the locus to higher frequencies, smaller loops are noted, with real-axis crossings of 120, 130, 140 and 150 cps, all nonharmonic multiples of 102 cps. These loops are taken to represent action of sybsystems (local

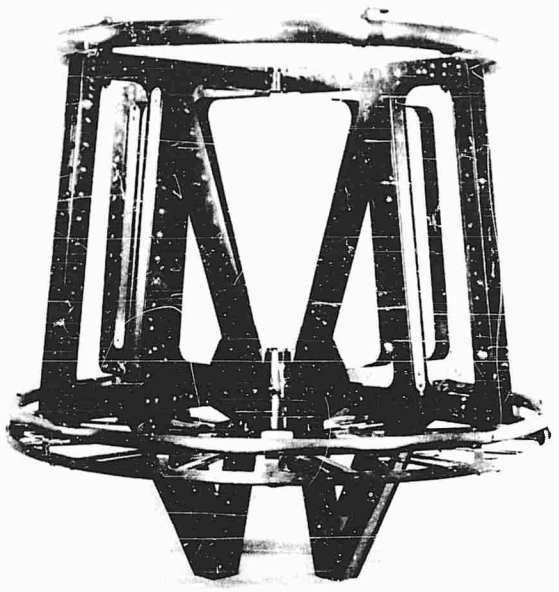

Fig. 5 - Photo of Relay spacecraft structure

spring-mass dampers) resonating by themselves. The loop at 175 cps is markedly offset from the origin, indicating the behavior of series-parallel connections. The loop with real-axis crossings of 198 and 205 cps is of particular note for it includes resonance of a subsystem at the first harmonic of the overall system. Such combination action would drive the subsystem very hard and would increase both its input levels and amplification factors. While the system shows other coincident resonances, as at 300 and 600 cps, the inputs are sufficiently lower to relieve the potential hazard of reinforcement of vibration among the parts of the system. When such coincidences occur at fundamentals or at first harmonics, adjustment of the subsystem resonance by altering the support stiffness and/or damping is indicated as a means of detuning. Identification of the offending subsystem can be made from the frequencies found during the general vibration survey, or from a frequency survey of the subsystem as a single item in a separate test.

A major benefit derived from impedance measurements is data with which to calculate the effective weight of the load presented to the vibrator as a function of frequency. The effective weight is a complex and generally inverse function of frequency, peaking at the resonances. The presence of this type of function means that the force reaction of the structure at the higher frequencies becomes rather low, irrespective of the g level output of the vibrator.

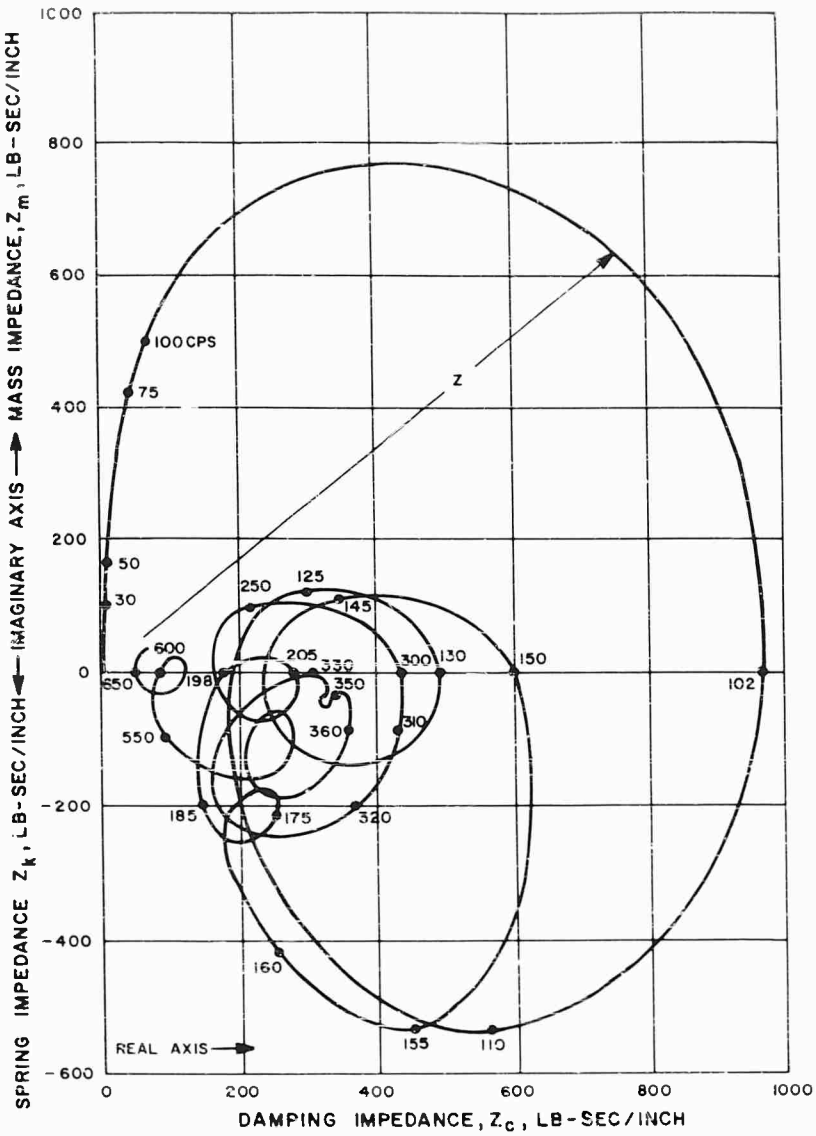

Fig. 6 - Impedance plot of Relay spacecraft structure

The force into the structure (and its reaction) at a given frequency is the product of the effective weight at that frequency and the g level output of the vibrator. This weight is required to ascertain the force which a given vibration machine (being characteristically limited in force output) is capable of imparting to the given body.

The structure used should be fabricated according to latest design as to geometry and materials and should be loaded with actual components. Since this latter condition is sometimes difficult to obtain, loads simulated by plates or blocks of proper weight, stiffness and c.g., location will usually not alter the structural response significantly. Simulation of component damping would be advantageous, but the difficulties involved and, particularly, the lack of knowledge as to the degree of damping simulation attained make this additional procedure questionable.

The instrumentation includes a strain gage and an integrating accelerometer for measuring force and velocity, respectively. These are to be located on the structure as close as possible to the separation plane, for their location defines the driving point. Since most structures are neither symmetrical in all planes nor isotropic in their response to force inputs in various directions, the choice of driving point

must, in general, be carefully made and the input applied in more than one direction. Spacecraft structures form a somewhat special class in that they are cantilever mounted with the driving point (plane) given as the separation plane. The only significant directions are the longitudinal, for steady state acceleration, shock and vibration inputs, plus such lateral directions as are significant to the particular structure, for the lateral components of these inputs. If, for any reason, the sensors are placed on the mounting fixture, the characteristics of that portion of the fixture between them and the separation plane are included in the response of the structure. Practically, this condition has the effect of shifting the position of the real axis vertically in the impedance plot. A major item in the test equipment, the Resolved Components Indicator, consists of a push-pull amplifier and phase detector to indicate the resolved magnitudes of the two input signals. The constant input velocity is taken as the reference component for phasing from the accelerometer, whose signal is also fed back to the servo controlling the vibrator. The strain gage signal is the force component and, as the frequency changes, it progresses through various phasal relationships with the velocity, becoming 180 degrees out of phase at resonance.

Calibration is performed by vibrating a known weight whose impedance varies only slightly with frequency, i.e., a lead block. The frequency used is very low, below any possible resonance of the weight or fixture, and the input is also low (0.5 to 1 g). The test is run by impressing a sine wave vibration of constant input velocity and sweeping slowly through the frequency range (1/4 octave per minute), recording the magnitudes of the velocity and force components at the driving point. Typical data appear in Table 1 together with a calculation scheme for finding the impedance and effective weight. The impedance is found by using the general expression, Eq. (4), simplified to $|Z| = A + jB$, or

$$|Z| = \left[c^2 + (2\pi fm - k/2\pi f)^2\right]^{1/2}, \quad (14)$$

in which the two component readings are substituted after conversion from millivolts to lb-sec/in. by use of the calibration factor.

The expression for the loading or effective weight $(W)_{eff}$ is derived from $F = ma$, $V = a/\omega$ and $Z = F/V$ by setting

$$|Z| = (ma)/(a/\omega) = \omega m,$$

TABLE 1
Data and Calculation Scheme for Impedance and Effective Weight

Freq., f (cps)	Driving Point Impedance Components					Z	$(W)_{eff}$
	Velocity (mv)	Force (mv)	K[a] (lb/in./mv)	Velocity	Force		
(1)	(2)	(3)	(4)	(2)/(4)	(3/4)		
0	0	0	1.9	0	0	-	125 (static)
20	15	75	1.9	7.9	40	40	128
30	20	200	1.9	10.5	105	106	216
50	30	340	↓	15.8	179	185	226
75	150	850	↓	79.0	520	545	330
102	2300	1100	↓	1210	580	1345	805
105	2000	0	↓	1050	0	1050	610
110	1200	-1050	↓	630	550	840	467
205	420	0	↓	226	0	226	67.1
210	470	-120	↓	248	63	255	73.5
220	60	-210	↓	32	110	116	32.2
550	80	-150	↓	42	-79	89.5	10.0
575	70	-80	↓	36.8	-42	55.8	5.9
600	100	-40	↓	52.5	-21	56.5	6.0
625	120	0	↓	63.9	0	63.2	6.2
650	50	5	↓	26.3	2.6	26.4	2.5

[a]Calibration factor.

from which

$$W_{eff} = (|Z|)/2\pi f . \qquad (15)$$

The value of impedance from Eq. (14) is then used in Eq. (15) for the effective weight at the selected frequency.

An illustrative example is formed using impedance, effective loading and resonance measurements made on the Relay spacecraft structure, Fig. 5. The calculations have been carried through the first two resonances, at 102 and 210 cps; and the peaking at resonance, followed by the general decrease in both impedance and effective weight, may be noted. The local peaks at each resonance are quite pronounced, indicating a sharp response. The fact that the fundamental frequency was 102 cps and the first harmonic came in at 210, not exactly twice 102, shows some experimental error present, but more significantly, that the response is not purely harmonic. The weight at zero frequency is included for comparison with the effective weight at some very low frequency, such as 20 cps, and the small difference, 128 pounds vs 125 pounds, was taken as adequate check on the accuracy of the test arrangements.

The low value of the effective loading in the higher frequency range is especially important. Certain rockets are known to impart forces as high as 600 pounds to the spacecraft in the frequency range of 550 to 650 cps. This condition, together with the fact that the g level output of many available vibrators is limited to about 50 g, may create a mismatch between test requirements and test equipment capacity. For this example, proper simulation requires a force of some 600 pounds, but only (6 lb) × (50 g) = 300 lb are available. Thus, if test specifications include complete simulation of the true physical situation, a vibrator output of 100 g would be required.

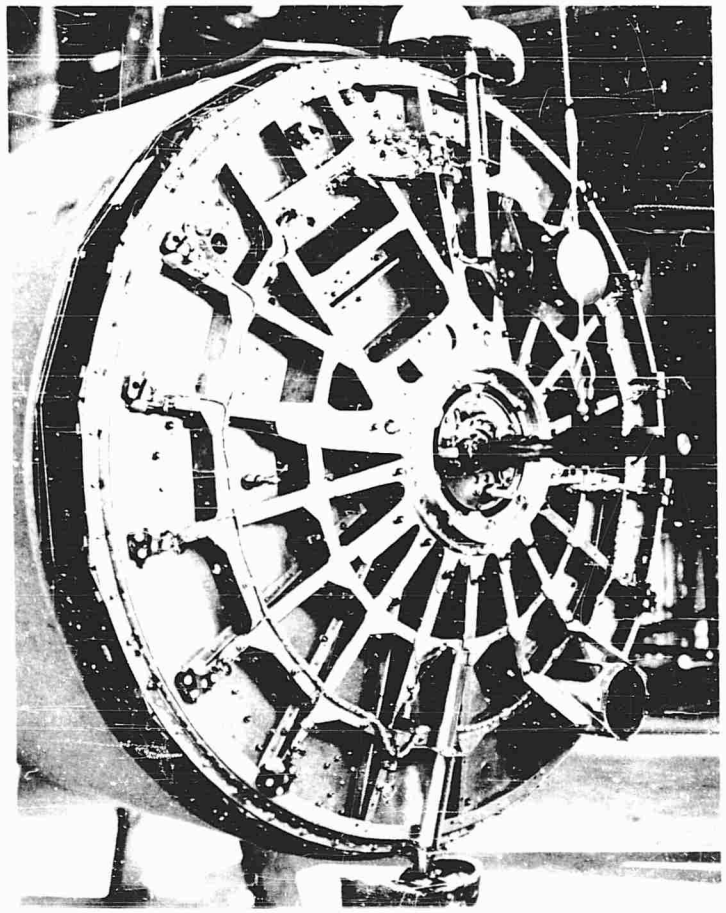

Fig. 7 - Photo ot Tiros spacecraft structure

The impedance characteristic of this cruciform arrangement of riveted trusses carrying shear-mounted loads was shown in Fig. 6. A general comparison is now formed using the Tiros structure (Fig. 7), basically a circular tension sheet to which radial ribs are riveted. This baseplate carries a cylindrical solar array that loads the plate rim but provides no stiffness. The majority of the component loads are compression mounted. An impedance plot for the Tiros baseplate is shown as Fig. 8 and several parameters of interest are given in Table 2.

It will be noted that the first three harmonics of the base plate are relatively distinct while the cruciform has shown a subassembly resonance between the fundamental and first harmonic. Further, the baseplate shows no well-defined subassembly resonances until the frequency reaches about 550 cps; the action between 340 and 550 cps is difficult to identify but is thought to be still that of the plate itself. Up to its first harmonic, the cruciform plot loops three times, indicating subassembly resonances or modes other than the longitudinal. Over the same total frequency range, the

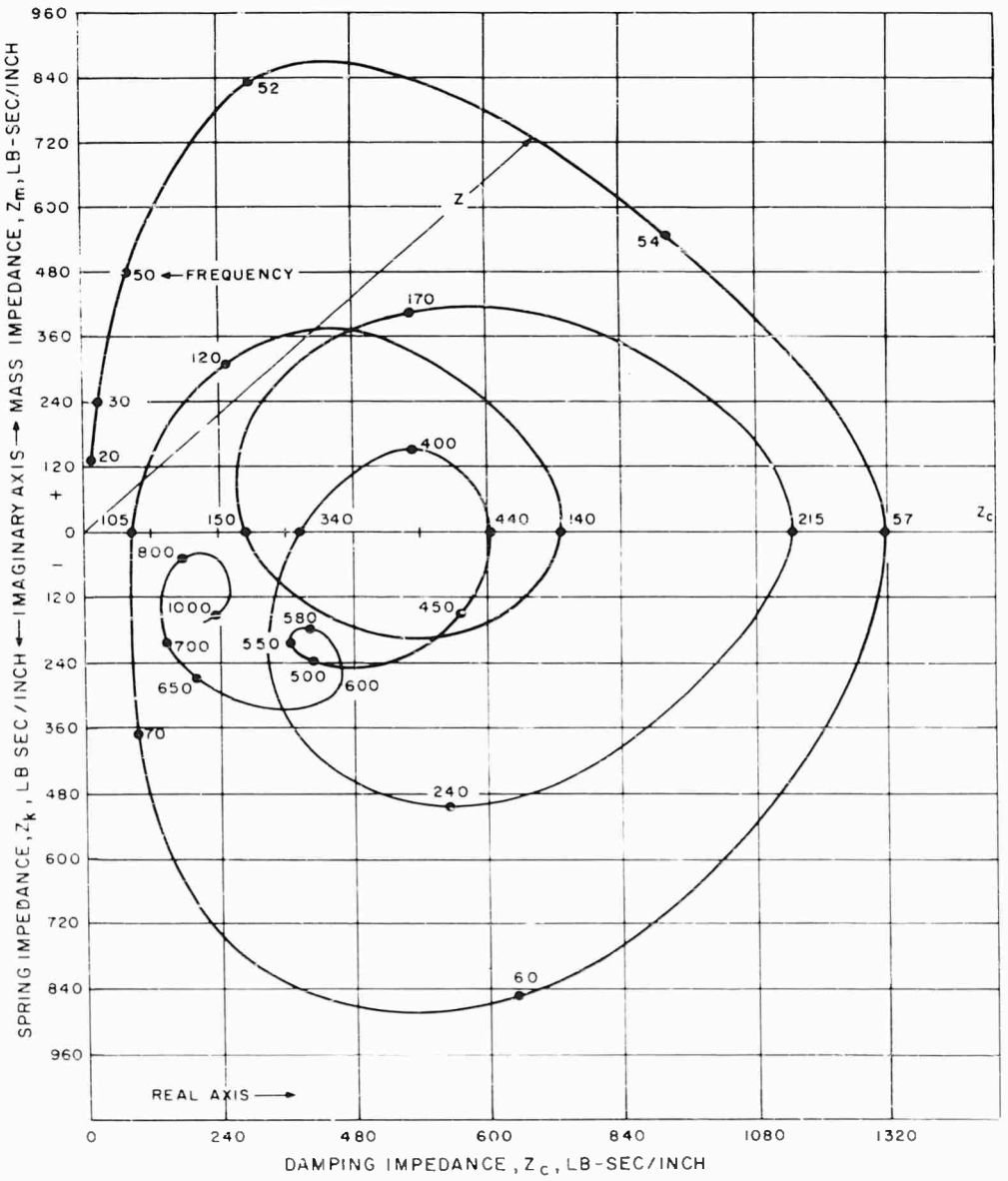

Fig. 8 - Impedance plot of Tiros spacecraft structure

TABLE 2
Impedance Comparison of Baseplate and Cruciform Truss

Parameters	Cruciform Truss	Baseplate
Static wt, W (lb)	125	275
Natural frequencies, 1st two	102, 198	57, 105
Stiffness impedance	Lower, Z_k = 550, max	Higher, Z_k = 880, max
Damping impedance	Lower, Z_c = 900, max	Higher, Z_c = 1,320, max
Mass impedance	Lower, Z_m = 750, max	Higher, Z_m = 870, max
Mass effect, or (velocity)$^{-1}$	$\frac{Z_m}{W} = \frac{750}{125} = 6.00$	$\frac{Z_m}{W} = \frac{870}{275} = 3.16$

cruciform shows about seven more loops. These conditions are in line with the higher stiffness noted in the baseplate, and mean that there are fewer portions (spring-mass-damper subsystems) resonating by themselves. The baseplate thus tends to act as the more rigid body. As another check on the accuracy of this type of data, the first natural frequency of the plate was calculated by the STODOLA method as 59 cps, with which 57 cps compares quite well.

The degree of mass dominance at the low end of the frequency range is greater for the cruciform, as is indicated by the greater slope of the locus. The cruciform has the sharper resonance, shown by a lesser number of cycles from that point where the spring and damping terms begin to take on significance to the real-axis crossing, approximately (102-100) vs (57-52). This condition is also borne out qualitatively by the lower rate at which $dZ/d\omega$ approaches zero.

As a further comparison, Fig. 9 is the plot for a plate very similar to that for Tiros, but smaller, 28 inches in diameter and carrying 150 pounds load. The fabrication was identical: radial flanged ribs riveted to a tension skin, all of 2024-T3 aluminum. As in Tiros, this plate carried a uniformly distributed load plus the rim load. The center of gravity here is much higher above the plate, accentuating the rocking modes. The plot indicates that the degree of mass dominance, at the low frequencies, is lower, and the resonance is more blunt, there being about 56 cycles vs 7 cycles between the end of mass dominance and resonance. The end of mass dominance is not a definitive point but is taken here at 80 cps and Z_m equal to 150 lb-sec/in. The most noticeable feature of this plot is that the first real-axis crossing is off-normal and that the zero point for $dZ/d\omega$ is below the real axis, in the spring-dominance region of frequency. These conditions indicate departure from ideal behavior, thought to be due to complex coupling between the first, or "umbrella," mode and a rocking mode. The first mode fundamental is undoubtedly the 136 cps, with the harmonic of 272 cps at another point where $dZ/d\omega = 0$, not the axis crossing at 280 cps.

The massive nature of the load together with the large moment from the high c.g. leads to the conclusion that the loop from 140 to 155 cps indicates the first rocking mode rather than a subsystem fundamental in axial translation. A subsequent survey with accelerometers located on the load to determine its modal axes confirmed the conclusion. Owing to its offset, the loop from 180 to 200 cps is most probably the fundamental of a subsystem of complex series-parallel connections, fortunately at a nonharmonic value of the spacecraft fundamental. The two crossings at 375 and 450 cps bracket the theoretical value of the second harmonic, 408 cps. By sequence, the values should be the second and third harmonics, respectively, but the numerical deviation is rather large, making the analysis somewhat inconclusive. About all that can be said is that these crossings represent peaks in the response curve of whatever mode is present at these frequencies. There is some indication that had the measurements been made at smaller increments of frequency, the plots for these systems would have shown more departure from ideal behavior.

As an inherent characteristic, impedance measurement is highly sensitive due to the manner in which the change of phase angle is

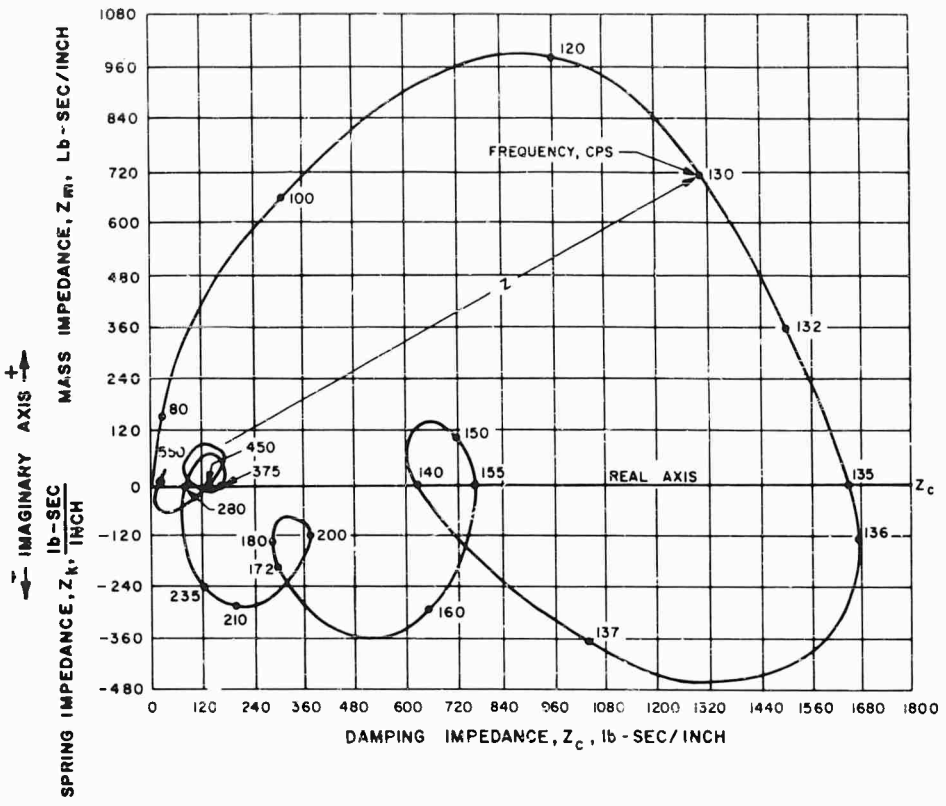

Fig. 9 - Impedance plot of circular plate structure

portrayed, which also follows the sequence of dominance of the spring, mass and damper elements. Further, the increase in the angular increment of the rotating impedance vector is greatest in the resonance regions. These accurate and essentially unmistakable indications of the resonance of an existing structure provide information by which to justify prior calculations, or on which to base detuning operations.

The principal reason for obtaining such data was to discover any subsystem which may be inadvertently tuned to the fundamental frequency of the spacecraft. Other methods are available, but the measurement of impedance and its plotting in the complex plane form a most sensitive and comprehensive view of a spacecraft's dynamic response.

* * *

PRELIMINARY STUDY OF AN EXPERIMENTAL METHOD IN MULTIDIMENSIONAL MECHANICAL IMPEDANCE DETERMINATION

Frank J. On
Goddard Space Flight Center
Greenbelt, Maryland

This paper presents a preliminary study of a method of resolving the driving point impedance at a terminal of a multidimensional structure into its six component impedances with respect to an orthogonal system of axes (i.e., three rectilineal and three rotational impedances). This problem exists in certain situations requiring combined driving point force and moment impedance measurements. A seemingly feasible method was studied theoretically, and a three-dimensional cross-shaped mechanical fixture was designed to be used with this method.

When the fixture is attached to a test specimen and forces are sensed at the cross extremities, the forces, moments, and velocities occurring at the attachment terminal can be obtained. Hence, under steady-state sinusoidal motions the appropriate ratios of net sinusoidal forces and moments, and their corresponding sinusoidal velocities at this terminal, define the components of driving point impedance of the test specimen. Some associated problems and experimental results are discussed in an evaluation of the method.

INTRODUCTION

One of the most vexing problems confronting an environmental engineer in his effort to measure mechanical impedance of realistic engineering structures is the effect of points of structures having motion in more than one direction. The frequent practice of measuring point impedance by simply force exciting the system at a point in a prescribed direction and measuring the velocity response at the same point in the same direction may lead to erroneous results. The tacit assumption that the system is one-dimensional is sometimes wrong. A description of the translational and rotational impedance at the terminal is needed. Three translational and three rotational impedances are required to describe completely the dynamic characteristic performance of the system.

In Fig. 1, applied forces F_1 and F_2 caused motion in directions 1 and 2. Accordingly, the performance equations are

$$F_1 = Z_{11}V_1 + Z_{12}V_2$$

and (1)

$$F_2 = Z_{21}V_1 + Z_{22}V_2 ,$$

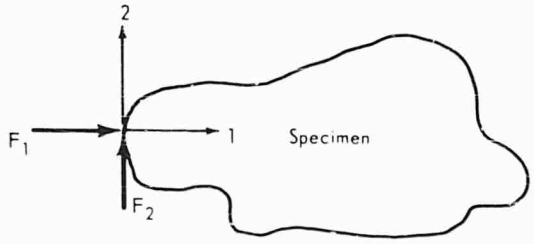

Fig. 1 - Example of multi-dimensional motion at a terminal

where Z_{11} and Z_{22} are point impedances, Z_{12} and Z_{21} are transfer impedances, and V_1 and V_2 are velocities, respectively, in Directions 1 and 2. Clearly the ratio of F_1 and V_1 defines the point impedance in Direction 1 only if V_2 is zero. This condition should not be assumed without substantiation.

The purpose of this paper is to present a preliminary study of an experimental method presently under way to determine impedance at a terminal possessing multidimensional motions.

GENERAL THEORY

The determination of mechanical impedance involving motions at one terminal in more than one direction requires the use of somewhat more complicated expressions and measurement techniques than the commonly assumed one-dimensional case. If a system of many masses, springs and dampers with fully defined reactions or constraints is linear, the vibration response to any one sinusoidal vibratory force is sinusoidal, of the same frequency, and proportional to the force. The amplitude of any one coordinate is, in general, different from that of any other so that

$$F_1 = Z_{11}V_1 ,$$
$$F_1 = Z_{12}V_2 , \qquad (2)$$
$$F_1 = Z_{13}V_3 , \text{ etc.}$$

In these equations, Z_{11}, Z_{12}, Z_{13}, etc., are complex numbers giving the ratio of the vibratory force at Coordinate 1 to the vibratory velocity at Coordinates 1, 2, 3, etc. They are functions of frequency and may be called impedance parameters; Z_{11} is called point impedance and Z_{12} or Z_{13} is called transfer impedance. If a force operates on Coordinate 2 alone, and none on Coordinate 1,

$$F_2 = Z_{21}V_1 ,$$
$$F_2 = Z_{22}V_2 , \qquad (3)$$
$$F_2 = Z_{23}V_3 , \text{ etc.}$$

If additional forces act at other coordinates at the same time and with the same frequency, the total amplitude of force required will be the sum of these:

$$F_1 = Z_{11}V_1 + Z_{12}V_2 + Z_{13}V_3 + \ldots ,$$
$$F_2 = Z_{21}V_1 + Z_{22}V_2 + Z_{23}V_3 + \ldots , \qquad (4)$$
$$F_3 = Z_{31}V_1 + Z_{32}V_2 + Z_{33}V_3 + \ldots , \text{ etc.}$$

or in the shorthand matrix notation,

$$\{F_i\} = [Z_{ij}]\{V_j\} , \qquad (5)$$

where Z_{ij} is the force at Point i due to a unit velocity of Point j when all other velocities corresponding to forces being considered are held zero; that is, all other forces must be replaced by rigid constraints. Under these conditions the reciprocity theorem $Z_{ij} = Z_{ji}$ still holds. In general, the values of the Z's will depend on how many forces are being considered.

As these conditions are seldom achieved physically during measurement, schemes must be devised whereby the impedance matrix $[Z_{ij}]$ can be obtained experimentally. One such scheme is based on the fact that if Eq. (5) is to describe truly the dynamic performance of a complex system, the complex coefficient matrix $[Z_{ij}]$ must be compatible with the set of velocities $\{V_j\}$ and forces $\{F_i\}$ measured on the system at the specified points. In general, this requires force and moment measurements along with translational and rotational velocities.

There are several possible combinations of experimental data sufficient for evaluating the coefficient matrix at a given frequency. Since these combinations are similar to one another, only one combination is presented here. The greatest difference is in the type of excitation to be employed, i.e., whether steady sinusoidal, transient, or random noise and whether the system is assumed to be active or passive. For convenience it will be assumed that steady sinusoidal excitation is applied to a passive system. Accordingly, if there are n coordinates of interest, n tests are generally required at each frequency to evaluate all elements of the coefficient matrix.

With the coordinates coupled to ground by connections of finite but not necessarily known stiffness, a force of a constant frequency is applied at some convenient terminal, possibly by an electrodynamic shaker. The resulting force phasors $F^{(1)}$ and the velocity phasors $V^{(1)}$ at these coordinates are then measured. Repeating Test 1, n number of times, each time using a different combination of external stiffness and denoting these measured force phasors by $F^{(n)}$ and velocity phasors by $V^{(n)}$, the resulting matrix equation

$$[Z(\omega)]\left\{V^{(k)}(\omega)\right\} = \left\{F^{(k)}(\omega)\right\} \quad k = 1, 2, \ldots n \qquad (6)$$

may be solved simultaneously for the elements of $[Z]$.

In this study a single terminal having six possible directions of motion was considered. To reference the force and moment impedances, an orthogonal system of Axes 1, 2, 3 may be established at the point of attachment. In accordance with this system of axes, a three-dimensional, cross-shaped mechanical fixture (Fig. 2) was studied. The fixture attachment to the specimen is at the origin O. When the specimen is excited at a convenient point, forces

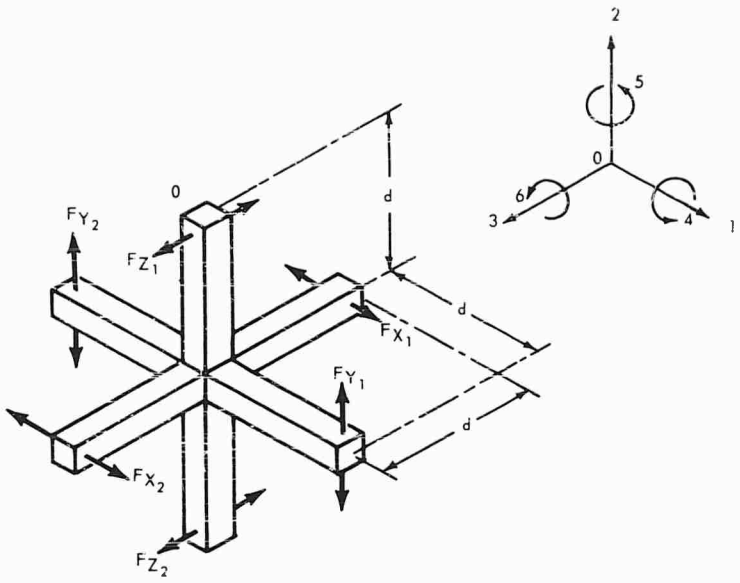

Fig. 2 - Three-dimensional cross-shaped mechanical fixture

are then sensed at the extremities by compliance elements appropriately oriented and coupled to ground. If these forces are designated F_{x_1}, F_{x_2}, F_{y_1}, F_{y_2}, F_{z_1}, and F_{z_2} as shown, by inspection the net forces and moments R_i ($i = 1, 2, \ldots, 6$) at the attachment Terminal O may be expressed in terms of the F's as

$$\begin{aligned} R_1 &= F_{x_1} + F_{x_2}, \\ R_2 &= F_{y_1} + F_{y_2}, \\ R_3 &= F_{z_1} + F_{z_2}, \\ R_4 &= -2F_{z_2}d, \\ R_5 &= (F_{x_2} - F_{x_1})d, \end{aligned} \tag{7}$$

and

$$R_6 = (F_{x_1} + F_{x_2} + F_{y_1} - F_{y_2})d .$$

For assumed small displacements, the corresponding velocities at Terminal O are

$$\begin{aligned} V_1 &= \frac{1}{2}(V_{x_1} + V_{x_2}), \\ V_2 &= \frac{1}{2}(V_{y_1} + V_{y_2}), \\ V_3 &= \frac{1}{2}(V_{z_1} + V_{z_2}), \\ V_4 &= \frac{1}{2d}(V_{z_1} - V_{z_2}), \end{aligned} \tag{8 (Cont.)}$$

$$V_5 = \frac{1}{2d}(V_{x_2} - V_{x_1}),$$

and

$$V_6 = \frac{1}{2d}(V_{y_1} - V_{y_2}). \tag{8}$$

Since six coordinates are involved at this terminal, six tests are required, each with a different combination of external compliance. By introducing a superscript to denote the test number, the matrix equation

$$[Z(\omega)]\ \left\{V^{(k)}(\omega)\right\} = \left\{R^{(k)}(\omega)\right\} \quad k = 1, 2, \ldots 6 \tag{9}$$

can be solved for the elements of the matrix $[Z]$. If the effect of the cross-shaped fixture is appreciable, it may be subtracted from the $[Z]$ of Eq. (9), provided its characteristic impedance is known.

EXPERIMENTAL REQUIREMENTS

To validate the method experimentally, certain requirements must be met. In designing a cross-shaped mechanical fixture, a material of sufficiently high elastic modulus and density must be selected so that fixture resonances occur sufficiently above the maximum frequency of interest. Accordingly, the physical dimension of the crossarm length should be sufficiently short, yet long enough to provide suitable

rotational impedance sensitivity, i.e., sufficient signal-to-noise ratios.

In this preliminary study, a cross-shaped fixture of aluminum alloy 2024-T4 with a crossarm length of 5-1/2 inches was considered. At the extremities, 33/64-inch diameter holes with centers 1/2 inch from the ends are tapped and appropriately oriented (Fig. 2). The holes are used for mounting impedance heads or external compliance elements. The cross sections of the arms are 1 inch square. The first resonant mode of the fixture calculated was a crossarm cantilever mode at approximately 2500 cps. Although it is desirable to have a higher fundamental mode frequency, the dimensions were limited to obtain sufficient rotational sensitivity within the force capability of the shakers employed.

DETERMINING CHARACTERISTIC IMPEDANCE OF MECHANICAL CROSS-SHAPED FIXTURE

To determine the impedance of a specimen, it is usually necessary to determine the loading effects of the fixture on the specimen. Figure 3 shows a typical experimental setup for measuring the characteristic impedance of the cross-shaped fixture. This setup was specifically employed to obtain the characteristic rectilineal impedance in direction 1 and the characteristic rotational impedance in direction 5. This was accomplished by suspending the fixture at O with a cable, sinusoidally shaking the two extremities in the direction 1 as shown, and obtaining the force and acceleration phasors by the impedance heads and a suitable electrical measuring circuit shown in Fig. 4. The magnitude of the force applied was such that sufficient rectilineal and rotational impedance measurement sensitivities were obtainable. The phase angle relationship of each measured signal was taken with reference to the output of the signal generator. Accordingly, the substitution of these phasors was made in the following expressions defining the appropriate ratios of the quantities of Eqs. (7) and (8) for the point rectilineal and rotation impedances, respectively:

$$Z_{R_1} = \frac{R_1}{V_1} = 2\omega \left[\frac{(Q_1Q_3 - Q_2Q_4) + i(Q_2Q_3 + Q_1Q_4)}{Q_3^2 + Q_4^2} \right], \quad (10)$$

where

$$Q_1 = \frac{F_{x_2}}{A_{x_2}} \cos\left(\beta_{22} + \frac{\pi}{2}\right) - \frac{F_{x_1}}{A_{x_2}} \cos\left(\beta_{12} + \frac{\pi}{2}\right),$$

$$Q_2 = \frac{F_{x_2}}{A_{x_2}} \sin\left(\beta_{22} + \frac{\pi}{2}\right) - \frac{F_{x_1}}{A_{x_2}} \sin\left(\beta_{12} + \frac{\pi}{2}\right),$$

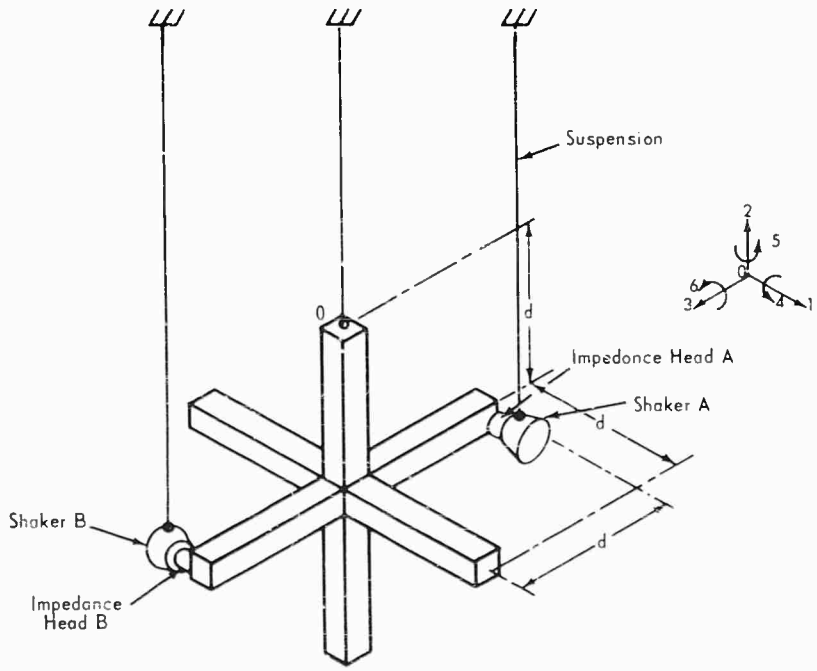

Fig. 3 - Typical experimental setup for measurement of characteristic rectilineal impedance in direction 1 and rotational impedance in direction 5 of cross-shaped fixture

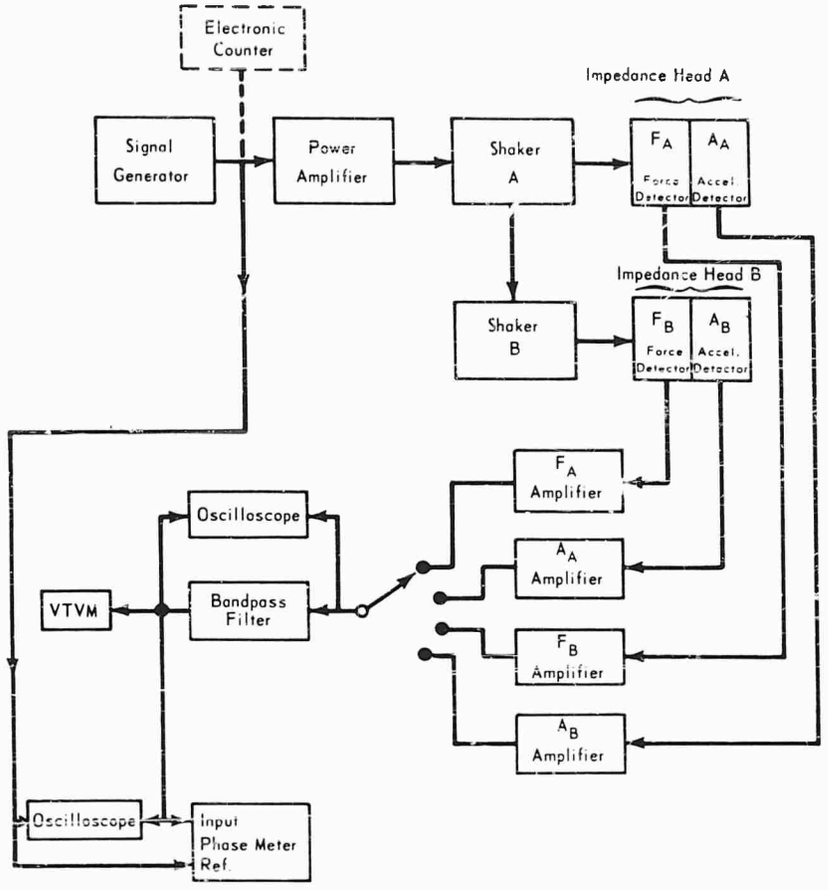

Fig. 4 - Typical electrical measuring circuit for experimental setup (Fig. 3)

$$Q_3 = 1 - \frac{A_{x_1}}{A_{x_2}} \cos \gamma_{12},$$

and

$$Q_4 = \frac{A_{x_1}}{A_{x_2}} \sin \gamma_{12},$$

and

$$Z_{R_5} = 2d^2\omega \left[\frac{(R_1R_3 + R_2R_4) + i(R_2R_3 - R_1R_4)}{R_3^2 + R_4^2} \right], \quad (11)$$

where

$$R_1 = \frac{F_{x_2}}{A_{x_2}} \cos \left(\beta_{22} + \frac{\pi}{2} \right) + \frac{F_{x_1}}{A_{x_2}} \cos \left(\beta_{12} + \frac{\pi}{2} \right),$$

$$R_2 = \frac{F_{x_2}}{A_{x_2}} \sin \left(\beta_{22} + \frac{\pi}{2} \right) + \frac{F_{x_1}}{A_{x_2}} \sin \left(\beta_{12} + \frac{\pi}{2} \right),$$

$$R_3 = 1 + \frac{A_{x_1}}{A_{x_2}} \cos \gamma_{12},$$

and

$$R_4 = \frac{A_{x_1}}{A_{x_2}} \sin \gamma_{12}.$$

A_{x_1} and A_{x_2} are, respectively, the acceleration response at extremities X_1 and X_2; β_{22} is the phase angle between signals F_{x_2} and A_{x_2}, β_{12} is that between F_{x_1} and A_{x_2}, and γ_{12} is that between A_{x_1} and A_{x_2}. If the input forces F_{x_1} and F_{x_2} are equal, Eq. (10) for the determination of rectilineal impedance becomes insensitive, and only the rotational impedance given by Eq. (11) can be obtained. Therefore, care should be exercised in using Eqs. (10) and (11) when only one experimental run is available.

As shown in Fig. 4, shaker B was wired in electrical series with shaker A to minimize unwarranted phase shifts between them. This was probably unnecessary as the common phase reference of the oscillator output provided a means of correcting for these shifts when used in Eqs. (10) and (11). The magnitudes of the forces and accelerations were measured by the VTVM, and the phase angles by an oscilloscope and a phasemeter. The bandpass filter was used to filter out harmonics and the additional oscilloscope to observe phase shift through the filter.

Equations (10) and (11) were computed by a digital computer program using these measured force and acceleration phasors. Figure 5(a) shows a plot of the experimental results compared to the theoretically calculated results for the characteristic rotational impedance magnitude. Figure (5b) is a plot of phase angle for this rotational impedance. Qualitatively, the magnitudes are in good agreement. The almost constant deviation will probably be lessened with improved calibration. As can be seen in Fig. 5(b), some of the phase angles differ from the others by approximately 180 degrees. On the basis of Fig. 5(a), these differences in phase angle are believed to be caused by the peculiarity of the computer program used in determining phase angles. No results for the rectilineal impedance were obtained because the particular set of forces applied resulted in insensitivity, as previously explained.

ADDITIONAL REQUIREMENT FOR EVALUATION OF THEORY

After the characteristic impedance of the cross-shaped fixture is determined, the fixture must be used to measure impedance of a symmetrical specimen whose characteristic impedance can be calculated with reasonably good accuracies. Figure 6 shows a typical experimental setup with the cross-shaped fixture. In this preliminary study, the specimen is a laminated cube of maple wood. Each laminate lies in a plane parallel to the top face. The laminates are arranged with cross-grain directions so that an isotropic condition of the material can be obtained. The specimen is suspended

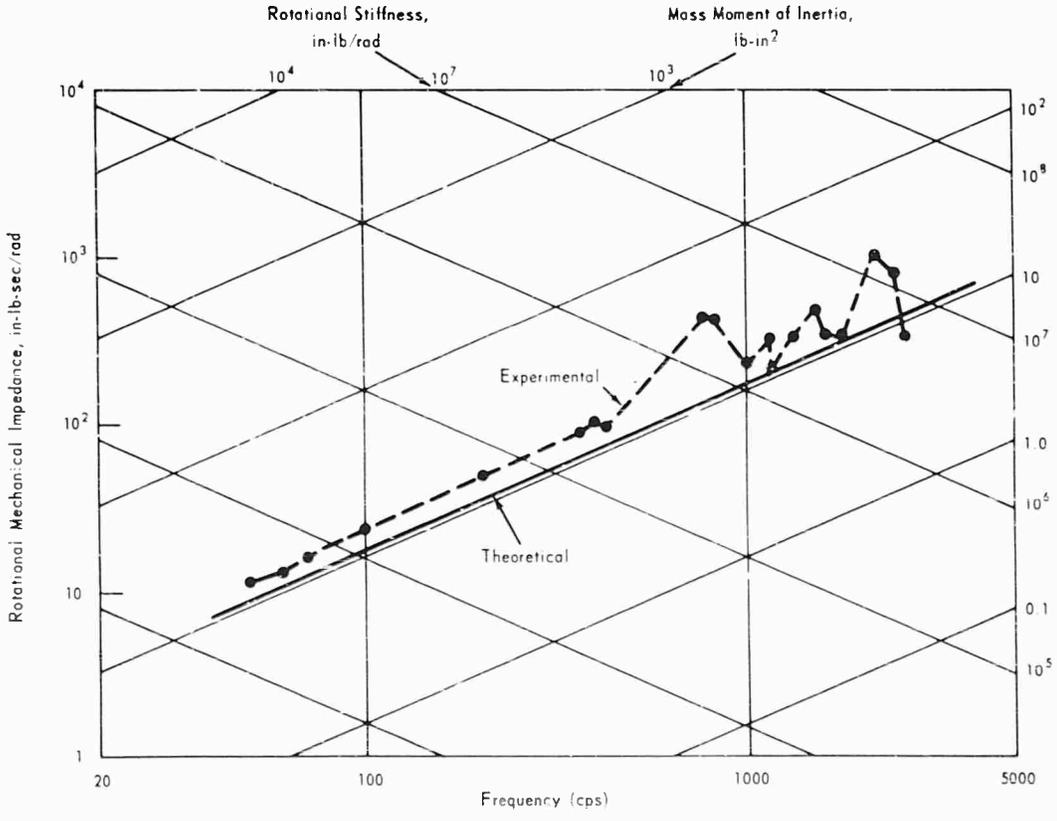

Fig. 5(a) - Characteristic rotational impedance at terminal O in direction 5--magnitude

at the center of the top face from an A-frame by a cable, thus providing a low-frequency suspension for the system. The attachment point O of the cross-shaped fixture is rigidly mounted to the center of the bottom face. At the extremities, compliance elements are coupled to ground in the directions as shown, and accelerometers are mounted on the other side of the extremities. Forces are then applied at points on the top face. The number of force application points and directions is arbitrary so long as there is sufficient response at each of the extremities to provide sufficient sensitivities for the impedance determinations by using Eq. (9).

Repeating this test six times, each time using a different combination of compliance elements, results in a set of measured force and acceleration phasors which, on substitution in Eq. (9), yields a set of simultaneous matrix equations. With the aid of a computer program, the complex impedance parameters of the coefficient matrix can be obtained. Because of symmetry of the specimen and the particular system of axes chosen, only the diagonal parameters will be non-zero. The indirectly determined complex impedances can then be compared to the calculated impedances

$$Z_{R_1} = Z_{R_2} = Z_{R_3} = i\omega M,$$

$$Z_{R_4} = i\omega I_1,$$

$$Z_{R_5} = i\omega I_2, \qquad (12)$$

and

$$Z_{R_6} = i\omega I_3,$$

where M, I_1, I_2, and I_3 are, respectively, the mass of the cube and mass moment of inertia about the respective axis through the point O.

CONCLUDING REMARKS

In this paper, a preliminary study of a method which seems to possess some merits in determining mechanical impedances at a point with motions in more than one direction is presented. Although the conditions assumed here are highly idealized, it is believed that this study can provide valuable guidelines in the treatment of more realistic complex systems. It was originally hoped that much experimental data could be presented. Unfortunately, due to equipment difficulties and subsequent computer program

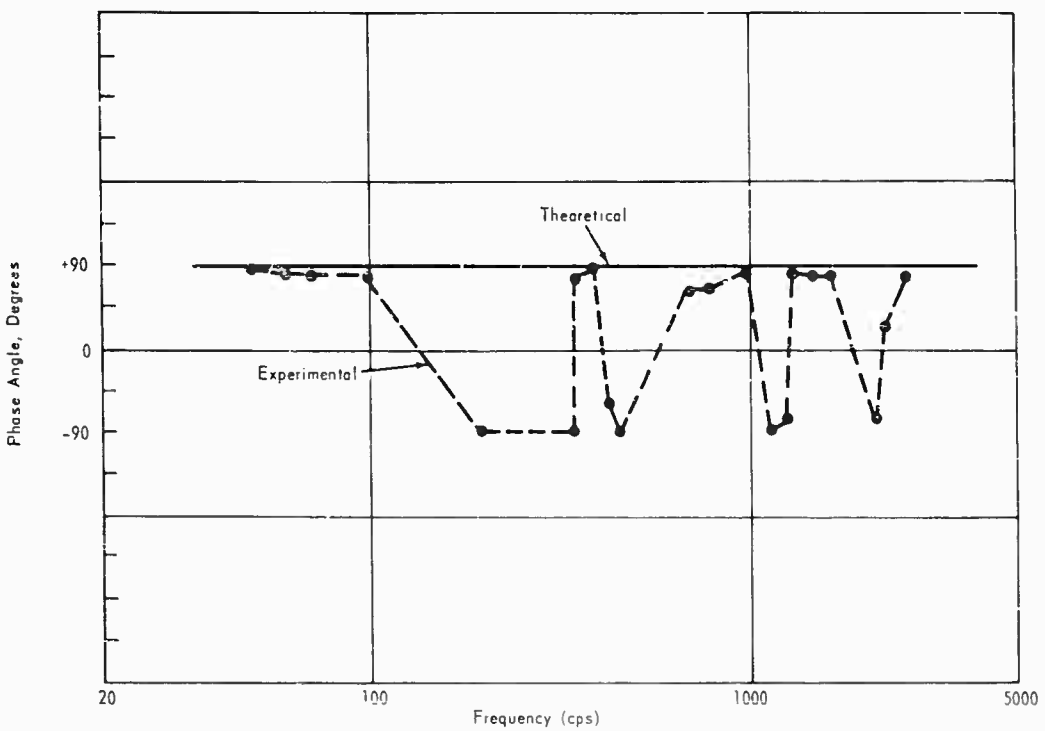

Fig. 5(b) - Characteristic rotational impedance at terminal O in direction 5--phase angle

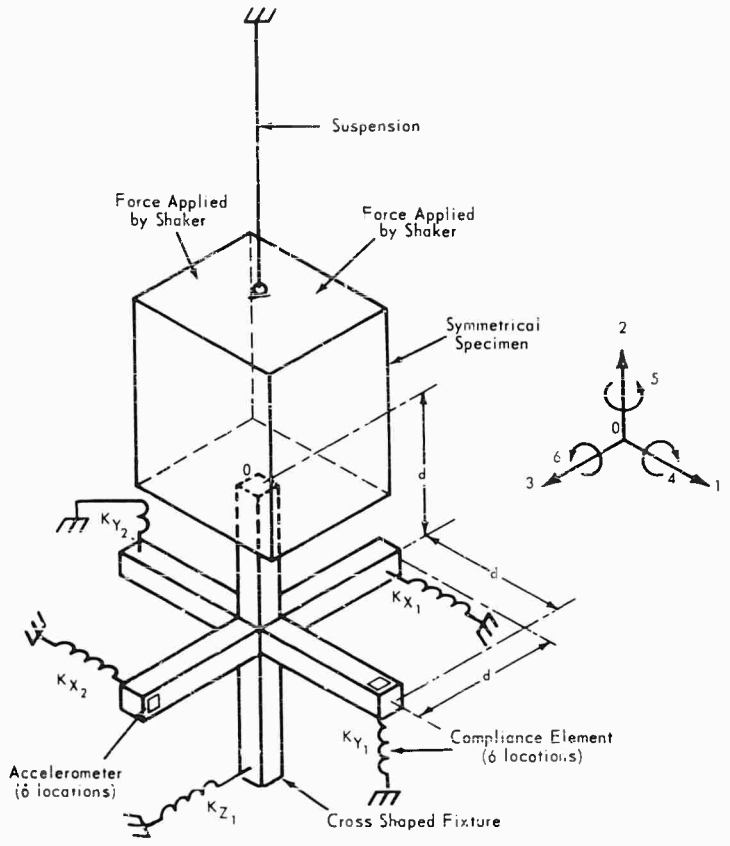

Fig. 6 - Typical experimental setup with cross-shaped fixture for impedance measurements of a symmetrical specimen

problems beyond our control, this is not now possible. Additional experimental results, when obtained, will be made available to those interested.

In general, the method presented appears theoretically feasible, and the preliminary experimental results seem to substantiate this. Future plans include the use of this method on more complicated specimens, with subsequent optimization of the experimental and computational procedures.

ACKNOWLEDGMENTS

The author is greatly indebted to T. G. Butler of the Goddard Space Flight Center for his most helpful suggestions during the preparation of this paper. He is also grateful to D. J. Hershfeld, J. F. Sutton, and A. J. Villasenor for their valuable assistance throughout this study.

DISCUSSION

F. Schloss (DTMB): You were mentioning that on a fixture the Young's modulus should be high. also the density should be high. Didn't you mean to say that the ratio of the Young's modulus to the density should be high or that the velocity of sound of the fixture material should be high, which means you should use something like beryllium. Secondly, I think you have the same possibility of running into trouble as you would have in measuring driving point impedances on known masses because of local deformation, especially at the higher frequencies. When you measure rotational impedances on a known structure, depending on the spacing

of your rotational impedance head, you can get different answers. This shouldn't happen unless it is due to local deformation of the structure.

Mr. On: With respect to the first question, that's correct. We used aluminum at first and found later on that wave effects were present in this fixture. You are right on the second point. That is why we decided to use the maple wood specimen. We took the laminated sections alternately in different grain directions hoping that we would get some near isotropic conditions of material properties.

* * *

EFFECTS OF TECHNIQUE ON RELIABILITY OF MECHANICAL IMPEDANCE MEASUREMENT

G. M. Remmers and R. O. Belsheim
Mechanics Division
U. S. Naval Research Laboratory
Washington, D. C.

Results of a recent "Round Robin" mechanical impedance measurement comparison (initiated by the ASA Shock and Vibration Committee) have shown that much improvement can be made in the reliability of data by better understanding the effects of and paying detailed attention to measurement procedures and techniques.

Variations reported by 19 organizations which measured the same test structures is discussed. Specific examples are related to experimental practices, many of which have shortcomings. Factors requiring increased attention to increase reliability and repeatability are listed.

INTRODUCTION

During the past six or seven years many authors have discussed mechanical impedance as a useful concept in solving complex problems of structural dynamics. A rough indication of the growing interest in the increasing number of papers presented at the Shock and Vibration Symposia. Figure 1 shows the results of a quick count of these papers published in the Bulletin during the last ten years.

Among the many questions which this research has produced is, "How reliable are the

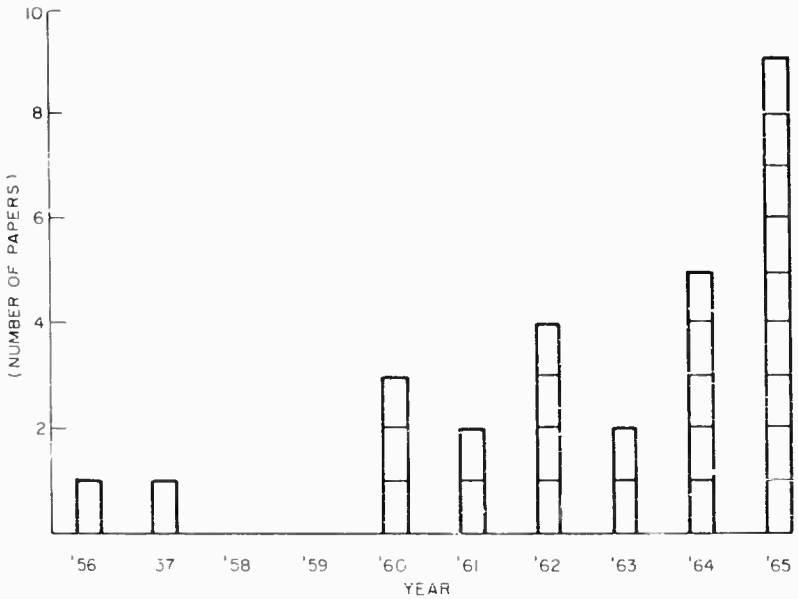

Fig. 1 - Number of mechanical impedance papers published in Shock and Vibration Bulletin

measurements of mechanical impedance?" This is obviously a question which can be answered only in a relative sense since the "exact" impedance of an actual structure is generally unknown. Thus, a paraphrase form of the question might be, "If several investigators measure the same structure, how well will their measurements compare?" To answer this question, the Shock and Vibration Committee of the Acoustical Society of America (ASA) asked the senior author to plan and conduct a series of "Round Robin" measurements on some "representative" structures. The plan was to circulate these structures among impedance experimentalists, have each make similar measurements, and correlate the results. This plan was carried out successfully, due largely to the cooperation of the 19 interested experimentalists. The results have been reported in preliminary fashion to the ASA Shock and Vibration Committee and were discussed at the Fall ASA meeting [1], as well as in a forthcoming NRL Report [2]. The purpose of this paper is to discuss some of the "Round Robin" results, with particular emphasis on the effects of measurement technique.

DESCRIPTION OF ROUND ROBIN STRUCTURES AND DATA-COLLECTION PROCEDURES

Considerable thought and computation preceded the selection of three structures as useful for collection of driving point data. Figure 2 shows the structures as finally constructed. These can be briefly described as follows:

Structure 1 - This is a solid aluminum cylinder, 7 inches in diameter and 7 inches long, weighing 24 pounds. The driving point impedance looking into one end of this cylinder is known at low frequencies and thus provides a relatively direct assessment of measurement capability.

Structure 2 - This is a symmetrical set of double-C shaped steel beams with low damping and a weight of 31 pounds. The several sharp system frequencies and high dynamic range of this structure within the frequency range brought out certain problems in the electronics of recording systems.

Structure 3 - This is an unsymmetrical pair of cantilevered aluminum beams weighing 15 pounds and having one beam constructed of high-damping sandwich material. During measurement of the driving point impedance at the tip of the undamped beam, problems were imposed by the nonsymmetry, the relatively large damping, and the presence of several system frequencies within the measurement range.

A common adaptor plug screws into each structure. Enough adaptor plugs were supplied so that each participant could attach the impedance transducer in his preferred manner without modifying the basic test structure

Letters were sent to potential participants, asking if they would make a set of measurements,

NOTE: References appear on page 57.

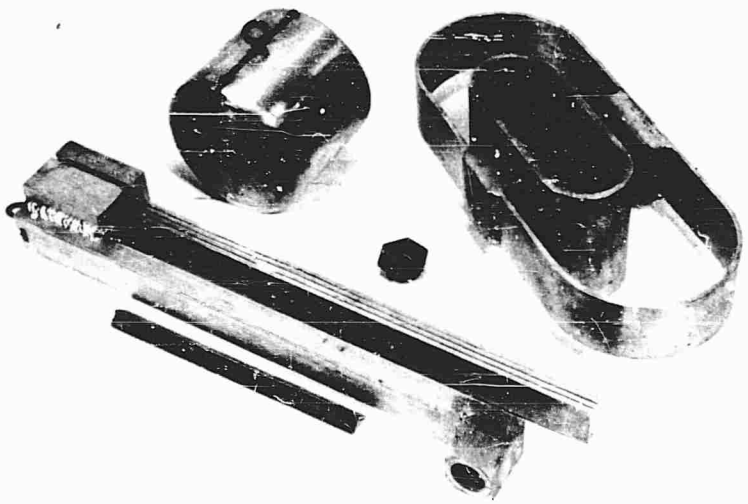

Fig. 2 - Round Robin test structures and adaptor plug

and 19 indicated interest. To reduce overall time for the program, two nominally identical sets of structures, labeled A and B (West Coast and East Coast, respectively) were manufactured. Reference [2] contains the information and instructions sent to each participant. To preserve anonymity the results were given a code designation even though this sometimes lost a useful result, such as identification of inadequate equipment. The collection of data has been compared in several ways [1], [2]; results of some of these are given in the following section.

OVERALL VARIATION IN ROUND ROBIN DATA

A general picture of how the data of the various groups compared with one another is best seen by examining a composite graph on which all curves for a structure are plotted.

Figure 3 is the composite plot of impedance magnitude for Structure 1 of set B. All data stays within an envelope about 3 db wide up to about 1 kc, after which the individual curves tend to peak at about 2 kc or above. This is the expected behavior. The frequency at which the peak occurs marks the point where the characteristic of the driving surface on the weight changes from predominantly mass-like to predominantly spring-like. The peak frequency measured is a function of the rigidity of the impedance head and of the structure being examined and is directly related to the contact stiffness of the impedance head-structure combination.

A composite graph of the phase angle curves for Structure 1B is shown in Fig. 4. Good agreement exists up to the lowest peak frequency, after which the envelope tends to diverge widely. Hence, its variation is directly comparable to

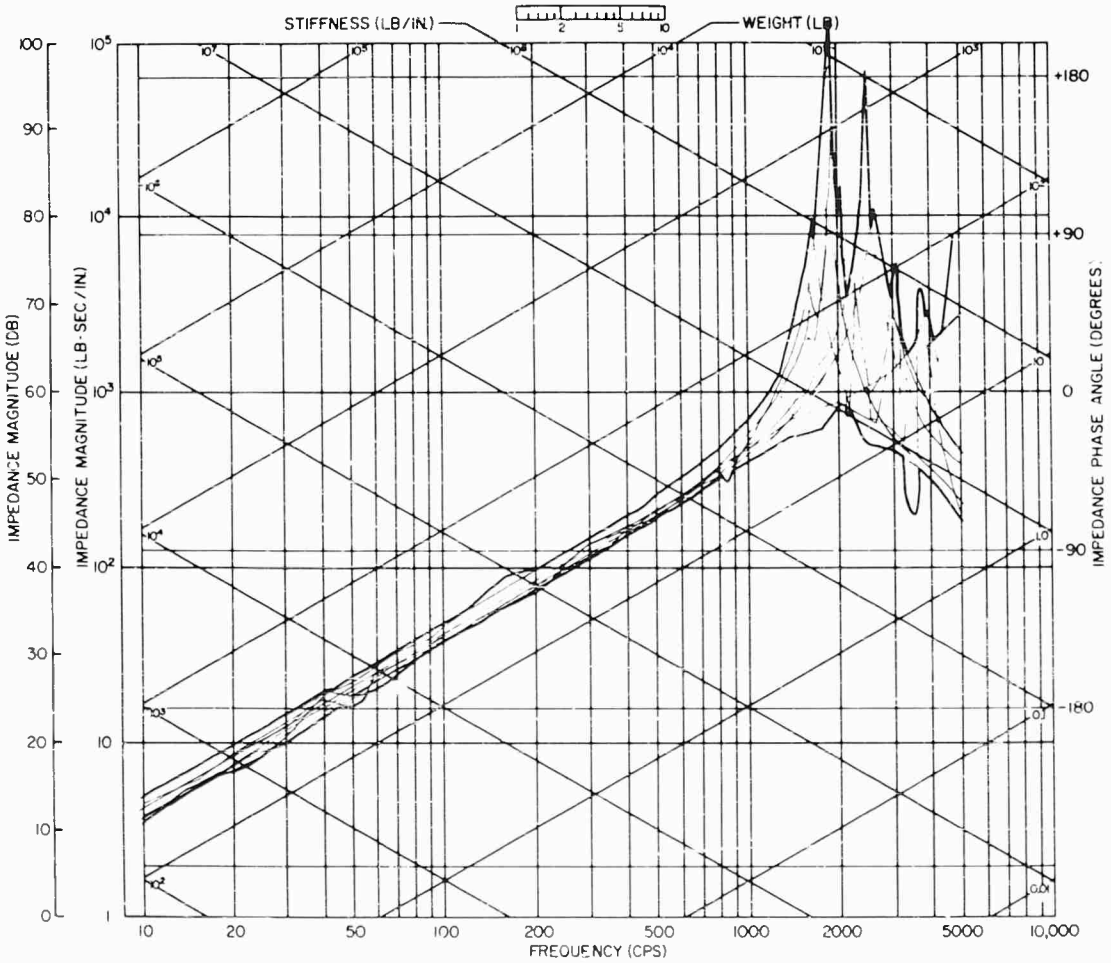

Fig. 3 - Envelope of impedance magnitude for Structure 1B

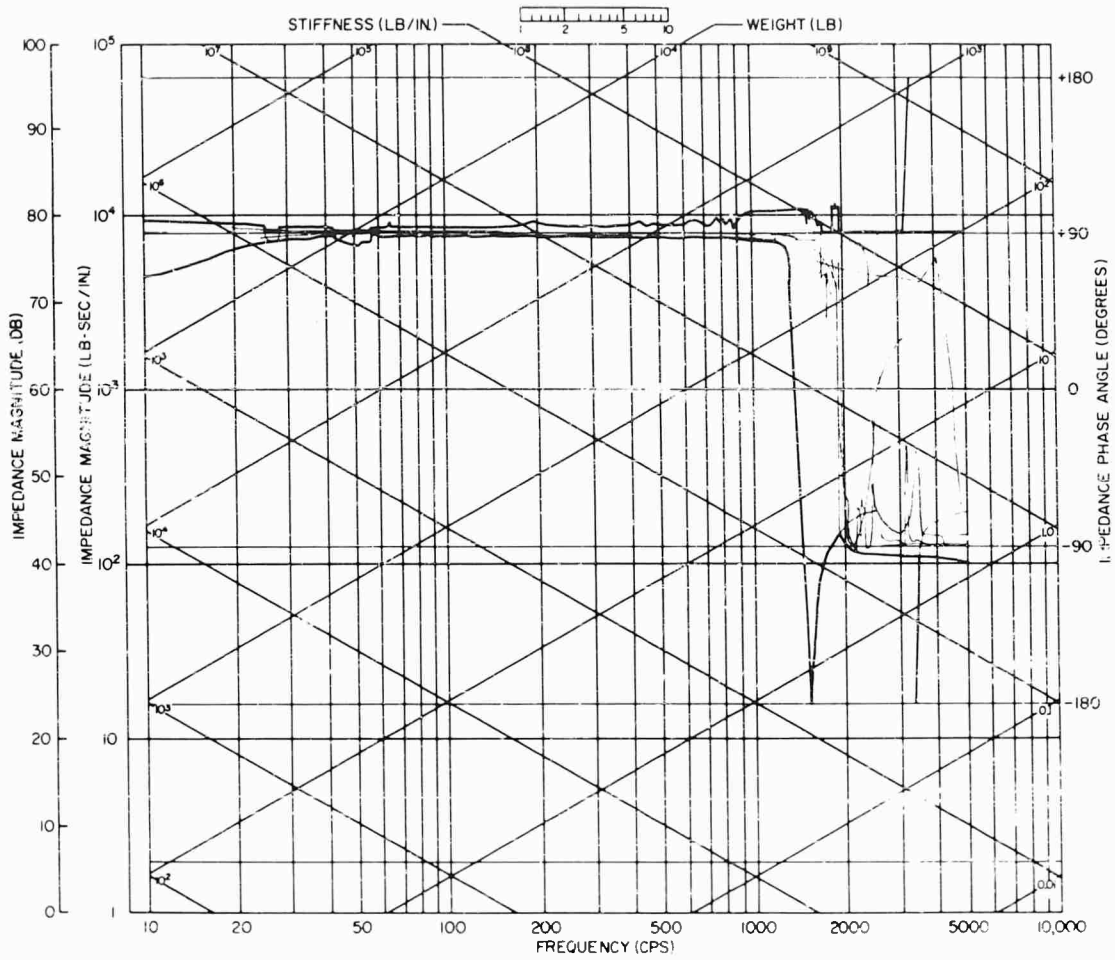

Fig. 4 - Envelope of impedance phase angle for Structure 1B

the variations seen in the magnitude data for 1B.

Figure 5 shows the magnitude envelope of the weight of Structure 1A. The individual curves do not appear here; extremes of the difference in curves are much greater than in the corresponding plot for 1B. However, omission of two curves gives an envelope of 1A results with about the same general character as the 1B envelope.

Table 1 contains the range of frequencies reported for the peak generally found in the magnitude curve of the weight. The 4500-cps peak was detected with an external accelerometer. The range of frequencies corresponds to the contact stiffness, which varies from 8.7×10^5 to 2.0×10^7 pounds per inch. A high contact stiffness indicates a high quality measurement in this sense. However, the contact

TABLE 1
Various Peak Frequencies
Measured for Structure 1

Frequencies (cps)	
Set A	Set B
1700[a]	1901
1403	2615
584	4500[a]
2300	1611
802	1826
1474	2473
2815	—[b]
1750	1950
1802	2412
2069[a]	—

[a]Frequency determined from 0-degree phase angle only, magnitude peak not clearly defined.
[b]No peak detected, external accelerometer used.

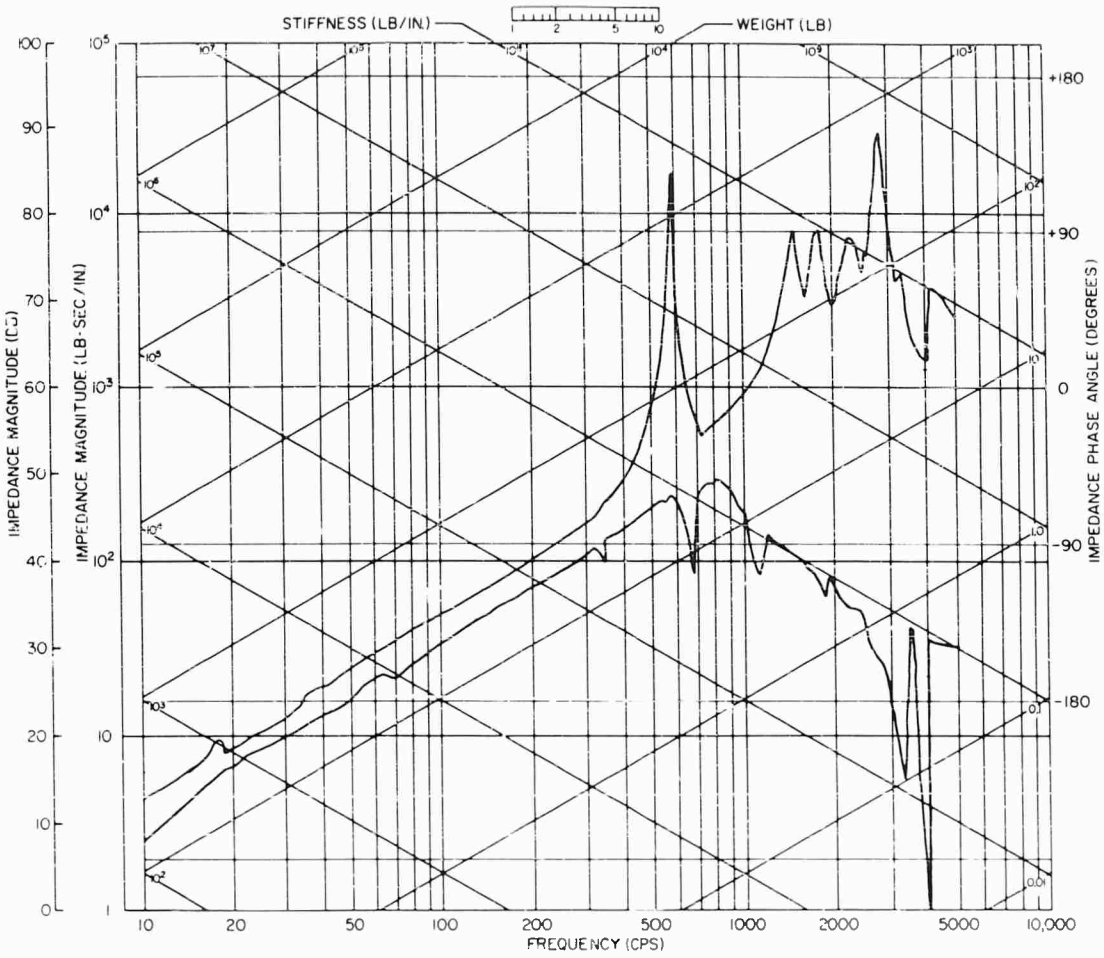

Fig. 5 - Envelope of impedance magnitude for Structure 1A

stiffness of an impedance head depends to a great extent on the area of contact; hence, variations can be expected with the use of different sizes of impedance heads. A calculated value, assuming a 1.5-inch diameter contact area, is roughly 4×10^7 pounds per inch; this stiffness corresponds to a peak at 3000 cps [3].

The contact stiffness is easily read from the log-log impedance plot, if the structure is mass-like, by extending the line of constant weight (corresponding to the dead weight of the structure) to where it intersects with the ordinate at the frequency of the peak. The line of constant stiffness passing through this intersection point corresponds to the contact stiffness.

A composite graph of the magnitude data reported for Structure 2B appears in Fig. 6. The impedance of this structure has seven peaks and seven notches over the frequency range measured, and seven peaks and notches were reported by most investigators. The very high dynamic range of the magnitude is seen in Fig. 6. The data ran off this graph in many cases, but this is not shown in the composite plot. The maximum dynamic range reported for 2B is 138 db. The average of the measurements on 2B is 120 db.

The spread of the envelope between the peaks and notches is considerable, but the values of magnitude reported for the peaks and notches are spread over a 25 to 35 db range. This is an astronomical error; however, the large dynamic range of this structure stretches the limits of even the most refined equipment.

Before we consider the causes of this difference in reported values, let us look at the envelope graph of Structure 3B. Magnitude, shown in Fig. 7, has a great deal of variation at frequencies below 100 cps (a factor of 10 or greater) and somewhat smaller variation at

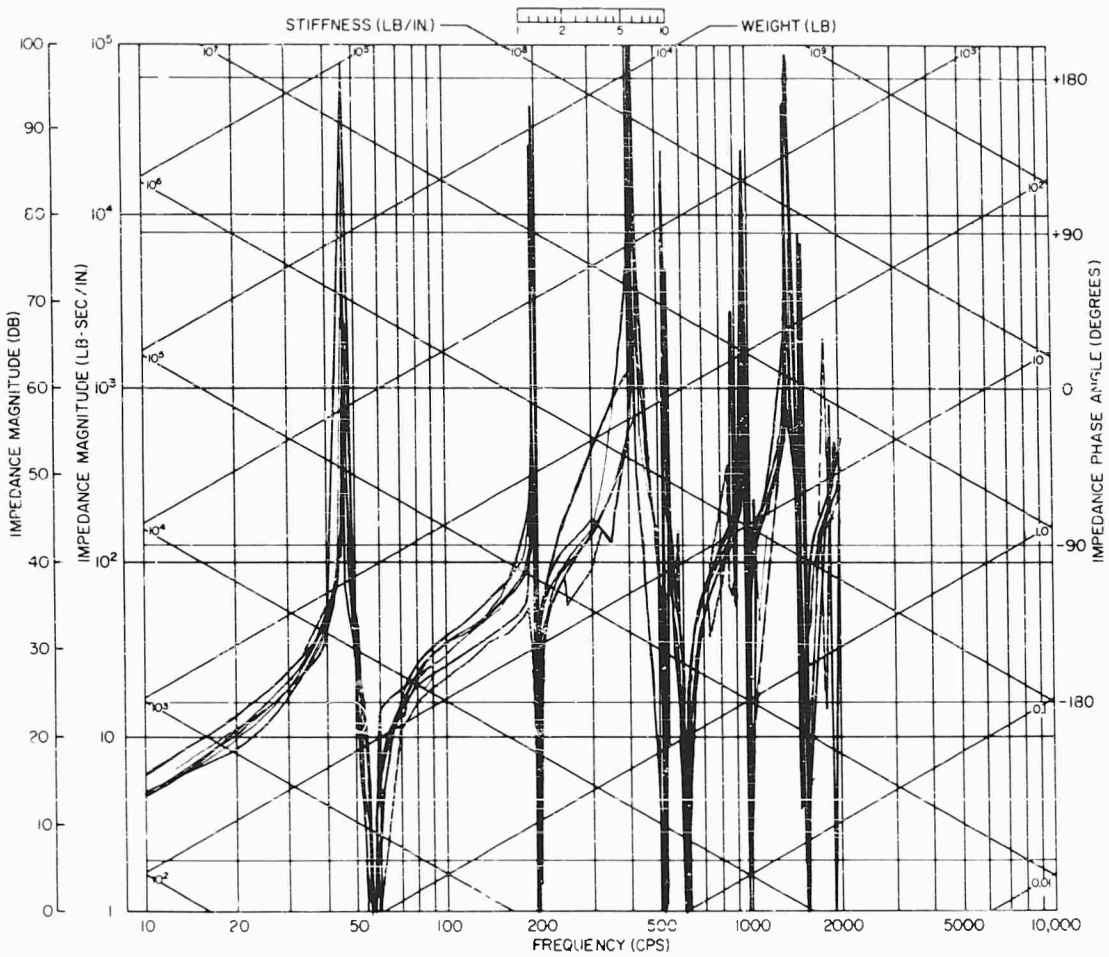

Fig. 6 - Envelope of impedance magnitude for Structure 2B

higher frequencies (roughly a factor of 3). This is to be expected for nonsymmetrical structures. In fact, this structure was designed to have large coupling with the driver and impedance head. Also magnifying the discrepancies is the small effective weight, which in turn is diminished somewhat by the large amount of damping present. Therefore, the attachment of an impedance head and shaker alters the boundary conditions of the structure and at least as many different results can be expected as there are driver-head combinations. This is also borne out in Fig. 8, since the phase envelope of 3B exhibits the same wild variations as the magnitude envelope.

It is interesting to note that the phase of 3B has a general tendency to shift past 0 degrees at only two pairs of frequencies. This is apparently due to the very large amount of damping present in the structure.

SPECIFIC EXAMPLES OF VARIATIONS RELATED TO RESPECTIVE PRACTICES AND TECHNIQUES

The repeatability of this relatively new field of measurement, as revealed by this 'Round Robin, is not as good as had been hoped for; however, with few exceptions this state-of-the-art had been expected by most active experimentalists. The source of much of this lack of reliability is found by examining the techniques and practices of measurement and noting their shortcomings.

Introducing fixturing — as depicted in Fig. 9 — between the face of the head and the test structure often has an adverse effect on the data. This conical adaptor reduces the inherent rigidity of the impedance head by introducing both a spring and extra mass. While the effect of a simple mass is easily canceled electronically,

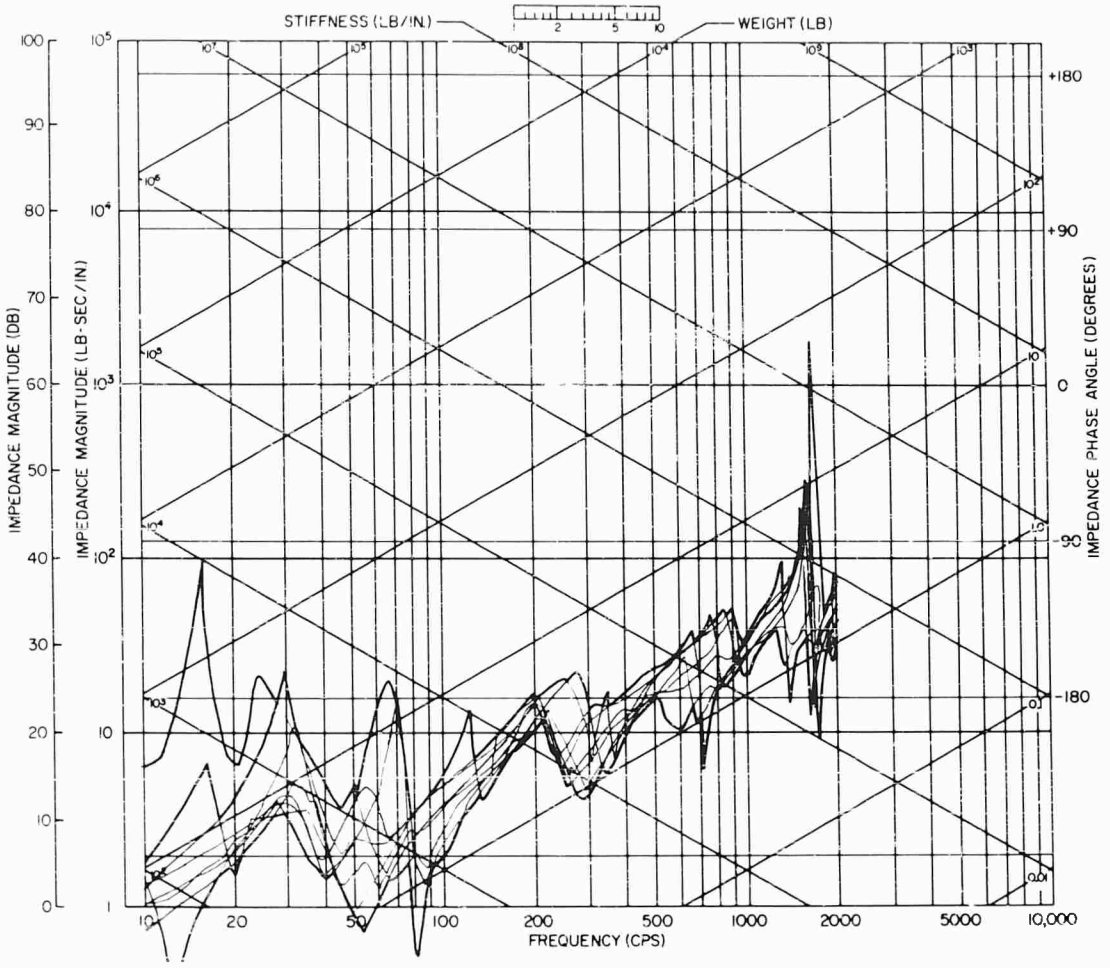

Fig. 7 - Envelope of impedance magnitude for Structure 3B

the effect of the spring-like character of fixing generally cannot be corrected.

Conical adaptors are supplied by impedance head manufacturers for measurements on specimens which require small contact area and, hence, are not extremely rigid specimens. In that case it is preferable to use a smaller impedance transducer. In general, conical adaptors should not be used for specimens like the Round Robin structures.

Figure 10 shows another example of unnecessary fixturing. This impedance head could have been attached to the adaptor plug directly. Blank plugs were provided for that purpose. Of secondary importance is the fact that this head is "medium sized," i.e., has a lower contact stiffness than that required for accurate measurements of a 25 pound structure over the frequency range considered in this project. One of the measurements made on the mass structure with this particular apparatus is shown in Fig. 11. The peak frequency of 584 cps corresponds to a contact stiffness of 8.7×10^5 pounds per inch. The data follow the weight line up to only about 200 cps.

A significant result of this program is to show that a widespread neglect of phase angle measurements exists. The phase plot corresponding to Fig. 11 is shown in Fig. 12. The dashed portion of the curve was estimated visually by using an oscilloscope. However, the reactance nulling technique was used for determining 0-, +90-, and -90-degree phase conditions. Several sets of phase data were determined without the aid of a phasemeter of any type. This is not recommended practice because the phase data must correlate directly with the magnitude data, as predicted by theory — and in this way serve as a self-check

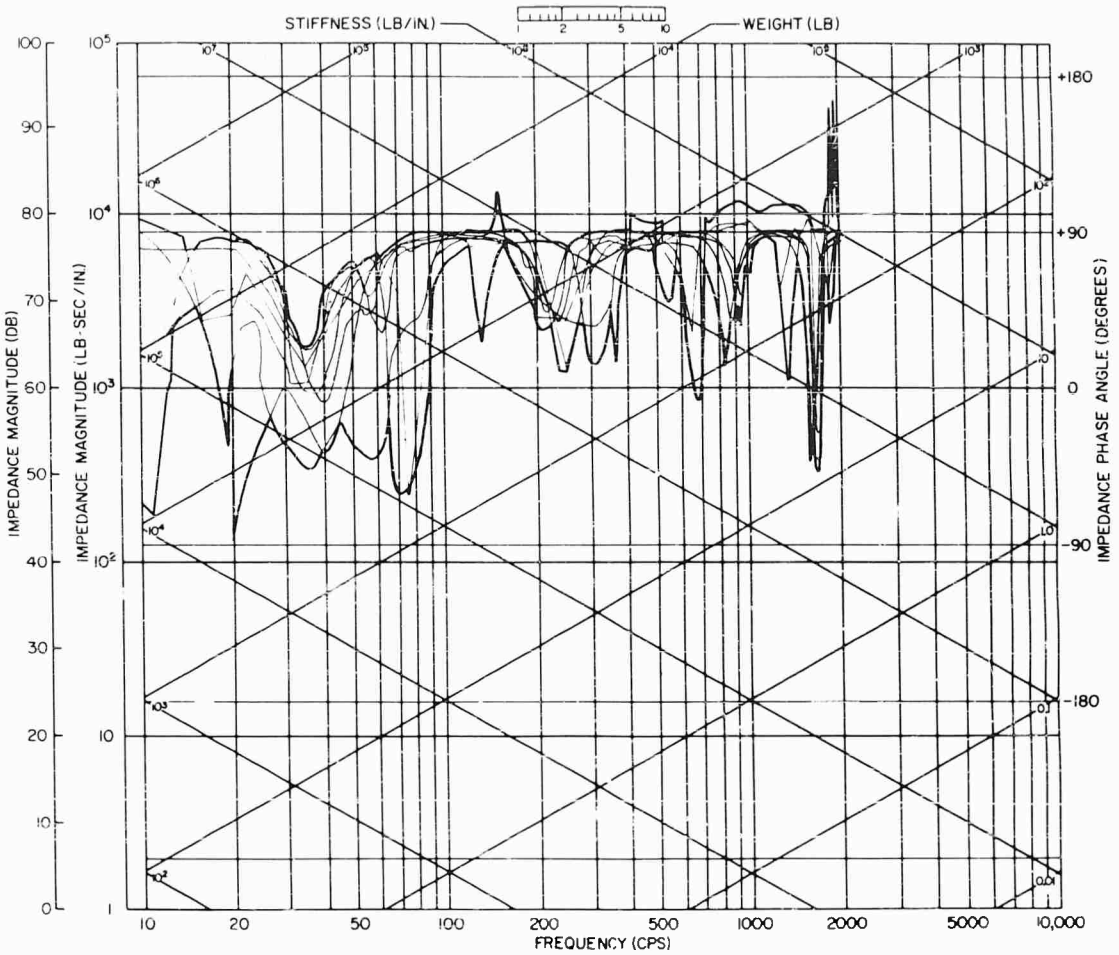

Fig. 8 - Envelope of impedance phase angle for Structure 3B

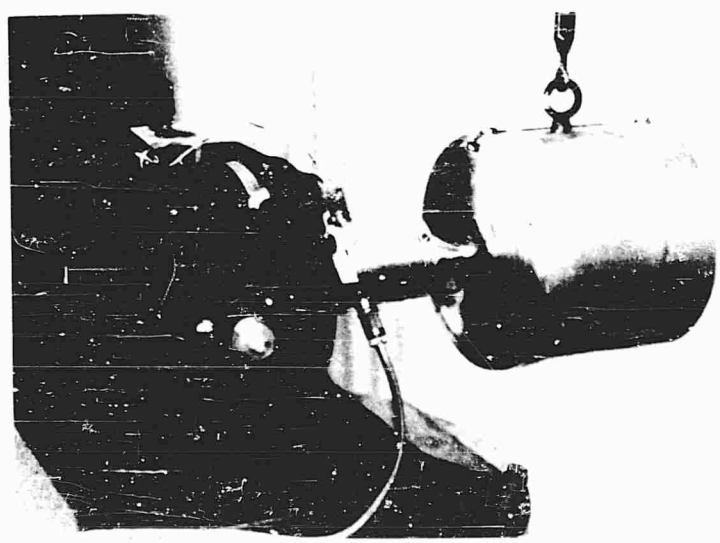

Fig. 9 - Fixturing between impedance head and structure

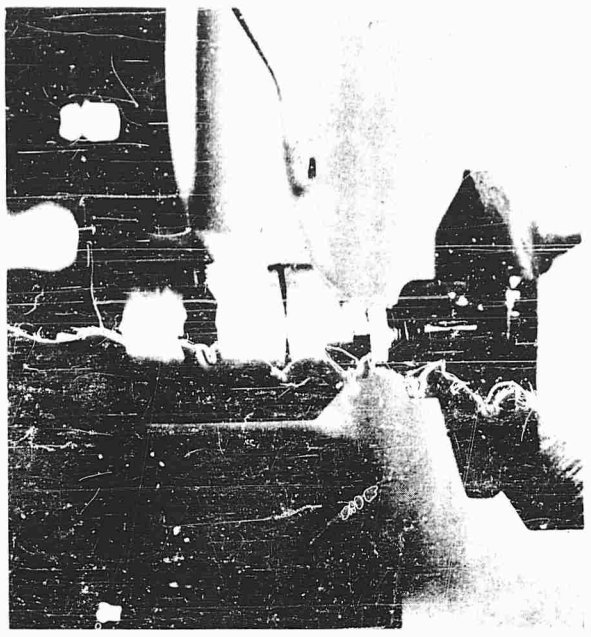

Fig. 10 - Faulty and unnecessary fixturing between impedance head and structure

on the measurements. But more importantly, many successful applications of impedance data depend on accurate knowledge of phase angles.

Another noteworthy fact is that four of the 19 participants did not use electronic filtering for either the force or acceleration signals. Even though the force input is a pure sinusoid, and harmonics and distortion are nearly always present. Data in Fig. 13 were measured without electronic filtering. A dip appears where the peak is expected. The existence of harmonics was reported in the remarks accompanying these data. Thus, it is easy to visualize this dip's occurrence -- the acceleration level at the driving frequency drops gradually to a very low value and suddenly the second harmonic appears and completely dominates. So a peak in impedance turns into a dip. This is not to say that every squiggle superimposed on a peak or dip is caused by a lack of electronic filtering; the dip-peak at 3200 cps has another cause. But electronic filtering of both channels is required if reliable impedance data are desired.

Shaker mounting, alignment, and suspension comprises another area in need of attention. The force generated should be uniaxial and free of lateral and rotational components or extra squiggles will appear in the data. This extraneous motion is easily seen on impedance plots of mass structures. One of the best sets of data, Fig. 14, contains an extraneous dip-peak at 3200 cps. The particular driver used here is of the same type and has the same suspension as that used to obtain the data in Fig. 13, which shows a similar squiggle at 3200 cps. Figure 15 shows the corresponding phase angle plot (to Fig. 14) without a complete phase shift at the squiggle frequency.

The conclusion that purity of shaker motion affected the spread of the data in this comparison is substantiated by noting the variety of force generators used by the participating groups. The shakers varied in maximum rated force output from 1/2 to 28,000 pounds. It is likely that each type of shaker has its own characteristics, so a considerable variation in forcing excitation could be expected. Also, large armature weight and corresponding stiff suspension required in large shakers designed for environmental testing are not generally well suited for impedance measurements on small structures.

Calibration errors contributed to the spread in the envelopes of these data. For example, the 2A magnitude data in Fig. 16 is nominally 6 db high. The low frequency effective weight of 65 pounds appears where the approximate scale weight of 31 pounds is expected.

A lack of resolution inherent in manual or point-by-point data contributed to the lack of repeatability in data for structures 2 and 3,

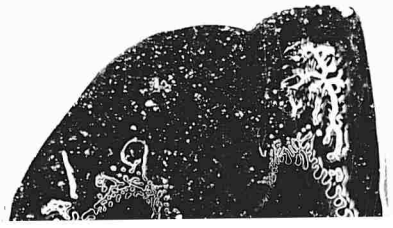

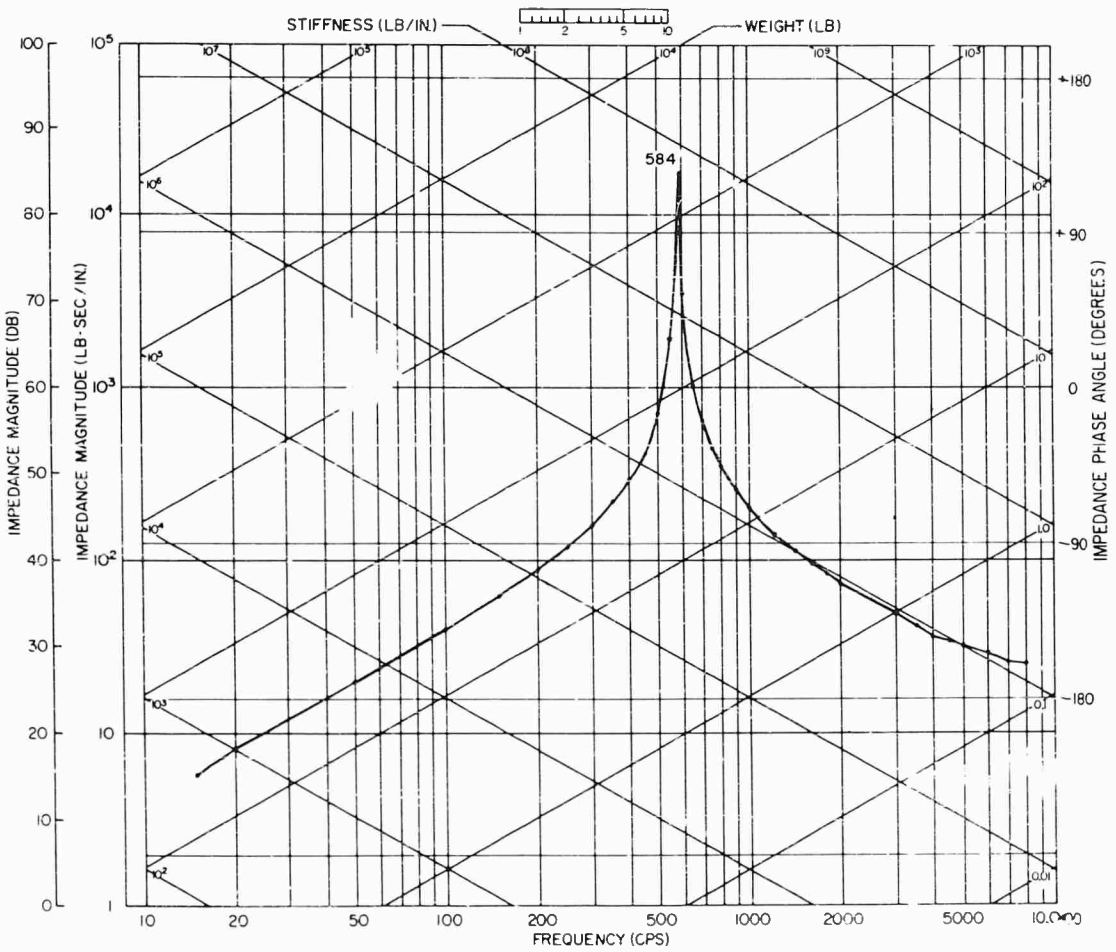

Fig. 11 - Impedance magnitude measured with faulty and unnecessa fixturing

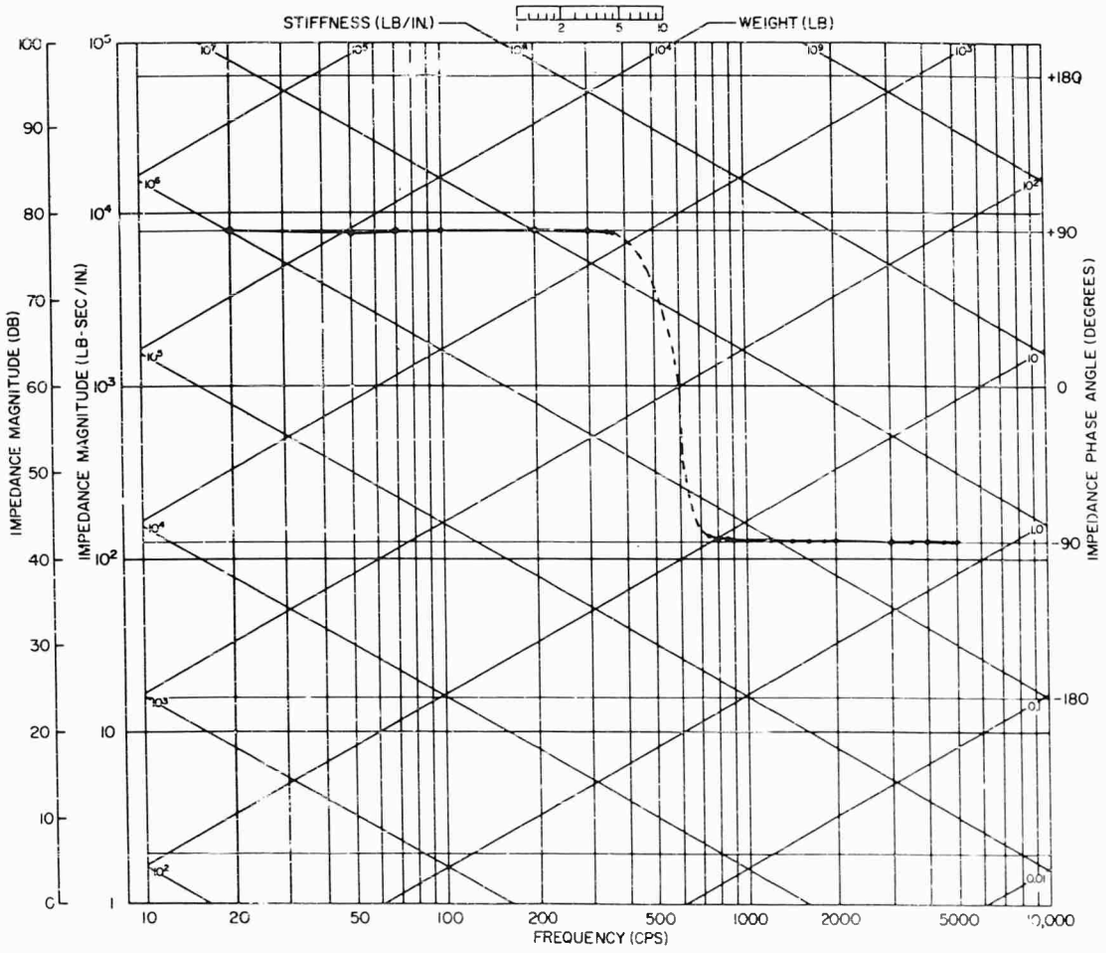

Fig. 12 - Impedance phase angle plot with estimated portion (dashed)

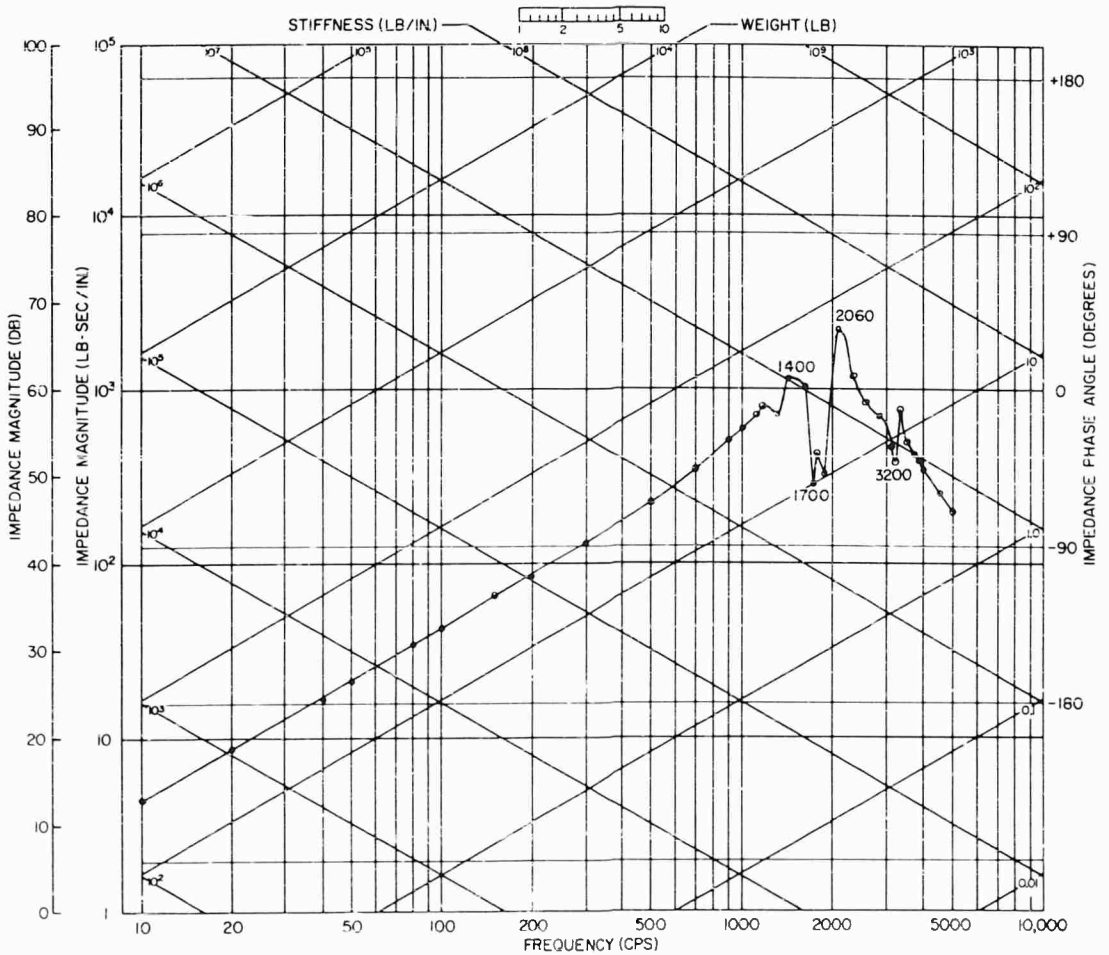

Fig. 13 - Impedance magnitude of 1A measured without electronic filtering

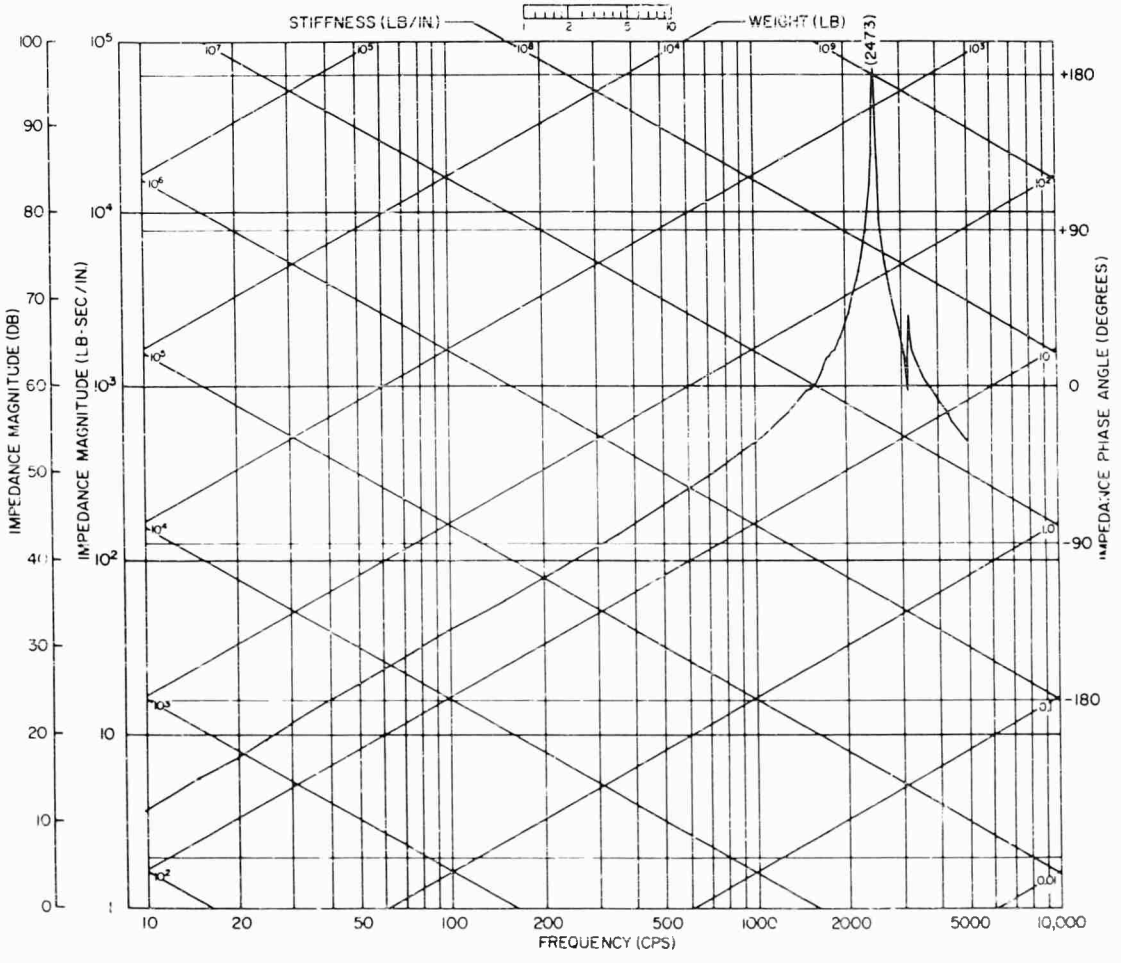

Fig. 14 - Example of good impedance-magnitude data for structure 1

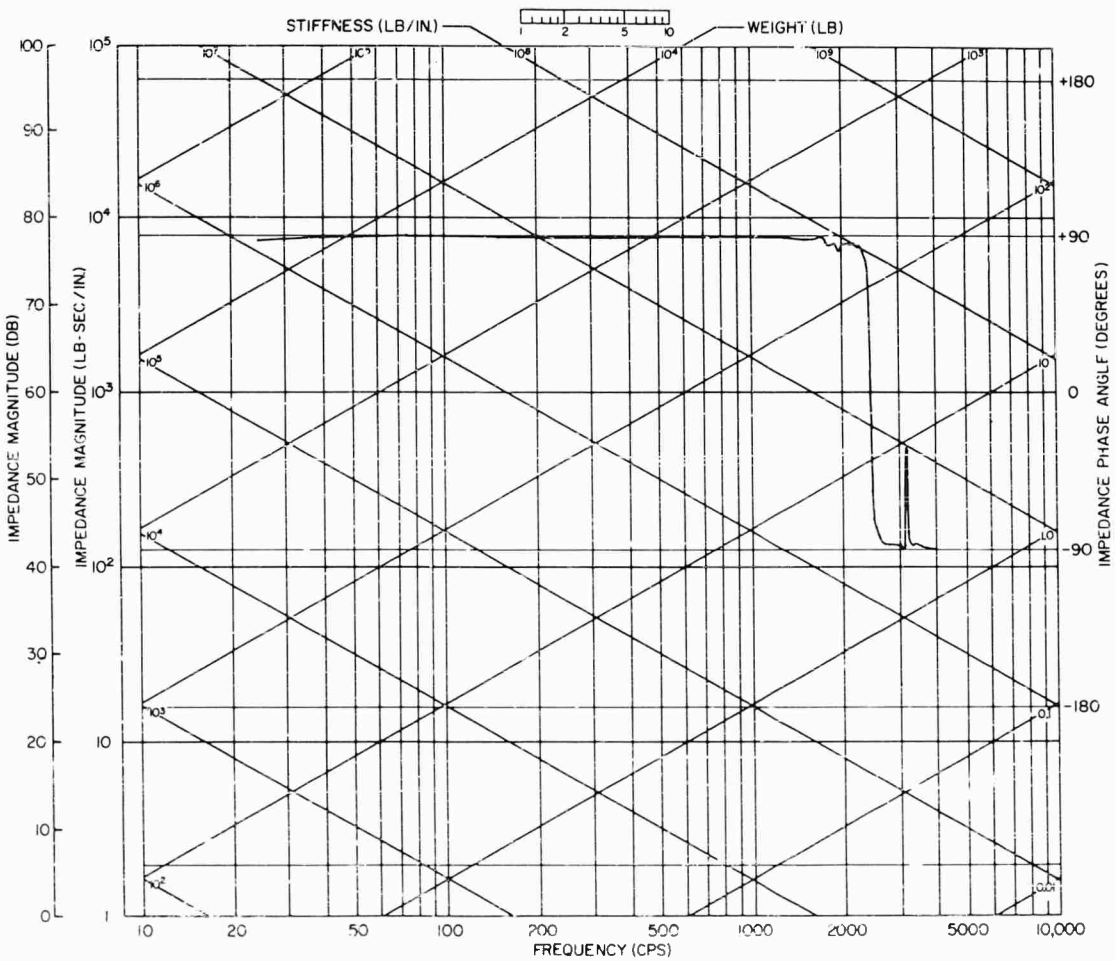

Fig. 15 - Impedance phase angle corresponding to Fig. 14

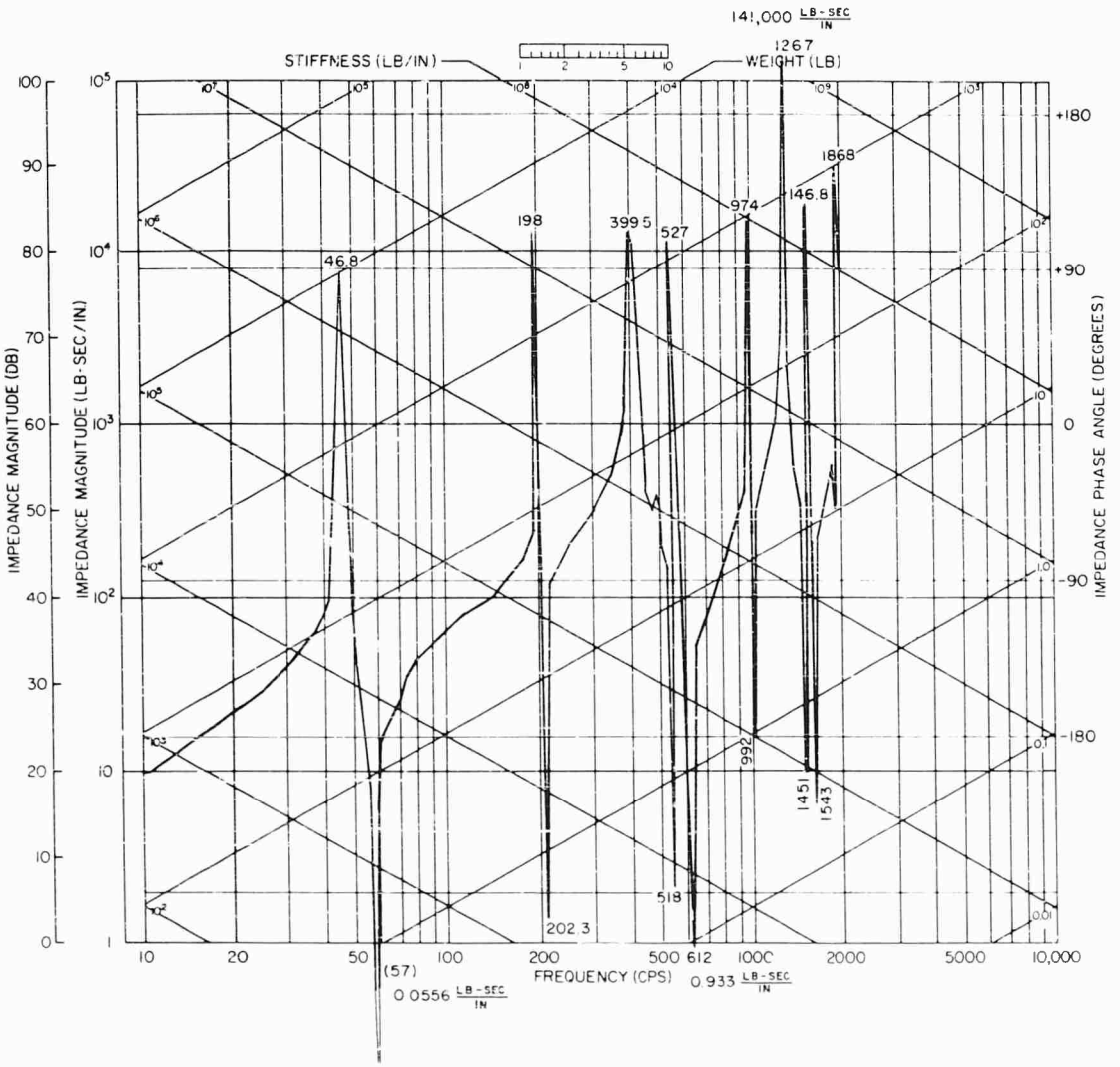

Fig. 16 - Example of calibration mistake in impedance magnitude

particularly. This is evidenced in Fig. 17, which show imaginative interpolation. It takes more than the 50 data points used here to resolve the impedance of a structure of this complexity.

Figure 18 (which is not the phase plot corresponding to Fig. 17) displays a similar quality in phase angle information for Structure 2A. This curve does not even pass through all 41 data points. Only one point was measured to verify the phase shifts in this case.

These two cases of inadequate point-by-point measurements emphasize the virture of automatic impedance plotting equipment in getting reliable data. The human endurance required in tedious manual measurements is considerable; the expense of equipment that will make simultaneous and continuous plots of magnitude and phase is quickly offset by time saved and by their quick-look capabilities for troubleshooting an experiment. This is not to say that automatic plotting equipment is necessarily, in itself, more accurate than all types of manually controlled electronics, for some of the best data of this comparison came from high-precision manual apparatus.

Occasionally one hears the question, "Why do you hold the force constant and record the acceleration instead of holding the acceleration constant while recording the force?" The result of such an attempt for the double C-spring structure is seen in Fig. 19. All peaks are clipped off simply because the 25-pound force generating apparatus in use did not have the capability to produce the range of forces needed to hold acceleration constant in a structure with

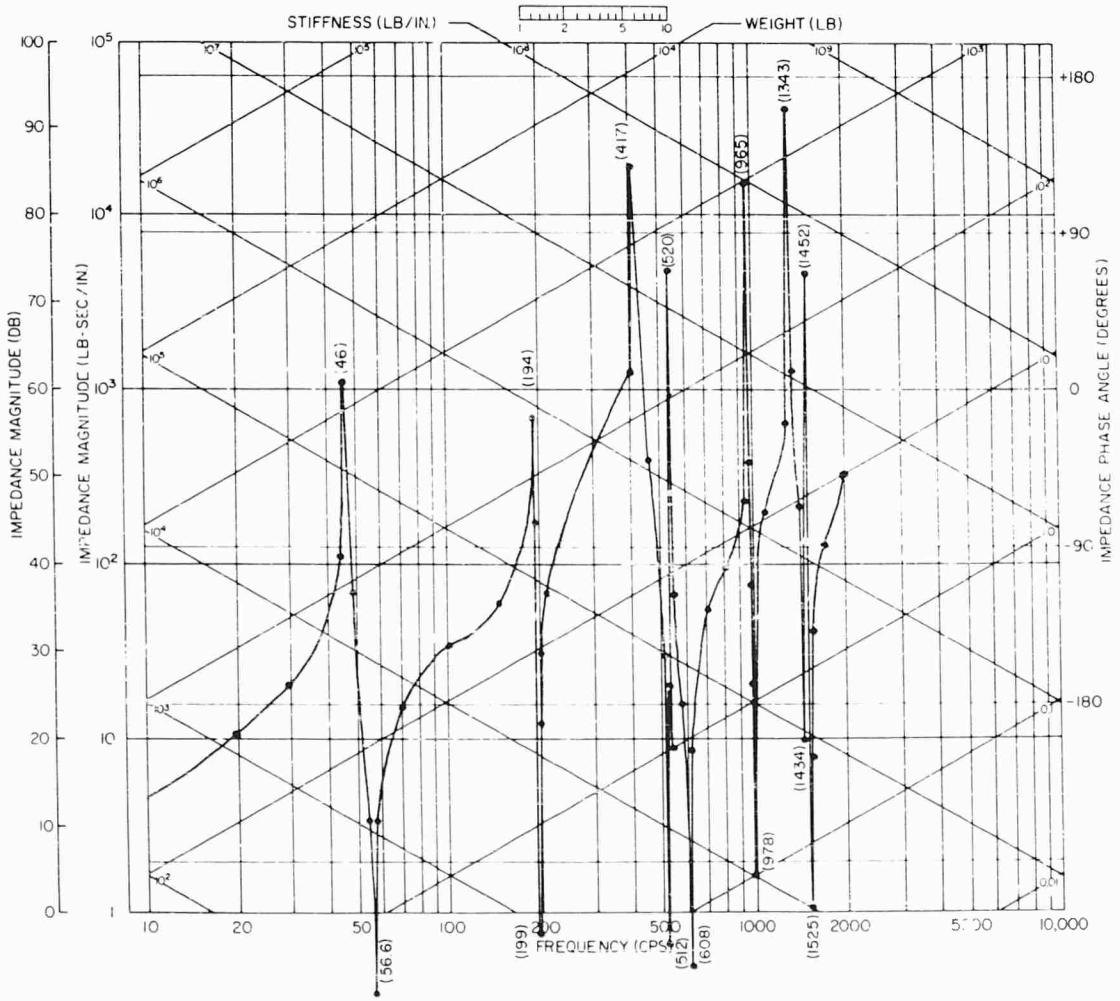

Fig. 17 - Example of inadequate resolution of impedance magnitude

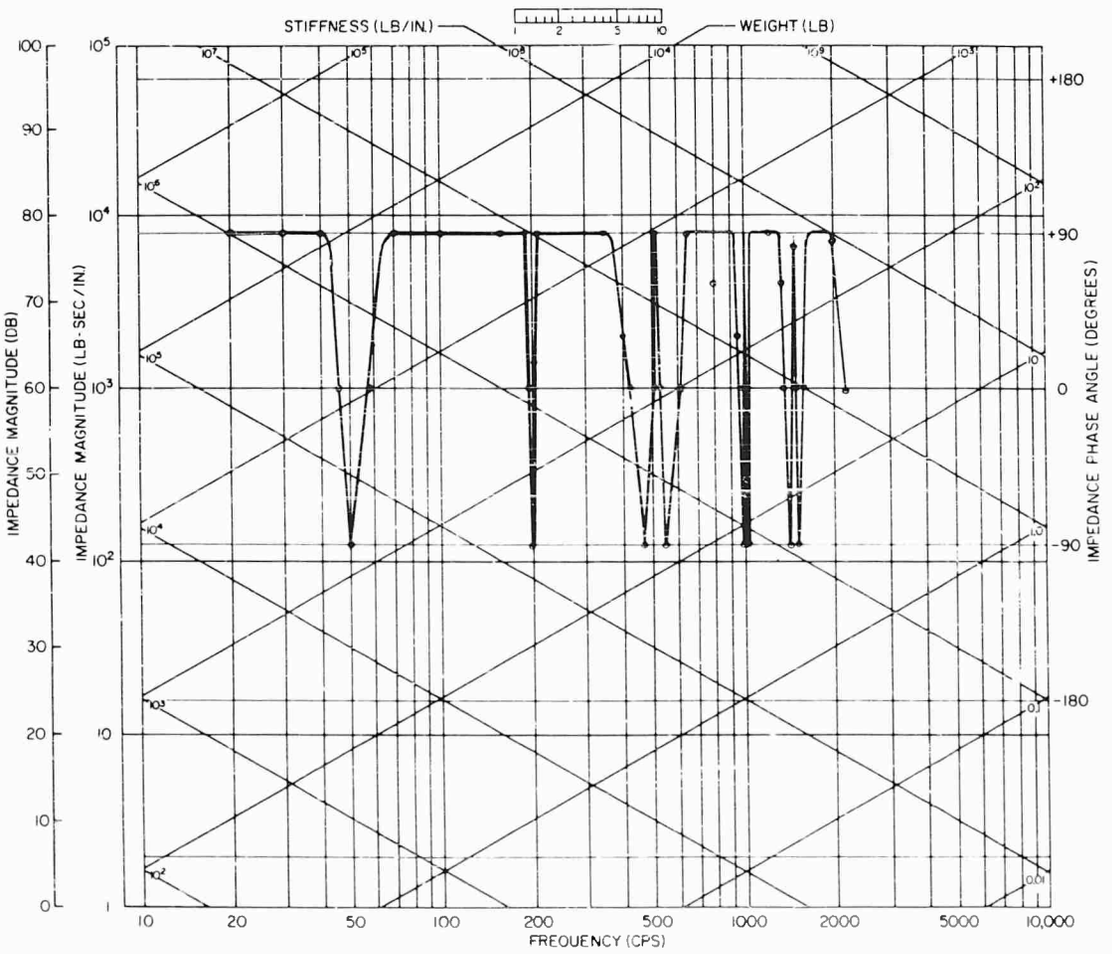

Fig 18 - Example of inadequate resolution of impedance phase angle

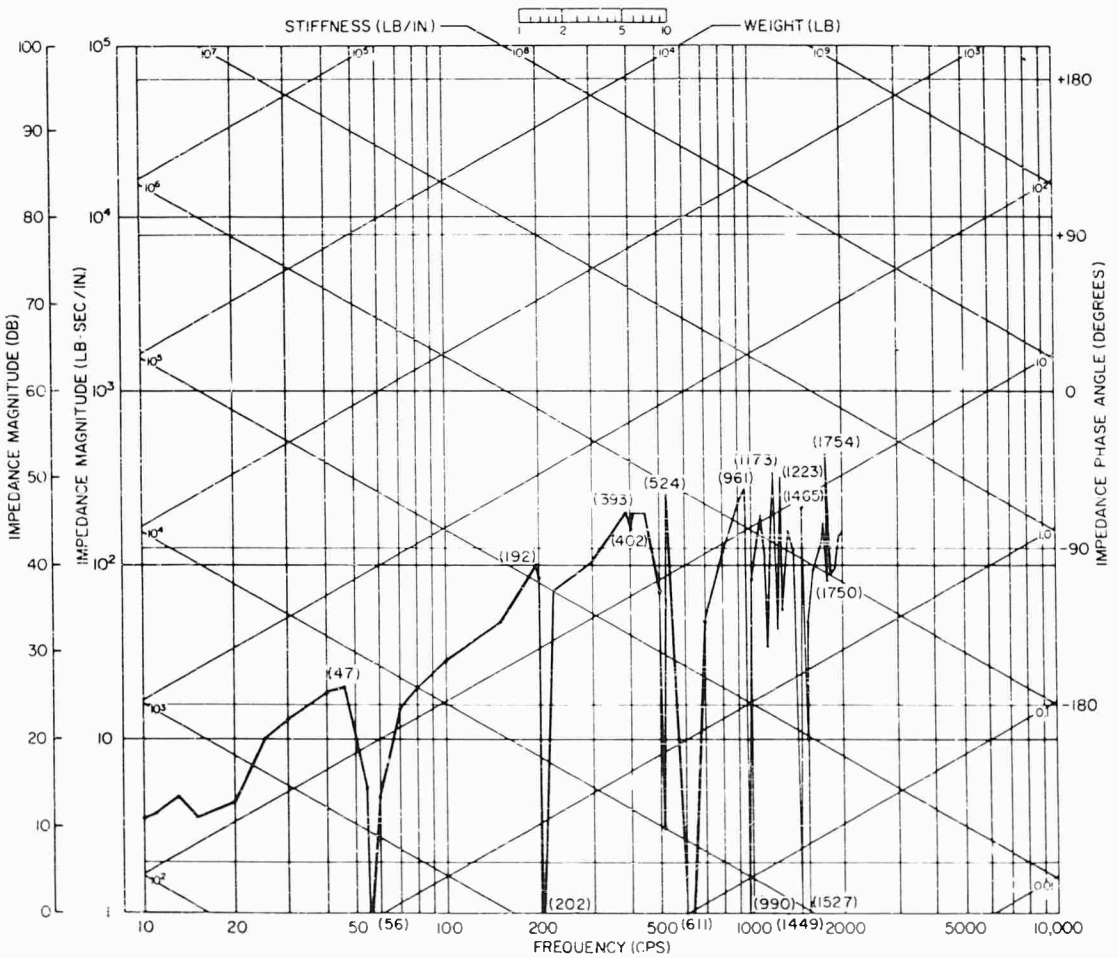

Fig. 19 - Example of impedance data gathered with compounded shortcomings in technique

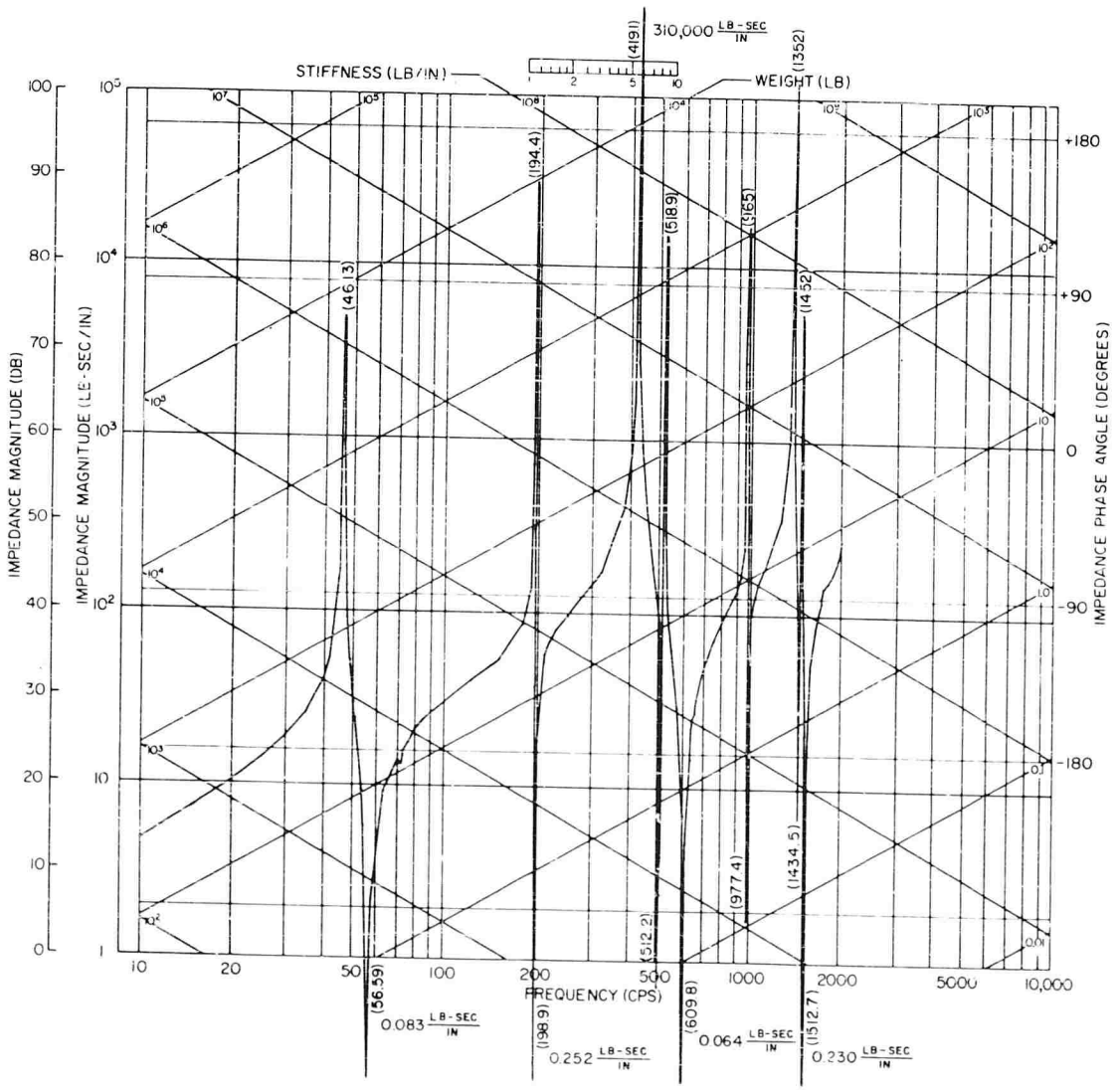

Fig. 20 - Example of best impedance-magnitude data

the dynamic range of 2A. In fact, no such system exists! Force tends to stay relatively constant even without regulation. Therefore, force can be regulated and only the widely varying quantity of acceleration need be recorded.

Two other practices, aside from holding acceleration constant, contributed to the complete ruination of the data of Fig. 19:

1. An unnecessary adaptor cone and a nut were inserted between the impedance head face and the specimen.

2. Neither force nor acceleration signals were filtered.

The preceding discussion has emphasized bad data in the hope that more attention will be focused on improved measurement techniques and practices. To gain perspective, Figs. 20 and 21 are presented as example of the best data collected in the Round Robin. A manual system was used, and enough data were taken for good resolution. The clarity of the graphs was enhanced by the use of a keyboard plotter.

SUMMARY

Reliable mechanical impedance measurements are rare if this Round Robin comparison is an accurate indication. The state of affairs in this relatively new area of measurement can be greatly improved simply by avoiding bad techniques. A list of factors is offered in Table 2 as a rule-of-thumb guide for more repeatable measurements. There are many other areas of difficulty needing improvement and research; however, great gains in reliability and repeatability can be made by following these ten recommendations.

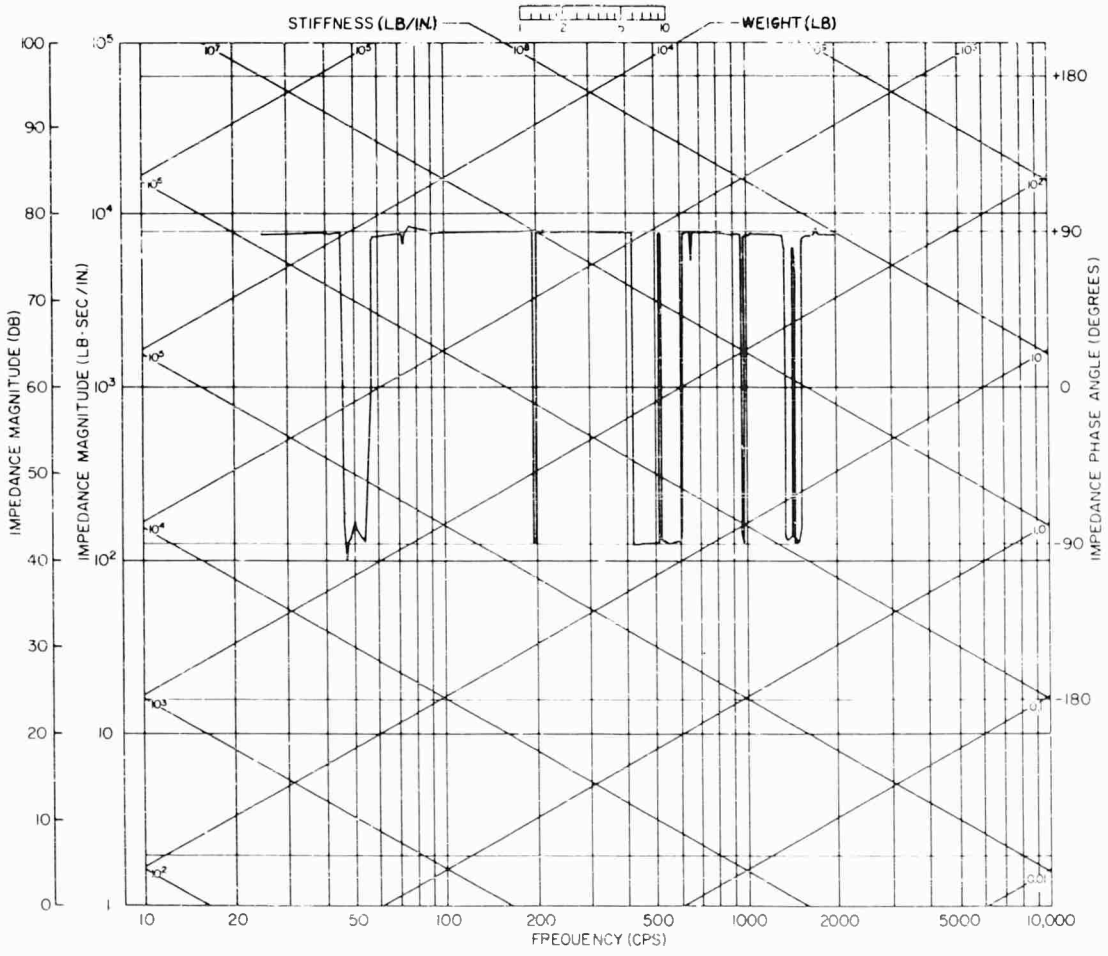

Fig. 21 - Impedance phase angle corresponding to Fig. 20

TABLE 2

Recommendations for Reliable Mechanical Impedance Measurements

1. Recognize limitations of impedance heads, electronics and force generating apparatus and use proper type of equipment for job.
2. Recognize effects of impedance head and shaker on boundary conditions and take steps to avoid coupling between shaker and structure and avoid changing structure stiffness by attachment of impedance head.
3. Introduce no unnecessary fixturing between the impedance head and structure.
4. Carefully align and suspend force generator so only a pure, lineal sinusoid is produced.
5. In general, servo force, not acceleration.
6. Filter both force and acceleration signals before regulation and before recording magnitude and phase.
7. Cancel effects of mass below force gage.
8. Calibrate entire system by measuring impedance of a "rigid" test weight before and after each data run.
9. Record sufficient number of data points for good resolution of magnitude and phase; use slow enough sweep rate for accurate resolution at peaks and dips if automatic plotter is used.
10. Pay extra attention to measuring accurate phase angles. Herein lies the key to success of many applications using circuit theorems of Thevenin and Norton.

REFERENCES

1. R. O. Belsheim and G. M. Remmers, "Results of the Mechanical-Impedance Round-Robin Measurements," Paper presented to 68th Meeting of Acoust. Soc. Am. Austin, Texas (Oct. 22, 1964).
2. R. O. Belsheim and G. M. Remmers, "NRL-ASA Round-Robin Mechanical Impedance Comparison," NRL Report, to be published.
3. F. Schloss, "Recent Advances in the Measurement of Structural Impedance," DTMB Report 1584 (Jan. 1963).
4. D. V. Wright, J. G. Akey, D. F. Miller, and A. C. Hagg, "Vibration Transmission and Impedance of Basic Foundation Structures," Westinghouse Res. Lab. Report 62-917-515-R1, pp. 231-232 (Oct. 1962).

DISCUSSION

Bouche (Endevco Corp): First of all, I would like to compliment you on doing a very good job of collecting these data, running the program, and reporting on the results. I notice in your presentation that you did discuss in detail some of the shortcomings of making mechanical impedance measurements; however, some of the slides showed particularly good agreement among many of the participants. Perhaps a little more discussion should be given on how well some agree as well as on those certain parts which disagree. I have a short two-part question. First, which of the three structures do you consider to be most typical of structures in the field; second, on which of the three structures were the data most in agreement from the various experimenters?

Mr. Remmers: I consider Structure 3 to be the most typical of those in the field because of its lack of symmetry. The agreement is quite good, if you pick the curves that agree; but once you pick two or three, you will find that one agrees in one portion of the frequency range, yet it might not agree in another portion of the frequency range. If you try to do this you are somewhat in a dilemma as to which ones to choose.

Dr. Mains (GE): Those curves that agreed best with each other in general were curves where identical impedance heads were used, is that not true?

Mr. Remmers: Not always.

Dr. Mains: Was there a significant agreement where markedly different impedance heads were used?

Mr. Remmers: Yes, there was a difference in the curves if the impedance heads were different in size. However, some very good results were obtained with certain types of heads in one case, where in the next case they were completely nullified by all other factors that must be taken into consideration. There are many details which have to be in place before you can get reliable measurements. One couldn't come up with a definite recommendation for a particular brand or type of equipment from the data.

Mr. Clevenson (Langley Research Ctr): You mention that many reliable results were obtained with different kinds of heads. Will you define which of the results you would consider as reliable since you had such a wide variation of results?

Mr. Remmers: Yes, I showed you slides of data taken on Structure 1 and Structure 2 which I consider to be reliable. I showed you two slides in the presentation taken on Structure 1. I think it is 2B-8 or set B, participant No. 8.

Mr. Clevenson: I recall seeing those. What was your basis for calling those reliable?

Mr. Remmers: I called them reliable by looking over the techniques used by the participants and procedures used. In most cases, one could find a serious defect in technique, but in that particular instance I didn't. That was the real criterion I used for determining which data I thought were best. It is based on my own judgment.

* * *

RESONANCE FREQUENCY OF LARGE SOLID PROPELLANT ROCKET MOTOR DETERMINED BY MECHANICAL IMPEDANCE

L. G. Flippin, L. W. Gammell, and G. S. Stibor
Thiokol Chemical Corporation
Wasatch Division
Brigham City, Utah

This paper presents the problems associated with vibration testing of full-scale Stage I MINUTEMAN motors. Vibration testing demonstrates the capability of the motor to perform its intended function after having undergone extensive dynamic loading simulating a transportation and handling environment. Solutions to these problems are discussed, in addition to test specifications, tooling, instrumentation, data acquisition, test procedures, and results.

INTRODUCTION

During the early development of the MINUTEMAN ICBM Weapon System, it became apparent that the separate stages, as well as the integrated missile, would be subjected to extensive transportation and handling environments during manufacture and final deployment. The effect of these transportation and handling environments on the reliability and end performance of the solid propellant rocket motors had to be determined.

Virtually no background information or reservoir of experience was available on which to base predictions of the durability of large solid propellant rocket motors when subjected to long-term shock and vibration. Detailed analyses were conducted wherever material stresses could be determined in response to known dynamic loads for the Stage I MINUTEMAN motor. These stresses were then compared to the basic fatigue limits of the material.

Stress problems readily lend themselves to analysis for simple beam-like structures; however, solid propellant rocket motors are complex structures, comprising a thick, cylindrical, rubber-like propellant grain bonded to a thin outer shell with a variable thickness bonding liner. Key areas of the case are insulated with a rigid material bonded to the shell interior. The large mass of viscoelastic propellant within the case has a star-shaped core chamber through the center. With such a composite structure, the classical Bernoulli-Euler beam analysis was considered inadequate to describe the dynamic translatory response of the rocket motor, even when the envelope geometry was idealized to that of a composite cylinder.

Thiokol engaged a consulting service in applied mechanics (Dyna/Structures, Inc.) to perform an analysis for predicting the dynamic response of the Stage I MINUTEMAN motor when subjected to a dynamic input.

A more exact analysis was used that took into account the effects of rotatory inertia and transverse shear deformation. Since the analysis was based on assumptions, some of which were questionable, full-scale vibration tests were required for verification. Some of the assumptions requiring verification were:

1. Does the propellant and case respond together as a beam?

2. Is the motor response a linear relation to the input force?

3. Does the predicted response of the idealized model match that of the actual motor?

The vibration tests were also used to verify the predicted resonant frequencies, case bending stresses, and case deflections. Propellant stresses or strains cannot be measured with current instrumentation; however, the computed values of propellant stress can be relied on if

the correlations between the idealized mathematical model and the actual motor are close for all other parameters.

Thiokol conducted air shipment, road, and multibump board course tests to determine the typical dynamic environment and the capability of the Stage I motor to withstand actual field conditions. Although useful information was obtained from these tests, the specimen sampling was insufficient in quantity to provide reliable conclusions. Motors tested in subsequent static firing performed well, but the margin of safe, reliable operation was still unknown. Environmental data from these tests could not be used for verification of the analyses because of frequency limitations.

At the direction of the U.S. Air Force Ballistic Systems Division (BSD), Thiokol designed and constructed a vibration test laboratory at the Wasatch Division with the capability for testing large rocket motors. This facility was initially used to conduct more sophisticated vibration tests on Stage I MINUTEMAN motors, under closely controlled test conditions.

This paper describes the problems encountered and the results obtained from the vibration tests of the Stage I MINUTEMAN motor.

DISCUSSION

Specifications

Prior to the development of the MINUTEMAN and POLARIS Weapon Systems, no standard military specifications had been written for vibration testing of large solid propellant rocket motors. The first task, then, was to write an applicable specification for research and development type vibration testing of these large motors. Thiokol realized that this specification [1] would require revisions from time to time as experience and knowledge were gained on the dynamic behavior of this type of vehicle; therefore, the specifications were based on the test objectives established by BSD in concurrence with Thiokol. These test objectives were to determine the resonant frequencies and corresponding mode shapes, the linearity of the response and the relative response of the propellant with the case, and to verify the computed displacements and stresses of the rocket motor.

Test Equipment

Once the test objectives were established and the test specifications documented, suitable vibration test equipment had to be designed and fabricated. This equipment included a suspension system for supporting the rocket motor during testing, force transmitting equipment for transmitting the output of the force generator to the test specimen, and safety equipment to restrain live motor specimens in case of an inadvertent ignition during testing.

The rocket motor was suspended by cables from a soft liquid spring suspension system with a calculated natural frequency below the proposed test frequency range to prevent feedback from the support structure. High-force drive rods for transmitting the exciter output force to the specimen loading fixtures were designed and fabricated for high-load fatigue and linearity of response tests. This loading included forces up to 100,000 vector force pounds. Low-force drive rods were designed and fabricated for resonance search tests at moderately high forces up to 30,000 vector force pounds. Loading or force input fixtures were designed for both longitudinal and transverse test configurations.

A cast aluminum cone force adapter was designed as an input fixture for the longitudinal test configuration, in which the stimulus is applied parallel to the longitudinal axis of the test specimen. This design proved to be adequate, exhibiting no major resonances throughout the test frequency range (Fig. 1). Two methods of applying the stimulus to the motor specimen in the transverse plane were considered. In the first design, large hard rings were considered as input fixtures. After further study, it was found that these rings might resonate at a frequency within the test frequency range and obscure the drive signal to the motor specimen even if they were large and heavy. A second design evolved consisting of aluminum drive shoes strapped to the motor with thin steel straps pretensioned beyond the dynamic driving force. This design proved to be workable and allowed the motor freedom to assume its natural mode shape corresponding to the forcing frequency. The drive shoe has a 90 degree contact surface on the motor and did cause some local distortion of the motor case at the higher forcing frequencies. A safety restraint harness (Figs. 2 and 3) was designed to restrain the motor in case of an accidental ignition.

Instrumentation

The proper type and amount of instrumentation had to be selected to measure the response

NOTE: References appear on page 72.

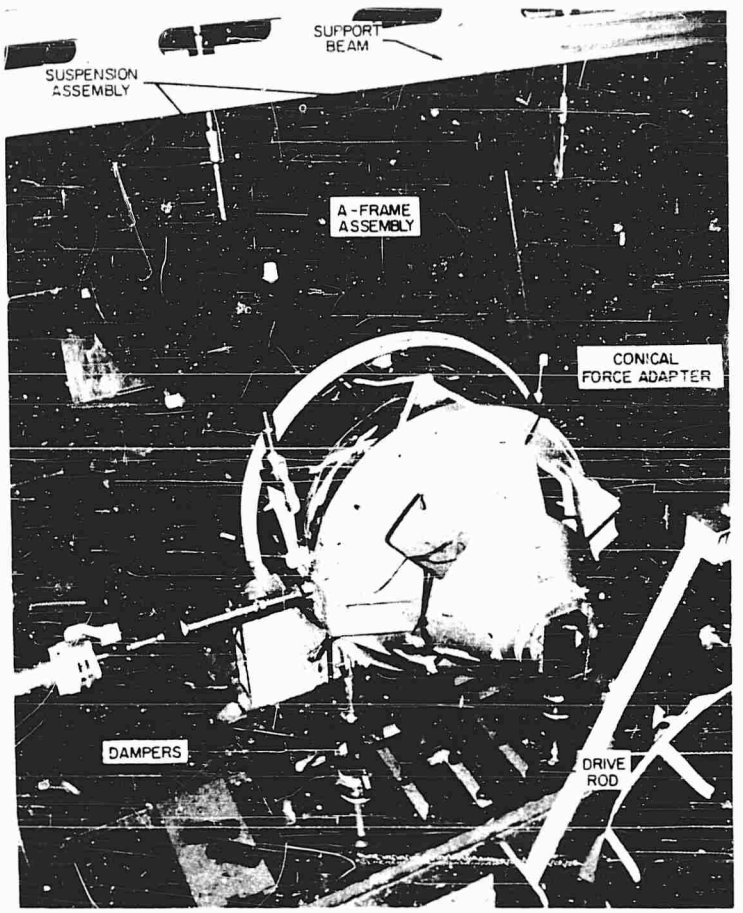

Fig. 1 - Longitudinal test configuration

of the rocket motor case and propellant during vibration testing. The amount of instrumentation required to define at least the first three elastic modes was selected. Since the responses of the entire propellant had to be measured, a method of embedding vibration measuring instruments within the propellant was required. A method of mounting instruments on the propellant surface had been developed during road and multibump board course testing. The Gulton (part number TA-32106) piezoelectric triaxial accelerometer [2] was selected for embedding in the propellant. The internal instrumentation embedment design concept is illustrated in Fig. 4. The test equipment was also instrumented and the responses were measured during each test.

Data Acquisition System

An 80-channel digital data acquisition system was selected for recording the rocket motor and dynamic test equipment responses during vibration testing. This system was selected because of channel capability, system accuracy, versatility, and the reduction in man-hours required to reduce the raw data to engineering units (Tables 1 and 2). A 48-channel oscillograph recording system was used as an interim system until the digital system became available. After the digital system was installed, the recorders were retained for backup and to increase channel capability. This approach proved valuable as the test progressed.

The size and complexity of the test specimens necessitated a significant number of data points to establish an accurate response curve, especially for higher order modes. Several response curves had to be obtained simultaneously for establishing characteristic relationships, such as the relationship of case behavior to propellant behavior. When the 80 digital channels are used in conjunction with the oscillograph recorders, a maximum of 128 channels of information can be recorded.

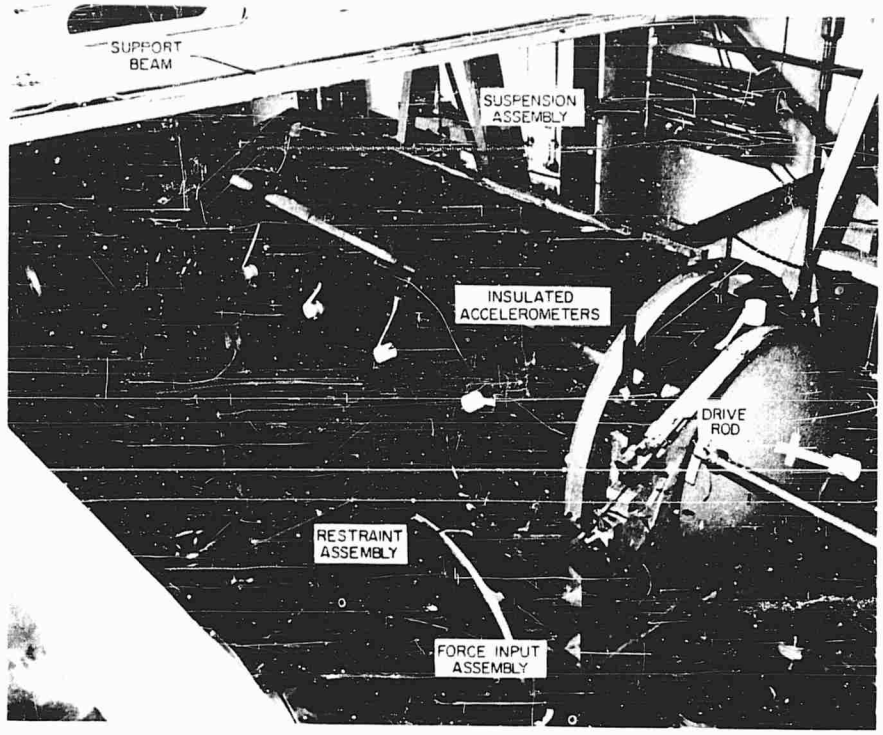

Fig. 2 - Transverse test configuration

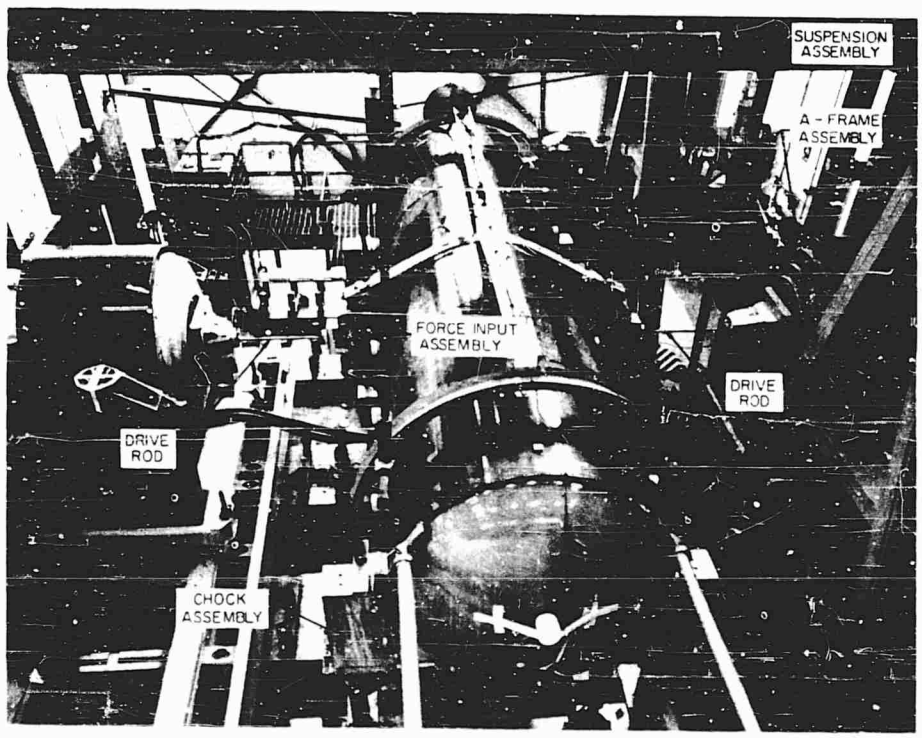

Fig. 3 - Center test configuration

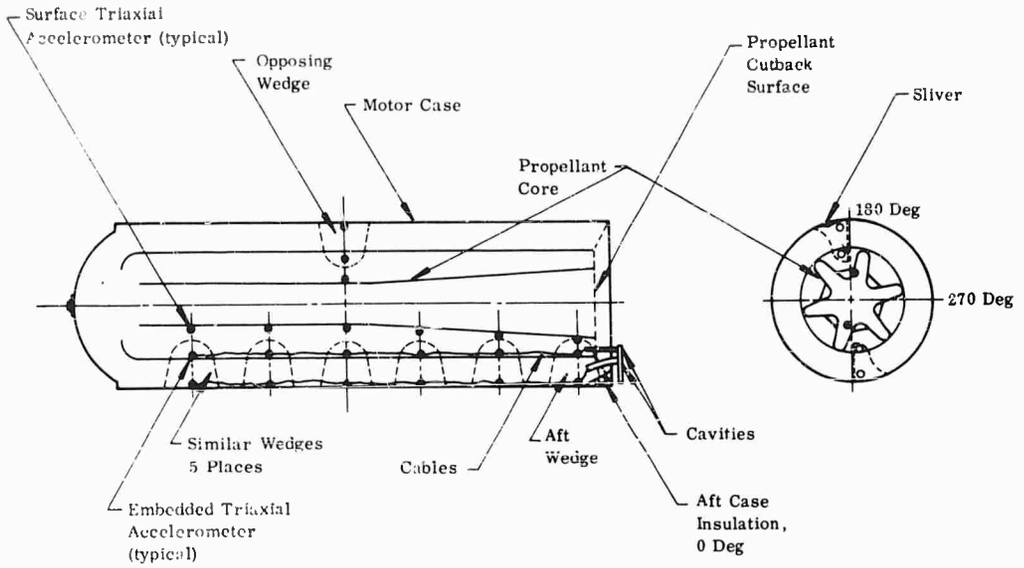

Fig. 4 - Internal instrumentation design concept

TABLE 1
Channel Capability

Transducers	Channels	Total Channels
Piezoelectric Accelerometers	1-46	46
Strain Gage Accelerometers	47-60	14
Strain Gage (Single Element)	61-76	16
Thermocouples	77-80	4

TABLE 2
Recording and Plotting Capability

Transducer Output	Ordinate Parameter	Abscissa Parameter
Acceleration	Amplitude Phase Distortion Amplitude Ratio	Time Transducer Location Frequency
Strain	Amplitude Phase Distortion	
Temperature	Amplitude	

The accuracy of the digital system is also n attractive feature. True root-mean-square r peak measurements for amplitude of acceler-tion, strain, displacement, and temperature or mplitude ratios can be obtained within ±1 per-ent accuracy. Also obtainable are phase meas-rements within ±5 percent with 100 percent distortion and within ±1 degree accuracy with 50 percent distortion on both the data and reference channels. This accuracy is possible because everything except the fundamental sine wave is filtered out for phase measurements. Distortion measurements can be obtained within ±3 percent accuracy for the range of 0.1 to 100

percent distortion. Frequency readings can be obtained within ±2 percent accuracy for the frequency range of 2 to 2,000 cps.

Another desirable feature is the versatility of the digital system. Any number of instrument channels from 1 to 80 can be stored on punch tape and/or plotted on an x-y plotter during a test. Direct read-out in engineering units is displayed for all parameters during the test. The data stored on punch tape may be plotted on x-y plots at a later date, choosing any one parameter, any group of parameters, or all of the parameters measured. The capabilities of the x-y plots are explained in Tables 1 and 2.

The digital data acquisition system also eliminates time-consuming and expensive hand reduction of raw data. The digital display and x-y plots are in engineering units and the system is compatible for use with a direct print-out system if the data are required in tabular form (Fig. 5).

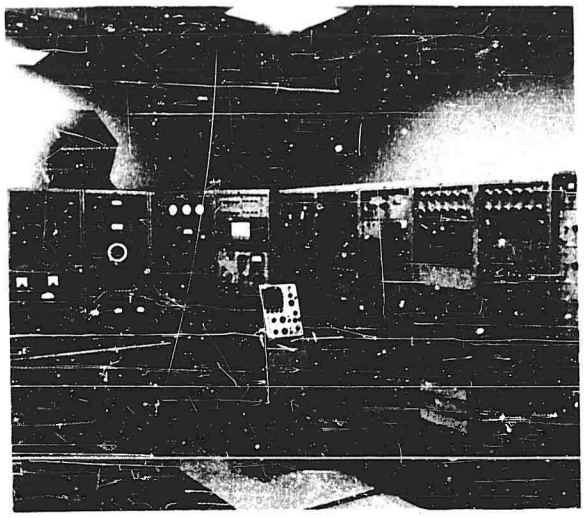

Fig. 5 - Control panel and data acquisition equipment

Test Procedures

Two basic test procedures were used in the MINUTEMAN test program. Each of these techniques was based on a different test philosophy. Early in the test program, all tests used a constant, automatically controlled, acceleration input to the test specimen. The block diagram in Fig. 6 illustrates the basic system used.

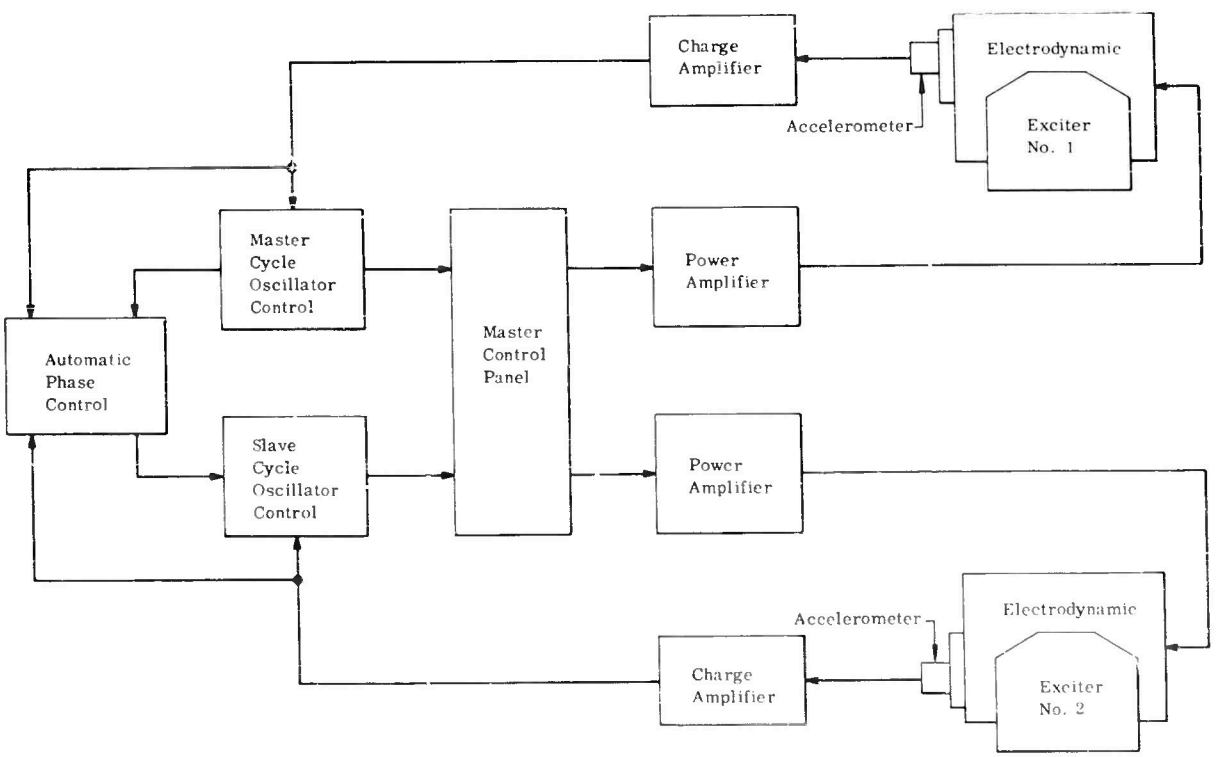

Fig. 6 - Constant acceleration-system signal flow diagram

By first performing frequency sweeps, the resonant frequency areas should be pinpointed by high acceleration amplitudes and phase shifts. These areas would then be investigated at discrete frequencies. This method should determine the frequency at which any change in the forcing frequency would cause a decrease in the amplitude of response of the specimen, indicating a resonance.

When this technique was first tried on a rocket motor specimen, several serious problems became immediately apparent. The instruments located on the rocket motor to measure the motor response to the applied stimulus would not reach a minimum or maximum response amplitude at the same frequency or instant in time. This seemed to indicate an unstable condition through some frequency ranges. The cause of this instability was not readily apparent but was later determined to be an unbalanced condition amplified at an antiresonance. The exciter power amplifier drew maximum current during these periods of instability, indicating a maximum force output by the exciter. A moderate increase in the response amplitude accompanied this phenomenon. At other forcing frequencies, the exciter power amplifier current draw apparently dropped to zero, and a moderate increase occurred in the response amplitude. Both of these conditions were accompanied by phase shifts.

Since the acceleration level is automatically controlled for this technique, no sudden amplification of the response is experienced at resonance. Only at resonance, a small force is required to drive the specimen, and as the amplitude of the response increases and the specimen becomes easier to excite, the force output of the exciter is automatically reduced, preventing any large buildup in amplitude. The change in amplitude is gradual and the peak appears to hold over several frequencies before slowly decaying. This prevents accurate determination of the exact frequency at which resonance occurs. When the motor response was plotted, the response curves showed no discernible differences over several frequencies. A more sensitive method of determining resonant frequencies and distinguishing between resonant and antiresonant conditions was required. The response of the motor specimen through several frequencies where there is an amplification buildup is shown in Fig. 7.

After a thorough search of available literature, it was decided that the driving point mechanical impedance would provide the necessary sensitivity required for pinpointing resonant and antiresonant frequencies. Since the driving point mechanical impedance is extremely sensitive to any change in driving force or resultant motion (velocity, acceleration or displacement), a plot of the driving point impedance vs the forcing frequency sharply defines the resonant and antiresonant frequencies for lightly damped structures. Once the resonant and antiresonant frequencies are established, the response of the motor specimen, when plotted, identifies the response mode shape. The phase relationship of the driving force to the resultant motion, plotted vs the forcing frequency, may be used to verify the frequencies identified by the impedance plots (Fig. 8).

Commercially produced impedance heads were not immediately available; therefore, an interim system was designed, using available materials and instruments to measure the driving force and resultant motion at the input point to the motor specimen. This system consisted of 1-inch diameter drive rods necked down to 3/8 inch diameter at each end for a 5-inch gage length, and strain gages mounted 180 degrees apart at the gage lengths to measure force output of the exciters and force input to the test specimen (Fig. 2). Accelerometers measured the exciter output and input acceleration to the test specimen. These measured parameters were then used to calculate the point impedance of the exciter and the motor specimen, using Eq. (1):

$$Z_o = \frac{Ea_1 \epsilon 2\pi f}{GA} = \frac{lb}{in./sec} , \qquad (1)$$

where

E = modulus of elasticity of drive rod material,

a_1 = cross-sectional area of drive rod gage length,

ϵ = strain measured on drive rod gage length,

f = forcing frequency,

G = gravity (in./sec^2), and

A = acceleration in units of gravity.

The test setup, a sample impedance plot, and a sample motor response plot are shown in Figs. 2 and 9. The impedance values are only relative. A calibrated system was not required, since only identification of resonant and antiresonant frequencies were the prime objectives, and relative values provided this information.

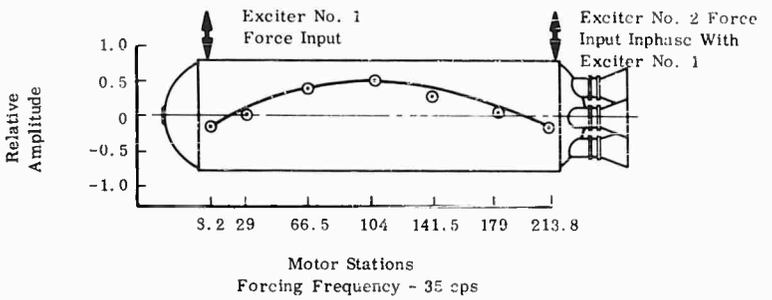

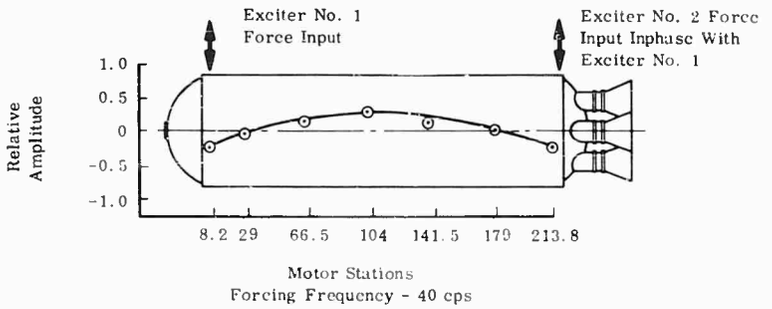

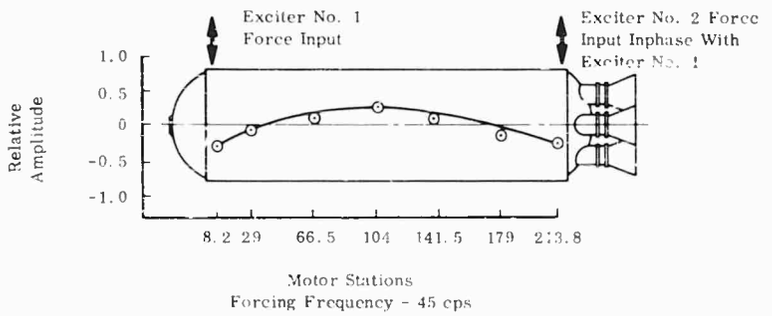

Fig. 7 - Motor bending response for constant acceleration input of 0.25 g at each driving point

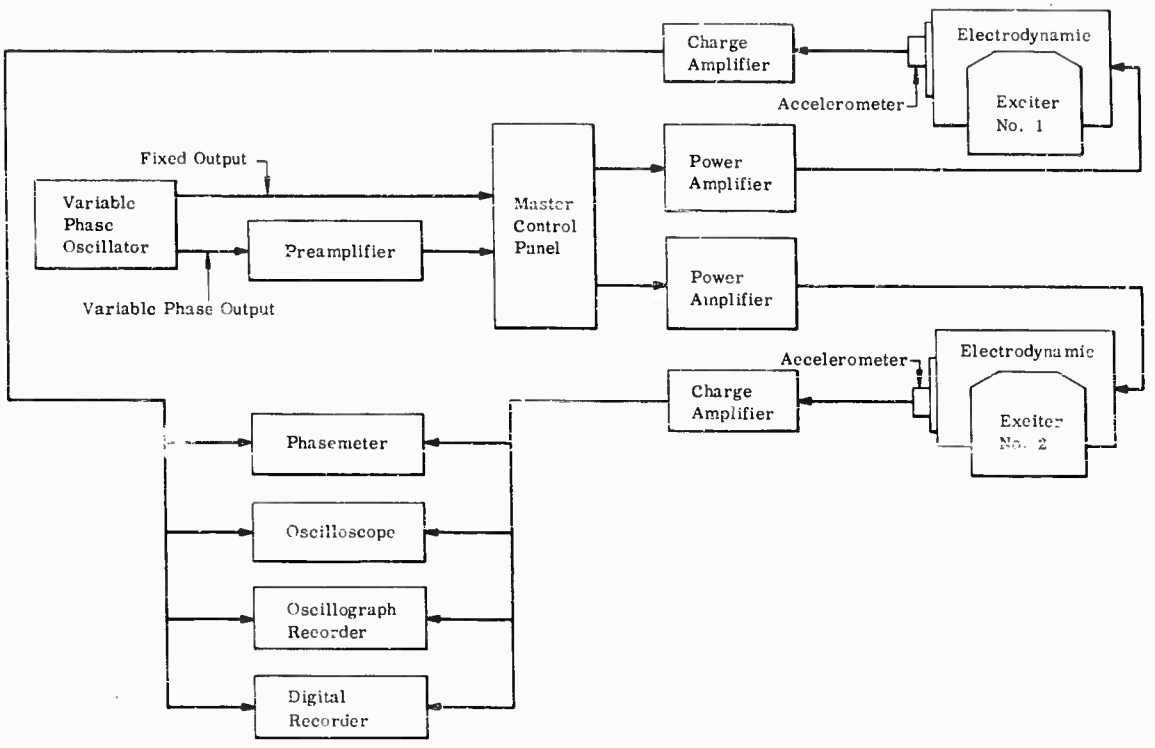

Fig. 8 - Constant force-signal flow diagram

RESULTS

One longitudinal coupled rod and propellant thickness shear mode and two transverse bending modes (first fundamental hinged-hinged and first fundamental free-free bend modes) were excited in a live Stage I MINUTEMAN motor, using the technique of maintaining a constant acceleration input to the motor specimen (Fig. 7). Positive identification of these resonant frequencies and corresponding mode shapes was not made, however, until the test techniques were changed to constant force input to the specimen and impedance measurements pinpointed the resonant and antiresonant frequencies.

Two longitudinal modes and three fundamental bending modes were excited in a live Stage I MINUTEMAN motor by maintaining a constant force input of known value to the test specimen and calculating the driving point mechanical impedance. The longitudinal modes were the coupled fixed-free rod (case) and propellant thickness shear mode and the coupled free-free rod and thickness shear mode (Fig. 10). The fundamental bending modes were the hinged-hinged bending mode, the free-free bending mode, and the center fixed-ends free or double cantilever bending mode (Figs. 9 and 11). Added confidence in the identification of the resonant frequencies and response mode shapes was gained by exciting the motor in more than one test configuration, with force inputs applied at different points on the motor for each test configuration. A good example is the free-free bending mode that was excited with inputs at the effective beam ends, and again with inputs at the motor center (Figs. 9 and 11). The response of the two configurations were in excellent agreement.

The vibration test results were compared with the mathematical analysis of the rocket motor. Primarily, the purpose of the mathematical analysis was to predict the induced stresses in the rocket motor as a result of a transportation environment. This environment was determined from road, multibump board course, and air shipment tests. To predict these induced stresses, the dynamic response of the rocket motor had to be determined first for the environment. In the analytical approach, the rocket motor was considered to be a tubular elastic beam with an annular propellant grain firmly bonded inside. The harness-band support used in the transport configuration was considered to be a simple (hinged-hinged) beam support through which end displacements were transmitted to the beam-like structure. The governing equations for the dynamic behavior

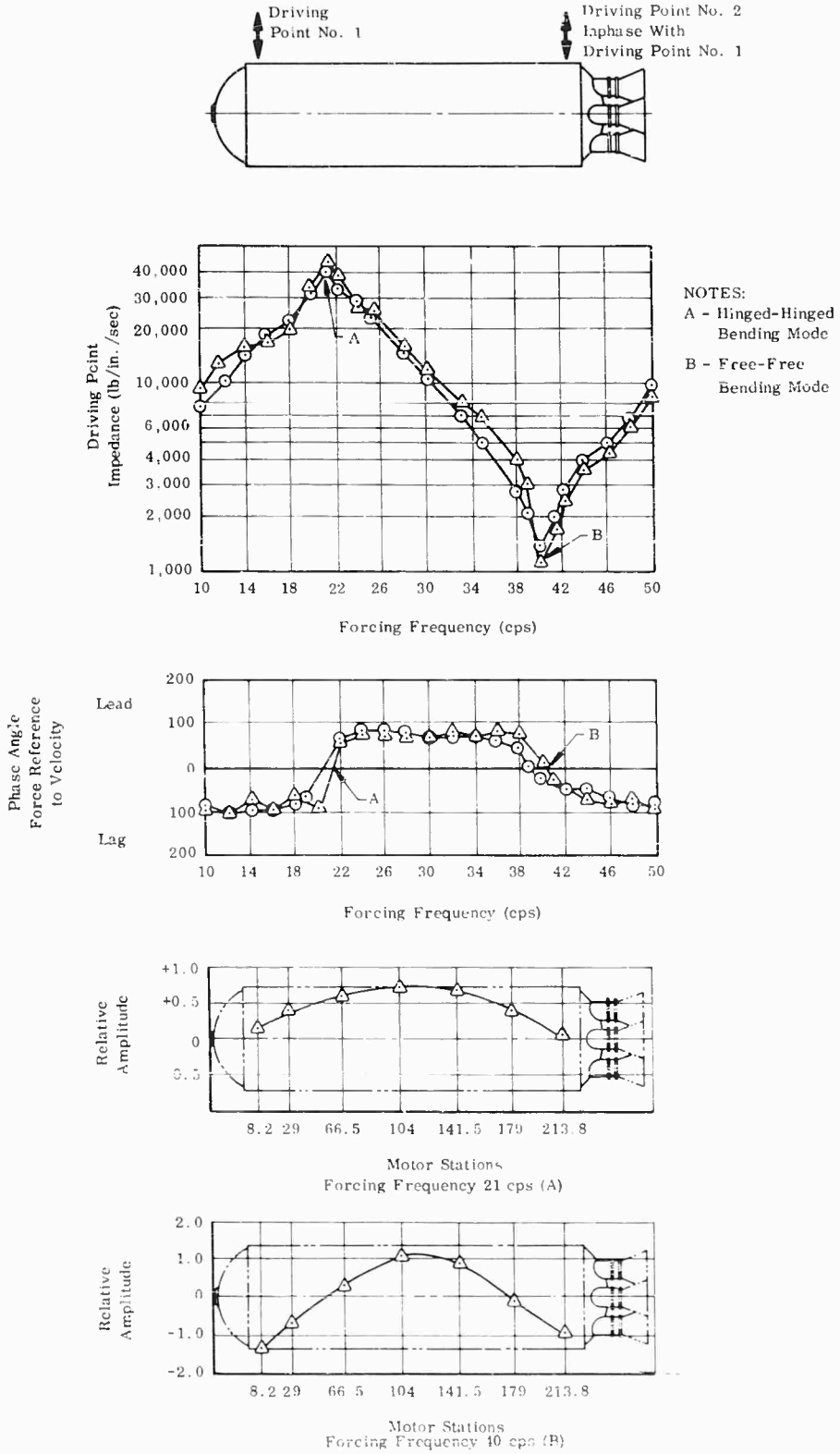

Fig. 9 - Driving point impedance; phase angle; hinged-hinged and free-free bending response for constant force input of 8,000 pounds at each driving point

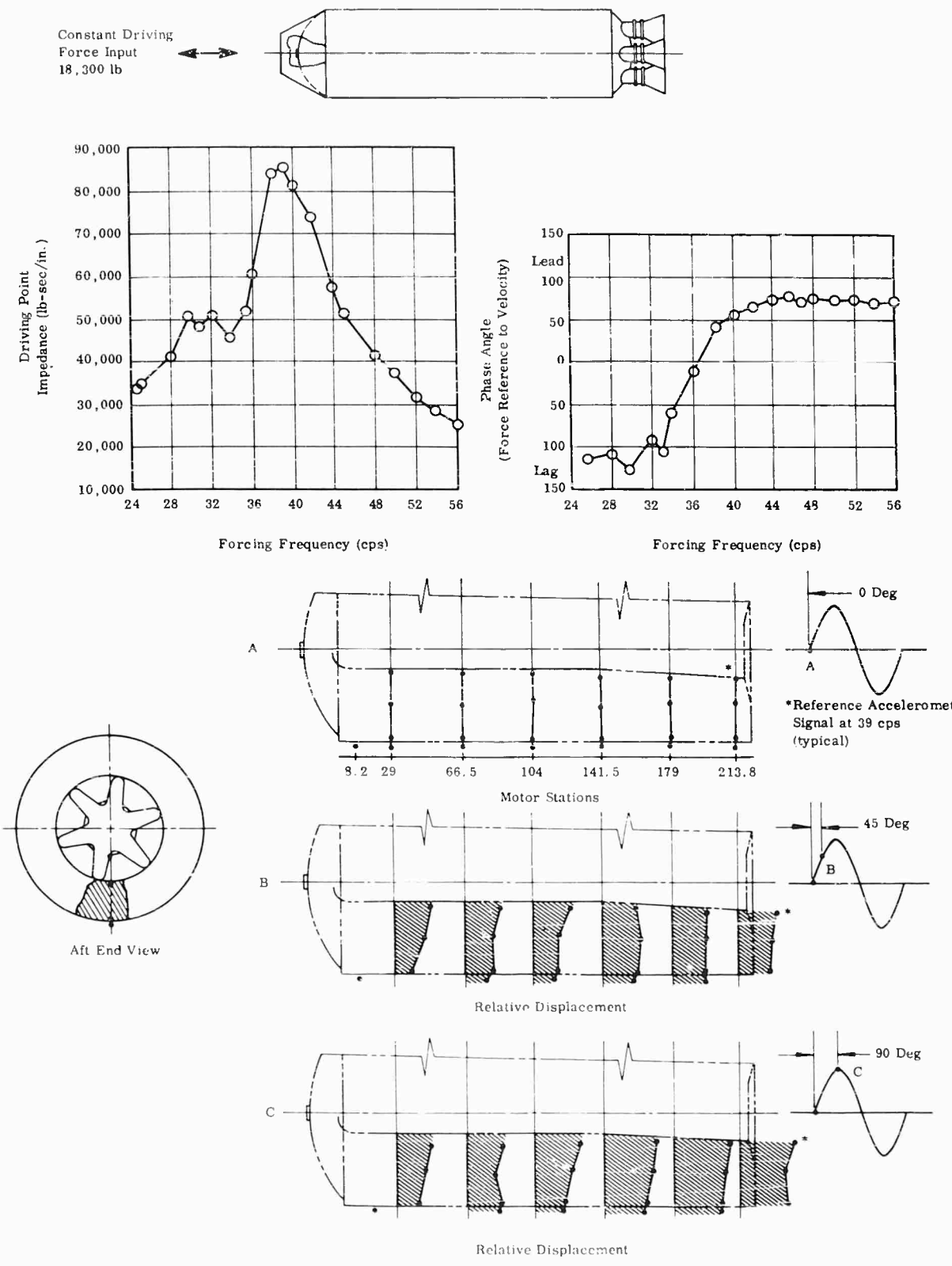

Fig. 10 - Driving point impedance; phase angle; longitudinal response for constant force input of 18,300 pounds

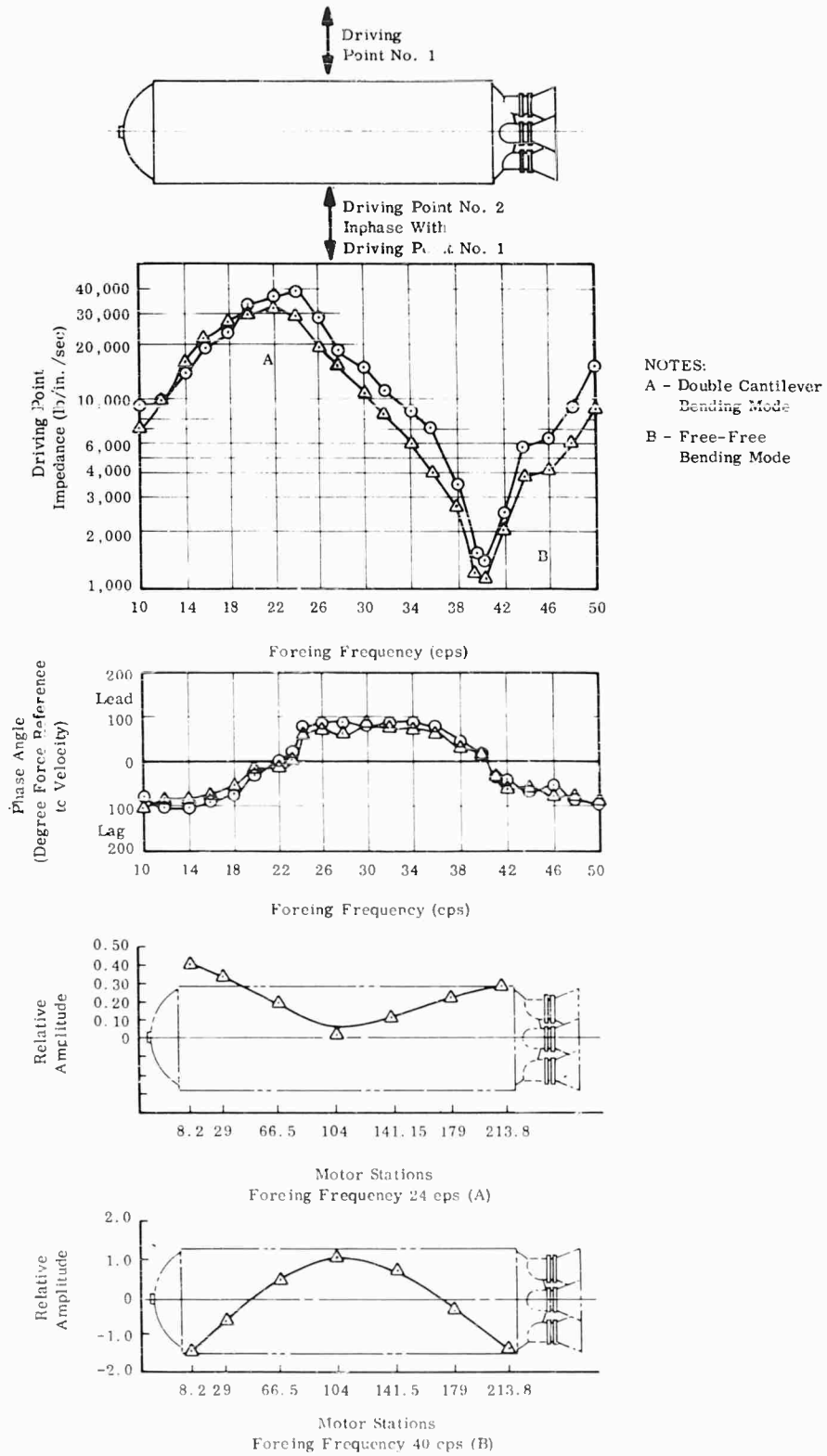

Fig. 11 - Driving point impedance; phase angle; double cantilever and free-free bending response for constant force input of 10,300 pounds at each driving point

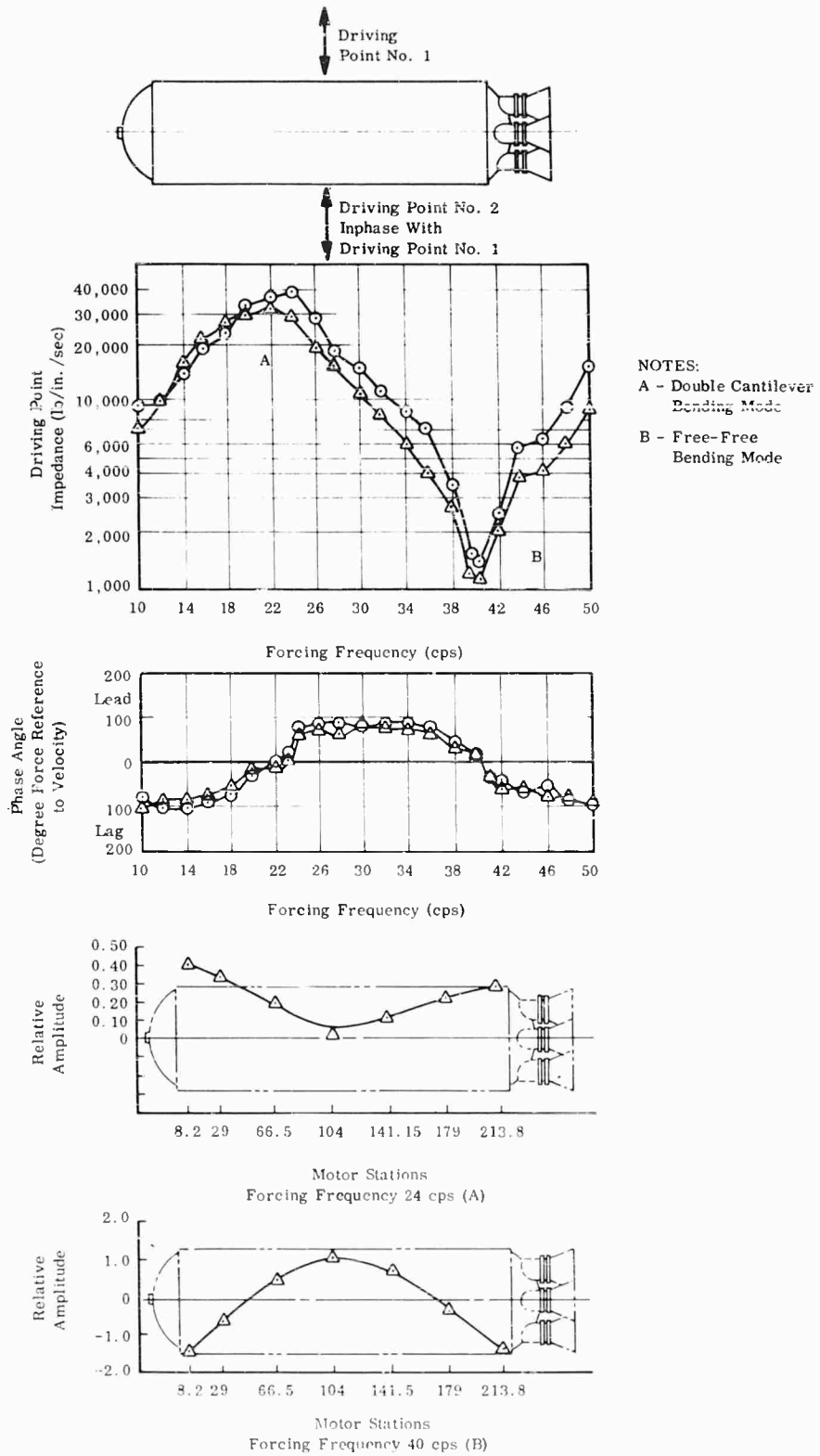

Fig. 11 - Driving point impedance; phase angle; double cantilever and free-free bending response for constant force input of 10,300 pounds at each driving point

of this idealized structure were obtained by application of Reissner's variational theorem and Hamilton's principle [3].

In performing the vibration tests, it was convenient to vary the boundary conditions in the transverse vibration configuration by exciting the motor, first at two input points, one at each motor end, and second, by one cross-sectional input point at the motor center. This procedure allowed the analysis to be checked for three different configurations; hinged-hinged, free-free, and ends free with center fixed (double cantilever).

For the hinged-hinged configuration, the effective length of the vibrating beam was taken as the length between the driving or input points. The portion of the motor length extending beyond the driving points was ignored, since it consisted primarily of rigid forward and aft domical closures. The effective length of the vibrating beam for both the free-free and double cantilever configurations had to include a portion of the forward and aft domical closures. This effective model length was determined by trial to match the free-free resonance obtained from tests. The resulting length appeared as a good average for the actual shear diagram.

This same effective length was used in the analysis of the double cantilever configuration as that used for the free-free condition, since the lengths for the two configurations had to be exactly the same. The computed fundamental resonance of the double cantilever mode was in excellent agreement with the test results, thus substantiating the analysis. Results of the analysis, which accounted for the effect of transverse shear deformation and rotatory inertia, were compared with frequencies obtained by slender beam theory. The latter were found to be unsatisfactory. Effects of rotatory inertia were small but the transverse shear deformation could not be ignored. Table 3 summarizes the frequency investigation.

The hinged-hinged configuration closely approximated the transport condition; therefore, this configuration was used to compute the displacements and strains for transverse oscillations. Table 4 summarizes the displacement and strain investigations.

For longitudinal oscillations, the analysis treated the propellant grain as a hollow elastic cylinder firmly bonded to a rigid case cylinder on the outer periphery and to one flat end. The first fundamental frequency found by this method was 42.5 cps. The first fundamental frequency encountered during vibration tests was 39 cps. However, the case elongated appreciably during tests so that the rocket motor behaved as a fixed-free rod (case) coupled with a shearing propellent grain. If the rocket motor is treated as a fixed-free rod of case stiffness

TABLE 3
Computed vs Experimental Frequencies

Configuration	Computed Frequency	Test Result	Computed Slender Beam Theory Frequency
Hinged-Hinged Mode	24.65	21	31.4
Free-Free Mode	40[a]	40.5[a]	52.5
Fixed-Free Mode	24.1	24	32.9

[a]Model length selected to force agreement.

TABLE 4
Calculated vs Experimental Displacement and Strain

Frequency (cps)	Calculated		Test Result	
	Displacement (in.)	Strain (μin./in.)	Displacement (in.)	Strain (μin./in.)
10	0.0236	102	0.023	82
			0.0266, 0.0344	92
15	0.0316	136.5	0.0362, 0.0313	127
			0.0345	130

and case plus propellant mass in the analysis, the first fundamental frequency is 45 cps. Since the propellant shearing and case rod fundamental frequencies are close together, it is extremely difficult to perform a valid analysis, due to the coupling of the two modes. Longitudinal accelerations experienced during transport tests were very small; therefore, no further analysis was attempted, since precise determination of induced stresses for this configuration was not considered vitally important.

Transverse bending response of the motor specimen was limited to the fundamental modes. Above 50 cps, an inplane propellant mode was excited in both the center and end forcing tests; however, the motor response could no longer be described by beam theory because local case distortion accompanied the propellant amplification. Since transportation frequencies are well below 50 cps, the theory used was considered adequate.

CONCLUSIONS

Vibration test programs conducted for the U.S. Air Force indicate that discretionary use of single point mechanical impedance measurements, combined with phase relationship of driving force to resultant motion, can be a very useful tool for determining resonant and antiresonant frequencies of large solid propellant rocket motors. Acceleration data obtained at several motor stations simultaneously with the impedance measurements yield the corresponding response mode shape.

Repeatability of this type of test with exactly the same results is excellent. The results obtained agree very closely with those obtained by analytical methods. The values obtained by analytical methods for transverse beam response of the motor may be used with confidence to refine the motor design, to confirm the adequacy of the motor design, or to predict the life expectancy of the motor for a transport environment.

REFERENCES

1. Thiokol Chem. Corp. Spec. IT801, Rev. 1-8 (Apr. 17, 1961).

2. R. L. Allen and L. G. Flippin, "A Method of Embedding Accelerometers in Solid Propellant Rocket Motors," Shock, Vibration and Associated Environments Bull. No. 33, Part III, pp. 27-43 (March 1964).

3. M. A. Brull, "On the Flexural Vibrations of Solid Propellant Rocket Motors," Proc. AIAA Launch and Space Vehicle Shell Structures Conf. (Apr. 1-3, 1963).

BIBLIOGRAPHY

R. O. Belsheim, "Mechanical Impedance," Shock, Vibration and Associated Environments Bull. No. 30, Part II, pp. 1 (Jan. 1962).

R. O. Belsheim and G. L. Remmers, "Comparability of Mechanical-Impedance Measurements," J. Acoust. Soc. Am., 34: 731 (May 1962).

R. E. Blake, "Applications of Impedance Information," Shock, Vibration and Associated Environments Bull. No. 30, Part II, pp. 29 (Jan. 1962).

W. Bradley, Jr., "Mechanical Impedance Testing," Repr. Tech. Paper, Endevco Corp., Pasadena, Calif. (1960).

R. R. Bouche, "Instruments and Methods for Measuring Mechanical Impedance," Shock, Vibration and Associated Environments Bull. No. 30, Part II, pp. 18 (Jan. 1962).

D. Burger, "Mechanical Impedance and Mobility Useful but Unused," Wright Eng. Co. Symp. (Sept. 1957).

C. M. Harris and C. E. Crede, Shock and Vibration Handbook, Vol 2 (McGraw-Hill Book Co., Inc., New York 1961).

R. C. Lewis and D. L. Wrisley, "A System for the Excitation of Pure Natural Modes of Complex Structure," J. Aero. Sci., 17, 11 (Nov. 1950).

R. Plunkett, "Analytical Determination of Mechanical Impedance," Shock, Vibration and Associated Environments Bull. No. 30, Part II, pp. 8 (Jan. 1962).

J. C. Snowdon, "Mechanical Impedance and Transmissibility of Simple Supported Beams," J. Acoust. Soc. Am., 35, 2 (Feb. 1963).

Thiokol Chem. Corp. Report 3368, "Final Report-Analytical Studies of the Phase II Transportation and Handling Program," Vol. I, Bk. 1 and 2 (Nov. 1962).

DISCUSSION

Mr. Ott (Sandia Corp): I noticed you use a strain gage in your force determination.

Mr. Flippin: We used strain gages for measuring force. We did not have a commercially produced impedance head.

Mr. Ott: What force magnitudes were you considering?

Mr. Flippin: We considered forces up to about 28,000 pounds.

Mr. Ott: We have had considerable trouble detecting or getting sensitivity from a strain gage-type measurement system. Did you notice any trouble?

Mr. Flippin: We had no trouble except in the antiresonances. We had more trouble getting enough acceleration to measure because we were putting a force in at a node point.

Mr. Sanders (Rocketdyne): Your data curves all appear to be the composite nature of a resonance. Did you detect any internal component resonance by mechanical impedance, such as the internal star points of your grain configuration?

Mr. Flippin: Up to about 70 cps the motor case acted as a beam loaded by the propellant and the propellant went along with the motor case. Above that, as I said in the conclusions, the propellant went asymmetric to the case and we stopped our test there.

* * *

USE OF MECHANICAL IMPEDANCE IN DYNAMIC MEASUREMENT OF SOLID ROCKET MOTORS

R. E. Coleman
Rocketdyne
McGregor, Texas

Test stand mechanical frequency response limits dynamic thrust measurement during solid rocket static firings. A Thévenin system of rocket representation using mechanical impedance is developed which leads to a 0 to 1000 cps response.

INTRODUCTION

Test stand mechanical frequency response has always limited the accuracy with which solid rocket thrust-time history could be measured. Although steady-state accuracy is approaching the order of 0.1 percent, dynamic data often fails to provide even a qualitative picture of true thrust during transient periods. Situations during which such transients exist include rocket malfunction, ignition phase (including igniter shock), tailoff, thrust reversal, and thrust vector control duty cycle.

Various investigators have analyzed the problem giving attention to ways of increasing system frequency response. This paper discusses an approach combining experimental and analytical techniques of mechanical impedance to obtain dynamic thrust measurements in the 0 to 1000 cps range, within test fixture design limitations.

PROBLEM DESCRIPTION

Background

Several factors motivate the dynamic measurement effort. First, solid rockets are characterized by fast thrust rise times. Figure 1 shows a reproduction of a typical ignition phase thrust-time oscillograph trace obtained during a static firing. The motor thrust is not

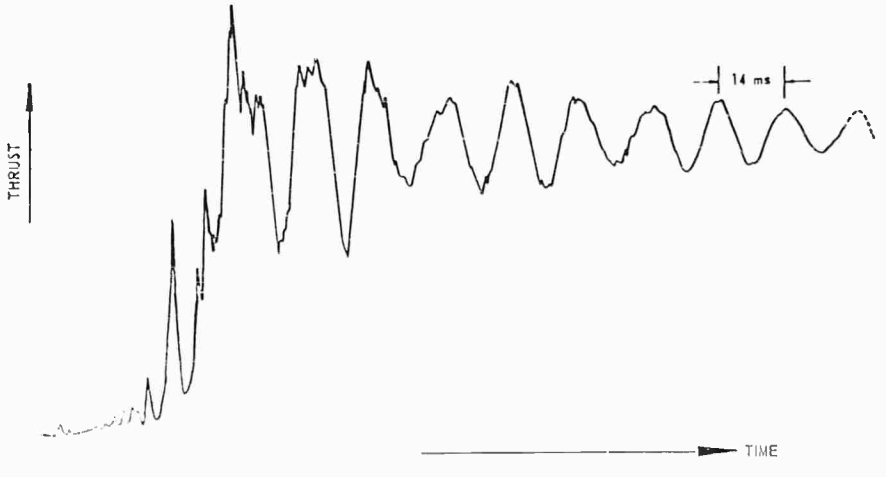

Fig. 1 - Representation of ignition phase thrust-time oscillograph trace

really oscillating, although the trace displays a 71-cps oscillation. The rapid thrust increase shocked the thrust stand system into oscillation at its resonant frequency. (By "thrust stand system" is meant rocket, thrust stand, force transducer, and test cell reaction wall.) Future rocket performance requirements will lead to even faster ignition characteristics.

Some rockets must deliver special thrust-time functions involving sudden changes. Specifications may require a complete thrust reversal within 5 milliseconds. A variety of special functions may be encountered among thrust vector control duty cycles. For example, a qualification test procedure may require measuring thrust vector vs time while actuating the nozzle at 20 or 30 cps.

To gain knowledge of the rocket shock spectrum, the dynamic environment presented by the thrust stand system must be studied. A valid shock spectrum obtained during a rocket static firing is difficult to obtain, even by making allowances for the stand environment.

A whole class of dynamic problems present themselves throughout countless malfunction reports. The thrust stand is usually shocked into oscillation during culmination of rocket failure. In many instances, stand vibrations are so predominant that the general trend of true thrust is misinterpreted. As an example, assume the key to a given malfunction is the knowledge of one piece of qualitative information – that thrust decreased abruptly at the same instant pressure increased. This infers nozzle blockage. Yet, the information could be lost as a result of prior perturbations exciting stand resonances.

A unique dynamic problem results when the solid propellant grain shifts inside the rocket case, perhaps imparting a forward impulse to the case as it breaks loose, followed by a reverse impulse at impact on the aft head.

The classic dynamic problem is, of course, oscillatory burning. The mechanism of the unstable burning propellant, sometimes coupling with pressure chamber acoustic resonances, has been the subject of intense research [1-3].* The oscillating pressure frequency range extends from around 100 cps beyond 35 kc. Special purpose pressure transducers and thermocouples are the most useful tools for this type of work. However, development of dynamic thrust and acceleration measurement techniques may prove valuable in the lower frequency range, particularly when special internal transducer installation is prohibited by motor design.

*NOTE: References appear on page 82.

Thrust Stand System Limitations

Any one of the many components comprising the complete measurement system may limit dynamic response, e.g., rocket motor, thrust stand, force transducer, electrical signal cable, signal conditioning circuitry, amplifier, and recording equipment (such as recording oscillograph, tape station, or digital system). Dynamic capability of the electronic end of the measurement problem (shielded cables, 100 kc dc amplifiers, 20 kc tape stations, 5 kc galvanometers, 15,000 samples per second digital system) has long since exceeded thrust stand system capability by orders of magnitude, leaving the mechanical system the limiting factor in achieving frequency response. Thrust stand systems for typical medium-sized rockets (weighing from a few hundred to a few thousand pounds, usually show first major resonances ranging from 20 to 100 cps.

The limitation will be more clearly understood after considering the standard method of thrust measurement diagramed in Fig. 2. The rocket thrust is transferred to the concrete abutment through a thrust adaptor cone and force transducer column. Flexures are used to support the motor and carriage with minimum restraint in the direction of thrust. (Restraint less than 0.2 percent of thrust level is obtained with good flexure design.) The force transducer is isolated by flexures to minimize effects of side forces. Thus, thrust measurement is based on Newton's third law: "For every action there is an equal and opposite reaction." From the measured deflection of a steel column (the force transducer), the total reaction to the rocket action may be derived using Hook's Law.

One way of explaining the limitation is to say that during transient periods, the action is not being totally reacted by the thrust transducer spring. Part of the thrust is reacted by inertia of accelerating masses and viscous reaction of the transducer. Furthermore, since the thrust stand system is underdamped, vibration forces are usually induced.

A simplified mechanical circuit representation of Fig. 2 is shown in Fig. 3. The basic input forces to the rocket are represented by force generators, F_1, F_2, F_3 and F_4. The physical locations of these forces are also illustrated in Fig. 4.

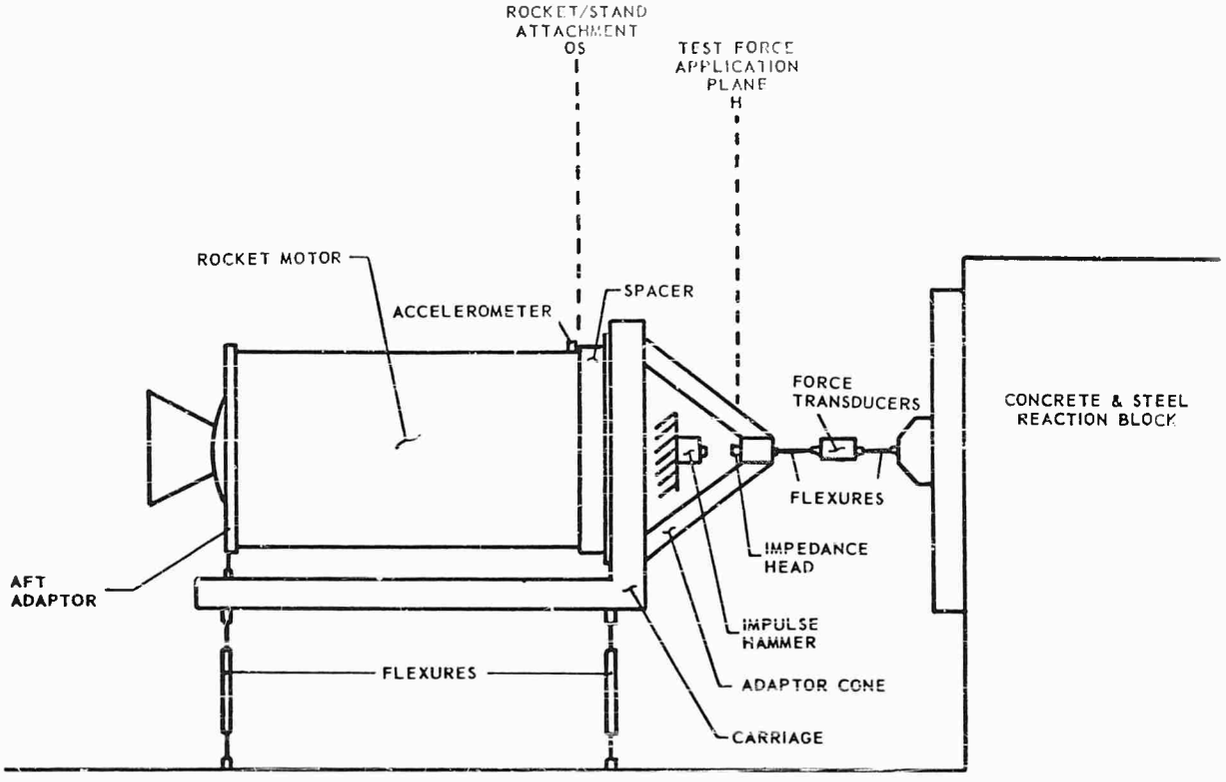

Fig. 2 - Static-firing test setup; impulse hammer and impedance head are included for mechanical impedance measurements

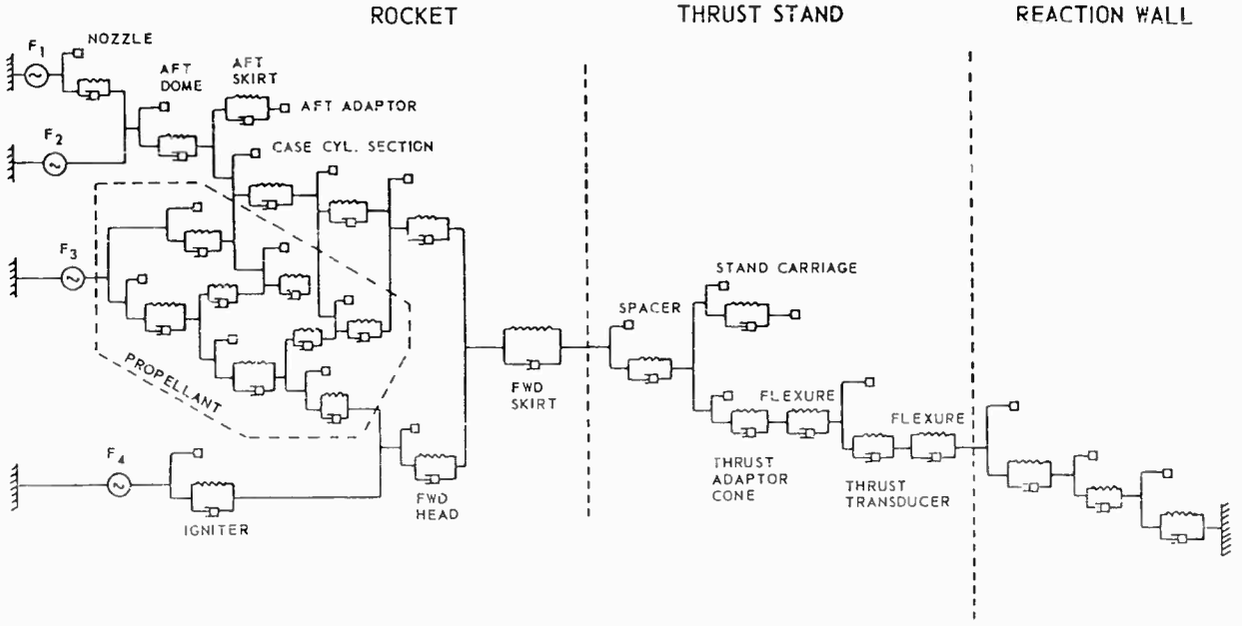

Fig. 3 - Simplified mechanical circuit diagram of rocket motor in thrust stand during static firing

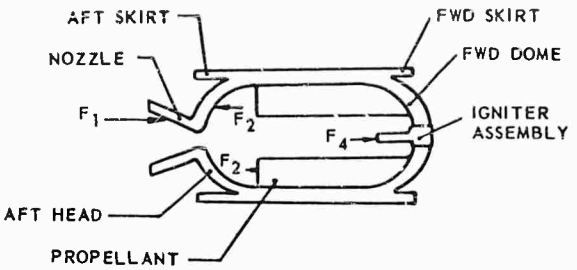

Fig. 4 - Physical location of circuit elements diagramed in Fig. 3

Usually, the first major resonance may be approximated analytically [4] by modeling the thrust stand system as a mass, spring and dashpot in parallel as shown in Fig. 5. Setting the sum of forces acting on the mass equal to the product of mass and acceleration leads to the differential equation of motion,

$$M\frac{d^2x}{dt^2} + C\frac{dx}{dt} + Kx = F(t), \qquad (1)$$

where

M = sum of moving mass in thrust stand system,

K = spring constant (primarily force transducer and flexures),

C = damping constant,

x = displacement,

t = time, and

F(t) = thrust-time function.

Since the oscillograph thrust trace originates with a displacement measurement of the spring, this thrust-time trace is directly proportional

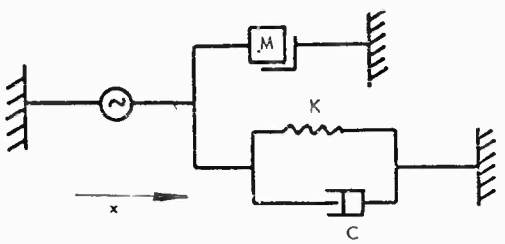

Fig. 5 - Rocket in thrust stand during static firing, modeled as single-degree-of-freedom system to approximate first major resonance

to the solution of the differential equation. The resonant frequency is taken from the oscillograph thrust trace (Fig. 1) or derived [5] from the analytical function, x(t):

$$f_n = \frac{1}{2\pi}\sqrt{\frac{K}{M} - \left(\frac{C}{2M}\right)^2}, \qquad (2)$$

where f_n = natural frequency. In view of this equation, thrust stand design engineers attempt to keep mass as low and stiffness as high as possible for best fidelity.

Another way to consider thrust stand limitation in this case is by noting that the thrust transducer measurement, represented by the Kx term in Eq. (1), is equal to true input thrust only when velocity and acceleration are zero:

$$M(0) + C(0) + Kx = F(t). \qquad (3)$$

Since values for M, C, and K are easily obtained experimentally, and taking first and second derivatives presents no great problem, the erroneous thrust measurement may be adjusted by adding on the inertia and viscous terms, $M(d^2x/dt^2)$ and $C(dx/dt)$, respectively. If this approach is taken, the measured thrust function kx(t) must first be taken through a low pass filter set just below the second major resonance of the thrust stand system (automatically establishing the limit of frequency response). Otherwise, errors introduced by resonant vibrations above the first major resonance will be compounded. Some attempts to correct dynamic malfunction data in this manner have failed completely due to presence of two or more resonances close to the first major resonance.

This is in contract to the very general character of mechanical impedance approach to dynamic measurements when systems even more realistic than that shown in Fig. 3 must be faced.

MECHANICAL IMPEDANCE APPLICATION

When discussing rocket thrust it is usually not important to specify the location of forces or whether the input or output is being considered. However, any discussion of the dynamic problem is meaningless unless the location of forces and transfer functions involved are specified.

The location of forces to be derived depends on original test objectives. The various problems that arise generally lead to analysis under two categories: input characteristics and output characteristics. Problems related to the first

category are of primary concern throughout the static-firing stage of rocket development. Too frequently, the second category goes unattended until problems arise during flight tests. This situation is steadily improving [6-10].

Input Characteristics

The numerous force application points and the environment inside a rocket pressure chamber and nozzle discourage efforts to solve the input force problem. Yet, during the development phase, internal ballistic performance and structural component stress analysis are most important. When malfunction occurs the question is, "What was the true input thrust?" It would be good to be able to assign values to each element of Fig. 3.

Nevertheless, until promising experimental techniques allowing measurement of pertinent rocket motor transfer functions are presented, only the output characteristics will be pursued. This, at least, is a step closer to the input problem and initiates efforts toward achieving compatibility between the rocket motor and other parts of the missile system.

Output Characteristics

Output characteristics are measured to develop an equivalent Thévenin system representation of the rocket motor. Thévenin's theorem states that a complex mechanical network may be represented by a force generator and an impedance in parallel, one side clamped and the other free for external load connection. The rocket motor Thévenin system mechanical circuit is shown in Fig. 6 with an external load impedance to indicate manner of attachment.

The value of Thévenin force is that which would be delivered to a load of infinite impedance. If the rocket motor (Fig. 4) were attached at the forward skirt to an infinite mass, the force applied to the infinite mass would be Thévenin's force or rocket output force F_o.

Thévenin's impedance in this case is simply the driving point impedance at the forward skirt. This is the ratio of applied force to velocity at the forward skirt, or the ratio of Thévenin's force F_o to the free velocity measured at the forward skirt during free flight of the rocket alone. We shall call this the rocket output impedance Z_{oo} (as opposed to input impedances at internal points of thrust application).

Once these two functions are determined (varying with frequency and time) the response to the rocket excitation of any other structure of known impedance can be predicted. Or, if the impedance looking into the thrust stand system (corresponding to Z_{LL} in Fig. 6) and the rocket output impedance are known, the rocket output force transient $F_o(t)$ during static firing may be determined. For example, if electronic components in a missile have failed repeatedly during flight tests, and transient forces during rocket ignition phase are suspect, it is first desirable to know the output force F_o of the rocket. During static firing, the rocket is connected to the thrust stand as represented by the circuit diagram, Fig. 7. (Figures 6 and 7 are alternate diagrams.) After Z_{oo} and Z_{ss} (input impedance to thrust stand) have been determined, the force F_o is derived by summing the effective forces applied at the connection point of the two impedances. These forces are expressed in terms of the impedances and a velocity measurement v at the rocket/stand attachment:

$$F_o = (Z_{oo} + Z_{ss})\,V\,. \qquad (4)$$

After measuring the driving point impedance Z_{mm} at the missile upper stage input attachment, the force F_m applied to the upper stage is predicted:

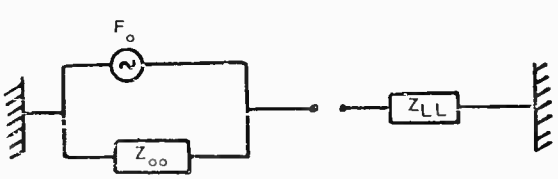

Fig. 6 - Thévenin equivalent system representation of rocket (equivalent force F_o and impedance Z_{oo}) in relationship to any load impedance Z_{LL}

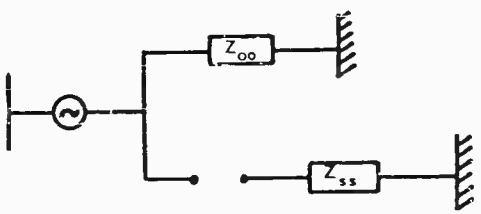

Fig. 7 - Thévenin equivalent system representation of rocket in relationship to thrust stand and wall with input impedance Z_{ss}

$$F_m = F_o \frac{Z_{mm}}{Z_{oo} + Z_{mm}} . \quad (5)$$

Further testing of the upper stage includes determination of the transfer impedance Z_{mE} between the upper stage attachment and the electronic package. Measurement of the input impedance Z_{EE} allows derivation of the force applied to the package F_E since

$$F_E = F_m \frac{Z_{EE}}{Z_{mE}} . \quad (6)$$

This information provides a sound basis for additional analysis and test, probably leading to solution along one or more of the following lines:

1. Fix electronic package by altering Z_{EE}, thereby reducing F_E.

2. Fix electronic package by increasing its strength. (This could be harmful if impedance is not watched.)

3. Alter impedance of passive elements between rocket and package.

4. Alter rocket output characteristics (redesign igniter or propellant geometry or alter rocket impedance).

Practical Obstacles

Once the theory has established the direction for specific test effort, experimental obstacles immediately appear. The following is a brief review of some of the problems to be considered in the experimental determination of the Thévenin system for a rocket. The determination is based on the test setup diagramed in Fig. 2.

Bilateral System - Forces must transmit equally well in both directions. The fact that most transients encountered will ride on a large dc force component is helpful here.

Linear System - Linearity is assumed but is questionable. The solid propellant is the main problem. Impedance measurements should be repeated using different force levels. Linearity of most springs would be established by in-place force vs deflection measurements.

Symmetry at Skirt/Thrust Stand Attachment - Point impedances around motor skirt or stand spacer should not vary appreciably.

Unaltered System During Test - System impedance should not change during time between impedance measurement and occurrence of transient force to be measured or during transient period. Obviously, measurements are meaningless after gross structural failure. Since impedance changes as propellant burns, it may be necessary to take measurements during static firing close to the transient force time. This requires the impulse method (Fig. 2), including Fourier analysis. Any alteration to system impedance introduced by the impulse hammer must be considered.

Lumped-Parameter System - Acoustic velocities and material dimensions should be considered to assure the problem is not one bordering on acoustics, analogous to electrical transmission line problems.

Difficulty of Measurements - Not all thrust stands conform to the configuration represented by Fig. 2; nor do all rocket motors resemble Fig. 4. Also, objectives vary from one test to another. Therefore, different tests may represent widely different measurement problems. Impedance functions often must be measured indirectly. Generally, four basic operations may be required to obtain the Thévenin equivalent system of a rocket for some transient period of rocket action:

1. Stand input impedance Z_{ss} is measured at the plane of rocket attachment with motor out of stand (test plane "S" in Fig. 8). The attachment plane diameter makes direct measurement quite difficult. An indirect approach involves attaching known impedances to the test plane.

2. Rocket output impedance Z_{oo} is measured at the forward skirt (test plane "0" in Fig. 8). The problem is similar to Operation 1 if measurement prior to test is valid. A particularly difficult problem arises when Z_{oo} must be measured during the static firing. As mentioned before, this is necessary when rocket impedance changes as propellant burns (mass decreases with time). Impedance must then be measured indirectly.

3. To determine output force F_o and output impedance Z_{oo}, the transfer impedance $Z_{(H-oS)}$ must first be measured. Impulse-type forces (F_H) are applied to test plane H (Fig. 9) at predetermined times during static firing prior to some thrust transient of interest. When the time of the transient event cannot be anticipated, some probability of applying a test force at the moment of rocket transient exists. This probability can be regulated from around 0.04 to 0.1, assuming typical motor firing times and transient

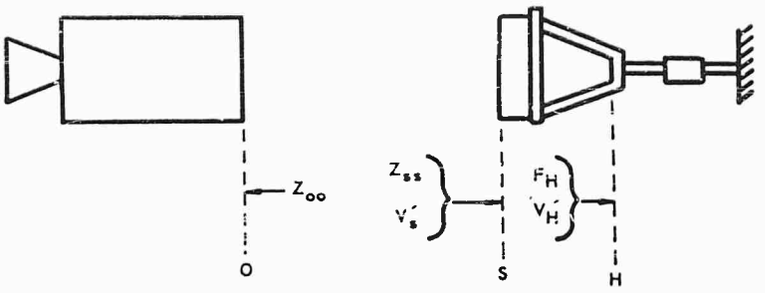

Fig. 8 - Locations of measured and derived functions with motor disconnected from thrust stand

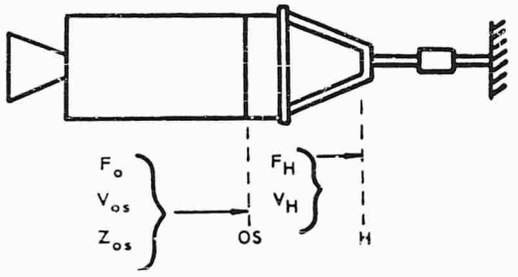

Fig. 9 - Locations of measured and derived functions with motor connected to thrust stand

durations. The transfer impedance can then be determined:

$$Z_{(H-oS)} = \frac{F_H}{V_{o_S}} . \qquad (7)$$

4. During the rocket transient of interest, the velocities, V_{o_S} and V_H (Fig. 2 or 9) must be measured. The output force is obtained from Eq. 7 measurements and the reciprocity theorem for mechanical impedance,

$$F_o = Z_{(oS-H)} V_H = Z_{(H-oS)} V_H . \qquad (8)$$

Referring again to Fig. 7, the total input impedance Z_{oS} at the point OS, as seen by the output force, is

$$Z_{oS} = \frac{F_o}{V_{oS}} . \qquad (9)$$

Having measured F_o and V_{oS} during the rocket transient period and Z_{ss} during Operation 1, the rocket output impedance Z_{oo} may be calculated:

$$Z_{oo} = Z_{oS} - Z_{ss} . \qquad (10)$$

To maintain continuity and avoid the inconvenience of additional subscripts and functional notation, the Fourier analysis has not been explicitly indicated in previous notation. In each case where a transient signal is measured, that function must be handled in the form of its Fourier integral [11]. The function V_H, for example, may be represented by the Fourier integral,

$$V_H(t) = \int_{-\infty}^{+\infty} g_V(\omega)\, e^{i\omega t}\, d\omega , \qquad (11)$$

where

$$g_V(\omega) = \frac{1}{2\pi} \int_{-\infty}^{+\infty} V_H(t)\, e^{-i\omega t}\, dt . \qquad (12)$$

Equations (11) and (12) are referred to as a Fourier transform pair. Treating all previous transient measurements in a similar manner, the Thévenin force F_o in Eq. (8) is

$$F_o(t) = \int_{-\infty}^{+\infty} Z_{(H-oS)}(\omega)\, g_V(\omega)\, e^{i\omega t}\, d\omega . \qquad (13)$$

A 100-channel high speed (15,000 samples per second) automatic digital acquisition system is used at Rocketdyne for recording data for computations such as Eq. (13) [11,12]. The data are recorded automatically on digital tape compatible with available computers. A typical test requires transient analysis over a 15- to 300-millisecond period. The time increment chosen for summations is about 0.2 millisecond in order to maintain good effective 1000 cps response. The choice of frequency increment is based

partly on expected response characteristics of most underdamped thrust stand system components. It is expected that 1 cps frequency increments will be more than adequate.

Based on these assumptions, the data processing should be well within computer practicability, requiring perhaps from 10 to 60+ minutes computer time, depending on transient and desired dynamic thrust measurement accuracy.

REFERENCES

1. F. T. McClure, R. W. Hart, and J. F. Bird, "Solid Propellant Rocket Motors as Acoustic Oscillators," Progress in Astronautics and Rocketry, Vol. 1, Ed. by Martin Summerfield (Academic Press, Inc., New York, 1960), pp. 295-358.

2. T. A. Angelus, "Unstable Burning Phenomenon in Double-Base Propellant," Progress in Astronautics and Rocketry, Vol. 1, Ed. by Martin Summerfield (Academic Press, Inc., New York, 1960), pp. 527-560.

3. E. W. Price, "Review of Experimental Research on Combustion Instability of Solid Propellants," Progress in Astronautics and Rocketry, Vol. 1, Ed. by Martin Summerfield (Academic Press, Inc., New York, 1960), pp. 561-602.

4. V. C. Plane, "Total Impulse Measuring System for Solid-Propellant Rocket Engine," Rocketdyne Report R-5162 (June 1963).

5. L. A. Pipes, Applied Mathematics for Engineers and Physicists (McGraw-Hill Book Co., Inc., New York, 1958), pp. 194-201.

6. R. O. Belsheim and J. W. Young, Jr., "Mechanical Impedance As A Tool for Shock or Vibration Analysis," NRL Report 5409 (Feb. 15, 1960).

7. J. W. Young, Jr., and R. O. Belsheim, "Experimental Measurement of Mechanical Impedance," NRL Report 5458 (May 24, 1960).

8. R. O. Belsheim and J. J. Harris, "Apparent-Weight Measurements of Rocket Payload and Test Structures," NRL Memorandum Report 1099 (Dec. 1960).

9. R. R. Bouche, "Instruments and Methods for Measuring Mechanical Impedance," 30th Symposium on Shock, Vibration and Associated Environments, p. 18. Mechanical Impedance Session, Edited by R. O. Belsheim (U.S. Naval Research Laboratory, Washington, D.C.).

10. E. L. Hixon, "Mechanical Impedance and Mobility," Shock and Vibration Handbook, Vol. 1, Ed. by C. M. Harris and C. E. Crede (McGraw-Hill Book Co., Inc., New York, 1961), Chap. 10.

11. C. R. Wylie, Jr., Advanced Engineering Mathematics (McGraw-Hill Book Co., Inc., New York, 1960), Chap. 7.

12. P. Gottlieb, "Final Report on High Speed Digital Data Acquisition System," Rocketdyne Report ETS 64-2.

13. D. L. Bietendorf, "Accuracy of Data Acquired from the Digital System," Rocketdyne Report ETS 64-5.

* * *

PREDICTING MAXIMUM RESPONSE OF A VIBRATION-EXCITED ELASTIC SUBSTRUCTURE

L. J. Pulgrano
Grumman Aircraft Engineering Corporation
Bethpage, New York

A method is presented for estimating the maximum response of an elastic substructure attached to a vibrating elastic supporting structure. The two structures, whose dynamic characteristics are represented by their apparent masses, are coupled together using impedance techniques. The system parameters are then varied to determine the conditions that produce the greatest response on the substructure. The substructure response is plotted for these conditions in terms of the effective masses of the two structures and the uncoupled response of the supporting structure. The resulting curves predict maximum vibration levels which are generally significantly lower than the levels predicted by neglecting interactions between the two structures and assuming that the supporting structure acts as a motion generator.

INTRODUCTION

When an elastic substructure (e.g., electronic equipment, mechanical component) is connected to a vibrating elastic supporting structure (e.g., airframe), vibration is transmitted through the connection into the substructure. To design the substructure to avoid vibration failure, the magnitude of the transmitted vibration must be known.

In the simplest and most widely used approach for determining the vibration level of the substructure, it is assumed that the reaction forces generated by the substructure do not interact with and, hence, do not influence the motion of the supporting structure. This, in effect, means that the supporting structure imposes a motion input on the substructure. Because the substructure does, in fact, load down the supporting structure, this assumption can yield a gross overestimate of the vibration level for all but the lightest substructures [1].

An attempt is sometimes made to correct for this overestimate by assuming that the vibration of the supporting structure is attenuated in direct proportion to the weight of the attached substructure. Although this approach has some merit, it fails to consider that under dynamic excitation the apparent weight of a structure can differ greatly from its static weight.

The response of the substructure can theoretically be calculated in detail, considering interactions between the two connected structures, by using impedance methods. Considerable work has been done in this field and methods for applying impedance concepts to structural vibration problems have been widely reported [2,3] The impedance approach, in its classical form, provides a complete solution for the response of connected structures, but it requires that the vibration levels of the unloaded supporting structure and the driving point impedances of both structures at their connection points be known in detail. Unfortunately, for most practical applications this information is not available.

Impedance methods are used here to develop a different approach, directed at predicting the maximum response that can occur on a simple substructure for the worst combination of substructure antiresonant and supporting structure resonant frequencies. This maximum response approach yields a conservative vibration design level, but it does not produce the extreme conservatism often obtained when interaction effects are completely neglected.

NOTE: References appear on page 94.

For the maximum response approach, the dynamic characteristics of the two connected structures are represented by their apparent masses. The expression for the apparent mass of a simple spring-mass resonator is used for the substructure, while a more general expression containing the basic characteristics of a multi-modal system is used for the supporting structure. The two structures are coupled together using impedance techniques, and the system parameters are varied to determine the conditions for which the substructure response is greatest. The response of the substructure under these conditions is then used as the basis for a set of curves giving the maximum possible substructure response in terms of the properties of the two connected structures.

LIST OF SYMBOLS

- a,b Subscripts indicating supporting structure and substructure, respectively
- $A, \bar{A}$ Constants
- F Force
- m Apparent mass
- M Point effective mass
- n,r Subscripts indicating antiresonant and resonant frequencies, respectively
- R Ratio of maximum acceleration response on substructure to uncoupled resonant response of supporting structure, Eq. (21)
- x Translational displacement at connection point
- x' Modified displacement after substructure is attached
- y Translational displacement on substructure
- α ω_b^2/ω_a^2
- β M_b/M_a
- μ Parameter defined by Eq. (4)
- η Structural damping factor
- ω Circular frequency
- ω_a Resonant frequency of supporting structure
- ω_b Antiresonant frequency of substructure
- ω_c Resonant frequencies of coupled system
- λ_c ω_c^2/ω_a^2

APPARENT MASSES OF STRUCTURES

The apparent mass is one of the basic impedance relations used to specify the dynamic properties of a mechanical system. It is defined as the complex ratio of the harmonic exciting force to the resulting acceleration response; thus,

$$m_{ij} = \frac{F_j}{\ddot{x}_i} , \qquad (1)$$

where the subscripts i, j denote coordinate locations in the system. If the force and acceleration are measured at the same coordinate (i.e., if $i = j$), the ratio is called the direct or driving point apparent mass.

The driving point apparent mass of any unrestrained linear mechanical system with hysteretic damping can be expressed in the general form [4,5]*

$$m = A \frac{(\omega^2 - \omega_r^2 - i\eta_r\omega_r^2)(\omega^2 - \omega_{2r}^2 - \eta_{2r}\omega_{2r}^2)\cdots}{(\omega^2 - \omega_n^2 - i\eta_n\omega_n^2)(\omega^2 - \omega_{2n}^2 - i\eta_{2n}\omega_{2n}^2)\cdots} , \qquad (2)$$

where ω_{ir} and ω_{jn} are the ith and jth resonant and antiresonant frequencies of the system, respectively. It can be shown [5] that these resonant and antiresonant frequencies must alternate, such that one and only one resonant frequency lies between every two adjacent antiresonant frequencies.

If the system is lightly damped and its resonances are well separated, the variation in apparent mass with frequency in the vicinity of the jth resonance will be due primarily to the influence of the terms corresponding to the jth resonance and to the two closest antiresonances bracketing the jth resonant frequency (e.g., the ith and kth antiresonances). Contributions from the remaining terms will vary slowly with frequency in this range and can be approximated by a constant. Under these restrictions the general form of the apparent mass given by Eq. (2) will reduce to the approximate expression

*The relations given in these references require slight modification to be put into this form.

$$m = \bar{A}\,\frac{(\omega^2 - \omega_{jr}^2 - i\eta_{jr}\omega_{jr}^2)}{(\omega^2 - \omega_{in}^2 - i\eta_{in}\omega_{in}^2)(\omega^2 - \omega_{kn}^2 - i\eta_{kn}\omega_{kn}^2)}\,, \qquad (3)$$

where the constant A has been modified to $\bar{A}$ to account for the remaining terms.

An expression similar to Eq. (3) is used here to represent the apparent mass of the supporting structure. The study is thus restricted to behavior in the vicinity of a single resonance of a lightly damped supporting structure with well-separated resonant frequencies. Further simplification is introduced by assuming that the two adjacent antiresonant frequencies bracket the resonant frequency with a symmetry described by the following relations:

$$\left(\frac{\omega_{in}}{\omega_{jr}}\right)^2 = \left(\frac{\omega_{jr}}{\omega_{kn}}\right)^2 = \mu\,, \qquad (4)$$

where μ is a constant between zero and unity. With this restriction, the apparent mass of the supporting structure becomes

$$m_a = \bar{A}\,\frac{\omega^2 - \omega_a^2 - i\eta_a\omega_a^2}{(\omega^2 - \mu\omega_a^2 - i\eta_a\mu\omega_a^2)\left(\omega^2 - \frac{\omega_a^2}{\mu} - i\eta_a\frac{\omega_a^2}{\mu}\right)}\,, \qquad (5)$$

where the i and r subscripts have been dropped since they are no longer significant, and an a subscript has been introduced in their place to denote the characteristics of the supporting structure.

At resonance $(\omega = \omega_a)$, the apparent mass given by Eq. (5) is

$$(m_a)_{res} = \frac{i\eta_a\mu}{\omega_a^2}\,\frac{\bar{A}}{(1-\mu)^2(1+i\eta_a) + \eta_a^2\mu}\,. \qquad (6)$$

Since it is desired that the resonant apparent mass be independent of the resonant and antiresonant frequencies (i.e., independent of ω_a and μ), the constant $\bar{A}$ is chosen as follows:

$$\bar{A} = -\frac{\omega_a^2 M_a}{\mu}\left[(1-\mu)^2(1+i\eta_a) + \eta_a^2\mu\right]. \qquad (7)$$

This choice for $\bar{A}$ gives a resonant apparent mass of the same form as that of a single-degree-of-freedom oscillator:

$$(m_a)_{res} = -i\eta_a M_a\,. \qquad (8)$$

The constant M_a is called the point effective mass of the structure in the vicinity of the resonance under consideration. It can be determined directly from Eq. (8), or in cases where the apparent mass near resonance is dominated by a single mode, M_a will approximately equal the generalized mass of the mode divided by the square of the normalized modal displacement at the driving point.

Substitution of Eq. (7) into Eq. (5) yields a final expression for the apparent mass of the supporting structure:

$$m_a = -M_a\omega_a^2\left[(1-\mu)^2(1+i\eta_a) + \eta_a^2\mu\right] \frac{\omega^2 - \omega_a^2 - i\eta_a\omega_a^2}{(\omega^2 - \mu\omega_a^2 - i\eta_a\mu\omega_a^2)(\mu\omega^2 - \omega_a^2 - i\eta_a\omega_a^2)}\,. \qquad (9)$$

This expression is shown graphically in Fig. 1.

If μ approaches zero in Eq. (9), the antiresonant frequencies approach zero and infinity. The apparent mass then approaches

$$(m_a)_{\mu\to 0} = \frac{M_a}{\omega^2}(\omega^2 - \omega_a^2 - i\eta_a\omega_a^2)\,, \qquad (10)$$

which is the expression for the apparent mass of a single-degree-of-freedom oscillator.

The attached substructure is assumed to behave as a simple spring-mass oscillator of the type shown in Fig. 2. The apparent mass for the substructure is then given by

$$m_b = -\frac{\omega_b^2 M_b(1+i\eta_b)}{\omega^2 - \omega_b^2 - i\omega_b^2\eta_b} = -\frac{\alpha\omega_a^2 M_b(1+i\eta_b)}{\omega^2 - \alpha\omega_a^2 - i\eta_b\alpha\omega_a^2}\,, \qquad (11)$$

where the b subscript denotes the substructure and $\alpha = \omega_b^2/\omega_a^2$ is a tuning parameter defining the nearness of the substructure antiresonant frequency to the supporting structure resonant frequency. These two frequencies are coincident for the case of $\alpha = 1$. The substructure apparent mass is also shown graphically in Fig. 1.

COUPLED SYSTEM

The substructure and supporting structure connected together form a coupled system with new resonant frequencies. If the excitation acting on the supporting structure is relatively

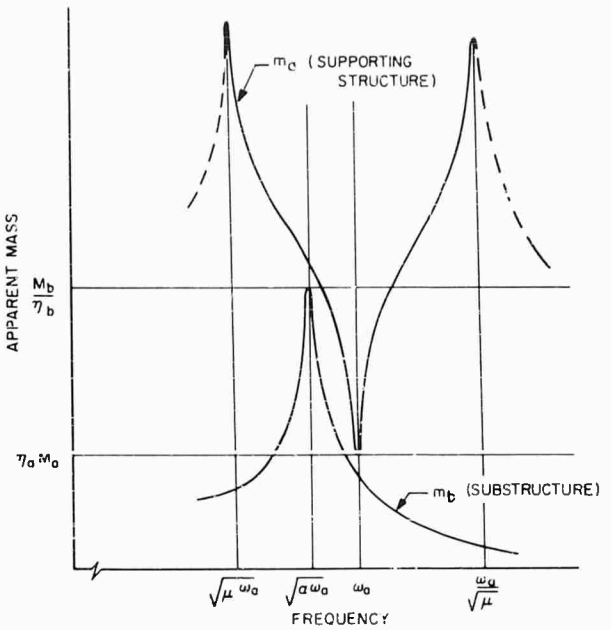

Fig. 1 - Apparent mass curves for substructure and supporting structure

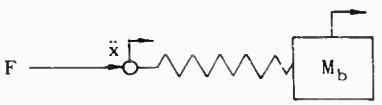

Fig. 2 - Simple spring-mass oscillator

constant over the frequency range of interest, the maximum response will occur at these coupled system resonances. For the structures under consideration, the single supporting structure resonance at ω_a will be replaced by two resonant frequencies after the structures are connected. Only the cases for which the substructure antiresonant frequency lies between the two antiresonant frequencies of the supporting structure (i.e., $\mu < \alpha < 1/\mu$) will be investigated, since this is the range where the greatest interactions between the two structures occur, and also the range over which Eq. (9), the approximate expression for the apparent mass of the supporting structure, is most valid. For these cases the coupled system resonant frequencies must also lie within this frequency range. This conclusion follows from a theorem for coupled systems which states that if the antiresonant frequencies of the two separate structures are listed in order of increasing frequency, then one, and only one, resonant frequency of the coupled system will lie between successive antiresonances [6]. The significance of this fact is that the results of greatest interest will also be confined to the frequency range over which the simplified representation of the supporting structure is applicable.

A schematic representation of the structures is shown in Fig. 3. Before coupling, the supporting structure vibration level at the connection point is $\ddot{x}_a$. This motion is in response to external forces acting on the structure. When the substructure is attached, a reaction force F is generated at the connection. The response of the supporting structure to this reaction force is $\ddot{x}_F = -(F/m_a)$. The modified response at the connection point $\ddot{x}_a$ is the sum of the original and the response due to the reaction force, or

$$\ddot{x}'_a = \ddot{x}_a + \ddot{x}_F = \ddot{x}_a - \frac{F}{m_a} . \qquad (12)$$

The response of the substructure at the connection point, which is due only to the reaction force, is given by

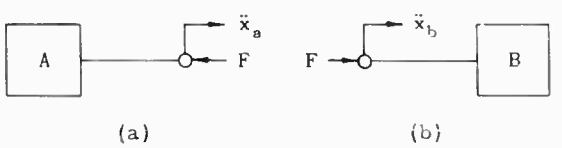

Fig. 3 - Representation of (a) supporting structure, and (b) substructure

$$\ddot{x}_b = \frac{F}{m_b} . \qquad (13)$$

Compatibility of the motions at the connection point requires that

$$\ddot{x}_b = \ddot{x}'_a . \qquad (14)$$

Combining Eqs. (12), (13), and (14) results in

$$\frac{\ddot{x}'_a}{\ddot{x}_a} = \frac{m_a}{m_a + m_b} , \qquad (15)$$

which gives the ratio of the acceleration at the connection point after the substructure is attached to the acceleration before attachment is made, in terms of the apparent masses of the two structures.

SUBSTRUCTURE RESPONSE

The resonant frequencies of the coupled system are those for which $\ddot{x}'_a/\ddot{x}_a$ becomes infinite, or equivalently, the frequencies for which the denominator of Eq. (15) vanishes. The frequency equation is, therefore,

$$m_a + m_b = 0 . \qquad (16)$$

The effect of damping is temporarily suppressed when determining the resonant frequencies by setting $\eta_a = \eta_b = 0$. Substitution of Eqs. (9) and (11) into Eq. (16) then results in

$$M_a(1-\mu)^2(\omega_c^2 - \omega_a^2)(\omega_c^2 - \alpha\omega_a^2) + \alpha M_b(\omega_c^2 - \mu\omega_a^2)(\mu\omega_c^2 - \omega_a^2) = 0 , \qquad (17)$$

where ω_c represents the two coupled system resonant frequencies. Equation (17) can be solved for the coupled system resonant frequencies to obtain

$$\lambda_c = \left(\frac{\omega_c}{\omega_a}\right)^2 = \frac{1}{2}\left[\frac{(1+\alpha)(1-\mu)^2 + \alpha\beta(1+\mu^2)}{(1-\mu)^2 + \alpha\beta\mu}\right] \pm \left[\frac{1}{4}\left(\frac{(1+\alpha)(1-\mu)^2 + \alpha\beta(1+\mu^2)}{(1-\mu)^2 + \alpha\beta\mu}\right)^2 - \alpha\left(\frac{(1-\mu)^2 + \beta\mu}{(1-\mu)^2 + \alpha\beta\mu}\right)\right]^{1/2} , \qquad (18)$$

where $\beta = M_b/M_a$ is a mass ratio parameter and $\lambda_c = \omega_c^2/\omega_a^2$ is a frequency ratio parameter.

The coupled system resonant frequencies are given by Eq. (18) in terms of the nondimensional parameters α, β, and μ. The response of the connection point at these resonant frequencies must next be determined. Substituting Eqs. (9) and (11) into Eq. (15), and setting $(\omega/\omega_a)^2 = \lambda_c$ yields

$$\frac{\ddot{x}'_a}{\ddot{x}_a} = \frac{[(1-\mu)^2(1+i\eta_a) + \eta_a^2\mu](\lambda_c - 1 - i\eta_a)(\lambda_c - \alpha - i\eta_b\alpha)}{[(1-\mu)^2(1+i\eta_a) + \eta_a^2\mu](\lambda_c - 1 - i\eta_a)(\lambda_c - \alpha - i\eta_b\alpha) - \alpha\beta(1+i\eta_b)(\lambda_c - \mu - i\eta_a\mu)(1 - \lambda_c\mu + i\eta_a)} . \qquad (19)$$

It is not the response at the connection point that is being sought, but rather the maximum response on the substructure (i.e., $(\ddot{y}_b)_{\omega=\omega_c}$) in terms of the maximum response that occurred on the supporting structure before the substructure was attached (i.e., $(\ddot{x}_a)_{\omega=\omega_a}$). A response ratio R containing the desired information is, therefore, defined as

$$R = \frac{(\ddot{y}_b)_{\omega_c}}{(\ddot{x}_a)_{\omega_a}} = \frac{(\ddot{y}_b)_{\omega_c}}{(\ddot{x}'_a)_{\omega_c}} \frac{(\ddot{x}'_a)_{\omega_c}}{(\ddot{x}_a)_{\omega_c}} \frac{(\ddot{x}_a)_{\omega_c}}{(\ddot{x}_a)_{\omega_a}} . \qquad (20)$$

There are two values for R, one corresponding to each of the coupled system resonances, but only the larger value is of interest.

The center member of the product in Eq. (20) is given by Eq. (19). The left-hand member is obtained from the equations relating the response to the input for the spring-mass system (Fig. 2):

$$\frac{\ddot{y}_b}{\ddot{x}_a} = -\frac{\alpha(1+i\eta_b)}{\lambda_c - \alpha - i\alpha\eta_b} . \qquad (21)$$

To specify the third member of the product in Eq. (20), a detailed description of the supporting structure and the excitation acting on it are required. This information has not been given for the structure under consideration. It is, therefore, assumed that the response of the structure at the connection point is inversely proportional to its apparent mass at the same point. This assumption is evidently valid for any excitation acting at the connection point, but it should also provide a reasonable approximation to the response for excitation at other locations in the structure. Thus, from Eq. (9)

$$\frac{(\ddot{x}_a)_{\omega_c}}{(\ddot{x}_a)_{\omega_a}} = \frac{(m_a)_{\omega_a}}{(m_a)_{\omega_c}}$$

$$= -i\eta_a \frac{(\lambda_c - \mu - i\eta_a\mu)(1 - \lambda_c\mu + i\eta_a)}{[(1-\mu)^2(1 + i\eta_a) + \eta_a^2\mu](\lambda_c - 1 - i\eta_a)} . \quad (22)$$

The expression for the response ratio R is now obtained by substituting Eqs. (19), (21), and (22) into Eq. (20):

$$R = \frac{i\eta_a\alpha(1 + i\eta_b)(\lambda_c - \mu - i\eta_a\mu)(1 - \lambda_c\mu + i\eta_a)}{[(1-\mu)^2(1 + i\eta_a) + \eta_a^2\mu](\lambda_c - 1 - i\eta_a)(\lambda_c - \alpha - i\eta_b\alpha) - \alpha\beta(1 + i\eta_b)(\lambda_c - \mu - i\eta_a\mu)(1 - \lambda_c\mu + i\eta_a)} . \quad (23)$$

The discussion is restricted at this point to the case of structures with equal damping (i.e., $\eta_a = \eta_b = \eta$). Structures with unequal damping will be considered later. With this restriction, Eq. (23) can be rearranged to give the following expression for the magnitude of R:

$$|R| = \left(\frac{N_1^2 + N_2^2}{D_1^2 + D_2^2}\right)^{1/2} , \quad (24)$$

where

$$N_1 = \eta\alpha[\lambda_c^2\mu - 2\lambda_c(1 + \mu^2) + \mu(3 - \eta^2)] ,$$

$$N_2 = \alpha[\lambda_c^2\mu - \lambda_c(1 + \mu^2)(1 - \eta^2) + \mu(1 - 3\eta^2)] ,$$

$$D_1 = \eta\{\lambda_c^2\mu + \lambda_c[(1 + \mu^2)(1 + \alpha + \alpha\beta) - 3\mu(1 + \alpha)] - \alpha[3(1 - \mu)^2 - \mu(1 - \eta^2 - 3\beta)]\} ,$$

and

$$D_2 = \{\lambda_c^2[(1 - \mu)^2 + \alpha\beta\mu + \eta^2(1 + \alpha)] - \alpha[(1 - \eta^2)[(1 - \mu)^2 + \alpha\beta\mu] + 2\eta^2\mu]\} .$$

DISCUSSION OF RESULTS

Equations (18) and (24) are the most significant relations in this discussion. Equation (18) gives the new resonant frequencies of the coupled system; Eq. (24) gives the maximum response on the substructure at these frequencies. The coupled system resonances and the substructure response have been determined for a typical range of the parameters α, β, and μ and the results plotted in a series of curves.

Figures 4 and 5 show the effect of parameter variations on the coupled system resonant frequencies. In Fig. 4, μ equals zero, giving the greatest separation between the supporting structure antiresonant frequencies. The coupled system resonant frequencies are plotted as functions of the tuning parameter α for various mass ratios β. For small values of β, representing weak dynamic coupling, the coupled system resonances occur near the resonant frequency of the supporting structure and the antiresonant frequency of the substructure. As β is increased, the interactions become more significant, and the coupled system resonances shift farther away from these frequencies.

Figure 5 shows the effect of β on the resonant frequencies for various separations of the supporting structure antiresonant frequencies. In this figure, α is fixed at unity, which represents the case of coincident substructure antiresonant and supporting structure resonant frequencies. Resonant frequencies are confined to the range between $\sqrt{\mu}\,\omega_a$ and $\omega_a\sqrt{\mu}$, as discussed previously, and approach these boundaries for large values of β.

The response ratios, the more significant results of this study, are shown in Fig. 6 as functions of the tuning parameter α for various values of the mass ratio β. For these curves $\mu = 0$ and $\eta = 0.1$. The largest values of the response ratio occur at approximately α equals unity for the range of β of greatest interest. This result is consistent with the prevailing impression that the condition of coincident supporting structure resonant and substructure antiresonant frequencies generates the largest vibration on the substructure. Although not shown by the curves, the response obtained for $\alpha = 1$ was very close to the maximum for all values of μ.

The effect on maximum response of varying the separation between the supporting structure antiresonances is shown in Fig. 7, where the maximum value of the response ratio is plotted as a function of μ. These curves reveal that the largest substructure response is obtained for either $\mu = 0$ or $\mu = 1$. Narrowing the separation of the antiresonances at first reduces the response, but for some values of α and η this trend is reversed as μ approaches unity, and the response ratio becomes larger than that obtained for $\mu = 0$.

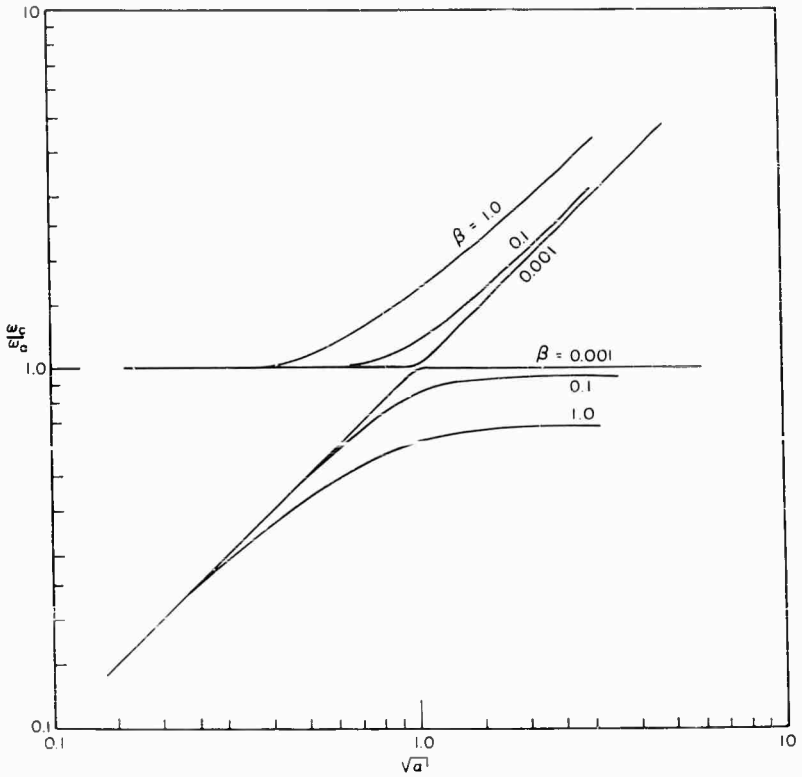

Fig. 4 - Effect of tuning parameter α and mass ratio β on coupled system resonant frequencies ($\mu = 0$)

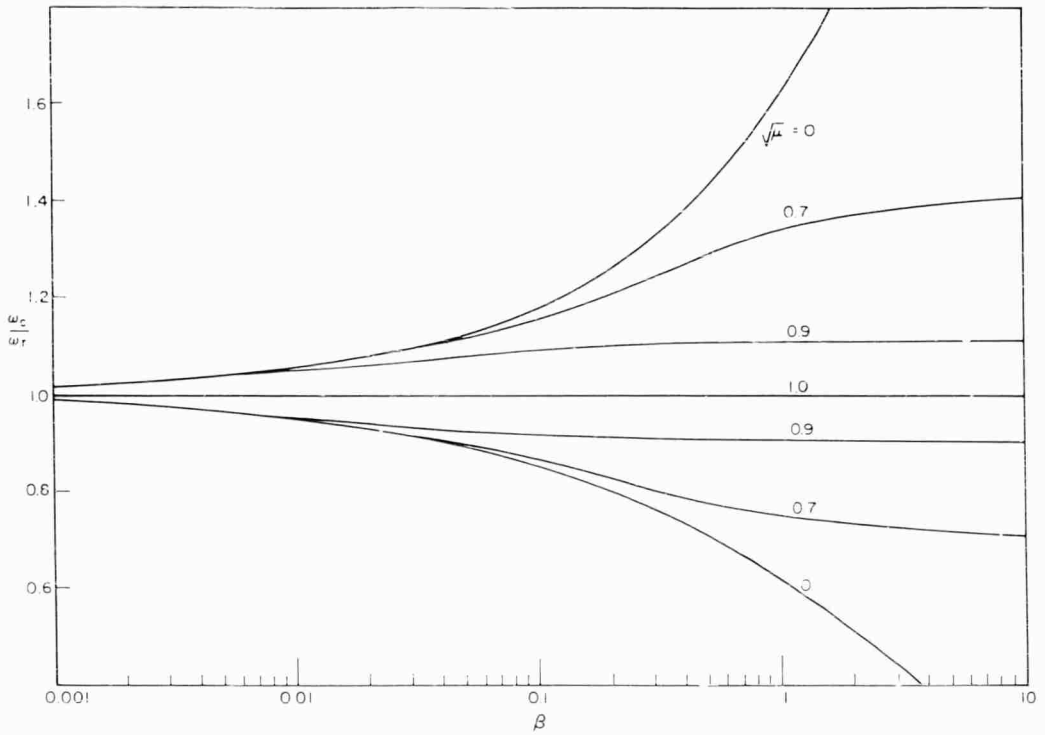

Fig. 5 - Effect of mass ratio β and antiresonant separation parameter μ on coupled system resonant frequencies ($\alpha = 1$)

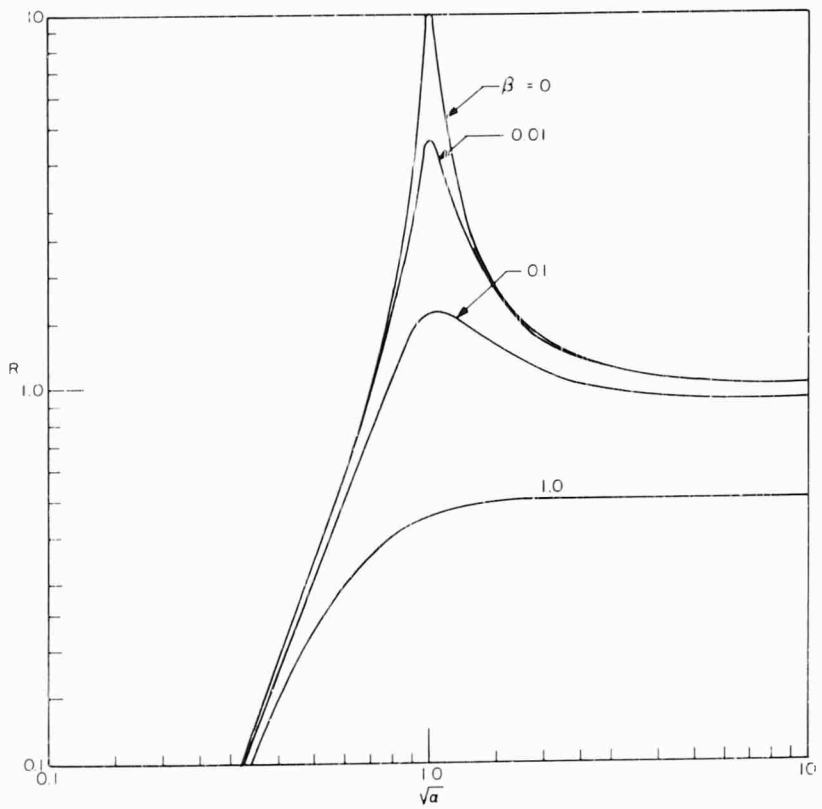

Fig. 6 - Effect of tuning parameter α and mass ratio β on response ratio ($\mu = 0$, $\eta = 0.1$)

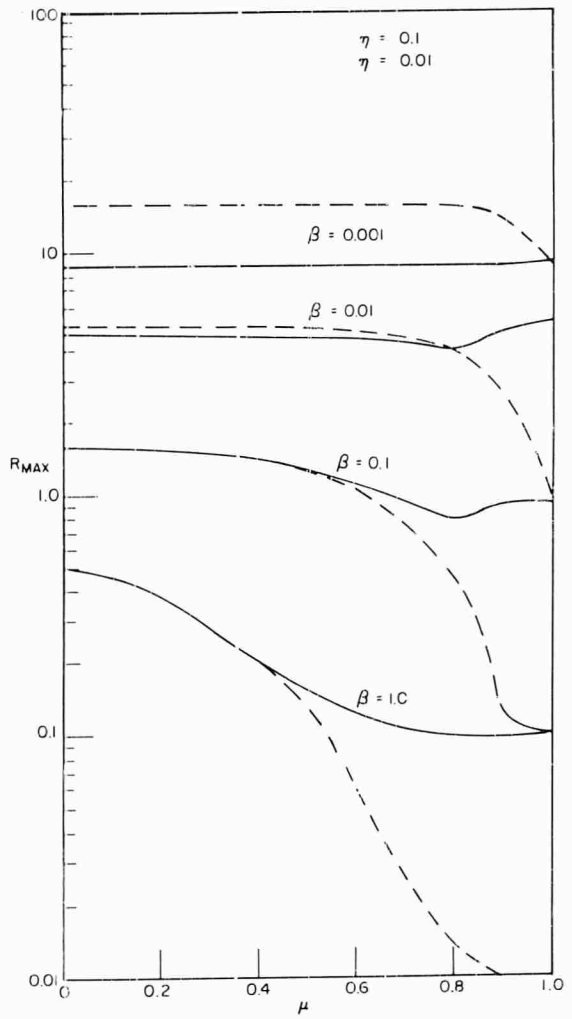

Fig. 7 - Effect of antiresonant separation parameter μ on maximum response ratio

Figure 8 shows the maximum response ratios for the cases of $\mu = 0$ and $\mu = 1$ as functions of β for various values of η. These curves show the range for which the response ratio corresponding to $\mu = 0$ is greater than that corresponding to $\mu = 1$, and vice versa. It is seen that the $\mu = 0$ case gives the greatest response for large values of β, whereas for intermediate values of β, the $\mu = 1$ case becomes more severe. For very small values of β, the curves corresponding to $\mu = 0$ and $\mu = 1$ converge to the same response ratio.

The information contained in Fig. 8 is presented in a more convenient form in Fig. 9, where the maximum possible values of the response ratio are plotted as functions of β and η. These results are obtained by choosing, for any value of β and η, that combination of μ and α giving the greatest substructure response. The curves indicate that only for very small values of β does R_{max} approach $1/\eta$, the value obtained when interactions are neglected. For intermediate values of β, R_{max} is significantly lower than $1/\eta$. It must be emphasized that β is the ratio of the substructure effective mass to the point effective mass of the supporting structure, and not simply the ratio of the rigid body masses. Since the point effective mass of the supporting structure will generally be considerably smaller than its rigid body mass, particularly at frequencies well above the first resonance, interaction effects may be quite important even when the ratio of rigid body masses is very small.

One important characteristic of the results, as indicated by the curves in Fig. 8, is the relative insensitivity of R_{max} to changes in η in the range of significant coupling (i.e., $\beta > 10^{-3}$). Since η is generally the parameter whose values are known with the least accuracy, this behavior is quite favorable. In addition, R_{max} is less sensitive to changes in β than might be expected, varying approximately as $\beta^{1/2}$ over much of the range. This is in contrast to the usual forced response calculations, for which the response varies inversely as the mass to the first power.

EFFECT OF UNEQUAL DAMPING

The discussion of the effect of unequal damping in the two structures is restricted to the case of $\alpha = 1$ and $\mu = 0$, which gave results closely approximating (within about 15 percent) the worst case for equal damping in the two structures. Since the resonant frequencies are assumed to be unaffected by damping, Eq. (18) remains applicable, and with the substitution of $\alpha = 1$ and $\mu = 0$ it reduces to

$$\lambda_c = \left(\frac{\omega_c}{\omega_a}\right)^2 = 1 + \frac{\beta}{2} \pm \left[\beta + \frac{\beta^2}{4}\right]^{1/2} . \qquad (25)$$

Rewriting Eq. (23) with $\alpha = 1$ and $\mu = 0$ yields

$$R = \frac{i\eta_a \lambda_c (1 + i\eta_b)}{(\lambda_c - 1 - i\eta_a)(\lambda_c - 1 - i\eta_b) - \beta\lambda_c(1 + i\eta_b)} . \qquad (26)$$

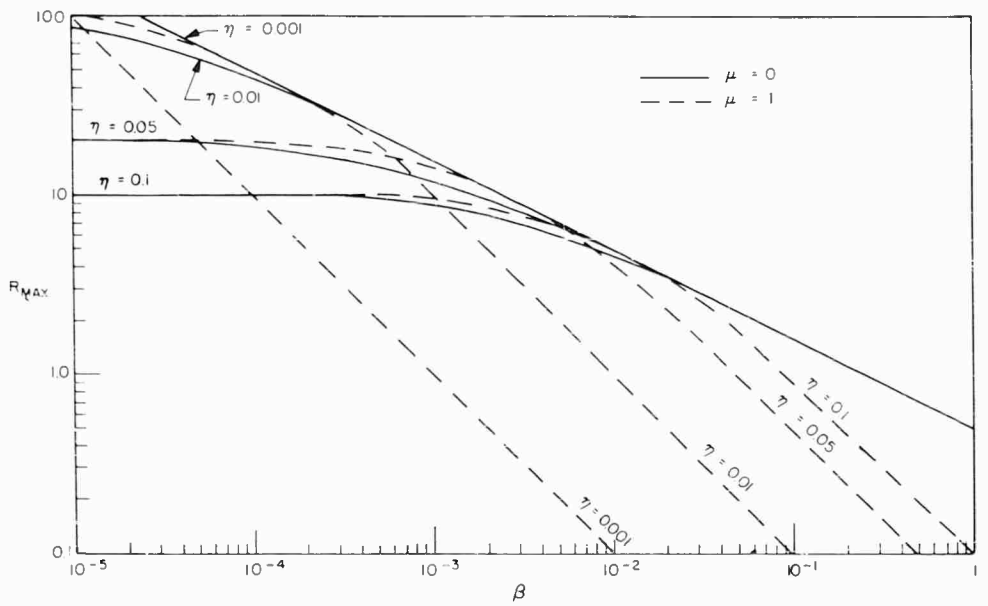

Fig. 8 - Maximum response ratio for $\mu = 0$ and $\mu = 1$

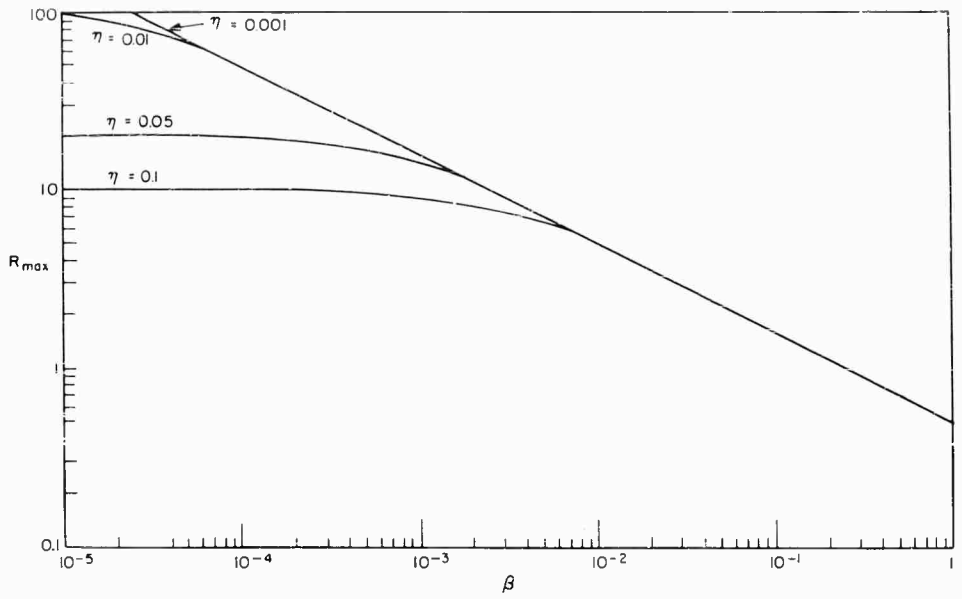

Fig. 9 - Maximum response ratio for equal damping case

Rearrangement of Eq. (26) to obtain the magnitude of R yields

$$|R| = \lambda_c \left[\frac{1 + \eta_b^2}{\eta_b^2 + \left[\frac{\eta_b}{\eta_a} \lambda_c^2 + \left(1 - \frac{\eta_b}{\eta_a} \right) \lambda_c - 1 \right]^2} \right]^{1/2} \tag{27}$$

This expression is plotted in Figs. 10, 11, and 12 for a typical range of damping values. The curves are similar to the equal damping curves of Fig. 9, but the variation of R with damping is more pronounced than for the equal damping case, particularly when the damping of the supporting structure is small. It is still concluded, however, that over much of the typical range, R is not strongly sensitive to errors in the damping η or the mass ratio β.

CONCLUDING REMARKS

A new approach for conservatively estimating the response on a vibration-excited elastic substructure has been considered. The approach is restricted to singly interconnected, lightly damped structures with well-separated resonances. Interactions between the two structures are considered, and the maximum response that can occur on the substructure under the worst conditions of dynamic coupling is predicted. This maximum response is generally found to be significantly lower than the response predicted by a conventional motion input approach, in which interactions between the connected structures are neglected.

The use of the maximum response approach requires that the effective masses and damping of the two structures, as well as the vibration levels at the connection point, be known. However, useful results can usually be obtained even with rough values for these structural characteristics, since the response ratio is not strongly sensitive to variations in η and β; thus, the estimates of maximum substructure response will generally be more accurate than the knowledge of either η or β.

Impedance methods, such as the one presented here, could be used to greater advantage in estimating the response of connected systems if environmental vibration data were accompanied by rough measurements of the associated impedances. It is urged that such measurements be made more frequently in the future.

ACKNOWLEDGMENTS

The assistance of L. Mitchell and C. E. Squires of the Dynamic Analysis Section of Grumman Aircraft with the work reported here is gratefully acknowledged.

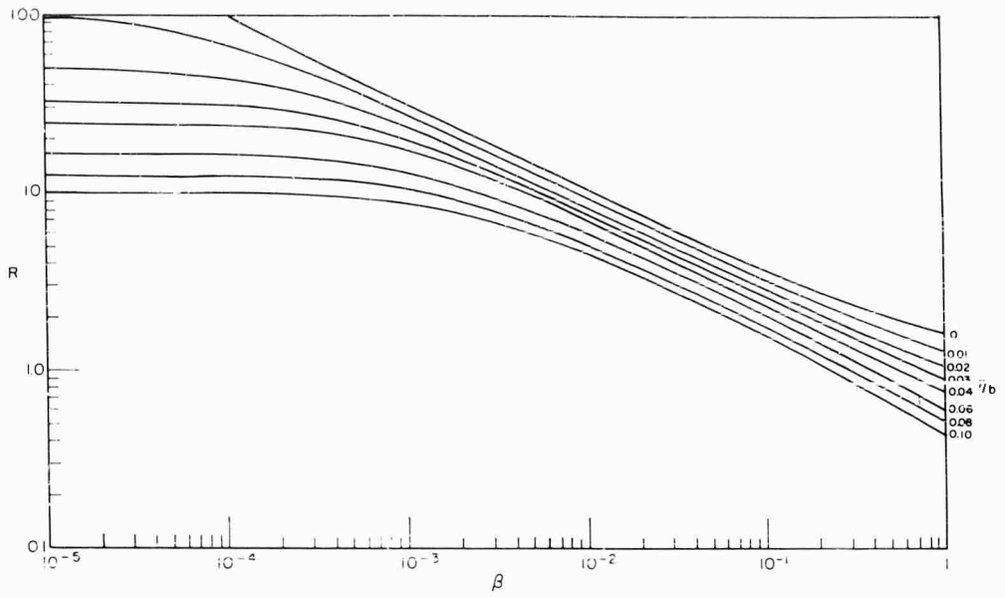

Fig. 10 - Response ratio for unequal damping case ($\mu = 0$, $\alpha = 1$, $\eta_a = 0.1$)

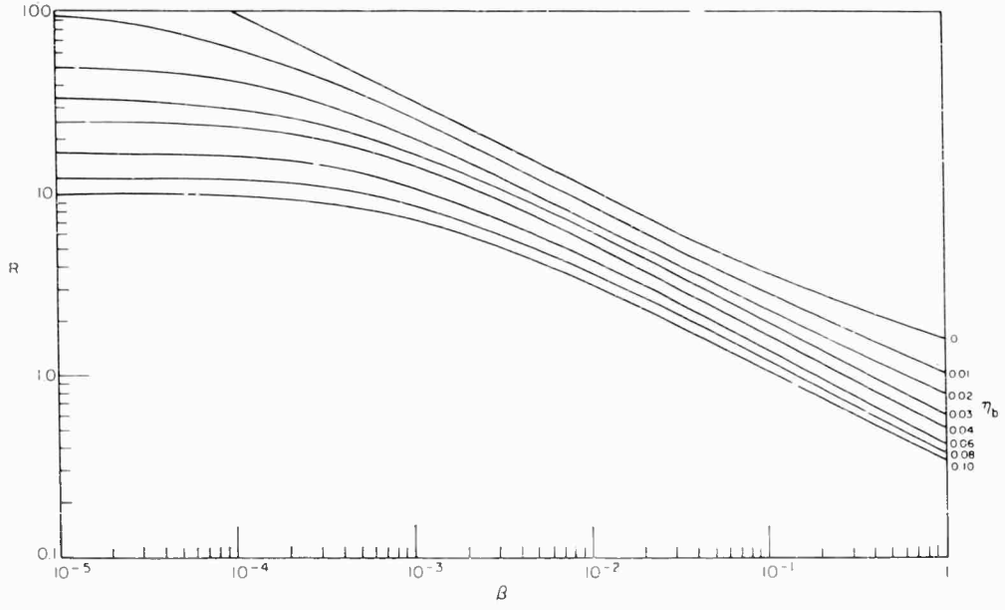

Fig. 11 - Response ratio for unequal damping case ($\mu = 0$, $\alpha = 1$, $\eta_a = 0.05$)

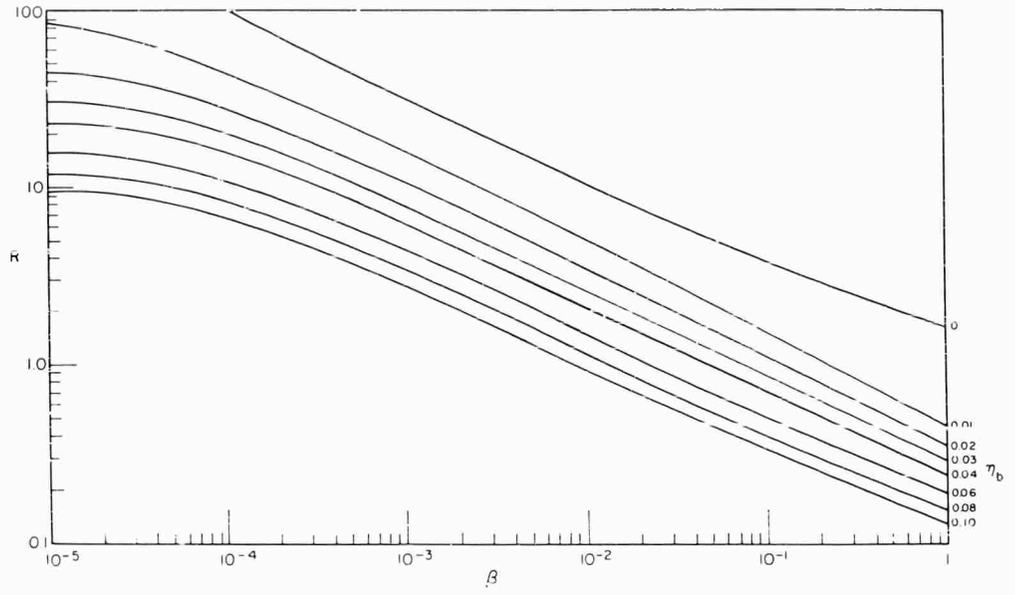

Fig. 12 - Response ratio for unequal damping case ($\mu = 0$, $\alpha = 1$, $\eta_a = 0.01$)

REFERENCES

1. L. J. Pulgrano, "Impedance Considerations in Vibration Testing," Shock, Vibration and Associated Environment Bull. No. 31, Part II, p. 236 (Mar. 1963).

2. R. Plunkett, Ed., "Mechanical Impedance Methods," ASME (1958).

3. E. L. Hixson, "Mechanical Impedance and Mobility," Shock and Vibration Handbook, Vol. 1 (McGraw-Hill Book Co., Inc., New York, 1961), Chap. 10.

4. R. E. D. Bishop and D. C. Johnson, The Mechanics of Vibration, Cambridge University Press, 1960.

5. S. Levy, "Form of Analytical Expressions for Mechanical Impedance and Mobility," J. Acoust. Soc. Am., p. 31 (Jan. 1963).

6. R. H. MacNeal, "Vibrations of Composite Systems," Cal. Tech. Report No. 4 for ARDC (DDC No. AD 63118) (Oct. 1954).

* * *

DETERMINATION OF SYSTEM FIXED BASE NATURAL FREQUENCIES BY SHAKE TESTS

R. E. Kaplan and L. P. Petak
U. S. Naval Research Laboratory
Washington, D. C.

INTRODUCTION

A shock design-analysis method [1] developed at the U. S. Naval Research Laboratory for shipboard equipment requires the use of design shock spectra in the analysis of a contemplated equipment. The development of these design shock spectra requires that the fixed base natural frequencies of certain in-place systems be known. (The fixed base natural frequencies of a system are the frequencies which the system would have if it were mounted on a base of infinite mass and stiffness.) At present, the most convenient method of finding these frequencies for complicated in-place system is that of "shake" tests. This involves exciting the structure with a sinusoidal force at various frequencies and recording the response at significant locations. Since shipboard equipment is not attached to a fixed base, its base in reality being a boundary between the equipment-foundation system and a supporting structure, peaks occurring in the responses of shipboard equipment are at the natural frequencies of the complete system (equipment foundation, base, and supporting structure). The ratio of the amplitudes of equipment motion and base motion is the quantity considered in determining the frequencies of the shipboard equipment-foundation system.

Previous techniques used in conducting shake tests have not given correct frequencies. A study of the theory of resonance testing was made to determine why the results were incorrect, and how shake tests should be properly conducted to obtain correct results. An analog computer study was then performed to illustrate that the previous method was incorrect and to verify that the proposed new method would provide the correct frequencies. A five-mass (M_1, M_2, M_3, M_4 and M_5) system with conveniently chosen parameters (Fig. 1) was simulated on the computer. Uniform viscous damping was introduced into the model to assure computer stability. Since the quantity of this type of damping increases with frequency, the motion at high frequencies was suppressed.

PAST METHOD

Previous techniques used during shake tests on ships were based largely on expediency. The massiveness of the equipment system to be analyzed influenced the placing of the driving point. The crowded shipboard conditions and limited handling techniques placed a severe restriction on the size of shaker, and hence, on the force that could be applied. A driving point was chosen on the equipment such that significant response could be obtained. An attempt was then made to select the desired frequencies by noting prominent peaks in a ratio plot of equipment driving point motion to base motion.

This method of conducting shake tests and analyzing the data can not give correct results.

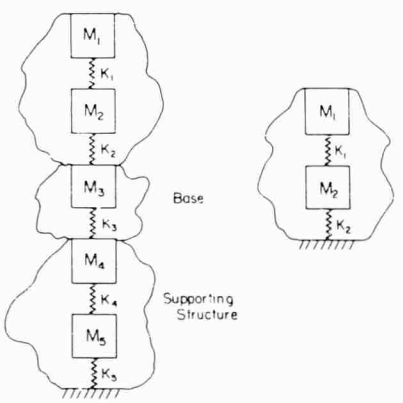

Fig. 1 - Simulation of an equipment-foundation system not mounted on a fixed base

NOTE: References appear on page 99.

Its errors was illustrated by application to the analog simulated system. The five-mass system was driven at M_1; the ratio of the driving point motion M_1 to base motion M_3 is shown in Fig. 2. Peaks were expected at the two fixed base natural frequencies of the simulated equipment foundation system. A prominent peak occurs at 58 cps; it is difficult to select the second frequency. By this method then, the first fixed base frequency of the equipment-foundation system is 58 cps. The calculated frequencies of the two-mass system in the simulated problem are 37.1 and 107.1 cps; therefore, there is an error of 21 cps in choosing the first frequency.

An inspection of the equations of motion for a linear, undamped, five-degree-of-freedom system was made to explain the discrepancy. The review revealed that if the five-mass system is excited at the top mass, M_3 nulls at the frequencies of the two-mass system below itself. (The two-mass system is fixed at M_3 and the base.) The plotted ratio will show peaks at the frequencies of this two-mass system. The calculated frequencies for this system in the simulated problem are 58.7 and 113.0 cps; the former agrees well with that yielded by the experimental ratio plot.

PROPOSED METHOD

The equation review showed that if a mass of a dynamic chain is driven with a sinusoidal force and response is recorded at any mass, this response will approach zero at the fixed base frequencies of the system on the side of the response mass away from the driven mass, and at the fixed base frequencies of the system on the side of the driven mass away from the response mass. For example, in Fig. 3, when driving at M_3 of the five-mass system, the response of M_2 nulls at the frequency of the one-mass system above M_2 and at the frequencies of the two-mass system below M_3. If the response of the driven mass is recorded, it will

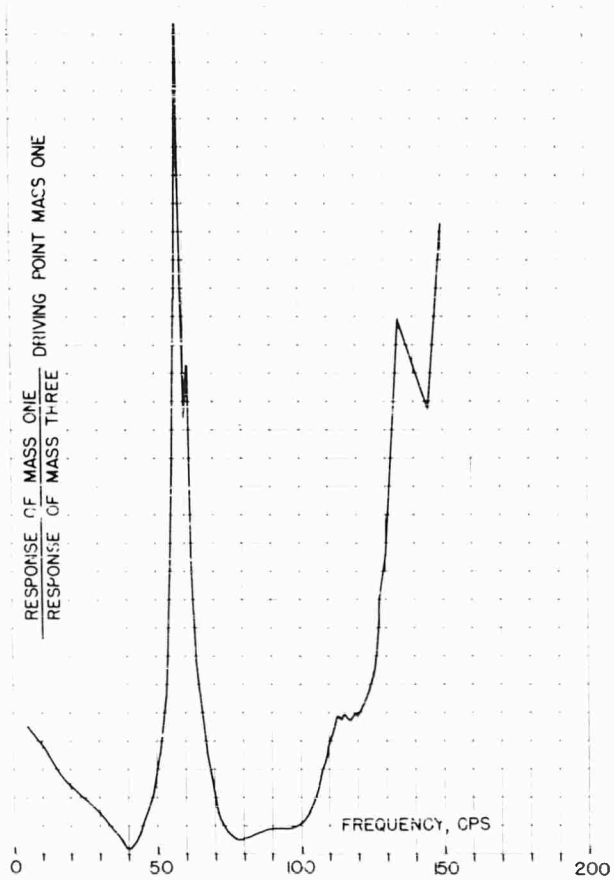

Fig. 2 - Ratio of response of M_1 to that of M_3 when driving force is at M_1

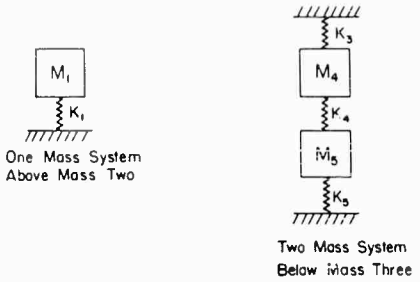

Fig. 3 - Systems at whose frequencies minima occur in response of M_2 when exciting force is at M_3

approach zero at the fixed base frequencies of the systems on either side of the mass.

An in-place system should be excited at its base or at some point below its base. Then the record of base response will exhibit valleys at the fixed base frequencies of the equipment-foundation system and at the fixed base frequencies of the structural system below the driving point. The recorded response of a point on the equipment-foundation system will display valleys at the extraneous subbase system frequencies and appreciable response at the fixed base frequencies of the equipment-foundation system. Therefore, a ratio plot of equipment motion to base motion will cause the fixed base frequencies of interest to show as dominant peaks and will eliminate the extraneous frequencies.

The proposed technique was applied to the analog simulated problem. The system was excited at M_3; the response of this mass is shown in Fig. 4a. Valleys occur at 37, 60, and 110 cps. The ratio of the response of M_2 to that of M_3 is given in Fig. 4b; prominent peaks occur at 36 and 107 cps. Since these peaks coincide approximately with valleys at 37 and 110 cps in the previous figure, frequencies of 36 and 107 cps were chosen as fixed base natural frequencies of the simulated equipment-foundation system. As stated before, the calculated frequencies are 37.1 and 107.1 cps. The new method resulted in selection of correct frequencies.

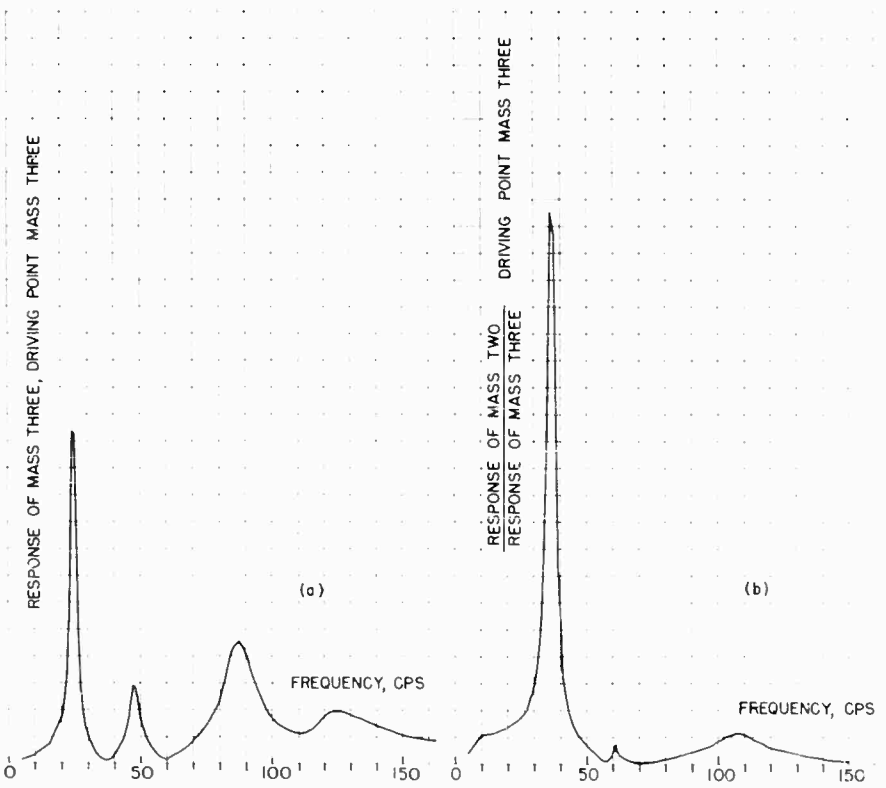

Fig. 4 - Driving point at M_3: (a) response of M_3 and (b) ratio of response of M_2 to that of M_3

SPECIAL CASES

Several special cases were investigated on the analog computer to determine if this technique could be employed. For example, a five-mass system was programed (Fig. 5) so that the frequency of the one-mass system above M_2 equaled one of the three frequencies of the three-mass system below M_2. This frequency, 43.6 cps, then also became one of the five frequencies of the complete system. The response of interest in this case was that of M_2 when the system was excited at M_2. As seen in Fig. 6a, there is a prominent dip at 43 cps. This dip occurs in place of the peak normally anticipated. The ratio plot of the response of M_1 to that of M_2 (Fig. 6b) displays a peak at 43 cps. The new method gave correct results for this case. Similar distinctive cases were simulated, and in each the technique produced the desired fixed base frequencies.

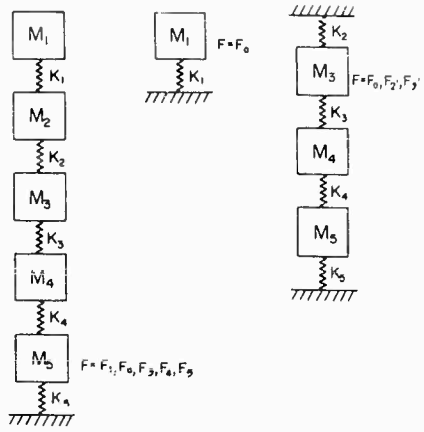

Fig. 5 - Special case: fixed base subsystems with common natural frequency also frequency of complete system

CASE INVOLVING ROTATION AND TRANSLATION

An investigation [2] was made of resonance testing in a case involving small rotation, as well as translation. The model of a system is that of Fig. 7, where the upper massless bar with lumped masses represents the equipment and the lower represents the equipment base. All joints are hinged and the system is assumed

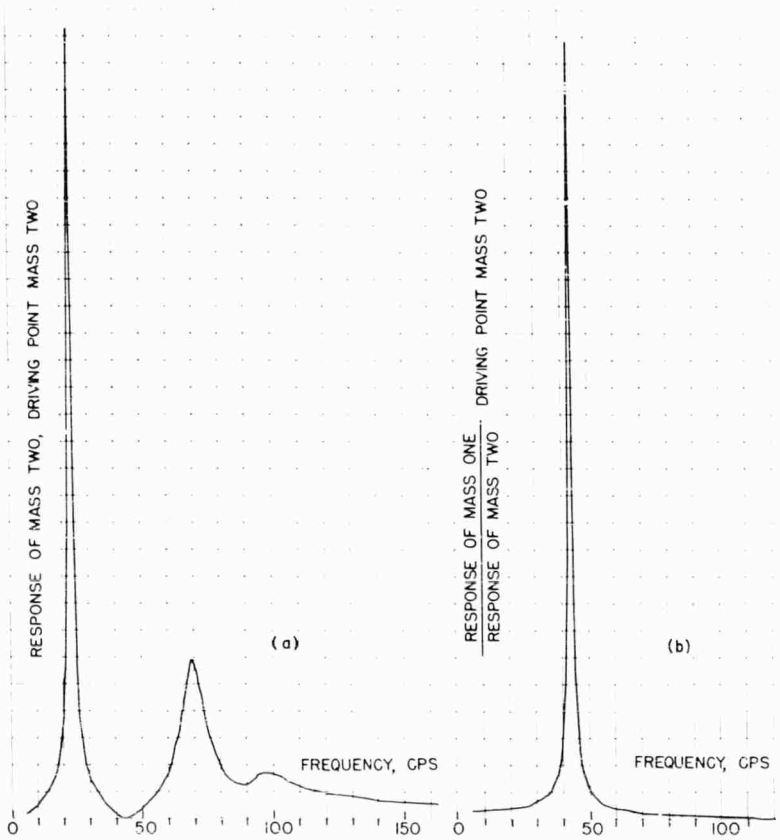

Fig. 6 - Special case: driving point at M_2: (a) response of M_2, and (b) ratio of response of M_1 to that of M_2

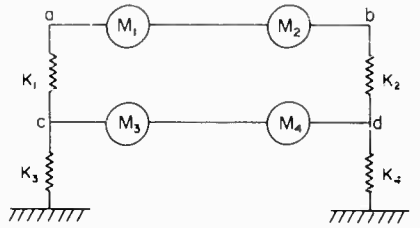

A MODEL INCLUDING ROTATION AND TRANSLATION

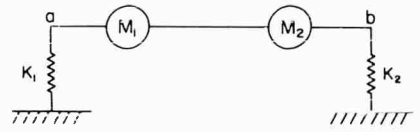

EQUIPMENT SYSTEM ON FIXED BASE

Fig. 7 - Simulation of system including capability for small rotation and translation

to be constrained only for stability. The equipment system has two fixed base natural frequencies with two associated mode shapes. These modal distortions cause displacements across the springs and resultant spring forces. The investigation revealed that if a sinusoidal force is located at each spring with magnitude proportional to the respective transmitted spring force and at the fixed base frequency of the mode, the equipment system will undergo the fixed base mode of vibration. The motion of the equipment base tends to a minimum. Thus, with the extra shakers required, the new method could be employed to find the desired fixed base natural frequencies

SUMMARY AND CONCLUSIONS

In the past, correct fixed base natural frequencies of in-place shipboard equipment-foundation systems have not been found. This paper presents a method that will provide the correct frequencies. It includes an analog computer proof of the new technique's validity. Although the method functioned well in simulation, it will cause field difficulties. The shaker must be placed at or below the base of the equipment and must have sufficient force to excite the modes of interest. These specifications are difficult to fulfill because of limited shaker size and handling techniques. Also, case involving rotation and translation require additional shakers with varying force, as well as frequency. However, once these field difficulties are overcome, shake tests can be utilized to obtain the fixed base natural frequencies of an in-place equipment – foundation system.

REFERENCES

1. R. O. Belsheim and G. J. O'Hara, "Shock Design of Shipboard Equipment – Part I – Dynamic Design-Analysis Method," NRL Report 5545 (Sept. 16, 1960).

2. P. F. Cunniff and G. J. O'Hara, "Shipboard Shock Fundamentals – Frequency Determination of Structural Systems by Shake Tests," to be published in Rept. NRL Progr.

DISCUSSION

L. Balazer (Sylvania): What is the proof, practical if possible, that the first method of analysis was incorrect and that your new methods are correct?

Mr. Petak: Practical proof that the old method was incorrect consists of a series of shake tests conducted in Norfolk last summer, I believe. The frequencies derived from the data, were, in fact, incorrect. Since they did not agree with calculated frequencies which were known. In fact, the frequencies which we got from the shake tests were absurd. With respect to the new method, so far the only proof we have is the analog computer proof and, of course, the equation study. However, we do hope to make some practical field tests in the lab.

* * *

EXPERIMENTAL PROGRAM TO DETERMINE DYNAMIC ENVIRONMENT OF LAUNCH VEHICLES

Irvin P. Vatz
Brown Engineering Co.
Huntsville, Alabama

Empirical methods, derived from a large quantity of precise and controlled data by statistical methods, show the best promise of short-term benefits in predicint launch vehicle self-induced vibration environments. This paper covers the pre-test study of a long-range research program where large quantities of impedance, response and acoustic input data are to be taken. A study was made of available analytical techniques, expanded to accept test data allowing multi-modal impedance evaluations from driving point impedance measurements. Acoustic coupling equations were revised for determination of empirical constants relating input to response. The analytical aspects were covered in sufficient detail that improved knowledge can lead to refinements in the prediction methods. From the analytical requirements a study was made to develop a suitable test facility. A description is included of the test equipment chosen and the background influencing the decisions. A test philosophy is propounded; objective thoughts as well as pilot testing are described. The chief problem is how to keep the data to a practical minimum. Methods of data use are discussed with the program objectives as a guide.

INTRODUCTION

A definition of the self-induced dynamic environment of a launch vehicle is necessary for the design and qualification testing of structural elements and components. The accuracy required by this definition is dependent on the margin within the alloted safety factors. Presently used definitions, although rather primitive in scope, are generally adequate to meet the requirements of current objectives. It is expected that future vehicles, although requiring complete reliability, will have refinements that will better balance the design parameters. This will result in lower safety factors and, therefore, the definition of the self-induced dynamic environment will have to be more precise. Marshall Space Flight Center (MSFC) has initiated a long-range applied research program, "Integrated Dynamic Study for Model and Full-Scale Vehicles," to meet the anticipated need. Langley Research Center (LRC) has shown interest in modeling techniques and has independently embarked on its own research program. At some future time, the work of both MSFC and LRC will be integrated, e.g., to perform tests at like representative locations on both full-scale and model vehicles.

At the time the research program was initiated, a survey of the requirements revealed many problem areas. Theoretical analysis techniques were not adequate or were too complicated. Testing equipment had frequency, dynamic range, and size (mass) limitations. Models could not be produced in perfect enough detail to be representative of some of the dynamic factors that included damping. There were electronic problems of phase retention and data storage and processing. Perhaps the two major problems in determining structural response to acoustic excitation were lack of precise mathematical definitions of the rocket-generated acoustic field and the nonlinear practical response of the structure, where applicable.

The search for problem solution led to the division of the research into four distinct areas.

1. Modeling techniques and model testing.

2. Laboratory testing of controlled isolated phenomena to examine or determine specific details.

3. Development of theoretical analysis techniques and methods.

4. Testing of full-scale models to arrive at empirical and/or statistical methods of environment prediction.

As the vehicles get larger it will become less practical to use full-size vehicles for test purposes; it will be considerably more economical to test small-scale models. Laboratory tests are necessary to advance the state-of-the-art in many of the parametric details of vibration analysis and acoustic coupling. The ultimate in prediction methods should be based on pure analytical techniques. This may prove to be difficult; therefore, the empirical/statistical techniques promise the best short-term improvements in dynamic response prediction methods. This paper is limited to reporting some of the initial pre-test investigations to arrive at these methods. It includes the determination of the test philosophy, test equipment, test procedures, analysis procedures and examples from some pilot test data.

DYNAMIC ENVIRONMENT PREDICTION TECHNIQUES FOR LINEAR SYSTEMS WITH DISTRIBUTIVE MASS

Many prediction techniques have been developed. In general, those that are specific in detail become too complicated for practical solution when all necessary structural details are included. As these methods are refined to make solution more practical, the results become less accurate or have confining limitations. Almost all analytical methods deal with reactive response only and solve for natural frequencies and mode shapes. Actually, the qualification test engineer is more interested in the envelope of maximum response which defines his requirements. This envelope is dependent on the real portion of the complex response equations. Although interested in mode shape, the structure design engineer must also know the maximum deflection. He superimposes this on the static deflections to arrive at loads and stresses. It follows that the needs of design engineering and qualification testing are not met by reactive analysis.

Damping controls the magnitudes of steady state response by physically equating the input energy to dissipated and radiated energy. In distributed mass systems, the impedance measured at a resonance is not necessarily representative of the structural damping coefficient; modal and measurement location considerations must be taken into account. Within the present state-of-the-art, structural damping of complex structures cannot be predicted accurately by analytical means. One of the prime objectives of the pre-test studies was the analysis of test data to determine damping values accurately.

The dynamic environment of a launch vehicle has many sources. The scope encompassed by this test program is initially limited to conditions at the instant of lift-off. When there is only one prime source — the rocket engines. The dynamic energy generated by the engines will travel to the various locations of the vehicle by three paths: structure, air, and fluid systems and filled tanks. The fluid paths will not be investigated during this test program, thereby limiting the scope to the structural and acoustic paths. The first phases of the program will investigate local and transfer impedances and the second group of tests will measure the response to acoustic excitation.

A literature search revealed two representative approaches to analysis of acoustic excitation of distributed mass structures. The first, by Allen Powell [1], develops the equations representative of excitation by random pressures and considers the statistical parameters of the induced vibration. R. W. White [2] extends this analysis to the mean square response of thin flat plates, with some modifications by this author to the most general case, as follows:

$$\bar{\xi}^2(x,y,t) = \sum_{m,n} \frac{S^2 \alpha^2_{m,n}(x,y)}{\left[\int_s \alpha^2_{m,n}(x,y)\, M dS\right]^2 \omega^4_{m,n}} H^2_{m,n}(\omega) \times \int_{x=0}^{a} \int_{y=0}^{b} \int_{x'=0}^{c} \int_{y'=0}^{d} PSD \times [P(x,y,t), P(x',y',t), \omega]\, \alpha_{m,n}(x,y) \times \alpha_{m,n}(x',y')\, dx\, dy\, dx'\, dy' \quad (1)$$

For those instances where the pressure fluctuations at the boundary layer are spatially homogeneous and cross correlation of pressures at two points is independent of location as long as the distance between the points is constant, the following simplified equation may be developed:

NOTE: References appear on page 121.

$$\left[\frac{\bar{\xi}^2(x,y,t,\omega,\Delta\omega)}{\Delta\omega}\right] = \sum_{m,n} \frac{S^4 \alpha^2_{m,n}(x,y)}{\left[\int_s \alpha^2_{m,n}(x,y)\ MdS\right]^2 \omega^4_{m,n}}$$

$$\times H^2_{m,n}(\omega,\Delta\omega) \left[\frac{\bar{P}^2(t,\omega,\Delta\omega)}{\Delta\omega}\right]$$

$$\times j_x^2(\omega,\Delta\omega,\alpha_{m,n})\ j_y^2(\omega,\Delta\omega,\alpha_{m,n}).^{*} \quad (2)$$

where

$\frac{\bar{\xi}^2(x,y,t,\omega,\Delta\omega)}{\Delta\omega}$ = power spectral density, PSD, of response displacement integrated over bandwidth $\Delta\omega$,

m,n = plate mode numbers,

S = plate area,

$\alpha_{m,n}$ = mode shape,

$\omega_{m,n}$ = undamped natural frequency of the m,nth modes,

M = total plate mass,

$H_{m,n}(\omega)$ = frequency response function for the m,nth mode of a plate,

$$H^2_{m,n}(\omega) = \frac{1}{\left[1 - \frac{\omega^2}{\omega^2_{m,n}}\right]^2 + \frac{1}{Q^2_{m,n}}\left[\frac{\omega}{\omega_{m,n}}\right]^2},$$

$Q_{m,n}$ = resonant quality factor of the m,nth mode,

$\Delta\omega$ = frequency bandwidth,

$\left[\frac{\bar{P}^2(x,y,t,\omega,\Delta\omega)}{\Delta\omega}\right]$ = excitation pressure PSD to bandwidth $\Delta\omega$, and

$j^2_{x,y}(\omega,\Delta\omega,\alpha_{m,n})$ = joint acceptance of a rectangular plate in the x or y direction, average value over bandwidth $\Delta\omega$ centered at frequency ω.

Modal impedance may be substituted for the square of the response factor by the following relationship:

$$|Z(\omega)|^2_{m,n} = \frac{\omega^4_{m,n}\left[\int_S \alpha^2_{m,n}\ MdS\right]^2}{\omega^2 S^2} \times \left[\left(1 - \frac{\omega^2}{\omega^2_{m,n}}\right)^2 + \frac{1}{Q^2_{m,n}}\right]. \quad (3)$$

In a narrow frequency band centered between antiresonances, $\omega^2/\omega^2_{m,n} \approx 1$, and within this limitation, Eq. (3) can be revised to:

$$\left[\left(1 - \frac{\omega^2}{\omega^2_{m,n}}\right)^2 + \frac{1}{Q^2_{m,n}}\left(\frac{\omega^2}{\omega^2_{m,n}}\right)\right] \approx \frac{|Z_{m,n}|^2 \omega^2 S^2}{\omega^4_{m,n}\left[\int_S \alpha^2_{m,n}(x,y)\ MdS\right]^2}. \quad (4)$$

By substituting Eq. (4) into the equation for $H^2(\omega)$ and inserting the bandwidth dependency,

$$H^2_{m,n}(\omega,\Delta\omega) \approx \frac{\omega^4_{m,n}\left[\int_S \alpha^2_{m,n}(x,y)\ MdS\right]^2}{|Z_{m,n}(\omega,\Delta\omega)|^2 \omega^2 S^2}. \quad (5)$$

By substituting Eq. (5) in Eq. (2),

$$\left[\bar{\xi}^2(x,y,t,\omega,\Delta\omega)\right] \approx \sum_{m,n} \frac{\alpha^2_{m,n}(x,y)}{\omega^2|Z_{m,n}(\omega,\Delta\omega)|^2} S^2 \frac{\bar{P}^2(t,\omega,\Delta\omega)}{\Delta\omega} \times j_x^2(\omega,\Delta\omega,\alpha_{m,n})\ j_y^2(\omega,\Delta\omega,\alpha_{m,n}). \quad (6)$$

It should be pointed out that in the process of using Eq. (5) in Eq. (2), the accuracy of the resulting equation is dependent on the quantitative value of damping. When no damping is present, Eqs. (6) and (2) are precisely equivalent. The equivalence diminishes as damping increases, so that Eq. (2) should be used for lightly damped structures.

The right side of Eq. (6) is defined as equivalent to the power spectral density of the generalized force by

$$\left[\frac{\bar{F}^2(t,\omega,\Delta\omega,\alpha_{m,n})}{\Delta\omega}\right] = S^2\left[\frac{\bar{P}^2(t,\omega,\Delta\omega)}{\Delta\omega}\right] \times j_x^2(\omega,\Delta\omega,\alpha_{m,n})\ j_y^2(\omega,\Delta\omega,\alpha_{m,n}). \quad (7)$$

*In the mathematical filtering of the bandwidth, all frequency dependent variables also become bandwidth dependent.

In terms of random mechanical excitation, Eq. (6) becomes

$$\left[\frac{\bar{\xi}^2(x,y,t,\omega,\Delta\omega)}{\Delta\omega}\right] = \sum_{m,n} \frac{\alpha^2_{m,n}(x,y)}{\omega^2 |Z_{m,n}(\omega,\Delta\omega)|^2} \times \left[\frac{\bar{F}^2(t,\omega,\Delta\omega,\alpha_{m,n})}{\Delta\omega}\right] . \quad (8)$$

At this point the first problem arises reducing test data taken at discrete locations and applying the results to equations involving mode shape. The mechanical excitation, in cases of impedance testing, is performed at a discrete location (x,y) which may be defined as location (A); therefore, the PSD of the generalized force is more accurately described in this case by $[\bar{F}^2(t,\omega,\Delta\omega,A)]/\Delta\omega$. The mode shape is defined by

$$\alpha_{m,n}(x,y) = \frac{\xi_{m,n}(x,y,t)}{\beta_{m,n}(t)} . \quad (9)$$

It is convenient to normalize the response $\xi_{m,n}(x,y,t)$ to the response at (A) which would be $\xi_{m,n}(A,t) = \beta_{m,n}(t)$. Then Eq. (9) becomes

$$\alpha_{m,n}(x,y) = \frac{\xi_{m,n}(x,y,t)}{\xi_{m,n}(A,t)} . \quad (10)$$

This is the basis of the second analytical approach to acoustic excitation to be used here. It is reported by Skudrzyk [3] and is founded on the usual set of differential equations describing a distributed mass mechanical system. However, Skudrzyk does not analyze in terms of random excitation. Here normalization to the input location response will be superimposed on the random process equation. The end result, of course, will be the equivalent of Skudrzyk's equation

$$M \frac{\langle \xi^2_{m,n}(x,y,t)\rangle}{\xi^2_{m,n}(A,t)} \left[-\omega^2 + \omega^2_{m,n}(1+j\eta)\right] \xi_{m,n}(A,t) = \int_x \int_y P(x,y,t) \frac{\xi_{m,n}(x,y,t)}{\xi_{m,n}(A,t)} \, dx\, dy , \quad (11)$$

where

$$\frac{\langle \xi^2_{m,n}(x,y,t)\rangle}{\xi^2_{m,n}(A,t)} = E_{m,n} = \frac{\int_x \int_y \xi^2_{m,n}(x,y,t)\, dx\, dy}{S\,\xi^2_{m,n}(A,t)} ,$$

S = area,

$E_{m,n}$ = mode constant,

$ME_{m,n}$ = modal mass ($M_{m,n}$), and

$$\int_x \int_y P(x,y,t) \frac{\xi_{m,n}(x,y,t)}{\xi_{m,n}(A,t)} \, dx\, dy$$

= generalized force.

Returning to the random excitation analysis, substitution of Eq. (10) into Eq. (8) yields:

$$\left[\frac{\bar{\xi}^2(x,y,t,\omega,\Delta\omega)}{\Delta\omega}\right] = \sum_{m,n} \frac{1}{\omega^2} \frac{\xi^2_{m,n}(x,y,t)}{\xi^2_{m,n}(A,t)} \frac{\left[\frac{\bar{F}^2(t,\omega,\Delta\omega,A)}{\Delta\omega}\right]}{|Z_{m,n}(\omega,\Delta\omega)|^2} . \quad (12)$$

The impedance term of Eq. (12) also contains a normalized term $E_{m,n}$ and is bandwidth dependent as follows:

$$|Z_{m,n}(\omega,\Delta\omega)| = \frac{1}{\Delta\omega} \int_{\omega_c - \frac{1}{2}\Delta\omega}^{\omega_c + \frac{1}{2}\Delta\omega} |Z_{m,n}(\omega)| d\omega , \quad (13)$$

where ω_c = center frequency of bandwidth $\Delta\omega$. The mode shape $[\xi_{m,n}(x,y,t)]/[\xi_{m,n}(A,t)]$ will not vary with frequency but is constant for mode mn throughout the entire frequency spectrum. If measured only at location (A), the equation of these measurements will be

$$\left[\frac{\bar{\xi}^2(A,t,\omega,\Delta\omega)}{\Delta\omega}\right] = \sum_{m,n} \frac{1}{\omega^2} \frac{\xi^2_{m,n}(A,t)}{\xi^2_{m,n}(A,t)} \frac{\left[\frac{\bar{F}^2(t,\omega,\Delta\omega,A)}{\Delta\omega}\right]}{|Z^2_{m,n}(\omega,\Delta\omega)|^2} , \quad (14a)$$

which reduces to

$$\left[\frac{\bar{\xi}^2(A,t,\omega,\Delta\omega)}{\Delta\omega}\right] = \sum_{m,n} \frac{1}{\omega^2} \frac{\left[\frac{\bar{F}^2(t,\omega,\Delta\omega,A)}{\Delta\omega}\right]}{|Z_{m,n}(\omega,\Delta\omega)|^2} . \quad (14b)$$

Equation (14b, is the exact counterpart of the equation,

$$\xi(A,t) = \sum_{m,n} \frac{1}{\omega} \frac{F(A,t)}{\sqrt{|Z_{m,n}(\omega)|^2}} , \quad (15)$$

which would result from Skudrzyk's work.

Equations (14b) and (15) are in reality nothing more than the definition of velocity impedance

$$Z = \frac{F}{j\omega\xi} . \quad (16)$$

and they form the basis of the mechanical excitation data analysis described later. These equations also describe the equivalent of an electrical-parallel system where

$$\frac{1}{Z_t} = \sum_{m,n} \frac{1}{Z_{m,n}} .$$

This leads to the final reduction of Eq. (14b) to be representative of total response measurements:

$$\left[\frac{\overline{\xi}^2(A,t,\omega,\Delta\omega)}{\Delta\omega}\right] = \frac{\left[\frac{\overline{F}^2(t,\omega,\Delta\omega,A)}{\Delta\omega}\right]}{\omega^2 |Z_t(\omega,\Delta\omega)|^2} . \quad (17)$$

Analysis of the acoustic excitation data is not as straightforward as that of the mechanical excitation data in Eq. (5). In complicated structures, $\alpha^2_{mn}(x,y)$, S^2, $j_x^2(\omega,\Delta\omega,\alpha_{mn})$ and $j_y^2(\omega,\Delta\omega,\alpha_{mn})$ will probably not be determinable by analysis. Measuring the mode shapes and determining the proper areas requires a quantity of testing not consistent with basic objectives. Putting these values to mathematical description and solving for the joint acceptance factors would also be a Herculian task. It was decided to use a first-order approach to the problem and to solve empirically for an all-inclusive coupling factor K that is defined by

$$K^2 = \frac{\alpha_t^2 S^2 j_x^2 j_y^2}{\omega^2} . \quad (18)$$

Equation (6) now becomes

$$\left[\frac{\overline{\xi}^2(x,y,t,\omega,\Delta\omega)}{\Delta\omega}\right] = \frac{K^2(x,y,\omega,\Delta\omega,s)}{|Z_t(\omega,\Delta\omega)|^2}\left[\frac{\overline{P}^2(t,\omega,\Delta\omega)}{\Delta\omega}\right] . \quad (19)$$

The test procedures will measure all quantities but K^2 which now becomes calculable.

The basic objectives of the test program can now be outlined. Mechanical testing will be used to determine the impedance and to help give a definition of the measurement locations. Acoustic excitation will determine the coupling factor K^2, thereby setting up Eq. (19) as a prediction method with K and Z as statistical quantities. The use of Eq. (19) will not be considered as final but as an interim prediction method. As the analytical methods improve, K will be broken down into its basic parts as shown in Eq. (18).

ANALYSIS OF MECHANICAL EXCITATION TEST DATA OF LINEAR DISTRIBUTED MASS SYSTEMS

Multi-modal response to a point force excitation may be considered equivalent to a parallel electric circuit with each of the parallel branches made up of the impedance elements of a single mode in series. Mathematically, this circuit is represented by

$$\frac{1}{Z_t} = \frac{1}{Z_1} + \frac{1}{Z_2} + \frac{1}{Z_3} \cdots + \frac{1}{Z_n} . \quad (20)$$

For convenience, each of the modes will be given a single number representative of their natural frequency sequence. The modal (structural branch) impedance [3] of the nth mode is

$$\frac{1}{Z_n} = \frac{j\xi_n^2(A,t)\omega}{M\langle\xi_n^2(x,y,t)\rangle\left[-\omega^2 + \omega_n^2(1+j\eta)\right]} , \quad (21)$$

where

$j = \sqrt{-1}$,

$\xi_n(x,y,t)$ = modal response displacement vector at (x,y),

M = total mass of system,

$$\xi_n^2(x,y,t) = \frac{1}{S}\int_a\int_b \xi_n^2(x,y,t)\,dx\,dy ,$$

a,b = area boundaries,

ω_n = mode undamped natural frequency,

η = complex loss factor, and

$\xi_n(A,t)$ = modal response displacement vector at drive location (A).

Next, the mode factor E and its inverse B is defined as

$$E = \frac{1}{B} = \frac{\xi_n^2(x,y,t)}{\xi_n^2(A,t)} . \quad (22)$$

Substitution of Eqs. (22) and (21) into Eq. (20) yields the mobility (M_t) equation

$$M_t = \frac{1}{Z_t} = \frac{jB_1\omega}{M\left[-\omega^2 + \omega_1^2(1+j\eta_1)\right]} + \frac{jB_2\omega}{M\left[-\omega^2 + \omega_2^2(1+j\eta_2)\right]} + \cdots + \frac{jB_n\omega}{M\left[-\omega^2 + \omega_n^2(1+j\eta_n)\right]} . \quad (23)$$

To facilitate the data analysis it is assumed that the systems are lightly damped and the natural and antiresonant frequencies are readily recognizable from the data. When this is so, little accuracy will be sacrificed in the first several steps of the analysis by assuming no damping present, and Eq. (23) becomes

$$\overline{M}_t = \frac{1}{\overline{Z}_t} = \frac{jB_1\omega}{M\left[\omega_1^2-\omega^2\right]} + \frac{jB_2\omega}{M\left[\omega_2^2-\omega^2\right]} + \ldots + \frac{jB_n\omega}{M\left[\omega_n^2-\omega^2\right]} . \tag{24}$$

At antiresonance with no damping the mobility is zero. If the antiresonant frequency between the mth and m+1th modes is designated as $\omega_{m,m+1}$. Eq. (24) reduces to

$$0 = \frac{B_1/M}{(\omega_1^2 + \omega_{m,m+1}^2)} + \frac{B_2/M}{(\omega_2^2 - \omega_{m,m+1}^2)} + \ldots + \frac{B_m/M}{(\omega_n^2 - \omega_{m,m+1}^2)} . \tag{25}$$

The objective use of Eq. (25) is to set up a matrix equation that will solve for the inverse of the modal mass. It is also desirable to calculate for the mode constant B_1 where possible. The reactive portion of the mobility $\overline{M}_i(\omega_a)$ at frequency a, b etc., may be measured. Equation (24) is transposed to

$$0 = \frac{-M_i(\omega_a)}{\omega_a} + \frac{B_1}{(\omega_a^2 - \omega_1^2)} + \ldots + \frac{B_n}{(\omega_a^2 - \omega_n^2)} . \tag{26}$$

By combining Eqs. (25) and (26), a matrix equation is formed as follows:

$$0 = \begin{vmatrix} \frac{1}{\omega_1^2-\omega_{1,2}^2} + \frac{1}{\omega_2^2-\omega_{1,2}^2} + \ldots + \frac{1}{\omega_n^2-\omega_{1,2}^2} + 0 & \frac{1}{M_1} \\ \frac{1}{\omega_1^2-\omega_{2,3}^2} + \frac{1}{\omega_2^2-\omega_{2,3}^2} + \ldots + \frac{1}{\omega_n^2-\omega_{2,3}^2} + 0 & \frac{1}{M_2} \\ \vdots & \vdots \\ \frac{1}{\omega_1^2-\omega_a^2} + \frac{1}{\omega_2^2-\omega_a^2} + \ldots + \frac{1}{\omega_n^2-\omega_a^2} + \frac{\overline{M}_i(\omega_a)}{\omega_a} & \frac{1}{M_n} \\ \frac{1}{\omega_1^2-\omega_b^2} + \frac{1}{\omega_2^2-\omega_b^2} + \ldots + \frac{1}{\omega_n^2-\omega_b^2} + \frac{\overline{M}_i(\omega_b)}{\omega_b} & 1 \end{vmatrix} \tag{27}$$

The square matrix is made up entirely of acquired test data. The column matrix is formed of the unknowns and unity; Eq. (27) will solve for the inverse of the modal masses. The modal mass is equated to the total mass by

$$M_n = E_n M = \frac{M}{B_n} . \tag{28}$$

The matrix equation should have read

$$0 = |X| \begin{vmatrix} B_1 \\ B_2 \\ \cdot \\ \cdot \\ \cdot \\ B_n \\ M \end{vmatrix} \tag{27a}$$

but this forms an indeterminant equation. By dividing the column matrix by total mass M, the equation is solvable. In instances where any mode constant B_n or the total mass M is available, Eq. (27a) is solvable and may be used. In some cases when the measurement location is at an anti-node (except for the first few of the lowest numbered modes), the mode constant $E_n = 1/4$. The numeral 4 can be substituted for B_n in Eq. (27a) for the proper mode and the total mass is solvable. The definition of $E_n = 1/4$ is for a rectangular plate with simply supported edges. This is equivalent to the mode shape taking the form of an undamped sine curve. This system must be lightly damped and reasonably small — several wavelengths in size — or the mode shape will approach a damped sine wave. In this case $E \neq 1/4$ and from a mathematical viewpoint for an infinite plate the total mass is indeterminant. The conclusions may be summarized as follows:

1. The modal masses of the vehicle structure are calculable from the data of the launch vehicle.

2. The total mass and mode constant are calculable from the test data of controlled laboratory setups but not generally from the launch vehicle data.

The solution accuracy of the column matrix of Eq. (27) is dependent on the ability of the data to define the required frequencies and true mobility of the square matrix. Widely spaced stepped frequencies on wide-band swept frequency analysis will affect results. The selection of test and data processing equipment and procedures should be influenced by the analysis requirements. Narrow-band PSD or filtered measurements should suffice for the determination of the frequencies. Care should be taken

when determining $\mathcal{M}_i(\omega_a)$ from filtered PSD data. Figure 1 will illustrate this point. Where the mobility curve has a relatively flat slope across the bandwidth, wide- and narrow-band filtered PSD signals have about the same quantitative value. Where the mobility curve slope is steep, especially near resonance and antiresonance, marked differences will appear due to bandwidth. ω_a and ω_b must be selected to give reasonable accuracy to $\mathcal{M}_i$.

The selection of undamped antiresonant frequencies as the prime basis for analysis does not prevent the use of resonant frequency data to determine quantitative damping. When it is assumed that there is no damping coupling between modes, then the impedance at each resonance is the real value of the associated modal impedance. At resonance

$$Z_n = \frac{M E_n \omega_n^2 \eta_n}{\omega_n} = M E_n \omega_n \eta_n = M_n \omega_n \eta_n , \quad (29)$$

which may be solved for η_n as follows:

$$\eta_n = \frac{Z_n}{M E_n \omega_n} = \frac{B_n Z_n}{M \omega_n} = \frac{Z_n}{M_n \omega_n} . \quad (30)$$

The loss factor η_n of the nth mode is related to other conventionally used damping quantities [4]:

$$\eta_n = \left(\frac{2c}{c_c}\right)_n = \frac{\delta_n}{\pi} = \frac{2\pi\Delta f_n}{\omega_n} = \frac{1}{Q_n} = \frac{\psi_n}{2\pi} . \quad (31)$$

where

$(c/c_c)_n$ = critical damping ratio of the mode,

δ_n = logarithmic decrement of the nth mode,

Δf_n = half-power bandwidth of the nth mode,

Q_n = resonant quality factor of the nth mode, and

ψ_n = specific damping capacity of the nth mode.

The mode factor E_n greatly affects the apparent influence of damping on a mode, Eq. (29). When E_n is large, the resonance impedance will be relatively high. From a single-degree-of-freedom system point of view this would imply heavy damping; however, this effect in a distributed mass system may take place in a lightly damped mode if the measurement point (A) is near a node. Equation (30) should produce an accurate plot of resonant damping values with respect to frequency where the modal constants can be determined.

Equation (27) has practical size limitations. A convenient matrix size will cover only a portion of the desired frequency range of this test program. In finite small structures, the total mass may be considered constant throughout all modes. In a very large structure such as a

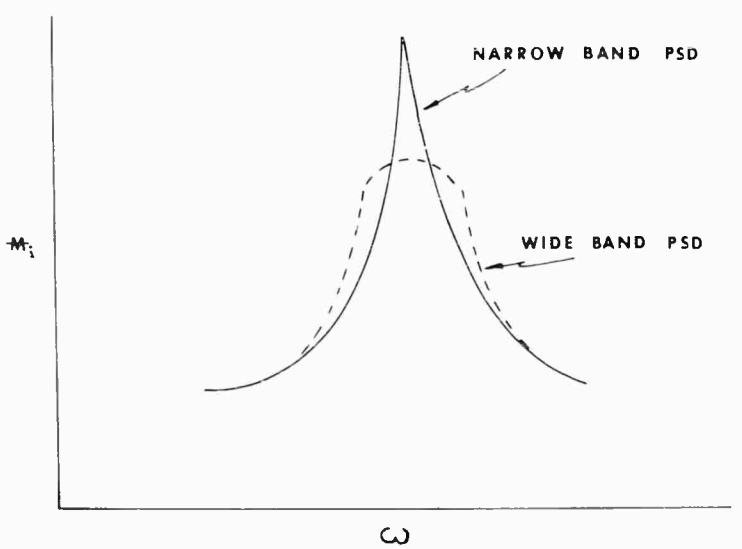

Fig. 1 - Bandwidth effect on mobility

launch vehicle, the areas influenced by the excitation and the total mass M may be frequency dependent. This comes from the fact that high-frequency waves will be damped out in a shorter distance than low-frequency waves. Equation (27) can be arranged to analyze the mth through the nth mode by

$$0 = \begin{vmatrix} \frac{1}{\omega_m^2 - \omega_{m,m+1}^2} + \frac{1}{\omega_{m+1}^2 - \omega_{m,m+1}^2} + \ldots + \frac{1}{\omega_n^2 - \omega_{m,m+1}^2} + 0 \\ \frac{1}{\omega_m^2 - \omega_{m+1,m+2}^2} + \frac{1}{\omega_{m+1}^2 - \omega_{m+1,m+2}^2} + \ldots + \frac{1}{\omega_n^2 - \omega_{m+1,m+2}^2} + 0 \\ \cdot \quad \cdot \quad \cdot \quad \cdot \\ \cdot \quad \cdot \quad \cdot \quad \cdot \\ \cdot \quad \cdot \quad \cdot \quad \cdot \\ \frac{1}{\omega_m^2 - \omega_a^2} + \frac{1}{\omega_{m+1}^2 - \omega_a^2} + \ldots + \frac{1}{\omega_n^2 - \omega_a^2} + \frac{\bar{M}_i(\omega_b)}{\omega_b} \end{vmatrix} \times \begin{vmatrix} \frac{1}{M_m} \\ \frac{1}{M_{m+1}} \\ \cdot \\ \cdot \\ \cdot \\ 1 \end{vmatrix} \qquad (32)$$

or by a similar rearrangement of frequencies and equations to also solve for M_n', the total modal mass effective at higher frequencies. The calculation of M_n or M_n' for successively higher mode combinations will also show the frequency dependency of the area because in relatively uniform structures it should be directly proportional to mass.

For structures where the mass is independent of frequency or for all structures in suitable frequency bands, an interesting high-frequency parameter (E_{av}) can be derived. Figure 2 shows the principles involved. With any mode n, the total impedance near ω_n will follow the electrical parallel rules. In addition, the modal impedance of the 1st to n - 1th modes at ω_n will be mass controlled and for the n + 1 to ∞ modes, the modal impedance will be stiffness controlled. The modal mass lines will generally fall in a band with a limiting value. However, the stiffness of each mode will be increasingly greater with modal number. The impedance near ω_n can be equated as

$$\frac{1}{Z_t} = \frac{1}{\sum_{1 \text{ to } n-1} Z_n} + \frac{1}{Z_n} + \frac{1}{\sum_{n+1 \text{ to } \infty} Z_n} . \qquad (33)$$

Since the impedance of all modes with modal numbers greater than n at ω_n is very large, the last term of Eq. (33) will have a very small value and may be eliminated after inserting the modal mass into the lesser numbered modes; Eq. (33) becomes, therefore,

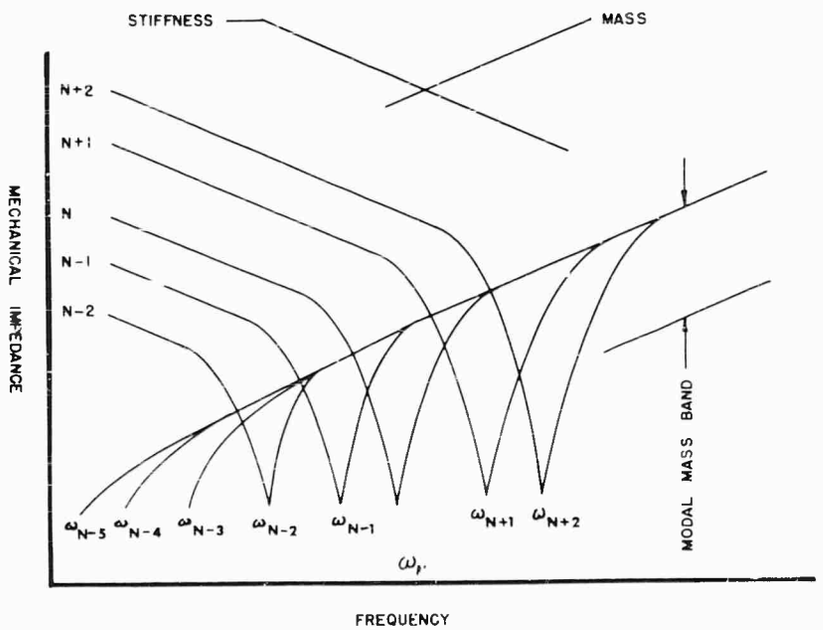

Fig. 2 - Analysis of impedance by independent modes

$$\frac{1}{Z_t} = \left[\sum_{1}^{n-1} \frac{1}{j\omega E_n M}\right] + \frac{1}{Z_n} \quad . \tag{34}$$

The summed term can be substituted for as follows:

$$\sum_{1}^{n-1} \frac{1}{E_n M} = \frac{n-1}{E_{av} M} = \frac{\omega}{[\Delta\omega]\, E_{av} M} \quad , \tag{35}$$

with $(n-1) \approx \omega/[\Delta\omega]$ and $[\Delta\omega]$ being the average frequency difference between mode resonances. Equation (34) now becomes

$$\frac{1}{Z_t} = \frac{(n-1)}{j\omega_{n,n-1} E_{av} M} + \frac{\omega_{n,n-1}}{jE_n M(\omega_n^2 - \omega_{n,n-1}^2)} \quad , \tag{36}$$

with $\omega_{n,n-1}$ being the antiresonant frequency between the nth and n - 1th modes. If zero damping is assumed, $1/Z_t = 0$, Eq. (36) can now be solved for E_n and the total mass M cancels out:

$$E_n = \frac{E_{av}[\omega_{n,n-1}]^2}{[n-1]\left[\omega_{n,n-1}^2 - \omega_n^2\right]} = \frac{E_{av}[\Delta\omega]\,[\omega_{n,n-1}]^2}{\omega\left[\omega^2_{n,n-1} - \omega_n^2\right]} \quad . \tag{37}$$

Equation (37) can be substituted into Eq. (20):

$$Z_n = \frac{[\omega_{n,n-1}]^2 E_{av} M\left[-\omega^2 - \omega_n^2(1 + j\eta)\right]}{\left[\omega_{n,n-1}^2 - \omega_n^2\right]\omega[n-1]} \quad . \tag{38a}$$

Equation (38) can also be written as

$$Z_n = \frac{[\omega_{n,n-1}]^2 E_{av} M\left[-\omega^2 + \omega_n(1 + j\eta)\right][\Delta\omega]}{\left[\omega_{n,n-1}^2 - \omega_n^2\right]\omega^2} \quad . \tag{38b}$$

Damping (loss coefficient) has been reinserted in the numerator of the equation, making the impedance curve accurate near resonance. Since the ω_n^2 term in the denominator was used under the assumption of no damping, it should stay unmodified by the damping influence.

When n is a large enough number, E_{av} will not vary with small changes in n. Therefore, E_{av} becomes a property of the system and location. Equation (38b) can be further reduced. When n is a high number, $\omega_{n,n-1}^2$ will be about the quantitative value of ω^2 in the frequency band between antiresonances. This approximation reduces Eq. (38b) to

$$Z_n \approx \frac{E_{av} M[\Delta\omega]\left[-\omega^2 + \omega_n(1 + j\eta)\right]}{\left[\omega_{n,n-1}^2 - \omega_n^2\right]} \quad . \tag{38c}$$

Substitution of Eq. (38c) into Eq. (36) yields

$$\frac{1}{Z_t(\Delta\omega_n)} \approx \frac{[n-1]}{j\omega_{n,n-1} E_{av} M} + \frac{\left[\omega_{n,n-1}^2 - \omega_n^2\right]}{E_{av} M[\Delta\omega]\left[-\omega^2 + \omega_n^2(1 + j\eta)\right]} \quad , \tag{39}$$

which may be simplified to

$$\frac{1}{Z_t(\Delta\omega_n)} \approx \frac{1}{j\,[\Delta\omega]\, E_{av} M} + \frac{\left[\omega_{n,n-1}^2 - \omega_n^2\right]}{E_{av} M[\Delta\omega]\left[-\omega^2 + \omega_n^2(1 + j\eta)\right]} \quad .$$

Collection of the two fractions into one results in

$$\frac{1}{Z_t(\Delta\omega_n)} \approx \frac{1}{j\,[\Delta\omega]\, E_{av} M}\left[\frac{-\omega^2 + j\eta\omega_n^2 + \omega_{n,n-1}^2}{\left[-\omega^2 + \omega_n^2(1 + j\eta)\right]}\right] \quad . \tag{40}$$

Z_t calculated by Eq. (40) is limited to a narrow frequency band centered at ω_n. This band is not as broad as $[\Delta\omega]$. This limitation is inferred by $Z_t(\Delta\omega_n)$. By neglecting damping and revising Eq. (40), $E_{av}M$ can be solved from available test data, $X_t(\omega)$ being the reactive portion of impedance:

$$E_{av} M = \frac{[X_t(\omega)]}{[\Delta\omega]}\left[\frac{-\omega^2 + \omega_{n,n-1}^2}{-\omega^2 + \omega_n^2}\right] \quad . \tag{41}$$

Once the average modal mass $E_{av}M$ is calculated, each of the higher numbered modal impedances can be determined near resonance by Eq. (40) without resource to a matrix equation. By using Eq. (37) E_nM can be calculated. Thus, $E_{av}M$ allows the analyst to investigate higher frequency modes without going through the complete spectrum analysis.

The preceding analysis was developed for local point impedance measurements. Transfer impedance measurements also lend themselves to Skudrzyk's normalization by the addition of a transfer function. Skudrzyk's equation can be modified to PSD measurements as follows:

$$M^2\left[\frac{\langle \xi_n^2 \rangle}{\xi(A)^2}\right]^2 \int_{\omega_c - \frac{\Delta\omega}{2}}^{\omega_c + \frac{\Delta\omega}{2}} \left[-\omega^2 + \omega_n^2(1 + j\eta)\right]^2 d\omega \left[PSD_{\xi(A)}\right] = PSD_{f(A)} . \quad (42)$$

A simple revision will produce

$$M^2\left[\frac{\langle \xi_n^2 \rangle}{\xi^2(A)}\right]^2 \left[\frac{PSD_{\xi(A)}}{PSD_{\xi(B)}}\right] \int_{\omega_c - \frac{\Delta\omega}{2}}^{\omega_c + \frac{\Delta\omega}{2}} \left[-\omega^2 + \omega_n^2(1 + j\eta)\right]^2 d\omega \times \left[PSD_{\xi(B)}\right] = PSD_{f(A)} . \quad (43)$$

The two bracketed ratios make up a transfer mode constant $E_n(t)$. $E_n(t)$ and transfer impedance may be applied to all preceding analytical methods.

A reverse transfer function is represented in the equation:

$$M\left[\frac{\langle \xi_n^2 \rangle}{\xi_n^2(B)}\right]^2 \left[\frac{PSD_{\xi_n(B)}}{PSD_{\xi_n(A)}}\right] \int_{\omega_c - \frac{\Delta\omega}{2}}^{\omega_2 + \frac{\Delta\omega}{2}} \left[-\omega^2 + \omega_n^2(1 + j\eta)\right]^2 d\omega \times \left[PSD_{\xi_n(A)}\right] = PSD_{f(B)} . \quad (44)$$

The transfer impedance from (A) to (B) is not expected to be reversible because the area of excitation will be different; E_n, M and ω_n will differ with location. In a small finite structure with clearly defined modes, transfer impedance should be reversible. Of course, this concept applies to a linear system. A further complication of the space vehicle test is that the response is not expected to be linear.

NONLINEAR ANALYSIS

A large structure such as a launch vehicle will most likely respond as a nonlinear system. The basic causes of this nonlinearity are: intermodal coupling, harmonic and subharmonic response, nonlinear damping, pre-stressing and stiffness nonlinearity, amplitude dependent response area (nonlinear mass), and high-amplitude transition from bending to membrane type response. Any attempt to define the nonlinear response completely by analytical equations would open a Pandora's box of troubles. However, by working backwards from the test data all nonlinear effects can be lumped into the modal masses, making them location, frequency and amplitude dependent. Skudrzyk's equation then becomes

$$M^2[\xi_n(A), \omega] \int_{\omega_c - \frac{\Delta\omega}{2}}^{\omega_c + \frac{\Delta\omega}{2}} \left\{-\omega^2 + \omega_n^2[\xi(A), \omega][1 + j\eta]\right\}^2 d\omega \times PSD_{\xi_n(A)} = PSD_{f(A)} . \quad (45)$$

Since the change in mass also changes natural frequency, ω_n^2 becomes dependent on location, displacement and frequency. Detailed empirical analysis will produce trends for each specific mode. Abramson [5] has a good listing of idealized nonlinear equations to which the results can be compared for best fits. An anticipated problem here is that more than one cause of nonlinearity will probably be present, making quick identification difficult. Another problem is that the mechanical shaking amplitudes will probably not be as large as expected from acoustic excitation. Therefore, the data may not extend to the usable range.

The investigation of nonlinearities will be an important analysis task. Analysis methods will have to bend with experience and will involve considerable analytical research before full use is made of the data. In locations where nonlinearity is not great, linear prediction methods will, in cases of nonlinear hardening, produce safe specifications with only reasonable error. It is hoped that this approach will put value in the direct use of the linear equations listed herein.

INSTRUMENTATION AND DATE ACQUISITION SYSTEMS

The instrumentation diagram (Fig. 3) is descriptive of the three major data systems. The primary system is an analog to digital converter with readout to a magnetic tape recorder. The test site monitoring system is an analog calculating system with graphic readouts. An auxiliary analog magnetic tape system is included to make multi-channel real time analysis possible. The purchased equipment differs slightly from the diagram but all the schematic functions are built into the equipment. The equipment listed in Fig. 3 and Table 1 is being built into or stored in a 50- by 10-foot trailer (Fig. 4) that will be a self-sufficient test facility. The instrumentation capabilities do not meet ultimate requirements; therefore, the instrumentation and data processing systems are themselves part of the developmental research associated with the project. The following discussion does not include all factors leading to equipment solution but does include the interesting highlights.

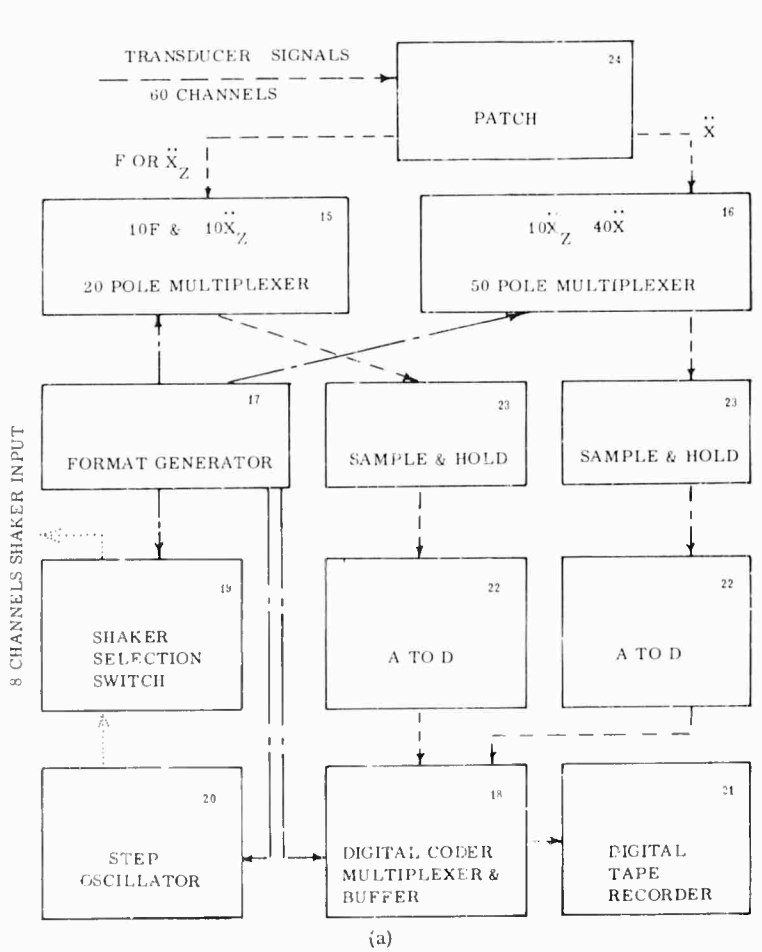

(a) - Digital system

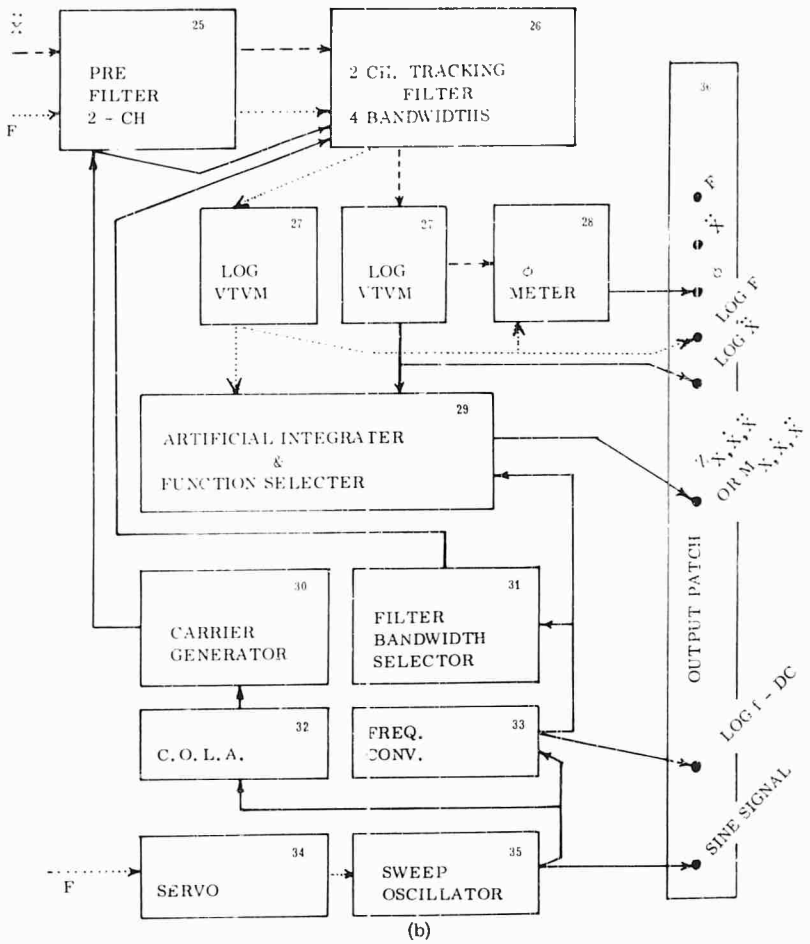

(b) - Analog system

Fig. 3 - Instrumentation diagram

TABLE 1
Peripheral List of Equipment

Item No.	Quantity	Description
		Shakers
1	2	3/4 lb, 40-3000 cps
2	8	1-1/2 lb, 40-3000 cps
3	8	50 lb, 10-10,000 cps
		Transducers
4	2	High response Z heads
5	8	Wide-range Z heads
6	10	Lightweight accelerometer
7	40	General use accelerometer
8	20	Microphones
		Amplifiers
9	60	Charge
10	—	Power supply
11	6	Voltage
12	—	Power Supply
13	--	Internal cables
14	—	External cables
15-36[a]	—	—
37	1	Wattmeter
38	3	VTVM
39	1	dc differential voltmeter
40	8	250 w shaker power amplifiers
41	1	Krohnite variable bandpass filter
42	1	White noise generator
43	1	40-channel tape recorder
44	13	ac to ac log converter
45	1	8-channel oscillograph
46	1	Electronic counter
47	2	Oscilloscope
48	4	x-y plotter

[a]See Fig. 3.

The objective of the equipment selection was the design of a research facility with the broadest scope of performance and the longest technical life within practical procurement feasibility. The equipment must be compatible with the large quantity of data to be taken and must have the best possible retention of real time and signal amplitude. The data will be stored in a manner compatible with efficient recognition and in a form suitable for the numerous calculations of the analysis techniques. The systems will be flexible enough to be expansible to new developments in the state-of-the-art. The systems will have the capability of on-site monitoring of impedance and transfer functions and will include random vibration capabilities.

It was quickly learned that no one system had all the desirable characteristics. Four types of systems were investigated: direct analog magnetic taping, on line analog computation and graphic readout, multiplexed magnetic taping and digital conversion with IBM compatible magnetic taping. The data acquisition capability will become part of the projected research with three of the four systems to be investigated. The multiplexed system was omitted in favor of the digital system because of phase and dynamic range problems associated with the

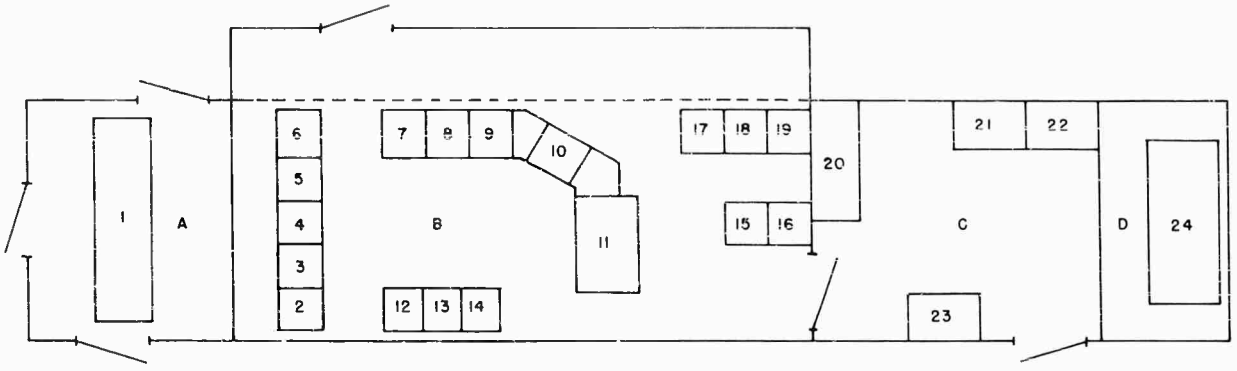

A	- Cable room	4, 5, 6	- Automatic impedance plotting equipment	15, 16	- Shaker power amplifiers
B	- Data-processing room	7	- 40-channel tape recorder	17, 18, 19	- Spare racks
C	- Storage and work room	8	- Spare rack	20	- Work bench
D	- Facility room	9, 11	- Digital system	21, 22, 23	- Storage racks
1	- External cable reels	10	- Desk		
2, 3	- Signal amplifiers and patch panels	12, 13, 14	- Desk and storage	23	- Air-conditioning equipment

Fig. 4 - Integrated dynamics test trailer

analog taping. Direct taping will give the characteristics of the multiplexed system for practical research purposes. If and when multiplexing is deemed desirable, it can be easily added to the trailer.

Excitation will be from three sources. Items 42 and 41 will provide white random noise in suitable bandwidths. Item 20 is an automatic programmed step oscillator and Item 35 is a sweep oscillator with a built-in servo mechanism. The excitation signals are switched to the desired shakers by Item 19. Item 40 amplifies the excitation signals to desired levels. There is a choice of three types of shakers with ratings up to 50 pounds of force. The shakers will excite the structure through impedance heads. Local response will be measured by the impedance heads and transfer response by remote accelerometers.

There were no excessive problems in selecting input signal equipment. The current status of transducer capability leaves something to be desired. The impedance of the transducers is reflected as an error in the measurements. Transducer frequency response, in general, does not have an upper limit suitable for small-scale modeling. This is especially true of impedance heads where the lower limits also are not ideal. The following equations were worked out to calculate the upper limit cutoff frequency ω_x due to transducer attachment [3,6]:

Plates:

$$\omega_x = \frac{N E_v M}{2\pi M_2}, \tag{46}$$

Rectangular bar:

$$\omega_x = \frac{4N(E\rho h^4)^{1/2}}{\sqrt{3}\, M_2}, \tag{47}$$

Beam:

$$\omega_x = \frac{8N^2\rho^2 S^4 C_\rho r}{M_2^2}, \tag{48}$$

Lumped mass and impedance head:

$$\omega_x = \left[\frac{NED}{M}\right]^{1/2}, \quad \text{and} \tag{49}$$

Lumped mass and accelerometer:

$$\omega_x = \left[\frac{NE^2}{\rho M_2 a}\right]^{1/2}, \tag{50}$$

where

N = allowable error ratio, e.g., 1/10,

E_v = frequency difference between modes (ω),

M = total mass of test specimen,

M_2 = mass of transducer or effective mass of impedance head,

E = Young's modulus,

h = plate or bar thickness,

ℓ = bar length,

c_p = wave propagation velocity in material,

S = cross-sectional area of a beam,

r = radius of gyration,

ρ = mass density of material,

a = acceleration of accelerometer, and

D = transducer attachment diameter.

The desirability of remote installation led to the decision of standardizing with charge amplifiers. For those instances where the noise background of the charge amplifiers would be excessive, six voltage amplifiers are included in the equipment list. Phase retention through the amplifiers is not completely satisfactory; this problem will be investigated after the system is assembled. However, in recognition of possible poor phase determination the data analysis as reviewed in earlier sections is dependent on phase angle only to a minor degree.

The dynamic range of the charge amplifiers will exceed 55 pounds. This is made possible by the use of solid state components especially selected for low noise level. Since the entire system is dependent on the amplifier dynamic range, prime consideration had to be given to input noise and its amplification. Voltage amplifiers are intrinsically quieter than charge amplifiers. After reviewing at some length the advantages and disadvantages of both systems, it was decided that the dynamic range of the selected charge amplifiers would be satisfactory. The retention of transducer signals without loss to the amplifiers through 300-foot cables had many advantages, such as no remote installation of equipment, better phase retention, fewer weather problems, convenient standard checkout of equipment and radio-frequency shielding of the amplifiers. Transducers, as far as possible, were selected to perform within the same calibration setting and thus improve phase correlation. When considering the precision of the digital conversion, the amplifiers are certainly the weak link of the data system.

The amplified signals are fed to a patch panel where the readout systems can be conveniently wired. Preliminary checks can be performed using the electronic counter, the watt- and voltmeters and the oscilloscopes. The analog system will accept any two of the channels and will calculate the impedance or transfer function referenced to either displacement, velocity or acceleration. The analog system has a sweep oscillator that activates both the excitation filters and plotters. The oscillator will also sweep the filter system and the plotter through a random spectrum for power spectral analysis. This flexibility gives good on-site monitoring capability. However, the paradox here is that this quick-look device is orders of magnitude slower than the digital long-look capability. Cost eliminated a digital computer capability within the trailer; its use as a quick analysis device would have been ideal. The analog system will plot spectra of force, displacement, velocity, acceleration, mobility, impedance or transfer ratios and the phase angle between the two signals. All readouts except phase are based on rms amplitude values integrated over a constant filter bandwidth of 2, 5, 10, 20 or 50 cps. To increase the sweeping rate at higher frequencies an automatic bandwidth selection device is incorporated into the system. It will program the filters to four successively larger bandwidths as the frequencies increase.

The analog system uses artificial integration which it performs by summing or subtracting the log of the volt-mean-square potentials including frequency. Modification and relatively simple additions to the system will increase its capability to cover most of the standard quantities used in random vibration analysis. It is expected that developmental projects will be performed on the system to increase its accuracy and capabilities. An interesting aspect of the developmental research is the combined use of the analog system and the magnetic tape recorder to perform some of the data analysis. Several examples follow:

Equation (19) can be rewritten as

$$k\ \text{db} = Z\ \text{db} + \xi\ \text{db} - \text{SPL}\ ,$$

or

$$k\ \text{db} = Z\ \text{db} + a\ \text{db} - \omega^2\ \text{db} - \text{SPL}\ , \tag{51}$$

where

$$k\ \text{db} = 20 \log \frac{K}{K_o}\ ,$$

$$Z \text{ db} = 20 \log \frac{Z}{Z_o} ,$$

$$\xi \text{ db} = 20 \log \frac{\xi}{\xi_o} ,$$

$$a \text{ db} = 20 \log \frac{a}{a_o} ,$$

$$\text{SPL} = 20 \log \frac{\rho}{\rho_o} ,$$

$$\omega^2 \text{ db} = 20 \log \omega^2 ,$$

and

$$\log K_c = \log Z_o + \log \xi_c - \log \rho_o$$

or

$$\log K_o = \log Z_o + \log a_o - \log \rho_o .$$

Equation (51) can be set up on the analog system with the input coming from either direct or taped signals. The readout would be the acceptance factor K plotted against frequency. Since KP is the generalized force,

$$F \text{ db} = Z \text{ db} + \xi \text{ db} ; \qquad (52)$$

this quantity also can be plotted as a spectrum.

The FM tape recorder has basically the same two problems of the other signal processing equipment — retention of amplitude and phase. The ideal recorder would have a dynamic range of 100 db and good phase retention on both record and playback. Practical considerations limit the dynamic range to about 40 db and playback will have some error in both amplitude and phase. However, the recorder represents the best presently available means of retaining the true time response and phasing of a multi-channel system. Here also is an area requiring developmental research to arrive at the best results.

The dynamic range problem can, to some extent, be bypassed by log converting the signals ac to ac before recording. To investigate this process, thirteen log converters are included in the equipment list. In some of the analog calculation processes, ac to dc log converters would be helpful, but they are not well suited to the recording process. Therefore, none were included in the first equipment list.

An eight-channel oscillograph is included to monitor time-amplitude relationships of a number of channels. The use of this equipment is limited but it will be very helpful in specific analysis problems.

The digital system is designed to accept signals excited by the step oscillator and from random sources. The system processes two signals at a time in true phase relationship. Two multiplexers, Items 15 and 16, switch the signals so that each signal fed to Item 15 is matched in turn with each signal fed to Item 16. In practice, all impedance ratios may be had by feeding the force signals to Item 15 and the response signals to Item 16. Where transfer functions are desired, the base responses are fed to Item 15 and the remote to Item 16. For step-oscillator signals, all combinations of signal pairs are taped for each frequency before the next step frequency is excited. The digital data is recorded in prefixed blocks and each block of data is identified. The system will have sampling capabilities to cover frequencies up to 10,000 cps, except for tape recorder which is limited to about 3000 cps.

When the full capacity of the digital system is put to use under step-oscillation excitation, each test run will process about 1,400,000 signals or 700,000 ratios. If the force amplitude is changed to monitor nonlinear response, five times, a single test run will be made up of 7,000,000 signals. This gives some comprehension of the magnitude of the data acquisition and processing scope. It also points to the desirability of the use of broadband random excitation.

The power amplifiers and shaker system will produce less force input within a narrow bandwidth under broadband random input than under discrete sine input because of the total power limitations. This will affect the nonlinear response investigations and also point out another test procedure developmental research objective — determination of the most expeditious manner of test excitation giving the required data detail.

The trailer (Fig. 4) in which the equipment is housed will be 10 feet wide and 50 feet long and will have an expandable side to allow rear access to the side-mounted electronic equipment. There will be four distinct areas within the trailer. The cable room will house the external lead cables stored on reels. There will be about 80 cables, 300 feet long. The data-processing room will house the functional electronic systems which operate the tests and process and store the data. There will be two desks to be used by the project personnel. The storage and workroom will house the portable equipment and have an electronic equipment work bench. The facility room will house the air conditioning and the electrical power service.

FORMULATION OF TEST PHILOSOPHY

The chief concern in developing the test procedures is the quantity of test data that need be taken. The digital data acquisition system has the capability to produce more data than can be reasonably processed. Thus, a practical minimum is a prime concern. With the limited supporting facts now available, any decision of defining minimum test procedures would be difficult. A pilot test run is now being performed with an analog automatic impedance plotting system on a S-IV vehicle to determine local and transfer impedance, damping and the extent of nonlinearity. This data should help decide which approaches to data acquisition will be the most informative. It will also supply input for trial runs of the various data processing methods that may be used in the main program.

The test procedures should take into account the quality of the data. The acoustic environment surrounding a test vehicle is influenced by such transient sources as trains, trucks, aircraft, construction activities, production activities and other test performances. The response of the test specimen to these sources can result in unreliable impedance test data. The complexity of the structure induces a high density of modes which tends to mask the precise resonant and antiresonant frequencies, as well as the significance of local modes. Low-amplitude excitation will lack clear modal boundary conditions and will show a loss of energy through damping that is not present under very high amplitudes of excitation. Pressurization and filling of tanks will change stiffness, mass, mode shape and damping characteristics. Measurements will be influenced by certain response readout characteristics that are location dependent. The instrumentation itself imposes apparent response measurements not representative of the test structure.

Figure 5 is a typical impedance plot where the structure is a composite of beams and plates; Fig. 6 is the phase plot. Several of the previously mentioned measurement problems

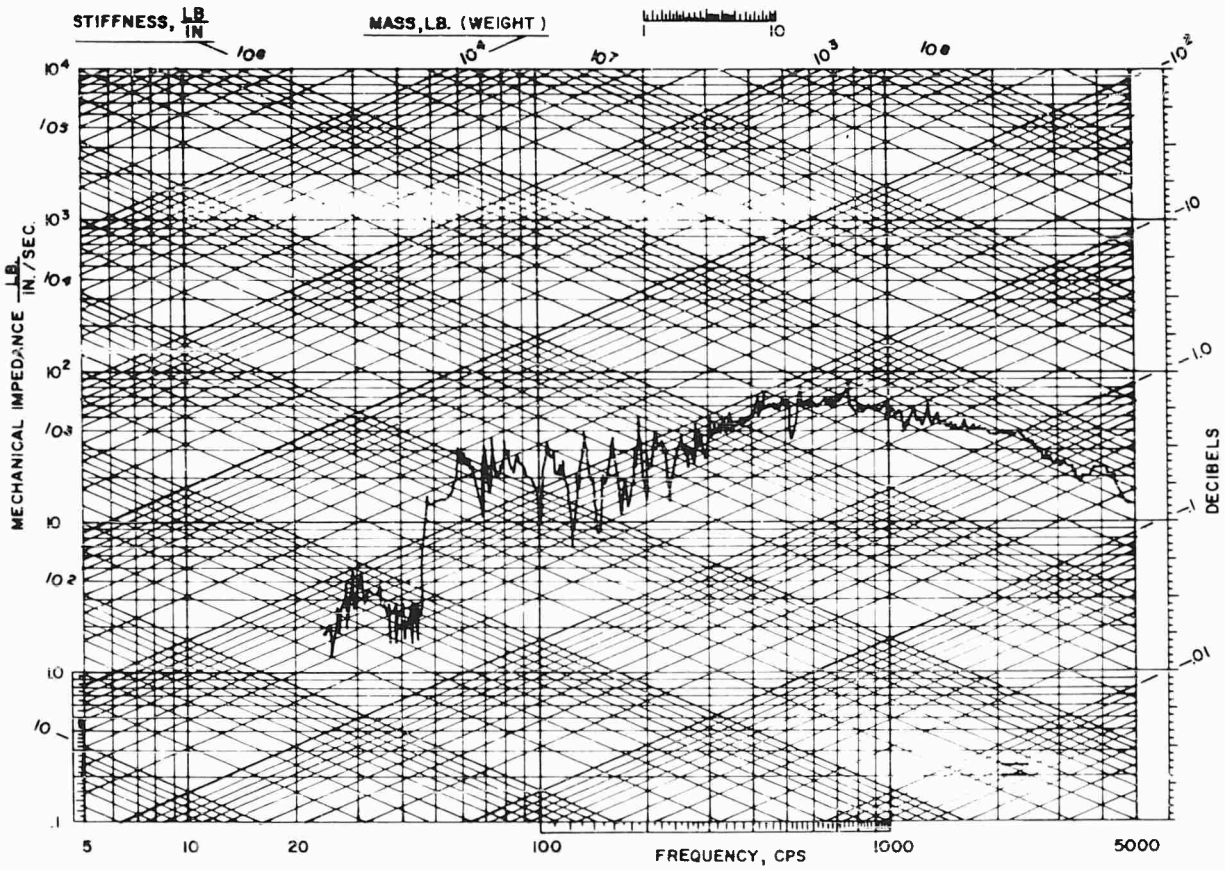

Fig. 5 - Impedance at tank frame location

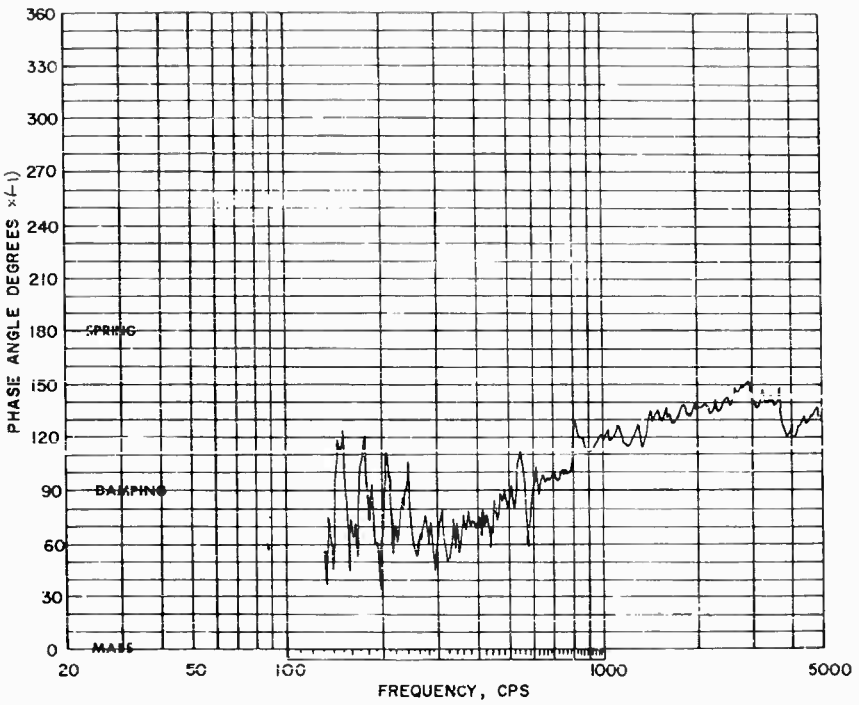

Fig. 6 - Phase angle

are identifiable. At low frequencies (below 60 cps) the shaker prevents the force transducer from reading correctly and the impedance measurement is too low. Also in this range, 50 to 60 cps, the electronic noise overrides the acceleration signal and the high values of impedance are masked. There is a high density of low response modes and local modes at 68, 100, 127, 150, 180, etc , are readily identifiable. The phase plot helps comprehension of the impedance graph. A phase angle located above 90 degrees shows response in the stiffness-controlled region; response located below 90 degress shows mass effect and at 90 degrees the system is damping controlled at either resonance or antiresonance. As the frequency increases and the phase angle decreases as it passes through 90 degrees, the 90-degree passover frequency is at resonance; when the phase angle increases as it passes through 90 degrees the passover frequency is at antiresonance. The graphs shown in Figs. 5 and 6 follow typical modal response up to 200 cps. At about this frequency the system starts to be affected by the quantity of lower numbered modes. Skudrzyk [3] integrates the multimodal system impedance at high frequencies as follows:

$$\frac{1}{Z_d(A)} = \int_{\omega}^{\infty} \frac{\omega}{\xi_v M_v \left[\omega_v^2 (\eta - j) + j\omega^2\right]} d\omega_v \quad (53a)$$

and for a system such as a bending rod

$$Z_d(A) = \frac{\xi_v}{\pi} M_v(A)[1 + j] . \quad (53b)$$

For longitudinal or torsional vibratiens and for transverse vibrations of a point excited plate or shell, the equation becomes

$$Z_d(A) = \xi_v M_v \frac{2}{\pi} , \quad (53c)$$

where

$Z_d(A)$ = driving point impedance at (A),

ξ_v = $\Delta\omega$ between modes,

M_v = modal mass for the nearest mode to ω, and

$j = \sqrt{-1}$.

Equation (52) leads to a prediction of a phase difference between real and reactive impedance of +45 degrees since they are of equal quantities. The real acceleration impedance has a phase angle of -90 degrees; then the system at high frequencies should have a phase angle of -45 degrees. Also the impedance $Z_d(A)$ is relatively constant and varies not as a frequency dependent but with modal mass. Inspection of

Fig. 6 shows that this effect is being formed at frequencies between 250 and 450 cps. The impedance curve in Fig. 5 is relatively constant with nearly a flat slope. This substantiates response equivalent to Eq. (52). Above 450 cps the phase angle increases in value and shows an increase in stiffness effect. The phase angle then falls off toward a resonance. It is believed that the impedance at these high frequencies is controlled by the stiffness of the attachment glue and the attachment system will go into resonance above the frequency range of the graphs.

The purpose of the preceding description is to illustrate the complexity of choosing measurement locations and analyzing the data. The usable data is in the frequency band between 60 and 400 cps with the remainder somewhat questionable. Only about 10 percent of the recorded spectrum represents good data.

The measurements of Fig. 5 are taken at a location of relatively high impedance, a ring stiffener with a tank bell attached. Figure 7 was taken at a tank midpoint and, therefore, at a low impedance location. The impedance, in general, lies about a decade below that of Fig. 5. Which measurement location is most typical of the data requirements? The high impedance locations are indicative of equipment attachments and the low impedance locations represent the area of maximum acoustic energy acceptance. It follows that both are necessary to meet the objectives of the test program. Measurements shown in Figs. 7 and 8 were taken at a location where considerable damping is present due to the attachment of fitted pads to the internal surface of the tanks. When the tank is filled with liquid the temperature will affect the stiffness and damping; mass and damping will be added to the impedance by the liquid. Under realistic environmental conditions, Figs. 7 and 8 would not be typical. The dynamics of the vehicle must be investigated under actual premission conditions to determine which of the other measurements have representative values for lift-off evaluation.

The experience to date has shown that considerable additional information is necessary

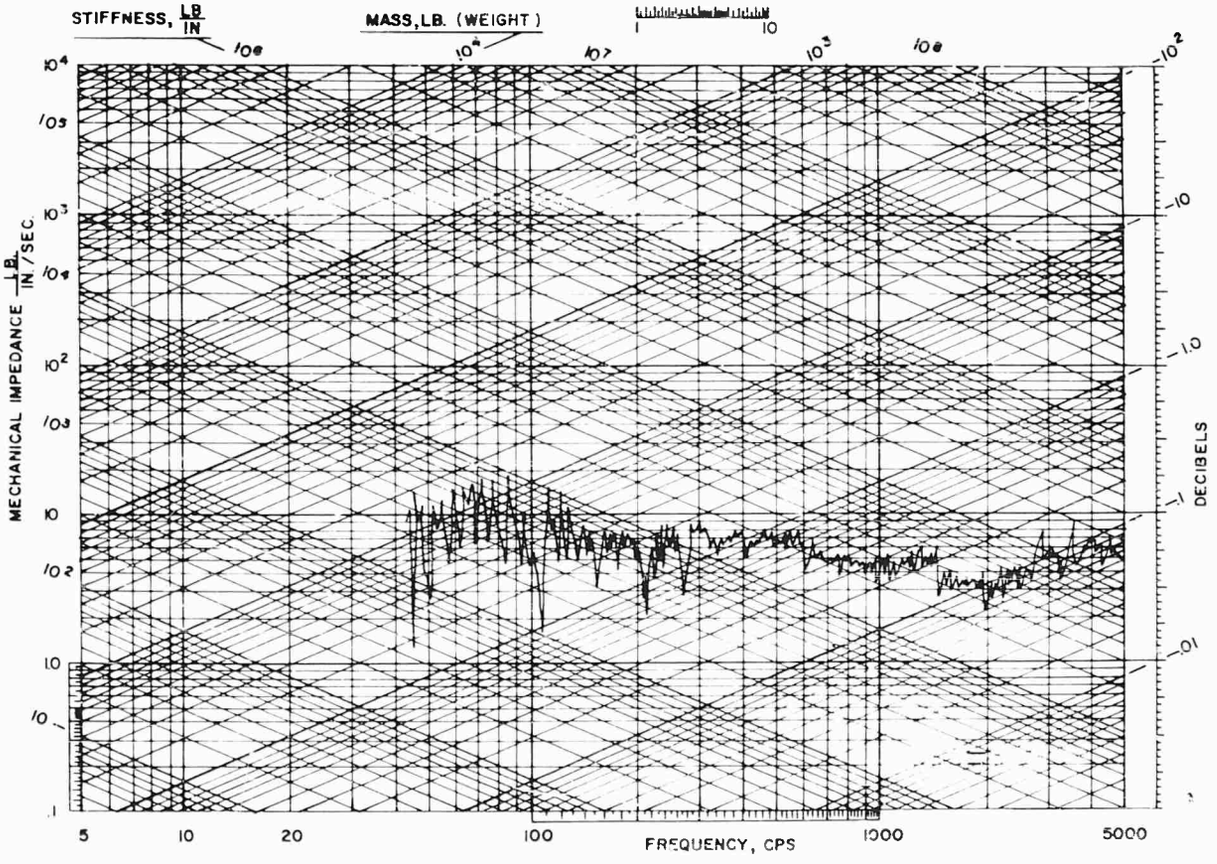

Fig. 7 - Impedance -- damped tank

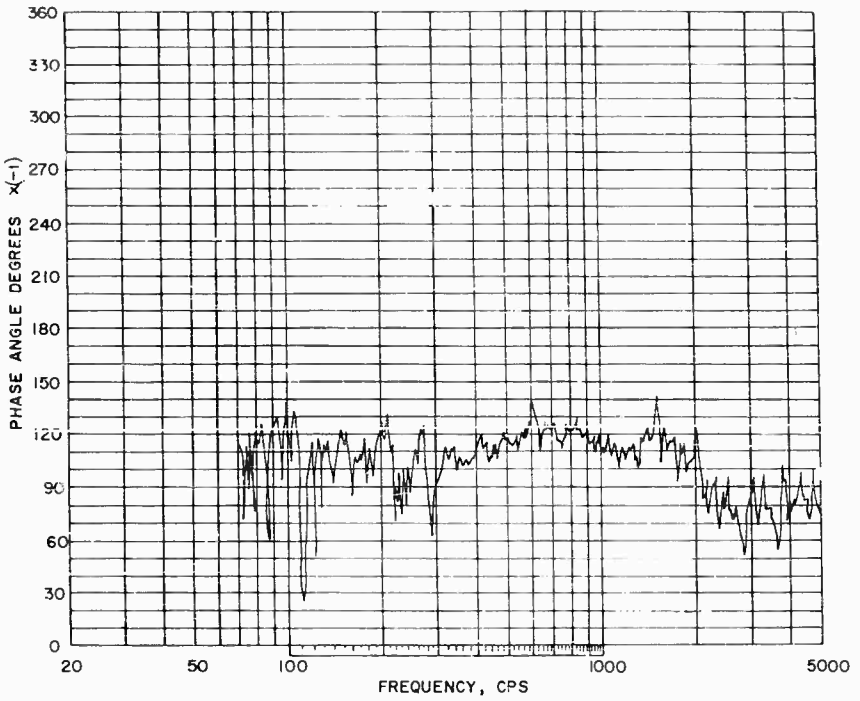

Fig. 8 - Phase angle

before an efficient test program can be produced. The test procedures must develop from an auxiliary research effort that in itself is a major task. It will not be an easy undertaking to balance the scope of the total program with the almost infinite quantity of objective considerations and keep the test program within practical bounds. A system of priorities will have to be developed so that the most useful information is given preference.

About a year ago, an anticipated test procedure was produced that was used as the basis of equipment procurement. At that time this test program was superimposed on a Saturn I vehicle as illustrated in Fig. 9.

The total vehicle had 18 measurement groups. Each of these groups were located on the surface of the vehicle, equidistant and in an axi-perpendicular plane. The number of measurements per group was proportional to the vehicle diameter at the group location. These measurements locations were given two importance levels. The heavy dots were measurement locations to be monitored during all tests. The light dots were at locations monitored only when excitation is nearby. In addition, locations of typical configurations were to be monitored

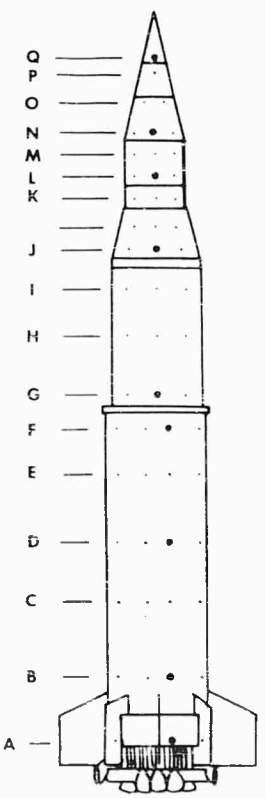

Fig. 9 - Measurement locations

when the response was measurable. Shaking was to be performed through impedance heads attached to the structure. For the first setup, the shakers were to be attached to engine gimbals at A. Four directions of excitation were to be performed: X-axis, Y-axis, Z-axis and 45 degrees to the three axis. Response was to be monitored at B, C, D, etc., as well as the typical structure locations to the capacity of the test equipment (about 40 remote locations). Roughly, with excitation at location A the following response measurements would be made: A, 8 through impedance heads, F and A; B, 8 acceleration measurements; C, 8 acceleration measurements; D, 1; E, 1; F, 1; G, 1; H, 1; I, 1; J, 1; M, 1; O, 1; R, 1; typical structure, 14 acceleration measurements. Excitation would be both sine and random with response field phasure changes induced by changing the polarity of some of the shakers.

On completion of each setup, the shakers were to be moved to the next higher group location with a corresponding logical shift in measurement locations. All shaking above location A was to be radial only. Each measurement location was to have a special local impedance test. Estimating 40 typical structural locations, the total test consists of 187 local impedance tests, 21 shaking setups each for random excitation and stepped sine excitation, and several with change in shaker polarity. Each test was to be performed at enough amplitude levels to determine linearity trends.

At the time this test program was conceived it was considered an ideal maximum effort and the scope would probably be reduced. The philosophy propounded by this program will be used as the basis of the final test procedure with the details modified as experience expands.

USE OF ACQUIRED DATA

The objective of the "Integrated Dynamics Study for Modal and Full-Scale Vehicles" is to produce improved methods of predicting the self-induced dynamic response of launch vehicles. The first phase of this study is to be related to the vehicle only, not to any of the energy sources. The second phase will study the acoustic coupling and other dynamic energy inputs. The prediction equation for acoustic excitation is

$$\frac{\bar{F}^2(x,y,t,\omega,\Delta\omega)}{\Delta\omega} \qquad \frac{K^2(x,y,\omega,\Delta\omega,s)}{Z_t(\omega,\Delta\omega)^2} \qquad \frac{\bar{P}^2(t,\omega,\Delta\omega)}{\Delta\omega} , \tag{54}$$

or for forced excitation the $K^2\,\bar{P}^2$ related quantities are replaced by $[\bar{F}^2(x,y,\omega,\Delta\omega,t,\tau)]/\Delta\omega$. The impedance is to be acquired in such a manner that statistical approaches can be used to correlate data. The analysis of the impedance parameters will help identify like structures as to both local response and transfer coefficient. The structural parameters of like locations will be compared to determine the normalized parameters influencing the impedance characteristics. This should lead to methods of predicting the impedance of a proposed structure. To implement the statistical approach good description of each measurement location must be taken.

As the program continues into the second phase, a like statistical approach will be applied to F, K, and P. Once these are predictable, response estimates will follow.

There are several aspects of the data usage that should help simplify prediction methods. The coupling factor K^2 will pass from maximum to minimum values very sharply with changes in frequency when discrete values are analyzed. There will be some optimum filter frequency band $\Delta\omega$ that will smooth the function curve into a simple mathematical form. This form will be used with the envelope of minimum values of the impedance (also across a bandwidth) to calculate specification requirements. This method has been used very successfully by the author in other impedance-response prediction calculations.

The force parameter as calculated by the equation

$$F = \frac{az}{\omega} \tag{55}$$

is a very useful analytical tool. It is equivalent to the complex summation of the forces acting at the point of measurement. The acceleration at the measurement location will have a wide dynamic range in narrow frequency bands. The force parameter F, when filtered, will have a more orderly character and will be more easily analyzed. Figure 10 is descriptive of a F db spectrum character analysis, Eqs. (51) and (52). Figure 10(a) is a typical acoustic spectrum for a rocket engine; Fig. 10(b) is the phasure sum of the structural forces acting on location A. The coupling or efficiency factor K is the ratio of F to P. If a deviation in the force parameter is due to a source other than acoustic pressure, the force curve will be distorted as in Fig. 10(c). By looking at the force spectrum at locations B, C, and D, an evaluation can be made of the location of the source and the cause possibly may be isolated. Figure 10 and its description is an

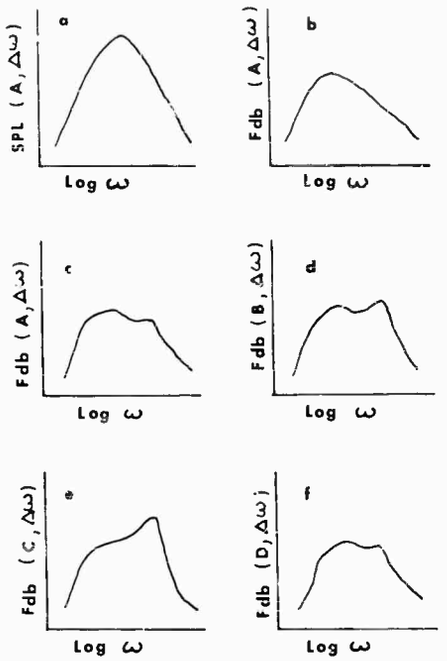

Fig. 10 - F db spectrum character analysis

oversimplification of a practical situation but it does put forth the value of logic gained by peak frequency identification and area of influence. In addition to developing self-induced vibration environment prediction procedures, the results of the "Integrated Dynamics Study for Model and Full Scale Vehicles" will provide a better understanding of the vehicle which should lead to design refinements and analytic techniques that will upgrade ability to meet the objectives of production of better launch and space flight vehicles.

REFERENCES

1. S. H. Crandal, Ed., Random Vibration (John Wiley & Sons, Inc., New York, 1958).
2. R. W. White, "Structural Response to Boundary Layer Pressure Fluctuations and Oscillating Shock, Wyle Lab., Huntsville, Ala., Report WR63-12.
3. E. J. Skudrzyk, "Vibrations of a System with a Finite on an Infinite Number of Resonances," J. Acoust. Soc. Am., 30:12 (Dec. 1958).
4. Giger & Hamme Lab., Ann Arbor, Mich., The Concept of Damping of Structure-Borne Sound and Vibration for Noise Control," Report USN No. 1 (Apr. 1961).
5. H. Norman Abramson, Shock and Vibration Handbook, Ed. by C. M. Harris and C. E. Crede (McGraw-Hill Book Co., Inc., New York, 1961), Chap. 4.
6. Wilcoxan Res. Tech. Bull. No. 1 (Aug. 1963).

DISCUSSION

Mr. Himelblau (North American Aviation): I saw quite a bit of the trees, but not the forest. I'm trying to understand the type of environment whose effects you are trying to determine.

Mr. Vatz: That is explained in some detail in the paper and I just skimmed over the highlights. Our first primary interest will be at the instant of lift-off.

Mr. Himelblau: Is this due to the acoustical forcing function or the direct vibration transfer?

Mr. Vatz: We are interested in both. The first phase of our program that I have reported here is primarily an investigation of the vehicle itself. The second phase of the first part of the test will also take acoustical data and the response to acoustical data to get to that simplified equation I showed on the screen.

Mr. Himelblau: It appears from your slides that you are going to put your shaker at various discrete locations.

Mr. Vatz: Every location!

Mr. Himelblau: All locations simultaneously?

Mr. Vatz: All locations that will be monitored at any time will have an impedance evaluation.

Mr. Himelblau: How are you going to control the force into the various shakers and the phasing between them?

Mr. Vatz: I'd like to say that this is a research program and we will change our concept as our experience gets better, but right now we intend to use eight shakers as a maximum. We will use the shakers in phase for one test and half the shakers out of phase for a second distinct test.

Mr. Himelblau: Is there a particular reason why you chose that combination?

Mr. Vatz: Because it is easy to achieve.

Mr. Himelblau: But still there is no intent to try and relate that to the field environment?

Mr. Vatz: Yes, that is why we are doing it. If we find that we can uncover specific problems by this phase mismatching, we will go further into it but we have to limit it to some practical approach. That's where we stopped at this time. This is a horrendous test the way it now stands.

Mr. Himelblau: Well, this thing is going to be, if you will, bathed in a fairly progressive sound field that has distinct phasing within a narrow frequency band within itself. I'm trying to relate that with your shaker position and the phasing in the shakers.

Mr. Vatz: We are going to shake it first and then try to get it into an acoustic field. Hopefully we can come up with some areas of pressure and response correlation. This is part of the program and we're distinctly aware of it and of the fact that we can't work it now. But we want to get to that point.

Mr. Himelblau: Are you going to be interested in phase?

Mr. Vatz: That's why we went to digital equipment. We didn't feel that any analog or taping device would be as retentive of phase as would be our digital system.

Mr. Himelblau: But I thought you said you were going to apply noise in narrow band?

Mr. Vatz: That is correct.

Mr. Himelblau: How do you plan to get phase information?

Mr. Vatz: We will be able to get phase mathematically at certain frequencies. If we find that this is not enough we can take some spotting of it with our analog system. In other words we want to check this out. I stated that we wanted sine excitation. We had to have some of that. We'll check our random analysis with our sine and see how well we do. If we don't do well we'll have to go to sine excitation.

Mr. Himelblau: I guess that leads me to my next question. What sort of bandwidth were you planning for your random?

Mr. Vatz: We're planning 50 cycles at the present time. In other words, the frequency spectrum will be scanned by 50 cycle random bands stepped.

* * *

SMALL DISPLACEMENT KINEMATIC ANALYSIS OF BAR LINKAGES*

C. S. O'Hearne
Martin Company
Orlando, Florida

There appears to be no method for the small displacement kinematic analysis of bar linkages presented in the general reference literature. A simple method developed by the author is described in this paper. The motivation for the development of the method was a need to obtain certain transformations on measured impedance functions and to establish test geometric data requirements in a laboratory measurement of the mechanical impedance of a missile air vane position control actuation system. In the measurement, the impedance head was mounted on a pushrod which was an element in a three-dimensional, four-bar, load applying linkage. The analysis performed is used as an illustrative example of the method.

INTRODUCTION

It may be thought curious that a paper on the kinematics of linkages is included with a set of papers on mechanical impedance. It is here because the analytical problem considered was first investigated by the author in planning a mechanical impedance measurement. Moreover, the problem is one that arises quite naturally in this particular kind of impedance measurement.

In the impedance measurement described here, the impedance head transducer was located in a linkage. The motivation for this measurement and the manner in which it was carried out, of interest in themselves, are described briefly. The particular kinematic analysis requirement which arose is explained, and the analysis is carried out using the general analytical method developed in the paper. The full power of the method is not really necessary in this case; however, it was retained as an example because of its simplicity and because of the intrinsic interest of the impedance measurement.

The aspects of the motion of a mechanism of concern to its designer and to a vibration analysis engineer may be rather different. Furthermore, the vibration analysis engineer may have difficulty understanding the designer because design techniques have little generality and are often graphical instead of mathematical. The vibrations engineer should rely on his own devices in this area expecting little assistance from designers or the literature. Small displacement oscillatory motion of mechanisms is not a topic considered in textbooks.

Fortunately, the problem is not difficult. The formalities are easily stated. They are developed here briefly, the mechanical impedance measurement which motivated a linkage analysis is then described, and finally the analysis is carried out as a concrete application of the method.

GENERAL METHOD

It is intuitively clear that the position state of a mechanism in which the output is a given one-to-one function of the input is completely specified by a single position vector in ordinary three-space. Therefore, if N variable-position vectors are required to describe the positions of the elements of such a mechanism, N-1 of them will be explicit one-to-one functions of the Nth, which may be considered the input or

*This paper was not presented at the Symposium.

driving element. Consideration of singular points and multi-branched solutions is excluded here. Most mechanisms of interest (e.g., control mechanisms) will not have singularities in their operating range.

The states of the system may be visualized as a set of points constituting a curve in 3N dimensional linear vector space. The components of the 3N vector defining the curve are an arrangement of the components of the N 3-vectors in ordinary 3-space.

Since, for the 3N dimensional position state mechanism postulated, there will exist N-1 vector functions of the input vector, there will be 3(N-1) scalar functions which may be expressed implicitly:

$$f_i(X_1, X_2, \ldots, X_{3N}) = 0, \quad i = 1, 2, \ldots, 3(N-1). \quad (1)$$

These equations express properties of geometric invariance and constraint. By the Implicit Function Theorem, a solution of these equations exists at each point $P = (X_i)_P$ on the state curve in the abstract space at which the Jacobean

$$J_P = \left| \frac{\partial f_i}{\partial X_j} \right|_P \qquad i, j = 1, 2, \ldots, 3(N-1) \quad (2)$$

is nonvanishing and the

$$\frac{\partial f_i}{\partial X_j} \qquad \begin{matrix} i = 1, 2, \ldots, 3(N-1) \\ j = 1, 2, \ldots, 3N \end{matrix} \quad (3)$$

are continuous in the neighborhood. To obtain small displacement output motion, $(\omega_i) = (X_i) - (X_i)_P$, about P in terms of the small displacement input motion, the Taylor expansion of the f_i is written up to the linear term. Since the column matrices, (f_i) and $(f_i)_P$, which constitute the left-hand side and the zero th order term of the expansion, respectively, are both the zero vector, the desired equations are expressed:

$$\begin{bmatrix} \frac{\partial f_1}{\partial X_1} & \frac{\partial f_1}{\partial X_2} & \cdots & \frac{\partial f_1}{\partial X_{3(N-1)}} \\ \frac{\partial f_2}{\partial X_1} & \frac{\partial f_2}{\partial X_2} & \cdots & \frac{\partial f_2}{\partial X_{3(N-1)}} \\ \cdots & \cdots & \cdots & \cdots \\ \frac{\partial f_{3(N-1)}}{\partial X_1} & \frac{\partial f_{3(N-1)}}{\partial X_2} & & \frac{\partial f_{3(N-1)}}{\partial X_{3(N-1)}} \end{bmatrix} \begin{Bmatrix} \omega_1 \\ \omega_2 \\ \cdots \\ \omega_{3(N-1)} \end{Bmatrix}$$

$$= \begin{bmatrix} -\frac{\partial f_1}{\partial X_{3N-2}} & -\frac{\partial f_1}{\partial X_{3N-1}} & -\frac{\partial f_1}{\partial X_{3N}} \\ -\frac{\partial f_2}{\partial X_{3N-2}} & -\frac{\partial f_2}{\partial X_{3N-1}} & -\frac{\partial f_2}{\partial X_{3N}} \\ \cdots & \cdots & \cdots \\ -\frac{\partial f_{3(N-1)}}{\partial X_{3N-2}} & -\frac{\partial f_{3(N-1)}}{\partial X_{3N-1}} & -\frac{\partial f_{3(N-1)}}{\partial X_{3N}} \end{bmatrix} \begin{Bmatrix} \omega_{3N-2} \\ \omega_{3N-1} \\ \omega_{3N} \end{Bmatrix}. \quad (4)$$

This method of analysis will be applied to the small displacement kinematic analysis of a spatial four-bar linkage. (Spatial means three dimensional, i.e., not planar.) First, the mechanical impedance measurement and the way in which the analysis requirement arose is described.

MECHANICAL IMPEDANCE MEASUREMENT

A set of mechanical impedance functions for a missile air vane control actuator were to be measured. The functions were to be indexed primarily by values of vane rotation mean angle and static hinge moment. The impedances were to be used in conjunction with a Winson type flutter analysis to predict the missile flutter stability boundary.

An air vane airload simulator, designed for systems testing, was with minor adaptations well-suited to serve as test object. The airload simulator is shown in Fig. 1. The section of the missile containing the air vane actuation system is supported in a relatively rigid mounting structure. Loads are applied externally to the air vane shafts through the linkage shown. Inboard thrust, air vane shaft normal load, and shaft hinge moments are applied simultaneously through the connecting rod. The connecting rod has ball joint connectors at both ends. A gas cylinder at the end of the rocker arm controls the magnitude of the load.

A special connecting rod, extended beyond the rocker arm connector to provide a point for shaker attachment, was made for the impedance measurement. It was designed to accommodate an Endevco 2110 impedance head near the vane end of the shaft.

IMPEDANCE MEASUREMENT ANALYTICAL PROBLEM

The impedance desired and the impedance sensed by the transducer in the connecting rod

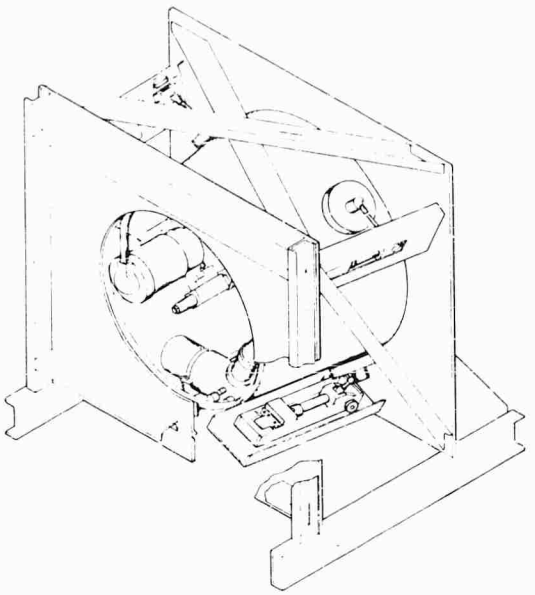

(a)

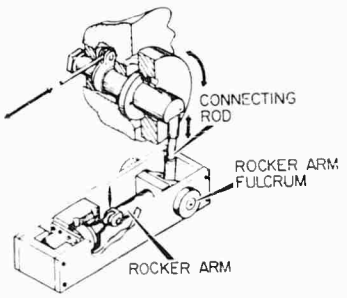

(b)

Fig. 1 - Airload simulator

are not the same. A linearized transformation must be obtained from the one to the other. This transformation determines also the geometric data requirements associated with the measurement.

The primary assumption made was that the loading linkage moved only in its design trajectory, that it did not significantly deform.

The transformation requirement will be explained using Fig. 2. In Fig. 2, upper case roman letters are used to designate vectors. The notation used here and subsequently is defined as follows:

Fig. 2 - Vector scheme for spatial, four-bar linkage of airload simulator

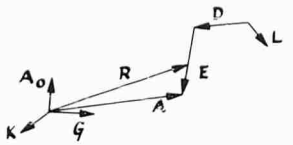

A_0, K, G = Orthonormal set of basis vectors, right-handed in the order given (the direction of K is the outboard direction of the air vane shaft centerline, and the direction of A_0 is the direction of the air vane shaft crank in the neutral position)

A = Position vector locating the driving point of the air vane shaft crank

E = Difference of the two position vectors locating the ball joints on the connecting rod

D = Difference of two position vectors locating the points of connection of the rocker arm to the connecting rod and to the rocker arm fulcrum pin

L = Unit vector directed along the centerline of the rocker arm fulcrum pin

R = Position vector locating the impedance head on the connecting rod

C = Position vector, not shown in the figure, locating the rocker arm fulcrum pin-rocker arm connection point; may be considered to lie in the fixed link of the four-bar linkage ($C = A - E - D$).

If the connecting rod is excited longitudinally by an oscillatory force containing a sinusoidal component at frequency Ω and $H(t)$ is the magnitude of the force in the connecting rod, positive in compression, at each instant of time t, then the sensed, force/acceleration, complex impedance function is:

$$I_S(\Omega) = \frac{\langle H(t) \rangle}{\frac{1}{|\bar{E}|} \langle \ddot{R} \cdot E \rangle} , \qquad (5)$$

where

$$< * > = \int_{t}^{t+\frac{2\pi}{\Omega}} * \, e^{j\Omega t} \, dt \, .$$

The desired function, the impedance seen in rotation by the air vane looking into the control actuator is:

$$I_D(\Omega) = \frac{\frac{1}{|\bar{E}|} <H(t)\, E \times A \cdot K>}{\frac{1}{|A|^2} <\ddot{A} \times A \cdot K>} \, , \qquad (6)$$

and the desired transformation is

$$T(\Omega) = I_D^*(\Omega)/I_S^*(\Omega) \, , \qquad (7)$$

where the asterisks denote that the expressions have been linearized.

R is expressed as a combination of A and E and the notation is augmented to express the nature of the motion as small displacement from a reference state. If

$$R = A - \lambda E \, , \quad \lambda = |A-R|/|E|$$

$$A = A_P + A_\omega \, , \quad \ddot{A} = \ddot{A}_\omega \, ,$$

and

$$E = E_P + E_\omega \, , \quad \ddot{E} = \ddot{E}_\omega$$

then

$$I_S(\Omega) = \frac{<H>}{\frac{1}{|E|} <(\ddot{A}_\omega - \lambda \ddot{E}_\omega) \cdot E_P>} \, , \qquad (8)$$

and

$$I_D^*(\Omega) = \frac{\frac{1}{|E|} <H> (E_P \times A_P \cdot K)}{\frac{1}{|A|^2} <\ddot{A}_\omega \times A_P \cdot K>} \, . \qquad (9)$$

Higher order terms have been dropped in Eq. (9). The ratio simplifies to:

$$\frac{I_D^*}{I_S} = \frac{|A|^2 (E_P \times A_P \cdot K)}{|E|^2} \, \frac{<(\ddot{A}_\omega - \lambda \ddot{E}_\omega) \cdot E_P>}{<\ddot{A}_\omega \times A_P \cdot K>} \, . \qquad (10)$$

It could be shown quite simply at this point that $L_\omega \cdot E_P$ and, hence, $\ddot{E}_\omega \cdot E_P$, are of higher order than $\ddot{A}_\omega \cdot E_P$. This is easily visualized if it is considered that E is a free vector of fixed length. Its displacement from a reference position E_P is, therefore, a pure rotation and a small increment E_ω is orthogonal to E_P. This course, however, would obviate immediately the need for a small displacement kinematic analysis of the form developed. To give an example of the analysis method in application, the formal step of expressing E_ω as a function of A_ω is taken.

The problem variables continue to be differences of position vectors as well as position vectors. This is, of course, no basic departure from the general method. The equations are developed from the following invariance or constraint properties of the system:

$$\begin{aligned}
(A - E - D - C) \cdot A_0 &= 0 \, , \\
(A - E - D - C) \cdot K &= 0 \, , \\
(A - E - D - C) \cdot G &= 0 \, , \\
A \cdot K &= 0 \, , \\
D \cdot L &= 0 \, , \\
A \cdot A - |A|^2 &= 0 \, , \\
E \cdot E - |E|^2 &= 0 \, ,
\end{aligned} \qquad (11)$$

and

$$D \cdot D - |D|^2 = 0 \, .$$

$|A|^2$, $|E|^2$ and $|D|^2$ are fixed constraints. The two equations in A alone are not used directly; the remainder are six scalar equations in the components of D and E. By application of the general method, the small displacement components of D and E may be found as functions of the small displacement components of A. Writing the first-order term of the expansion yields the equations

$$\begin{bmatrix}
1 & 0 & 0 & 1 & 0 & 0 \\
0 & 1 & 0 & 0 & 1 & 0 \\
0 & 0 & 1 & 0 & 0 & 1 \\
L \cdot A_0 & L \cdot K & L \cdot G & 0 & 0 & 0 \\
0 & 0 & 0 & E_P \cdot A_0 & E_P \cdot K & E_P \cdot G \\
D_P \cdot A_0 & D_P \cdot K & D_P \cdot G & 0 & 0 & 0
\end{bmatrix}$$

$$\times \begin{Bmatrix}
D_\omega \cdot A_0 \\
D_\omega \cdot K \\
D_\omega \cdot G \\
E_\omega \cdot A_0 \\
E_\omega \cdot K \\
E_\omega \cdot G
\end{Bmatrix}
\begin{bmatrix}
1 & 0 \\
0 & 0 \\
0 & 1 \\
0 & 0 \\
0 & 0 \\
0 & 0
\end{bmatrix}
\begin{Bmatrix}
A_\omega \cdot A_0 \\
A_\omega \cdot G
\end{Bmatrix} \qquad (12)$$

Multiplying both sides of the equation by

$$\begin{bmatrix} 1 & 0 & 0 & 0 & 0 & 0 \\ 0 & 1 & 0 & 0 & 0 & 0 \\ 0 & 0 & 1 & 0 & 0 & 0 \\ 0 & 0 & 0 & 1 & 0 & 0 \\ E_P \cdot A_0 & E_P \cdot K & E_P \cdot G & 0 & -1 & 0 \\ 0 & 0 & 0 & 0 & 0 & 1 \end{bmatrix}$$

places the left-hand coefficient matrix in a more suitable form for solution by partitioning:

$$\begin{bmatrix} 1 & 0 & 0 & 1 & 0 & 0 \\ 0 & 1 & 0 & 0 & 1 & 0 \\ 0 & 0 & 1 & 0 & 0 & 1 \\ L \cdot A_0 & L \cdot K & L \cdot G & 0 & 0 & 0 \\ E_P \cdot A_0 & E_P \cdot K & E_P \cdot G & 0 & 0 & 0 \\ D_P \cdot A_0 & D_P \cdot K & D_P \cdot G & 0 & 0 & 0 \end{bmatrix}$$

$$\times \begin{Bmatrix} D_\omega \cdot A_0 \\ D_\omega \cdot K \\ D_\omega \cdot G \\ E_\omega \cdot A_0 \\ E_\omega \cdot K \\ F_\omega \cdot G \end{Bmatrix} = \begin{Bmatrix} A_\omega \cdot A_0 \\ A_\omega \cdot G \\ 0 \\ 0 \\ A_\omega \cdot E_P \\ 0 \end{Bmatrix} . \qquad (13)$$

It is observed that the coefficient matrix is nonsingular if neither D_P and E_P nor L and E_P are co-linear. These are states unlikely to appear in a practical design, and do not occur in the present case. The partitioned matrix is easily solved for the E_ω components:

$$\begin{Bmatrix} E_\omega \cdot A_0 \\ E_\omega \cdot K \\ E_\omega \cdot G \end{Bmatrix} = \begin{Bmatrix} A_\omega \cdot A_0 \\ A_\omega \cdot G \\ 0 \end{Bmatrix} - \begin{bmatrix} L \cdot A_0 & L \cdot K & L \cdot G \\ E_P \cdot A_0 & E_P \cdot K & E_P \cdot G \\ D_P \cdot A_0 & D_P \cdot K & D_P \cdot G \end{bmatrix} . \qquad (14)$$

Once again the solution has been carried to this point for the purpose of illustration. In deriving the equations, the relationship $E_\omega \cdot E_P = 0$, previously established by geometric argument, appeared again.

In the transformation problem, the portion of the ratio appearing within operator symbols $<*>$ is now

$$\frac{<\ddot{A}_\omega \cdot E_P>}{<\ddot{A}_\omega \times A_P \quad K>} =$$

$$\frac{<(\ddot{A}_\omega \cdot A_0)(E_P \cdot A_0) + (\ddot{A}_\omega \cdot G)(E_P \cdot G)>}{<-(\ddot{A}_\omega \cdot A_0)(A_P \cdot G) + (\ddot{A}_\omega \cdot G)(A_P \cdot A_0)>} . \qquad (15)$$

Using $\ddot{A}_\omega \cdot A_P = 0$,

$$(\ddot{A}_\omega \cdot G) = -\frac{(A_P \cdot A_0)}{(A_P \cdot G)} (\ddot{A}_\omega \cdot A_0) \qquad (16)$$

is obtained and substituted in the bracketed terms, yielding

$$\frac{<\ddot{A}_\omega \cdot A_0>}{<\ddot{A}_\omega \cdot A_0>} \frac{\left[(E_P \cdot A_0) - (A_P \cdot A_0)(E_P \cdot G)/(A_P \cdot G)\right]}{\left[-(A_P \cdot G)(A_P \cdot A_0)(A_P \cdot A_0)/(A_P \cdot G)\right]}$$

$$= \frac{E_P \times A_P \cdot K}{|A|^2} , \qquad (17)$$

and the linearized transformation, now a constant function of Ω, is

$$T(\Omega) = \frac{(E_P \times A_P \cdot K)^2}{|E|^2} ,$$

which is certainly an intuitively satisfactory term which an experienced analyst would write immediately on inspection.

CONCLUDING REMARKS

The method developed was applied to a spatial, four-bar linkage problem, and the title of this paper alludes only to bar linkages. The method is, however, generally applicable to any system in which states are specified by a set of implicit equations satisfying the hypothesis of the Implicit Function Theorem

* * *

A PRACTICAL METHOD FOR PREDICTING ACOUSTIC RADIATION OR SHOCK EXCURSIONS OF NAVY MACHINERY*

R. A. Darby
Noise Transmission Branch
U.S. Navy Marine Engineering Laboratory

A practical method to predict the machinery noise radiated from Navy ships is developed. The method uses experimentally determined vibration spectra from resiliently mounted machines as the input, transfer impedance information to characterize flexible isolation devices, force transmissibility factors to account for machinery foundations, and an acoustic transfer factor relating dynamic forces on the hull to far-field sound pressure. Simplifications are necessary to make the technique practical. For example, large matrices with many elements to account for multidirectional motion and multiterminal structures are treated as single transfer factors. The possibility of utilizing the technique in reverse, to specify the pressure pulse outside the hull and then predict the dynamic forces on the mounted machinery, is discussed briefly.

INTRODUCTION

A method to predict the machinery noise radiated to the far field and to the ship's own sonar has been developed by the Marine Engineering Laboratory (MEL) [1]. In this paper is considered only the component of the radiation that results via transmission through a purely structure-borne path from a resiliently mounted machine to the hull. The technique may be of some value in predicting the shock forces on a machine if the pressure pulse in the sea is known. In either case, the problem of relating the motion of the machine (whether it be the vibration when considered as a source or the resultant transient excursions due to a shock impulse) to the dynamic pressure in the sea, is a function of the actual shipboard installation with the isolation devices, foundations, hull and the sea all serving as important transfer factors [2]. It is probable that the requirements for a practical prediction scheme in the shock problem also parallel the requirements established for radiated noise predictions. These requirements are:

1. A flexible plan capable of using all available analytical and experimental factors and of being updated as more data become available;

2. An approach aimed at obtaining solutions to the most immediate problems, which are considered to be the establishment of meaningful vibration specifications for machinery and quantitative specifications for isolation devices and the generation of effective and practical design criteria for machinery installations accenting such items as foundations, piping configuration, and optimum machine locations; and

3. A practical prediction scheme sufficiently accurate to aid designers in the preliminary design stages of new ships or machinery modifications.

RIGOROUS ANALYSIS OF GENERAL MACHINERY NOISE PROBLEM

The use of resilient isolation mounts and flexible couplings in a machinery installation allows the analysis of the noise transmitted to the system because the actual vibratory sources in the machine do not have to be characterized and specified; only the resultant velocity spectra above the isolation mounts need be measured. The basic method of analysis was developed by Wright [3] for dealing with noise

*This paper was not presented at the Symposium.
NOTE: References appear on page 137.

transmission through systems with isolation mounts. The approach has been extended to include flexible fluid couplings [4] by treating these devices as pure structure-borne paths and neglecting the acoustic effects occurring inside the device. As long as the mechanical transfer impedance across the isolation device is small compared to the mechanical impedances at either termination, the device can be quantitatively evaluated as an isolation mount. It is believed any significant acoustic energy transfer phenomena can be treated separately and entered independently into the analysis.

In a resiliently mounted machine with n isolation mounts on a foundation which attaches to the hull at m locations, and with p isolation devices flanking the mounts (Fig. 1), the areas of attachment, or interfaces, of interest are assumed to remain plane throughout the vibration frequency range under consideration. Thus, it is meaningful to assign six degrees of freedom to these interfaces with all velocity or force components evaluated as though they were acting at the centroid of the area.

The dynamic forces $[F_p]$ out of the machine at the interface on the hull-side termination of an isolation mount are

$$[F_f] = [Z] \cdot [V] , \qquad (1)$$

where $[Z]$ is a 36-element matrix of transfer impedance parameters Z_{ij} needed to fully describe the isolation mount and $[V]$ is a column matrix representing the six velocity inputs to the top of the isolation mount. There are n such relationships as Eq. (1) representing all the forces out of the machine driving a common structure, the foundation. Also, there are p expressions

$$[F'_f] = [Z'] \cdot [V'] \qquad (2)$$

representing the forces out of a particular isolation device and driving its respective structure, i.e., a piping system clamped to hull after a run of pipe from the coupling.

The force systems at the foundation-hull interfaces driving the hull can be found by the expression:

$$[F_n] = [T] \cdot [F_f] , \qquad (3)$$

where the column matrix $[F]$ represents an arrangement of all n expressions for $[F]$ in Eq. (1). These forces serve as the input for the force ratio matrix $[T]$. This matrix contains $6n \times 6m$ elements ratioing specific combinations of individual output and input forces (T_{ij}). Also, driving the hull are p force matrices:

$$[F'_h] = [T'] \cdot [F'_f] , \qquad (4)$$

where it is assumed that any of these structural systems are characterized by only one input interface, but may have any number of output interfaces, each with six degrees of freedom.

The assumption that there are acoustic transfer factors S_i available relating radiated sound pressure $P(w)$ to force (or moment) driving the hull yields

$$P(w) = [S] \cdot [T] \cdot [F_f] + \sum_{i=1}^{p} [S']_i \cdot [T']_i \cdot [Z']_i \cdot [V']_i . \qquad (5)$$

A rigorous analysis, including all parameters, immediately becomes too complicated for practical prediction purposes. For example, a small resiliently mounted pump with four isolation mounts, four foundation attachment points,

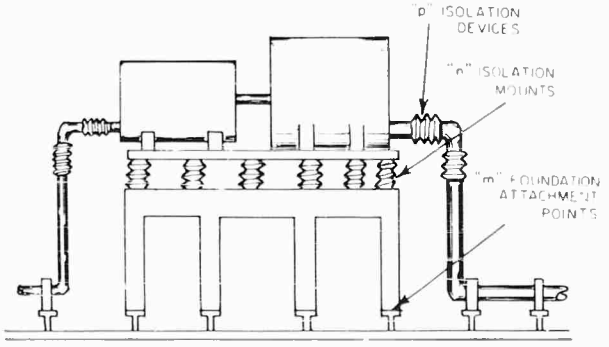

Fig. 1 - Typical machinery system

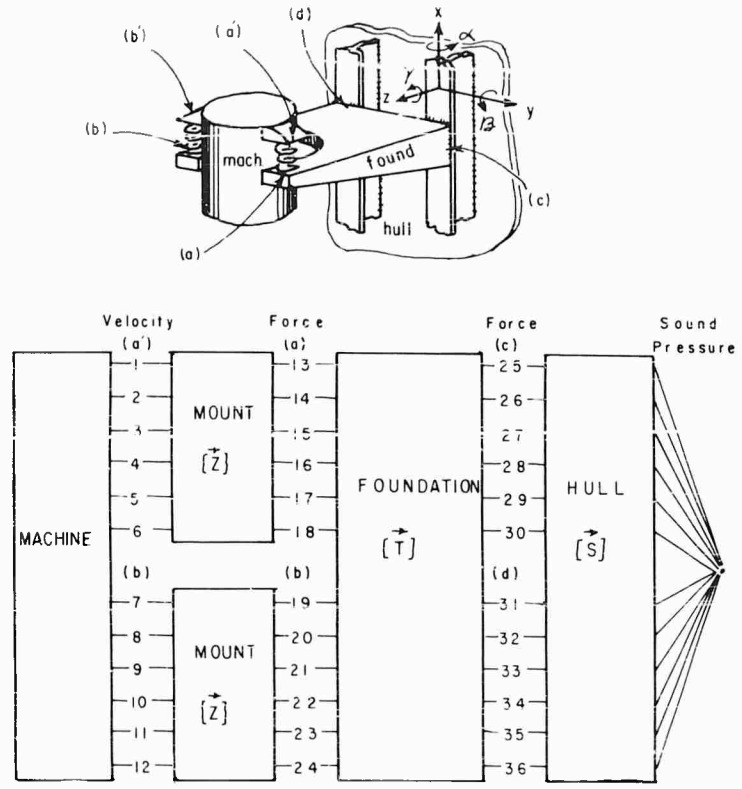

Fig. 2 - Simple machine installation and analysis scheme

and two flexibly coupled piping systems would require 36 velocity spectra with magnitude and phase information, 36 of the Z_{ij} elements for the type of isolation mount used, 36 Z'_{ij} elements for each of the two flexible couplings used as they would not be similar, 576 elements of Y_{ij} to specify the foundation, 36 Y'_{ij} elements for each piping system, and minimum of 6 S_i elements, if all interfaces on the hull could be assumed to have similar characteristics. Obviously, such a rigorous analysis is not practical for many reasons.

A SPECIFIC EXAMPLE AND COMMENTS ON PROBLEMS OF A RIGOROUS ANALYSIS

To understand the problem better, the simplified model shown in Fig. 2 will be considered. Here is a simple three-dimensional system consisting of a machine with two isolation mount interfaces (a,b) on a foundation with two attachment interfaces (c,d) on the hull. The terminal pairs are numbered continuously through as shown in the figure with the convention that at a given interface the first three terminal pairs are the translational coordinates (x, y, z) in that order, and the last three are the rotational (α, β, γ) in that order.

Analysis as above would lead to the following results:

1. The column matrix of force spectra out of the machine at interface a would be:

$$\begin{vmatrix} F_{13} \\ F_{14} \\ F_{15} \\ F_{16} \\ F_{17} \\ F_{18} \end{vmatrix} = \left[\begin{array}{ccc:ccc} Z_{13/1} & Z_{13/2} & Z_{13/3} & Z_{13/4} & Z_{13/5} & Z_{13/6} \\ Z_{14/1} & Z_{14/2} & Z_{14/3} & Z_{14/4} & Z_{14/5} & Z_{14/6} \\ Z_{15/1} & Z_{15/2} & Z_{15/3} & Z_{15/4} & Z_{15/5} & Z_{15/6} \\ \hdashline Z_{16/1} & Z_{16/2} & Z_{16/3} & Z_{16/4} & Z_{16/5} & Z_{16/6} \\ Z_{17/1} & Z_{17/2} & Z_{17/3} & Z_{17/4} & Z_{17/5} & Z_{17/6} \\ Z_{18/1} & Z_{18/2} & Z_{18/3} & Z_{18/4} & Z_{18/5} & Z_{18/6} \end{array}\right] \cdot \begin{vmatrix} V_1 \\ V_2 \\ V_3 \\ V_4 \\ V_5 \\ V_6 \end{vmatrix} \quad (6)$$

A similar matrix would exist for the forces at interface b involving velocity inputs $V_7, V_8, \ldots V_{12}$

and force outputs $F_{19}, F_{20}, \ldots F_{24}$. It is current practice to measure spectra defining the three translation velocity input magnitudes, $|V_1|$, $|V_2|$, $|V_3|$ and $|V_7|$, $|V_8|$, $|V_9|$. With present instrumentation, relative phase information on these measurements may be obtained but not generally in routine specification and evaluation tests. Attempts to measure rotational motion at an interface have been made [5], but practical transducers and techniques to do so are just now being considered at MEL. The measurement of the elements in the transfer impedance matrix is such that presently only a few elements can be measured with confidence [6]. Also, it should be noted that phase information on all transfer measurements is difficult and tedious to obtain with present instrumentation because the phase angle is not confined to the first and last quadrants, if the system is continuous.

2. The operation to obtain the matrix of forces that drive the hull is:

$$\begin{vmatrix} F'_{25} \\ \cdot \\ F'_{28} \\ \cdot \\ F'_{31} \\ \cdot \\ F'_{34} \\ \cdot \end{vmatrix} = \begin{vmatrix} T_{25/13} & T_{25,16} & T_{25/19} & T_{25/22} \\ \cdots & \cdots & \cdots & \cdots \\ T_{28/13} & T_{28/16} & T_{28/19} & T_{28/22} \\ \cdots & \cdots & \cdots & \cdots \\ T_{31/13} & T_{31,16} & T_{31,19} & T_{31,22} \\ \cdots & \cdots & \cdots & \cdots \\ T_{34/13} & T_{34,16} & T_{34,19} & T_{34/22} \\ \cdots & \cdots & \cdots & \cdots \end{vmatrix} \cdot \begin{vmatrix} F_{13} \\ \cdot \\ F_{16} \\ \cdot \\ F_{19} \\ \cdot \\ F_{22} \\ \cdot \end{vmatrix} \quad . \quad (7)$$

The elements of the force transmissibility matrix can be obtained in several ways. Analytical techniques for calculating the elements for relatively simple structures have been described [7,8,9]. Efforts to extend the results from simple structures to more realistic, and, therefore, more complex, structures by a module or "building block" technique are presently under way at Westinghouse Research Laboratory. Individual T elements for complex foundation structures can be obtained experimentally by ratioing radiation-transfer factors, or mechanical mobility measurements made on the hull without the foundation in place, with those obtained on the foundation [10,11]. There are many technical problems involved in applying and measuring the unidirectional forces on the interfaces required in the definition of the radiation transfer factors and mechanical mobilities [6].

3. The final operation yielding the radiated pressure in the field is:

$$P = |S_{25} \quad S_{28} \quad S_{31} \quad S_{34}| \cdot \begin{vmatrix} F'_{25} \\ \cdot \\ F'_{28} \\ \cdot \\ F'_{31} \\ \cdot \\ F'_{34} \\ \cdot \end{vmatrix} \quad . \quad (8)$$

An analytic method for the calculation of the acoustic transfer factor caused by a force normal to the hull and the factor caused by a moment (similar to S_4) has been devised by Junger and compared to experimental efforts [12]. One of the main difficulties is that the S factor should utilize a far-field pressure measurement free of surface and bottom effects. This condition is difficult to achieve readily.

A Practical Approach

Superimposed on the specific measurement problems mentioned is the fact that there are many different machines and different installation geometries involved in any major analysis. This condition results primarily from the fact that ships and submarines are not produced in large quantities and, therefore, do not have interchangeable, or nearly identical, machinery installations. For example, there may be significant differences in machine-source characteristics, as well as in structural details, on installations performing identical functions on sister ships constructed in different shipyards. Thus, there is the need to categorize the necessary input [13] and transfer parameters in terms of such general properties as function, size, and power for machines, and basic geometric shape, normalized dimensions, and location in hull for machinery foundations. A program to do this can be commenced with existing techniques, if the analysis scheme is simplified to account for the previously mentioned technical problems.

The first simplification is the combination of velocity or force components at a given interface. All translatory components at an interface must obviously be in phase with each other, and the same applies to the rotational components. The square root of the sum of the square correctly defines the magnitude of the resultant velocity or force, i.e.,

$$F_t^* \quad F_t \quad \left(F_x^{\,2} + F_y^{\,2} + F_z^{\,2} \right)^{1/2}$$

and

$$F_r^* \quad |F_r| = \left(|F_\alpha|^2 + |F_\beta|^2 + |F_\gamma|^2\right)^{1/2} . \quad (9)$$

When a structure has many such interfaces and they are grouped into input and output interfaces for analysis purposes, a second simplification is the spatial summation or integration of the velocities and forces of like units across all input interfaces (or all output interfaces), thereby further reducing the bulk of data to be processed. This step demands an assumption about the relative phasing of the resultant quantities F^* or V^* among the interfaces, if accurate phase information is to be neglected. The extremes are to assume that all quantities are in phase or that they pair up in combinations 180 degrees out of phase. A logical assumption for the complicated systems and the broad frequency ranges under consideration is a power summation of the resultants:

$$F_t^* = \left(\sum_{i=1}^{n} F_{t_i}^{*2}\right)^{1/2} , \quad F_r^* = \left(\sum_{i=1}^{n} F_{r_i}^{*2}\right)^{1/2} . \quad (10)$$

These simplifications for treating input and output quantities infer that a simple transfer function also exists in each case in the analysis. For example, with the expression $[F'] = [T] \cdot [F]$ for a structure with one output and one input interface, if only the translatory input and output force components are considered,

$$T_t^* \quad \frac{F_t'^*}{F_t^*} = \frac{\left(|F_x'|^2 + |F_y'|^2 + |F_z'|^2\right)^{1/2}}{\left(|F_x|^2 + |F_y|^2 + |F_z|^2\right)^{1/2}} . \quad (11)$$

Then it can be shown that T_t^* relates to the elements in $[T]$ by

$$T_t^* \quad \frac{1}{\sqrt{3}} \left(|T_{xx}|^2 + |T_{xy}|^2 + \cdots + |T_{zz}|^2\right)^{1/2} . \quad (12)$$

Thus, T_t^* is equal to the square root of the sum of the squares of the magnitudes of all the T_{ij} elements in $[T]$ which involve only translational coordinates. The $1/\sqrt{3}$ is a normalization coefficient needed to make Eq. (12) compatible with Eq. (11). In general, the coefficient would be the reciprocal of the square root of the number of input quantities. For a rigorous analysis including rotational components, a minimum of four T^* factors ($T_t^*, T_r^*, T_{r/t}^*, T_{t/r}^*$) are necessary to define a very complex system. Applying this technique to the system in Fig. 2, the forces out of the isolation mount in Eq. (6) would become:

$$\begin{vmatrix} F_t^* \\ F_r^* \end{vmatrix} = \begin{vmatrix} Z_t^* & Z_{t/r}^* \\ Z_{r/t}^* & Z_r^* \end{vmatrix} \cdot \begin{vmatrix} V_t^* \\ V_r^* \end{vmatrix} , \quad (13)$$

where

$$F_t^* = \left(|F_{13}|^2 + |F_{14}|^2 + |F_{15}|^2\right)^{1/2} ,$$

$$Z_t^* = \frac{1}{\sqrt{3}} \left(|Z_{13/1}|^2 + |Z_{13/2}|^2 + \cdots + |Z_{15/3}|^2\right)^{1/2}$$

$$V_t^* = \left(|V_1|^2 + |V_2|^2 + |V_3|^2\right)^{1/2} , \text{ etc.}$$

The spectrum V_t^* can be obtained by a manual summation of the individual spectra or by obtaining it automatically at the time of measurement [14]. The forces operating on the hull after being modified by the foundation become from Eq. (7):

$$\begin{vmatrix} F_{t_c}' \\ F_{r_c}'^* \\ F_{t_d}'^* \\ F_{r_d}'^* \end{vmatrix} = \begin{vmatrix} T_{t_{ca}}^* & T_{t/r_{ca}}^* & T_{t_{cb}}^* & T_{t/r_{cb}}^* \\ T_{r/t_{ca}}^* & T_{r_{ca}}^* & T_{r/t_{cb}}^* & T_{r_{cb}}^* \\ T_{t_{da}}^* & T_{t/r_{da}}^* & T_{t_{db}}^* & T_{t/r_{db}}^* \\ T_{r/t_{da}}^* & T_{r_{da}}^* & T_{r/t_{db}}^* & T_{r_{db}}^* \end{vmatrix} \cdot \begin{vmatrix} F_{t_a}^* \\ F_{r_a}^* \\ F_{t_b}^* \\ F_{r_b}^* \end{vmatrix} . \quad (14)$$

As before, it can be seen that force transfer factor

$$T_{t_{ca}}^* = \frac{1}{\sqrt{3}} \left(|T_{25/13}|^2 + |T_{25/14}|^2 + \cdots + |T_{27/15}|^2\right)^{1/2}$$

represents all elements involving translation force ratios between interfaces a and c.

The expression for obtaining the pressure in the sea would become from Eq. (8):

$$P^* = |S_{t_c}^* \quad S_{r_c}^* \quad S_{t_d}^* \quad S_{r_d}^*| \cdot \begin{vmatrix} F_{t_c}'^* \\ F_{r_c}'^* \\ F_{t_d}'^* \\ F_{r_d}'^* \end{vmatrix} , \quad (15)$$

where

$$S^*_{t_c} = \frac{1}{\sqrt{3}} \left(|S_{25}|^2 + |S_{26}|^2 + |S_{27}|^2 \right)^{1/2}$$

which intuitively can be approximated by $S^*_{t_c} \approx |S_{25}|$ or at least by

$$S^*_{t_c} \approx \frac{1}{\sqrt{2}} \left(|S_{25}|^2 + |S_{26}|^2 \right)^{1/2} .$$

In view of the present state-of-the-art, where data involving rotational coordinates are not available, the following simplifications for the system in Fig. 2 would result for the total force output of the machine:

$$\begin{aligned} F^*_{t_a} &= Z^*_{t_a} V^*_{t_a} , \\ F_{t_b} &= Z^*_{t_b} V^*_{t_b} . \end{aligned} \qquad (16)$$

F^*, V^* and Z^* are defined for the system by the expression:

$$Z^* = \frac{F^*}{V^*} = \frac{\left(F^{*2}_{t_a} + F^{*2}_{t_b} \right)^{1/2}}{\left(V^{*2}_{t_a} + V^{*2}_{t_b} \right)^{1/2}} , \qquad (17)$$

where

$$Z^* = \frac{1}{\sqrt{2}} \left(Z^{*2}_{t_a} + Z^{*2}_{t_b} \right)^{1/2} .$$

If $Z^*_{t_a} = Z^*_{t_b} = Z^*_o$ (that is, the mounts are identical) $Z^* = \sqrt{2}\, Z^*_o$. The forces driving the hull now would become from Eq. (14):

$$\begin{vmatrix} F'^*_{t_c} \\ F'^*_{t_d} \end{vmatrix} = \begin{vmatrix} T^*_{t_{ca}} & T^*_{t_{cb}} \\ T^*_{t_{da}} & T^*_{t_{db}} \end{vmatrix} \cdot \begin{vmatrix} F^*_{t_a} \\ F^*_{t_b} \end{vmatrix} . \qquad (18)$$

Again by defining F'^* and T^* for the system by:

$$T^* = \frac{F'^*}{F^*} = \frac{\left(F'^{*2}_{t_c} + F'^{*2}_{t_d} \right)^{1/2}}{F^*} , \qquad (19)$$

it can be shown that

$$T^* = \frac{1}{\sqrt{2}} \left(T^{*2}_{t_{ca}} + T^{*2}_{t_{cb}} + T^{*2}_{t_{da}} + T^{*2}_{t_{db}} \right)^{1/2} . \qquad (20)$$

Similarly, the system acoustic transfer factor is defined as

$$S^* = \frac{\left(P^{*2}_{(c)} + P^{*2}_{(d)} \right)^{1/2}}{F'^*} , \qquad (21)$$

which is equivalent to

$$S^* = \frac{1}{\sqrt{2}} \left(S^{*2}_{t_c} + S^{*2}_{t_d} \right)^{1/2} . \qquad (22)$$

Thus, the system pictured in Fig. 2 can be approximated by the simple expression

$$P^* = S^* T^* Z^* V^* \qquad (23)$$

with a single spectrum plot representing each of the parameters considered in the analysis; i.e., the hull radiation characteristics S^*, the effect of transmission through internal structural paths T^*, the effect of the isolation mounts Z^*, and the input velocity spectrum V^*.

This technique can be applied to very complicated systems as shown in Fig. 1 and Eq. (5) would become:

$$P^* = \left[(S^* T^* F^*_f)^2 + \sum_{i=1}^{p} (S^{*\prime}_i T^{*\prime}_i Z^{*\prime}_i V^{*\prime}_i)^2 \right]^{1/2} . \qquad (24)$$

Considering the limited number of measurements that are commonly available, it is reasonable to let the one velocity spectrum V^* represent all velocity inputs ($V^* = V^{*\prime}_i = V^{*\prime}_j \ldots$). Also, let all n isolation mounts be of the same type, allowing F^*_f to be equivalent to $\sqrt{n}\, Z^*_o V^*$. Furthermore, the geometry of the hull construction (particularly of a submarine) is often symmetrical enough to allow a common S^* factor to be used in the analysis without too much loss of confidence. Then Eq. (24) becomes:

$$P^* = S^* V^* \left[(T^* \sqrt{n}\, Z^*_o)^2 + \sum_{i=1}^{p} (T^*_i Z^{*\prime}_i)^2 \right]^{1/2} . \qquad (25)$$

In practical prediction problems [1], one may be required to compare the radiated and self-noise signatures of entire propulsion systems, each involving many primary and auxiliary machines. Furthermore, it may be required to predict the benefit of effecting noise reduction features that can be quantitatively interpreted in the source and transfer factors used in this analysis. Presently, the lack of time and nonavailability of desired data usually force a rough

Type of Machine	No. of Machines per Ship	Isolation Mount Type	"n" No. of Mounts	T_i^* Foundation Factor Category	Type of Flanking Path	No. per Type	$Z_i^{*\prime}$ Category	$T_i^{*\prime}$ Category

Fig. 3 - Heading of typical data sheet used in itemizing factors for machinery noise predictions

estimate of the factors in Eq. (25) with the result that they serve as simple weighting functions. Figure 3 represents the heading from a typical data sheet utilized in the prediction for the major components in an entire machinery system. Figure 4 shows a combination of measured and estimated transfer impedances for common isolation devices. The value shown for most of the isolation mounts was obtained by utilizing the dynamic spring constant data available for common Navy mounts in three translational directions and allows for a "flattening off" of the curve at high frequencies to account for standing wave phenomena [15].

Figure 5 represents a typical velocity spectrum that may be used to represent a small resiliently mounted pump. Appropriate values for Z_o^* and $Z_i^{*\prime}$ are chosen from the data in Fig. 4. The effect of the foundation and piping systems is estimated by the factors shown in Fig. 6. The T_{db}^* factors are considered to be flat and positive (therefore, representing only amplifications of the input force). It is believed that such factors for a complicated foundation would actually be curves having many extrema both in the positive and negative portions of the T_{db}^* plot [16]. Figure 7 depicts what is considered as the typical trend of the S_{db}^* curve. Figure 8 shows the resultant contributions to the radiated sound pressure from energy transmitted through each of the piping systems in the pump installation, as well as through the foundation structure.

PREDICTING DYNAMIC FORCES ON RESILIENTLY MOUNTED EQUIPMENT

As mentioned earlier, the possibility of utilizing the technique in reverse, to specify the pressure pulse spectrum outside the hull and

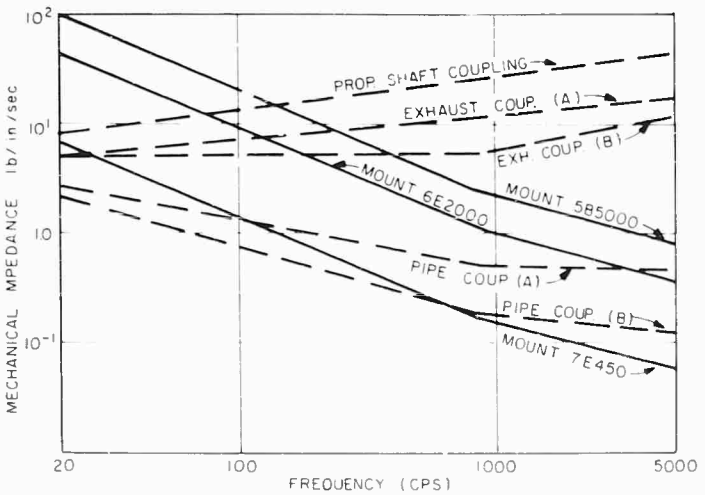

Fig. 4 - Transfer impedances of isolation devices

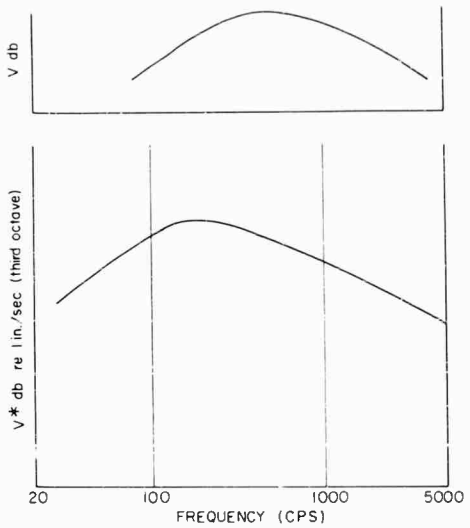

Fig. 5 - Typical velocity spectrum for pump

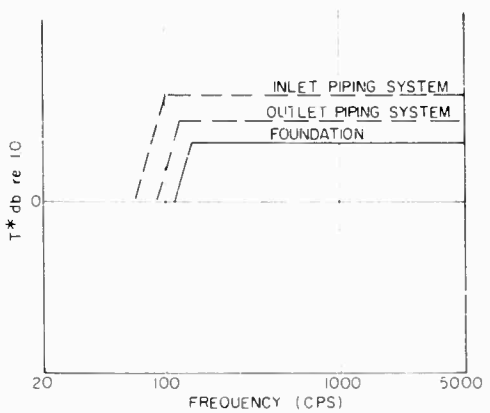

Fig. 6 - Typical structural force ratio factors

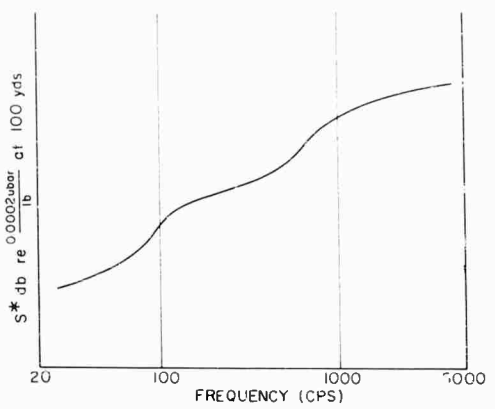

Fig. 7 - Typical acoustic transfer factor

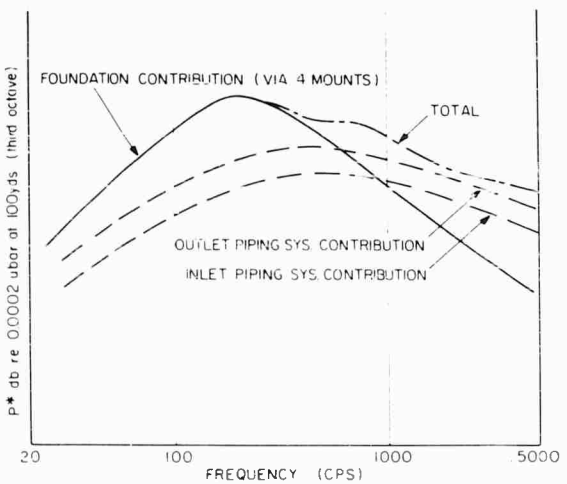

Fig. 8 - Predicted radiated sound pressure from pump

then predict the dynamic forces at the hull-side interfaces of isolation devices, is intriguing because it would mean that investigators working in both disciplines would be interested in defining and cataloging similar transfer functions.

A thorough investigation of the significance of the acoustic transfer factor is needed to evaluate the method's applicability to the shock problem. Junger [17] calculates the S factor by relating the dynamic response of the hull to the force on the hull by a summation of the modal mobilities. It seems that if the radiation problem can be solved from knowing the dynamic response of the hull and the boundary conditions in the acoustic field, a special reciprocity condition can be obtained [18,19] allowing the dynamic response of the hull to be found if the acoustic pressure spectrum is given. Then this response may be related, by the hull mobility, to the reaction force existing at a foundation attachment interface. The force ratio transfer factor [T] or T^* may be used to calculate the force magnitudes applied to the isolation devices. These force spectra could be used in establishing levels for shop shock tests of resiliently mounted machines. The prediction of excursions of the mounted machinery would probably involve using Z^* parameters for isolation devices which would include amplitude and strain-rate nonlinearities [20] that do not

have to be considered for the small motions involved in the noise transmission problem.

Programs are now under way to assay existing data and to obtain new data which may be used as transfer functions for predicting machinery noise radiation from Navy surface ships and submarines. Eventually the MEL acoustic library could be expanded to include categorized transfer factors for isolation devices and foundations, as well as the machinery vibration data now being stored in digital form. This data will be readily available as inputs for the calculation of far- and near-field radiation predictions.

REFERENCES

1. R. A. Darby, "A Method for Predicting the Radiated Acoustic Noise from Machinery on Navy Ships," MEL Report 67 102 B (Mar. 12, 1964) (Confidential).

2. M. C. Junger et al., "Foundation Design Procedure Based on Radiated Noise Specifications," Cambridge Acoust. Assoc. Tech. Memorandum TM C-150-128 (Jan. 19, 1963) (Confidential).

3. D. V. Wright, "Impedance Analysis of Distributed Mechanical Systems," ASME Colloquium on Mechanical Impedance Methods, Ed. by R. Plunkett (Dec. 2, 1958).

4. R. A. Darby, "The Quantitative Evaluation of Vibration Isolation Devices for Mounted Naval Machinery Installations," MEL Report 82 287E (Aug. 29, 1963).

5. R. C. Hirsch, "Experimental Mobility Parameters of a Clamped Circular Plate," MEL Report 137/64 (to be published).

6. R. A. Darby, "Mechanical Impedance Measurements in Foundation Studies," Shock, Vibration and Associated Environments Bull. No. 33, Part IV, pp. 55 (Mar. 1964).

7. D. V. Wright, "Sound Radiation and the Force Ratios of Foundation Structures," USN J. Underwater Acoust., 13:1009 (Oct. 1963) (Confidential).

8. D. V. Wright et al., "Vibration Transmission and Impedance of Basic Foundation Structures," Westinghouse Res. Lab. Report 62-917-515-R1 (Oct. 1962).

9. J. G. Akey, "Transfer-Matrix Method and Computer Program for the Vibration Analysis of Series Plane-Frame Structures Having Material Damping and Complex Terminations," Westinghouse Res. Lab. Report 63-917-515-R4 (Sept. 1963) (Proprietory).

10. R. A. Darby and E. V. Stanley, "Impedance Studies of Tubular Columns as Basic Machine Foundation Elements," EES (MEL) Report 820287B (July 6, 1962).

11. R. C. Hirsch, "Impedance Studies of an Asymmetrical Angle-Iron Column as a Basic Machine Foundation Element," MEL Report 82 287D (Aug. 1963).

12. M. C. Junger and W. Thompson, Jr., "Spectrum Level Curves Relating Submarine Radiated Noise at 100 Yards to Forces and Moments on Hull Frames," USN J. Underwater Acoust., 13:955 (Oct. 1963) (Confidential).

13. H. W. Moody and R. W. Achurch, "Structure-borne Noise Survey of Nuclear Submarines," USN J. Underwater Acoust., 13:965 (Oct. 1963) (Confidential).

14. R. M. Bell, "Vibration Cross-Talk Control Through Instrumentation," Reprint from ISA Show, New York (Sept. 26-30, 1960).

15. F. J. Cingel, "Mechanical Impedance Characteristics of Navy Type 7E450 Resilient Mounts," EES (MEL) Report 82 288 E (Nov. 1962).

16. E. V. Thomas, "Development of a Highly Damped Submarine Machinery Foundation," Shock, Vibration and Associated Environments Bull. No. 34, Part V (Feb. 1965).

17. M. C. Junger, "Noise Radiation from Submarine Hulls, Part I," Cambridge Acoust. Assoc., Inc., Report C-129-64 (Mar. 1962) (Confidential).

18. G. Chertoch, "General Reciprocity Theorem," J. ASA, 34:989 (1962).

19. E. L. Shenderov, "Radiation of Sound From a System of Sources Through an Elastic Cylindrical Shell," Soviet Physics-Acoustics, 9:313 (Jan.-Mar. 1964).

20. R. E. Baker, "Response of 5B5,000 Resilient Mounts to Dynamic Loading," DTMB Encl. to ltr Ser. 7-178 (July 30, 1964).

* * *

A STEADY STATE RESPONSE ANALYSIS OF COMPLEX STRUCTURES USING IMPEDANCE COUPLING TECHNIQUES*

M. J. Baruch and S. Telles
Republic Aviation Corp.
Farmingdale, L. I., New York

A generalized method has been developed to obtain the damped steady state response of a structure to a sinusoidal force, applied at any point on the structure, or a base motion input. Using matrix methods in conjunction with impedance coupling techniques, the steady state response of a free-free or motion-constrained structure can be obtained.

By matrix methods the structure is represented as a system of lumped mass points and a set of influence coefficients. A resulting matrix equation, including the mass distribution and influence coefficients, must then be inverted to obtain the response. To handle a complete structure with a large number of degrees of freedom in this manner requires the inversion of large complex $(a + ib)$ matrices, equal in size to the total number of degrees of freedom describing the structure. The numerical difficulties encountered in the inversion of large complex matrices severely limits the size of systems (degrees of freedom) that can be considered.

The method presented allows the structure to be divided into smaller substructures that are analyzed as individual systems. Constraint (coupling) forces, at the points of interconnection between substructures, act as external forces on each substructure. The substructure is divided into mass stations, and the influence coefficients are developed with respect to reference stations. The constraints imposed by the reference stations depend on the mathematical idealization of the substructure; in most cases a substructure can be represented as fixed ended or simple supported for lateral degrees of freedom and as fixed ended for longitudinal or in-line degrees of freedom.

A set of matrix equations have been developed which define the response of the substructure to the unknown coupling forces and any known input forces or motions acting on the substructure. Each substructure is analyzed with these equations. The substructure response equations are then coupled, noting that compatibility of motions and equilibrium of constraint forces must exist at the points of interconnection of the substructures. The resulting matrix, whose size is a function of the total number of interconnections, is inverted to obtain the values of the constraint forces. Substitution of the values of the constraint forces back into the substructure response equations yields the absolute steady state response and phase angle of all mass points in the structure. By performing this analysis for a range of frequencies, a response or transmissibility curve can be developed from which the damped steady state response at the natural frequencies can be obtained.

*This paper was not presented at the Symposium.

INTRODUCTION

During the payload boost phase, steady state excitations can be induced at the booster-payload interface, resulting in the transmission of high g levels to the payload and its components. In the design of the payload an estimate of these dynamic loads can be made from a steady state response analysis of the payload with an assumed sinusoidal input at the interface or of the booster-payload combination considered as a free body in space. Many of today's spacecraft are complex structures consisting of many interconnected components, making it necessary to have a method of analysis that can handle a large structure without excessive simplification of the structural model.

An analytical procedure has been developed to obtain the damped steady state response of a structure to sinusoidal force or motion excitations. Using matrix methods in conjunction with impedance coupling techniques, the steady state response of a free-free, or motion constrained structure can be obtained.

The method presented here assumes that any structure can be divided into a set of statically determinate substructures, where each substructure is separated from adjoining substructures at discrete interconnections (coupling coordinates). The redundant (coupling) forces transmitted at these interconnections act as external forces on each substructure. Therefore, each substructure can be treated as an isolated free-free or motion constrained system which can be analyzed separately; i.e., a response equation can be developed for each substructure as a function of the unknown coupling forces as well as any external excitation functions applied to the structure.

Each substructure is represented by a lumped mass structural model with up to six degrees of freedom for each mass station. A set of influence coefficients is developed for each substructure with respect to the reference coordinates. These may be assumed to have fix-ended or simple-supported boundary conditions.

A set of matrix equations is derived which define the absolute motion response at each degree of freedom in a particular substructure to the unknown coupling forces and any known force or motion excitations acting on a substructure. The matrix response equations obtained for all substructures combined to obtain the coupled responses at all degrees of freedom in the complete structure. The individual substructure response equations contain a coefficient matrix of complex elements which multiply the column vector of redundant coupling forces. Based on the definition of mechanical impedance, i.e., $[Z] = \{\phi\}/\{q\}$, the coefficient of the coupling force column vector is $[Z]^{-1} = \{q\}/\{\phi\}$, known as the mobility matrix. These mobility matrices and the matrices defining the known excitations are combined, noting that compatibility of motions and equilibrium of coupling forces must exist at the interconnections of the substructures. A resulting matrix, whose size is a function of the total number of interconnections in all the substructures, is inverted to obtain the values of the coupling forces. Substituting these values into the substructure response equations yields the steady state responses of the coupled structure. By performing the analysis for a range of frequencies, a response or transmissibility curve can be developed from which the damped steady state responses at the natural frequencies can be obtained.

LIST OF SYMBOLS

n	Number of mass station coordinates (degrees of freedom) in substructure
m	Number of reference station coordinates in substructure
[ ]	Brackets indicating rectangular or square matrix
{ }	Braces indicating column matrix
x, y, z	Translational Cartesian coordinates (in.)
$\theta_x, \theta_y, \theta_z$	Rotational Cartesian coordinates (rad)
y_o	Rigid body translation at Station Zero (in.)
θ_o	Rigid body rotation at Station Zero (rad)
F_i	Applied external force at ith mass station (lb)
M_i	Applied external moment at ith mass station (lb-in.)
i j	Subscripts: i 1...n, j 1...m
y_i	Absolute coordinate translation of ith mass station (in.)

θ_i Absolute rotational coordinate of ith mass station (rad)

$\ddot{y}_i, \ddot{\theta}_i$ Absolute translational and rotational acceleration, respectively, of Mass Station (i) (in./sq sec)

x_i Distance of Station (i) from Station Zero (in.)

F_i' Total external force at ith mass station (lb)

M_i' Total external moment at ith mass station (lb-in.)

$[\alpha]$ Influence coefficient matrix (size: $n \times n$) (in./lb)

m_i Mass of ith mass station (lb-sq sec/in.)

I_i Mass moment of inertia of ith mass station (lb-in.-sq sec)

$[M]$ Mass matrix (size: $n \times n$) (lb-sq sec/in.)

$[L]$ Geometry (rigid body motion) matrix (size: $m \times n$)

$[L]^T$ Transpose of geometry matrix

q_i Absolute response of ith mass station coordinate of substructure (in.)

δ_j Rigid body motion of jth reference station coordinate

ϕ_i Coupling load (force or moment) applied to ith mass station coordinate (lb or lb-in.)

λ_i Known external load (force or moment) applied to ith mass station coordinate

$[\alpha]_c$ Complex influence coefficient matrix (in /lb)

μ $2b = 2x(c/c_c)$, where c/c_c = damping ratio

$e^{-i\mu}$ Complex damping modulus

i Imaginary value, $\sqrt{-1}$

ω Excitation frequency (rad/sec)

t Time (sec)

$[I]$ Unit matrix (size: $n \times n$)

$[\beta]$ Dynamic matrix (size: $n \times n$)

$[F]$ Free-free matrix (size: $n \times n$)

$[Q]$ Mass unbalance matrix (size: $m \times m$)

$[E]$ Given by Eq. (42)

$[N]$ Given by Eq. (43)

$[P]$ Given by Eq. (39)

$(q_R)_j$ Responses of jth reference station coordinate

$(\lambda_R)_j$ Input load (force or moment) applied to jth reference station coordinate (lb or lb-in.)

$(\phi_R)_j$ Redundant (coupling) load (force or moment) at jth reference station coordinate (lb or lb-in.)

$|q|$ Amplitude of steady state response

ψ Phase angle

ANALYSIS OF INDIVIDUAL SUBSTRUCTURES

The mass point degrees of freedom in a substructure are defined as follows:

1. Reference Station Coordinates: those degrees of freedom in a statically determinate substructure that are assumed a fixed reference for obtaining the influence coefficients of the substructure.

2. Mass Station Coordinates: those degrees of freedom in a statically determinate substructure for which influence coefficients are obtained with respect to the reference station coordinates.

The equation used to obtain the responses of a particular substructure is dependent on the type of boundary conditions existing at the assumed reference station coordinates of the substructure and the types of excitation functions applied to the substructure. The types of boundary conditions considered are fixed free, simple supported, and free-free. In the first two cases the excitation functions are a displacement, velocity or acceleration input to a reference station coordinate and a known external force

or coupling force applied at a mass station coordinate. Such substructures are referred to as motion constrained. Under free-free conditions the excitation functions can only be a coupling force applied to the substructure at a reference station coordinate (for a coupling-constrained free-free substructure),* a known external force applied at a reference station coordinate (for an unconstrained free-free substructure), or a known external or coupling force applied at a mass station coordinate (contained in either of the latter two types of substructure).

The equations of a motion-constrained substructure are developed in the following section. The response equations of a free-free substructure are then obtained by considering the equilibrium of forces and moments on the substructure.

Derivation of Substructure Equations of Motion

The beam shown in Fig. 1 is represented by a lumped mass distribution and a set of influence coefficients referenced to Station Zero. It is considered to contain (n) mass points, each with the capability of up to six degrees of freedom.

For simplicity the derivation considers only the translational motions in the y direction and the rotational motions about the z axis. The extension to six degrees of freedom per mass point can be achieved once the form of the equations of motion has been established.

*In this case, the reference station coordinate is a coupling coordinate, and the motion of the reference station coordinate is a function of the coupling between substructures.

In Fig. 1, y_o and θ_o are the rigid body translational and rotational motions, respectively, at Station Zero, having the positive directions indicated. The influence coefficients, a_{ij} are referenced to Station Zero as though the beam were cantilevered from that point. It is assumed that a set of applied external forces $\{F_i\}$ and moments $\{M_i\}$ act at each mass point on the beam y_i and θ_i are the absolute translational and rotational coordinates of Station (i) relative to the equilibrium position, and x_i is the distance of Station (i) from Station Zero. The elastic translation and rotation of the beam at Station (i), assuming θ_o to be small, can be defined as

$$(y_i)_e = y_i - y_o - \theta_o x_i \qquad (1)$$

and

$$(\theta_i)_e = \theta_i - \theta_o , \qquad (2)$$

and the elastic translation and rotation of a Station (i) due to a force or moment at a Station (j) can be written

$$y_i - y_o - \theta_o x_i = \sum_{j=1}^{n} a_{ij} F'_j + \sum_{j'=1}^{n} a_{ij'} M'_j$$

and (3)

$$\theta_i - \theta_o = \sum_{j=1}^{n} a_{ij} F'_j + \sum_{j'=1}^{n} a_{ij'} M'_j .$$

where F'_j and M'_j are the total external loads at Station (j) and the a_{ij} are the influence coefficients, $i, j = 1 \ldots n$.

The elastic motions at each of the mass stations can then be described by the matrix form of Eq. (3).

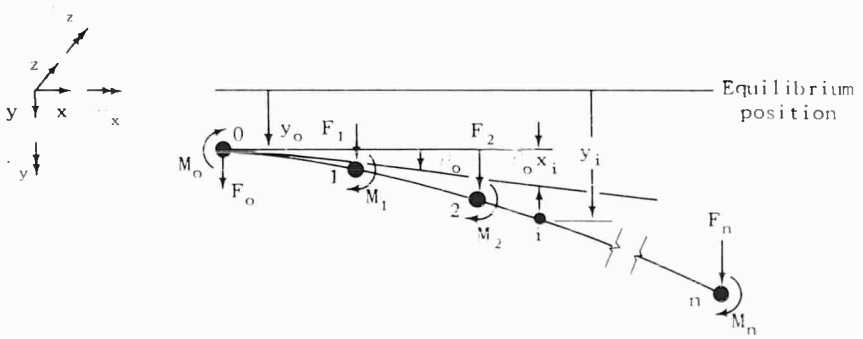

Fig. 1 - Beam with "n" mass points

$$\begin{Bmatrix} y_i - y_o - \theta_o x_i \\ \vdots \\ y_n - y_o - \theta_o x_n \\ \hline \theta_1 - \theta_o \\ \vdots \\ \theta_n - \theta_o \end{Bmatrix} =$$

$$\begin{bmatrix} a_{11} & \cdots & a_{1n} & a'_{11} & \cdots & a_{1n'} \\ \vdots & & \vdots & \vdots & & \vdots \\ a_{n1} & \cdots & a_{nn} & a_{n1'} & \cdots & a_{nn'} \\ a_{1'1} & \cdots & a_{1'n} & a_{1'1'} & \cdots & a_{1'n'} \\ \vdots & & \vdots & \vdots & & \vdots \\ a_{n'1} & \cdots & a_{n'n} & a_{n'1'} & \cdots & a_{n'n'} \end{bmatrix} \begin{Bmatrix} F'_1 \\ \vdots \\ F'_n \\ \hline M'_1 \\ \vdots \\ M'_n \end{Bmatrix} \quad (4)$$

The influence coefficient matrix $[a_{ij}]$ will henceforth be denoted by the symbol $[\alpha]$.

Since the motions of a given Station (i) vary with time, the inertia forces $(-m_i\ddot{y}_i)$ and $(-I_i\ddot{\theta}_i)$ act at this mass. The sum of the inertia load and applied external load at a Station (i) equals the total external load at the Station (i). This can be written as follows:

$$\begin{aligned} F'_i &= -m_i\ddot{y}_i + F_i \\ M'_i &= -I_i\ddot{\theta}_i + M_i \end{aligned} \quad (5)$$

In matrix form, Eq. (5) for all stations (1...n) is:

$$\begin{Bmatrix} F'_1 \\ \vdots \\ F'_n \\ \hline M'_1 \\ \vdots \\ M'_n \end{Bmatrix} = \begin{bmatrix} m_1 & & & & 0 \\ & \ddots & & & \\ & & m_n & & \\ & & & I_1 & \\ & & & & \ddots \\ 0 & & & & I_n \end{bmatrix} \begin{Bmatrix} \ddot{y}_1 \\ \vdots \\ \ddot{y}_n \\ \hline \ddot{\theta}_1 \\ \vdots \\ \ddot{\theta}_n \end{Bmatrix} + \begin{Bmatrix} F_1 \\ \vdots \\ F_n \\ \hline M_1 \\ \vdots \\ M'_n \end{Bmatrix} \quad (6)$$

where the matrix of elements $\begin{bmatrix} m_i & \\ & I_i \end{bmatrix}$ is the mass matrix and is denoted by the symbol $[M]$.

Substitution of Eq. (6) into Eq. (1) for the total external loads F'_i and M'_i and rearrangement of terms yields

$$\begin{Bmatrix} y_1 \\ \vdots \\ y_n \\ \hline \theta_1 \\ \vdots \\ \theta_n \end{Bmatrix} = -[\alpha][M] \begin{Bmatrix} \ddot{y}_1 \\ \vdots \\ \ddot{y}_n \\ \hline \ddot{\theta}_1 \\ \vdots \\ \ddot{\theta}_n \end{Bmatrix} + [\alpha] \begin{Bmatrix} F_1 \\ \vdots \\ F_n \\ \hline M_1 \\ \vdots \\ M_n \end{Bmatrix} + \begin{Bmatrix} y_o + \theta_o x_i \\ \vdots \\ y_o + \theta_o x_n \\ \hline \theta_o \\ \vdots \\ \theta_o \end{Bmatrix} \quad (7)$$

The term involving the rigid body motions y_o and θ_o can be rewritten in the form:

$$\begin{Bmatrix} y_o + \theta_o x_i \\ \vdots \\ y_o + \theta_o x_n \\ \hline \theta_o \\ \vdots \\ \theta_o \end{Bmatrix} = \begin{bmatrix} 1.0 & x_i \\ \vdots & \vdots \\ 1.0 & x_n \\ \hline 0 & 1.0 \\ \vdots & \vdots \\ 0 & 1.0 \end{bmatrix} \begin{Bmatrix} y_o \\ \theta_o \end{Bmatrix} \quad (8)$$

The coefficient matrix of

$$\begin{Bmatrix} y_o \\ \theta_o \end{Bmatrix}$$

is the transpose of the geometry matrix discussed later and is denoted by $[L]^T$.

Equation (7) can be rewritten as

$$\begin{Bmatrix} y_i \\ \theta_i \end{Bmatrix} = -[\alpha][M] \begin{Bmatrix} \ddot{y}_i \\ \ddot{\theta}_i \end{Bmatrix} + [\alpha] \begin{Bmatrix} F_i \\ M_i \end{Bmatrix} + [L]^T \begin{Bmatrix} y_o \\ \theta_o \end{Bmatrix} \quad (9)$$

which is the equation of motion of the two-dimensional beam shown in Fig. 1.

To extend this analysis to six degrees of freedom per mass point a new coordinate $\bar{q}_i$ is defined where the subscript i refers to a particular mass station coordinate of the substructure. In addition, the external loads F_i and M_i are replaced by the sum of two new forces $\bar{\varphi}_i$ and $\bar{x}_i$ where the $\{\bar{\varphi}_i\}$ are the redundant coupling forces which exist at the points of interconnection of adjoining substructures and the

$\{\bar{\lambda}_i\}$ are the known externally applied forces. The motions at Station Zero are called $\bar{\delta}_j$, where $j = 1, \ldots m \leq 6$, and are the possible rigid body motions at a reference station. Equation (9) can now be written as

$$\{\bar{q}_i\} = -[\alpha][M]\{\ddot{\bar{q}}_i\} + [\alpha]\{\bar{\phi}_i\} + [\alpha]\{\bar{\lambda}_i\} + [L]^T\{\delta_i\}, \quad (10)$$

where

$\bar{q}_{i(i=1..n)}$ = motion of ith mass station coordinate of substructure,

$\bar{\delta}_{j(j=1..m)}$ = rigid body motion of jth reference station coordinate,

$[\alpha]$ = influence coefficient matrix of substructure, with six degrees of freedom per mass point, referred to reference station coordinates (size: $n \times n$),

$[M]$ = mass matrix for (n) mass station coordinates (size: $n \times n$),

$[L]^T$ = transpose of geometry matrix for (m) reference station coordinates and (n) mass station coordinates (size: $m \times n$),

$\bar{\phi}_{i(i=1...n)}$ = coupling force applied at ith mass station coordinate, and

$\bar{\lambda}_{i(i=1...n)}$ = known external force applied at ith mass station coordinate.

Equation (10) has been developed using a structural model with cantilevered boundary conditions for influence coefficients. However, any statically determinate structural model could have been used.

Introduction of Damping into Equations of Motion

The equations of motion given by Eq. (10) have been developed omitting the effects of damping. Damping is introduced into the analysis by considering the structural of hysteretic energy dissipated within the structure. Myklestad [1] has developed a complex damping modulus $e^{i\mu}$ where $\mu = 2b$ and $b = c/c_c$ for low damping, which when multiplied by the elastic modulus E, results in a complex elastic modulus $\bar{E} = Ee^{i\mu}$. Since the elements of the influence coefficient matrix are inversely proportional to E, a complex influence matrix

$$[\alpha]_c = [\alpha]\, e^{-i\mu} = [\alpha](\cos\mu - i \sin\mu) \quad (11)$$

can be used to define the damping in the structure. The resulting damping force is a displacement dependent function.

By substitution of $[\alpha]_c$ for $[\alpha]$ in Eq. (10) and rearrangement of terms, the damped equations of motion of a substructure become

$$[\alpha]_c[M]\{\ddot{\bar{q}}_i\} + [I]\{\bar{q}_i\} = [\alpha]_c\{\bar{\phi}_i\} + [\alpha]_c\{\bar{\lambda}_i\} + [L]^T\{\delta_j\}, \quad (12)$$

where $[I]$ = a unit matrix.

Response Equations of Motion-Constrained Substructure

It is assumed that the forces and motions vary harmonically so that

$$\{\bar{\phi}_i\} = \{\phi_i\}\, e^{i\omega t},$$

$$\{\bar{\lambda}_i\} = \{\lambda_i\}\, e^{i\omega t},$$

and

$$\{\bar{\delta}_i\} = \{\delta_j\}\, e^{i\omega t},$$

and Eq. (12) has a solution of the form

$$\{\bar{q}_i\} = \{q_i\}\, e^{i\omega t}, \quad (13)$$

where

ω = frequency (rad/sec), and

i = imaginary value $\sqrt{-1}$.

Equation (12) then becomes

$$\left[[I] - \omega^2[\alpha]_c[M]\right]\{q_i\} = [\alpha]_c\{\phi_i\} + [\alpha]_c\{\lambda_i\} + [L]^T\{\delta_j\}. \quad (14)$$

Substitution for $[\alpha]_c$ from Eq. (11) with

$$[\beta] = \left[[I] - \omega^2[\alpha][M]\, e^{-i\mu}\right], \quad (15)$$

yields

NOTE: Reference appears on page 154.

$$[\beta]\{q_i\} = [\alpha]\, e^{-i\mu}\{\phi_i\} + [\alpha]\, e^{-i\mu}\{\lambda_i\} + [L]^T\{\delta_j\}\,. \quad (16)$$

If both sides of Eq. (16) are premultiplied by the inverse of $[\beta]$, the steady state response equation of a motion constrained substructure is obtained:

$$\{q_i\} = [\beta]^{-1}[\alpha]\, e^{-i\mu}\{\phi_i\} + [\beta]^{-1}[\alpha]\, e^{-i\mu}\{\lambda_i\} + [\beta]^{-1}[L]^T\{\delta_j\}\,, \quad (17)$$

where $\{\delta_j\}$ is the motion input column vector.

Equation (17) gives the response at all mass station coordinates $(1 \ldots n)$ in a substructure due to the coupling forces and known force and motion inputs. Several inherent properties of Eq. (17) should also be mentioned:

1. If $\{\delta_j\} = 0$, a substructure fixed to ground at the reference station can be analyzed.

2. If $\{\phi_i\} = 0$, coupling forces do not exist in the substructure; i.e., Eq. (17) also obtains the responses of a structure that has not been divided into substructures.

Response Equations of Free-Free Substructure

The summation of forces acting on the beam in Fig. 1 and the summation of moments about Station Zero are given by the following equations:

$$-F_o = -m_o\ddot{y}_o - \sum_{i=1}^{n} m_i\ddot{y}_i + \sum_{i=1}^{n} F_i \quad (18)$$

$$-M_o = -I_o\ddot{\theta}_o - \sum_{i=1}^{n} m_i x_i\ddot{y}_i - \sum_{i=1}^{n} I_i\ddot{\theta}_i + \sum_{i=1}^{n} F_i x_i + \sum_{i=1}^{n} M_i \quad (19)$$

where

m_o, I_o = mass and mass moment of inertia, respectively, at Reference Station Zero, and

F_o, M_o = force and moment at Reference Station Zero.

The terms of the equations can be written in matrix form as follows:

$$\sum_{i=1}^{n} m_i\ddot{y}_i = \left[[1,\ldots 1]_n, [0,\ldots 0]_n\right][M]\begin{Bmatrix}\ddot{y}_i\\ \ddot{\theta}_i\end{Bmatrix} \quad (20)$$

and

$$\sum_{i=1}^{n} m_i x_i\ddot{y}_i + \sum_{i=1}^{n} I_i\ddot{\theta}_i = \left[[x_1,\ldots x_n], [1,\ldots 1]\right][M]\begin{Bmatrix}\ddot{y}_i\\ \ddot{\theta}_i\end{Bmatrix}, \quad (21)$$

where $[M]$ = mass matrix defined by Eq. (6); also

$$\sum_{i=1}^{n} F_i = \left[[1,\ldots 1]_n, [0,\ldots 0]_n\right]\begin{Bmatrix}F_i\\ M_i\end{Bmatrix} \quad (22)$$

and

$$\sum_{i=1}^{n} F_i x_i + \sum_{i=1}^{n} M_i = \left[[x_1,\ldots x_n], [1,\ldots 1]_n\right]\begin{Bmatrix}F_i\\ M_i\end{Bmatrix}. \quad (23)$$

By using Eqs. (18) through (23), the following matrix equation can be written:

$$-\begin{Bmatrix}F_o\\ M_o\end{Bmatrix} = -\begin{bmatrix}m_o & 0\\ 0 & I_o\end{bmatrix}\begin{Bmatrix}\ddot{y}_o\\ \ddot{\theta}_o\end{Bmatrix} - \begin{bmatrix}[1,\ldots 1]_n, [0,\ldots 0]_n\\ [x_1,\ldots x_n], [1,\ldots 1]_n\end{bmatrix}[M]\begin{Bmatrix}\ddot{y}_i\\ \ddot{\theta}_i\end{Bmatrix} + \begin{bmatrix}[1,\ldots 1]_n, [0,\ldots 0]_n\\ [x_1,\ldots x_n], [1,\ldots 1]_r\end{bmatrix}\begin{Bmatrix}F_i\\ M_i\end{Bmatrix}\,, \quad (24)$$

where

$$\begin{bmatrix}m_o & 0\\ 0 & I_o\end{bmatrix} = [M_{Ref.}] = \text{reference station mass matrix.}$$

By noting Eq. (8) which defines $[L]^T$, it can be observed that

$$[L] = \begin{bmatrix}[1,\ldots 1]_n, [0,\ldots 0]_n\\ [x_1,\ldots x_n], [1,\ldots 1]_n\end{bmatrix}\,. \quad (25)$$

and Eq. (24) can be simplified to

$$-\begin{Bmatrix} F_o \\ M_o \end{Bmatrix} = -[M_{Ref.}]\begin{Bmatrix} \ddot{y}_o \\ \ddot{\theta}_o \end{Bmatrix} - [L][M]\begin{Bmatrix} \ddot{y}_i \\ \ddot{\theta}_i \end{Bmatrix} + [L]\begin{Bmatrix} F_i \\ M_i \end{Bmatrix}. \tag{26}$$

Equation (26) is the combined force and moment equilibrium equation for the two-dimensional structure in Fig. 1.

To extend Eq. (26) to six degrees of freedom per mass point, the motion coordinate q_i is introduced as discussed in the previous section. The externally applied forces F_i and M_i are again replaced by the summation of forces $\bar{\phi}_i$ and $\bar{\lambda}_i$. The rigid body motions and forces at Reference Station Zero are called $(\bar{q}_R)_j$ and $(\bar{\phi}_R)_j$, respectively, where $j = 1 \ldots m \leq 6$ are the rigid body degrees of freedom at the reference station. Equation (26) can be written for up to six degrees of freedom per mass point as follows:

$$-\{(\bar{\phi}_R)_j\} = -[M_{Ref.}]\{(\ddot{\bar{q}}_R)_j\} - [L][M]\{\ddot{\bar{q}}_i\} + [L]\{\bar{\phi}_i\} + [L]\{\bar{\lambda}_i\}, \tag{27}$$

where

$[M_{Ref.}]$ = reference station mass matrix (size: $m \times m$),

$(\bar{q}_R)_{j(j=1\ldots m)}$ = motion of jth reference station coordinate,

$(\bar{\phi}_R)_{j(j=1\ldots m)}$ = coupling force at jth reference station coordinate, and

$\bar{q}_{i(i=1\ldots n)}$ = motion of ith mass station coordinate.

Since the forces and motions are assumed to vary harmonically as in Eq. (13), Eq. (27) becomes

$$-\{(\phi_R)_j\} = \omega^2[M_{Ref.}]\{(q_R)_j\} + \omega^2[L][M]\{q_i\} + [L]\{\phi_i\} + [L]\{\lambda_i\}. \tag{28}$$

which is the general equilibrium equation of a statically determinate substructure.

The free-free response of a substructure can be obtained using Eq. (14) in conjunction with Eq. (28). The known motions of the reference station $\{\delta_j\}$ in Eq. (14) may be replaced by $\{(q_R)_j\}$, which are the unknown motions of the reference stations in the free-free substructure. On rearrangement of terms, Eq. (14) becomes

$$[I]\{q_i\} = \omega^2[\alpha]_c[M]\{q_i\} + [\alpha]_c\{\phi_i\} + [\alpha]_c\{\lambda_i\} + [L]^T\{(q_R)_j\}. \tag{29}$$

Premultiplying both sides of Eq. (29) by $[L][M]$ yields

$$[L][M]\{q_i\} = \omega^2[L][M][\alpha]_c[M]\{q_i\} + [L][M][\alpha]_c\{\phi_i\} + [L][M][\alpha]_c\{\lambda_i\} + [L][M][L]^T\{(q_R)_j\}. \tag{30}$$

If Eq. (28) is solved for $[L][M]\{q_i\}$ and the result is substituted into Eq. (30), the following equation is obtained:

$$-\frac{1}{\omega^2}\{(\phi_F)_j\} - [M_{Ref.}]\{(q_R)_j\} - \frac{1}{\omega^2}[L]\{\phi_i\} - \frac{1}{\omega^2}[L]\{\lambda_i\} = \omega^2[L][M][\alpha]_c[M]\{q_i\} + [L][M][\alpha]_c\{\phi_i\} + [L][M][\alpha]_c\{\lambda_i\} + [L][M][L]^T\{(q_R)_j\}. \tag{31}$$

If Eq. (31) is solved in terms of $[Q]\{(q_R)_j\}$, where

$$[Q] = [L][M][L]^T + [M_{Ref.}], \tag{32}$$

$\{(q_R)_j\}$ may be obtained by premultiplying both sides of the resulting equation by the inverse of $[Q]$:

$$\{(q_R)_j\} = -\frac{1}{\omega^2}[Q]^{-1}\{(\phi_R)_j\} - \frac{1}{\omega^2}[Q]^{-1}[L]\left[[I] + \omega^2[M][\alpha]_c\right]\{\phi_i\} - \frac{1}{\omega^2}[Q]^{-1}[L]\left[[I] + \omega^2[M][\alpha]_c\right]\{\lambda_i\} - \omega^2[Q]^{-1}[L][M][\alpha]_c[M]\{q_i\}. \tag{33}$$

By substituting Eq. (33) into Eq. (29) for $\{(q_R)_j\}$ and rearranging terms, the following equation is obtained:

$$\left[[I] - \omega^2[F][\alpha]_c[M]\right]\{q_i\} - \frac{1}{\omega^2}[L]^T[Q]^{-1}\{(\phi_R)_j\} \tag{34 (Cont.)}$$

$$+ \left[[F][\alpha]_c - \frac{1}{\omega^2} [L]^T [Q]^{-1} [L] \right] \{\phi_i\}$$

$$+ \left[[F][\alpha]_c - \frac{i}{\omega^2} [L]^T [Q]^{-1} [L] \right] \{\lambda_i\} , \quad (34)$$

where

$$[F] = \left[[I] - [L]^T [Q]^{-1} [L] [M] \right] . \quad (35)$$

The matrix

$$[\beta] = \left[[I] - \omega^2 [F] [\alpha]_c [M] \right] \quad (36)$$

is identical to the $[\beta]$ matrix given by Eq. (15) for a motion-constrained substructure when $[F] = [I]$.

The steady state responses of the mass station coordinates $\{q_i\}$ are obtained by premultiplying both sides of Eq. (34) by the inverse of $[\beta]$:

$$\{q_i\} = -\frac{1}{\omega^2} [\beta]^{-1} [L]^T [Q]^{-1} \{(\phi_R)_j\}$$

$$+ [\beta]^{-1} \left[[F][\alpha]_c - \frac{1}{\omega^2} [L]^T [Q]^{-1} [L] \right] \{\phi_i\}$$

$$+ [\beta]^{-1} \left[[F][\alpha]_c - \frac{1}{\omega^2} [L]^T [Q]^{-1} [L] \right] \{\lambda_i\} . \quad (37)$$

If Eq. (37) is substituted into Eq. (33) for $\{\dot{q}_i\}$ and the terms are rearranged, the steady state responses of the reference station coordinates $\{(q_R)_j\}$ are obtained:

$$\{(q_R)_j\} = -[P]\{(q_R)_j\} - [R]\{\phi_i\} - [R]\{\lambda_i\} , \quad (38)$$

where, by using Eq. (11) for $[\alpha]_c$

$$[P] = -\frac{1}{\omega^2} [Q]^{-1}$$

$$- [Q]^{-1} [L] [M] [\alpha] [M] [\beta]^{-1} [L]^T [Q]^{-1} e^{-i\mu} \quad (39)$$

and

$$[R] = [Q]^{-1} [L] \left[\frac{1}{\omega^2} [I] + [M] [\alpha] e^{-i\mu} \right]$$

$$+ [Q]^{-1} [L] [M] [\alpha] [M] [\beta]^{-1} e^{-i\mu} \left[\omega^2 [F] [\alpha] e^{-i\mu} - [L]^T [Q]^{-1} [L] \right] . \quad (40)$$

Eq. (37) can be rewritten in the following form:

$$\{q_i\} = -[E]\{(\phi_R)_j\} + [N]\{\phi_i\} + [N]\{\lambda_i\} \quad (41)$$

where, by using Eq. (11) for $[\alpha]_c$

$$[E] = -\frac{1}{\omega^2} [\beta]^{-1} [L]^T [Q]^{-1} \quad (42)$$

and

$$[N] = [\beta]^{-1} \left[[F][\alpha] e^{-i\mu} - \frac{1}{\omega^2} [L]^T [Q]^{-1} [L] \right] . \quad (43)$$

Equations (38) and (41) define the steady state damped responses of the free-free substructure.

Since $[R] = [E]^T$ if the mass matrix $[M]$ is symmetric, the substructure responses at the mass station coordinates (i) and reference stations (j) can be written in the following matrix form:

$$\begin{Bmatrix} (q_R)_j \\ \hline q_i \end{Bmatrix} = \begin{bmatrix} \begin{bmatrix} -P \\ (m \times m) \end{bmatrix} & \begin{bmatrix} -E^T \\ (m \times n) \end{bmatrix} \\ \begin{bmatrix} -E \\ (n \times m) \end{bmatrix} & \begin{bmatrix} N \\ (n \times n) \end{bmatrix} \end{bmatrix} \begin{Bmatrix} (\varphi_R)_j \\ \hline \phi_i \end{Bmatrix}$$

$$+ \begin{bmatrix} \begin{bmatrix} -E^T \\ (m \times n) \end{bmatrix} \\ \begin{bmatrix} N \\ (n \times n) \end{bmatrix} \end{bmatrix} \{\lambda_i\} , \quad (44)$$

where

$j = 1 \ldots m$, and

$i = 1 \ldots n$.

Equation (44) gives the steady state response of a coupling-constrained free-free substructure having coupling forces $\{(\phi_R)_j\}$ at the reference station coordinates (j) and coupling forces $\{\phi_i\}$ at the mass station coordinates (i). These forces are dependent on the coupling coordinate interactions of a particular substructure with external substructures, which together comprise the overall structure. The procedure for combining the substructures is developed in the following section.

In general, a complete structure will either be excited by motion and/or force inputs, as is the case of a motion-constrained structure, or by force inputs, as is the case of a free-free structure. In the former case, one substructure (input substructure) must feel the motion input directly at its reference station, while the adjoining substructures (coupling-constrained free-free substructures) feel the input only through the coupling forces at the interconnection between the substructures. In this case the

input substructure is analyzed using Eq. (17) and the coupling constrained substructures are analyzed using Eq. (44).

To analyze a free-free structure, none of the substructures can be motion constrained. In fact, all substructures must be analyzed as free-free structures having forces at the reference station coordinates (j) and input or coupling forces at the mass station coordinates (i). If coupling forces exist at the reference station coordinates of all the free-free substructures (i.e., all substructures are coupling constrained), Eq. (44) is used for all substructures. If the reference coordinates of a free-free substructure are not coupling coordinates, the forces at the reference coordinates are defined by known forces. The force will be zero if no force exists at a reference coordinate. This substructure is designated as an unconstrained free-free substructure and may be analyzed by the following modification of Eq. (44):

$$\begin{Bmatrix} (q_R)_j \\ q_i \end{Bmatrix} = \begin{bmatrix} [-E^T] \\ [N] \end{bmatrix} \{\mu_i\} + \begin{bmatrix} [-P] & [-E^T] \\ [-E] & [N] \end{bmatrix} \begin{Bmatrix} (\lambda_R)_j \\ \lambda_i \end{Bmatrix} . \tag{45}$$

where $\{(\lambda_R)_j\}$ = known forces at reference station coordinates. By using Eqs. (44) and (45) all substructure responses are obtained for a free-free structure.

Since there are three steady state response equations for the substructure response analysis, an option designation has been assigned to each equation:

Equation (44) - Option I, for a coupling-constrained free-free substructure;

Equation (17) - Option II, for a motion-constrained substructure; and

Equation (45) - Option III, for an unconstrained free-free substructure.

COMBINATION OF SUBSTRUCTURES

The substructures are combined by maintaining compatibility and equilibrium at each discrete interconnection of two or more substructures; i.e., the motions of the substructure at each interconnection must be equal and the summation of the coupling forces acting on each substructure at an interconnection must equal zero. (It is assumed that an excitation force $\{\lambda_i\}$ applied at a coupling mass station coordinate acts on only one of the substructures at an interconnection.) The procedure for manipulating the response equations obtained for each substructure (using the appropriate option), so that the compatibility and equilibrium equations can be applied, is outlined in Steps 1 through 5 of the Flow Diagram.

For explanatory purposes it is assumed that there are r substructures and that Substructure 1 is motion constrained, so that its response equation is obtained by using Option II. The remaining substructures (2...r) are assumed coupling constrained, so that the response equations are obtained by using Option I. However, the procedure for combining substructures, in general, can be used with any set of options contained in this analysis.

In the equation defined by Option II and indicated functionally in the Flow Diagram (Step 1), the column matrix $\{q_i\}$ defines the responses at all mass stations coordinates (1...n) in the substructure, including the responses at each of the coupling coordinates. At a coupling coordinate, the coupling force, contained within the column matrix $\{\mu_i\}$, acts as an external force to the substructure. A force in $\{\mu_i\}$ corresponding to a noncoupling coordinate equals zero.

In the response equations for the coupling constrained substructures (2.. r) as developed from Option I, the column matrix $\{(q_R)_j/q_i\}$ defines the responses at the reference station coordinates (j 1...m) as well as the mass station coordinates (i 1...n). For this case the reference station coordinates (j) are all coupling coordinates and the coupling forces at these coordinates act as external forces on the substructure. The responses and coupling forces at the mass station coordinates (i 1...n) have been discussed above.

Before the compatibility and equilibrium conditions can be applied to obtain the values of the coupling forces as a function of any known excitation functions, an equation must be obtained relating responses at the coupling coordinates in each substructure to the coupling forces at these coordinates; i.e., an equation must be developed of the form $\{q_c\}$ $[A]$ $\{\lambda_c\} + \{a_c\}$ as shown in Step 5 of the Flow Diagram. This relationship is developed in Steps 2 through 5.

Once the above relationship (i.e., Step 5) has been obtained, the compatibility and equilibrium conditions can be applied with a knowledge of which responses in $\{q_c\}$ and coupling forces in $\{\lambda_c\}$ exist at the same interconnections in the complete structure. Steps 7 through

10 describe the application of the compatibility and equilibrium conditions from which a reduced matrix [A"] is obtained. The coupling forces are then obtained (Step 11) from the product of the inverse of the [A"] matrix and the reduced input column vector $\{a'_\lambda\}$. (The original form of the input column vector $\{b_\lambda\}$, given in Step 3, contains the terms $[L]^T\{\delta_j\}$ from Option II and

$$\begin{bmatrix}[-E^T] \\ [N]\end{bmatrix} \{\lambda_i\}$$

from Option I.) Upon substitution of these coupling forces back onto the equation of Step 3, the steady state responses at all coordinates in the structure are obtained (Steps 13 and 14).

Since the responses include the effects of damping and are in complex form, the output of this analysis will be the absolute value or amplitude of the steady state response and the phase angle with respect to the forcing function (Steps 14 through 18). An example, using symbolic response equations, has been included in the Appendix to help clarify the above procedure.

Since the purpose of a steady state response analysis is to determine the responses over a frequency spectrum, a frequency response curve must be developed for each of the more significant mass points in the structure. This requires that the procedure be repeated for as many frequencies as is necessary to define clearly the frequency vs response curve.

GEOMETRY MATRIX

The geometry matrix [L] describes the rigid body motions of the mass station coordinates (i) caused by the rigid body motions of the reference station coordinates (j). For a unit rigid body motion of each reference coordinate (row designation of the [L] matrix), each mass station coordinate (column designation of the [L] matrix) receives a rigid body motion corresponding to its geometrical relationship to the reference station.

For example, in the [L] matrix, Eq. (25), developed from the analysis of a cantilevered structural idealization (Fig. 1), the rigid body motions at the mass station coordinates (i) due to a unit displacement of reference coordinate y_o are equal to $\{y_i\} = \{1.0\}$ for the displacement coordinates $\{y_i\}$ and zero for the rotational coordinates $\{\theta_i\}$. However, a unit rotation of θ_o causes displacements at the mass station coordinates of $\{y_i\} = \theta_o$, $x_i = x_i$, as well as rotations at the mass stations (i) equal to $\{\theta_i\} = 1.0$.

To illustrate an [L] matrix for a substructure with up to six degrees of freedom per mass point, the structural model shown in Fig. 2 is discussed.

Station R is considered the reference station with six degrees of freedom and Stations 1 and 2 as mass stations with six degrees of freedom. Stations 1 and 2 are a distance ℓ_1 and a distance ℓ_2 from Station R, respectively. A positive sign convention for translation and rotation is designated by the right-handed coordinate system in Fig. 2.

If a unit motion is applied to each of the reference station coordinates separately, in the positive directions indicated in Fig. 2, the rigid body motions of the mass station coordinates are obtained in the [L] matrix. This matrix is developed by noting the magnitude and direction of a motion at a mass station coordinate due to a unit rigid body motion of a particular reference station coordinate. The resulting direction of the rigid body motion of a mass station coordinate, relative to a particular positive sign convention (in this case a right-handed

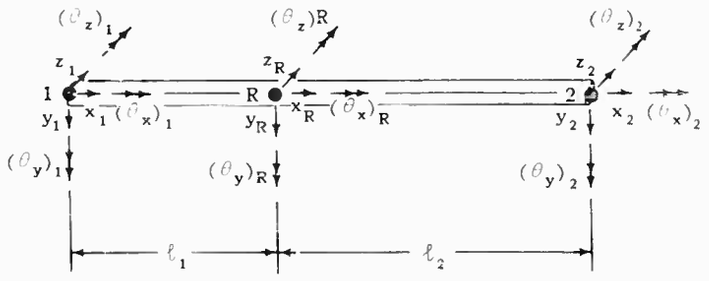

Fig. 2 - Structural model used to develop an illustrative [L] matrix

FLOW DIAGRAM

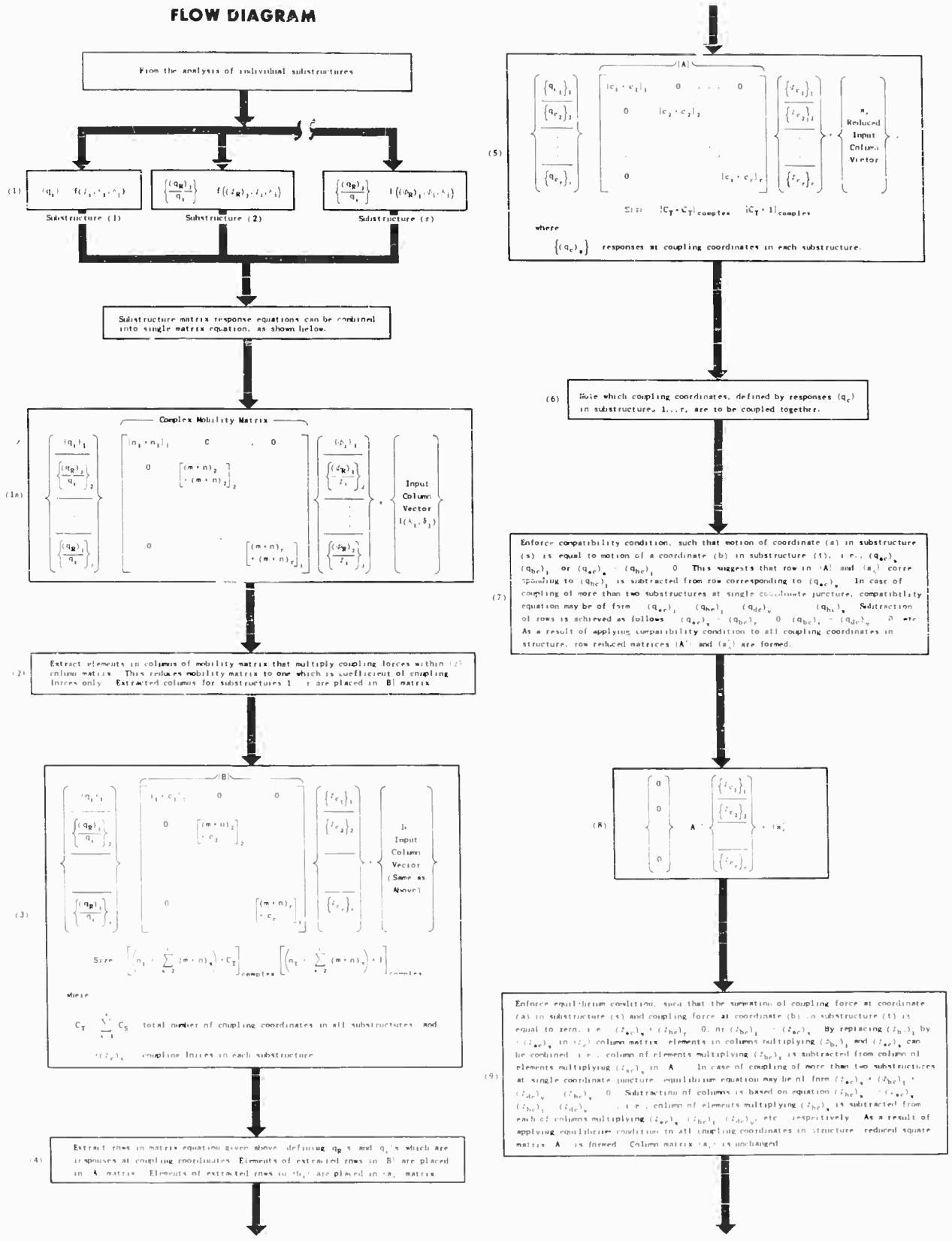

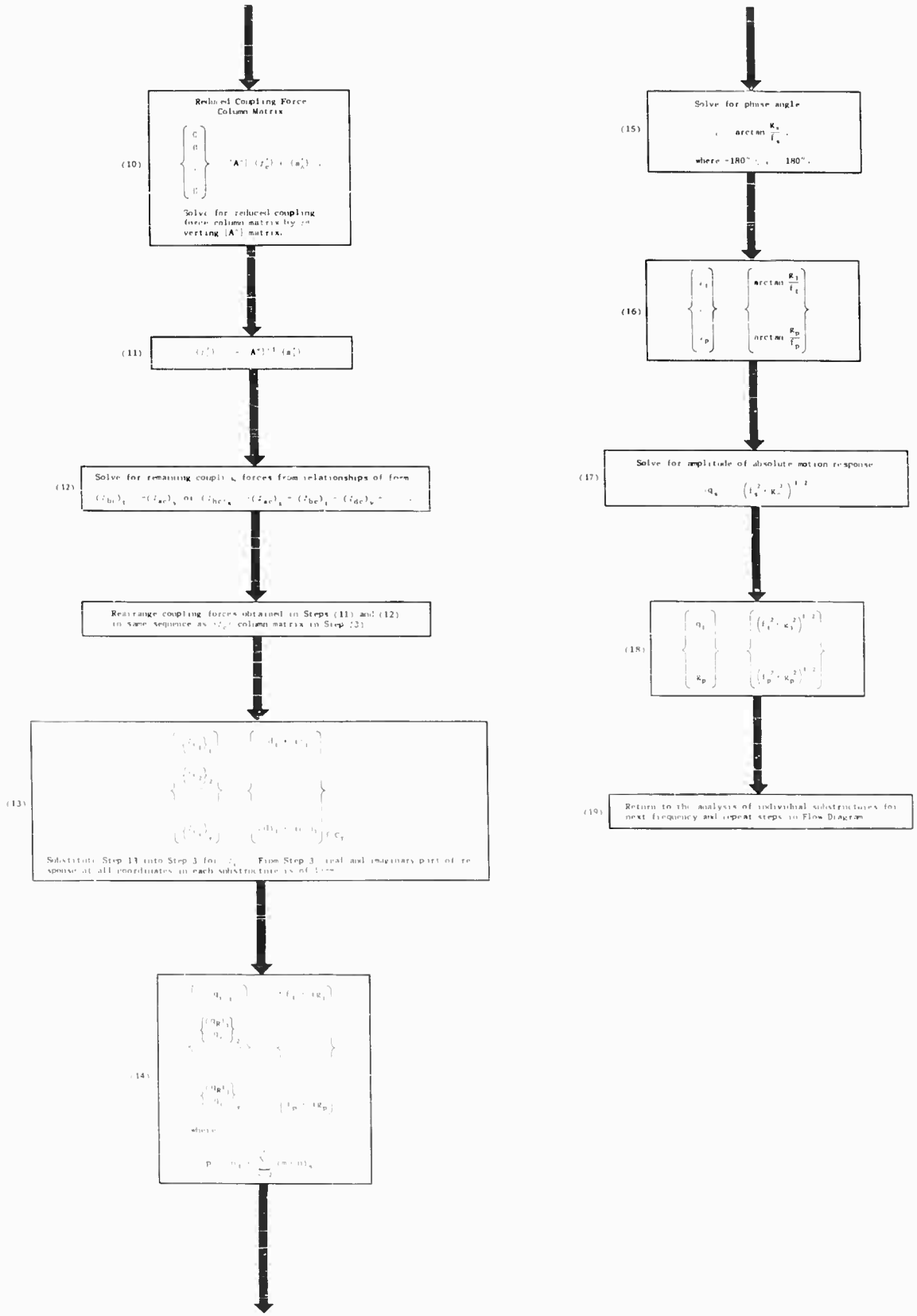
Reduced Coupling Force Column Matrix
(10)
Solve for reduced coupling force column matrix by inverting [A^-1] matrix.
(11)
(12)
Solve for remaining coupling forces from relationships of form
Rearrange coupling forces obtained in Steps (11) and (12) in same sequence as column matrix in Step (3)
(13)
Substitute Step 13 into Step 3 for
From Step 3 real and imaginary part of response at all coordinates in each substructure is of form
(14)
where
(15)
Solve for phase angle
where -180° 180°.
(16)
(17)
Solve for amplitude of absolute motion response
(18)
(19)
Return to the analysis of individual substructures for next frequency and repeat steps in Flow Diagram

coordinate system), determines the sign of a particular element in the [L] matrix. As an example, the motion of z_2 in Fig. 2 due to a positive unit rotation of $(\theta_y)_R$ is $(-\ell_2)$, since the resulting motion is in the negative z direction at Station 2. The elements in the [L] matrix are developed in this manner, since the magnitudes and directions can be determined visually from particular statically determinate structural idealization.

$$[L] = \begin{array}{c|cccccc} \text{Ref. Station Coordinates} & \multicolumn{6}{c}{\text{Mass Station Coordinates}} \\ & x_i & x_2 & y_1 & y_2 & z_1 & z_2 \\ \hline x_R & 1.0 & 1.0 & 0 & 0 & 0 & 0 \\ y_R & 0 & 0 & 1.0 & 1.0 & 0 & 0 \\ z_R & 0 & 0 & 0 & 0 & 1.0 & 1.0 \\ (\theta_x)_R & 0 & 0 & 0 & 0 & 0 & 0 \\ (\theta_y)_R & 0 & 0 & 0 & 0 & \ell_1 & -\ell_2 \\ (\theta_z)_R & 0 & 0 & -\ell_1 & \ell_2 & 0 & 0 \end{array}$$

$(\theta_x)_1$	$(\theta_x)_2$	$(\theta_y)_1$	$(\theta_y)_2$	$(\theta_z)_1$	$(\theta_z)_2$
0	0	0	0	0	0
0	0	0	0	0	0
0	0	0	0	0	0
1.0	1.0	0	0	0	0
0	0	1.0	1.0	0	0
0	0	0	0	1.0	1.0

A definite sequence of rows and columns must exist to develop a correct [L] matrix:

1. The sequence of the columns, corresponding to the mass station coordinates (i), must correspond to the columns of the [a] matrix and [M] matrix, as well as to the sequence of the coordinates in the $\{q_i\}$ response matrix.

2. The sequence of the rows, corresponding to the reference coordinates (j) must correspond to the sequence of the elements of the reference station mass matrix $[M_{Ref.}]$, as well as to the sequence of the coordinates in the $\{(q_R)_j\}$ response matrix.

SUMMARY

This analytical procedure can be summarized by listing the steps to be followed in using this analytical method.

1. Establish a set of statically determinate substructures to represent the structure. Four factors determine the selection of substructures: the substructures must be separated at discrete interconnection coordinates; the number of interconnections between substructures should be minimized to maintain the size of the [A"] matrix (Step 10 in the Flow Diagram) at a reasonable value; the dynamic model for each substructure should adequately describe the substructures; and the damping characteristics of each substructure should be reasonably homogeneous since a constant damping factor is assumed for each substructure. A typical structure is shown represented by a set of substructures in Fig. 3.

2. Establish a consistent sign convention for the coordinates in all substructures to obtain the [a] matrix and [L] matrix. A right-handed coordinate system has been used for developing the previous analytical equations; however, any consistent coordinate system can be used.

3. Establish the mass point distribution for each substructure and define the reference station coordinates (m). For a motion-constrained substructure, the reference station coordinates are the motion input coordinates. For a free-free substructure, the reference station coordinates are either coupling-constrained or unconstrained. The remainder of the degrees of freedom in a substructure are mass station coordinates (n).

4. Define the interconnection (coupling) coordinates in each substructure. It is suggested that each degree of freedom in all the substructures be given a numerical designation so that each coordinate is uniquely defined. The coordinates coupling at specific interconnections can then be established to apply the compatibility and equilibrium conditions.

The following steps apply to each substructure:

5. Develop the influence coefficient matrix [a] and mass matrix [M].

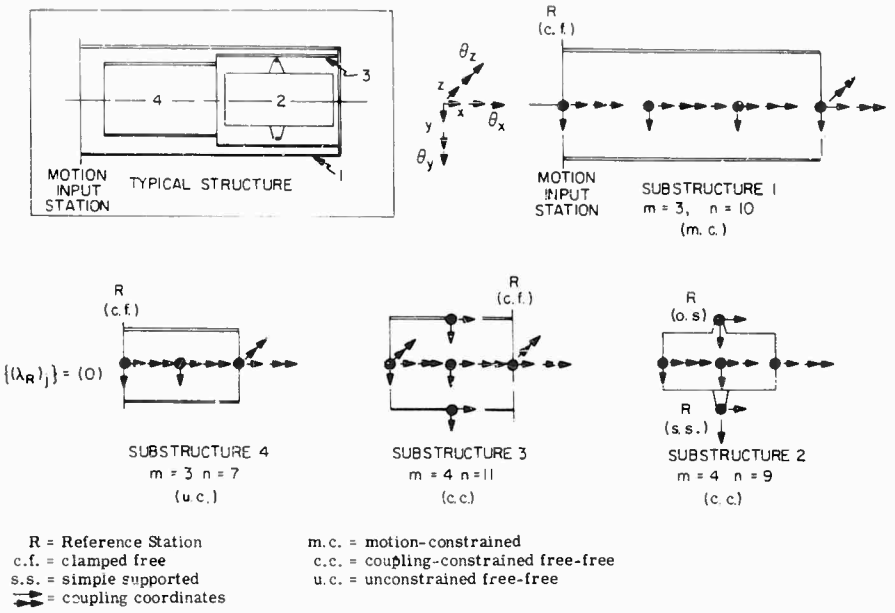

Fig. 3 - Substructure breakdown and mass distribution for typical structure

6. Develop the geometry (rigid body motion) matrix [L].

7. Assume a value for the damping ratio and solve the following relationship for the complex damping modulus: $e^{-i\mu} = \cos\mu - i \sin\mu$, where $\mu = 2(c/c_c)$ = radians.

8. If a substructure is motion constrained, solve for $[\beta]$ from Eq. (15) for a particular excitation frequency, invert the $[\beta]$ matrix and substitute into Eq. (17).

9. If a substructure is free-free, develop the reference mass matrix $[M_{Ref.}]$ and $[L]^T$, compute [Q] from Eq. (32), the inverse of [Q], and [F] from Eq. (35). For a particular excitation frequency, compute $[\beta]$ from Eq. (36), the inverse of $[\beta]$, [P] from Eq. (39), [E] from Eq. (42) and develop $[E]^T$, and compute [N] from Eq. (43). If the substructure is coupling-constrained free-free, substitute the values for [P], [E], $[E]^T$ and [N] into Eq. (44). If the substructure is unconstrained free-free, substitute these values into Eq. (45).

10. When the response equations are developed for all substructures, the procedure outlined in Steps 1 through 19 of the Flow Diagram is followed.

11. The procedure outlined in Steps 8, 9f through 9ℓ, and 10 must be repeated for a range of excitation frequencies to obtain a response vs frequency curve for critical coordinates in the structure. The peak responses define the damped natural frequencies of the structure.

The response to a particular motion input i.e., displacement, velocity, or acceleration) will have the units of the input function. If a force excitation is applied to the structure the response will be in displacement units.

In many steady state analyses a transmissibility curve is desired for critical coordinates in a structure, due to a motion input. The transmissibility can be obtained directly by substituting a value of unity for a single coordinate (j) in Eq. (17).

REMARKS

In any steady state analysis, the accuracy of the peak responses is a function of the estimated damping in a structure; therefore, test confirmation of the damping factor is required to improve the confidence in the analysis. If a reasonable damping factor is assumed, the analysis can be used for estimating dynamic loads and stresses in a structure at the natural frequencies by observing the distribution of responses over the structure. The analysis can also be used for establishing sinusoidal environments for components of structures which must be vibration tested separately.

The analytical procedure in this paper has involved dividing a structure into a set of substructures. The advantages of this substructure approach are:

1. Complex structures can be analyzed. Since the method of substructures treats each substructure as a lumped mass distribution represented by a set of influence coefficients, it may be more feasible to develop several smaller influence coefficient matrices rather than one large influence coefficient matrix.

2. It allows a structure, with internal changes in mass distribution or structural characteristics, to be analyzed without reanalyzing the entire structure; the unchanged part of the structure may be treated as one substructure and the variable portion of the structure as another substructure. Such a case exists if the basic frame of a structure is unchanged but the components housed within the structure are changed to establish a different overall structure. In this case the basic frame is analyzed once using one of the matrix equations developed in the first section. The component substructures are reanalyzed for each change in structural characteristics and mass distribution, and these substructures are combined with the basic frame substructure to obtain the new steady state responses of the overall structure. Therefore, a structure with internal changes need not be reanalyzed as a complete structure, thus reducing the time for developing the input parameters to a steady state response analysis.

3. The damping characteristics throughout a structure need not be homogeneous. If a part of a structure appears to have different damping characteristics from the rest of the structure, it can be treated as a separate substructure.

4. The largest square matrix which may require an inversion is not a function of the total number of degrees of freedom in the overall structure as would be the case if an analysis were performed on the overall structure directly; the sizes of the matrices inverted in this analysis are either equal to the number of mass station coordinates in each substructure or are a function of the total number of interconnection (coupling) coordinates in all substructures.

To obtain the steady state response of complex structures, a large number of degrees of freedom may be required to simulate the structure accurately. To use this analytical procedure to obtain the frequency vs response curve for the more significant degrees of freedom of such a structure, it becomes necessary to program the analytical procedure for the digital computer. This has been done and has been successfully applied to obtain the steady state response of the AOSO spacecraft in the launch configuration.

ACKNOWLEDGMENT

This work has been done in part under NASA (Goddard Space Flight Center) Contract NAS 5-3587, Project AOSO.

REFERENCE

1. N. O. Myklestad, J. Appl. Mech. (Sept. 1952).

BIBLIOGRAPHY

R. H. Scanlon and R. Rosenbaum, Introduction to the Study of Aircraft Vibration and Flutter (The MacMillan Co., New York, 1962), pp. 177-178.

Appendix

AN EXAMPLE OF PROCEDURE OF COMBINING SUBSTRUCTURES

The response equations of three substructures may be considered to have the following form:

Substructure I

$$\begin{Bmatrix} q_1 \\ q_2 \\ q_3 \end{Bmatrix} = \begin{bmatrix} C_{11} & C_{12} & C_{13} \\ C_{21} & C_{22} & C_{23} \\ C_{31} & C_{32} & C_{33} \end{bmatrix} \begin{Bmatrix} \phi_1 \\ 0 \\ \phi_3 \end{Bmatrix} + \begin{Bmatrix} I_1 \\ I_2 \\ I_3 \end{Bmatrix}, \quad \text{(A1)}$$

where Stations 1 and 3 are coupling coordinates;

Substructure II

$$\begin{Bmatrix} q_4 \\ q_5 \end{Bmatrix} = \begin{bmatrix} d_{44} & d_{45} \\ d_{54} & d_{55} \end{bmatrix} \begin{Bmatrix} \phi_4 \\ 0 \end{Bmatrix} + \begin{Bmatrix} 0 \\ 0 \end{Bmatrix}, \quad \text{(A2)}$$

where Station 4 is a coupling coordinate; and

Substructure III

$$\begin{Bmatrix} q_6 \\ q_7 \end{Bmatrix} = \begin{bmatrix} e_{66} & e_{67} \\ e_{76} & e_{77} \end{bmatrix} \begin{Bmatrix} \phi_6 \\ 0 \end{Bmatrix} + \begin{Bmatrix} 0 \\ 0 \end{Bmatrix} , \quad \text{(A3)}$$

where Station 6 is a coupling coordinate.

The elements c, d, e, and I are in complex form. The following steps are performed with reference to the Flow Diagram:

Step 1(a)

$$\begin{Bmatrix} \begin{Bmatrix} q_1 \\ q_2 \\ q_3 \end{Bmatrix}_I \\ \begin{Bmatrix} q_4 \\ q_5 \end{Bmatrix}_{II} \\ \begin{Bmatrix} q_6 \\ q_7 \end{Bmatrix}_{III} \end{Bmatrix} = \begin{bmatrix} C_{11} & C_{12} & C_{13} & \cdots & \cdots & \cdots & 0 \\ C_{21} & C_{22} & C_{23} & & & & \\ C_{31} & C_{32} & C_{33} & & & & \\ \cdot & & & d_{44} & d_{45} & & \\ \cdot & & & d_{54} & d_{55} & & \\ \cdot & & & & & e_{66} & e_{67} \\ 0 & & & & & e_{76} & e_{77} \end{bmatrix}$$

$$\cdot \begin{Bmatrix} \phi_1 \\ 0 \\ \phi_3 \\ \phi_4 \\ 0 \\ \phi_6 \\ 0 \end{Bmatrix} + \begin{Bmatrix} I_1 \\ I_2 \\ I_3 \\ 0 \\ 0 \\ 0 \\ 0 \end{Bmatrix} , \quad \text{(A4)}$$

Steps 2 and 3

[B] Matrix

$$\begin{Bmatrix} \begin{Bmatrix} q_1 \\ q_2 \\ q_3 \end{Bmatrix} \\ \begin{Bmatrix} q_4 \\ q_5 \end{Bmatrix} \\ \begin{Bmatrix} q_6 \\ q_7 \end{Bmatrix} \end{Bmatrix} = \begin{bmatrix} C_{11} & C_{13} & 0 & 0 \\ C_{21} & C_{23} & 0 & 0 \\ C_{31} & C_{33} & 0 & 0 \\ 0 & 0 & d_{44} & 0 \\ 0 & 0 & d_{54} & 0 \\ 0 & 0 & & e_{66} \\ 0 & 0 & & e_{76} \end{bmatrix} \begin{Bmatrix} \phi_1 \\ \phi_3 \\ \phi_4 \\ \phi_6 \end{Bmatrix} + \begin{Bmatrix} I_1 \\ I_2 \\ I_3 \\ 0 \\ 0 \\ 0 \\ 0 \end{Bmatrix} ; \quad \text{(A5)}$$

Steps 4 and 5

[A] Matrix

$$\begin{Bmatrix} q_1 \\ q_3 \\ q_4 \\ q_6 \end{Bmatrix} = \begin{bmatrix} C_{11} & C_{13} & 0 & 0 \\ C_{31} & C_{33} & 0 & 0 \\ 0 & 0 & d_{44} & 0 \\ 0 & 0 & 0 & e_{66} \end{bmatrix} \begin{Bmatrix} \phi_1 \\ \phi_3 \\ \phi_4 \\ \phi_6 \end{Bmatrix} + \begin{Bmatrix} I_1 \\ I_3 \\ 0 \\ 0 \end{Bmatrix} ; \quad \text{(A6)}$$

Stations 1 and 4 and Stations 3 and 6 are to be coupled; therefore, $q_1 = q_4$ and $q_3 = q_6$ are compatibility equations and $\phi_1 + \phi_4 = 0$ and $\phi_3 + \phi_6 = 0$ are equilibrium equations.

Steps 7 and 8 - Compatibility of motions

$$\begin{Bmatrix} 0 \\ 0 \end{Bmatrix} = \begin{bmatrix} C_{11} & C_{13} & -d_{44} & 0 \\ C_{31} & C_{33} & 0 & -e_{66} \end{bmatrix} \begin{Bmatrix} \phi_1 \\ \phi_3 \\ \phi_4 \\ \phi_6 \end{Bmatrix} + \begin{Bmatrix} I_1 \\ I_3 \end{Bmatrix} ; \quad \text{(A7)}$$

Steps 9 and 10 - Equilibrium of forces

$$\begin{Bmatrix} 0 \\ 0 \end{Bmatrix} = \begin{bmatrix} (C_{11} + d_{44}) & C_{13} \\ C_{31} & (C_{33} + e_{66}) \end{bmatrix} \begin{Bmatrix} \phi_1 \\ \phi_3 \end{Bmatrix} + \begin{Bmatrix} I_1 \\ I_3 \end{Bmatrix} ; \quad \text{(A8)}$$

Step 11 - Computing coupling forces

$$\begin{Bmatrix} \phi_1 \\ \phi_3 \end{Bmatrix} = - \begin{bmatrix} (C_{11} + d_{44}) & C_{13} \\ C_{31} & (C_{33} + e_{66}) \end{bmatrix}^{-1} \begin{Bmatrix} I_1 \\ I_3 \end{Bmatrix}$$

$$= \underset{\text{Form}}{A} \begin{Bmatrix} r_1 + i s_1 \\ r_2 + i s_2 \end{Bmatrix} ; \quad \text{(A9)}$$

Step 12

$$\begin{aligned} \phi_4 &= -\phi_1 = -(r_1 + i s_1) , \\ \phi_6 &= -\phi_3 = -(r_2 + i s_2) ; \end{aligned} \quad \text{(A10)}$$

Step 13

$$\begin{Bmatrix} \phi_1 \\ \phi_3 \\ \phi_4 \\ \phi_6 \end{Bmatrix} = \begin{Bmatrix} r_1 + i s_1 \\ r_2 + i s_2 \\ -(r_1 + i s_1) \\ -(r_2 + i s_2) \end{Bmatrix} ; \quad \text{(A11)}$$

Substitute Step 13 into Step 3 for $\{\psi_c\}$

$$\begin{Bmatrix} q_1 \\ q_2 \\ q_3 \\ q_4 \\ q_5 \\ q_6 \\ q_7 \end{Bmatrix} = \underset{\text{Form}}{A} \begin{Bmatrix} t_1 + i\,v_1 \\ \cdot \\ \cdot \\ \cdot \\ \cdot \\ \cdot \\ t_7 + i\,v_7 \end{Bmatrix} ; \quad \text{(A12)}$$

Steps 15 and 16 - Phase Angle

$$\begin{Bmatrix} \psi_1 \\ \cdot \\ \cdot \\ \cdot \\ \psi_7 \end{Bmatrix} = \begin{Bmatrix} \tan^{-1} \dfrac{v_1}{t_1} \\ \cdot \\ \cdot \\ \cdot \\ \tan^{-1} \dfrac{v_7}{t_7} \end{Bmatrix} ; \quad \text{(A13)}$$

Steps 17 and 18 - Amplitude of response

$$\begin{Bmatrix} |q_1| \\ \cdot \\ \cdot \\ \cdot \\ |q_7| \end{Bmatrix} = \begin{Bmatrix} \left(t_1^2 + v_1^2\right)^{1/2} \\ \cdot \\ \cdot \\ \cdot \\ \left(t_7^2 + v_7^2\right)^{1/2} \end{Bmatrix} .$$

* * *

Section 2
SHOCK AND VIBRATION ISOLATION

INVESTIGATION OF A RATIONAL APPROACH TO SHOCK ISOLATOR DESIGN

R. A. Eubanks
IIT Research Institute
Chicago, Illinois

INTRODUCTION

Little work has been done in the general area of the synthesis of mechanical devices. Classically, mechanical design has been a repetitive process of conception, initial design, analysis, design improvement, re-analysis, re-improvement, ad infinitum. There is a crying need for procedures which will permit the engineer to state his problem and utilize the statement of the problem in a constructive and organized way to lead directly to the determination of the optimal design solution. Development of such procedures would not only be a boon in the ordinary design process, it would lay a foundation for an organized attack on many of the appalling problems of the reliability of mechanical devices.

Synthesis of engineering design is not an unattainable dream. The literature of control systems theory and electrical network theory abounds with analytical procedures for an organized and straightforward synthesis of transfer functions, and, in some cases, even complete systems; the basis for this design residing in a mathematical statement of the results to be obtained. Furthermore, isolated investigations have shown the feasibility of optimizing specific mechanical designs; in some cases, straightforward optimal synthesis procedures have been introduced.

The present paper presents a status report on several closely associated projects which are being conducted by IIT Research Institute under the auspices of the Office of Naval Research, the Air Force Weapons Laboratory, and the Army Research Office. The goals of these programs are threefold:

1. An organized and detailed inquiry into the several synthesis techniques which have been proposed.

2. The development of each technique to a stage which will permit a rational estimate of its desirability and applicability to be formed.

3. The development of the initial phases of synthesis approaches which appear most fruitful, culminating in a firm establishment of approaches to be used in extension of scientific efforts in the general field.

POSSIBLE APPROACHES

Several approaches to the problem of optimal mechanical synthesis have been initiated. Specifically, these developments include:

1. Application of variational techniques to determine optimal distribution of parameters in systems which have been designed. This is a relatively common procedure. It is exemplified by the work in minimum weight design, maximum stiffness design, peak response minimization, optimal damping, and many others. The approach does not attempt to synthesize; the major purpose is that of improving a completed design.

2. Direct application of the calculus of variations to the problem of synthesis. Here only the gross outlines of a design are presented and variational methods are applied to determine the mechanism required as well as the parameter values thereof.

3. Application of experimental design and response surface techniques. This procedure

normally involves the specification of a quite general possible solution to the design problem. A controlled selection procedure which utilizes an experimental design or a "dynamic program" is then applied to specialize the very general solution to one which is specific and is optimal within the class of all designs considered. This procedure commonly requires extensive computation on high-speed digital computers.

4. Recent work in control systems and aerospace trajectory analysis, have utilized an adjoint procedure which was recently introduced by the Russian academician Pontryagin. While this approach appears to have some applicability as a direct approach to mechanical design, it may well serve its major function as an adjunct to the previously discussed dynamic programming procedures.

5. Some work has been done on organized iterative procedures which utilize analog computers. The basic philosophy involved here is similar to that of the "experimental design" or "optimal dynamic program" approach; the details differ because analog computers rather than digital computers are the basic tool.

6. Direct analogies between electrical networks and mechanical systems motivate the belief that investigation in the frequency domain may lead to direct synthesis procedures which are similar to those which are presently used in electrical engineering to synthesize passive and active networks and transfer functions. No work of this type for mechanical systems is known to the writer.

No attempt will be made to discuss these different procedures in the present discourse. Instead, reference is made to the incomplete bibliography which is included herein. On the other hand, it is worthwhile to sketch briefly some of the more important approaches in order that the reader may more fully realize the differences as well as the similaritics in the several methods of attack.

Optimization of Parameters in a Completed Design Concept

The literature in this area is too extensive to encourage a complete study. The majority of the work has been done for static design procedures. Representative are developments in minimum weight design [1-5] and optimum stiffness design [6-8]. The procedures of this work should be observed, but the principal need for new developments is in the area of the optimization of time-dependent systems.

Plunkett [9], Springfield and Raney [10], Henney [11], Lewis [12], Den Hartog [13], and others have examined the optimum damping of dynamic systems. The basic phenomenon involved can be observed in terms of the frequency response of the two-degree-of-freedom system of Fig. 1. For infinite damping a curve similar to that of curve "a" of Fig. 2 is obtained. On the other hand, if there is zero damping the system has two degrees-of-freedom and the double-peaked curve, curve "b" of Fig. 2., results. Clearly, for any intermediate value of damping the frequency response curve must lie in the shaded area of Fig. 2. Furthermore, for all values of damping the response curve must pass through the "invariant points" P and Q for a given value of the spring constant K. If the response curve is adjusted so that it has a maximum at the invariant point of greater amplitude (curve "c" of Fig. 2 is adjusted this way), then the maximum response for the whole range of possible damping constants has been minimized. If we can vary the spring constant K we can "tune" the system so that the curve for minimum damping (curve "a") is shifted relative to the curve for zero damping until the two invariant points are of equal amplitude. In this case we have an absolutely minimum response for the system. This basic idea has been evaluated experimentally and has been studied for a variety of more complex systems including those of a large finite number of degrees-of-freedom, as well as continuous beams with damping applied at end supports or internal to these supports. Although this is one of the simplest cases of optimized dynamic

NOTE: References appear on page 167.

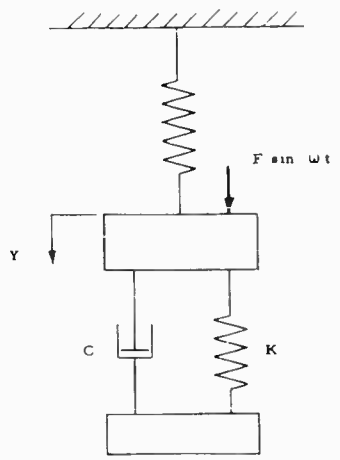

Fig. 1 - Two-degree-of-freedom system

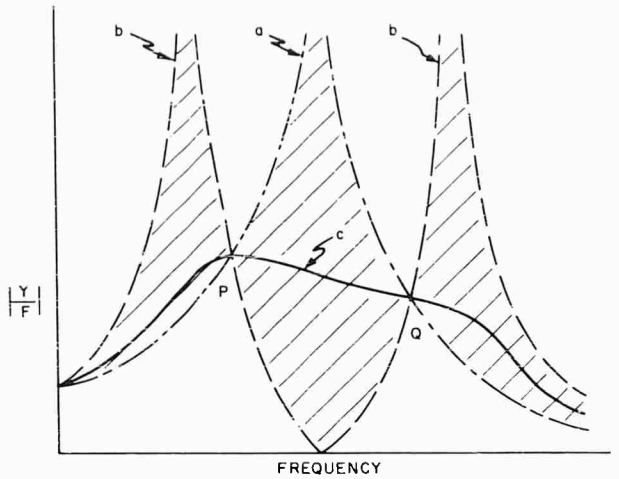

Fig. 2 - Response of two-degree-of-freedom system

response, it does have significant application to mechanical engineering design.

Brach and Sevin [14] attacked a different phase of optimum dynamic design. Briefly, the problem is that of the synthesis of flexible mechanical systems or structures in cases where the total system weight is to be held constant and where the response to transient loadings is to be minimized. The completed work restricts itself to flexible systems which have discrete flexible members and which may be approximated by linear single-degree-of-freedom systems. The mass of the flexible members is included in the response calculations by constructing an equivalent single-mass system. The response of the system is expressed in terms of the mass of the flexible members through the use of stiffness-mass relationships. The response is then minimized with respect to the mass of the flexible members whose optimum mass distribution results. Specific relationships are developed for a system which consists of a given concentrated mass which is supported by two series-connected flexible members. The basic mathematical approach is, however, applicable to an arbitrary number of series-connected flexible members. Figure 3 is an example of a system which can be idealized to correspond to the explicit design curves which are presented. In this approach, as in that which was previously discussed, a full design is completed and the parameter values are then selected to optimize required responses. It is apparent that true synthesis would eliminate many of the pre-analysis steps.

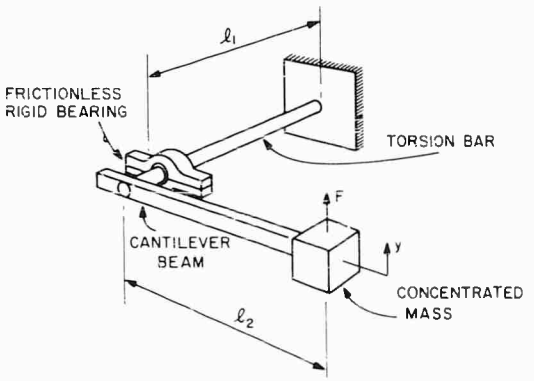

Fig. 3 - Example system

Direct Synthesis Through the Calculus of Variations

A very general approach to the problem of optimal design is one which considers methods whereby the optimum system characteristics can be deduced from information concerning the desired system output. An example of a firm statement of a problem of this type can be given in the case of a shock isolation system.

> "Given an external excitation, find a mechanism that will minimize the maximum values of the acceleration while keeping the values of the displacement within prescribed bounds, or alternatively, find a mechanism that will minimize the maximum

displacement, while keeping maximum values of the acceleration within prescribed bounds."

It is apparent that, in all cases, the equations of motion for the shock isolation system under discussion can be written in the general form

$$\ddot{x} + g(x,\dot{x}) \quad A(t) ,$$

where

$A(t)$ = the external excitation (the forcing function),

x = the displacement of the isolated mass,

$\dot{x}$ = the velocity, and

$\ddot{x}$ = the acceleration.

The function $g(x,\dot{x})$ characterizes the restoring force. It can be referred to as the "shock absorber function." We have here assumed that the properties of the shock absorber depend directly on the displacement and on the velocity, but that the shock absorber does not have time dependence which is independent of these fundamental parameters. From a mathematical point of view, the shock absorber problem can be formulated in the following abstract fashion: "Given the differential equation

$$\ddot{x} + g(x,\dot{x}) = A(t) ,$$

with specified forcing function $A(t)$, develop procedures for the determination for the shock isolator function $g(x,\dot{x})$ which will minimize the maximum value of the acceleration, subject to the restriction that the displacement does not exceed the specified bound."

A similar problem can clearly be formulated for the minimization of the displacement, with bounds on the acceleration. This abstract problem falls into the area of the calculus of variations. On the other hand, there are technical difficulties which preclude its being attacked through the utilization of techniques which are in the presently recorded state of the art.*

*Some of the technical difficulties include the fact that the function g which we seek to determine depends on state variables rather than the independent variable t. A second departure from conventional problems is that, here, inequality constraints are placed on the state variables rather than on the control variables. The calculus of variations provides no machinery for determining optimum functions of the dependent variables and normal inequality constraint procedures are invariably used for bounded control variables.

A theory has been established which reduces the shock absorber design problem as stated to the form of the "simplest problem of the calculus of variations." In a later section of this paper we will show that this problem, while solvable, does not yield information of engineering significance. The possibility still remains that problem modification and restriction will permit useful results to be obtained through this elegant approach.

The single degree-of-freedom oscillator is a basic building block for dynamic analyses. It does not seem unreasonable that approaches which can be used successfully in connection with this oscillator can be directly applied to the synthesis of more complex mechanical systems. IIT Research Institute is of a belief that gains can be made through the reduction to practical usefulness of the methods involved in this new variational approach.

Application of Experimental Design and Response-Surface Methods

The preceding discussion introduced an approach which, if successful, yields the required physical characteristics of a system as the result of a firm statement of the job that the system is required to do. In a case of that type we have the determination of an unknown function of several variables. Conversely, the first approach discussed is based on the assumption that the characterizing functions (and hence the conceptual physical setup) are known, but that parametric values must be determined for best operation. A third approach to the optimum design of mechanical systems has some of the characteristics of both of the preceding methods. In this approach, we introduce a limited number of possible functional representations (hence physical configurations), and, simultaneously, select the best configuration which is a member of the limited class introduced for comparison and determine the parametric values of this selected function which will optimize the design. Hence, in a shock isolation problem of the type discussed in the calculus of variations approach, we specify that the isolator must consist of a linear spring, static friction, viscous friction, a pneumatic isolator, and a viscoelastic plastic, or any combination of these; the procedure then selects the combination of isolation mechanisms which will do the best job, and determines the parametric values.

It is clear that an approach of the type described, wherein the system is defined in terms of a large family of parameters, is representative

of a wide class of problems reducible to that of minimizing (or maximizing) a function of many variables (defined in a closed region) subject to certain constraints. The method of solution is that of searching the parameter space in some manner. It is well known and easily demonstrated that the brute force approach to the "search" in a multi-dimensional parameter space rapidly becomes impractical with increasing order of the space, even when employing the largest computers. Various selective methods of search ranging from gradient techniques to random sampling techniques have been proposed and have found application to a host of varied problems.

One very promising method for this search lies within the framework of the statistical design of experiments. The specific searching technique is the method of ridge analysis, an extension of steepest ascent techniques introduced by Hoerl [15]. Methods of statistical design of experiments are essentially empirical in nature and generally are applied to situations wherein either a functional relationship between the system parameters and system output or response is unknown, or the "yield" of an "experiment" involves a burdensome degree of effort (i.e., time and cost). In the present application the functional relationship between system parameters and response is known implicitly, being given by the differential equations of motion of the isolator (or other mechanical systems). The "experiment" consists merely of solving the differential equations of motion for a desired characteristic of the motion. For example, in the case of an isolator, parameter values would be specified and the maximum value of the acceleration, as well as the maximum values of the displacement, would be determined. This maximum acceleration and maximum displacement become additional values associated with the specified parameters. Another set of parameters is then specified and the differential equation is solved again to determine the yield. We thus get a group of parametric sets. Now, if we consider that, in general, it will be prohibitive to solve the differential equations for each possible combination of system parameters, the possibility of establishing an implicit or explicit functional relationship between the desired response characteristic and the system parameters based on a very limited number of experiments becomes attractive. This functional relationship or response surface then provides a basis for selecting the optimum system parameter values according to the desired response characteristics. Geometrically speaking, the searching technique becomes the means whereby the topology of the response service is investigated to establish local "hills," "valleys," and "ridges."

This general approach has been used successfully in problems involving optimal controls; limited private investigations have indicated its applicability to mechanical systems. The approaches which were numbered 4, 5, and 6 all have their origin in control systems analysis and servomechanisms studies. They also have in common the fact that, to the best knowledge of the writer, they have not been successfully applied to the problem of optimal mechanical design or synthesis. On the other hand, control systems and electronic networks are, in many ways, similar to dynamic mechanical systems. It would therefore appear to be quite probable that methods which apply to one art may be transferable to a second. The three procedures which we are discussing in this connection are, first, an adjoint procedure which was recently introduced by Pontryagin [16]. The approach is usually confined to control systems whose behavior can be described by a system of ordinary differential equations in the independent variables and auxiliary control variables. The problem is that of determining a "trajectory" which satisfies a given criterion of optimality. The major strength of this approach lies in the fact that, in many cases, additional variables can be introduced and a simple set of differential equations can be derived; the solutions of these equations give the optimal trajectory as well as the variations of the control variables.

It has also been suggested that mechanical synthesis be approached by means of iterative solutions on analog computers. This iterative approach is usually of a trial and error nature. On the other hand, in some cases, control system designers have developed organized rational selection procedures which greatly reduce the effort involved in cut and try solution methods. The fact that the trial solutions can be immediately displayed graphically, and engineering intuition can be used to expedite parameter changes, had made this approach very appealing to electrical designers. Although analog computer iteration does not presently appear to be the best available approach for improvement of mechanical design, it may prove to be useful.

The final approach which was mentioned is that of transferring the optimization investigations to the frequency domain. Most electrical network studies are presently conducted in this way. Direct procedures [17] which utilize the properties of continued fractions and direct

correspondences between canonical mathematical forms and specific network building blocks, are often applied to synthesize very complex and efficient filters, wave shapers, and other electrical networks. There is a direct analogy between the principal linear mechanical elements (masses, springs, and dashpots) and the principal linear electrical elements (inductances, capacitances, and resistances). It seems reasonable that a continuation of this analogy with a view toward synthesis of mechanical designs can yield results and approaches which will be fully as rewarding as the corresponding introduction of mechanical impedance techniques has been in an analogous transferral of electrical results to mechanical systems.

PROBLEM FORMULATION

The system of Fig. 4 is governed by a differential equation of the form

$$\ddot{z} + g(x,\dot{x}) = 0 , \tag{1}$$

where

$$z = x + y(t) \tag{2}$$

and $y(t)$ is a known function of time.

It is desired to find that $g(x,\dot{x}) = g_o(x,\dot{x})$ for which the solution of Eq. (1) under the initial conditions,

$$x(0) = \dot{x}(0) = 0 , \tag{3}$$

has the following properties:

1. The maximum absolute acceleration $\ddot{z}$ is a minimum for $g = g_o$ as compared to any other $g(x,\dot{x})$ admissible.

2. The relative displacement and velocity must satisfy the following inequalities:

$$-X \le x \le X$$

and (4)

$$-V \le \dot{x} \le V ,$$

where X and V are given constants.

The Direct Approach

If the conditions on the problem are relaxed to permit the condition

$$|\ddot{z}_{max}| \le \beta \tag{5}$$

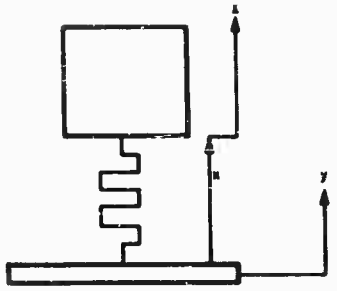

Fig. 4 - Generic system

instead of absolute minimization of $\ddot{z}_{max}$, an infinity of solutions can be found. To see this, let $f(t)$ be any function in $0 \le t < \infty$ which is, together with its first two derivatives, continuous and bounded. For convenience, we shall assume that $f(t)$ has a single-valued inverse, and that $f(0) = \dot{f}(0) = 0$. Define

$$\left.\begin{aligned} x &= \epsilon f(t) \quad (a) \\ \dot{x} &= \epsilon \dot{f}(t) \quad (b) \\ \ddot{x} &= \epsilon \ddot{f}(t) \quad (c) \end{aligned}\right\} , \tag{6}$$

where ϵ is a constant to be determined. Now Eqs. (2), (4), and (5) imply

$$\left.\begin{aligned} |\epsilon f(t)| &\le X \\ |\epsilon \dot{f}(t)| &\le V \\ |[\epsilon \ddot{f} + \ddot{y}(t)]_{max}| &\le \beta . \end{aligned}\right. \tag{7}$$

If $\ddot{y}(t)$ is bounded (a physically realistic assumption) and if

$$|\ddot{y}(t)_{max}| \le \beta$$

then a single ϵ can be found which guarantees satisfaction of Eq. (7). Let the inverse of Eq. (6a) be

$$t = f^{-1}(x/\epsilon) = F(x) , \tag{8}$$

hence

$$\left.\begin{aligned} \dot{x} &= \frac{1}{F'(x)} \\ \ddot{x} &= \frac{F''(x)}{F'^3(x)} \end{aligned}\right\} , \tag{9}$$

but

$$g(x,\dot{x}) = -\ddot{x} - \ddot{y}(t) \tag{10}$$

by Eq. (9), (8)

$$g(x,\dot{x}) = -\frac{F''(x)}{F'^3(x)} - \ddot{y}[F(x)] . \qquad (11)$$

In this case, g has been determined as a function of x alone. Should a single-valued inverse of Eq. (6b) exist, g can be expressed in many ways as a function of x and $\dot{x}$.*

This procedure results in a "solution class" which is very large. Practical considerations will dictate the desirability of one class member over another. The procedure does not, however, attack the full problem as stated.

The Rosenberg Lagrange Approach

At the instant of maximum acceleration the jerk is zero. Let that instant be $t = T$. By differentiating Eq. (1), one has

$$\dot{x}\frac{\partial g}{\partial x} + \ddot{x}\frac{\partial g}{\partial \dot{x}} = 0 \qquad (t = T) \qquad (12)$$

or, by Eq. (2), the stationary value of the acceleration is

$$\ddot{z} = \ddot{y} - \frac{\dot{x}\dfrac{\partial g}{\partial x}}{\dfrac{\partial g}{\partial \dot{x}}} \qquad (t = T) . \qquad (13)$$

Consider the integral

$$I = \int_0^T \frac{d}{dt}\left(\ddot{y} - \dot{x}\frac{g_x}{g_{\dot{x}}}\right)dt \qquad (14)$$

and

$$I \quad \ddot{y}(T) - \dot{x}(t)\frac{g_x[x(T),\ \dot{x}(T)]}{g_{\dot{x}}[x(T),\ \dot{x}(T)]} - \ddot{y}(0) . \qquad (15)$$

Since $\ddot{y}(0)$ is a constant, it follows that we required

$$I = \text{minimum} . \qquad (16)\dagger$$

*It should be observed that the requirement of existence of single valued inverses is over-restrictive. Our aims are satisfied if only it is possible to solve for time, t, from Eq. (6a) and (6b). Solutions of this type can often be obtained explicitly.

†This defines a Meyer problem in the calculus of variations. See, for example, Optimization Techniques, by George Leitmann, Academic Press, New York, 1962. The Lagrange approach is used here because it is assumed to be more familiar to the reader.

For convenience, let

$$\left.\begin{aligned} \dot{x} &= v \\ g_x &= f \\ g_{\dot{x}} &= h \end{aligned}\right\} . \qquad (17)$$

We have

$$\frac{d}{dt}\left(\ddot{y} - \dot{x}\frac{g_x}{g_{\dot{x}}}\right) = \dddot{y} - \frac{d}{dt}\left(v\frac{f}{h}\right)$$

$$= \dddot{y} - \dot{v}\frac{f}{h} - \frac{v}{h}(f_x v + f_v \dot{v})$$

$$+ \frac{vf}{h^2}(h_x v + h_v \dot{v})$$

but, by Eq. (17), (1) and (2)

$$\dot{v} = \ddot{z} - \ddot{y} = -(\ddot{y} + g)$$

so that

$$\frac{d}{dt}\left(\ddot{y} - \dot{x}\frac{g_x}{g_{\dot{x}}}\right) = \dddot{y} + (\ddot{y} + g)\frac{f}{h} - \frac{v}{h}(f_x v - \ddot{y} f_v - g f_v)$$

$$+ \frac{vf}{h^2}(h_x v - h_v \ddot{y} - h_v g) . \qquad (18)$$

Thus, we desire to find $g(x,\dot{x})$ to minimize

$$I = \int_0^T \left\{ \dddot{y} + (\ddot{y} + g)\frac{f}{h} - \frac{v}{h}(v f_x - \ddot{y} f_v - g f_v) \right.$$

$$\left. + \frac{vf}{h^2}(v h_x - \ddot{y} h_v - g h_v) \right\} dt \qquad (19)$$

under the equations of constraint

$$\left.\begin{aligned} &\dot{v} + g(x,v) = -\ddot{y}(t) \\ &-V \le v \le V \\ &-X \le x \le V \\ &\dot{x} = v,\ g_x = f,\ g_v = h \end{aligned}\right\} . \qquad (20)$$

where

$$x(0) = v(0) = 0 \qquad (21)$$

and

$$\left.\begin{aligned} \dot{v} &= -\frac{vf}{h} \\ &= -\dot{y} - g \end{aligned}\right\} \text{at } t = T . \qquad (22)$$

Introduce new variables z_1, z_2 through the bounds

$$\left.\begin{aligned} z_1^2 &= V^2 - v^2 \\ z_2^2 &= X^2 - x^2 \end{aligned}\right\}. \tag{23}$$

The bounds imply that z_1 and z_2 are real. The constrained problem can be stated as follows.

J is stationary, where

$$J = \int_0^T \left\{ \frac{d}{dt}\left(\dot{y} - v\frac{f}{h}\right) + \lambda_1\left[z_1^2 - (V^2 - v^2)\right] + \lambda_2\left[z_2^2 - (X^2 - x^2)\right] + \lambda_3(v - \dot{x}) + \lambda_4(g_x - f) + \lambda_5(g_v - h) + \lambda_6(\dot{v} + \ddot{y} + g)\right\} dt, \tag{24}$$

or

$$J = \int_0^T F(x, \dot{x}, v, \dot{v}, f, h, g, z_1, z_2, g_x, g_v)\, dt. \tag{25}$$

To the Euler equations, we append the natural boundary conditions and the transversality condition. We note, by Courant-Hilbert [18], that we need not consider

$$\left(\frac{d}{dt}\quad \ddot{y} - v\frac{f}{h}\right)$$

in deriving the Euler equations.

Euler Equations

$$-\frac{d\lambda_3}{dt} - 2\lambda_2 x = 0, \tag{26}$$

$$\lambda_3 + 2\lambda_1 v = 0, \tag{27}$$

$$+\lambda_4 = 0. \tag{28}$$

$$+\lambda_5 = 0, \tag{29}$$

$$\lambda_6 = 0. \tag{30}$$

$$\lambda_1 z_1 = 0, \tag{31}$$

and

$$\lambda_2 z_2 = 0. \tag{32}$$

Natural Boundary Conditions

At $t = T$,

$$\lambda_3 = \lambda_6 = 0. \tag{33}$$

Transversality Condition

At $t = T$,

$$F = 0. \tag{34}$$

(Note): There are many transversality conditions but one of them implies Eq. (34) and all others are satisfied by this specification.

Euler Equations

Eliminate λ_3 between Eq. (26) and Eq. (27), thus

$$\frac{d}{dt}(\lambda_1 v) - \lambda_2 x = 0, \tag{35}$$

$$\lambda_1 z_1 = 0, \tag{36}$$

and

$$\lambda_2 z_2 = 0. \tag{37}$$

We now discuss the different cases:

Case I: $\lambda_1 = \lambda_2 = 0$

In this case, the entire expression vanishes. The integrand of J, Eq. (24), is a divergence expression. This case has the following interpretation:

> If neither x nor v is required to assume and retain an end value, any sufficiently smooth $g(x, \dot{x})$ is a "stationary shock absorber" over the time range $0 \le t \le T$, provided

$$\ddot{y} + g - \frac{\dot{x}\dfrac{\partial g}{\partial x}}{\dfrac{\partial g}{\partial \dot{x}}} = 0 \tag{A}$$

and

$$\frac{d}{dT}\left[\ddot{y} - \dot{x}\frac{\dfrac{\partial g}{\partial x}}{\dfrac{\partial g}{\partial \dot{x}}}\right] = 0, \tag{B}$$

simultaneously at $t = T$.

The above case is the major conclusion of this section. For completeness we consider the other very simple cases.

Case II: $\lambda_1 = 0,\ \lambda_2 \neq 0$

By Eq. (37), (23)

$$\left.\begin{aligned} z_2 &= 0 \\ x^2 &= X^2 \end{aligned}\right\}, \tag{38}$$

by Eq. (35)

$$X = 0 . \tag{39}$$

Equations (38) and (39) can hold simultaneously only if $X = 0$, a trivial case.

Case III: $\lambda_1 \neq 0,\ \lambda_2 = 0$

By Eq. (36) and (23),

$$\left.\begin{aligned} z_1 &= 0 \\ v^2 &= V^2 \end{aligned}\right\}, \tag{40}$$

by Eq. (35)

$$\frac{d}{dt}(\lambda_1 v) = 0 , \tag{41}$$

thus λ_1 is constant.

Equation (40) implies that

$$x = \pm Vt + \text{constant} . \tag{42}$$

Thus, the mass can move back and forth between bounds at constant velocity. This solution is acceptable only if the forcing displacement y and the absorber g are such that the absolute acceleration is finite at the turning points. The solution violates our (restrictive) continuity assumptions.

Case IV: $\lambda_1 \neq 0,\ \lambda_2 = 0$

By Eq. (37), (23)

$$\left.\begin{aligned} z_2 &= 0 \\ x^2 &= X^2 \\ z_1 &= 0 \\ \dot{x}^2 &= V^2 \end{aligned}\right\}. \tag{43}$$

Equations (43) and (35) yield the triviality of Case II.

Re-Interpretation of Problem

The preceding results can be obtained through a different line of reasoning. By basic arguments there is an instant $t = T$ at which the stationary value of the acceleration is

$$\ddot{z}(T) = \ddot{y}(T) - \frac{\dot{x}(T)\,\frac{\partial}{\partial x}\, g\,[x(T),\ \dot{x}(T)]}{\frac{\partial}{\partial \dot{x}}\, g\,[x(T),\ \dot{x}(T)]} . \tag{44}$$

Utilization of Eq. (1) with Eq. (44) yields Eq. (A) in Case I. Now, as the functional form of g varies, the point at which $\ddot{z}$ is stationary will vary. If g is $C\,[2]$ in both its arguments in the neighborhood of a given T, and $\ddot{y}(T)$ is differentiable, we then have that the stationary value of $\ddot{z}$ is, itself stationary at T if

$$\frac{d\ddot{z}(T)}{dT} = 0 , \tag{45}$$

by Eq. (44) and (45), we obtain Eq. (B) in Case I.

We must observe that the Lagrange-Rosenberg approach CAN NEVER yield the results we desire. The problem, as formulated, contains a single independent variable (x) and a single dependent variable, time. Thus NO constraints can be applied. If an attempt is made to apply constraints one obtains results which are independent of these constraints. Thus, to be successful, the formulation must introduce additional dependent or independent variables.

We have reached the conclusion that the solution of our minimization problem depends only upon conditions at the end-point of time and that the path between the end-point is, itself, immaterial. This conclusion is not as strange as it may seem. Let us refer to a geometric problem for an interpretation. Assume that the problem depicted in Fig. 5 is prescribed. Here we define a curve in the xy plane which connects the points x_0 and x_1 on the axis $y = 0$. We demand that, at the end-points, the curve be perpendicular to the abscissa. It is otherwise unrestricted except that we demand that the curve have minimal length. In a formal sense the problem has no solution. If any curve is presented which is perpendicular at the end-points another curve can be found which is also perpendicular but whose length is less. One can approach arbitrarily close to the minimal

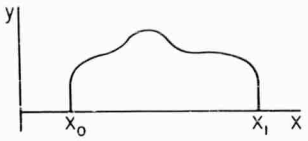

Fig. 5 - Geometric problem

curve between x_0 and x_1 (namely, the straight line segment of the abscissa) but this limit is not a solution of the completely prescribed problem.

This conclusion reinforces that which can be obtained from the direct approach to the problem; it would appear that should any purported solution to the stated minimization problem be presented, a better solution can always be found.

Alternative Approaches

Problem Modification. It is apparent that the determination of solutions of engineering utility will require some alternative approach. A possibility in this regard is in the modification of the statement of the problem. The direct approach which was presented is one approach of this type. Here we did not require minimization of the relative acceleration. Instead, we only demanded that the relative acceleration be bounded. Solutions of this problem are, clearly, in no way unique. Furthermore, the "best" solution is not necessarily obtained. This approach does, however, present the possibility of yielding useful engineering results.

A second possible problem modification involves introduction of additional subsidiary conditions which reflect engineering restrictions which must be met. One example of this type is that in which the shock isolator must also serve as a noise isolator. A simple problem modification would require that the shock isolator function, g, be such that the velocity response to a sinusoidal input is bounded. System stability, system weight, system cost, and energy restriction are other possible subsidiary conditions which can be imposed. All of these problems are presently under investigation.

Specialization of Isolator. The primary statement of the shock isolator problem yields a formulation which can, at best, result in a description of the behavior of the shock isolator function in phase space. Actual mechanization of a function which satisfactorily complies with the continuous conditions may be difficult or impossible. Hence, there are certainly advantages which can accrue from a prespecification of the shock isolator function which demands that the mechanical isolator itself be constructed of elements each of which can definitely be fabricated. An approach of this type is basically no more than an extension of the parameter variation methods which were described earlier in the paper. Conversely, the possible generality of isolator specification is great. A typically specified isolator might include springs, viscous dampers, hydraulic mechanisms with variable orifices, pneumatic springs, and regions of free fall. Such basic isolator parameters as the variation of orifice area with displacement can be left open and determined by means of relatively simple minimization procedures. Although difficulties exist in this approach it appears to offer much promise.

Interpretative Analysis. A third analytical procedure involves attempts to determine basic qualitative problem restrictions. Hence, it is possible to construct "trade-off diagrams" which show the relationship between maximum relative displacement and maximum absolute acceleration for a particular end-point function and shock isolator functions. Although many procedures of this type are conceptually simple they can yield basic information which is of importance to the designer in search of better isolation systems. Such analyses are presently under study although definite conclusions cannot be stated at this time. It does appear probable that quantitative as well as qualitative conclusions can result from conscientious application of basic physical principles.

It is clear that the general problem of optimal mechanical design is in its infancy. Many of the results which have been obtained to date have led to negative conclusions rather than positive solutions. It is felt that the present paper is justified by the novelty of the problem and the tremendous utility of any possible solutions which may be obtained. Much additional work in this general area is needed. It is hoped that this introduction will motivate additional independent investigations.

REFERENCES

1. F. R. Shanley, "Principles of Structural Design for Minimum Weight," J. Aeronaut. Sci., Vol. XVI, No. 3 (Mar. 1949).

2. F. R. Shanley, Weight-Strength Analysis of Aircraft Structures (Dover Publications, Inc., New York, 1960).

3. G. Gerard, Minimum Weight Analysis of Compression Structures (New York University Press, New York, 1956).

4. H. B. Howard, "Merit Indices for Structural Materials," Report 105, for North Atlantic Treaty Organization, Palais de Chaillot (Apr. 1957).

5. G. A. Hoffman, "Optimum Tolerances of Sheet Materials for Flight Vehicles," ASME Paper No. 59-A-70.

6. R. L. Barnett, "Selection of Material in Minimum Weight Design," ASME Paper No. 63-MD-25.

7. R. L. Barnett, "Minimum-Weight Design of Beams for Deflections," Journal of the Engineering Mechanics Division, Proc. Am. Soc. Civil Engrs. (Feb. 1961).

8. R. L. Barnett, "Lightweight Structures and Prestressed Launcher Components - Phases I and II," for Rock Island Arsenal under Contract No. DA-11-070-508 (Oct. 1958).

9. R. Plunkett, "The Calculation of Optimum Concentrated Damping for Continuous Systems," J. Appl. Mech., Trans. ASME, Vol. 80 (1958).

10. J. F. Springfield and J. P. Raney, "An Experimental Investigation of Optimum End Supports for a Vibrating Beam," Annual Meeting, SESA, Milwaukee, Wisconsin (Oct. 1962).

11. A. R. Henney, "The Damping of Continuous Systems," The Engineer (Mar. 1963).

12. F. M. Lewis, "The Extended Theory of the Viscous Vibration Damper," J. Appl. Mech., ASME, Vol. 77 (1955).

13. J. P. Den Hartog, Mechanical Vibrations, Fourth Edition (McGraw-Hill, New York, 1956).

14. R. M. Brach and E. Sevin, "Optimum Design for Transient Loading," The Soc. Aeronaut. Weight Engrs., SAWE Nat'l. Conference (May 1962).

15. A. E. Hoerl, "Optimum Solution of Many Variable Equations," Chemical Engineering Progress, Vol. 55 (Nov. 1959).

16. C. A. Desoer, "Pontryagin's Maximum Principle and the Principle of Optimality," Journal of the Franklin Institute, Vol. 271.

17. E. R. Guillemin, Synthesis of Passive Networks (John Wiley and Sons, Inc., New York, N. Y., 1957).

18. Courant-Hilbert, Methods of Mathematical Physics, Vol. I (Interscience Publishers, New York, 1961), p. 196.

* * *

VIBRATION ISOLATION SYSTEMS FOR ELECTRONIC EQUIPMENT IN THE B-52 AIRPLANE LOW-LEVEL ENVIRONMENT

R. W. Spring
The Boeing Company
Wichita, Kansas

This paper discusses the equipment mounting inadequacies found when the mission capability of the B-52 airplane was revised to include low-level flight operation and the steps taken to resolve the problem. It describes the program by which over 200 items of vibration isolated equipment were evaluated to determine the adequacy of their mounting provisions. Selection and development of various types of isolaters to replace the inadequate parts are discussed. A limited amount of service data is presented to show the improvement resulting from use of the new vibration isolators

INTRODUCTION

The B-52 airplane was utilized from its first appearance in 1954 until 1961 solely as a high-altitude bomber and missile platform. In 1958, the requirement for low-level flight operation was added. This additional capability was reflected in many changes to structure and equipment. The new mission profile also resulted in a severe change in the vibration environment of the airplane and made necessary a reevaluation of equipment mounting provisions.

LOW-LEVEL VIBRATION ENVIRONMENT

The B-52 low-level vibration environmental characteristics are established by airplane rigid and elastic body responses excited by atmospheric turbulence. These responses are of very low frequency, 0 to 10 cps, and are not considered as shock excitation but are transients by nature and decay at a rate determined by the structural damping of the airplane. The vibrational energy is not constant over the frequency range to 0 to 10 cps, but is concentrated at several frequency intervals with the highest concentrations below 5 cps. Most severe vibration occurs in the vertical and lateral directions, but excitation may occur in all directions simultaneously. The most severe environment is generally in the aft fuselage, forward fuselage, and wing tips.

A representative sample of the low-level vibration environment is difficult to obtain because of the large number of variables having a significant effect on the measured vibration data. These variables include air speed, altitude, gross weight, fuel distribution, equipment location, gust velocity, and turbulence intensity distribution. Accordingly, the B-52 vibration envelopes for the low-level vibration environment have been calculated rather than measured.

Because of the low g forces involved at these low frequencies, virtually all equipment items that are rigidly mounted to a support structure are expected to function without difficulty in the low-level vibration environment. A problem may exist in such items if the components have low resonant frequencies; however, required design loads criteria normally prevent this condition. In contrast to the negligible effects induced in rigidly mounted equipment, items mounted on vibration isolaters are subject to low-frequency isolator conditions that magnify the vibration transmitted from structure. Isolator and/or equipment damage will result if the isolator frequency corresponds to, or is relatively close to, an airplane rigid or elastic body response frequency excited by the low-level environment.

EQUIPMENT MOUNTING SURVEY

In February 1961, Boeing was authorized to accomplish a study [1] of all equipment mountings in B-52C through H model aircraft to determine their adequacy under conditions of low-level flight. This study was initiated at the request of the Air Materiel Command because of numerous mounting failures which Boeing discovered after early exploratory flight tests at low level. Prior to the start of this study, 16 different equipment installations acquired a history of being inadequate as a result of the flight tests.

The probability of failure or damage to a B-52 Vibration Isolation System (VIS) or the mounted equipment is greatly increased if one or more of the VIS natural frequencies coincides with or is near one of the airplane low-level response frequencies. For this reason, the lowest natural frequency of a vibration isolation system is the primary indicator of the adequacy of such a system to withstand the low-level environment. A large portion of the equipment mounting study was devoted to determining the lowest natural frequency of the existing B-52 vibration isolation systems, considering the mounted equipment as a rigid body. A frequency criteria was established considering the VIS transmissibility and the low-level vibration environment characteristics to determine the minimum permissible value of the lowest natural frequency. By applying this frequency criteria to the existing B-52 VIS, their adequacy or inadequacy could be determined. The number of vibration isolation systems involved precluded testing each one to determine the lowest natural frequency; therefore, a combination of experimental vibration testing and theoretical vibration analysis was used.

Eleven mockup configurations were established to obtain experimental values of natural frequencies. Six of the configurations were base mounted because this is representative of the majority of items in the B-52. The configurations differed in mass distribution, isolator spacing, and center-of-gravity (cg) location. The remaining configurations included vertically aligned cg mounting, horizontally aligned cg mounting, inclined cg mounting, and triangular base mounting.

Four sets of vibration isolators were chosen for the test. Two were representative of the existing type in the B-52 which was suspected to be inadequate. The other two were of the type thought to be adequate.

Frequency scans from 2 to 50 cps at an input of 0.06-inch double amplitude were conducted in three axes on each of the 11 configurations with each of the four sets of isolators. However, the vibration input level was lowered to 0.036-inch double amplitude for one of the sets of existing isolators to prevent snubbing. Transmissibility curves were plotted for each frequency scan. Figures 1 and 2 show typical test setups.

For the analytical portion of the study, the basic configurations described in the experimental procedures were idealized as undamped, linear spring-supported masses for simplicity of solution. The mass and inertia properties were determined analytically and the isolator stiffness properties were estimated from load deflection tests performed on each type of isolator. It was assumed that the isolators could be replaced by lateral and vertical springs equivalent to the lateral and vertical stiffness of the isolator. This representation allowed a

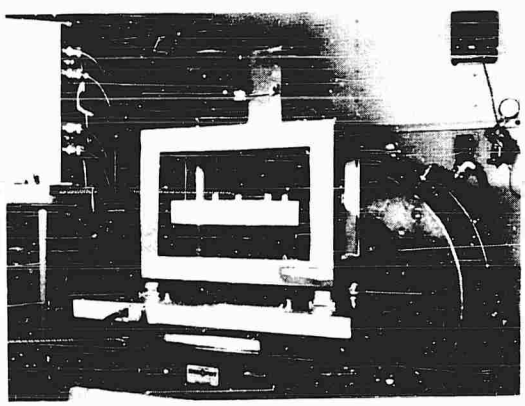

Fig. 1 - Base-mounted test configuration

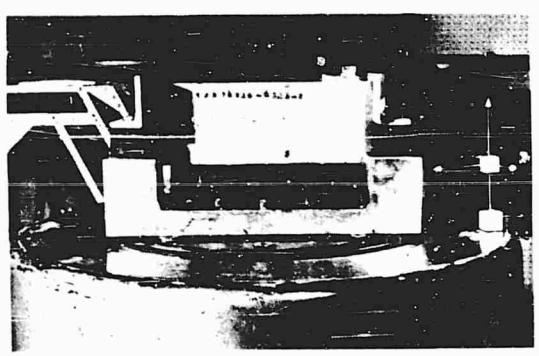

Fig. 2 - Center-of-gravity mounted test configuration

NOTE: References appear on page 175.

TABLE 1

Comparison of Experimental and Analytical Values of First Mode Frequency for Three Base Mounted Configurations

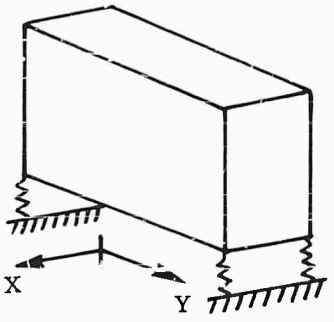

Configuration Number	Axis	Frequency of First Mode (cps)	
		Experimental	Analytical
Isolator A			
1	X	3.5	2.9
	Y	5.0	4.5
2	X	4.0	3.5
	Y	5.6	5.0
3	X	4.5	4.1
	Y	6.0	5.4
Isolator B			
1	X	10.0	9.8
	Y	15.0	16.5
2	X	12.5	12.2
	Y	18.0	19.0
3	X	14.5	14.5
	Y	19.0	21.2

matrix iteration method of solution to determine the rigid body natural frequencies and associated mode shapes. The iteration procedure used was similar to that described previously [2] and was programed for solution on an IBM 7090 digital computer.

A comparison of the experimental and analytical results indicated that the correlation was adequate for the purposes. Table 1 presents a typical comparison of results from three configurations with two different isolators. Isolators A and B were of the types suspected to be inadequate, respectively. An analytical tool was then available for classifying, which with reasonable assurance, the B-52 VIS as either adequate or inadequate for the environment associated with low-level flight based on the criteria of lowest natural frequency.

The next step was to obtain from the various B-52 design groups the physical parameters of each item of isolated electronic equipment for which they were responsible. This included weight, cg location, isolator spacing, and isolator details. With the aid of the digital computer program, the natural frequencies of each mounting system could then be determined.

The study encompassed 211 items of vibration isolated equipment on C through H Model airplanes. Of these, 75 had adequate mountings and 136 were classed as potential trouble items, based on the frequency criteria. Because

considerations of economy and time might make it impossible to replace all 136 mounting systems, these items were further categorized by their weight, aircraft location, and essentialness so that effort could be concentrated on the most critical. Using these criteria, 50 of the 136 items were classified as inadequately mounted for the environment associated with low-level flight; these included the 16 items previously known to be inadequate. The remaining 86 items were listed as potential trouble items to be monitored for future replacement as required.

PROPOSED SOLUTION

Because of the severely limited space available for electronic equipment on present combat aircraft and the large excursions associated with very low-frequency vibration isolation systems, it is not practical to build, for aircraft use, an isolation system for frequencies in the 1 to 5 cps range. Therefore, the approach utilized was to develop VIS whose lowest resonant modes were above the frequency range of the disturbances. The first step was to decide how far above the forcing frequencies to go. Theoretically, all frequencies below the natural frequency of VIS are amplified to some degree. However, isolators with the high degree of damping necessary to control excursion at resonance would not significantly amplify forcing frequencies lower than 40 percent of the isolator resonant frequency. To insure minimum amplification of the major disturbances below 5 cps, all resonant modes of the VIS should be above $5/0.4 = 12.5$ cps. For the specification requirement 13 cps was used.

CONFIGURATION PROBLEM

The majority of electronic equipment items in the B-52 are base mounted. In this configuration the lowest resonant frequency, a coupled horizontal mode, is determined by the spring system and the geometry of the equipment. If the cg is high, or the distance between isolators is short, the isolators must be extremely stiff in the horizontal direction to control the inertia forces resulting from the unfavorable width-height ratio.

One of the ground rules of the program was that, as much as possible, the new VIS would retain the existing attachment points to the support structure; therefore, the isolator spacing could not be expanded. Relocating the cg of existing government furnished equipment was out of the question, so we had to contend with the existing width-height ratios.

Even with such unfavorable configurations, it is possible, of course, to keep all resonances of the mounted system above 13 cps by increasing the stiffness of the springs. In so doing, the frequency at which effective isolation is achieved is also increased. This results in a more severe ride for the equipment with an increased probability of damage. Almost without exception, the equipment had been designed to ride on MIL-C-172 mounts and in that specification there is no lower limit on resonant frequencies. Consequently, the mounts had very little stiffness, especially in the lateral directions, and the resonant points were quite low. The transmissibility of that type mount was less than one from approximately 16 cps on up, thus providing very good isolation of the frequencies which are normally detrimental to electronic equipment. However, this "very good isolation" provided by MIL-type mounts will not be present if the mounts are snubbed, deteriorated, or broken due to the vibrational inputs associated with low-level flight.

EQUIPMENT FRAGILITY CONSIDERATIONS

Many equipment items were susceptible to vibration damage at much lower frequencies than had been suspected. For example, one modulator contained a cantilevered, high-voltage relay shelf resonant at 26 cps in the vertical axis. With MIL-C-172 type mounts, the input at this frequency was greatly attenuated. The new low-level VIS had a vertical resonant frequency of 24 cps which was quite incompatible with the shelf resonance. Fortunately, this was a cg mounted item so that there were no coupled modes. On a subsequent redesign of the VIS; a system was obtained with resonant modes at approximately 14 cps in each of the three principal axes and a transmissibility of 0.4 at 26 cps. This experience pointed up a situation foreseen from the start of this program: keeping all resonances above 13 cps and still obtaining isolation of frequencies that could be detrimental to the function of the equipment gave a very narrow frequency range in which to place the response frequencies of the mounting system. It was apparent that some compromises would have to be made.

The original design criteria for the equipment was based on the protection afforded by a soft, efficient, isolation system. Any significant increase in isolator stiffness could create equipment problems. Because equipment modification or redesign is an expensive undertaking, it was considered as the last resort. Therefore, it was decided to deviate, where testing indicated

it was necessary, from the 13 cps requirement and to accept a limited risk in the low-level environment.

The lower limit of deviation was not a firmly defined frequency; it varied with geometry, weight, airplane location, fragility, and essentialness of the particular equipment item in question. If, for any item, a point was reached such that the "softest" VIS that could be tolerated under low-level considerations did not provide sufficient isolation for reliable equipment operation, equipment modification was recommended.

HARDWARE DEVELOPMENT

In the hardware development stage three companies were involved; each approached the problem by tailoring a more or less "standard" product to meet specific requirements. One company utilized an isolator with opposed helical load-carrying springs and friction damper. Another company proposed their elastomeric mounts in either standard or focalized configurations. The third company offered an adaptation of their knitted wire mesh resilient mount.

The features of these three types of mounts as observed in their application to the B-52 program are briefly summarized below:

1. Wire Mesh Type. The wire mesh isolators provided satisfactory performance in cg mounting applications and on base-type mounting systems where the width-height ratio of the equipment was favorable. Transmissibility at resonance was greater than the spring and damper type but less than the elastomeric type. Temperature effects on performance were negligible and isolation of high frequencies was good. The wire mesh isolators were practically "on-the-shelf" items with the manufacturer so that development time and delivery were not problems. The wire mesh isolators were not very successfully used on base-mounted systems in which there was a considerable offset of the equipment cg from the elastic axis because the damping was not sufficient to limit the rocking mode transmissibility to an acceptable level. With additional time this type could have been tailored to perform satisfactorily in the adverse configurations, but, the timing of the program did not permit extended development effort.

2. Elastomeric Type. The performance of the elastomeric isolators was generally satisfactory for base-mounted equipment with favorable dimensions. If the isolator spacing was adequate, the elastomeric mounts were used in a focalized configuration and provided excellent performance. Since isolator spacing could not be expanded, proper focalization could not be achieved in many cases. On narrow items, the elastomeric isolators in a cg mounting configuration had to be used because the internal damping of the elastomer was not sufficient to control the rocking modes. For this same reason, the transmissibility at resonance was higher than that of the other two types. It took longer to revise the elastomeric-type isolators than the metal-type if performance was not as desired. The elastomeric isolators could not be revised, but rather, had to be replaced with new mounts containing a differently compounded elastomer. This would be of little consequence in most mount development efforts but it became a factor in the program because of the compressed time schedule.

3. Spring and Damper Type. The performance of the spring and damper isolators was satisfactory in all mounting configurations. This type was utilized in nearly all applications involving unfavorable width-height ratios of base-mounted equipment. Because the stiffness and damping can be varied independently, this type of isolator was ideally suited to the "tailoring" process by which it was hoped to keep all resonances in the optimum frequency range. In those cases where it was necessary to deviate much below 13 cps, the high lateral damping obtained with this type of isolator kept the transmissibility of the lower rocking mode to a safe level. As might be expected these highly damped isolators did not provide as good isolation at high frequencies as was wished. As the program evolved, the high-frequency performance was greatly improved by use of a damper control technique which approached the sprung damper method. The damper was amplitude sensitive so that it was most effective at high amplitudes in the low-frequency range.

VIBRATION ISOLATION SYSTEM QUALIFICATION

All vibration testing of the new VIS was accomplished with the use of sinusoidal inputs. The input spectrum is shown in Fig. 3. Relatively high amplitude is required at the low-frequency end because of the low-level environment. The expected performance, or transmissibility limit, is shown in Fig. 4. Amplification at resonance is limited to 3.5 and this is in the narrow frequency range of 13 to 21 cps. The maximum allowable input to the equipment is 2.85 g which could occur at 21 cps. The specification required that there be no resonances below 13 cps, in accordance with the idealized solution; however, it

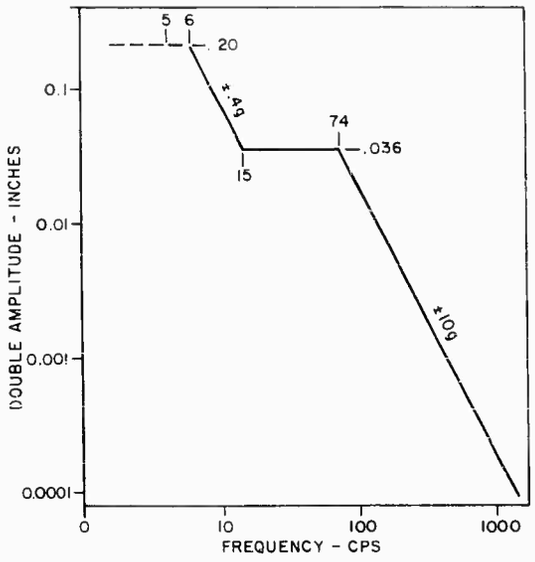

Fig. 3 - Vibration test envelope

also stated that resonances slightly below 13 cps be coordinated with Boeing for possible deviation.

The vendors of the VIS utilized weighted, rigid mockups to represent the electronic equipment during qualification testing. Accelerometers were mounted at the extremities of the mockups to obtain maximum transmissibility measurements. The "extremities" are sometimes construed to be only the upper corners on a base mounted equipment, but the lower corners were included as well. At the lower coupled mode frequency, the upper edge of the equipment has the greatest displacement; however, with these stiff isolators, the response at the upper coupled mode frequency is sometimes greatest at the lower edge of the equipment.

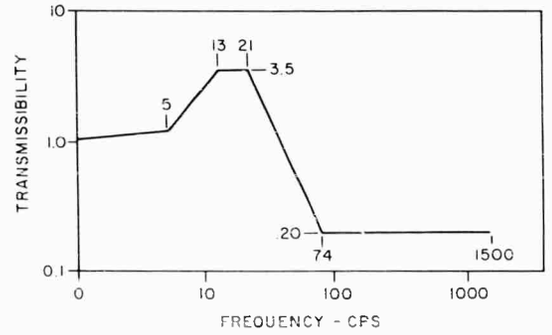

Fig. 4 - Transmissibility limit for vibration isolation systems subjected to input levels on Fig. 3

The majority of "out-of-specification" conditions found during VIS qualification fell in the categories of resonances below 13 cps, upper rocking mode "out of specification" in the 40 to 70 cps range, or a combination of these. The isolators were revised or tailored to optimize these deviations where possible

EQUIPMENT TEST PROGRAM

Thirty-eight of the 53 new VIS were shipped to the various equipment vendors for compatibility testing with live equipment. In some cases, hardware was concurrently being installed in the fleet; in other cases, retrofit was not to be considered until the compatibility testing was successfully completed. The remaining 15 types of VIS were procured in small quantities and installed on a limited number of aircraft without any equipment testing. It should be explained here that the 53 VIS developed did not include all 50 items classified as inadequate by the study. Several were omitted for various reasons. Replacements were developed for several potential trouble items where they were part of a subsystem in which the majority of mounting provisions were inadequate and were being redesigned.

The results of the live equipment testing were generally very satisfactory. The only serious incompatibility between equipment and VIS was on the modulator, as previously mentioned. There were, however, a number of equipment failures during the test program. These failures exposed the weaker points of the original equipment design and a suitable fix should improve the overall reliability of the item.

Several equipment items were from the bombing-navigation system and were being modified to provide electronic functions required for low-level navigation; therefore, the fixes for significant vibration failures were incorporated along with the function modifications.

Other failures were categorized as random in nature and so no fix was provided or else one was devised and shelved until such time as an in-service failure occurs. Because the test was accelerated, it is quite conceivable that many of these laboratory failures will seldom, if ever, occur during the service life of the equipment.

IN-SERVICE RESULTS

The value of the mounting program can be measured by the effect on the in-service maintenance requirements of the equipment. This is based on the assumption that if a particular item of equipment is used on a large quantity of aircraft, and failure information is segregated

according to whether the aircraft have old or new VIS, any difference in failure rate is due to the VIS. For maximum confidence in this assumption aircraft of the same model and from the same base should be compared over a long time period.

For several reasons a large amount of failure data has not yet been accumulated: the VIS retrofit program is not complete, some items of equipment are mounted only on the new VIS, and some items of equipment are installed on new VIS in H model aircraft and on old VIS in earlier model aircraft. Table 2 presents a failure rate comparison using the limited data available. A very significant reduction in failures is apparent and represents a considerable saving in man-hours and money. Caution must be exercised in evaluating this impressive improvement in failure rate. The data were obtained from a limited sample of aircraft and over a relatively short time span. However, we are optimistic that future service experience will demonstrate the value of providing adequate vibration isolation systems for electronic equipment on the B-52 airplane.

TABLE 2

Comparison Of Failure Rates Of Equipment Mounted On New And Old Vibration Isolation Systems

Equipment	Failures Per 1000 hr.		Ratio New/Old
	Old[a] Vis	New[b] Vis	
1. BNS Computer Modules	37.38	23	0.62
2. Radio Rcvr.-Trans.	18.32	14	0.76
3. Astro Compass Mdles.	12.24	5	0.41
4. ECM Transmitter	10.84	7	0.65
5. ECM Power Supply	8.81	2	0.23
6. Doppler Rcvr.-Trans.	5.05	3	0.59
7. Radar Modulator	4.33	2	0.46

[a]Inadequate for vibration environment of low-level fleet.
[b]Adequate for vibration environment of low-level fleet.

REFERENCES

1. "A Study of B-52 Equipment Mounting Adequacy for Low Level Flight," Boeing Co. Doc. D3-4064 (Nov. 1, 1961).
2. S. H. Crandall and R. B. McCalley, "Numerical Methods of Analysis," Shock and Vibration Handbook, Vol. 2, Ed. by C. M. Harris and C. E. Crede (McGraw-Hill Book Co., Inc., New York, 1961), Chap. 28.

DISCUSSION

Dr. Morrow (Aerospace Corp): This is a good example of what can be done when you have the opportunity to take a good look at the excitations and also a good look at the character of what you are trying to mount. It causes me to reflect that one of the more critical difficulties in general purpose specifications is trying to select levels with a sufficient degree of realism so that the specifications are a help rather than a hindrance with respect to vibration isolator design.

* * * * *

DESIGN AND DEVELOPMENT OF LOW-FREQUENCY VIBRATION ISOLATORS WHICH EXHIBIT LOW SHOCK AMPLIFICATION CHARACTERISTICS

S. Balan and L. J. Pulgrano
Grumman Aircraft Engineering Corporation
Bethpage, Long Island, New York

INTRODUCTION

Many types of electronic equipment on board operational military aircraft are mounted on vibration isolators designed in accordance with the current applicable general specification, MIL-C-172C. The relatively low resonant frequency characteristics* of isolators of this type were established to provide high isolation efficiency of the low forcing frequencies of piston engine aircraft.

Typical commercial isolators designed in accordance with MIL-C-172C have essentially bilinear elasticity. The first element of the bilinear spring is designed to support the mounted equipment under normal level flight conditions; its relatively low stiffness, established by resonant frequency considerations, can usually accommodate dynamic loading not greater than 2.5 g within its deflection range. Hence, if the isolator is subjected to shock loading of substantially higher acceleration level, such as during hard aircraft carrier landings, the load capacity of the low-stiffness element is grossly exceeded, and the motion of the mounted equipment is arrested by abrupt bottoming on the much stiffer second, or snubbing, spring element. In commercial isolators the stiffness of this snubbing element is usually not related to the stiffness of the first-stage element, since, for manufacturing simplicity, the same snubber is generally used for a number of isolators of different load ratings in a particular isolator series. Thus, there is no specific relationship between first- and second-stage stiffnesses.

It has been conclusively demonstrated, both analytically and experimentally, that the abrupt bottoming of typical commercial low-frequency vibration isolators occurring during hard carrier landings causes the single long-duration landing shock pulse to be transformed into a series of several short-duration amplified shock response pulses.† Figure 1 shows representative oscillographic traces of a laboratory-produced long-duration shock pulse and the response of an equipment mockup mounted on typical low-frequency isolators. It is seen that when the system is subjected to a single 12-g, 125-millisecond shock pulse, the mockup experiences a series of four relatively short-duration amplified shock pulses, the highest of which is 35 g. The adverse effect on equipment performance and reliability of repeated exposure to such amplified shock forces has been widely recognized by airframe and electronic equipment manufacturers and by the military procurement agencies. It is reasonable to conclude that a reduction in shock exposure will produce a related increase in reliability.

By contrast with the low first-stage stiffness and abrupt change to high second-stage stiffness of typical low-frequency isolators, typical high-frequency (above 20 cps) isolators have four or more times higher initial stiffness, as well as a stiffness characteristic which increases gradually, in the form of a tangent or

*Although not explicitly stipulated by the specification, the relatively low resonant frequency characteristics of MIL-C-172C isolators are governed by vibration transmissibility requirements. Typical commercial isolators have resonant frequencies between 7 and 11 cps in vertical translation; the five other rigid body mode frequencies are functions of isolator stiffnesses and spacing and the inertial properties of the mounted equipment.

†The shock requirements of MIL-C-172C exercise inadequate control over the adverse effects of shock amplification produced by carrier landings, in two respects: first, the response of a mounted equipment to MIL-C-172C 11-millisecond shock pulses is considerably less severe than the response to typical 125-millisecond shock pulses; and second, the specification places no limit on shock amplification.

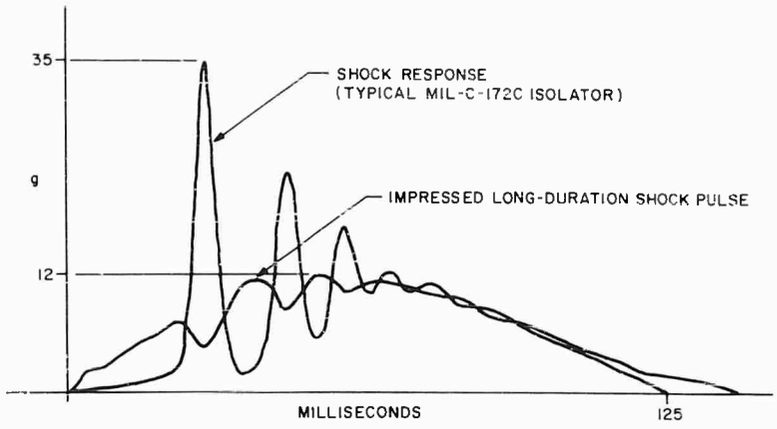

Fig. 1 - Measured response of typical MIL-C-172C isolator to 125-millisecond half-sine shock pulse

parabolic curve, with increasing deflection. With such isolators, the application of shock forces to the mounted equipment is much more gradual, and abrupt bottoming and associated detrimental shock amplification are greatly reduced or avoided.

It is evident that the problem of shock amplification could be eliminated by replacement of low-frequency isolators with high-frequency isolators of equivalent load rating, if the correspondingly lower vibration isolation efficiencies could be tolerated. Therefore when a compromise must be made between high isolation efficiency and high shock amplification of typical MIL-C-172C type isolators, and lower isolation efficiency and minimum or no shock amplification of high-frequency isolators, cognizant personnel have selected the latter alternative in many instances, particularly in jet engine aircraft applications, in spite of the fact that the vibration isolation efficiency requirements of MIL-C-172C are violated.

The low shock transmissibility of higher frequency isolators notwithstanding, their inherently lower isolation efficiency precludes their use on:

1. Existing items of equipment that have been qualification tested on low-frequency isolators, without requalification testing to establish that the item of equipment could withstand the higher vibration levels transmitted;

2. Items of equipment on board piston engine aircraft, due to the likelihood of excessive resonant excitation by the low forcing frequencies of the piston engine and propeller; and

3. Particularly sensitive items of equipment requiring the highest practical degree of isolation efficiency.

A need was thus evident for improved vibration isolators combining the superior vibration isolation characteristics of low-frequency isolators with the low shock amplification characteristics of high-frequency isolators, within the dimensional requirements of MIL-C-172C.

ISOLATOR DEVELOPMENT PROGRAM

In appreciation of the possibility of achieving a major increase in the reliability of airborne electronic equipment in operational aircraft without airframe or equipment modification, a program aimed at the development of improved isolators was undertaken.

Shock and Vibration Incompatibility

It is well established that no basic incompatibility exists between effective shock and vibration isolation; rather, a good vibration isolator could also be a good shock isolator (depanding on ratio of shock pulse duration to natural period of the system), if unlimited isolator deflection were permitted. However, the extremely limited sway space available in most aircraft installations precludes the use of isolators with large deflections; rather, shock deflection of typical low-frequency commercial isolators is severely limited by very stiff snubber cushions.

Since unlimited deflection of an isolator allows effective shock isolation, and deflection

limited by abrupt bottoming on a stiff snubber element produces shock amplification, there obviously exists some minimum deflection for which some combination of stiffness and damping characteristics will produce neither shock isolation nor amplification (i.e., unity shock transmissibility). Clearly, the possibility of designing low-frequency vibration isolators with no significant tendency to amplify long-duration shock pulses is dependent on whether this minimum amount of deflection exceeds the prevailing isolator defection limitations.

Computer Shock Transmissibility Analysis

As the first phase of the isolator development program, a variable parameter analog computer study of a nonlinear single-degree-of-freedom spring-mass system was performed to determine the lowest amplification of a 12-g, 125-millisecond half-sine shock pulse which could be obtained within the implicit deflection limitations of MIL-C-172C. Imposed conditions included 9-cps resonant frequency, a minimum of 2-g deflection capability in the linear range (i.e., 1 g above the static weight of the mounted equipment), and 0.25-inch maximum total deflection.

A schematic diagram of the single-degree-of-freedom system investigated in the analysis is shown in Fig. 2. The general equation governing the response of this system to excitation of the base is

$$M\ddot{z} + B(\dot{z}) + R(z) = -M\ddot{u}. \qquad (1)$$

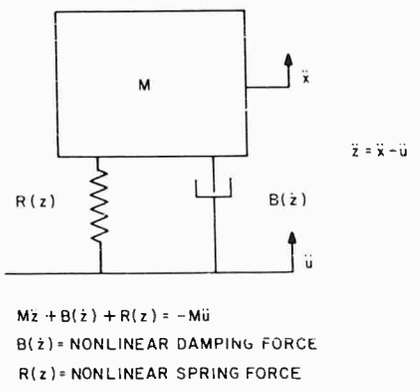

Fig. 2 - Nonlinear single-degree-of-freedom system, and associated forced response equation

Stiffness corresponding to the 9-cps natural frequency and viscous damping corresponding to 15 percent of critical (typical of commercial isolators) were assumed for the initial linear range in all cases.

Various second-stage combinations of nonlinear elasticity and damping were considered. The nonlinear elasticity investigated included bilinear hardening springs with various second-stage stiffnesses, (Fig. 3) and linear—constant-force springs that develop various constant restoring force levels (Fig. 4). The nonlinear damping investigated included viscous damping in the initial linear range, in effect at all amplitudes of motion, plus a stepped damper, either viscous or friction, in effect only during motion in the second stage.

The study revealed two configurations which, when subjected to a 12-g, 125-millisecond pulse, limited the response to approximately 13 g, corresponding to a transmissibility of 1.08, within

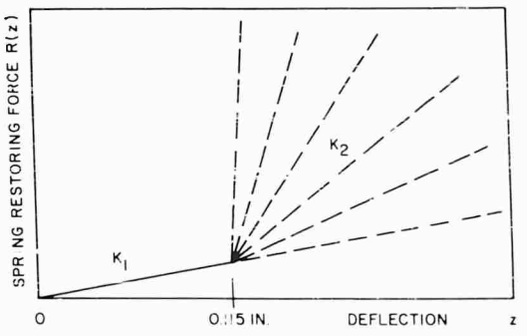

Fig. 3 - Bilinear hardening springs with various second-stage stiffnesses

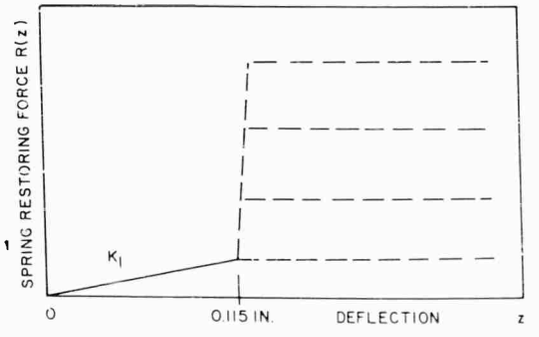

Fig. 4 - Linear-constant force springs with various constant restoring-force levels

a total deflection of approximately 0.25 inch. One of the configurations included a bilinear hardening spring with a stepped viscous damper, and the other a constant force spring with a stepped friction damper. The study also revealed a system response of 31 g for a configuration incorporating a stiffness ratio actually measured on a typical commercial low-frequency isolator. Computer traces comparing the responses of the best bilinear isolator and the typical commercial isolator are shown in Fig. 5. Complete details and results of the computer study are given in Ref. [1].

The computer shock transmissibilities of 1.08 strongly indicated that the goal of a shock transmissibility approaching unity was realizable in a practical isolator configuration.

Verification of Computer Results

The next phase of the program was an attempt to verify experimentally the results of the analog computer study. A mechanical model mounting system was assembled (using commercially available tube- and plate-form rubber isolators) to simulate the optimum nonlinear damping and stiffness characteristics of the mathematical model as closely as possible.

The mounting system was loaded with a mockup of appropriate weight and was subjected to 125-millisecond half-sine shock pulses of four different magnitudes, on a shock test machine specially built to produce long-duration shock pulses. Shock transmissibilities between 1.00 and 1.10 were recorded. Good agreement with the computer transmissibilities was thus obtained, in spite of the fact that it was not practical to make all computer and test conditions identical. For example, in the computer study, the test specimen was assumed to be in a 1-g condition at the time the shock pulse was applied; this is representative of actual constant-sink-speed landings. In the free-fall laboratory tests, the specimen was in a zero-g (weightless) condition while falling, and hence tended to rise above the static equilibrium position by an amount equal to the static deflection; thus, at the instant of impact the distance between the lower snubber and the spring-seat disk, and hence, the impacting velocity and resulting acceleration were greater than under the 1-g condition.

The possibility of developing low-frequency vibration isolators which would limit transmissibility of long-duration shock pulses to approximately unity, within the imposed excursion limitation, was thus verified experimentally as well as analytically.

Design of Practical Isolators

The final phase of the isolator development program was the design and development of a practical isolator meeting all dimensional and performance requirements of MIL-C-172C and also limiting shock transmissibility to approximately unity.

Of the two configurations of the computer study producing the lowest response, the bilinear configuration was considered preferable since a bilinear spring can be more readily designed and fabricated than a linear-constant force spring. Also, the bilinear configuration was less sensitive to variations in second-stage damping ratio. Therefore, an isolator with the following characteristics was selected as the design objective:

1. Linear range stiffness corresponding to 9-cps natural frequency,

NOTE: Reference appears on page 183.

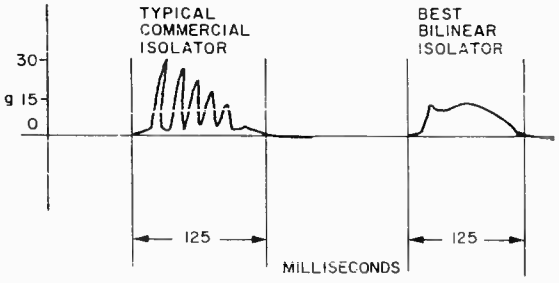

Fig. 5 - Comparison of theoretical responses of typical MIL-C-172C isolator and best bilinear isolator

2. Linear range allowable deflection (beyond static deflection) = 0.115 inch,

3. Ratio of second- to first-stage spring stiffnesses = 10,

4. First-stage critical damping ratio = 0.15, and

5. Second-stage critical damping ratio = 0.40.

Of the various isolator designs conceived and judged on the bases of anticipated mechanical complexity, cost and weight, the design shown in Fig. 6 was selected. The isolator consists basically of a spring, upper and lower snubber cushions, and three-stage amplitude-sensitive friction damper assembly. These components are described below.

For simplicity of design and fabrication, a helical music wire compression spring was selected as the first element of the bilinear spring.

The small rubber snubber, housed within the compression spring, constitutes the second element of the bilinear elasticity. Shock motions exceeding the linear range of the isolator compress the snubber between the isolator core and the spring-seat disk attached to the baseplate. As was expected, a snubber cushion of suitable size could not be fabricated with stiffness and damping characteristics exactly equal to the design objective values. Rather, the values were used as a guide in determining general proportions of the simple cylindrical snubber cushion (cut from a silicone rubber compound used in commercial high-frequency isolators). The load-deflection characteristic of the snubber more nearly resembled parabolic than linear elasticity, and its equivalent viscous damping ratio of approximately 0.17 was substantially less than the theoretical ratio of 0.40.

The three-stage amplitude-sensitive damper was developed to enhance the vibration rather than the shock transmissibility characteristics of the isolator under both high and low vibration amplitudes. The motivation was the fact that typical commercial friction-damped isolators, which contain only a single damping assembly adjusted to limit resonant amplification to 5 or less at 0.060-inch impressed excursion (per MIL-C-172C), are significantly overdamped at 0.020-inch excursion and grossly overdamped at very small excursions of, e.g., 0.002 inch. Consequently, at 0.020-inch excursion, isolation efficiency is compromised, and at 0.002-inch excursion, the isolator is to a large measure "shorted-out." By contrast, the three-stage amplitude-sensitive damper provides three different damping levels, namely zero, light, and heavy damping for small, intermediate, and large amplitudes of vibration, respectively, in both axial and radial directions. The damping levels were adjusted to provide minimum resonant amplification and maximum isolation of each of the three different vibration spectra of MIL-C-172C (0.020-inch double amplitude, 5 to 55 cps; 0.060-inch double amplitude, 5 to 55 cps; and ± 10 g vector, 55 to 500 cps), consistent with the least compromise in isolation of the other two spectra. Since the primary purpose of this paper is to discuss improvement of shock characteristics (which are not significantly affected by linear range damping characteristics), operation of the damper assembly is not described here. However, its operation may be deduced from Fig. 6.

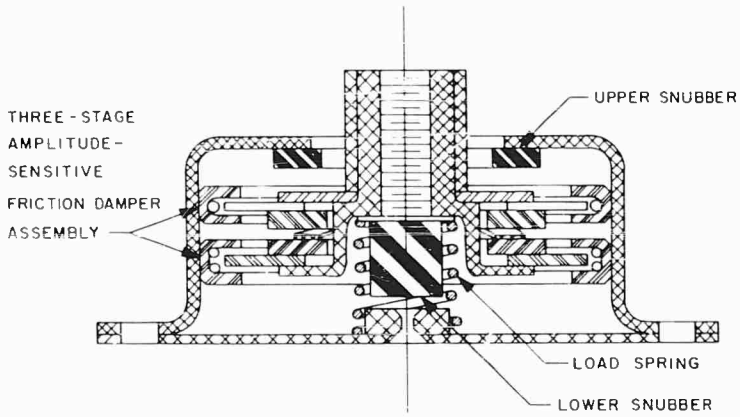

Fig. 6 - Cross section of GAEC improved MIL-C-172C type low-frequency isolator

As would be intuitively expected, the results of the analog computer study indicated that shock amplification increases with increase in clearance between the snubber cushion and the spring-seat disk. Accordingly, this clearance must be held as small as possible, consistent with clearance necessary to accommodate vibration at resonance and moderate dynamic loads imposed during gentle maneuvers (taken at 1 g in the computer study); any reduction in this clearance (due to overloading) would reduce shock transmissibility but would cause repetitive bouncing off the lower snubber cushion during vibration at resonance, whereas any increase in clearance (due to underloading) would both increase shock transmissibility and cause repetitive bouncing off the upper snubber cushion. It is apparent that accuracy of isolator loading and shock and vibration performance are closely related. This indicates that application of the shock optimization techniques discussed here would be more successful if applied to MIL-C-172C Class B isolators (where deflections are related to ± 15 percent deviation from rated load) than if applied to Class A isolators (where deflections are related to two-to-one load range). However, restriction of isolator selection to Class B types is not considered to be a serious limitation when applying isolators to items of equipment whose weights are even approximately known. The relatively widespread use of Class A isolators stems from logistic rather than technical considerations.

The springs of the experimental isolators used in the shock and vibration tests were designed for the specific load to be supported, within generous tolerances; shock and vibration performance of the isolators probably would not have been significantly affected at any loading within 15 percent of the design loading.

Test Procedures and Results

An experimental mounting system consisting of four isolators attached to an aluminum rack was assembled and loaded with a suitable mockup of an equipment. Shock and vibration transmissibility characteristics of the mounting system were optimized during alternate shock and vibration development tests in which trial and error changes were made in axial-to-radial spring stiffness ratio, axial and radial friction damping forces, lower snubber stiffness and snubber clearance.

The optimized configuration was subsequently subjected to MIL-C-172C vibration transmissibility tests; transmissibilities were generally very low and within allowable values under all test conditions. The configuration was then subjected to a series of 125-millisecond shock pulses in the vertical direction; included were shock pulses of different g levels intended to simulate different aircraft landing conditions. Peak shock transmissibilities recorded are given in Table 1.

TABLE 1
Results of Vibration Testing of Optimized Mounting System

Input[a] (g)	Response (g)	Transmissibility
12.0	14.8	1.23
9.0	12.0	1.33
6.7	9.2	1.37
5.0	6.8	1.36

[a] 125-millisecond pulses.

In view of the differences in damping and elasticity characteristics, as well as test conditions (zero g vs 19), between the experimentally and theoretically optimized isolators, agreement between predicted and measured shock responses is considered good.

As a comparison, Fig. 7 shows the oscillographic traces of the responses (to 12-g, 125-millisecond input pulses) of typical commercial isolators and the improved isolators. The large reduction in overall shock intensity and the marked reduction in peak accelerations are clearly evident.

CONCLUSIONS AND RECOMMENDATIONS

It has been demonstrated that it is possible to fabricate improved low-frequency vibration isolators which operate effectively under high and low vibration amplitudes and also have no significant tendency to amplify long-duration shock pulses, within the dimensional limitations of MIL-C-172C. It is accordingly reasonable to expect that the replacement of commercial low-frequency isolators in existing equipment installations in operational aircraft with improved isolators would produce a significant increase in equipment reliability, without aircraft or equipment modification.

It is recommended that airframe manufacturers encourage the use of improved isolators, in appropriate circumstances, in both existing and future airborne electronic equipment installations.

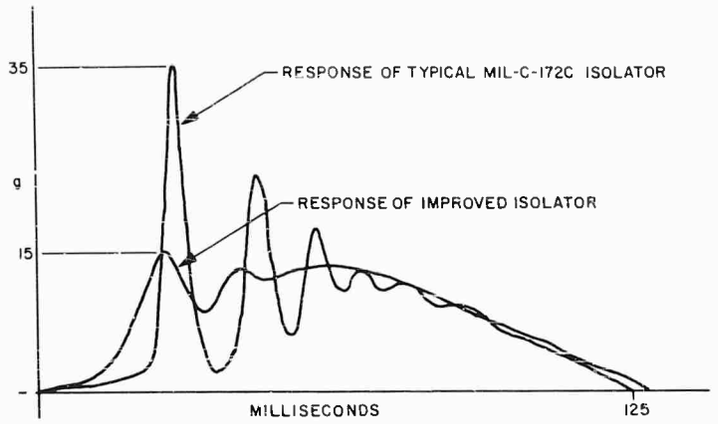

Fig. 7 - Comparison of measured responses of typical MIL-C-172C isolator and GAEC improved isolator

REFERENCE

1. Louis J. Pulgrano, "An Analog Computer Study of the Shock Response of Nonlinear Resilient Mounting Systems," Grumman Aircraft Eng. Corp. Note ADN 03-06-62.1 (Sept. 25, 1962).

DISCUSSION

Mr. Mullen (NADC): How about lateral isolation? I didn't see anything but snubbing for the lateral direction. You just had a vertical isolator there, and most aircraft shocks I'm sure are not vertical.

Mr. Balan: Well that is an excellent question. The diagram did show a snubber cushion which is operative in a lateral direction. As part of the program, which I did not describe here, we are attempting to optimize the response in the lateral direction as well as in the forward direction. It is important that we optimize the lateral characteristics as well as the vertical particularly since we are dealing with Naval aircraft where we have catapult launch and arrestment. However I can say that the acceleration levels in either catapult or arrestment are not nearly as severe as the vertical acceleration. Therefore we concentrated on that first, but we are taking care of the item that you mentioned.

* * *

PROTECTING THE "EYES" OF THE OAO SATELLITE*

J. T. Gwinn, Jr.
Lord Manufacturing Company
Erie, Pennsylvania

In addition to isolating and withstanding high levels of booster shock, vibration, and directionally combined acceleration loads, the OAO spectrometer instrument package isolation system had to be constructed in an unorthodox configuration.

Some established principles from classical vibration theory were combined with a new idea for providing truly velocity-sensitive system damping. The latter was necessitated by stringent displacement returnability requirements. Design, development, and testing of such a system proved successful, and a summary of system performance results is presented.

Basic theory for the design of velocity sensitive dampers which employ the shearing of thin fluid films is also presented.

Introductory comments orient the topic and discuss the nature of the overall system design problem before focusing on the theory of thin-film fluid-shear dampers. Substantial viscous damping forces can be achieved with such devices with relatively small expenditures in size and weight; specific examples illustrate this point.

PROBLEM BACKGROUND

The Orbiting Astronomical Observatory (OAO), a large 3600-pound satellite carrying a stabilized telescope platform, will survey the entire sky in three spectral bands, catalogue over 100,000 stars, and take spectrometric data on various celestial bodies starting with its first orbit in 1965. In accomplishing this feat, the dynamic environment to which this vehicle will be subjected will include uncommonly high levels of booster shock and vibration combined with multi-direction steady acceleration loading.

The spectrometer instrument package is the heart of this space vehicle and performs the fundamental task of converting the light signals into data which can be telemetered back to earth.

Protecting the instrument package from the dynamic environment was accomplished in a rather unorthodox fashion made necessary by the functional requirements of the spectrometer installation.

As shown in Fig. 1, the spectrometer package is "hung" in the telescope bore. The package and attached "spider legs," which are used to conduct heat to the spacecraft structure, partially obscure the incoming light rays.

Thus in designing a shock and vibration control system, the fundamental problem was to support the instrument package flexibly without obscuring any more of the bore cross section. This meant that the isolation system components had to be within the "shadow" of the instrument package elements. Obviously, conventional isolator configurations could not be employed.

In addition, while the suspension system had to permit relative motion of the spectrometer package with respect to the supporting structure (up to 3/8-inch amplitude) it still had to return the package within extremely small

*This paper was not presented at the Symposium.

tolerances of translational and rotational static displacement (Fig. 11) so that optical performance would not be impaired. The dynamic inputs and important performance requirements are given in Table 1.

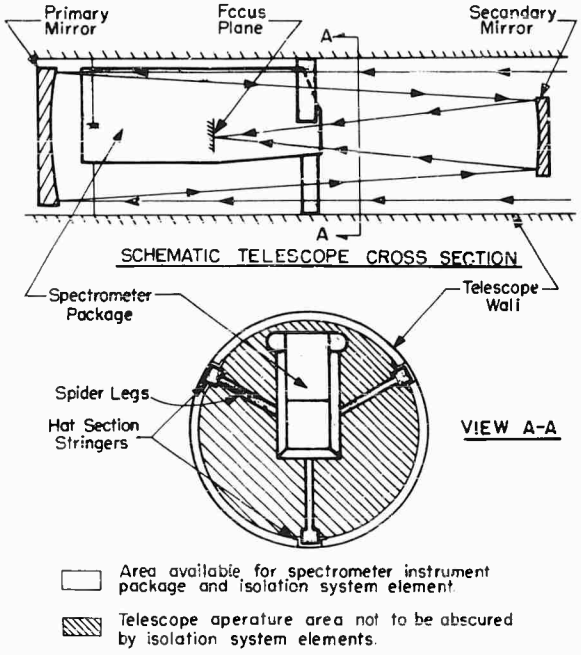

Fig. 1 - Schematic spectrometer instrument installation

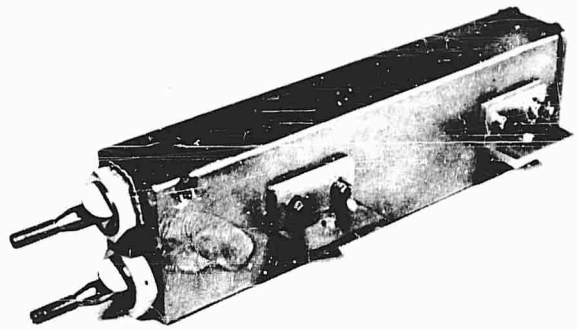

Fig. 2 - Spring-damper assembly

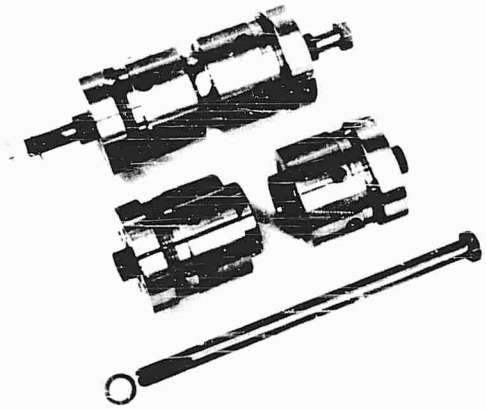

Fig. 3 - Elastomer isolator assembly and subassemblies

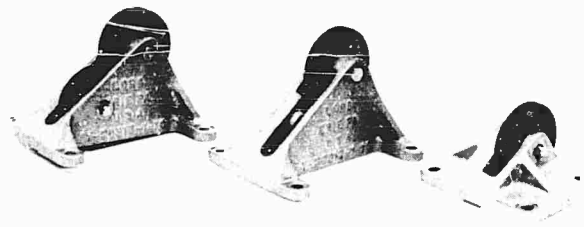

Fig. 4 - Sheave-bracket assemblies for routing cables from spring-damper assemblies to spectrometer instrument package

COMBINATION SYSTEM USED

A combination of elastomeric and viscous damped metallic isolators was used. The total system is comprised of six dual spring-damper assemblies, each attached by cables to the spectrometer package, plus four elastomeric isolators. This results in 16 attachment points between the package and the supporting structure. The elastomeric mountings provide about 40 percent of total suspension stiffness while the cable-spring-damper assemblies furnish the remaining 60 percent. The center of suspension system elastic and damping forces coincide with the instrument package center of gravity to provide decoupled modes of vibration. Figures 2, 3, and 4 show the main isolation system components and Figs. 5, 6, and 7 show the isolation system installed in the telescope tube with the spectrometer instrument package.

The system natural frequency of this arrangement is approximately 25 cps in all directions. This provides more than adequate high frequency isolation while affording a high degree of suspension stiffness to minimize sway space under dynamic conditions. A lower frequency system would have required greater clearances for dynamic response displacements. The 25 cps natural frequency is also low enough

TABLE 1
A Summary of Dynamic Inputs and Requirements for the
OAO Spectrometer Instrument Package Isolation System

Item No.	Description	Specification and Remarks
1	Sinusoidal Vibration Input	1/2" D.A., 5-10 cps 2.5" G, 10-50 cps 5 G, 50-400 cps 7.5 G, 400-3000 cps (approximately the same for all three coordinate axes[a])
2	Random Vibration Input	0.03 G^2/cps 15-75 cps 0.12 G^2/cps 75-500 cps 0.03 G^2/cps 500-2000 cps (approximately the same for all three coordinate axes[a])
3	Shock Input (Both Directions) (Three Times Each Axis)	8.5 G, 12 ms half-sine pulse - X axis 2.1 G, 10 ms half-sine pulse - Y and Z axes
4	Acceleration Inputs (Combined To Occur Simultaneously)	X Axis / Y Axis / Z Axis / Duration (min) +11.3 g / +2.3 g / --- / 4.5 +11.3 g / -2.3 g / --- / 4.5 +11.3 g / --- / +2.3 g / 4.5 +11.3 g / --- / -2.3 g / 4.5 - 3.0 g / +2.3 g / --- / 4.5 - 3.0 g / -2.3 g / --- / 4.5 - 3.0 g / --- / +2.3 g / 4.5 - 3.0 g / --- / -2.3 g / 4.5
5	Combination of Environments	Sinusoidal vibration combined with acceleration as given above.
6	Vibration Response	Maximum vibratory acceleration of mounted body is not to exceed 20 g, measured at location of and in direction of maximum acceleration (includes translational and rotational accelerations). Also see Fig. 10.
7	Shock Response	Shock response not to exceed 12.5-g peak.
8	Sway Space Limits	Translation (in.) / Rotation About Centroidal Axes (rad) X Axis, ±.38 / X Axis, $\pm 15 \times 10^{-3}$ Y Axis, ±.18 / Y Axis, $\pm 20 \times 10^{-3}$ Z Axis, ±.38 / Z Axis, $\pm 15 \times 10^{-3}$ NOTE: Sway space is defined as the total available envelope for Dynamic Response. The translational and rotational components of package motion in combination, including the deflections produced by steady-state acceleration forces must not exceed this envelope.
9	Returnability Limits	Upon removal of the dynamic environment specified in Items 1 through 5, the mounted body must return to its original equilibrium position within the limits specified in Fig. 11.

[a]Identification of Axes: X Axis - Telescope tube center line and booster thrust axes.
Y Axis - Telescope tube lateral axis and booster pitch axis.
Z Axis - Telescope tube lateral axis and booster azimuth axis.

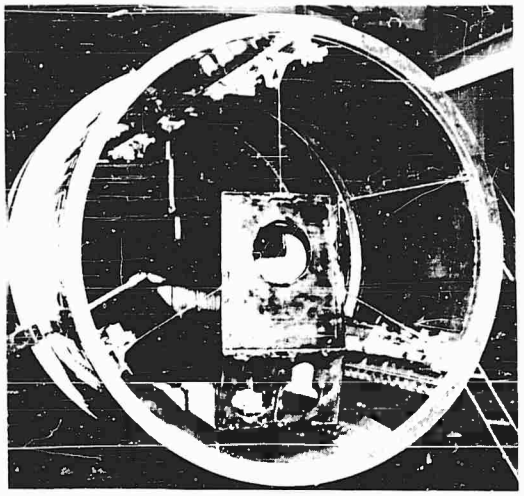

Fig. 5 - Isolation system installation, looking forward

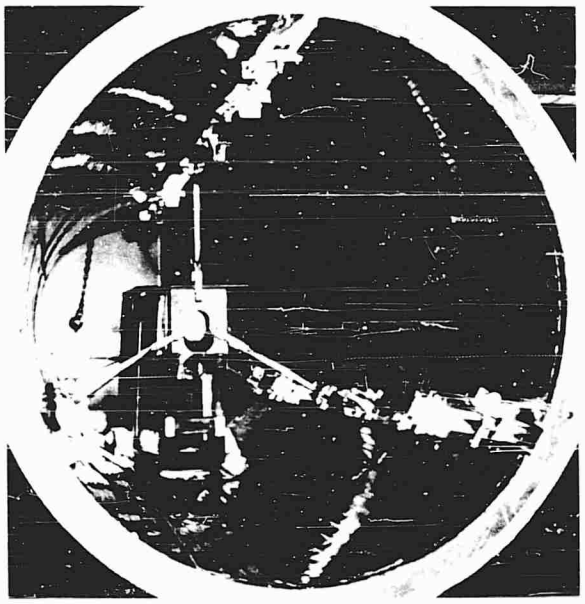

Fig. 6 - Isolation system installation, looking aft

to avoid problems with the fundamental instrument package and support structural modes, which were found to exist from 50 cps on up.

The geometric distribution of elasticity in the isolation system results in center of gravity support and high rotational constraint. The comparatively small elastomeric isolators, which support the equipment near its mid-point work out well with the severe limits on installation

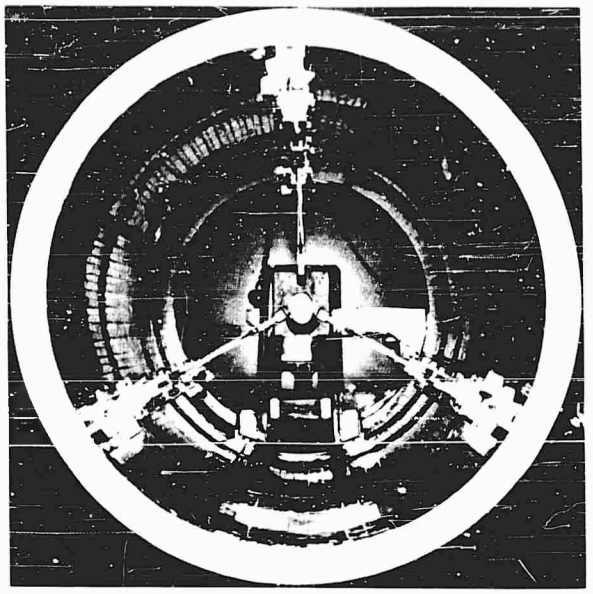

Fig. 7 - Isolation system installation, looking aft, head-on

space in that area. Viscous dampers in that part of the isolation system which provides most of the rotational constraint were necessary in order to optimize rotational displacement returnability.

VISCOUS DAMPER DETAILS

The means for achieving truly velocity-sensitive damping in the spring-damper assemblies is new and results in considerable economy in installation space.

Viscous, or velocity sensitive damping, may be obtained by the shearing of a film of Newtonian fluid. Such damping is desirable in shock and vibration control systems which must also maintain the precise translational and rotational position of the protected equipment. It minimizes the effect of residual static forces due to friction and/or hysteresis in the suspension system, which, in turn, affect returnability. Such damping utilized with closely matched elastic elements and arranged in a fashion so that the center of elastic and damping forces coincides with the equipment center of gravity assures decoupled dynamic response modes and maximum displacement returnability.

A determination of the damping force for a fluid shear damper composed of concentric rigid tubes follows (see Fig. 8). When the outer tube is displaced at velocity v, the shear stress in the film is

$$\tau = \mu \frac{\partial V}{\partial y} , \qquad (1)$$

the partial derivative, of velocity V, with respect to the film thickness y (or the velocity gradient) times the absolute viscosity. For the two concentric tubes this form of Newton's hypothesis may also be written as

$$\frac{F_D}{A} = \mu \frac{V}{t_o} . \qquad (2)$$

where

F_D = the damping force (lb),

A = area of fluid film being sheared (sq in.),

V = velocity of the moving tube (ips),

t_o = fluid film thickness (in.), and

μ = absolute viscosity (lb-sec/in.^{2}).

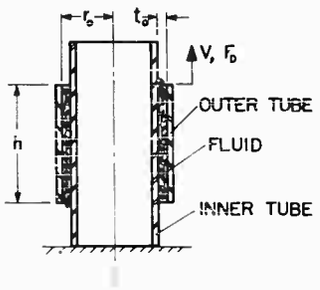

Fig. 8 - Schematic fluid-shear damper cross section and terminology

Since, for concentric tubes

$$A = 2\pi r_o h , \qquad (3)$$

$$\frac{F_D}{2\pi r_o h} = \mu \frac{V}{t_o} \qquad (4)$$

and

$$F_D = 2\pi r_o h \mu \frac{V}{t_o} . \qquad (5)$$

In terms of kinematic viscosity, a more common term,

$$\nu = \frac{\mu}{\rho} \qquad (6)$$

and

$$F_D \quad \frac{2\pi\nu\rho r_o h V}{t_o} , \qquad (7)$$

where ρ = mass density (lb-sec^2/in.^{4}).

NOTE: Kinematic Viscosity (Centistokes) = $(0.145 \times 10^{-6}) \times$ Absolute Viscosity (lb-sec/in.^{2}) for water with a specific gravity of 1 at standard conditions.

For viscous damping, the damping coefficient C is

$$C = \frac{F_D}{V} = \frac{2\pi\nu\rho r_o h}{t_o} . \qquad (8)$$

This formula may be used for design purposes and has proven to be accurate within about 10 percent for normal conditions of temperature and pressure. Examination of Eq. (8) indicates that to maximize C, the damping coefficient of such a device, highly viscous fluids and very thin films will optimize a given geometric configuration.

Considering the fact that most fluids show a variation of viscosity with temperature, it may be desirable to include "temperature compensation" in those cases where significant changes in C are undesirable. This is accomplished by choosing different materials for the inner and outer tubes so that changes in viscosity are offset by changes in film thickness for a given temperature variation. In other words, the ratio of kinematic viscosity to film thickness is approximately constant. Limits on r_o and h, the need for a given damping force F_D, along with the choice of available tube materials and fluids, of course, establish the practical bounds within which one must work.

Actual parts have been constructed where the variation in C over the temperature range of 0 to 200°F was within ± 20 percent.

Figure 9 shows the cross section details of the spring-damper assembly of Fig. 2. Note that in this particular design flexible elastomeric end seals were used to contain the damping fluid and allow motion of the tube within the housing bore. The damper is, of course, in parallel combination with the load spring. Dimensions and performance data for this damper are given below the cross section.

The peak damping force which can be generated by such a device is comparatively large considering the volume occupied by mechanical parts and the amount of fluid required. For instance, suppose a damper with a peak force of 100 pounds at a peak velocity of 10 inches per second in as small a space as possible is needed. If concentric cylinders with a bearing diameter of 1 inch are used and the gap is set at 0.005 inch, which is a minimum considering

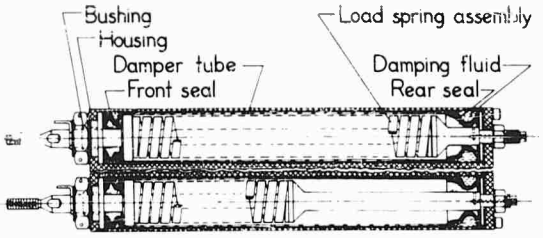

DAMPER DETAILS

Nominal gap - .021 inch, Tube length 8¼ inch
Fluid kinematic viscosity - 100,000 centistokes
damping coefficient - 6.5 lb sec/inch
damping force - 78 lb @ 12 in/sec peak velocity

Fig. 9 - Cross section details of spring-damper assembly

the practical tolerances of normal shop procedures, the length required will only be 1-1/8 inch if fluid of 100,000 centistokes viscosity is used. Certainly this illustrates the economy of space resulting from the use of this device.

PERFORMANCE

A complete assembly of spectrometer package and isolation system was qualification tested, and the vibration and returnability performance data are of particular interest.

Figure 10 shows the transmissibility characteristics of the spring-damper assemblies and the elastomeric isolators and compares these to the transmissibility of an idealized viscous damped system with the same natural frequency and peak transmissibility. Note that the transmissibility of these parts in the high frequency region is greater than would be expected from theory.

This may be attributed to the amplitude-sensitive elastic modulus of the damping fluid in the spring-damper assembly, and to nonlinear hysteresis damping in the elastomeric isolators.

That is, the fluid film exhibits both elastic and damping reactions when sheared as explained above, and the elastomer has strain and frequency dependent dynamic elastic and dynamic damping moduli. The result is that, in practice, actual performance in the isolation range is not as good as calculated performance based on an idealized system. The difference, however, is not enough to be of critical significance in most applications considering the advantages of small space and low weight of mechanical parts.

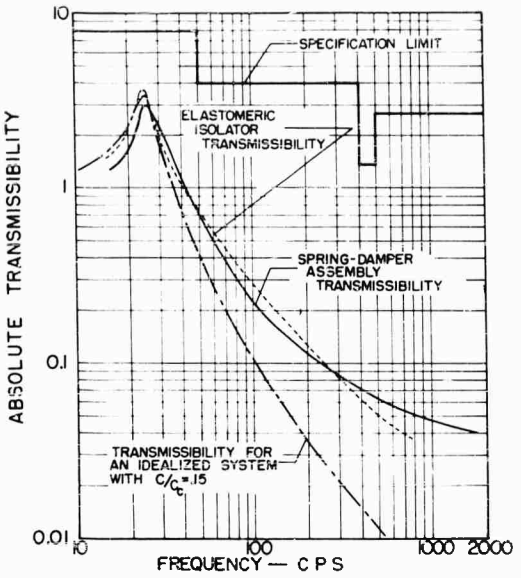

Fig. 10 - Transmissibility curves for isolation system components compared to theoretical equivalent viscous damped system

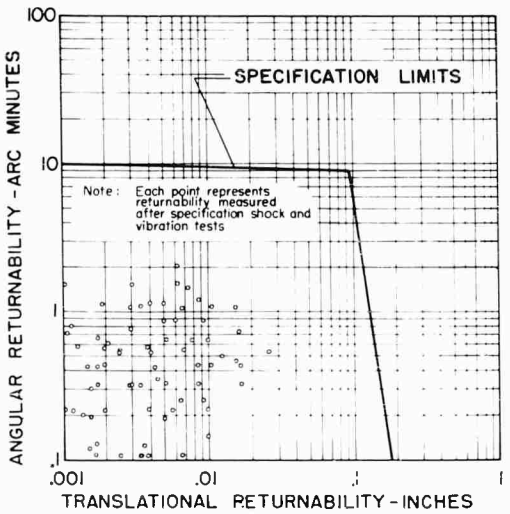

Fig. 11 - Returnability data obtained by test compared to specified limits

The returnability data shown in Fig. 11 are an order-of-magnitude better, in most cases, than the performance limits allowed. This and the foregoing discussions are good reason to consider the type of isolation system described here, for applications having similar requirements, in missiles and space vehicles.

ACKNOWLEDGMENT

The cooperation of the Perkin Elmer Corporation and the assistance and counsel of project engineer, James Greed, and task manager, Werner Loening, during the course of the design and testing of the OAO spectrometer instrument package isolation system is gratefully acknowledged.

* * *

DESIGN OF FOCALIZED SUSPENSION SYSTEMS*

L. S. Pechter and H. Kamei
Autonetics
Division of North American Aviation, Inc.
Anaheim, California

In designing isolation systems, the location of the isolators determines, to a large extent, the amount of decoupling possible in the six modes of vibration. Maximum decoupling is accomplished when the isolators are located so that their elastic centers coincide with the center of gravity (cg). When the elastic center is located away from the cg, as in the common base-mounted system, the vibration modes are coupled. Occasionally this coupling is intolerable as in a system supplying positional information, or where clearances are at a premium. To eliminate coupling, essentially, these isolators can be inclined toward the cg, thus achieving the effect of a center-of-gravity system.

This paper outlines isolation system requirements for a base-mounted system where any number of isolators may be used and where all the isolators are focused toward the cg. The description will be limited to the case where the isolators are all coplanar and have radial symmetry about the axis perpendicular to the plane and passing through the cg.

INTRODUCTION

High accuracy is an extremely important parameter of navigation systems. By use of digital computers, the vehicle's present position can be determined from inertial instrument outputs. Unless however, the inertial instruments are precisely aligned and shielded from the environment, the computational accuracy is of little value. At the heart of the problem is the stable element, a structure which provides mounting surfaces and relative alignment of the inertial instruments. A gimbal system isolates the stable element from the angular motion of the vehicle, while isolators may be employed in the gimbal system to reduce the level of vibration seen by the instruments. The total system is called a stable platform.

The conventional design of a gimbal system is one where the ring gimbals (or at least the outer ring gimbal) are located outside the stable element package. The center of gravity of the stable platform is invariably located within the gimbal rings and, therefore, the isolators can be symmetrically located in a plane passing through the center of gravity. With this design, a decoupled system can be obtained.

Another type of gimbal system has been developed for use with an inverted stable element. That is, the stable element is packaged around the outer gimbal which is reduced to half a ring (or a yoke) and cantilevered from the vehicle structure. This unique design has many advantages but is least desirable from a vibration standpoint in that it dictates that the suspension system be base-mounted. The base-mounted system, being cantilevered, permits a large amount of coupling between translation and rotation. Effects of this coupling are realized in the excessive amount of sway space required and, if the system is providing fire-control information, the angular position errors introduced under translatory vibration.

*This paper was not presented at the Symposium.

When a body is subjected to a translatory motion, the resultant of the applied forces is directed through the center of gravity. The rotation of the body when supported by isolators, occurs about the elastic center of the isolators; only the forces passing through this point will remain uni-directional (i.e., not couple with the other directions). To separate translation from rotation, the two centers must be coincident [1]. Where the isolators are located away from the cg, as in the base-mounted system, the centers can be made to coincide by inclining the isolators toward the cg and by selecting the stiffnesses such that the isolator becomes anisoelastic [2]. The following discussion outlines the requirements for a base-mounted system using any number of isolators and the location in which isolators are to be focused on the center of gravity.

BASIC RELATIONSHIPS

Figure 1 shows a rigid body with its principal axes, X, Y, and Z, passing through the cg. The body is supported by isolators all of which are located in a plane parallel to the X and Z axes and displaced a distance "a" below the cg. The isolators are focused toward the cg, so that the elastic center and cg are coincident. The orientation of the isolator with respect to the mass is shown in Fig. 2. Its position can be described by the angle of inclination of its principal axis, p; from the system Y axis, α; and the angle of rotation about the Y axis, β. The isolator is located a radial distance "r" from the cg. The principal axis is assumed to be parallel to the X-Z plane, and the other principal axis, q, is perpendicular to both p and r.

For the purpose of this analysis, the following assumptions are made:

1. All isolators have the same stiffness properties.

2. All isolators have the same angle of inclination to the vertical.

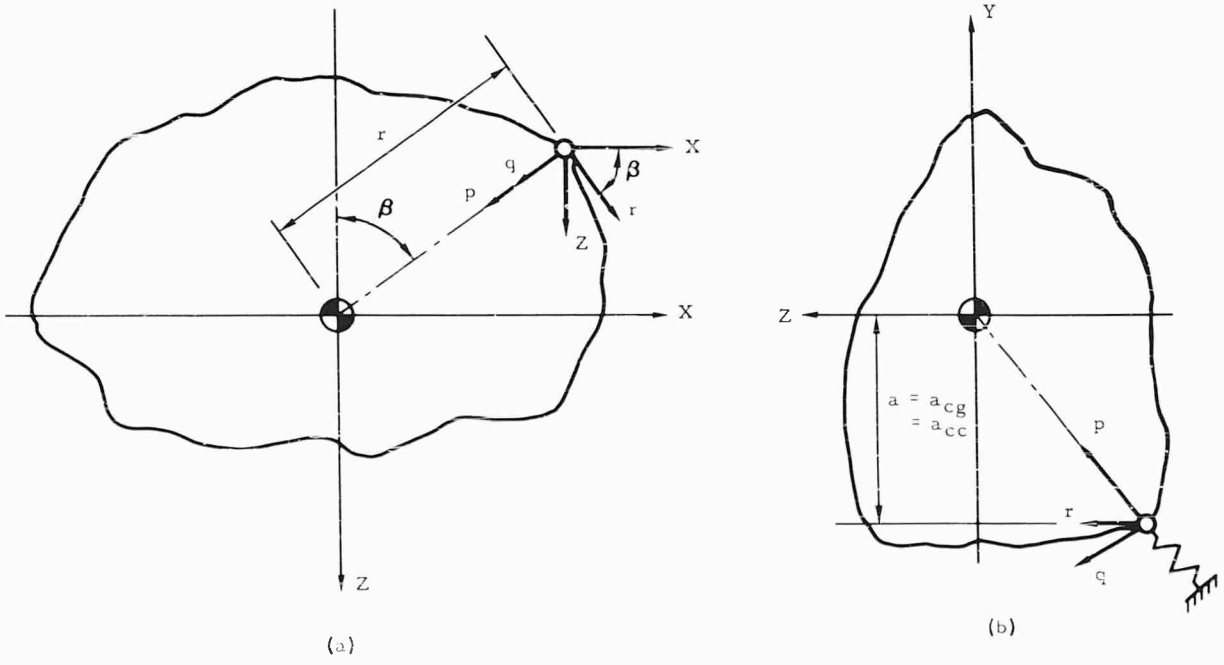

Fig. 1 - Rigid body at rest supported by resilient elements. A typical element is shown. The principal axes of the resilient elements, p, q, r, are inclined to the principal axes of the body, X, Y, Z. A plan is shown in (a) and an elevation is shown in (b).

NOTE: References appear on page 207.

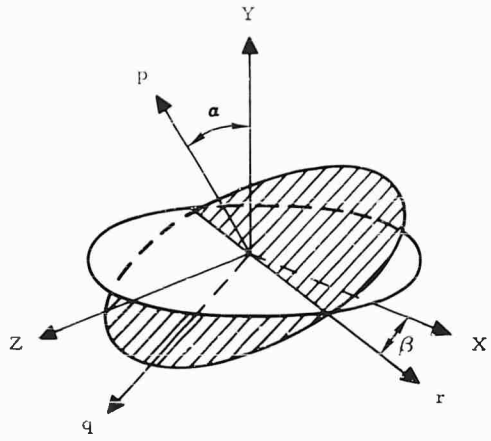

Fig. 2 - Relationship between the principal axes of the isolator, p, q, r, to the principal axes of the body, X, Y, Z.

3. The spring constants are the same for both tension and compression.

4. The isolator stiffnesses are the same along both lateral axes, q and r.

The last assumption will be utilized only in obtaining the graphical results so that the number of variables is kept to three. This assumption agrees with the common type of elastomeric mount which is circular in cross section and has two spring rates, radial and axial.

To find the elastic force of one isolator resulting from a small displacement along any of the system axes (X, Y, or Z), the displacement is first transformed to the isolator axes, multiplied by the appropriate isolator spring constants to get force, and then transformed back to system axes. For a positive displacement along the Y axis, δ_y, the forces along the isolator axes are:

$$F_{py} = K_p \delta_y \cos\alpha ,$$

$$F_{qy} = K_p \delta_y \sin\alpha , \qquad (1)$$

and

$$F_{ry} = 0 .$$

Relating these forces to the X, Y, and Z axes, the forces become:

$$F_{xy} = (K_p \delta_y \cos\alpha) \sin\alpha \sin\beta - (K_q \delta_y \sin\alpha) \cos\alpha \sin\beta ,$$

$$F_{yy} = -(K_p \delta_y \cos\alpha) \cos\alpha - (K_q \delta_y \sin\alpha) \sin\alpha , \qquad (2)$$

and

$$F_{zy} = (K_q \delta_y \sin\alpha) \cos\alpha \cos\beta - (K_p \delta_y \cos\alpha) \sin\alpha \cos\beta .$$

For a positive displacement along the X axis, δ_x, the forces along the isolator are:

$$F_{px} = K_p \delta_x \sin\beta \sin\alpha ,$$

$$F_{qx} = K_q \delta_x \sin\beta \cos\alpha , \qquad (3)$$

and

$$F_{rx} = K_r \delta_x \cos\beta .$$

These forces when related to the X, Y, and Z axes become:

$$F_{xx} = -(K_p \delta_x \sin\beta \sin\alpha) \sin\beta \sin\alpha - (K_q \delta_x \sin\beta \cos\alpha) \sin\beta \cos\alpha - (K_r \delta_x \cos\beta) \cos\beta , \qquad (4)$$

$$F_{yx} = (K_p \delta_x \sin\beta \sin\alpha) \cos\alpha - (K_q \delta_x \sin\beta \cos\alpha) \sin\alpha , \qquad \text{(Cont.)}$$

and

$$F_{zx} = (K_p \delta_x \sin\beta \sin\alpha) \cos\beta \sin\alpha + (K_q \delta_x \sin\beta \cos\alpha) \cos\beta \cos\alpha - (K_r \delta_x \cos\beta) \sin\beta . \quad (4)$$

Finally, for a positive displacement along the Z axis, δ_z, the forces along the isolator axes are:

$$F_{pz} = K_p \delta_z \cos\beta \sin\alpha ,$$

$$F_{qz} = K_q \delta_z \cos\beta \cos\alpha , \quad (5)$$

and

$$F_{rz} = K_r \delta_z \sin\beta .$$

When related to the X, Y, and Z axes, these forces become:

$$F_{xz} = (K_p \delta_z \cos\beta \sin\alpha) \sin\alpha \sin\beta + (K_q \delta_z \cos\beta \cos\alpha) \cos\alpha \sin\beta - (K_r \delta_z \sin\beta) \cos\beta ,$$

$$F_{yz} = (K_q \delta_z \cos\beta \cos\alpha) \sin\alpha - (K_p \delta_z \cos\beta \sin\alpha) \cos\alpha , \quad (6)$$

and

$$F_{zz} = -(K_p \delta_z \cos\beta \sin\alpha) \sin\alpha \cos\beta - (K_q \delta_z \cos\beta \cos\alpha) \cos\alpha \cos\beta - (K_r \delta_z \sin\beta) \sin\beta .$$

DERIVATION OF INCLINED ISOLATOR EQUATIONS

The relationship between the position of the isolators and the stiffness of the isolators is determined by setting up the moment equation for moments about each principal axis created by displacements along the other orthogonal axes. Since a decoupled system is desired, these displacements cannot produce any moments, and the equations can be equated in zero.

$$M_{zx} = r \sum_{i=1}^{i=n} F_{yx_i} \sin\beta_i + a \sum_{i=1}^{i=n} F_{xx_i} = 0 , \quad (7)$$

$$M_{xz} = r \Sigma F_{yz_i} \cos\beta_i - a \Sigma F_{zz_i} = 0 , \quad (8)$$

$$M_{yx} = r \Sigma F_{xx_i} \cos\beta_i + r \Sigma F_{zx_i} \sin\beta_i = 0 , \quad (9)$$

$$M_{yz} = r \Sigma F_{xz_i} \cos\beta_i + r \Sigma F_{zz_i} \sin\beta_i = 0 , \quad (10)$$

$$M_{xy} = r \Sigma F_{yy_i} \cos\beta_i - a \Sigma F_{zy_i} \quad 0 , \quad (11)$$

and

$$M_{zy} = r \Sigma F_{yy_i} \sin\beta_i + a \Sigma F_{xy_i} = 0 . \quad (12)$$

From Eq. (7),

$$\frac{a}{r} = \frac{-\Sigma F_{yx_i} \sin\beta_i}{\Sigma F_{xx_i}} .$$

After substituting and rearranging, the following is obtained:

$$\frac{a}{r} = \frac{1/2 \sin 2\alpha (K_p - K_q) \Sigma \sin^2\beta_i}{K_r \Sigma \cos^2\beta_i + K_q \Sigma \sin^2\beta_i + (K_p - K_q) \sin^2\alpha \Sigma \sin^2\beta_i} \quad (13) \text{ (Cont.)}$$

$$\frac{a}{r} = \frac{1/2\ (1 - K_q/K_p)\ \sin 2\alpha}{K_q/K_p + (1 - K_q/K_p)\ \sin^2\alpha + R K_r/K_p}\ ,$$

where

$$R = \frac{\Sigma \cos^2\beta_i}{\Sigma \sin^2\beta_i}\ . \tag{13}$$

Equation (8) can be solved in the same manner;

$$\frac{a}{r} = \frac{\Sigma F_{yz} \cos\beta_i}{\Sigma F_{zz}}$$

$$= \frac{1/2\ \sin 2\alpha\ (K_p - K_q)\ \Sigma \cos^2\beta_i}{K_r \Sigma \sin^2\beta_i + K_q \Sigma \cos^2\beta_i + (K_p - K_q)\ \sin^2\alpha\ \Sigma \cos^2\beta_i}$$

$$= \frac{1/2\ (1 - K_q/K_p)\ \sin 2\alpha}{K_q/K_p + (1 - K_q/K_p)\ \sin^2\alpha + \left(\frac{1}{R}\right) K_r/K_p}\ . \tag{14}$$

Since Eqs. (7) and (8) must be equal, the following relationship must exist:

$$\frac{1}{R} = R\ ,$$

$$R = 1\ , \tag{15}$$

$$\Sigma \cos^2\beta_i = \Sigma \sin^2\beta_i\ ,$$

and

$$\cos 2\beta_i = 0\ .$$

Equation (15) is a limitation on β. With this limitation, the equation for a/r for all values of β_i becomes

$$\frac{a}{r} = \frac{1/2\ (1 - K_q/K_p)\ \sin 2\alpha}{K_q/K_p + K_r/K_p + (1 - K_q/K_p)\ \sin^2\alpha}\ . \tag{16}$$

Two additional β limitations come from Eqs. (9) and (10). When the force expressions are substituted into Eq. (9) and the terms rearranged and cancelled, the resultant equation is

$$\Sigma \cos \beta_i = 0\ .$$

Similarly, Eq. (10) yields

$$\Sigma \sin \beta_i = 0\ .$$

Every term in Eq. (11) contains $\Sigma \cos \beta_i$, therefore this equation is zero. Also, every term in Eq. (12) contains $\Sigma \sin \beta_i$, thus this equation is zero. Therefore, to achieve decoupling about all axes, Eq. (16) must be satisfied, and for this equation to be valid, the following conditions are imposed on β:

$$\Sigma \cos 2\beta_i = 0\ ,$$

$$\Sigma \cos \beta_i = 0\ ,$$

and

$$\Sigma \sin \beta_i = 0\ .$$

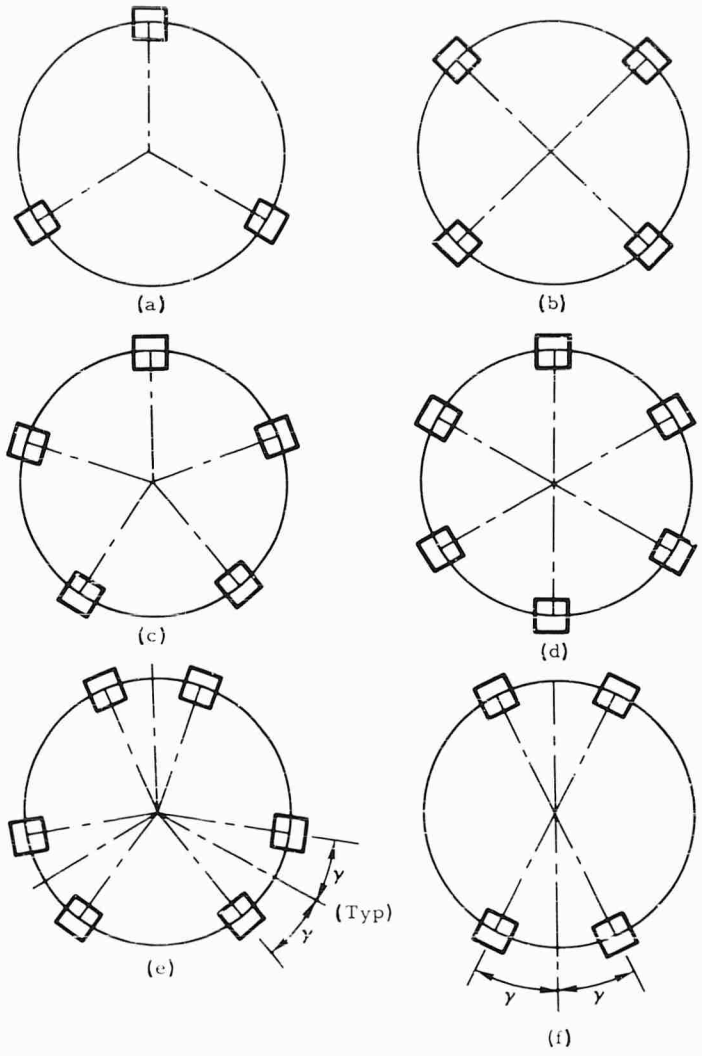

Fig. 3 - Plan view of isolators depicting several possible arrangements. (a) through (d) show three through six isolators, respectively, with equal spacing. In (e) the isolators are arranged in equally spaced pairs. In (f) the isolators have symmetrical but unequal spacing.

These conditions can be satisfied by having the isolators equally spaced around the vertical centerline as shown in Figs. 3(a) through 3(d). $\Delta\beta$, the spacing between two adjacent isolators, is equal to 360 degrees divided by the number of isolators.

Consider the arrangement in Fig. 3(f). The expressions $\Sigma \cos \beta_i = 0$ and $\Sigma \sin \beta_i = 0$ are satisfied, but $\Sigma \cos 2\beta_i$ is not. This means that the Y axis can be decoupled from the X and Z axes, but the X and Z axes cannot be decoupled from each other. Depending upon whether it is desired to decouple the Y and X axes or the Y and Z axes, Eq. (13) or (14) can be used to determine the a/r ratio for this system. The other equation is not valid as the moment is not zero.

In a similar manner, the case where the isolators are inclined in one plane only can be obtained by setting the angle, γ, equal to zero. The expression $(1/R)\ K_r/K_p$ in Eq. (14) becomes zero and

$$\frac{a}{r} = \frac{1/2\ [1 - K_q/K_p]\ \sin 2\alpha}{K_q/K_p + [1 - K_q/K_p]\ \sin^2\alpha}$$

$$= \frac{[1 - K_q/K_p]\ \tan \alpha}{K_q/K_p + \tan^2\alpha} \ . \qquad (17)$$

The primary concern of the analysis, however, is for decoupling of all modes; therefore, the remaining equations will be limited to these cases.

Figure 3(c) shows a system with six isolators arranged in three pairs. The centerlines of the pairs are equally spaced and the individual isolators of the pairs are equally spaced about the centerline. The six isolators can be located by the angles: $\beta_1 = +\alpha$, $\beta_2 = 120° - \alpha$, $\beta_3 = 120° - \alpha$, $\beta_4 = 240° - \alpha$, $\beta_5 = 240° + \alpha$, and $\beta_6 = -\alpha$. These angles will satisfy the conditions imposed by Eqs. (15), (17), and (18) which indicate that the system can be completely decoupled and that the a/r ratio is independent of the angle α. This independence can be extended to any number of isolator pairs arranged about equally spaced centerlines.

The rotational stiffness for the inclined isolator system is as follows: For a deflection θ about the X axis,

$$M_{x\theta} = r\Sigma F_{yi} \cos \beta_i - a\Sigma F_{zi}$$

$$= r\Sigma (F_{yzi} - F_{yyi}) \cos \beta_i - a\Sigma (F_{zzi} - F_{zyi}) \ . \qquad (18)$$

By substituting the expressions for F_i and by letting $\delta_z = a\theta$, $\delta_y = (r \cos \beta_i)\ \theta$ and $\Sigma \cos^2\beta_i = \Sigma \sin^2\beta_i = n/2$, the following is obtained:

$$M_{x\theta} = \frac{n\theta}{2}\left[ra \sin \alpha \cos \alpha (K_q - K_p) + (K_p \cos^2\alpha + K_q \sin^2\alpha)\, r^2 \right.$$

$$\left. + a^2 (K_p \sin^2\alpha + K_q \cos^2\alpha + K_r) + ar\,(K_q - K_p) \sin \alpha \cos \alpha\right]$$

and

$$K_{x\theta} = \frac{M_{x\theta}}{\theta} = \frac{n}{2}\left[K_q\,(r \sin \alpha + a \cos \alpha)^2 + K_p\,(r \cos \alpha - a \sin \alpha)^2 + a^2 K_r\right] \ .$$

For a deflection ϕ about the Y axis,

$$M_{y\phi} = r F_r = r(r\phi)\, nK_r$$

and

$$K_{y\phi} = \frac{M_{y\phi}}{\phi} = nr^2 K_r \ .$$

Because of symmetry, the stiffness about the Z axis is equal to that about the X axis,

$$K_{z\lambda} = K_{x\theta} \ .$$

To design an inclined isolator system, information is also required with regard to the six decoupled system natural frequencies. The ratio of the horizontal to vertical natural frequency is given by the following expression:

$$\frac{\omega_x}{\omega_y} = \frac{\omega_z}{\omega_y} = \sqrt{\frac{K_x \text{ (or } K_z)}{K_y}}$$

$$= \sqrt{\frac{K_r + K_p \sin^2\alpha + K_q \cos^2\alpha}{K_p \cos^2\alpha + K_q \sin^2\alpha}} \cdot \frac{\Sigma \cos^2 \beta_i}{n} \qquad (19)$$

For a system of equally spaced isolators,

$$\sum_{i=1}^{i=n} \cos^2 \beta_i = \frac{n}{2}.$$

The equation can now be simplified to its final form,

$$\frac{\omega_x}{\omega_y} = \frac{\omega_z}{\omega_y} = \frac{\sqrt{2}}{2} \sqrt{\frac{K_r/K_p + K_q/K_p \cos^2 \alpha + \sin^2 \alpha}{\cos^2 \alpha + K_q/K_p \sin^2 \alpha}}. \tag{20}$$

The natural frequency ratios for rotation are:

$$\frac{\omega_{x\theta}}{\omega_y} = \frac{K_{x\theta}/m \rho_x^2}{\Sigma K_y/m} = \frac{K_{x\theta}}{\rho_x^2 \Sigma K_y}$$

$$= \frac{\sqrt{2}}{2} \sqrt{\frac{\left(\frac{r}{\rho_x} \cos \alpha - \frac{a}{\rho_x} \sin \alpha\right)^2 + K_q/K_p \left(\frac{r}{\rho_x} \sin \alpha + \frac{a}{\rho_x} \cos \alpha\right)^2 + \frac{a^2}{\rho_x^2} K_r/K_p}{\cos^2 \alpha + K_q/K_p \sin^2 \alpha}}. \tag{21}$$

Similarly,

$$\frac{\omega_z}{\omega_y} = \frac{\sqrt{2}}{2} \sqrt{\frac{\left(\frac{r}{\rho_z} \cos \alpha - \frac{a}{\rho_z} \sin \alpha\right)^2 + K_q/K_p \left(\frac{r}{\rho_z} \sin \alpha + \frac{a}{\rho_z} \cos \alpha\right)^2 + \frac{a^2}{\rho_z^2} K_r/K_p}{\cos^2 \alpha + K_q/K_p \sin^2 \alpha}} \tag{22}$$

and

$$\frac{\omega_{y\phi}}{\omega_y} = \frac{r}{\rho_y} \sqrt{\frac{1}{2} \frac{K_r}{K_p}} \sqrt{\frac{1}{\cos^2 \alpha + K_q/K_p \sin^2 \alpha}}. \tag{23}$$

The vertical natural frequency is given by

$$\omega_y = \sqrt{\frac{\Sigma K_y}{m}} = \sqrt{\frac{nK_p}{m}} \sqrt{\cos^2 \alpha + K_q/K_p \sin^2 \alpha}. \tag{24}$$

It is interesting to note that the frequency ratios (Eqs. (20) - (23)) are independent of the number of isolators.

GRAPHICAL PRESENTATION

By equating the two radial spring constants, K_q and K_r, the inclined isolator equations can be plotted to simplify the design procedures.

$$\frac{a}{r} = \frac{\frac{1}{2}(1 - K_q/K_p) \sin 2\alpha}{2K_q/K_p + (1 - K_q/K_p) \sin^2 \alpha}. \tag{25}$$

$$\frac{\omega_x}{\omega_y} = \frac{\omega_z}{\omega_y} = \frac{f_x}{f_y} = \frac{f_z}{f_y} = \frac{\sqrt{2}}{2} \sqrt{\frac{\sin^2 \alpha + K_q/K_p (1 + \cos^2 \alpha)}{\cos^2 \alpha + K_q/K_p \sin^2 \alpha}}. \tag{26}$$

$$f_y = 3.13\sqrt{\frac{nK_p}{W}}\sqrt{\cos^2\alpha + (K_q/K_p)\sin^2\alpha} = C\sqrt{\frac{nK_p}{W}}. \quad (27)$$

Equation (25) can be rearranged so as to facilitate the situation where a/r is the known parameter. In this case, the equation becomes

$$\frac{K_q}{K_r} = \frac{1 - a/r \tan\alpha}{1 - a/r \tan\alpha + \dfrac{2a/r}{\sin\alpha\cos\alpha}}. \quad (28)$$

These equations are plotted as Figs. 4 through 7.

A point of interest in Fig. 6 is that for an inclination angle of 54° 44.1', the system is isoelastic (equal natural frequencies in all directions) regardless of the K_q/K_p ratio.

APPLICATION

Figure 8(a) shows a section through an actual stable platform. The vibration problem for this unit was not fully appreciated until after the assembly was designed into an integral structure and first stage pre-prototype fabrication was completed. At this stage of development, any vibration isolation of the stable element would require subsequent designing around existing hardware and in existing space. The electronics toroid and the general pedestal-like configuration of the stable platform, coupled with other structural and space considerations, all combined to dictate an inclined isolator system.

Studies indicated that the g level as seen by the gyro gas bearing was three times the theoretical allowable and that a resonance factor of two was required. Because of the noise specification, an attenuation of 40 db per decade was indicated. Space considerations indicated that the isolation system has natural frequencies of 20-35 cps.

To achieve the low resonance factor and rapid high frequency attenuation, special isolators were used. This type of isolator, known as a "combination shockmount," consists essentially of four rubber fluid-filled bellows mounted perpendicular to each other in the same plane and attached to a central hub [3]. The bellows are interconnected with one another through orifices which determine the damping and, in part, the spring rate. The mathematical model for the isolators would be an elastically-supported viscous-damped system [4]. By adjusting the orifice size, the mount can be made to give very high damping at resonance with attenuation at the higher frequencies as if the mass were undamped.

Use of this type of isolator does not affect the inclined isolator equations. The design of this system would be as follows.

Since the center of gravity of the system is known and the space requirements are established, there is little possible variation in the a/r ratio. This can be firmly established and in this case it is 1:1. By using this value and Fig. 5, the relationship between the stiffness ratio and the inclination angle can be determined. It should be noted that the curves vary from a circular shape to an open rectangle (at $a/r = 0$). By selecting points near the top of the curve, the inclination angle can be permitted to vary (as with tolerance) with a minimum of variation in stiffness ratio. At the sides of the curve, the situation is reversed. The stiffness ratio has very little effect on the inclination angle, especially at low a/r ratios. If there are no other restrictions on K_q/K_p or α, an evaluation of manufacturing procedures should be a factor in selecting values. For the system in question, it is desired that the dependency on inclination angle be reduced. The maximum K_q/K_p ratio is 0.085 with $\alpha = 22$ degrees. A lateral to vertical frequency ratio of 0.42 is obtained by checking Fig. 6. This value is too low to obtain the desired frequency ranges. The K_q/K_p ratio must then be lowered. To keep this value reasonable, a ratio of 0.067 is chosen ($K_p/K_q = 15/1$). This gives two possible inclination angles, 12 and 31 degrees. The larger angle is used because, as indicated in Fig. 6, a higher frequency ratio is obtained (0.52 as compared with 0.37).

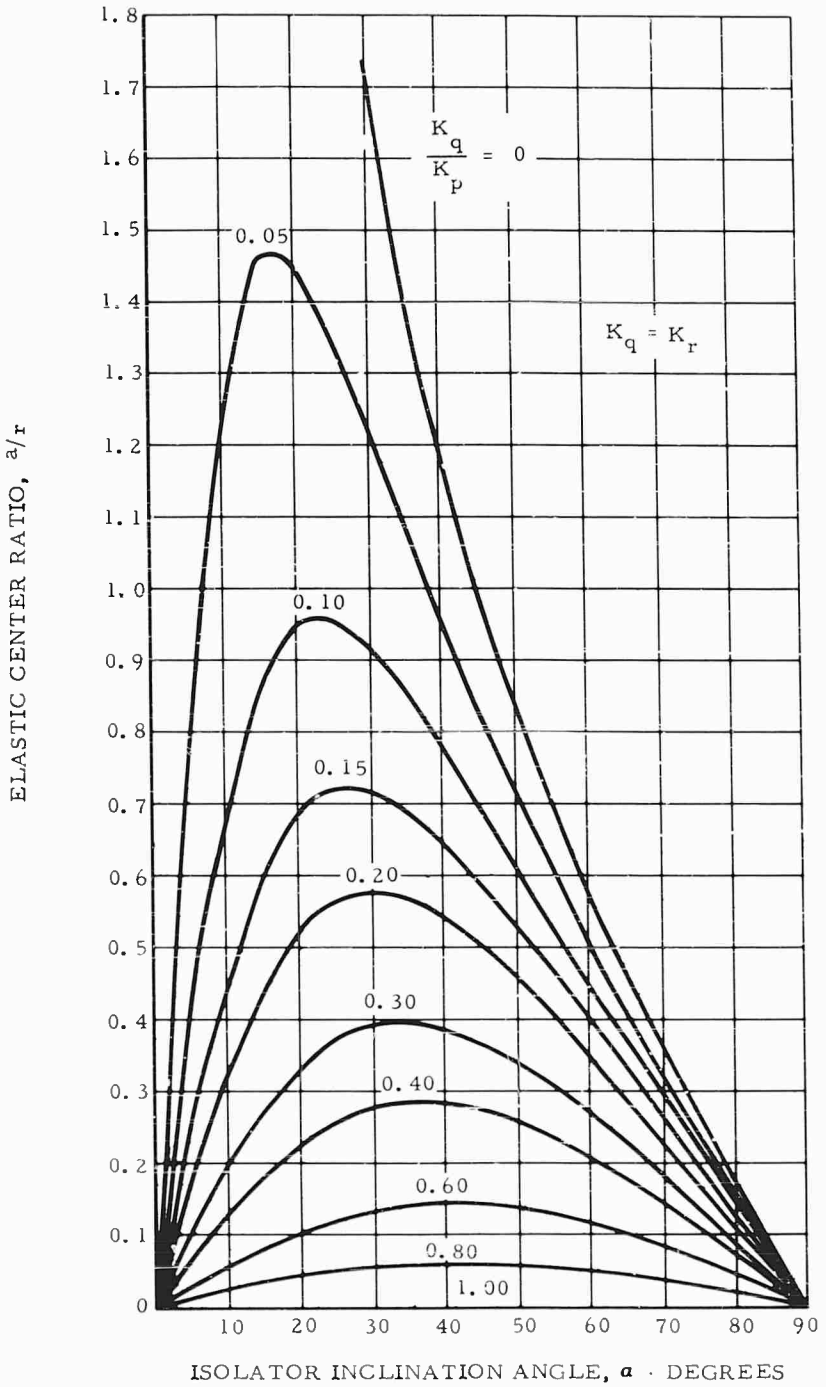

Fig. 4 - Elastic center ratio as a function of isolator inclination angle for varying stiffness ratio

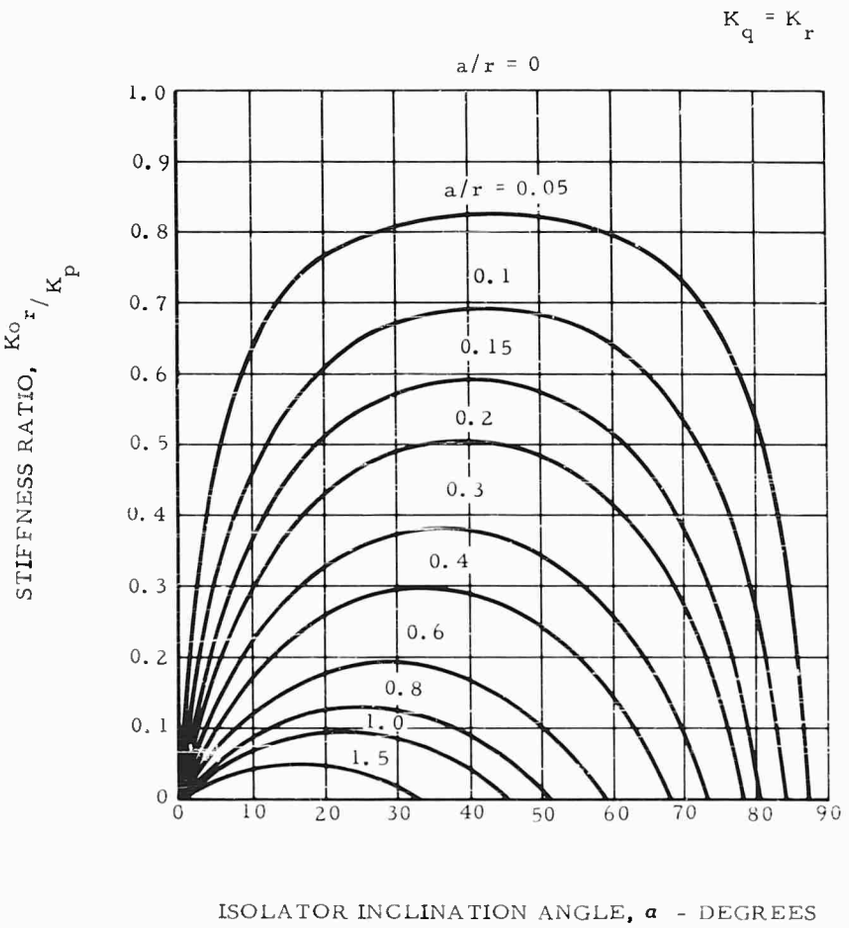

Fig. 5 - Stiffness ratio as a function of isolator inclination angle for varying elastic center ratio

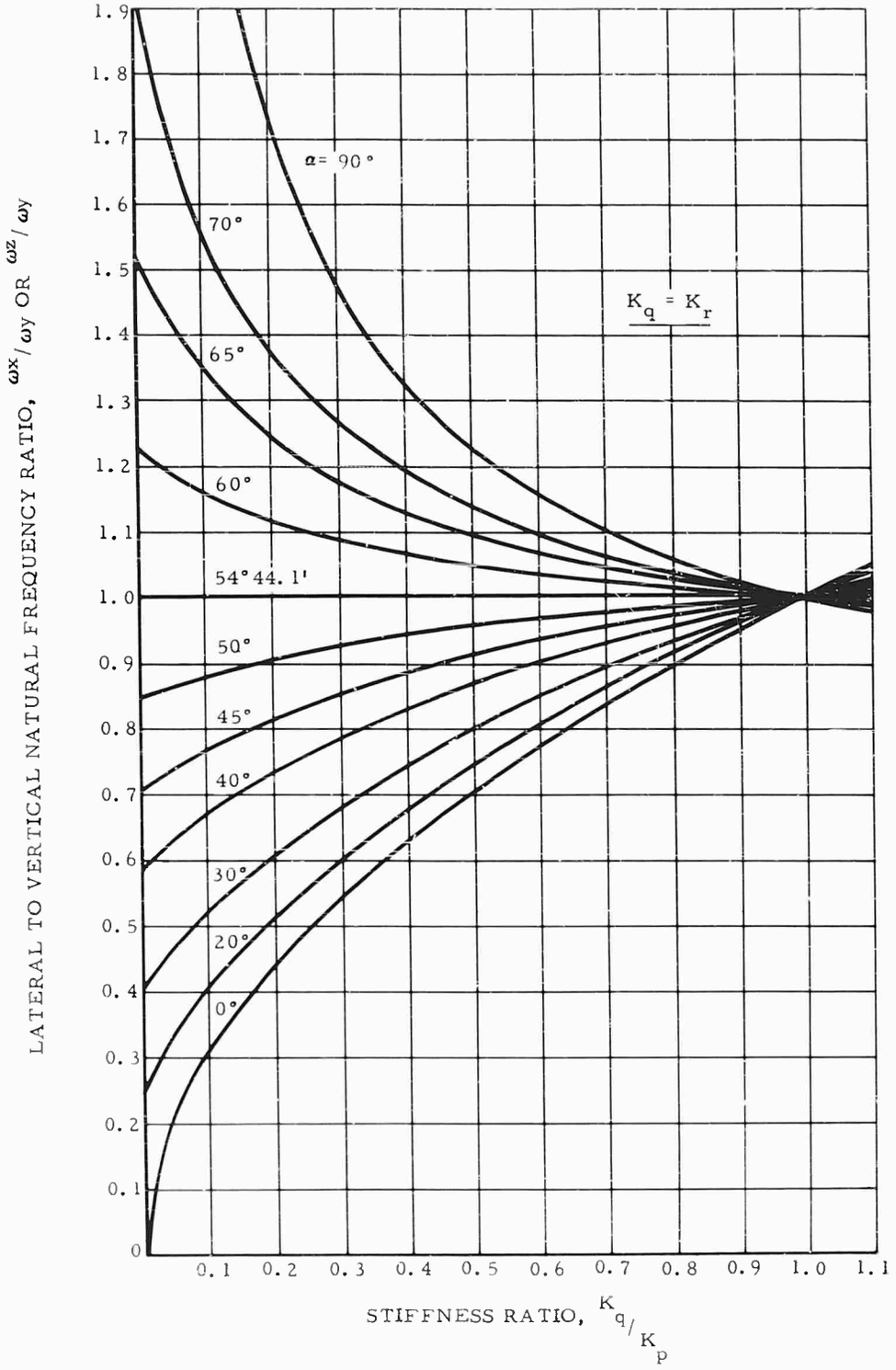

Fig. 6 - Lateral to horizontal natural frequency ratio as a function of stiffness ratio for varying angle of inclination

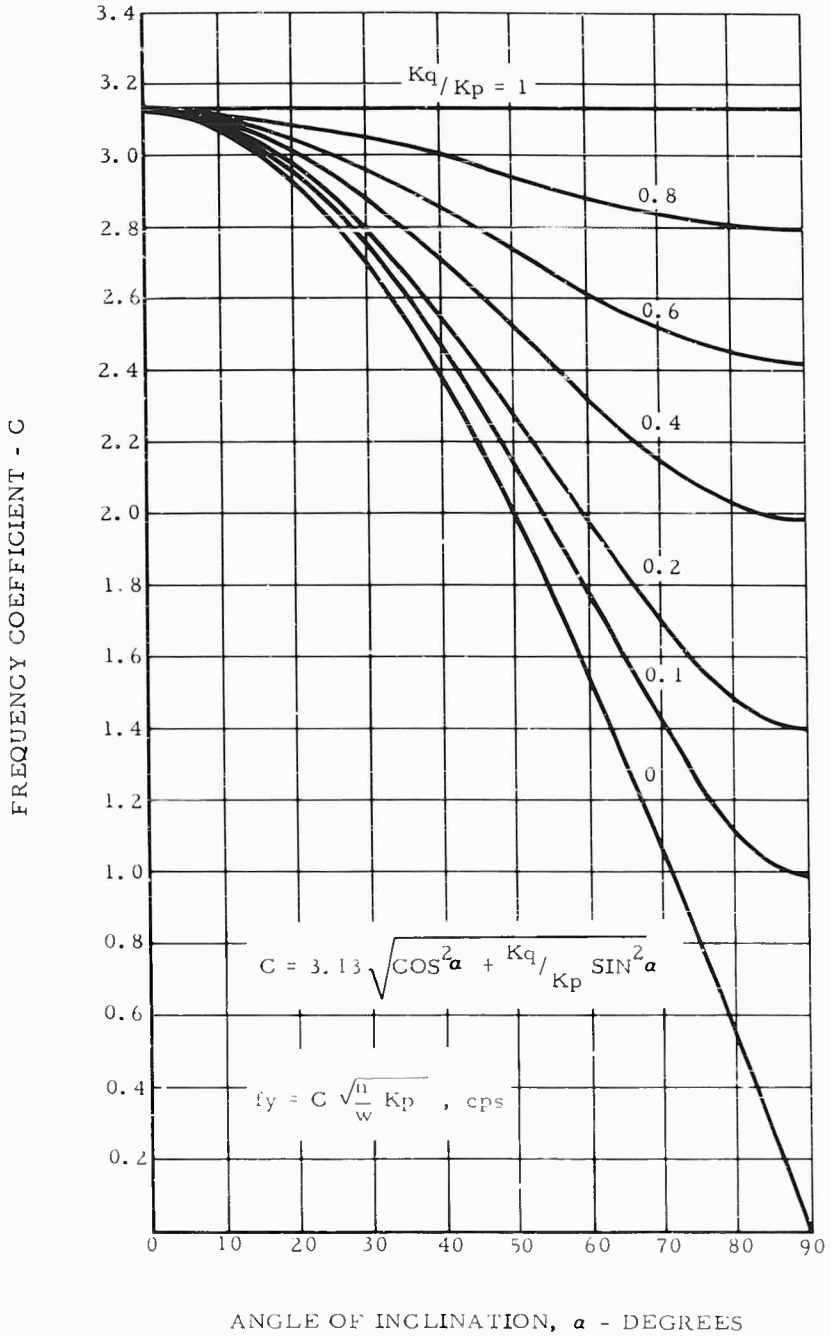

Fig. 7 - Frequency coefficient as a function of stiffness ratio and angle of inclination

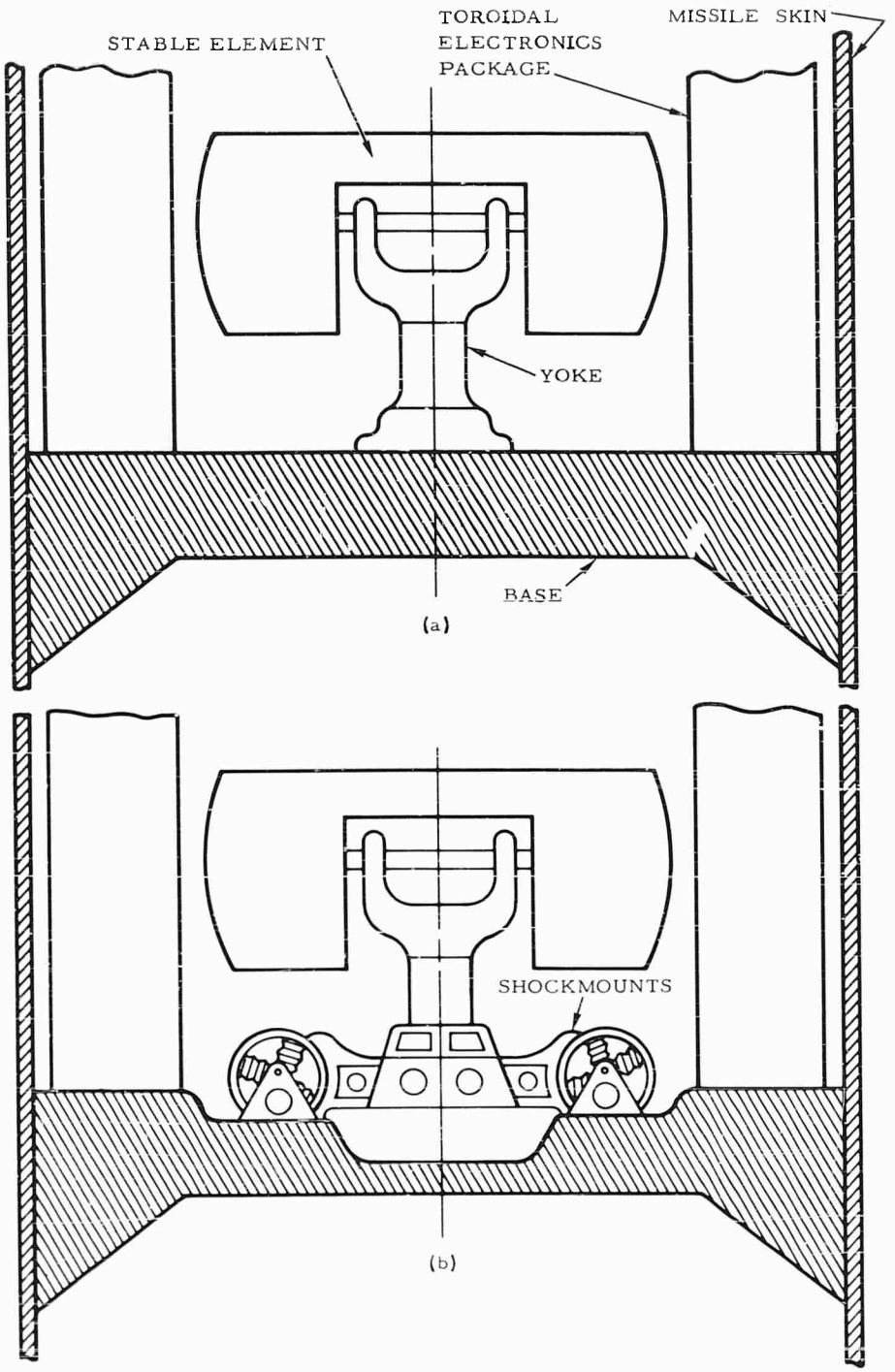

Fig. 8 - (a) Existing stable platform before application of mounts; (b) modification required to include mounts. Shockmounts structure replaces base structure.

The remaining properties can now be determined. From Fig. 7, the frequency coefficient is 2.67. Using the maximum desired vertical frequency, Eq. (27) becomes

$$35 = 2.67\sqrt{\frac{nK_p}{W}},$$

where

$$nK_p = 9463 \quad \text{and} \quad W = 55 \text{ lb}.$$

To keep the isolators as small as possible, six isolators spaced at 60-degree intervals will be used.

$$K_p/\text{isolator} = 9453/6 = 1575 \text{ lb/in}.$$

$$K_q = 0.067\ (1575) = 105 \text{ lb/in}.$$

The lateral natural frequency is

$$f_x = 0.52\ (35) = 18.2 \text{ cps}.$$

This figure is just below the minimum desired frequency but it represents a good compromise with the stiffness parameters. Its acceptability will be determined by the motion of the isolated mass and the resultant clearance.

This unit has been built and tested and the results are available to substantiate the analysis. The configuration is shown in Fig. 8(b) and the results are given in Figs. 9 and 10. For the 31-degree inclination angle that was calculated, a peak coupled transmissibility of 19 arc seconds per g input was obtained. While there is no available criteria for evaluating this result, it is felt that this is extremely satisfactory for a base-mounted system. Note that slight changes in inclination angle do not have a significant effect on the translation resonance peak, but do affect the coupling as evidenced by the 45 arc second/g rotation at $\alpha = 33$ degrees. The natural frequencies agree with the calculated values.

The above example should serve to indicate that the procedures for designing inclined isolator systems are relatively simple if isolator symmetry can be obtained.

ACKNOWLEDGMENT

The authors wish to acknowledge the efforts of Messrs. D. H. Mitchell, W. Stearns, and L. N. Tanner for their part in preparing the analysis and the design and testing of the illustrative system.

REFERENCES

1. C. W. Crede and C. M. Harris, Shock and Vibration Handbook (McGraw Hill Book Company, Inc., New York, 1961), Chap. 3.

2. C. E. Crede, Vibration and Shock Isolation (John Wiley and Sons, Inc., New York, 1951), pp. 73-87.

3. W. Stearns, "Combination Spring Piston Isolator," U.S. Patent 3,101,937 (1963) assigned to N.A.A., Inc.

4. J. E. Ruzickca and R. D. Cavanaugh, Machine Design, 30:114 (1958).

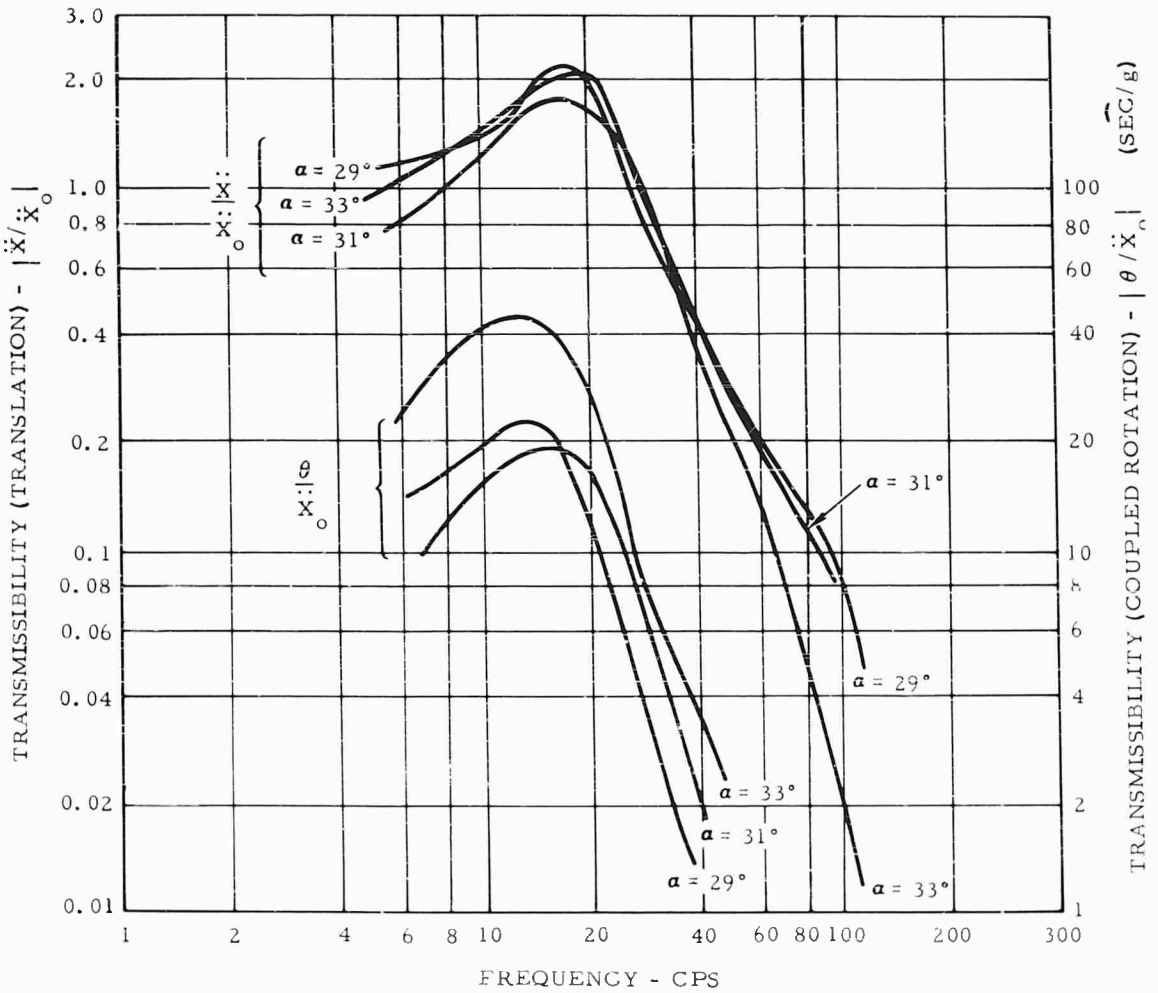

Fig. 9 - Results of tests showing the system response to a lateral acceleration, X_o, for various angles of inclination

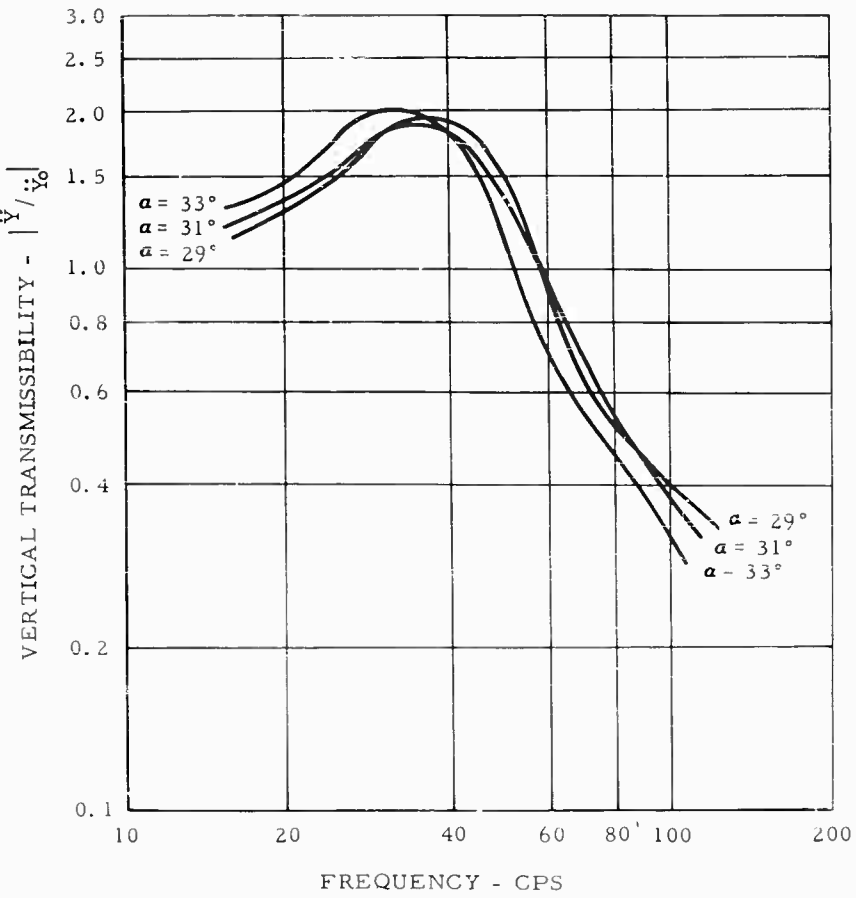

Fig. 10 - Results of tests showing the system response to a vertical acceleration, $\ddot{X}_o$, for various angles of inclination

Appendix A

LIST OF SYMBOLS

F	Force, lb
K	Spring constant, lb/in.^{2} or in.-lb/rad*
M	Moment, in.-lb*
X, Y, Z	Principal axes of body
a	Distance from XZ plane, in.
f	Natural frequency, cps
n	Number of isolators
p, q, r	Principal axes of isolators (used as subscripts)
r	Radial distance from Y axis, in.
α	Angle of inclination
β	Angle of rotation
γ	Angle of deviation
δ	Linear displacement
θ, ϕ, λ	Angular displacement about X, Y, and Z axes, respectively
ρ	Radius of gyration
ω	Natural frequency, radians per seconds.

*A double subscript notation is used. The first denotes the output axis and the second the input axis (i.e., F_{xy} is a force along the X axis caused by a displacement along the Y axis).

* * *

Section 3
SHOCK

ELEMENTARY CONSIDERATIONS OF SHOCK SPECTRA

Irwin Vigness
U. S. Naval Research Laboratory
Washington, D. C.

Various component parts of shock spectra, which are the product of concepts advanced during recent years, are described. Terminology, definitions, and methods of presentation of shock spectra are given. Information that can be obtained by quick inspection of spectra, when the spectra are plotted on four-coordinate log paper, is shown. Other uses and limitations of the shock spectra concept are briefly mentioned. It is suggested that spectra for complex shock motions be plotted dimensionally on a four-coordinate log graph paper in order to illustrate simultaneously the acceleration, velocity, and displacement shock spectra, and that spectra for simple shock pulses should be plotted nondimensionally on the same type of graph paper. A collection of shock spectra for simple shock pulses is included.

INTRODUCTION

Objective

In order to improve the ease of communication between diverse groups working in the field of mechanical shock, some suggestions as to terminology, definitions, and methods of presentation of shock spectra are made. These suggestions are not necessarily new or original. Except for a particular nondimensional presentation of shock spectra they represent the normal vocabulary, concepts, and methods of many of the specialists in this field. In addition stress is placed upon information, of an approximate and simple nature, which can be observed directly from shock spectral curves when they are plotted on a four-coordinate log paper.

Background

A shock spectrum, roughly defined, represents the maximum responses of a series of single-degree-of-freedom systems, as a function of the frequencies of the systems, to a given shock excitation. The concept of shock spectra was introduced by Biot [1-3], who was concerned with the damage potential of earthquake motions. He called this type of presentation earthquake spectra and used it to determine building responses to the earthquake motions and to provide a method of analysis of the effects of these motions. Mindlin [4] first suggested that this method of analysis be used for general types of shock motions. He suggested this as a concept to compare the damage potential of different shock motions. This essentially compared their effects on a standard system, the standard system being an assembly of single-degree-of-freedom systems as shown in Fig. 1. About this same time (about 1942) the David Taylor Model Basin constructed a "reed" gage which indicated directly a shock spectrum of a shock motion.

The terms "earthquake spectra" and "shock spectra" rather than response spectra were undoubtedly selected in order to make the terms more narrowly definitive. The broad term "response spectra" does not convey to the reader the nature of the field of study in sufficient detail.

More recently shock spectra have been used for the specification of shock tests [5], for design specifications [6], and their use has been extended by normal mode theories [7] to determine

NOTE: References appear on page 221.

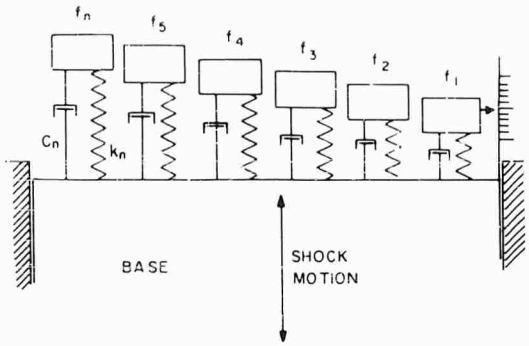

Fig. 1 - A series of single-degree-of-freedom systems with viscous dampers subjected to a common shock excitation

various types of responses of multi-degree-of-freedom lumped systems and systems of distributed mass.

More accurate and sophisticated techniques brought a demand for more information than was contained in the initial shock spectral presentations, which were merely spectra of the absolute values of the maximum responses. At the present time instead of using only absolute values, both positive and negative spectra are often given, damping is included as a parameter, primary and residual spectra are added, and spectra for nonlinear systems [8] are considered.

DEFINITIONS FOR SHOCK SPECTRA

Consider an assembly of single-degree-of-freedom systems as shown in Fig. 1. The definition of a shock spectrum is based primarily on the relative displacement responses of these systems to a shock excitation. Thus, a displacement [9] shock spectrum is the maximum relative displacement responses of an assembly of single-degree-of-freedom systems as a function of their natural frequencies when the assembly is excited by a given shock motion. Damping is a parameter and its value should be stated. If it is not stated it is assumed to be zero.

Unless it is otherwise stated only the absolute values of the responses are given. The signs of the responses may be considered, however. In this case the positive displacement shock spectrum is the maximum positive relative displacement responses of the single-degree-of-freedom systems to a given shock motion, and the negative displacement shock spectrum is correspondingly defined in terms of the negative responses.

It is also often desirable to know the maximum velocity and acceleration responses of the single-degree-of-freedom systems to the shock excitation. Unfortunately if precision is maintained the derivations of these responses and their relations one to another become very complicated. Therefore an approximate set of responses has been arbitrarily defined which provide the relations between the velocity and acceleration responses and that of displacement. The shock spectra [10] in terms of displacement, velocity, and acceleration are defined as:

$$\underline{\text{Displacement shock spectra}} = S_d = X, \qquad (1)$$

$$\underline{\text{Velocity shock spectra}} = S_v = \omega X, \qquad (2)$$

and

$$\underline{\text{Acceleration shock spectra}} = S_a = \omega^2 X, \qquad (3)$$

where X is the maximum relative displacement response as defined above, and ω is the angular natural frequency of a single-degree-of-freedom system.

It is to be noted that the velocity and acceleration shock spectra are not, in general, the true maximum responses of velocity and acceleration, although normally the approximation is good. In the case of the velocity shock spectra the maximum velocity responses occur at different times than for those of displacement, hence there is no reason for Eq. 2 to provide precise values of maximum velocity response. For this reason this velocity is called a pseudo velocity. Generally damping increases still further the difference between the velocity shock spectra and the maximum velocity responses.

Acceleration shock spectra and the maximum acceleration responses are the same if there is zero damping. This is obvious if one notes that for a single-degree-of-freedom system with no damping the mass experiences its greatest acceleration when the spring response is the greatest (maximum relative displacement), so

$$kX = ma_{max}$$

or

$$a_{max} = \frac{kX}{m} = \omega^2 X = S_a, \qquad (4)$$

where k is the spring constant, X is the maximum spring deflection, m is the mass, and a_x is the maximum acceleration of the mass. Small differences between acceleration shock spectra and acceleration responses occur as the damping becomes appreciable.

It has been shown [11] that the shock spectrum, for values that occur after the shock excitation for a condition of zero damping, is the same (except for a constant factor) as the Fourier spectrum of the shock motion. This fact, together with qualitative considerations concerning these long sustained vibrations, make it of value to decompose the shock spectrum so as to present values which occur during the time of excitation and values which occur after this time. A primary shock spectrum, or an initial shock spectrum, represents shock spectral values which occur during the time of excitation. A residual shock spectrum represents shock spectral values which occur after the time of excitation. It is sometimes necessary to distinguish between the complete shock spectrum and the residual and primary spectra. The term overall shock spectrum is used instead of shock spectrum if it is necessary to distinguish this term from residual or primary shock spectra.

TYPICAL APPLICATIONS OF SHOCK SPECTRA

Perhaps a principal reason for the success of the shock spectra concepts is its wide range of applications. These range from simple applications requiring no mathematical skill to complicated schemes that are a joy to the mathematician. They are useful to the field engineer, the test engineer, the specification writer, and the designer. Some of these uses and applications are listed below:

Comparison of the Severities of Different Shocks

The damage potential of a shock is estimated by its effect on a simple standard assembly as shown in Fig. 1. The probability of this assembly being damaged will increase as the relative displacements of the masses with respect to their common base increase, or as the accelerations of the masses increase. The magnitude of the values represented by the shock spectral curves therefore provide a measure of damage potential of the shock motion as a function of frequency of the item being subjected to the motion. It is not implied that there are no other factors involved which might cause damage or that the results obtained with other types of assemblies would be the same. It is only implied that this is a method of comparing the relative severities of dissimilar shock motions by their effects on a standard assembly of simple systems.

Nomograph for Determining Relative Displacement and Acceleration [12]

If an equipment is flexibly mounted on a center-of-gravity type mounting system, then the deflection of the mount and the acceleration transmitted by the mount can be read directly from the shock spectrum curve. The natural frequency of the mounting system is equal to that selected on the shock spectrum frequency scale. Items within the mounted equipment will experience the acceleration thereon indicated.

If any two of the three values of acceleration, displacement, and frequency are given, the third can be selected from the graph. If only one value is assigned then a choice can be had as to the other two. If the equipment does not have a center-of-gravity type mounting system some additional calculations may be necessary to determine the rocking mode response and the additional mount deflection caused by this mode.

Determination of Maximum Values of Acceleration, Inpulsive Velocity Change, Displacement and Natural Frequencies Involved in the Shock Motion [12]

As the frequencies for the shock spectral values become very high the single-degree-of-freedom systems (Fig. 1) become very stiff. They will eventually behave as a rigid mass. At high frequencies the acceleration shock spectral values will therefore be asymtotic to the maximum value of acceleration existent in the shock motion. This is shown as region A of Fig. 2. At some intermediate frequency, region B, peaks in the shock spectral curves indicate sustained frequencies of the shock motions. At some lower frequency (generally), a section of the shock spectral curve, region V, remains at a constant velocity value. This corresponds to a frequency region over which the shock motion can be considered to be an impulsive (step) velocity change. At very low frequencies, region D, the shock spectrum becomes asymtotic to the maximum displacement involved in the shock motion.

Determination of Continuous Fourier Spectrum of a Shock Motion

Most methods of analysis of shock motions to obtain shock spectra include residual shock spectra as an output. Since a residual shock

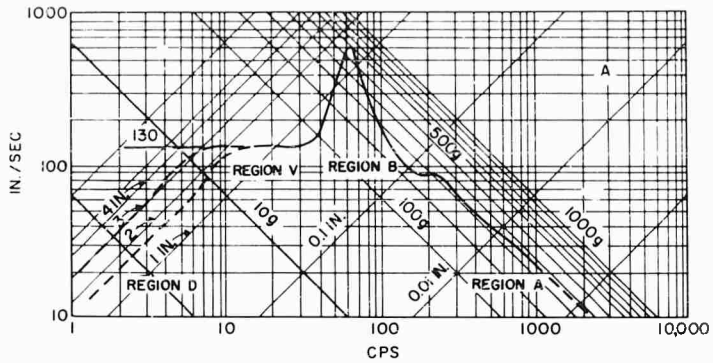

Fig. 2 - Shock spectrum for one particular loading and operating condition of the Navy High Impact Shock Machine for Lightweight Equipment

spectrum is the same as a continuous Fourier spectrum [11] of the shock motion (except for a constant factor), a general shock spectral analysis may be said to include a Fourier spectrum of the shock motion as one of its by products.

Design Calculations

Shock spectra can be used in various mathematical procedures [3,6,7], including normal mode theories, to determine upper limits of responses of either lumped mass or distributed mass systems. These responses may be stress, strain, displacement, or acceleration.

Specifications

Shock spectra may be used in lieu of shock motions to specify shock tests. It is generally simpler and more meaningful to give tolerances in terms of shock spectral limits rather than shock motion deviations. Generally the spectrum analysis of the shock machine output would be done only when it is necessary to calibrate or standardize the operation of the test machine. Machine-setting and motion measurements would be normal operating procedures; see Refs. [5] and [9], pp. 105-106.

APPROXIMATIONS AND ASSUMPTIONS INVOLVED IN SHOCK SPECTRA CONCEPTS

Shock spectra applications involve many approximations. While these detract from the accuracy of the results, there do not appear to be any competitive methods that are sufficiently simple and practical that can do better. Some of the shortcomings of the shock spectra approach are listed as follows:

Applies Only to Linear Systems

Some attempts [8] have been made to extend the method to nonlinear systems, however, at the present state of the art its practical application requires an assumption of linear systems.

Single-Degree-of-Freedom Concept Limitations

Damage potential and some other concepts are based only on single-degree-of-freedom systems.

Normal Mode Methods Over Conservative

In normal mode calculations, use is made only of the absolute spectrum values and the contribution of each mode is added without regard to phase or sign.

Fatigue Effects Disregarded

The effects of fatigue are generally disregarded although some attempts have been made to include this in three-dimensional shock spectra [14, 15].

Disregards the Concept of Mechanical Impedance

In this respect it is in the same category of other approaches wherein a motion is specified

for a shock or vibration test which is required to be maintained regardless of equipment reaction.

Application of Shock Spectra Obtained From Field Measurements May Cause Unrealistically Severe Shock Specifications

This is most likely to occur if the enveloped field data are translated into simple shock pulse types of excitation. Suitably damped spectra may be used to determine responses of damped systems, but this would not correct for the disregard of the mechanical impedance. If the field conditions are subjected to suitable analysis, the field shock spectra may be applied by methods other than enveloping to obtain design shock spectra [6].

METHODS OF GRAPHICALLY PRESENTING SHOCK SPECTRA

Four-way log paper

For many years the graph paper shown in Fig. 3 has been used to illustrate simultaneously the displacement, velocity, and acceleration amplitudes of a sinusoidal vibration versus frequency. The relationships between these three amplitude values and frequency are given respectively by:

$$A_d = A_d ,$$

$$A_v = \omega A_d , \qquad (5)$$

and

$$A_a = \omega^2 A_d .$$

These are the same as for the corresponding values of shock spectra (see Eq. (1-3)). One can therefore use this paper to represent simultaneously the corresponding three types of shock spectra.

A choice is permissible as to which type of amplitude is to be selected for the horizontal coordinate. The most commonly selected choice appears to be that of velocity as shown in Fig. 3. When this selection is made the acceleration amplitude coordinate have a 45-degree negative slope (when the scales are as shown) and displacement amplitude coordinates

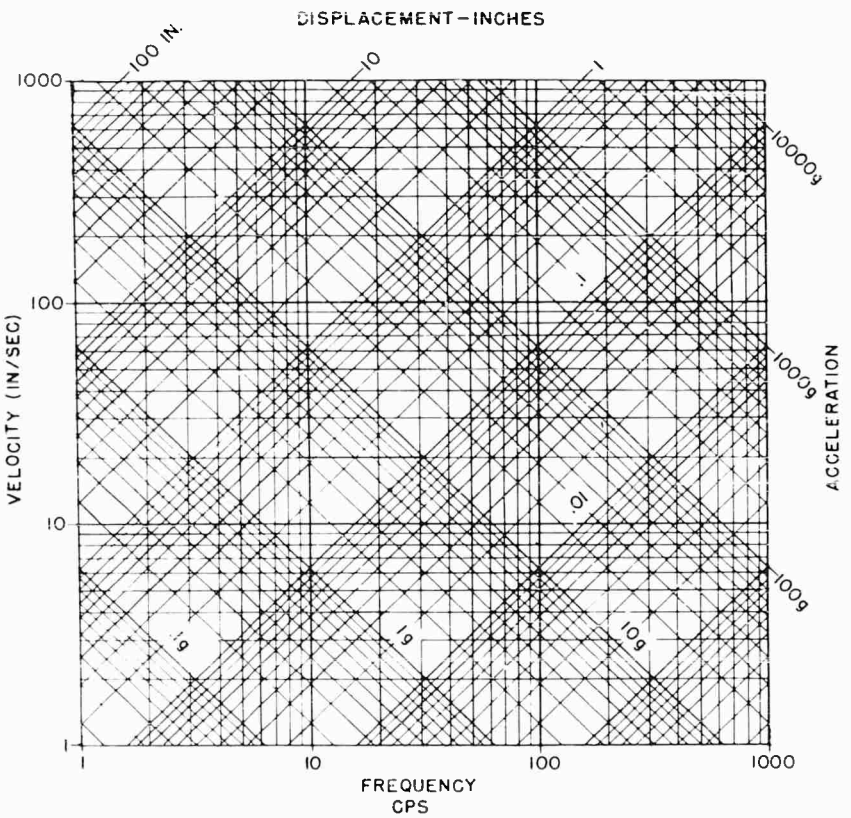

Fig. 3 - Four-coordinate shock spectra graph paper. This is also shock spectra for velocity shock, where the horizontal coordinate values are the values of the velocity shock.

have a 45-degree positive slope. The next most commonly selected choice is to have the displacement amplitude be the horizontal coordinate. This results in the velocity and acceleration amplitudes having slopes of -1 (45-degree negative slope) and -2, respectively. Morrow (Ref. [11], p. 110) has suggested that the acceleration amplitude be selected as the horizontal coordinate. This could cause the most used value, acceleration, to be the horizontal component.

The first of the above choices is considered most suitable, as the range of values to be covered by velocity is normally less than that of either acceleration or displacement, and accuracy is better preserved if the slopes of the dependent coordinates do not become too steep.

While the advantages of presenting shock spectra on four-coordinate log paper are emphasized at this time, it is not implied that linear scales and other forms of presentation may not be preferable for particular situations. When these situations exist then, of course, the method of presentation used should be that best able to illustrate the factors of most importance.

Dimensional Presentations

Shock spectra of typically complicated shock motions, such as those that occur in the field and for shock testing machines that do not generate simple pulse shapes, are plotted using conventional dimensions. The conventional four-way log paper is made so that the acceleration spectrum is given in units of g (gravity), and the velocity and displacement coordinates are then positioned so that the velocity is expressed in terms of inches per second and displacement in terms of inches. Frequency is, of course, given in terms of cycles per second. If different units are used the relative coordinate positions will be changed.

Examples of this type of presentation are shown in Figs. 2 and 4. Figure 2 is a shock spectrum for a shock motion generated by a Navy H. I. shock machine [15] for a given load and machine setting. From this graph it can be directly observed that: (1) the maximum acceleration generated is between 300 and 400 g and that this maximum value lasts sufficiently long that it is effective for all unisolated elements under test that have natural frequencies above 200 cps; (2) sustained vibrations are generated at about 60 cps and cause responses up to 600 g for undamped systems. The displacement amplitude (relative) of these responses is about 1.5 inches; (3) the impulsively obtained velocity, which is the velocity of the center-of-gravity of the shock machine table as the table moves between its stops, is 130 ips. This is the only factor that need be considered for unisolated equipment components having natural frequencies between 10 and 40 cps; and (4) the displacement involved in the shock motion is either about 1.6 or 3 inches (either can be obtained by machine adjustments). Unisolated equipment elements will

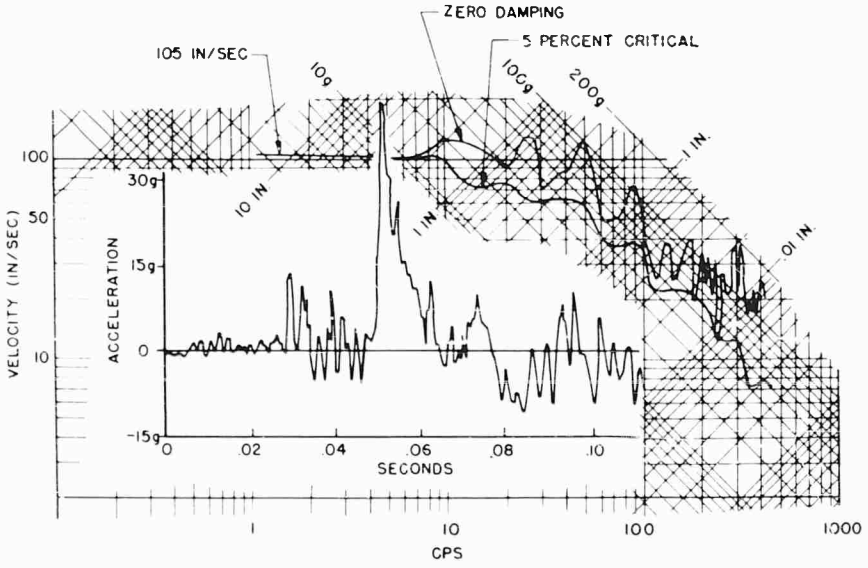

Fig. 4 - Shock motion and corresponding shock spectra replotted from a Sandia Corporation Report [14]

not be affected by this displacement value if their natural frequencies are above 10 cps. (There is an element of untruth in this statement that is neglected in this presentation.)

One can also observe directly from this graph that if one were to apply an isolator to limit the transmissibility of this shock to 10 g, then the natural frequency of the mounted equipment would be about 5.5 cps and one would have to provide a clearance of a little over 3 inches (6-inch excursion). If only about 0.6 inch clearance were available then the natural frequency of the mounted system would have to be between 30 and 40 cps and the transmitted acceleration would be about 100 g. An appreciably stiffer mount would aggravate the shock motion.

Figure 4 illustrates a shock motion, obtained by Sandia Corp. [16], and its corresponding shock spectra. The spectra have been replotted from the original linear scales. The shock motion is that resulting from the bumping of two railroad cars together at a speed of 9.0 mph (141 ips). The instrumented car was initially at rest. Spectra for zero damping and 5 percent critical are shown.

The following information is directly available from the graph. The velocity change resulting from the impact was 105 ips. This change took place in a time that was short compared with one seventh of a second, so that for unisolated elements having natural frequencies less than 7 cps the shock can be treated at a simple velocity change. A flexible mount designed to limit the transmitted acceleration to 10 g would require a clearance of 2.6 inches and an equipment-mount natural frequency of 6 cps. Many sustained frequencies are observable, the lower ones appear to be harmonically related. The large difference between the damped and the undamped spectra indicate that many cycles of coherent vibration (narrow-band random) are involved. Significant frequency components exist above 400 cps, as the two spectra must both become asymtotic to the maximum value of acceleration. It would appear from the damped spectrum curve that this value will be between 40 and 50 g.

Mostly Nondimensional Presentation

When shock spectra are given for shock pulses of simple shape it is advantageous to use nondimensional units in order that one graph will suffice for all sizes of pulses of similar shape.

It is nearly universal to express acceleration magnitudes in terms of units of g (gravity). If g is expressed in ips [2] then the same graph paper can be used for this type of plotting as is conventionally used for vibration and for the previous type of shock spectra. This has been done for the shock spectrum shown on Fig. 5. The frequency scale is made nondimensional. The frequency is f and the pulse duration is T.

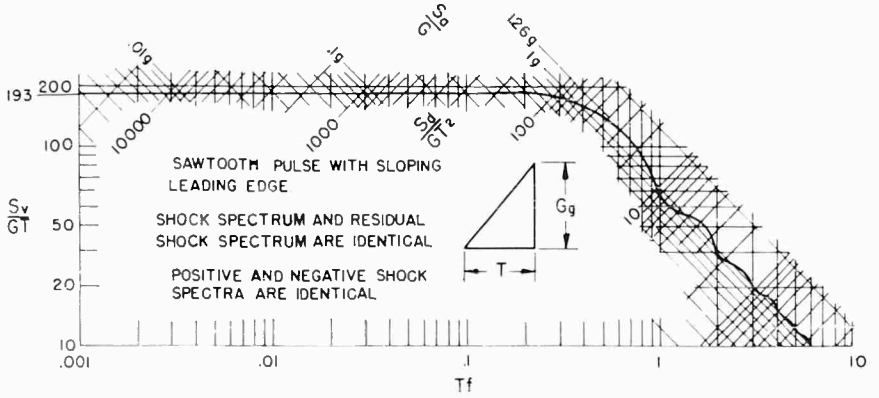

Fig. 5 - Shock spectrum of a terminal peak saw-tooth acceleration pulse. Abscissa is nondimensional. Ordinates are all in units of acceleration so that the usual graph paper for vibration amplitudes can be employed.

The peak value of acceleration of the pulse is Cg, so G is the acceleration expressed in units of gravity.

To obtain numerical values of shock, one multiplies the value of the acceleration, velocity, or displacement coordinate of the shock spectrum curve by G, GT, or GT^2, respectively. It may be observed that the dimensions of all of the above coordinates are in dimensions of acceleration. The values of S_v and S_d are in units of inches per second and inches, respectively.

Nondimensional Presentation

There are advantages in expressing a function nondimensionally. In this way one is able to use any consistent set of units. This can easily be done for the shock spectra by dividing each of the three dependent coordinates, shown in Fig. 5, by g. This is shown on Fig. 6. While it would be permissible to leave the acceleration coordinate the same as it was for the previous case, the g is brought into the coordinate symbol for consistency. This change to complete nondimensionality requires that the displacement and velocity coordinates be in different positions with respect to that of acceleration as compared with the conventional graph paper, Fig. 5. Thus a different graph paper is required. This method of presentation is preferred over the previous method, and should generally be used for shock spectra of simple pulses even though the coordinate paper is not consistent with that normally used for vibration amplitude presentations.

COLLECTION OF SHOCK SPECTRA OF SIMPLE SHOCK MOTIONS

A selection of some commonly used shock pulses and their spectra are included for reference. Except for the case of "velocity shock" i.e., a step change of velocity, these are all plotted nondimensionally. For velocity shock the simplicity of the dimensional representation makes it the better choice.

As plotted on the conventional four-coordinate log paper a shock spectrum of a velocity-shock is a horizontal line the value of which is equal to the value of the velocity-shock, or step-velocity change. The horizontal coordinate system of this graph paper therefore, in its unmodified form, respresents shock spectra of velocity shocks.

In Fig. 3 each of the horizontal coordinates represents a spectrum of a velocity shock. The values assigned to these coordinates are equal to the magnitudes of the corresponding velocity shocks. One can read directly from this graph the displacement (relative) and acceleration experienced by any simple flexibly mounted element when it is subjected to any sudden change of velocity.

Figures 6 through 11 illustrate the overall shock spectra and residual shock spectra for many simple pulses. If the pulse acceleration is considered positive, then the values shown are positive shock spectra. The negative overall and the negative residual shock spectra, are the same for the cases illustrated, and are numerically equal to the positive residual spectra.

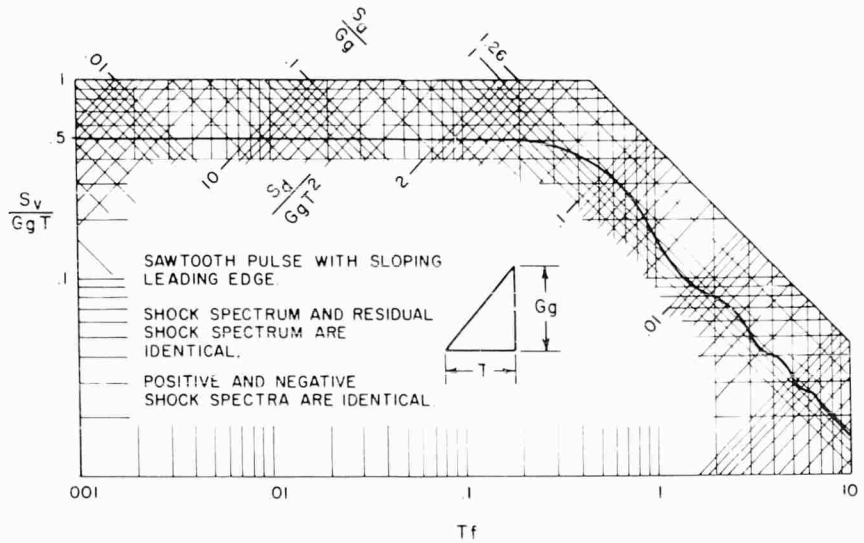

Fig. 6 - Nondimensional representation of a terminal peak sawtooth acceleration pulse

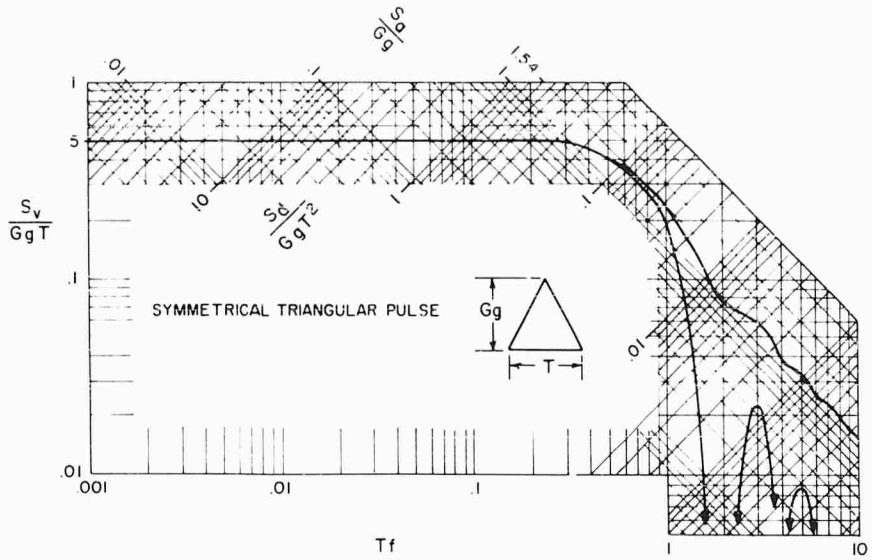

Fig. 7 - Nondimensional representation of a symmetrical triangular acceleration pulse

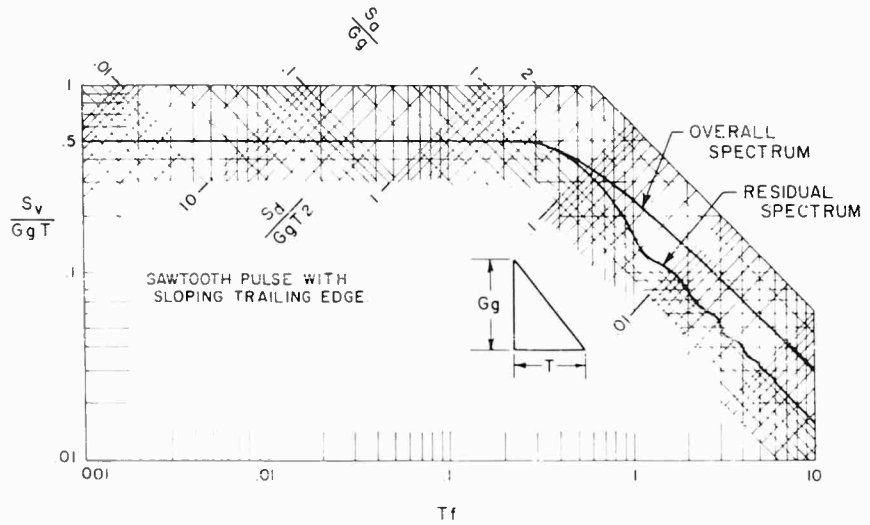

Fig. 8 - Nondimensional representation of an initial peak saw-tooth acceleration pulse

The velocity change caused by the acceleration pulse is indicated by the velocity shock spectrum value of the low-frequency horizontal section of the curves. It is observed that for frequencies less than $0.3/T$ that the shape of the pulse is unimportant, and that for frequencies above about $3/T$ the maximum acceleration is the most important factor. It is also observed that the overall shock spectra are much less dependent on the pulse shape than are the residual spectra.

It should be noted that the residual spectra of any symmetrical shock pulse periodically goes to very small values. This situation is generally not desirable for shock tests. Consequently, shock tests were devised [17] which required a saw-tooth pulse with a steep trailing edge. As shown in Fig. 6, under this condition the residual and overall spectra are the same, and the positive and negative spectra are also the same. These are desirable conditions for shock tests.

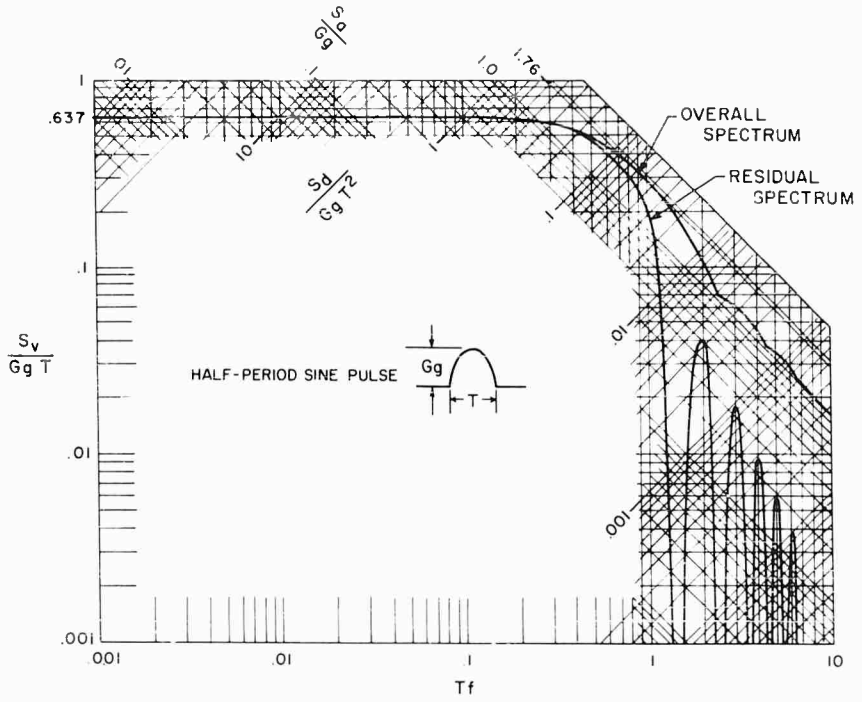

Fig. 9 - Nondimensional representation of a half-sine acceleration pulse

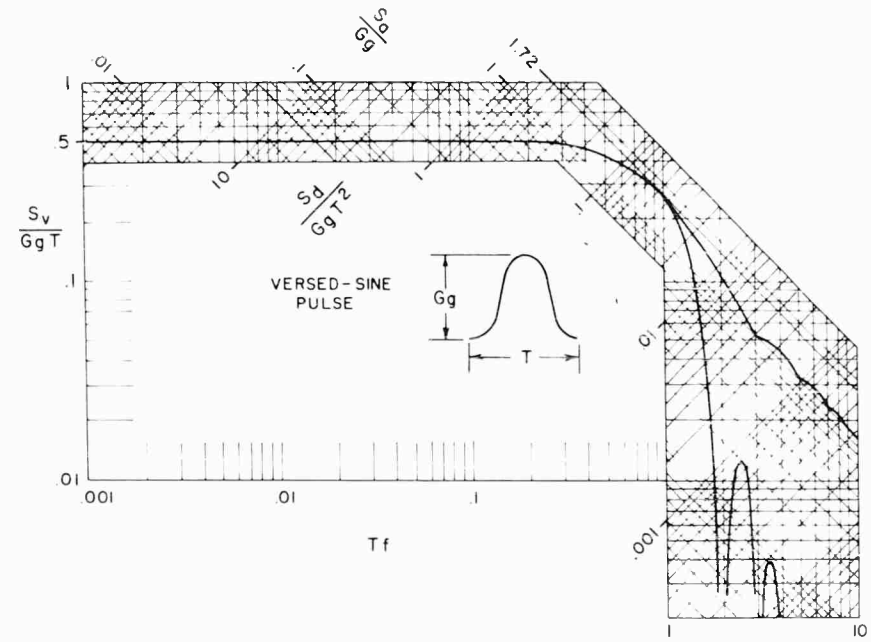

Fig. 10 - Nondimensional representation of a versed-sine acceleration pulse

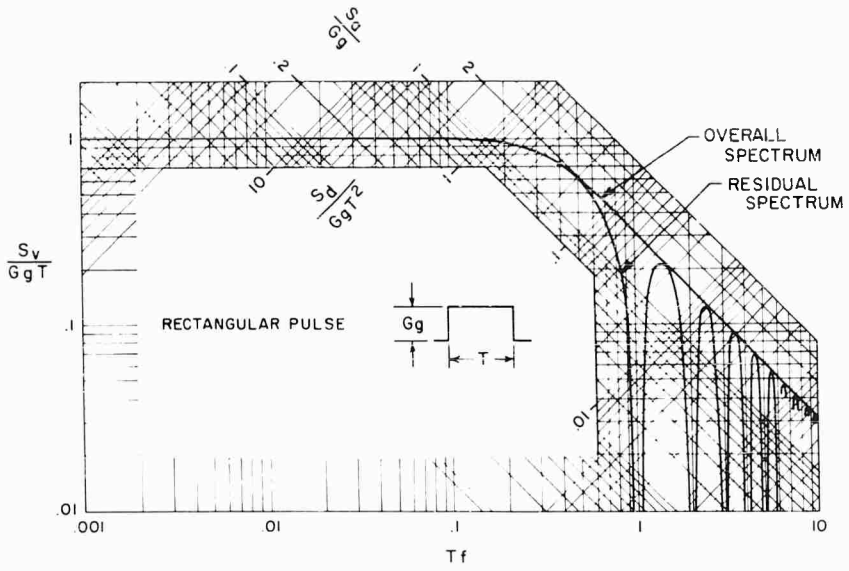

Fig. 11 - Nondimensional representation of a rectangular acceleration pulse

REFERENCES

1. Biot, M. A., "Theory of Elastic Systems Vibrating Under Transient Impulse," Proc. Natl. Acad. Sci. U.S., Vol. 19, pp. 262 (1933).

2. Biot, M. A., "A Mechanical Analyzer for the Prediction of Earthquake Stresses," Bull. Seismological Soc. Am., Vol. 31, No. 2, pp. 151 (1941).

3. Biot, M. A., "Analytical and Experimental Methods in Engineering Seismology," Trans. ASCE, No. 108, pp. 365 (1943).

4. Mindlin, R. A. Conversation with the author, 1942.

5. Morrow, C. T., "The Shock Spectrum," Electrical Manufacturing, Vol. 64, pp. 121 (1959).

6. Belsheim, R. O. and O'Hara, G. J., "Shock Design of Shipboard Equipment, Dynamic Design-Analysis Method," NAVSHIPS 250-423-30, Bureau of Ships, Navy Dept., Washington, D. C.

7. Young, D., "Response of Structural Systems to Ground Shock," Bull. of ASME of papers presented to a Colloquim on Shock and Structural Response during Nov. 1960. (See page 53.) Edited by M. V. Barton.

8. Fung, Y. C. and Barton, M. V., "Shock Response of a Nonlinear System," J. Appl. Mech., 29, 465-476 (1962).

9. The terms "displacement, velocity, and acceleration" are normally omitted if the meaning is otherwise apparent, or if the term is used generically.

10. The term, response spectra, is often used instead of shock spectra. In the author's opinion this should not be done. The term response spectra is general and it is not satisfactory to constrict its usage to a limited part of its normally conceived meaning. It does not convey, to the general reader, the particular area of work about which this response is of concern. Moreover the shock spectra represent arbitrarily defined responses of a standard assembly which should be distinguished from response spectra in general. The term shock spectra was especially coined for its use and it can be defined in a restricted sense with no confusion. It specifically defines the subject matter of concern. If, in unusual cases, there is a question of identity when spectra of both shock motion and shock responses are considered, then the shock spectra should be called "shock response spectra" in order to distinguish it from "shock motion spectra."

11. Morrow, C. T., Shock and Vibration Engineering (John Wiley and Sons, Inc., New York, N.Y., 1963). See especially sections beginning on pages 106 and 226.

12. These determinations are illustrated in greater detail in a later section (dimensional Presentation), A similar description has been made by Cavanaugh (Ref. 13, page 93).

13. Cavanaugh, R. C., "Shock Spectra," Proc. Inst. Environ. Sci. (1964), pp. 89-95.

14. Crede, C. E., "Concepts in Shock Testing Equipment," Bull. of ASME of papers presented at a Colloquim on Shock and Structural Response during Nov. 1960. (See especially page 42.) Edited by M. V. Barton.

15. Harris, C. M. and Crede, C. E., (Editors) "Shock and Vibration Handbook" (McGraw Hill Book Co., Inc., New York, N.Y., (1961). (See especially pp. 21 and 22 of chapter 23 by Sheldon Rubin)

16. Adams, P. H. "Shock Signatures and Spectra from Railroad Switching Loads," Sandia Corp., Tech. Memo No. 410-60(73) (Jan. 1961).

17. Morrow, C. T. and Sargeant, H. I., "Sawtooth Shock as a Component Test," Acoust. Soc. Am., 28, 959 (1956).

* * *

SPECTRAL CHARACTERISTICS OF SOME PRACTICAL VARIATIONS IN THE HALF-SINE AND SAW-TOOTH PULSES

E. H. Schell
Air Force Flight Dynamics Laboratory
Wright-Patterson Air Force Base, Ohio

This paper considers a two-part function composed of a ramp tangent to a half-sine pulse in which the rise times and drop-off times can be controlled independent of each other. This pulse is considered to be more representative of actuality than other analytical functions. Positive and negative response spectra with a range of damping from zero to critical are presented. Fourier spectra of amplitude are also presented as well as Fourier real and imaginary spectra.

The paper also shows the superiority of the saw-tooth pulse (and asymmetrical pulses in general) over the half-sine pulse (and symmetrical pulses in general) for producing failures due to proximity or collision of elements and proposes a proximity failure criterion.

INTRODUCTION

Much has been written concerning the advantages of a terminal peak saw-tooth wave for shock testing and design purposes [1-4]. The superiority of the waveform is demonstrated by showing the undamped positive and negative acceleration shock spectra. These spectra tend to nearly be constant above some selectable frequency as shown in Fig. 1, and the negative values are equal to the positive values. The latter feature has been used to justify testing in only one direction along each of the three principal axes of the equipment.

An important point was demonstrated by Lowe and Cavanaugh [2] when they studied an actual test pulse and were able to show that practical shock machine pulses are not quite as superior as would be indicated by the spectrum of the theoretically perfect saw-tooth. They used the work of Jacobsen and Ayre [5,6] to explain their results on a theoretical basis. This work shows that a finite drop-off time (rather than zero drop-off time as in the theoretically perfect pulse) results in a reduction of the magnitudes of the residual (and hence the negative) undamped spectrum particularly at higher frequencies. The pulse studied by Jacobsen and Ayre was a triangular pulse with a rise time independent of the drop-off time. This pulse, shown in Fig. 2(a) is useful in studying the responses of equipments to a saw-tooth test because it retains most of the essential features of the shock. None of the previous references, however, have considered the effects of damping which is always present in a realistic system. A report by Luke [7] of the University of Texas, considers the effect of damping on the positive response spectrum of the theoretically perfect saw-tooth. The negative response spectrum, and practical deviations from the theoretically perfect waveform, however, were not studied. Since both damping and drop-off time exert a different (and much larger) influence on the negative response spectrum, a gap in our knowledge exists in this area.

All of the previous studies used analytical functions which are only partially justifiable on the basis of physical reliability; i.e., the analytical pulse does not look like the oscillogram of an actual test pulse, nor can it be fully justified by reasoning from the physical phenomena present during the actual test.

In the past few years several publications [6,8,9] have dealt with the application of Fourier transform of shock analysis and design problems. Painter and Parry [10] have applied Fourier spectrum techniques to the problem of

NOTE: References appear on page 250.

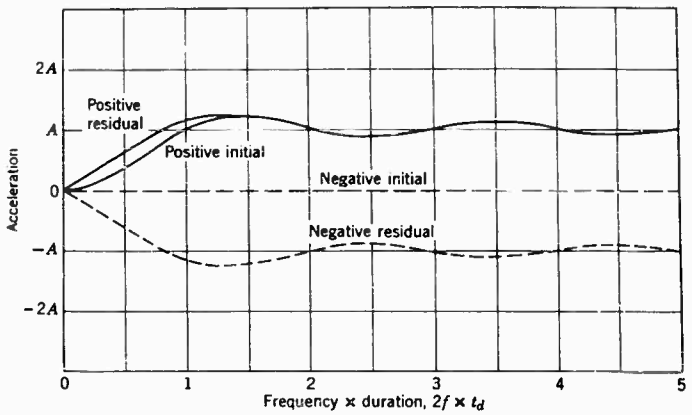

Fig. 1 - Ideal saw-tooth spectra (after Morrow [4])

laboratory simulation of the shock environment. It has also been suggested that the Fourier spectrum be used as a means of specifying shock test conditions [11]. Morrow [12] regards the Fourier spectrum as a more fundamental analytical tool and suggests that it may eventually supersede the shock spectrum for purposes of data reduction.

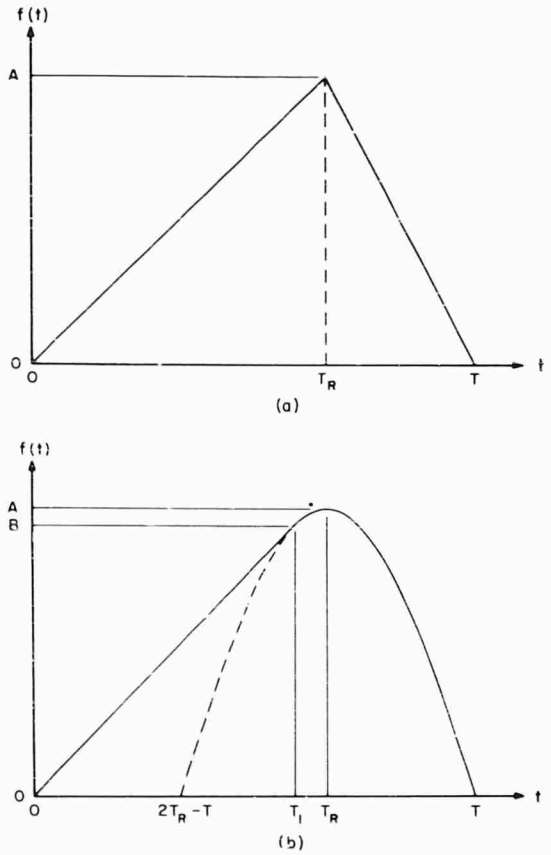

Fig. 2 - (a) Triangular function used in previous studies, and (b) Ramp-sine function studies in this paper

In view of the foregoing discussion, it was decided to undertake an effort designed to bring increased agreement between theoretical and practical results and to provide design information to be used in several different design methods. This was to be accomplished by selection of an analytical function with variable characteristics and reduction of the pulse to damped and undamped positive and negative shock spectra and to complex Fourier spectra for variations of the function over a given range of values of the ratio of the rise time to the drop-off time.

After the function was selected, it became apparent that the function could also be used to study the effects of distortion on the half-sine pulse and to study the effects of symmetry and asymmetry as represented by the half-sine and terminal peak saw-tooth waveforms. These studies were also included.

Finally, the work was expanded to include demonstration of the superiority of the terminal peak saw-tooth waveform for testing purposes when the failure criterion is the proximity or collision of two uncoupled simple systems.

Designers can make direct use of the pulse in the solution of preliminary design problems when the differential equations of motion of the system can be written, or with the convolution (Du Hamel's) integral for simple linear systems. These design methods are covered by most of the standard shock and vibration texts [4-6, 13-16] and engineering mathematics texts [17, 18]. The pulse may also be used with phase-plane

graphical techniques for the solution of a wide variety of linear and nonlinear, single and multi-degree-of-freedom problems including various types of damping [5,6,19]. The shock spectra may be used directly if the system can be considered to behave as a linear single-degree-of-freedom system or they may be used with normal mode theory [20-23] for more complex systems. The Fourier spectra may be used with a hypothetical transfer function in the preliminary design of linear systems. When the design reaches the hardware stage, the actual transfer function can be measured for use with the spectra. A recent paper by Mains [9] thoroughly explores Fourier design techniques. Several other publications [6,8,15] also treat the subject.

SELECTION OF THE ANALYTICAL FUNCTION

Theoretically, it is possible to produce shaped pulses which decay from a peak value to 1 g in zero time on a free-fall shock machine. This is done by dropping a perfectly rigid table onto a shaped plastic pellet resting on an infinitely massive perfectly rigid anvil. All of the kinetic energy of the table is absorbed by plastic deformation of the pellet. At the instant when all of the kinetic energy has been dissipated in doing work to deform the pellet, the acceleration will drop instantaneously to 1 g.

In a practical machine using a lead pellet as the plastic element, the ideal pulse is unobtainable due to elasticity in the pellet and elements of the machine. This is illustrated graphically in Fig. 3. The figure represents the major elements of the shock machine and the pellet after the shock is over and the elements shown are at rest. The test setup is shown schematically as a lumped parameter system consisting of masses and linear elastic elements. This is because the table and anvil are not perfectly rigid; i.e., K_2 and K_4 are not infinite, and the lead pellet is not perfectly plastic, but it does exhibit elasticity (K_3). Thus the pulse generation system is partially plastic and partially elastic.

The waveform for a perfectly elastic linear system has been shown many times to be a perfect half-sine. During this pulse the free fall velocity is reduced to zero at the peak of the pulse and then increased to the initial value in the opposite direction at the end of the pulse causing a rebound to the original drop height because elastic systems do not dissipate energy. During the rising portion of the pulse, the elastic element completely converts the kinetic energy of the free falling table and test item into potential energy stored in the spring at the peak acceleration. During the unloading portion of the pulse, the stored energy is returned to the table and test item thereby increasing their kinetic energy to the original value. The timing of events during the pulse is a function of the falling mass and the spring rate.

Figure 4 shows the results of this partially elastic pulse generation mechanism in a photograph of an actual machine generated terminal peak saw-tooth pulse. A superposed ideal saw-tooth pulse is included for comparison. This pulse was generated with a lead pellet on a standard, commercially available, gravity-powered impact machine.

The actual terminal peak saw-tooth test pulse differs from the theoretical pulse in the following ways:

1. The rising portion is not quite linear, although this pulse is exceptionally good in

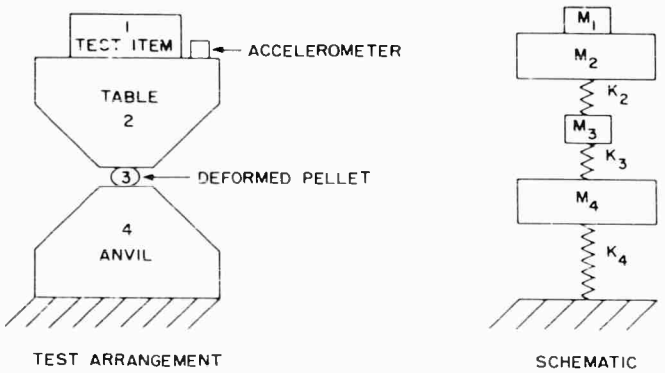

Fig. 3 - Test setup and schematic representation

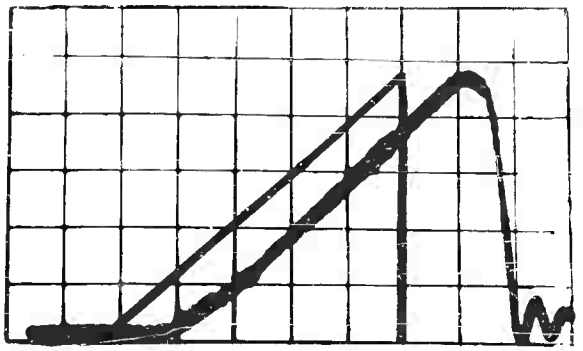

Fig. 4 - Comparison of a record of an actual test pulse with an ideal terminal peak saw-tooth pulse

this respect. (Pulses, normally, are more non-linear).

2. There are no discontinuities in the pulse, especially at the peak which rounds smoothly into the decaying portion of the curve.

3. A finite drop-off time is exhibited in the unloading portion of the pulse after the peak is reached.

4. A high-frequency, low-amplitude oscillation appears at the end of the pulse. The frequency is approximately 1750 cps. These observable differences are explained as follows:

1. The linearity of the rising portion of the pulse is a function of the pellet shape. With some effort, the rising portion can be made more linear by redesign of the pellet. The results, however, may not be worth the effort.

2. Physically generated pulses never exhibit discontinuities. The rounding at the peak is attributed to the partial elasticity of the generation system.

3. Any system with elasticity requires time to unload. During the drop-off era, the table and test item are being accelerated in a vertically upward direction due to the release of the energy stored in the elastic elements. The table then rebounds as a result of the upward acceleration. This is the same physical condition present in the generation of a half-sine shock pulse with a linear spring and the unloading portion of the pulse appears to be nearly a quarter-sine as it is with the half-sine pulse.

4. The structural ringing at the end of the pulse is associated with the predominant natural mode of the test machine. This structural response is excited by the high-rate-of-change of the acceleration (jerk) in the drop-off. This may or may not have important consequences depending on the frequencies and amplitudes involved and also the test item. Since this problem is a very specific problem, it cannot be treated as part of a generalized analytic function without vastly multiplying the complexity of the study. In future work, it is believed that the "tail-wagging" on the pulse can be handled as a separate damped sinusoid using super-position methods. This aspect will not be treated in this paper.

Although the previous discussion refers to the lead-pellet terminal peak saw-tooth pulse, some elasticity is a characteristic of all methods of pulse generation. As a result, all practical saw-tooth pulses have a rounded peak and require a finite drop-off time. An analytical function based on the previous development will, therefore, have general applicability.

The selected pulse is shown in Fig. 2(b). It has all the essential features of the actual test pulse except the structural ringing at the end. It is composed of a ramp tangent to a half-sine. The analytical statement of the function is as follows:

$$f(t) = f_1(t) + f_2(t)$$

$$f_1(t) = Bt/T_1 , \qquad 0 \le t \le T_1$$

$$f_1(t) = 0 , \qquad t \le 0 , \; T_1 < t$$

$$f_2(t) = A \sin \frac{\pi(t - 2T_R + T)}{2(T - T_R)} , \qquad T_1 \le t \le T , \; T_R \neq T$$

$$f_2(t) = 0 . \qquad t < T_1 , \; T \le t .$$

In addition to the physical significance, the ramp-sine function has several other niceties which make it useful for a variety of present and future studies.

1. When T_R and T are equal, the function is a theoretically perfect terminal peak saw-tooth.

2. When T_R equals half of T, the function is a theoretically perfect half-sine.

3. If the function is defined for negative values of time, when T_R is equal to T, the function is a theoretically perfect initial peak saw-tooth.

4. When the function is defined for negative values of T, it is the mirror image of the function defined for positive values of T.

These features make it possible to vary the function incrementally from an initial peak saw-tooth through a half-sine to a terminal peak

saw-tooth by varying the ratio of T_R to T. The present paper considers only positive values of time. Some of the pulses studied are shown in Fig. 5. In addition to these, spectra of one other pulse are presented in this paper. It has a T_R ratio of 0.909 and represents the condition of maximum decay for the nominal 10-millisecond shocks of MIL-STD-810A. The nominal 6-millisecond shock of MIL-STD-810A is covered by the pulse with a T_R to T ratio of 0.870. Minimum duration times for these tests are given by the ideal case where the T_R to T ratio is 1.0.

Shock Response Spectra

The response spectra were computed on a digital computer by determining the generalized response R from the generalized second order linear differential equation of a single-degree-of-freedom system. This equation was developed by Professor Ayre [6] and is quite useful:

$$\frac{\ddot{R}}{\omega_n^2} + \frac{2\zeta\dot{R}}{\omega_n} + R = E .$$

The advantages of this generalized form are discussed in a previous paper [24]. A table of specific excitations and responses is included in the appendix of this paper for those who are interested in the responses of systems to a pulse of this shape for other motional parameters as well as acceleration. The specific excitation used for this problem is the acceleration time function, $\ddot{u}$. The specific differential equation then becomes:

$$-\ddot{\delta} - 2\zeta\omega_n\dot{\delta} - \omega_n^2\delta = \ddot{u} ,$$

where δ is the relative displacement. Conversion of the generalized response to the specific response is as follows: $R = -\omega_n^2\delta$. The response spectra are shown in Figs. 6 through 12. The ordinates are in the normalized general form:

$$\frac{R_m}{E_p} = \frac{-\omega_n^2\,\delta_m}{\ddot{u}_p} ,$$

where the subscripts m and p refer to the maximum and peak values. The abscissa is the normalized product fT where f is the natural frequency of the responding system, and T is the time length of the excitation function. Each curve represents a different damping ratio ζ.

The maximum relative displacement response is obtained from the previous relationship:

$$\delta_m = \frac{-\ddot{u}_p}{\omega_n^2}\left(\frac{R_m}{E_p}\right) .$$

These spectra were computed for comparison on the basis of equal amplitudes and equal durations based on the assumption that it is much easier for a test engineer to control the peak value and duration of a specified shock motion than it is to match the specified shape. The study, therefore, was aimed primarily at showing the effects of deviation from specified shapes.

Examination of the ideal saw-tooth spectra of Fig. 12 indicates that the addition of damping smoothes out the ripples in the spectrum. It is also seen that damping has a greater effect in reducing negative responses than it does in reducing positive responses. Finally, the figure shows that the undamped negative responses

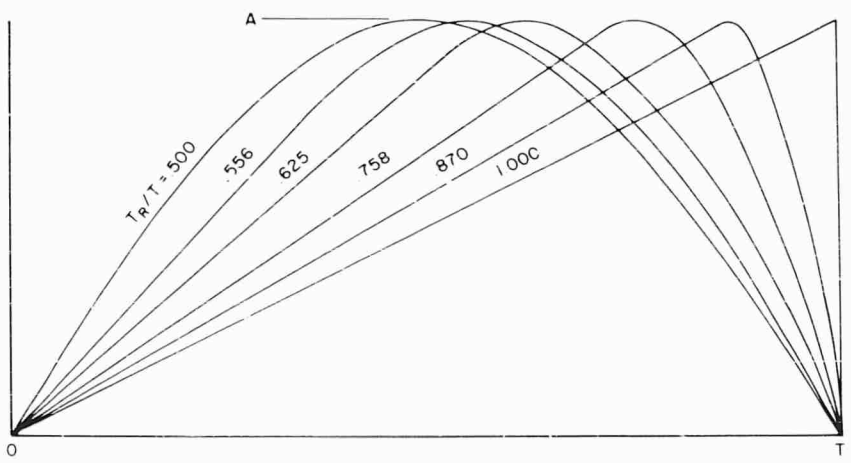

Fig. 5 - Ramp-sine pulses

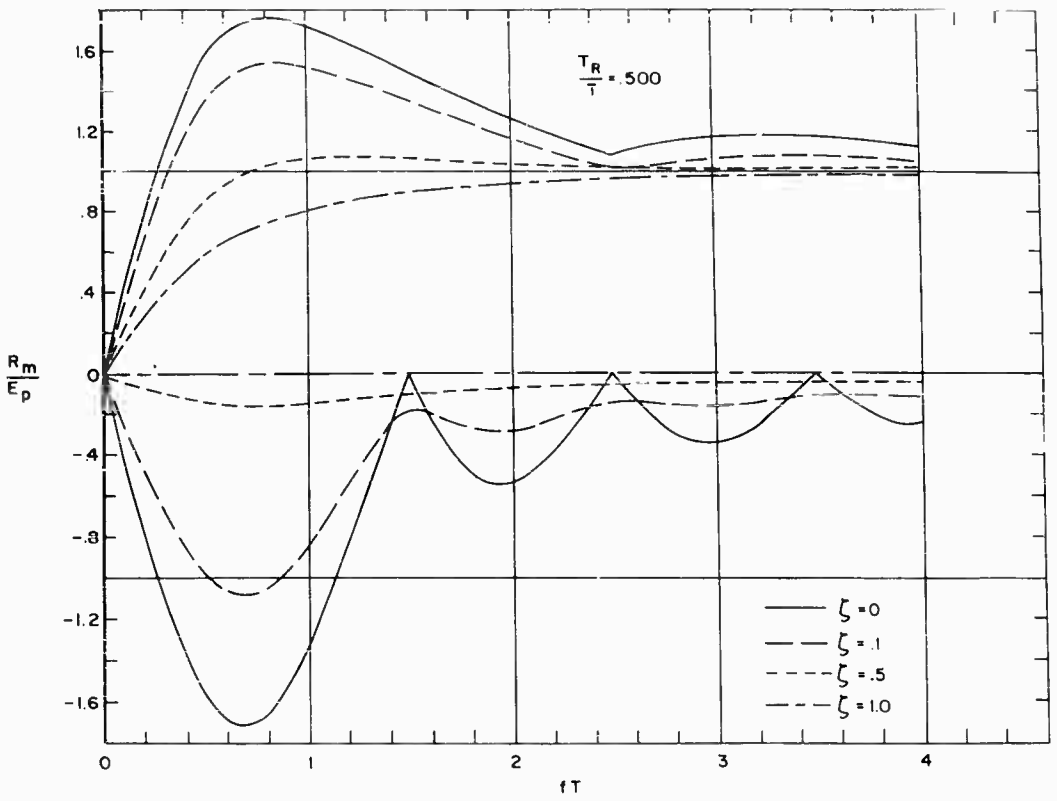

Fig. 6 - Half-sine response spectra for $T_R/T = 0.5$

are between 31 and 54 percent larger than the damped negative responses for $\zeta = 0.1$. This amount of damping is rather common for equipment on isolators or for equipment with damping intentionally built into it to control vibration responses. Such an amount of damping may also be unintentionally present due to the use of plastic and elastomeric insulation or other materials as well as coulomb damping between parts.

Figure 10 shows the spectra of a pulse which meets the requirements for the nominal 6-millisecond pulse of MIL-STD-810. It is seen that the undamped negative response at $fT = 4.0$ is somewhat less than that shown in the ideal case. The undamped negative response in the ideal case is 23 percent greater. The ideal case is 82 percent greater than the responses for $\zeta = 0.1$. This frequency is 581 cps. If we extrapolate to 1000 cps, the undamped negative spectrum for the ideal case is approximately 100 percent greater than the undamped negative spectrum of the assumed test pulse. At 1000 cps the undamped negative response for the ideal pulse is approximately 300 percent greater than the damped negative response for the condition $\zeta = 0.1$ for the assumed test pulse.

The point of these comparisons of assumed test spectra with the undamped negative spectra of the ideal terminal peak saw-tooth is to emphasize the fallacy of testing in only one direction along each of the three principal axes of the equipment. In other words, the assumption that positive and negative responses for a terminal peak saw-tooth test are equal is justifiable only under certain highly restricted circumstances.

Response spectra for the ideal half-sine case are shown in Fig. 6. Damped positive and negative half-sine spectra were previously presented by Shapiro and Hudson [24] and Rubin [6]. They were recomputed for comparison purposes for this study. The most important feature of these spectra are the low values in the negative spectra and the nulls or tendencies to nulls in the negative spectra at fT values of $1.5 + n$. Jacobsen and Ayre [5] have shown these nulls to be a characteristic of symmetrical pulses. It is also interesting to note that the addition of damping up to some maximum value increases the negative responses at these nulls. Increasing damping beyond this value causes a decrease in the negative responses until they become zero

for critical damping. Examination of the positive spectra of Figs. 7 through 12 indicates that an analogous condition is also present in the positive spectra.

Summary plots for each of the four values of damping are presented in Figs. 13 through 16. These graphs can be used for interpolation and extrapolation of the responses to a ramp-sine function of any T_R/T ratio. The first of these figures shows the undamped case. The following points can be deduced from the figure:

1. In the impulsive behavior region where fT is less than 0.25, the responses in both the positive and negative spectra are equal, except for sign, and the differences due to a change of Tr/T are at a minimum. The actual differences are proportional to the differences in the areas of the excitation functions.

2. The positive spectrum between $fT = 0.25$ and 2.0 is sensitive to changes of T_R/T. This is due to the combined effects of changes in shape and area of the excitation function.

3. The region above $fT = 2$ is approximately unity in the positive spectrum, which indicates that this area is relatively insensitive to the ratio of T_R/T.

4. The negative spectrum is quite sensitive to changes in T_R/T for values greater than $fT = 0.25$ with the single exception of values of fT near 1.2 where the values tend to be nearly equal and nearly unity for all exciting functions. Since T_R/T is a measure of the degree of symmetry present in the excitation function, it is evident that the effects of the degree of symmetry are more pronounced in the negative spectrum.

The same general statements apply to the case for a damping ratio of 0.1 shown in Fig. 14 except that sensitivities to differences of T_R/T have been somewhat deemphasized by the addition of damping.

When the damping ratio is 0.5, as shown in Fig. 15, the negative portion of the spectrum tends to become insignificant while the positive portion tends to be relatively insensitive to changes of T_R/T throughout the spectrum.

The final case considered is for critical damping. This case is shown in Fig. 16. Since the definition of critical damping implies a

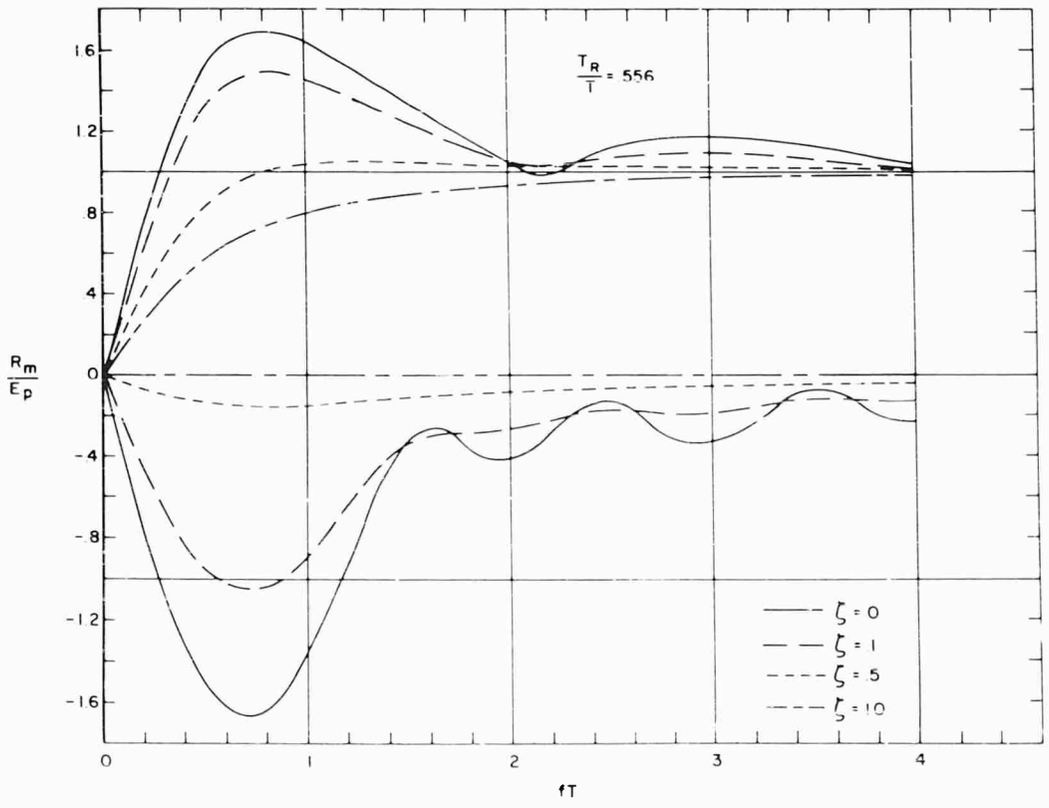

Fig. 7 - Ramp-sine response spectra T_R T = 0.556

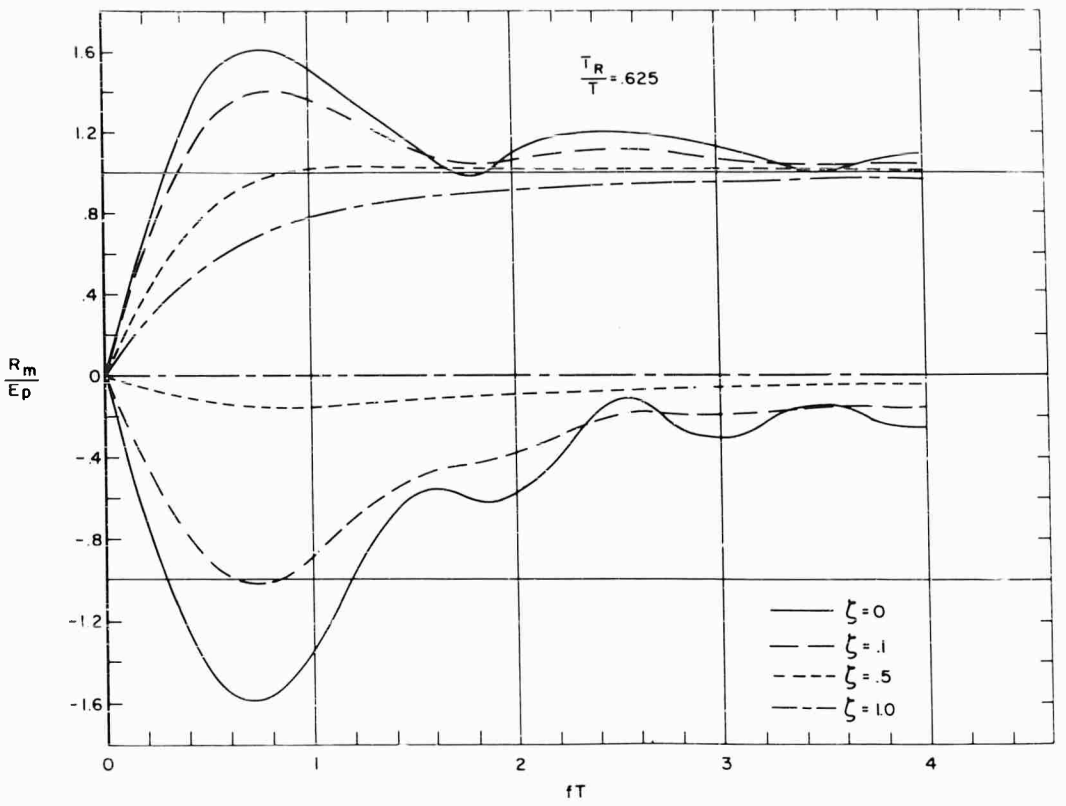

Fig. 8 - Ramp-sine response spectra for $T_R/T = 0.625$

minimum response of zero, there is no negative spectrum. The positive portion of the spectrum is even more insensitive than the previous case.

Fourier Spectra

The Fourier spectra were computed from the Fourier integral as follows:

$$F(\omega) \quad \int_0^T f(t)\, e^{-j\omega t}\, dt$$

$$F(\omega) \quad \int_0^T f(t) \cos \omega t\, dt - j \int_0^T f(t) \sin \omega t\, dt$$

$$F(\omega) \quad R[F(\omega)] + jI[F(\omega)] .$$

This equation provides data for the Fourier real and imaginary spectra. They are sometimes referred to as the cosine and sine spectra, respectively.

An alternative form of the Fourier spectrum which is preferred by some engineers is:

$$F(\omega) = |F(\omega)|\, e^{j\phi(\omega)}$$

$$|F(\omega)| = \left\{ R^2 [F(\omega)] + I^2 [F(\omega)] \right\}^{1/2}$$

$$\phi(\omega) = \tan^{-1} \frac{I[F(\omega)]}{R[F(\omega)]} .$$

The latter two equations provide data for the Fourier amplitude and phase spectra. Since both methods of presenting the spectra are useful, the small effort required to present them in both ways was considered worthwhile.

The Fourier amplitude and phase spectra are shown in Figs. 17 through 23. The abscissa is normalized for general applicability by multiplying the frequency of the Fourier component by the pulse duration. The ordinate values are normalized by dividing by the value of $F(\omega)$ at $\omega = 0$. This is merely the area of the forcing function. The values of $|F(\omega)|$ for any ramp-sine function can be interpolated by knowing the peak value of the function (A), the duration (T), and the rise time T_R. Values of F(0) AT can be interpolated from Table B1 of Appendix B. From these, $|F(\omega)|$ is obtained by multiplying

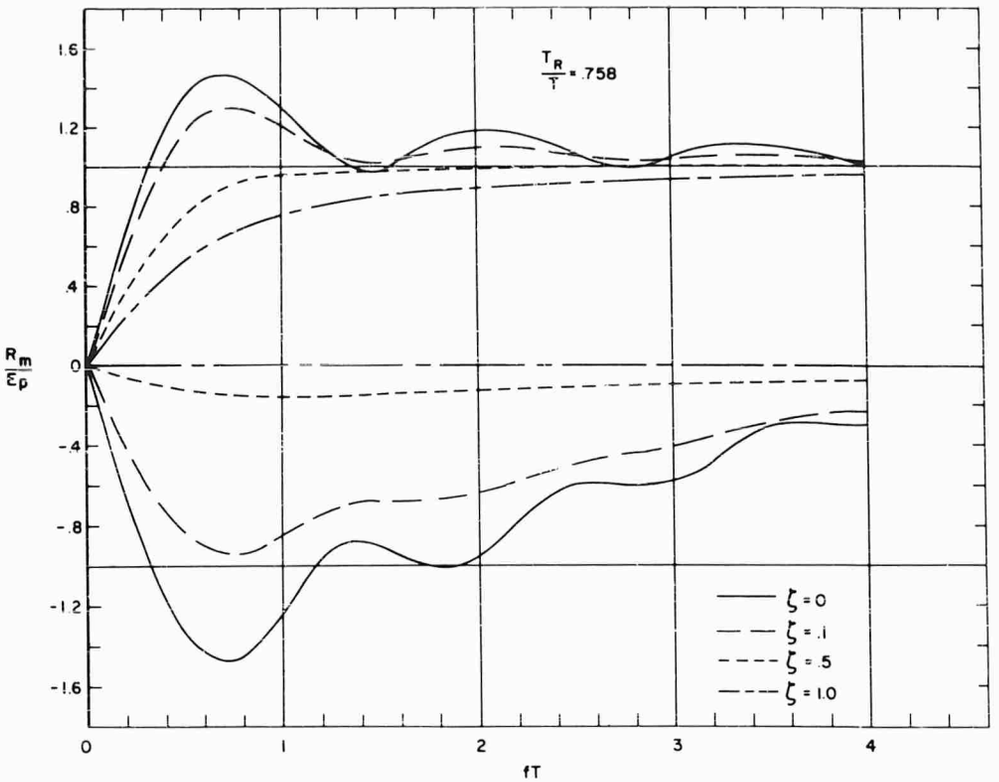

Fig. 9 - Ramp-sine response spectra for T_R/T = 0.758

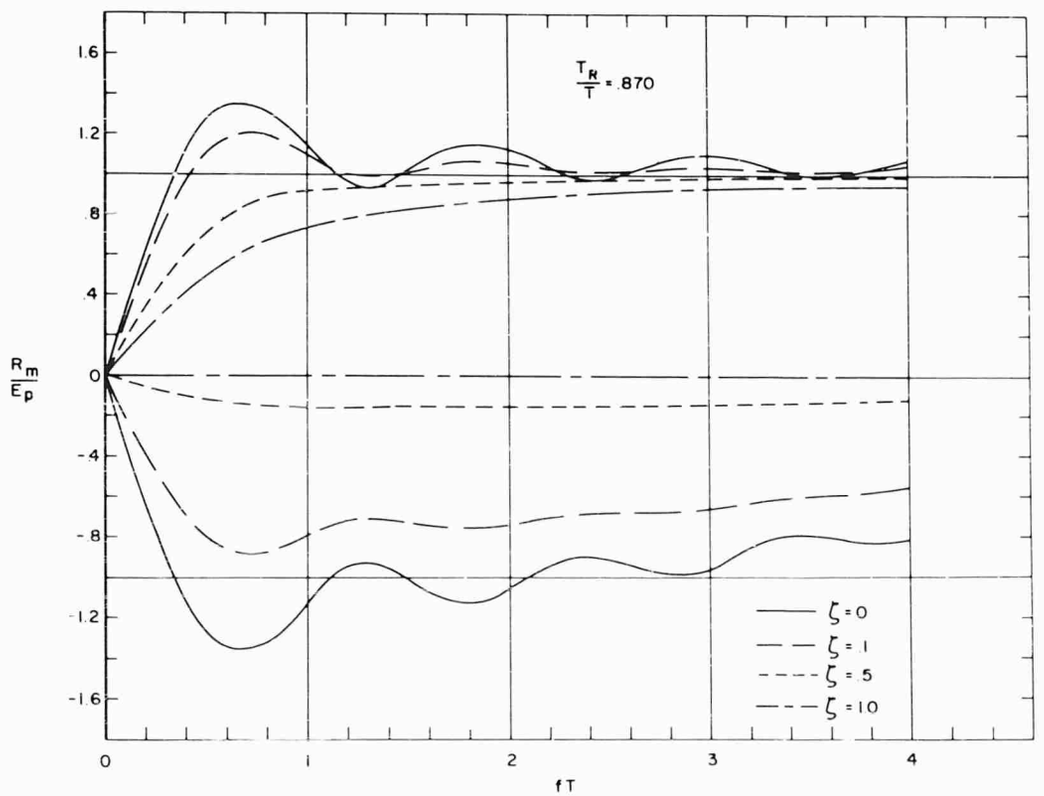

Fig. 10 - Ramp-sine response spectra for T_R/T = 0.870

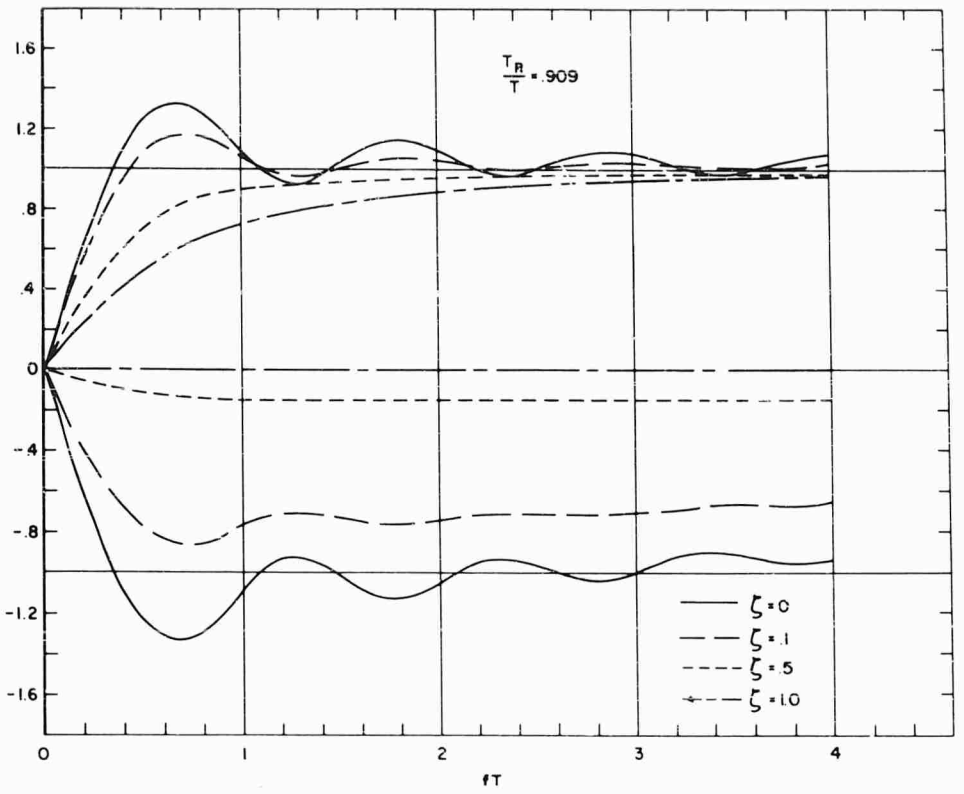

Fig. 11 - Ramp-sine response spectra for T_R/T = 0.909

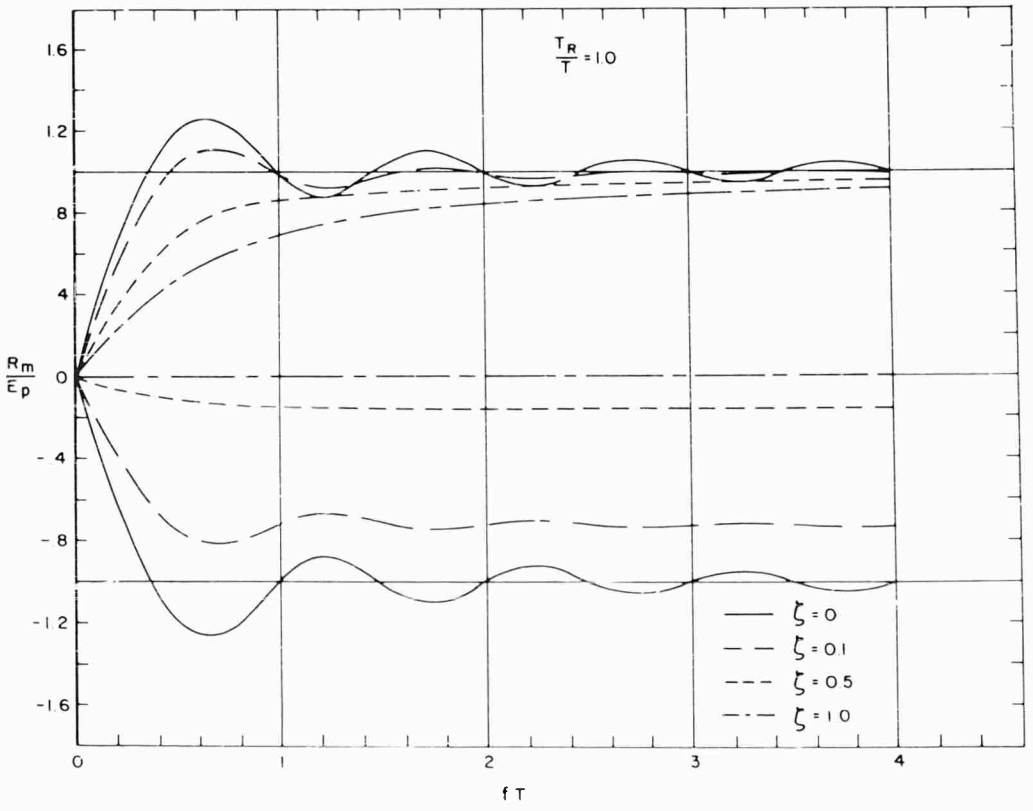

Fig. 12 - Ramp-sine response spectra for T_R T = 1.000

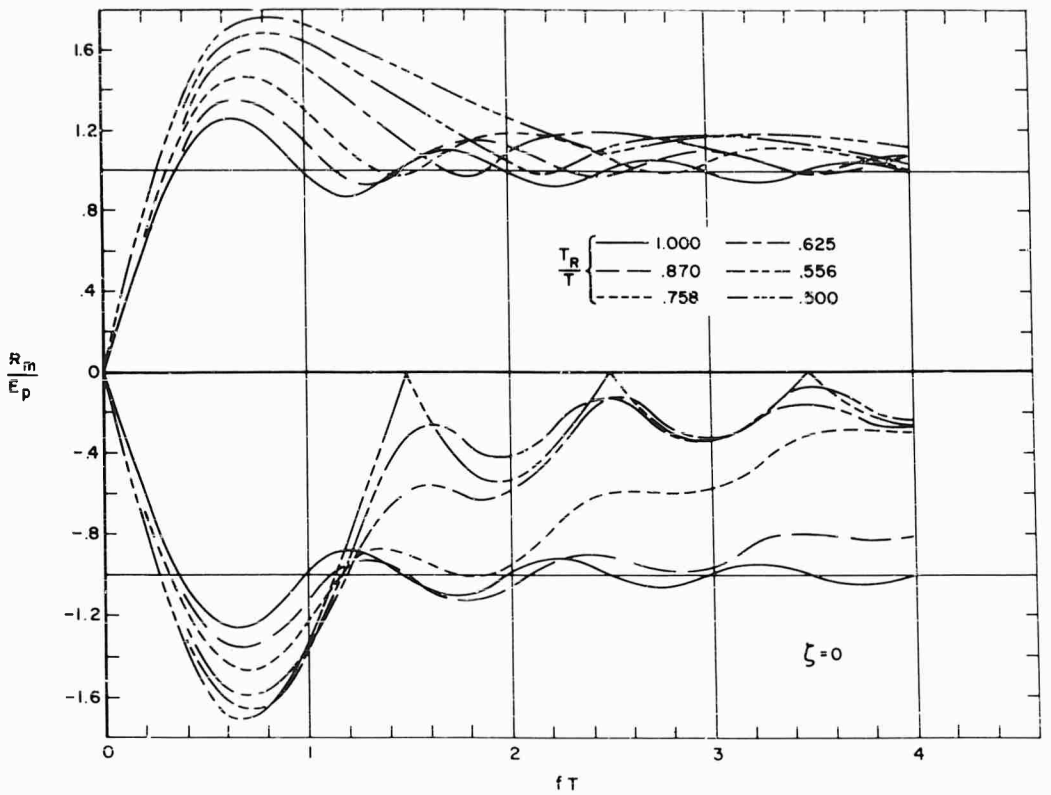

Fig. 13 - Variations in response spectra for $\zeta = 0$

the ordinate by $F(0)\,\Delta T$ from the table and the known amplitude and duration ΔT. The frequency f is obtained by dividing the abscissa by T. Phase angles $\phi(\omega)$ are determined directly from the curves. Examination of the half-sine spectra of Fig. 17 indicates that zeroes of the absolute value occur at $1.5 + n$. This is to be expected since the undamped residual shock spectrum is related to the Fourier spectrum by the constant frequency factor ω_n, and these zeroes were observed in the undamped shock spectrum. It is also seen that phase discontinuities exist wherever these zeroes exist. These can be shown to be true discontinuities since the sine of the angle is discontinuous at the same point.

In the other phase spectra, apparent discontinuities are seen. These, however, are not true discontinuities. They are merely the result of plotting the phase as an angle between 0 and 2π radians. It can be shown that the tangent of the phase angle at an apparent discontinuity is continuous. Therefore, the phase angles must also be continuous at the apparent discontinuity. Because the Fourier components exist forever, it can be shown that the phases of the components can be described by any angle which is different from $\phi(\omega)$ by the angle $\pm 2n\pi$.

A close study of the results obtained in the spectra of Figs. 17 through 23 has not been attempted. It is, however, obvious that major characteristics of the phase spectrum can be correlated with major characteristics of the amplitude spectrum. For example, the half-sine pulse shows discontinuities in the phase spectrum at the same frequencies that zeroes occur in the amplitude spectrum. In Fig. 18, the points of maximum curvature and points of inflection of the phase spectrum occur at odd and even multiples of $\pi/2$, respectively, and seem to be related to some corresponding point (as of now undetermined) in the amplitude spectrum. This suggests the possibility that the phase spectrum may be determined from the amplitude spectrum. Since the Fourier integral can be inverted to obtain the time history, this in turn implies the possibility of inversion of the undamped residual shock spectrum since it fully determines the Fourier amplitude spectrum. No conclusions will be made on this subject and it is reserved for future study.

A summary plot of the amplitude and phase spectra is shown in Fig. 24. Examination of the amplitude spectrum shows the low frequency values to be close together below $fT = 1.0$. At

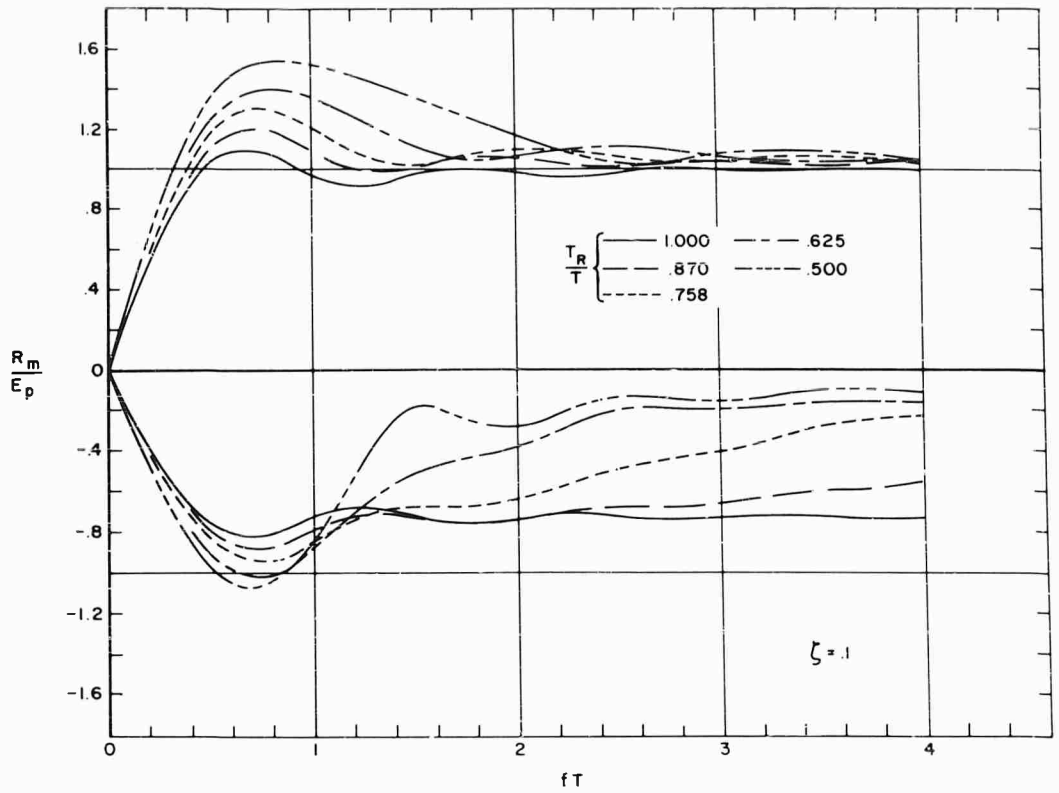

Fig. 14 - Variations in response spectra for $\zeta = 0.1$

fT = 0, all values converge to unity. This could have been predicted from the shock spectra.

The extreme effect of assymetry, as represented by the saw-tooth case $T_R/T = 1.0$, is to smooth out the spectra, both amplitude and phase. The extreme effect of symmetry, as represented by the half-sine case $T_R/T = 0.5$ is the introduction of discontinuities in both the amplitude and phase spectra. Intermediate cases provide a smooth transition from one extreme to the other. The case $T_R/T = 0.556$ is particularly interesting since it shows a rather large variation in the phase spectrum as it approaches the discontinuous spectrum of the symmetrical function $T_R/T = 0.5$.

The normalized real and imaginary spectra are plotted in Figs. 25 through 31. The values of the real and imaginary parts can be determined by multiplying the ordinate by the value of F(0)/AT from Table B1 of Appendix B and the known values of A and T. The frequency is determined by dividing fT by T as before.

In general, the greater the symmetry, the smoother the spectra, both real and imaginary. This is most evident at the higher frequencies.

It is interesting to note that the real part of the half-sine case $T_R/T = 0.5$ is negative for all values of fT greater than 0.5.

A summary plot of real and imaginary spectra is shown in Fig. 32. At the lower frequencies the curves converge to the values of unity and zero in the real and imaginary spectra indicating that the lower frequencies are less sensitive to differences in pulse shape.

CRITERION FOR PROXIMITY FAILURES

There are many types of equipment in which the change in distance between two elements due to the presence of a dynamic environment is a criterion for failure. A simple model of an equipment consisting of two mechanically uncoupled linear single-degree-of-freedom systems is shown schematically in Fig. 33. The proximity of the two masses can change in accordance with dynamic excitations. If the distance between the masses becomes zero, collision occurs which may result in deformation or fracture of mechanical systems or direct shorts in electrical systems. The clearance between adjacent parts in mechanical

systems may be either increased or decreased by the effects of an exciting motion. The results may lead to either malfunction or physical damage due to interaction of mechanical elements attributable to increased or decreased friction or interference between moving parts. In an electrical system, a multitude of failure can occur due to changes in the proximity of two elements. The direct result is a change of dielectric strength, magnetic or electrostatic field strengths. These in turn cause breakdowns in insulation, changes in capacitance, inductance, mutual inductance, and the like, leading to any number of malfunctions or to permanent damage to components of the electrical system.

If a ground acceleration $\ddot{u}(t)$ is applied to the simple equipment of Fig. 33, it causes a displacement of the base $u(t)$ which is transmitted to the two masses through the rigid frame and the springs and dampers of the equipment. The absolute motions of the adjacent surfaces of the two masses are $x_1(t)$ and $x_2(t)$. The relative displacements of these two masses are $\delta_1(t)$ and $\delta_2(t)$. The proximity of the masses at any time is the distance $D(t)$, and D_{st} is the static value when the system is at rest.

$$D(t) = x_2(t) - x_1(t) + D_{st}$$

$$x_1(t) = u(t) + \delta_1(t)$$

$$x_2(t) = u(t) + \delta_2(t).$$

By substituting for $x_1(t)$ and $x_2(t)$ in the first equation

$$D(t) = \delta_2(t) - \delta_1(t) + D_{st} = \Delta(t) + D_{st}.$$

The symbol D is called the "proximity" and Δ is called the "proximity criterion."

While the complete time history of the proximity function $D(t)$ might be enlightening, most engineers would find the extreme values more useful:

$$D_{max} = D_{st} + \Delta_{max}$$

$$D_{min} = D_{st} + \Delta_{min}.$$

If the equipment is excited in both positive and negative directions, the maximum absolute value of the proximity function is of most importance:

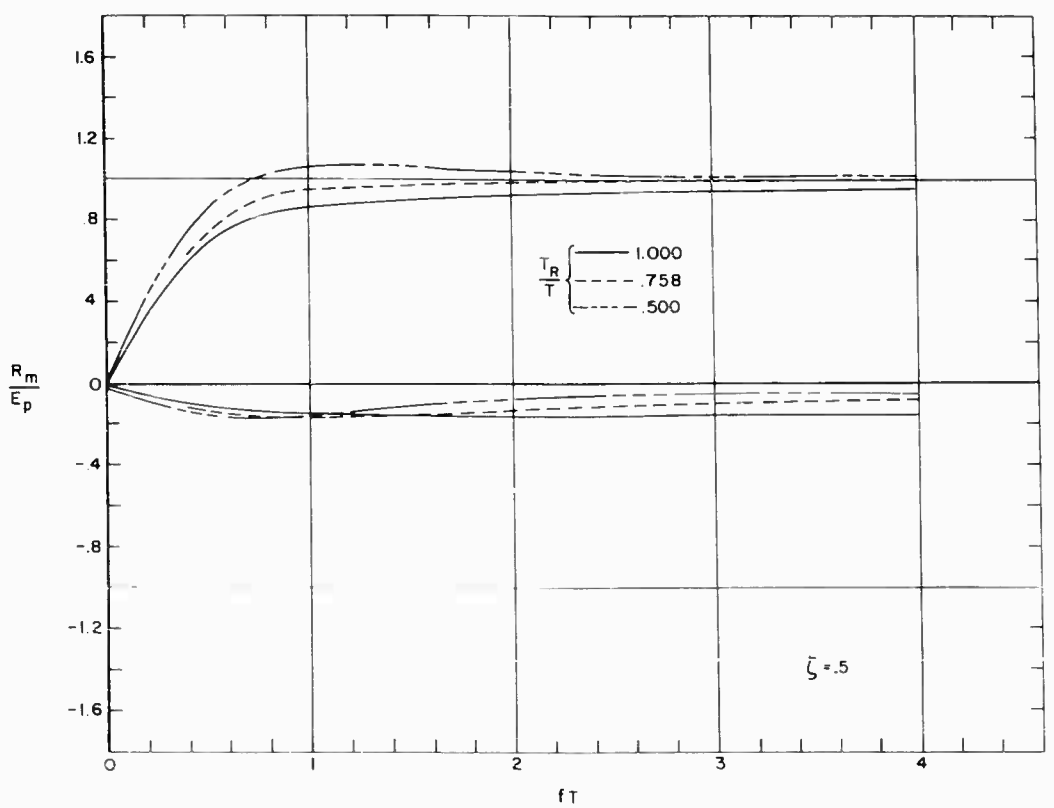

Fig. 15 - Variations in response spectra for $\zeta = 0.5$

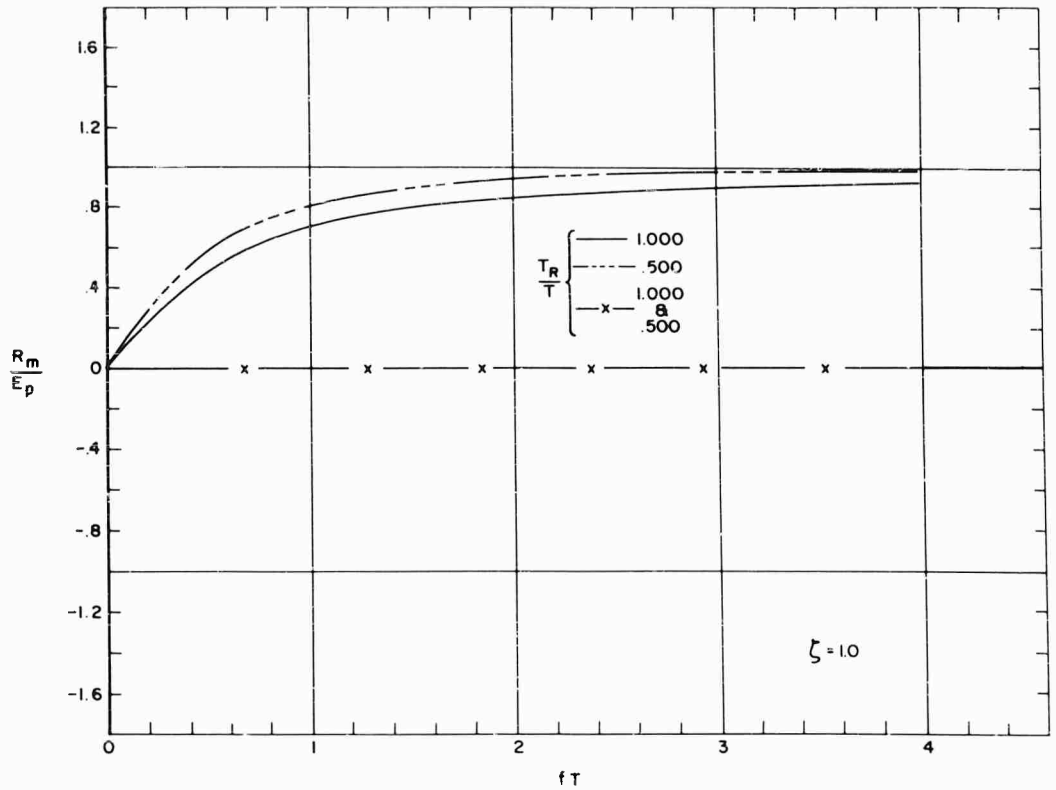

Fig. 16 - Variations in response spectra for $\zeta = 1.0$

$$|D|_{max} - |D_{st} + \Delta|_{max}.$$

Thus Δ is established as an important criterion for determining the proximity failure potential of an exciting motion. This is somewhat analogous to the equivalent static acceleration of a single degree-of-freedom system which Walsh and Blake [26] proposed as a criterion for the failure potential of a motion. The latter is usually plotted as a positive function of the frequency of an undamped system and called the shock spectrum.

This suggests the possibility that "proximity spectra" might be determined by plotting Δ_{max} and Δ_{min} for the two mass system of Fig. 33. Since an additional mass is present, it would require a second frequency axis. Such a scheme would generate two surfaces (Δ_{max} and Δ_{min}) on a three dimensional plot. The development of this idea, however, is beyond the scope of this paper.

An upper bound for the proximity criterion Δ can be obtained from the undamped positive shock spectrum by adding the relative displacements. Δ_{max} and $|\Delta|_{max}$ would be the positive value of this sum and Δ_{min} would be the negative value. This method provides a conservative estimate of the possibility of collision or proximity failures.

An indication of the possibility of overconservatism may be obtained by examining the undamped residual spectrum (or the undamped negative spectrum). If the proximity criterion has one or more extreme values in the residual era, i.e., after the excitation has ceased, its positive and negative values may be much less than those determined from the positive spectrum. This is particularly true if the pulse tends toward symmetry. Since it cannot be determined whether the extremes of proximity occur during the pulse, after the pulse is over, or in both eras, when the negative (or residual) spectrum is different from the positive spectrum, it will be necessary to compute the time history of the proximity criterion if an over-conservative estimate is unacceptable.

The preceding discussion also applies to the determination of the proximity criterion for the model equipment with damped spring mass systems.

Although the proximity criterion has been developed for study of shock excitations, there is

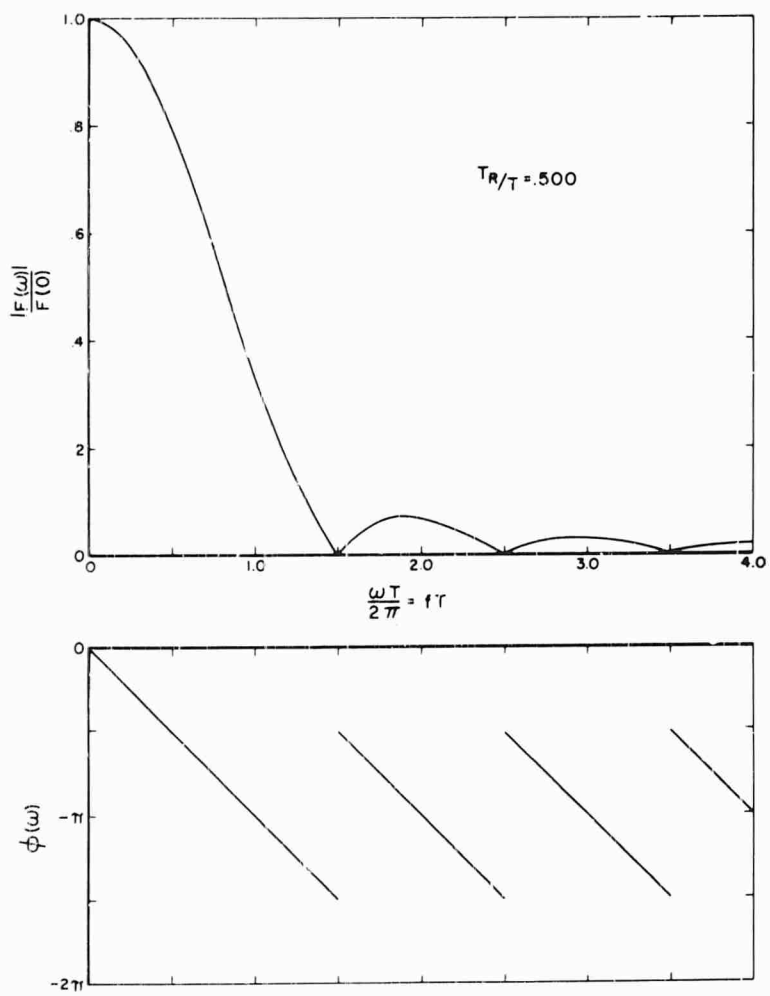

Fig. 17 - Fourier amplitude and phase spectra for $T_R/T = 0.500$

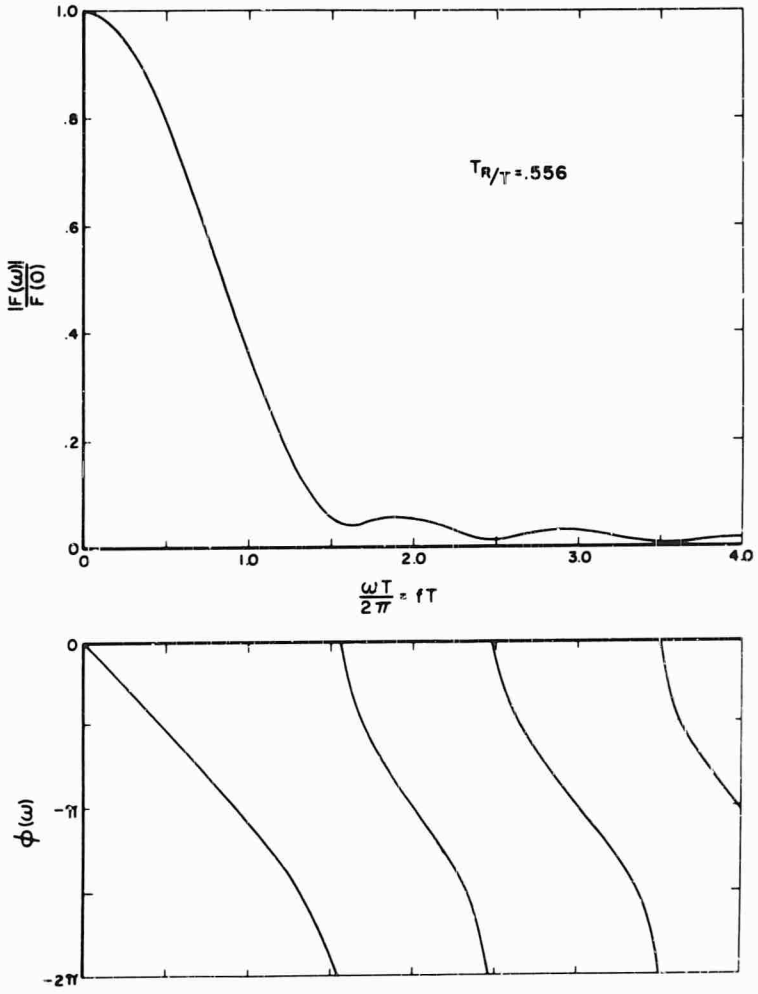

Fig. 18 - Fourier amplitude and phase spectra for $T_R/T = 0.556$

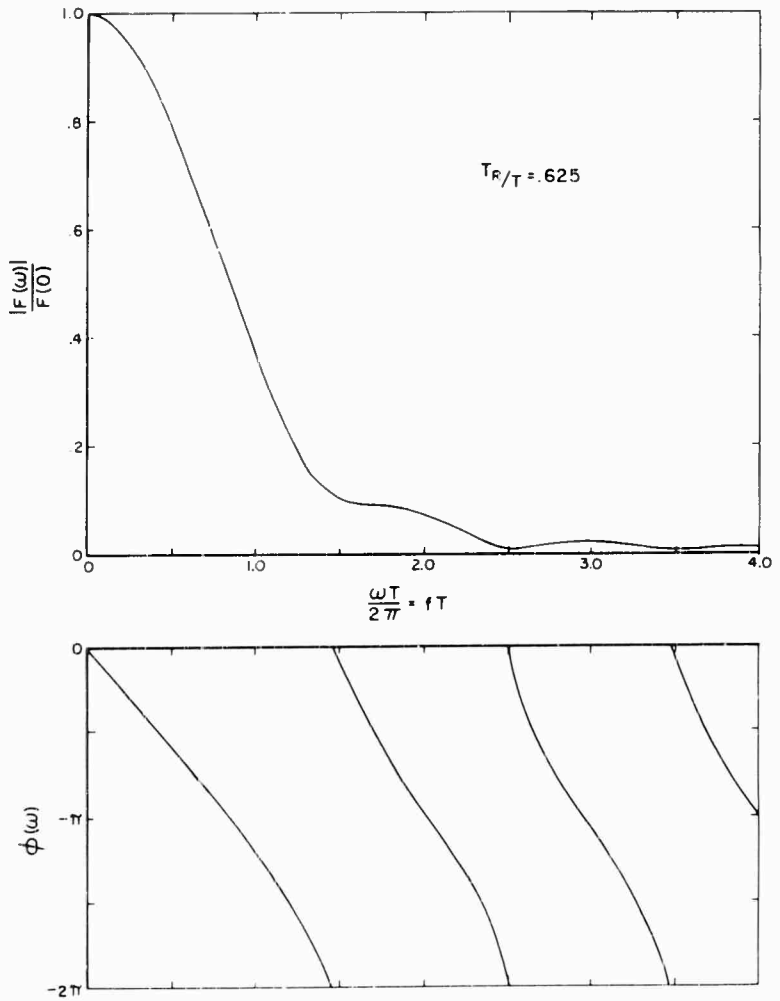

Fig. 19 - Fourier amplitude and phase spectra for T_R T = 0.625

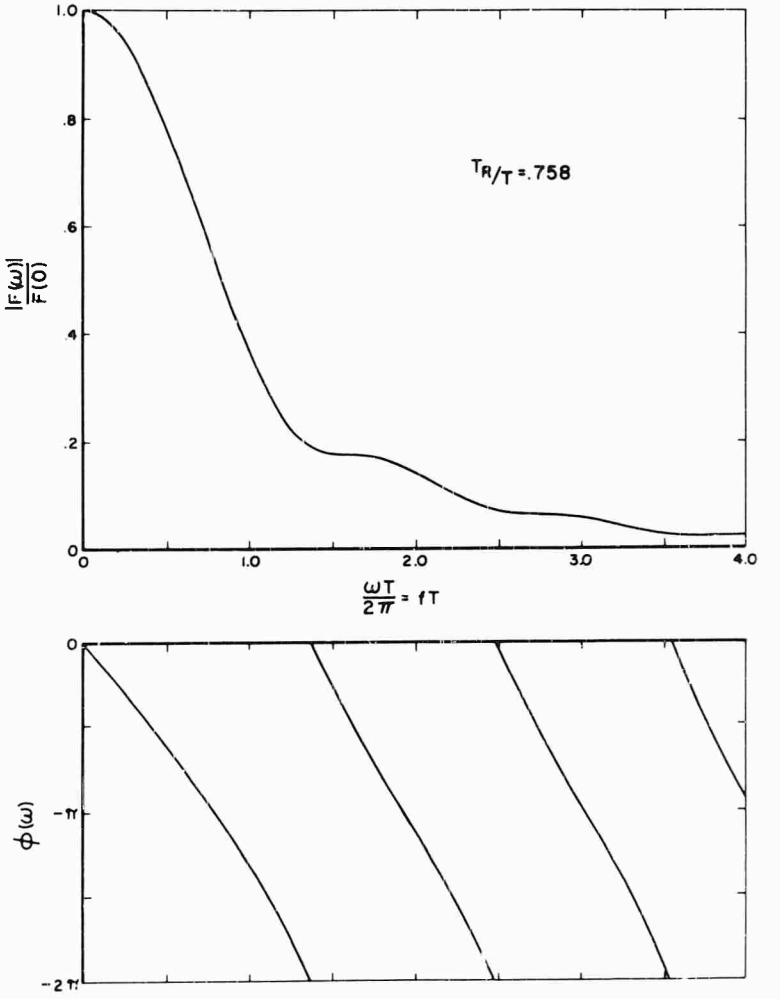

Fig. 20 - Fourier amplitude and phase spectra for T_R T = 0.758

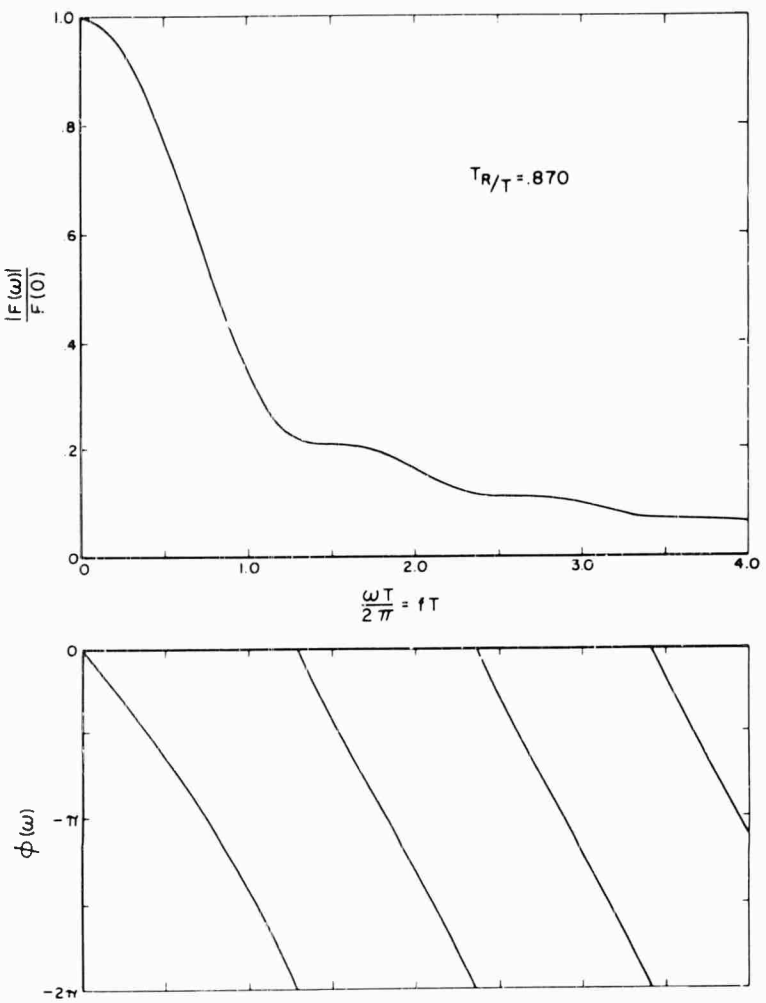

Fig. 21 - Fourier amplitude and phase spectra for $T_R/T = 0.870$

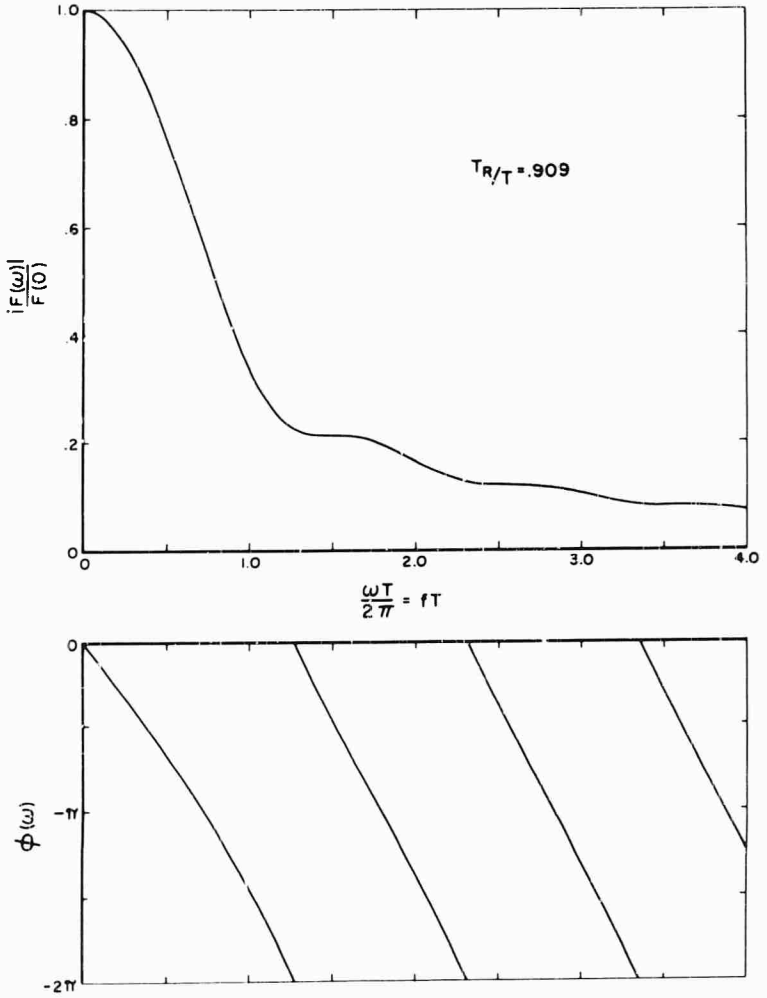

Fig. 22 - Fourier amplitude and phase spectra for $T_R/T = 0.909$

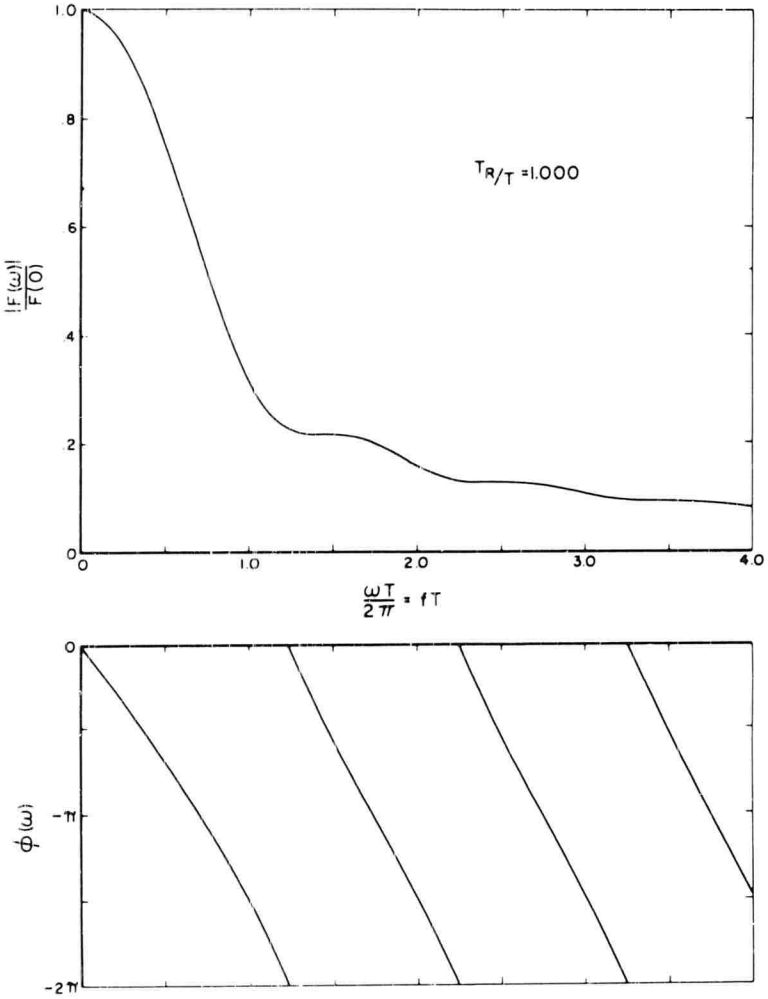

Fig. 23 - Fourier amplitude and phase spectra for T_R T = 1.000

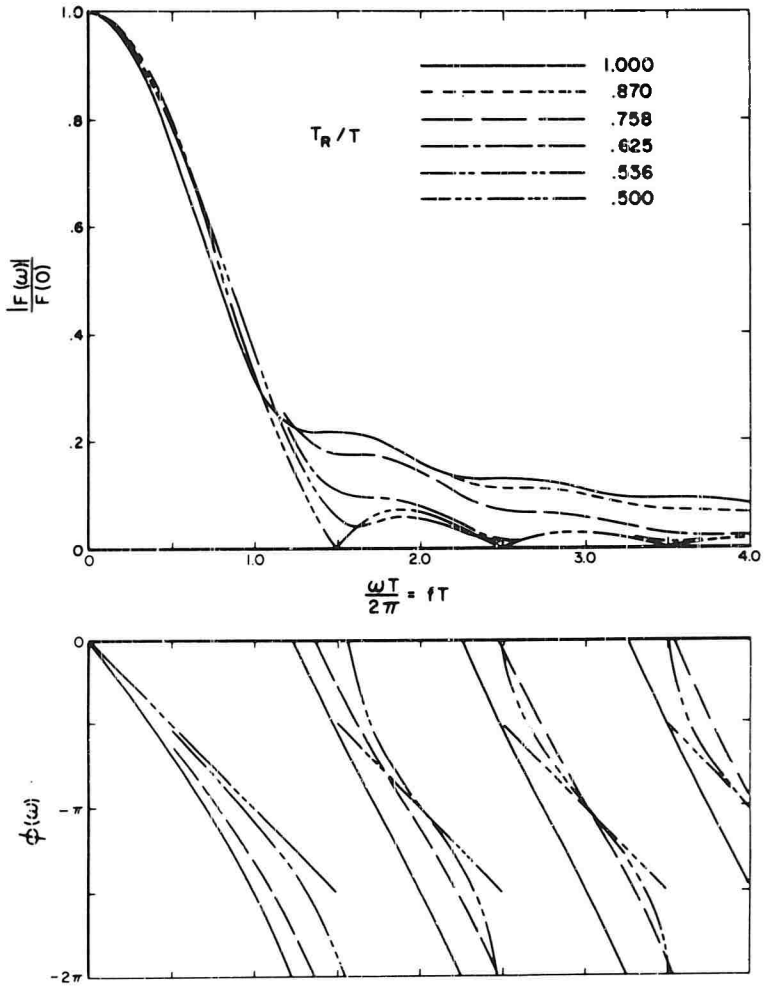

Fig. 24 - Variations in Fourier amplitude and phase spectra

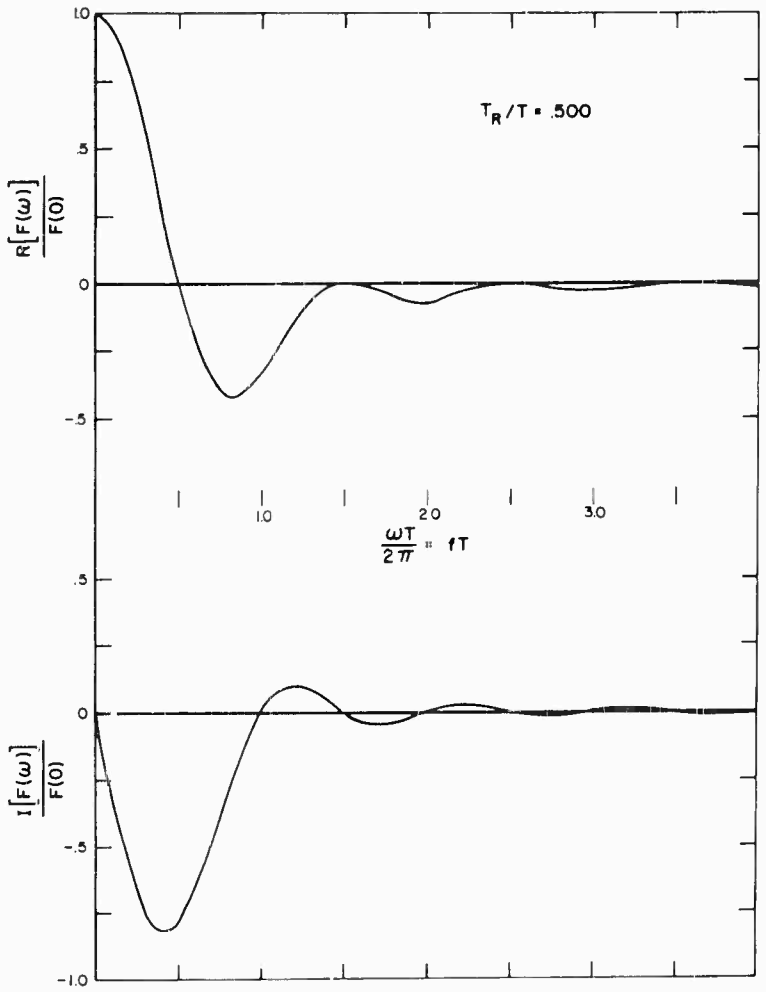

Fig. 25 - Fourier real and imaginary spectra for $T_R/T = 0.500$

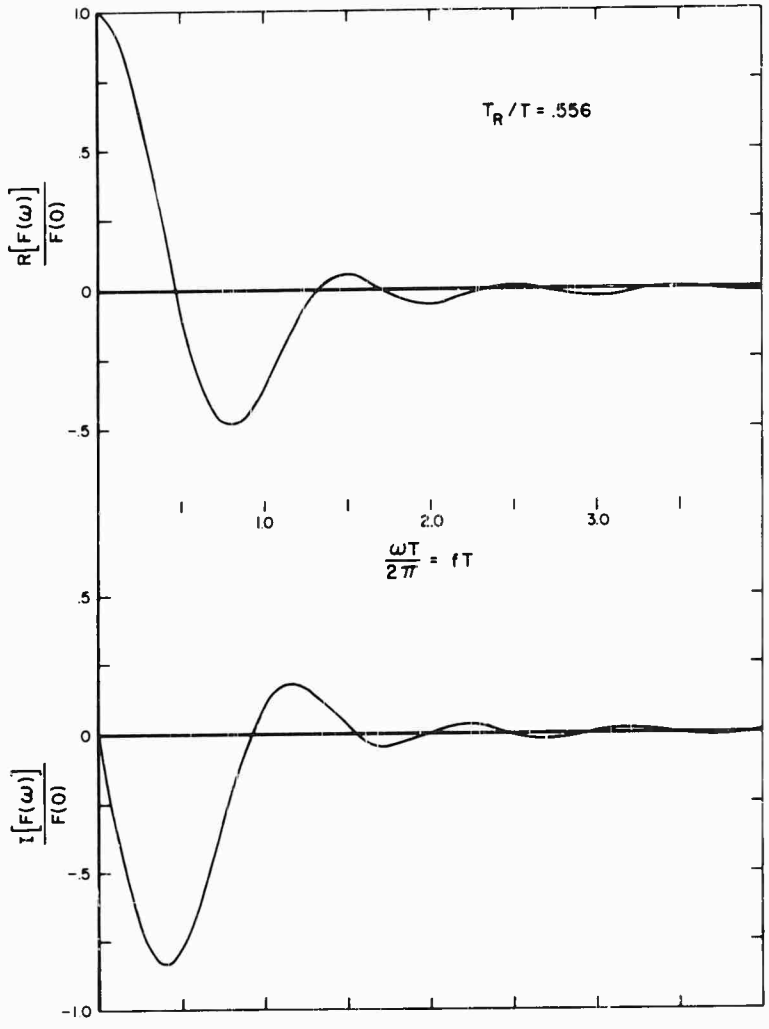

Fig. 26 - Fourier real and imaginary spectra for $T_R/T = 0.556$

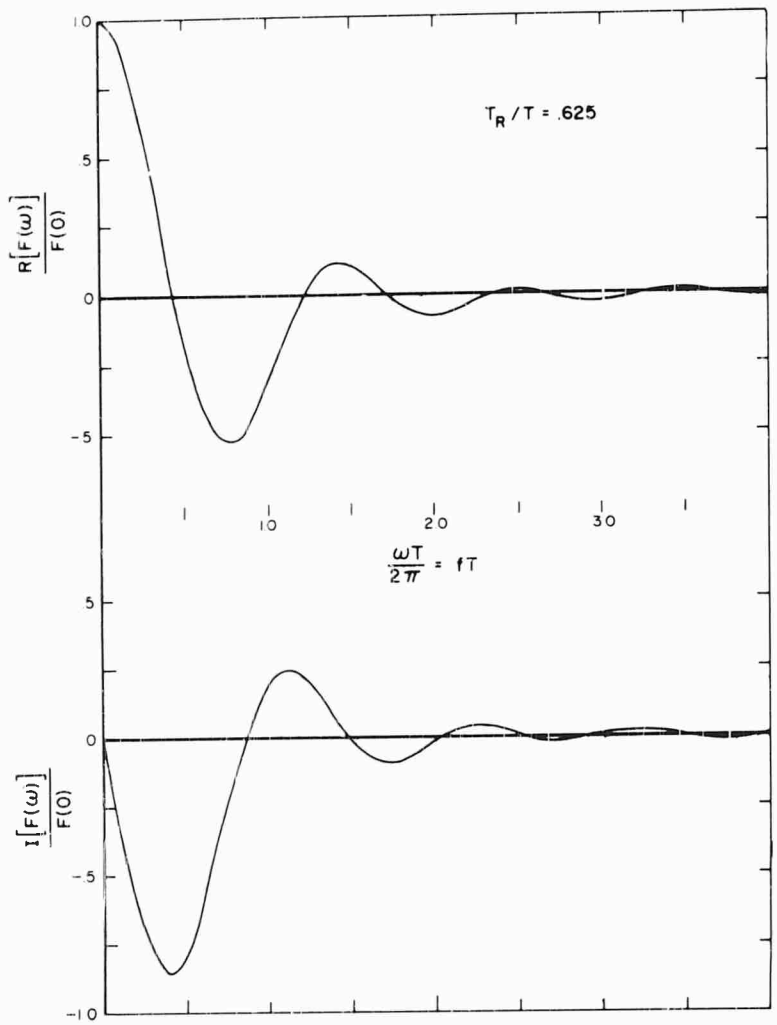

Fig. 27 - Fourier real and imaginary spectra for $T_R/T = 0.625$

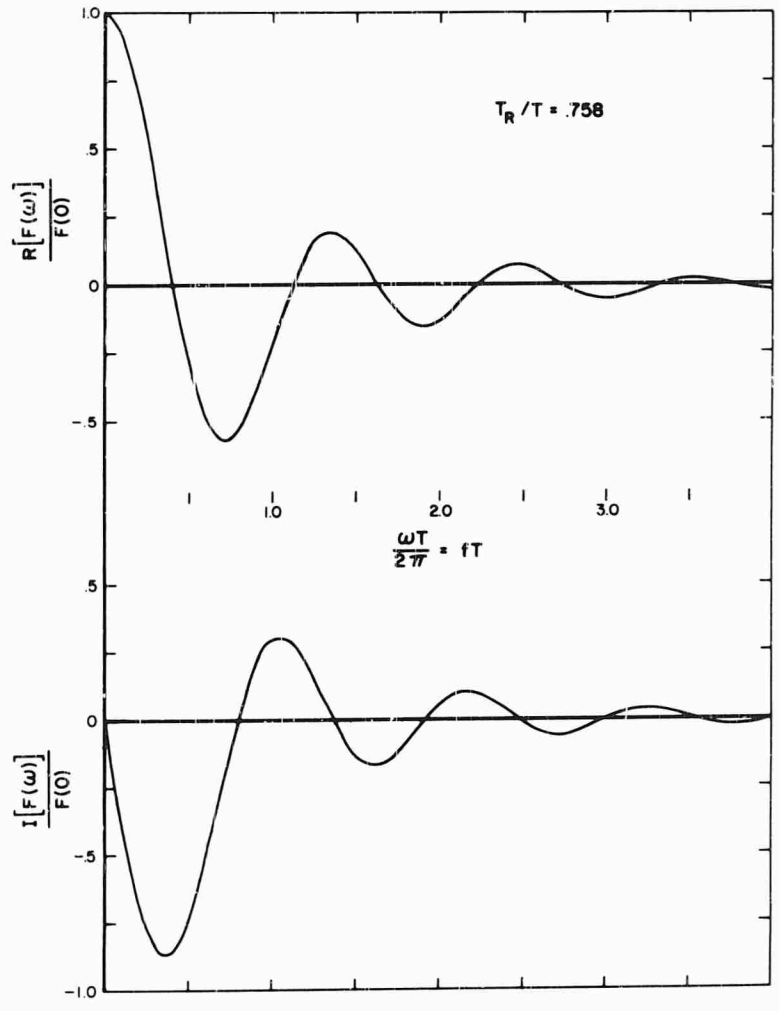

Fig. 28 - Fourier real and imaginary spectra for $T_R/T = 0.758$

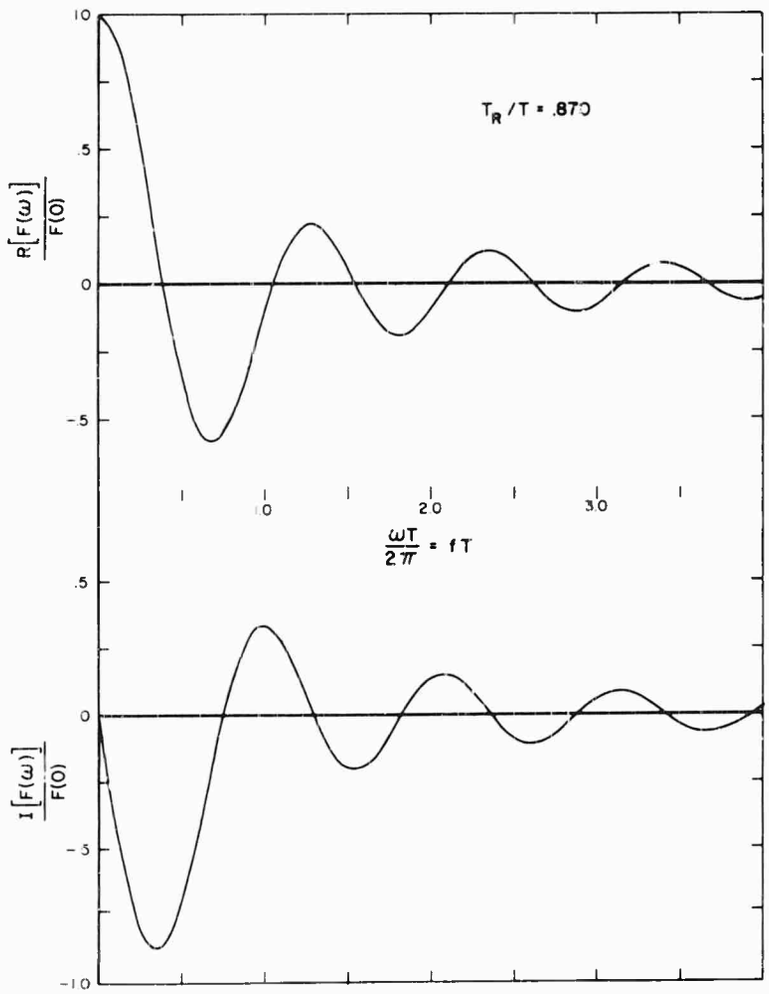

Fig. 29 - Fourier real and imaginary spectra for $T_R/T = 0.870$

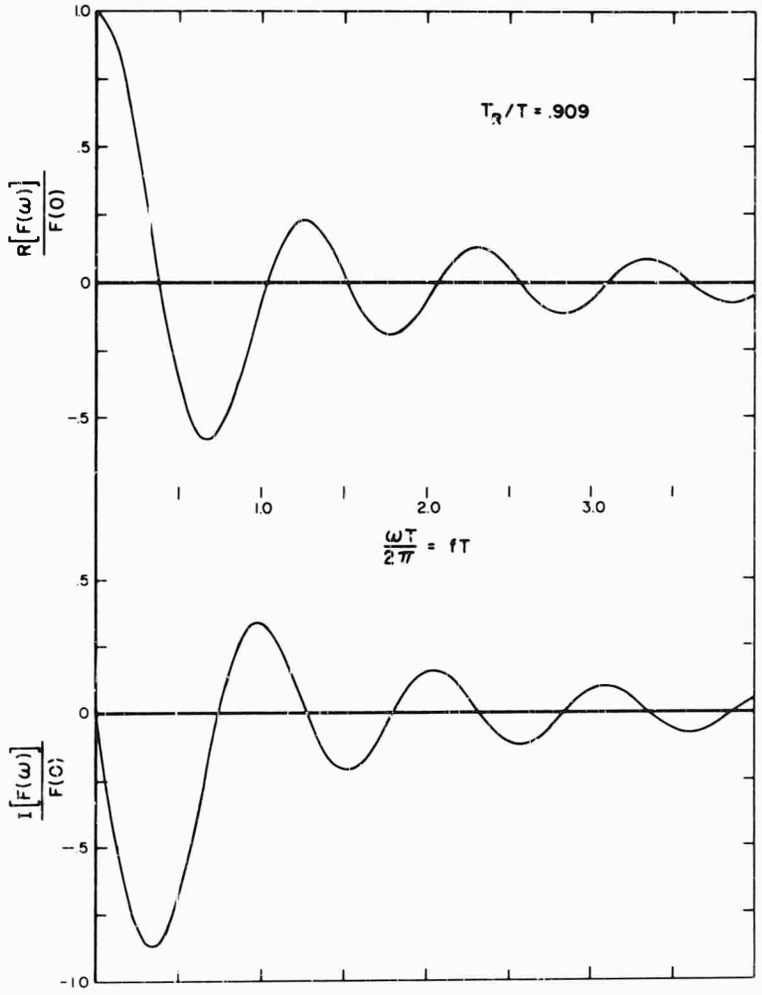

Fig. 30 - Fourier real and imaginary spectra for $T_R/T = 0.909$

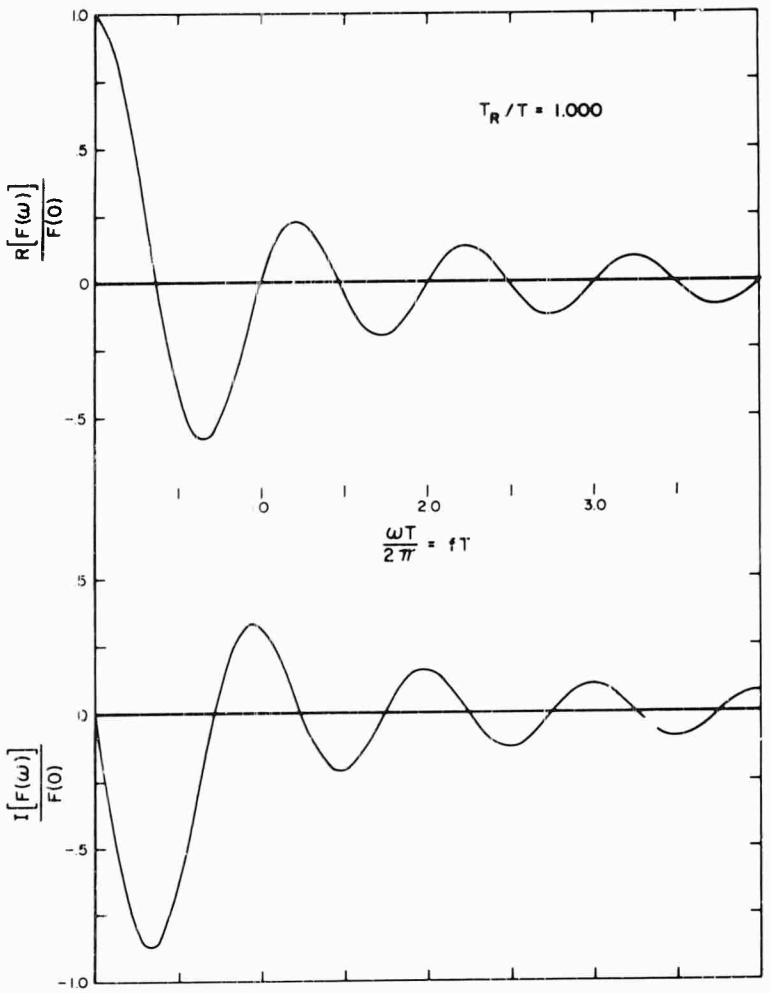

Fig. 31 - Fourier real and imaginary spectra for $T_R/T = 1.000$

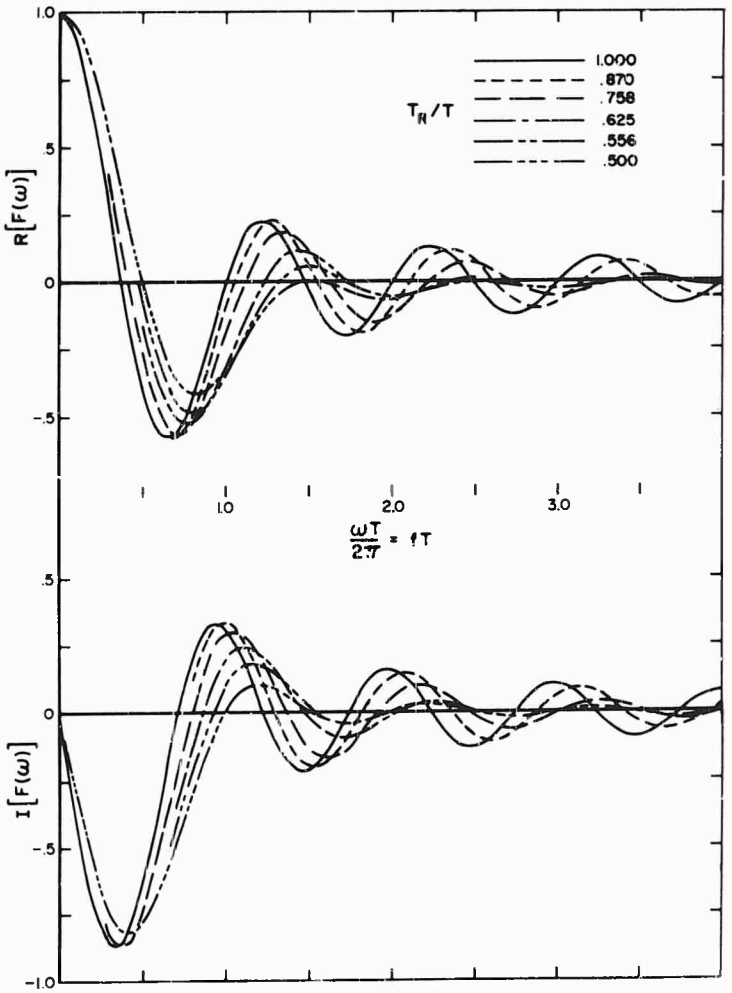

Fig. 32 - Variations of the Fourier real and imaginary spectra

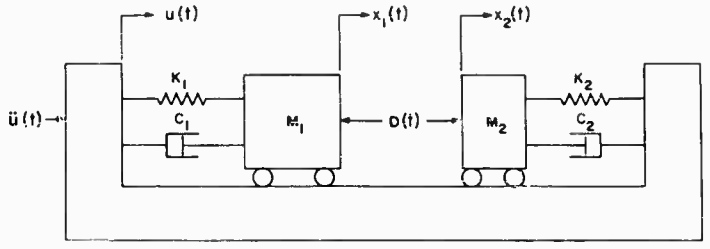

Fig. 33 - Model equipment for determining proximity failure criteria for a given excitation

no reason to limit it to shock. It can also be useful in the study of the proximity failure potential of random and multi-sinusoidal vibration and other forms of excitation.

SAW-TOOTH VERSUS HALF-SINE

Another reason will be advanced in this section for preference of the terminal peak saw-tooth for a general test. Two other reasons have already been discussed.

It has already been pointed out that the positive spectrum of the half-sine pulse is less constant than that of the saw-tooth and there are nulls in the negative spectrum. In other words, the half-sine pulse shows much more frequency discrimination than the saw-tooth. If it could be shown that the environment discriminated against these frequencies in the same way, one could say the half-sine would be an ideal test. Unfortunately, this is not so. The environment for a variety of equipments mounted in a variety of ways on a variety of structures in a variety of vehicles is largely unpredictable. The result is usually a somewhat arbitrary estimate of a positive and negative design shock spectrum of constant acceleration over a given frequency range. In other words, the design spectrum for a general test must be nondiscriminatory since we cannot predict how nature will discriminate against certain frequencies.

In the past, it has been assumed that if one were willing to overtest at some frequencies by as much as 76 percent, the half-sine would produce the minimum positive and negative values by testing in both positive and negative directions along the test axis of the equipment.

The half-sine pulses of military specifications were not based on shock spectra, but on expected acceleration inputs from the environment with no consideration of the spectral character of the environment.

There are several ways of judging the equivalence of the half-sine and saw-tooth waves for comparison purposes. The method used here was to assume that the pulses were equivalent if they were equal in area and duration. This means that the peak amplitude of the saw-tooth is $4/\pi$ times the peak amplitude of the half-sine. This is partially justified when it is realized that an environmental response spectrum based on half-sine inputs with various durations would be 1.76 times the input amplitude. The maximum response to the equivalent saw-tooth is 1.61 times the input. The energy requirements for both pulses are equal.

Proximity criteria (Δ) for the model equipment of Fig. 33 were computed on an analog computer for an ideal half-sine of unit amplitude and unit duration and an ideal saw-tooth having an amplitude of $4/\pi$ and unit duration. The frequencies f_1 and f_2 were 1.5 and 1.55, respectively. These frequencies are in cycles per unit time. If the unit of time is 10 milliseconds, the pulses would be 10 milliseconds long and the response frequencies would be 150 and 155 cycles per second. They were chosen so that the residual responses were at or near a null in the residual spectrum and were also close together. The first of these conditions insures that the residual responses will be at or near zero. The second condition would insure that the two responses would be very nearly in phase with each other during the excitation, and the proximity criterion in this era would also be nearly zero. This is shown to be true by examination of the first computer record from the left of Fig. 34. Positive, negative, and absolute values of the proximity criterion are all very small in comparison to the proximity criteria for the saw-tooth shown in the second record. The third and fourth records compare the proximity criteria when a goodly amount of damping ($\zeta = 0.1$) is present. These proximity criteria cannot be compared directly to those in the first and second records, because the amplitude scale is different. They are actually smaller than those for the undamped

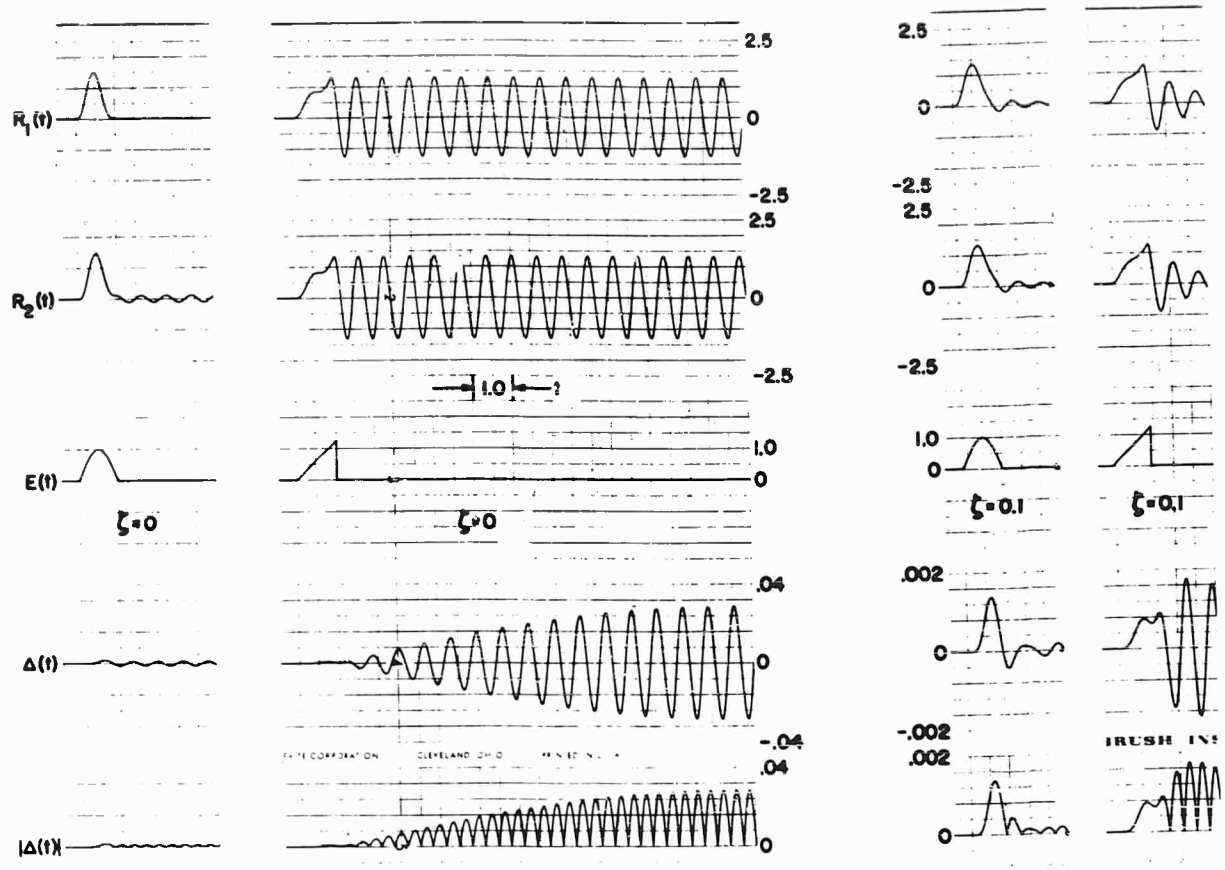

Fig. 34 - Proximity criteria for half-sine and saw-tooth pulses for a case causing a near-minimum half-sine proximity criterion

cases. It is seen that the addition of damping greatly reduces the proximity criterion in the residual eras, but has much less effect on those during the excitation era. Nevertheless, the saw-tooth still produces larger values of positive, negative, and absolute proximity criteria.

The same equipment was also subjected to pulses having a relative duration of 0.4333 as shown in Fig. 35. This pulse length was chosen to nearly maximize extreme values of the proximity criteria for the half-sine excitation. The same results would have been obtained if the duration had remained at unity and the frequencies of the two systems had been changed by the factor 0.4333 to 0.65 and 0.672. A change in the input is analogous to a change in the environment while a change in the response frequencies is analogous to a change of an equipment being tested. It is evident that even near frequencies of maximum values for the positive, negative, and absolute proximity criteria of the half-sine, the proximity criteria of the saw-tooth are 96 percent of those for the half-sine. It can be shown that a saw-tooth pulse which produces the same maximum response at the same frequency as the half-sine and has the same area will produce the same extremes of the proximity criterion. This is another pulse which can be considered equivalent. This criterion for equivalence was actually used in converting Air Force half-sine tests to saw-tooth tests.

CONCLUSIONS

1. The ramp-sine function is more closely related to the actual test waveform generated during a saw-tooth test than previous theoretical pulses and is more justifiable by physical reasoning.

2. Shock spectra and Fourier spectra for a variety of deviations from ideal half-sine and saw-tooth pulses have been determined. These spectra can be used in design work and in choosing test waveforms.

3. The proximity criterion (Δ) proposed in this paper provides insight into the ability of a

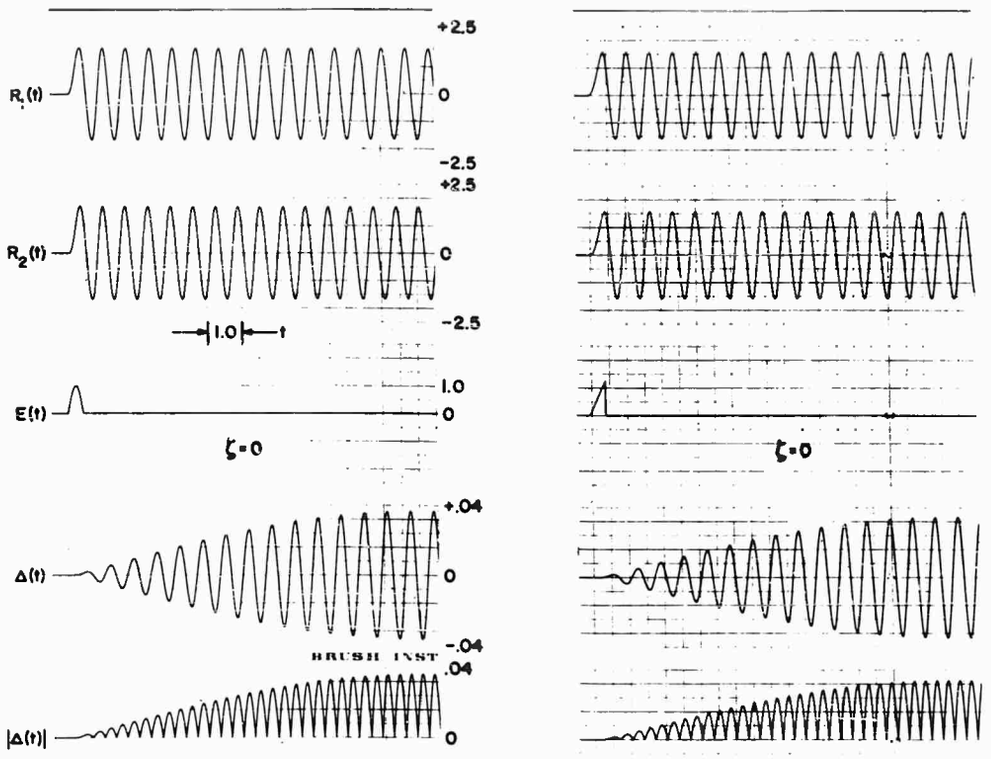

Fig. 35 - Proximity criteria for half-sine and saw-tooth pulses for a case causing a near-maximum half-sine proximity criterion

shock excitation to produce proximity or collision failures in a simple equipment which cannot be obtained from the shock spectrum. It can also be used to study other forms of excitation such as random vibration.

4. On the basis of present knowledge, the terminal peak saw-tooth is a considerably better waveform than the half-sine for creating proximity and collision failures in a simple equipment. This conclusion applies whether the test is applied in only one direction or in opposite directions along the test axis. Since the terminal peak saw-tooth and half-sine are representative of the effects of asymmetry and symmetry, the conclusion can be generalized to show the superiority of asymmetrical over symmetrical waveforms.

5. The effects of damping and drop-off in the saw-tooth pulse reduce the negative spectrum enough to warrant testing in both directions along each of the three principal axes. For example, damping and drop-off reduced the undamped negative response to an ideal pulse by 75 percent for a comparable 1000 cps system with 10 percent damping. (This does not mean that the negative spectrum is unimportant. It is quite important when proximity failures are considered).

6. Negative spectra should be plotted as part of any data reduction process which results in shock response spectra since this spectrum is important in assessing the possibility of proximity failures.

ACKNOWLEDGMENTS

The author wishes to acknowledge the very significant contributions of Ernst Tolle, Joseph Marous, John Sansom, and Dave La Jeunesse.

Appendix A

LIST OF SYMBOLS

A peak value of an excitation

B ordinate of the point of tangency of the ramp-sine function as shown in Fig. 2(b)

c viscous damping coefficient

D proximity (derivation in text)

D_{st} status value of D (see text)

e base of Napierian logarithms (2.7183)

E generalized excitation

f general function of a specific variable

f cyclic frequency

F complex Fourier spectrum

I the imaginary part or component (b) of the complex number a + jb

j $\sqrt{-1}$

K stiffness

M mass

m subscript meaning "the maximum value of"

n 0, 1, 2, 3 ---etc.

p subscript meaning "the peak value of"

R generalized response of a linear single-degree-of freedom system

R the real part or component (a) of the complex number a + jb

t instantaneous time

t_d duration of an excitation time function

T duration of an excitation time function

T_R time of rise to the peak value of an excitation

T_1 abscissa of the point of tangency of the ramp-sine function as shown in Fig. 2(b)

u absolute displacement excitation

x absolute displacement response

δ relative displacement response

Λ proximity criterion (derivation in text)

ζ fraction of critical damping

ϕ phase difference of Fourier amplitude components

ω angular frequency

ω_n angular natural frequency

Appendix B

FORMULAS AND TABLES

POINT OF TANGENCY OF THE RAMP-SINE FUNCTION

The point of tangency of the ramp-sine function (B, T_1) is determined from the condition that both $f_1(t)$ and $f_2(t)$ are equal at the time T_1 and their slopes are also equal at T_1. These conditions lead to the following pair of simultaneous equations:

$$B - A \sin \frac{\pi(T_1 - 2T_R + T)}{2(T - T_R)} = 0$$

$$\frac{B}{T_1} - \frac{\pi A}{2(T - T_R)} \cos \frac{\pi(T_1 - 2T_R + T)}{2(T - T_R)} = 0 .$$

The solution of this pair is:

$$T_1 = \frac{2(T - T_R)}{\pi} \tan \frac{\pi(T_1 - 2T_R + T)}{2(T - T_R)} .$$

This is a transcendental equation and an exact analytical solution cannot be obtained. It was evaluated by iterative methods on a digital computer. B was then evaluated by substituting T_1 in the first of the simultaneous pair. The evaluations of B and T_1 were carried out for various ratios of T_R/T. The normalized results of these computations are compiled in Table B-1. Values of B and T_1 for values of T_R/T not listed may be interpolated. B and T_1 may be obtained from the table value by multiplying by A and T, respectively.

DETERMINATION OF AREA OF RAMP-SINE FUNCTION

The determination of the value of F(0) for normalization of the Fourier spectra is as follows:

$$F(\omega) = \int_0^T f(t)\, e^{-j\omega t}\, dt .$$

When $\omega = 0$, this reduces to:

$$F(0) = \int_0^T f(t)\, dt .$$

This is simply the area between the excitation function and the time axis.

For the ramp-sine function:

$$F(0) = \frac{B}{T_1}\int_0^{T_1} t\, dt + A\int_{T_1}^{T} \sin\frac{\pi(t - 2T_R + T)}{2(T - T_R)}\, dt ;$$

the solution of this equation is:

$$F(0) = \frac{BT_1}{2} + \frac{2A(T - T_R)}{\pi}\left[\cos\frac{\pi(T - 2T_R)}{2(T - T_R)} \times \left(\cos\frac{\pi T_1}{2(T - T_R)} - \cos\frac{\pi T}{2(T - T_R)}\right) + \sin\frac{\pi(T - 2T_R)}{2(T - T_R)} \times \left(\sin\frac{\pi T}{2(T - T_R)} - \sin\frac{\pi T_1}{2(T - T_R)}\right)\right] .$$

TABLE B-1
Frequency and Area[a] Data for the Ramp-Sine Function

T_R/T	B/A	T_1/T	F(0)/AT
1.0000	1.0000	1.0000	0.500
0.9756	0.9999	0.9754	0.503
0.9524	0.9995	0.9514	0.507
0.9302	0.9989	0.9281	0.510
0.9091	0.9980	0.9054	0.513
0.8889	0.9968	0.8832	0.517
0.8696	0.9954	0.8615	0.520
0.8511	0.9937	0.8404	0.523
0.8333	0.9917	0.8196	0.526
0.8065	0.9880	0.7873	0.531
0.7813	0.9835	0.7559	0.536
0.7576	0.9781	0.7252	0.541
0.7353	0.9719	0.6952	0.546
0.7143	0.9647	0.6658	0.551
0.6897	0.9541	0.6296	0.557
0.6667	0.9417	0.5938	0.563
0.6452	0.9270	0.5583	0.569
0.6250	0.9096	0.5227	0.575
0.6061	0.8889	0.4867	0.581
0.5882	0.8641	0.4500	0.588
0.5714	0.8336	0.4118	0.595
0.5556	0.7955	0.3713	0.602
0.5405	0.7455	0.3272	0.609
0.5263	0.6756	0.2763	0.617
0.5128	0.5621	0.2108	0.625
0.5000	0.0000	0.0000	0.637

[a] F(0) is numerically equal to the area of the function.

This equation has been solved for a number of T_R/T ratios. The values computed have been normalized by division by the product AT. They are included in Table B-1.

ALTERNATE EXCITATIONS AND RESPONSES

Several alternate forms of excitation and responses are given in Tables B-2 and B-3. In general, an excitation which is the nth derivative or integral of any excitation in the tables results in a response which is the nth derivative or integral of the corresponding tabular response.

TABLE B-2
Alternate Forms of Excitation and Undamped Response

Excitation (E)		Response (R)	
Force Applied to Mass (Ground Immobile)	$\frac{F(t)}{K}$	Absolute displacement	x
Ground displacement	$u(t)$	Absolute displacement	x
Ground acceleration	$\frac{-\ddot{u}(t)}{\omega_n^2}$	Relative displacement	δ
Ground acceleration	$\ddot{u}(t)$	Absolute acceleration	$\ddot{x}$
Ground velocity	$\dot{u}(t)$	Absolute velocity	$\dot{x}$
nth derivative of ground displacement	$\frac{d^n u(t)}{dt^n}$	nth derivative of absolute displacement	$\frac{d^n x}{dt^n}$

TABLE B-3
Alternate Forms of Excitation and Damped Response

Excitation (E)		Response (R)	
Force Applied to Mass (Ground immobile)	$\frac{F(t)}{K}$	Absolute displacement	x
Ground acceleration	$\frac{\ddot{u}(t)}{\omega_n^2}$	Relative displacement	δ
Ground acceleration	$\ddot{u}(t)$	Relative displacement	$-\omega_n^2 \delta$

REFERENCES

1. C. T. Morrow and H. I. Sargeant, Acoust. Soc. Am., 28:959 (1956).
2. R. Lowe and R. D. Cavanaugh, "Correlation of Shock Spectra and Pulse Shape with Shock Environment," Environmental Engineering Vol. 1, No. 1 (Feb. 1959).
3. I. Vigness, and E. W. Clements, "Saw-tooth and Half-Sine Shock Impulses from the Navy Shock Machine for Medium Weight Equipment," NRL Report 5943 (1963).
4. C. T. Morrow, "Shock and Vibration Engineering" (John Wiley and Sons, Inc.) New York (1963), Vol. 1.

5. L. S. Jacobsen and R. S. Ayre, "Engineering Vibrations (McGraw-Hill Book Co., Inc., New York) (1958), Ch. 4, et al.

6. C. M. Harris and C. E. Crede, Shock and Vibration Handbook (McGraw-Hill Book Co., Inc., New York), Chaps. 8 and 23.

7. R. R. Luke, "The Impact Response of a Single-Degree-of-Freedom System with Viscous Damping," Structural Mechanics Research Laboratory, The University of Texas (1960).

8. C. T. Molloy, J. Acoust. Soc. Am., 29, 842-853 (1957).

9. R. M. Mains, "Structural Response to Dynamic Load," Shock, Vibration and Associated Environments Bull. No. 30, Part II, p. 66, Naval Research Laboratory, Washington (1962).

10. G. W. Painter and H. J. Parry, Shock, Vibration and Associated Environments, Bull. No. 33, Part III, p. 85, Naval Research Laboratory, Washington (1964).

11. Discussion MEMO of MIL-STD-810 Dynamics Conference, Flight Dynamics Laboratory, Wright-Patterson AFB, Ohio (1962).

12. C. T. Morrow, Shock, Vibration and Associated Environments, Bull. No. 33, Part II, p. 8, Naval Research Laboratory, Washington (1964)

13. C. E. Crede, Vibration and Shock Isolation (John Wiley and Sons, Inc. New York, 1951).

14. W. T. Thomson, Mechanical Vibrations (Prentice-Hall, Inc., Englewood Cliffs, N. J., 1953), 2d ed.

15. S. H. Crandall, et al., Random Vibration (The M.I.T. Press, Cambridge, Mass. 1958), Vol. I.

16. J. P. Den Hartog, Mechanical Vibrations (McGraw-Hill Book Co., Inc., New York, 1956), 4th ed.

17. T. von Karman and M. A. Biot, Mathematical Methods in Engineering (McGraw-Hill Book Co., Inc., New York, 1940).

18. C. R. Wylie, Jr., Advanced Engineering Mathematics (McGraw-Hill Book Co., Inc., New York, 1960).

19. R. O. Brooks, Shock, Vibration and Associated Environments, Bull. No. 33, Part II, p. 195, Naval Research Laboratory, Washington (1964).

20. M. A. Biot, Bull. Seismological Soc. Am., 31, 143 (Apr. 1941).

21. M. A. Biot, Trans. Am. Soc. Civil Engineers, 108, 365 (1943).

22. Y. C. Fung and M. V. Barton, J. Appl. Mech., 25, 365 (Sept. 1958).

23. S. Rubin, J. Appl. Mech., 25, 501 (Dec. 1958).

24. J. J. Marous and E. H. Schell, Shock, Vibration and Associated Environments, Bull. No. 33, Part II, p. 182 (1964).

25. H. Shapiro and D. E. Hudson, J. Appl. Mech., 20, 422 (Sept. 1953).

26. J. P. Walsh and R. E. Blake, "The Equivalent Static Acceleration of Shock Motions," NRL Report F-3302, Naval Research Laboratory, Washington (1948).

* * *

USE OF SHOCK FOR LOW FREQUENCY VIBRATION TESTING

A. J. Villasenor and T. G. Butler
Goddard Space Flight Center
Greenbelt, Maryland

The primary aim in bringing a satellite or satellite component to a vibration laboratory is to insure that it can withstand the various shocks and vibrations it will encounter during actual flight. An important set of vibrations occurs right at lift-off, but because these vibrations are often less than 10 cps, they are quite troublesome to reproduce on the shakers. What we have done in this paper to eliminate this problem is design a shock transient whose spectrum will contain these low frequencies. This transient can then be programmed into an electrodynamic shaker for actual use.

Given a discrete spectrum of N sets of resonant frequency and amplitude components ω_i and A_i ($i = 1$ to N), we can fit straight lines to the curve

$$f(t) = \sum_{i=1}^{N} A_i \sin(\omega_i t)$$

for a duration of τ seconds, $0 \leq t \leq \tau$. The choice of a particular arrangement of straight lines is aided by results obtained from studies of alternating saw-tooth and triangular wave curves. It was also revealed that in order to produce an absolute maximum peak in the spectrum at non-zero frequencies, the time curve must contain both negative and positive components.

The process of obtaining the time curve is followed by a process of reformulating it after considering its total energy relative to the energy of the given discrete spectrum. The aim here is to duplicate the discrete spectrum energy as well as possible.

Lastly we have to reformulate the curve again to take into account the impedance of the particular shaker being used for a test. This will give us our final result, in the form of the structural response of the testing system. The levels of this result should be very similar to the levels of the environment experienced by the satellite or satellite component at very low frequencies.

Our ultimate aim at the Test and Evaluation Division at Goddard is to link digital computers to the present vibration test apparatus in order to form the required shock transient on-line, with data coming from a shaker sweep test and then almost immediately using the computer formed shock to test the spacecraft in a type of combined environments analysis.

The primary aim in bringing a satellite or satellite component to our vibration labs is to insure that it can withstand the various shocks and vibrations it will encounter during actual flight. An important set of vibrations occurs right at lift-off, but because these vibrations are often less than 10 cps, they are quite troublesome to reproduce on the shakers. What we have done in this paper is to eliminate much of this trouble by using the shakers in a new way. This new approach uses negative shock components, which are made possible by the development of electrodynamic shakers. These shakers allow the designing of a shock

transient whose spectrum will contain the low frequencies.

In order for all of us to be sure what is meant by a transient, we define it here to be a sudden, nonperiodic disturbance in an otherwise steady state. A spectrum is a plot of frequency versus amplitude, revealing the frequency content of a time curve.

Suppose we are given the discrete spectrum shown below:

ω	A
5.45	5.0
11.00	1.4
21.00	1.4
26.70	1.0
34.50	1.4
35.10	1.0
40.20	1.0
72.40	1.0

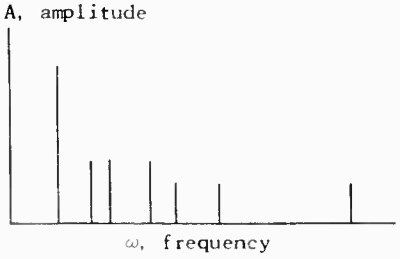

This is a "discrete spectrum" as opposed to a "continuous spectrum," such as that shown below for the half-sine transient:

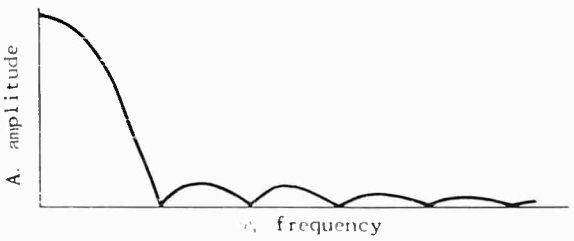

We want to obtain this spectrum on the shaker in one of two ways, either by feeding in the trigonometric polynomial

$$f(t) = \sum_{i=1}^{N} A_i \sin(\omega_i t),$$

or by designing a transient with a similar spectrum. Specifically, we wanted to feed some time function into the shaker and come out with a spectrum which contains the given discrete spectrum. With this in mind, our procedure was as follows: we first wanted to examine the characteristics of a typical shock transient, as for example, the trapezoidal time function, with the intention of discovering how slight modifications to this function affected its frequency content. Because of its frequent appearance in shock testing literature, we considered the trapezoidal curve shown here:

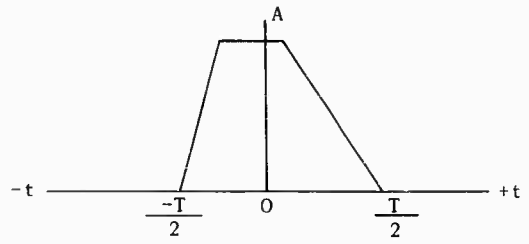

defined by the equations

$$f(t) = \begin{cases} yt + c & \text{for } t \text{ in } [-T/2, t_1] \\ s & \text{for } t \text{ in } [t_1, t_2] \\ ut + b & \text{for } t \text{ in } [t_2, T/2]. \end{cases}$$

The points t_i are computed from the equations

$$t_1 = AT - T/2$$

and

$$t_2 = BT - T/2$$

where the constants A and B were a measure of the slopes of the left and right sides of the trapezoid. By varying A and B, we got many different types of curves. For our investigations, s and T were kept fixed at unity and A and B were varied. It was believed that the slopes of the sides were related to the frequency content of the transient. A digital computer program calculated for a specific A and B, the real and imaginary parts of the spectrum, as well as the magnitude. A varied from 0.01 to 0.99 and for each value of A, B varied from A to 0.99.

Computer results showed that in the frequency range between 0 and 400 radians per second, no significant change occurred in the spectrum as a result of varying either A or B, except when A or B $\geq$ 0.95, in which case the spectrum had lower amplitude in the 0-10 rad/sec region. The average amplitude at high frequencies was always less than the average amplitude at low frequencies. No matter how A and B were varied, this character was still maintained. This was highly undesirable, because it indicated that we could not control the relative amplitudes of high and low frequencies. Obviously, we would want to do this because we might be given a steady acceleration plus a

low frequency to reproduce and no control, as we have here, would make this task impossible. Hence, this type of time curve would hardly be effective in generating a desired spectrum which was to have high amplitudes only at high frequencies. Further consideration of the pulse reveals that varying the height would have no effect on the relative amplitudes of the spectrum and no desired effect, therefore, on the character of the frequency content.

Another way to obtain high amplitudes at high frequencies would perhaps be to study pulses of unit height in which the only variables are the width of the pulse and the number of pulses. Let N be the number of slopes of the curve, and ω_f be the "fundamental frequency." A computer program was written to analyze these curves as they varied in ω_f and in N. These curves contained negative as well as positive components, inasmuch as completely positive shocks were giving unfruitful results. The philosophy here was that the negative components might combine with certain positive components and cancel amplitudes at low frequencies, thereby reinforcing amplitudes at high frequencies.

We considered the "alternating saw-tooth" curves shown in Fig. 1. We should point out here that we would not actually expect to program these waveforms on the shakers, because they are examples of just the low frequency curves we are hoping to avoid. They will, however, help us to solve the problem by serving as mathematical models. This set of curves does produce relatively high amplitudes at high frequencies. Numerical analysis of the data revealed several consistent patterns,* such as the frequency at which an absolute maximum peak is desired, its amplitude, and its spread or width. In this figure, we have the results obtained by varying N for a fixed $\omega_f = 10$. Figure 2 shows what happens when N gets larger. Figure 3 indicates the result obtained by keeping N = 4 and varying ω_f.

Thus, by using negative components, there are several things at our disposal to change. By varying N and/or ω_f, we can control the spread of the peaks, as well as their amplitudes. We can obtain a peak at any desired frequency and can even control the spectrum amplitudes at specific frequencies.

We now consider the problem of producing a desired spectrum with the alternating saw-tooth waves. Suppose we want to produce the spectrum:

*(a) If N is odd, a relative maximum will be at $\omega = 0$ and the absolute maximum will be at the $1/2(N+1)$ th peak. If N is even, the spectrum will be 0 at $\omega = 0$, increasing, and the absolute maximum will be at the $(N/2)$th peak.
(b) If ω_f is the fundamental frequency, then an absolute maximum will occur at the following frequencies:

N = 1		N = 4	$\omega = 6.0\ \omega_f$
N = 2	$\omega = 5.1\ \omega_f$	N = 5	$\omega = 6.1\ \omega_f$
N = 3	$\omega = 5.8\ \omega_f$	6 ≤ N ≤ 10	$\omega = 6.2\ \omega_f$

(c) The value of the absolute maximum amplitude is $(1 + 15N)/80\ \omega_f$).
(d) The spread of the maximum peak is approximately $25(\omega_f/N)$.

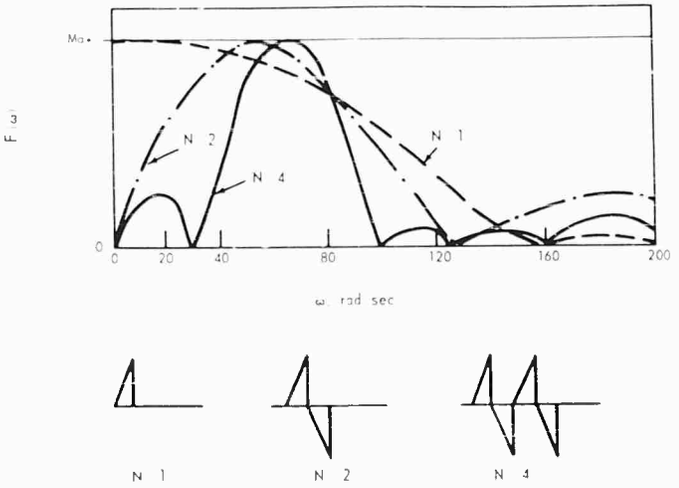

Fig. 1 - Alternating saw-tooth curves (N = 1, N = 2, N = 4)

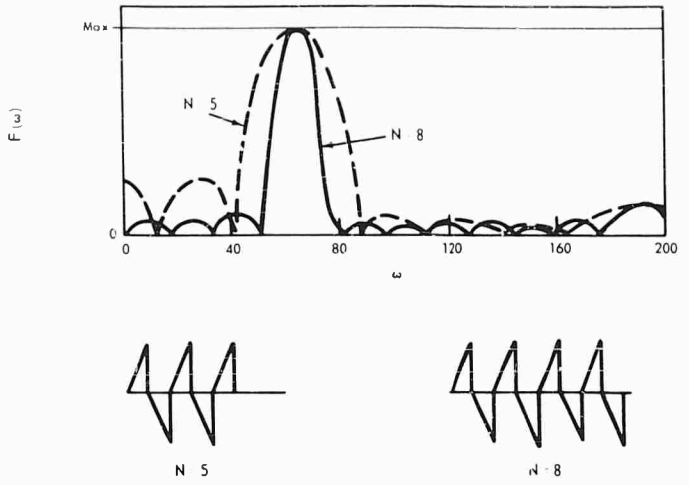

Fig. 2 - Alternating saw-tooth curves
(N = 5, N = 8)

ω	A
15.0	1.0
74.0	1.0

We have enough information about the nature of these curves to obtain, on first attempt, the result in Fig. 4. The lower half of Fig. 4 shows the actual curve set used to produce this highly agreeable spectrum.

Up to now we have only considered very simple waveforms. Let us recall the discrete spectrum shown at the beginning of this talk. We form the continuous time curve

$$f(t) = \sum_{i=1}^{N} A_i \sin(\omega_i t).$$

the beginning of which is shown in Fig. 5. This, incidently, is a trigonometric polynomial, not a Fourier series. This infinite time curve was then truncated and the truncated part treated as an isolated shock. Its duration was approximately 0.9 seconds. Of course, longer duration would give a closer correspondence with the input data; however, our aim here is to discover what kind of modifications, if any, to the truncated curve will yield a spectrum reasonably similar to the discrete data. It was expected

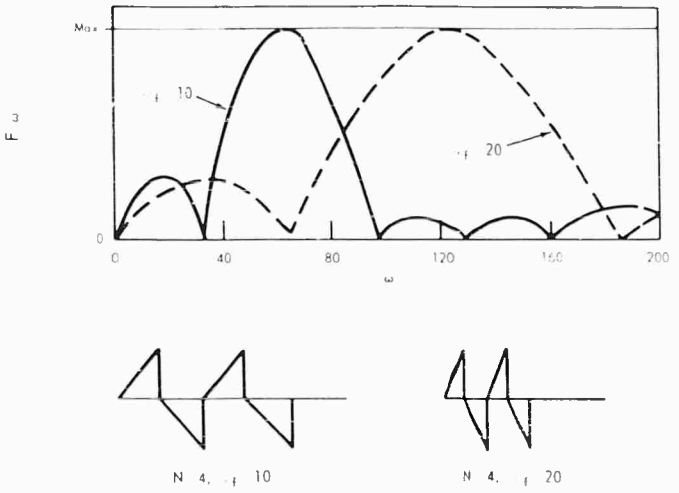

Fig. 3 - Alternating saw-tooth curves
(N = 4, ω_f = 10; N = 4, ω_f = 20)

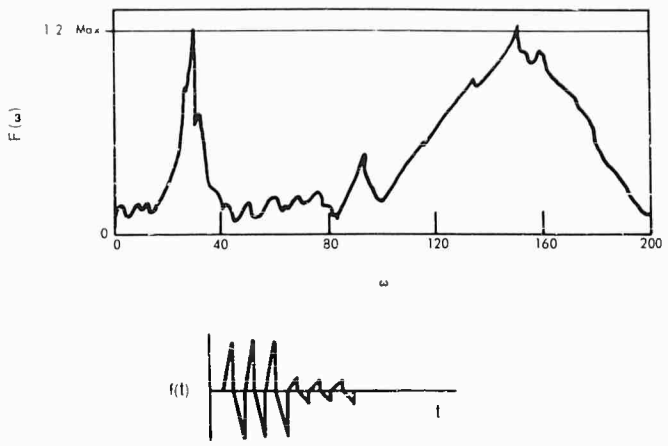

Fig. 4 - Specification

that the amplitude of the truncated curve's spectrum would be much smaller than the discrete spectrum amplitudes due to the energy difference between the two curves (one is infinite, while the other lasts for less than 1 second).

A computer program formed the infinite time curve which was immediately examined and truncated. Then the computer calculated the Fourier integral spectrum of this truncated curve, and the result subsequently compared with the input data, as shown in Fig. 6.

Suppose we choose 18 points on the truncated curve and connect them with straight lines. The Fourier spectrum of this linear fit curve is shown in the lower part of Fig. 7. This spectrum agrees well with the input data, although again, we cannot predict exactly what the complete spectrum will look like.

At this point we would like to summarize the results contained in this paper. Our original goal was to produce a shock pulse that efficiently contained a discrete spectrum. The results of this study show that this goal is possible. Although the technique is yet to be streamlined, the concept of making a straight line approximation to the infinite curve is justified, because the resulting spectra agree very well within certain tolerances. Using the knowledge of the need for negative components learned from the saw-tooth curves to help form this approximation, we see good prospects for nearly complete control for a large set of input data such as that considered in the discrete

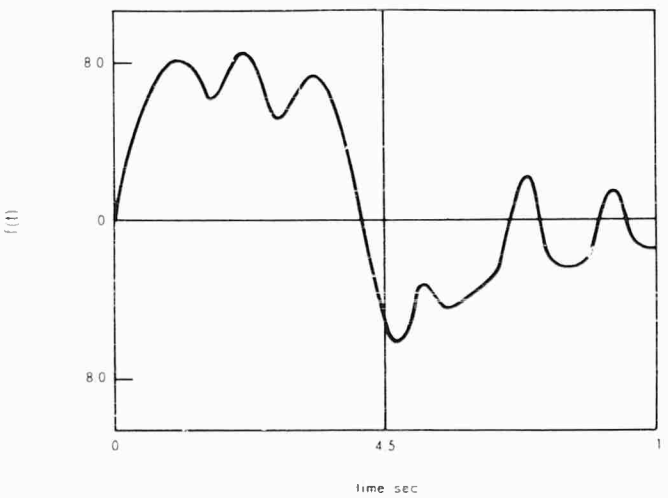

Fig. 5 - Truncated infinite time curve

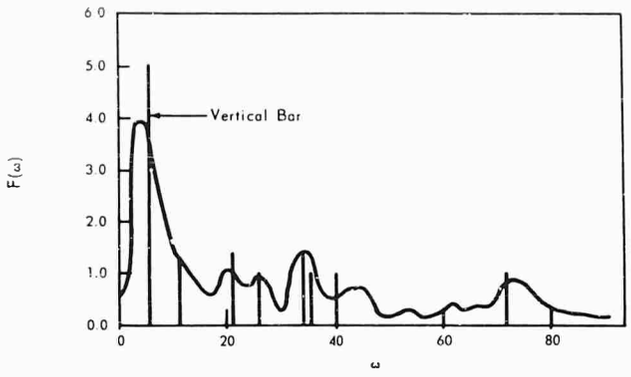

Fig. 6 - Comparison of spectrums of discrete and infinite time curve

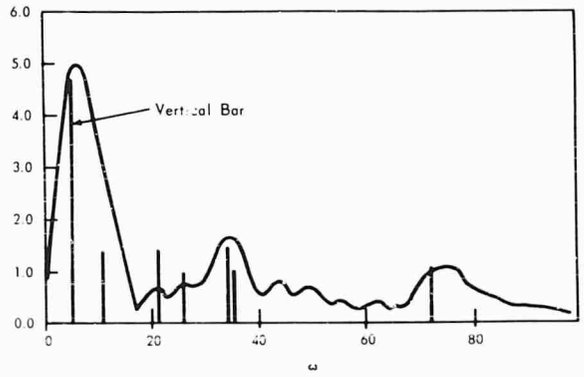

Fig. 7 - Comparison of spectrums of discrete data and approximated curve

spectrum. Our ultimate aim is to develop a system in which we first get a set of resonances and corresponding amplitudes from a low amplitude shaker sweep test, then feed this data into a digital computer which will form our trigonometric polynomial, truncate this polynomial and approximate it, then finally use the approximation to test the spacecraft in a type of combined environments analysis.

In this paper only two things were considered; the input time function $f(t)$, and the output frequency response $F(\omega)$. In actual testing, we would instead consider the structural response $R(\omega)$ defined by

$$R(\omega) = H(\omega) \cdot F(\omega)$$

where $H(\omega)$ is a transfer function, which is the reciprocal of the sum of the electrical impedance of the shaker armature and the mechanical impedance of the structure. For mathematical ease, we have chosen a unit transfer function for this paper.

This will link computers to the test area in a new type of testing procedure, which, although not yet in use, promises to rid us of previous low frequency problems. We hope this technique will ultimately become generally used by other spacecraft testing labs.

* * *

SPACECRAFT SHOCKS INDUCED BY ELECTRO-EXPLOSIVE DEVICES

D. A. Heydon and W. W. Aichroth
TRW Space Technology Laboratories
Redondo Beach, California

Actuation of electro-explosive devices (EED), and the energy they release, can induce significant mechanical shocks in spacecraft structure and components. These shocks are caused by such events as nose fairing separation, spacecraft separation from the booster, and actuation of high pressure gas valves. Effects of this type of induced shock may include structural or electronic component failure and premature sequencing of relay controlled events.

Separation and injection of the tandem Nuclear Detection Satellite (NDS) system involves 8 separate EED events, employing 24 cartridges and 2 rocket motors, exclusive of booster operation and nose fairing separation. The nose fairing is separated by a system involving approximately 42 feet of mild detonating fuse, with associated initiators.

A series of tests were performed to determine the effects on the spacecraft systems of the shock induced by some of these events. The last four events, rocket firing for injection and heat shield release from each of the two spacecraft, were not considered in this series of tests. Rocket firings were independently evaluated at an earlier time, while the heat shield release events involve very small energy levels and were therefore excluded as being negligible.

Events tested for shock effects included:

- Nose fairing separation by linear shaped charge,
- Separation of the tandem spacecraft from the booster by two actuators and a V-band clamp,
- Spinup of the tandem spacecraft pair by a cold gas nitrogen system using two cartridge actuated valves, and
- Separation of each spacecraft in succession from the spin interstage, using the basic booster V-band clamp and release assembly.

Test results indicate that shocks induced by normal spacecraft separation and spinup events, with relatively low energy, pose no significant design problems. Shock levels associated with higher energy events, such as nose fairing separation, require special attention to the location and mounting of sensitive components. Components and assemblies mounted close to any source of shock input, regardless of level, should be considered potentially susceptible.

Testing, required for development and design verification of electro-explosive actuated systems, should include shock level measurement as a routine parameter. Shock inputs representative of anticipated levels should be included in unit qualification and acceptance testing.

Where structural and other considerations permit, maximum use of material discontinuities to provide shock isolation should be employed. Structural design techniques providing high inherent damping, such as honeycomb sandwich panels, also provide a useful mechanism for attenuating induced shock effects.

INTRODUCTION

Actuation of electro-explosive devices (EED), and the energy they release, can induce significant mechanical shocks in spacecraft structure and components. These shocks are caused by such events as nose fairing separation, spacecraft separation from the booster, and actuation of high pressure gas valves. Effects of this type of induced shock may include structural or electronic component failure and premature sequencing of relay-controlled events. The nature of these shocks has been discussed by several previous authors [1-3].

Separation and injection of the tandem Nuclear Detection Satellite (NDS) system involves 8 separate EED events, employing 24 cartridges and 2 rocket motors, exclusive of booster operation and nose fairing separation. The nose fairing is separated by a system involving approximately 42 feet of mild detonating fuse, with associated initiators.

A series of tests were performed to determine the effects on the spacecraft systems of the shock induced by some of these events. The last four events, rocket firing for injection and heat shield release from each of the two spacecraft, were not considered in this series of tests. Rocket firings were independently evaluated at an earlier time, while the heat shield release events involve very small energy levels and were therefore excluded as being negligible.

Events tested for shock effects included:

1. Nose fairing separation by linear shaped charge,

2. Separation of the tandem spacecraft from the booster by two actuators and a V-band clamp,

3. Spinup of the tandem spacecraft pair by a cold gas nitrogen system using two cartridge actuated valves, and

4. Separation of each spacecraft in succession from the spin interstage, using the basic booster V-band clamp and release assembly.

Test results indicate that, in general, shocks induced by normal spacecraft and spinup events pose no significant design problems. Shock levels for nose fairing separation appeared marginal in some respects, and resulted in minor design changes by both the booster and spacecraft contractors. Two fully successful flight missions since the test series have confirmed the adequacy of the design.

SYSTEM DESCRIPTION

The tandem NDS spacecraft system is shown in Fig. 1. The overall height above the second stage is approximately 10 feet, and the total weight at launch is approximately 1000 pounds. Figure 2(A) illustrates location of the nose fairing electro-explosive devices, and Fig. 2(B) shows the locations of all spacecraft EED. The characteristics of these devices are given in Table 1.

To provide a more efficient structure, a very close interface has been maintained between the second stage booster contractor (LMSC) and the spacecraft contractor (STL). As a result, the nose fairing support ring is also used as the primary lower structural member of the spacecraft interstage. The eight bolts securing

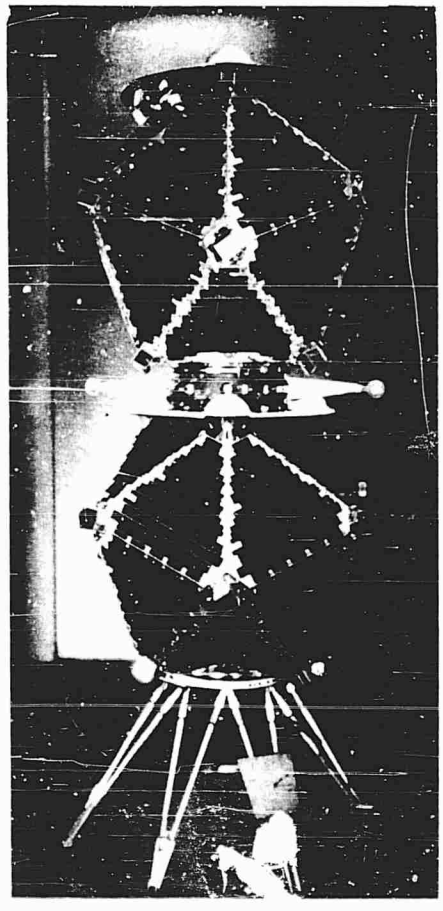

Fig. 1 - Tandem nuclear detection satellite system

NOTE: References appear on page 266.

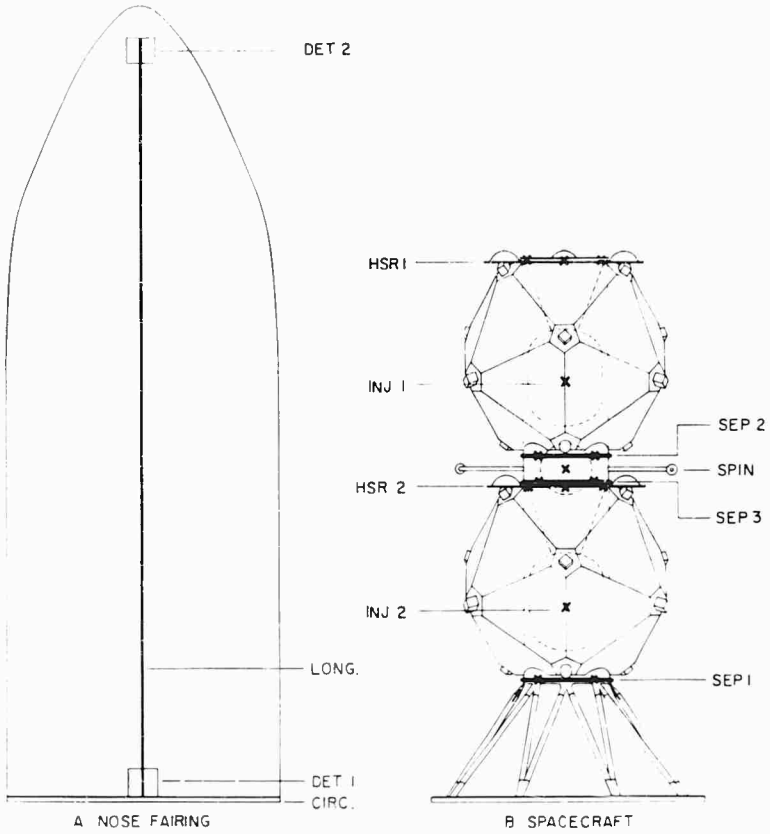

Fig. 2 - Locations of electro-explosive devices

TABLE 1
Characteristics of Electro-Explosive Devices

Location	Event	Type	Quan	Charge
DET 1	Fairing Sep.	Initiator	2	170 mg.
DET 2	Fairing Sep.	Initiator	2	100 mg.
CIRC	Fairing Sep.	MDF	~16'	10 gr/ft
LONG (initial)	Fairing Sep.	FLSC	~26'	5 gr/ft
LONG (final)	Fairing Sep.	MDF	~26'	10 gr/ft
SEP 1	Tandem Sep.	Cartridge	4	188 mg.
SPIN	Tandem Spinup	Cartridge	2	140 mg.
SEP 2	Upper S/C Sep.	Cartridge	4	188 mg.
SEP 3	Lower S/C	Cartridge	4	188 mg.
INJ 1	Upper S/C Inj	Initiator	2	N/A
HSR 1	Heat Shield Rel	Cartridge	3	30 mg.
INJ 2	Lower S/C Inj	Initiator	2	N/A
HSR 2	Heat Shield Rel	Cartridge	3	30 mg.

the interstage to the Agena forward bulkhead provide a common load path for all spacecraft and nose fairing loads. The nose fairing skirt is fastened to the ring by 192 bolts, so as to provide excellent mechanical coupling between the fairing and the interstage.

As indicated in Table 1, fairing separation charges for early tests consisted of 10-grain/foot mild detonating fuse (MDF) at the base of the nose fairing circumference, and 5-grain/foot flexible linear shaped charge (FLSC) along the length of the fairing. Detonator blocks were mounted on the fairing at the apex of the circumferential and longitudinal charges (+Y and -Y axes) and at the upper end of each longitudinal shaped charge. The final flight configuration employed 10-grain/foot MDF for all joints.

Spacecraft separation from the Agena interstage and spin interstage is accomplished by redundant explosive actuators and V-band clamps. Installation of the actuator and band on the Agena interstage is shown in Fig. 3. This particular photograph was taken during a series of band clearance tests, to ensure that the bands would not damage the lower detectors.

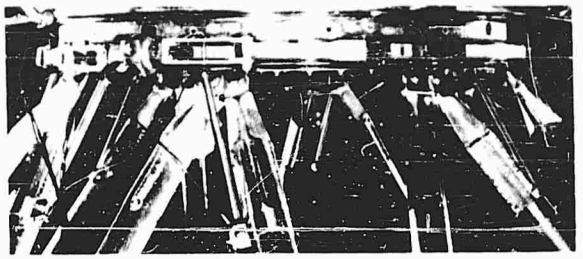

Fig. 3 - Separation V-band clamp installation

Tandem spacecraft spinup is accomplished by redundant explosive valves, which release nitrogen stored at 4,000 psi. The relationship of the valves, pressure vessel, lines, and nozzle booms is illustrated in the spin interstage photograph, Fig. 4. The valves are mounted inside the "A-Frame" pressure vessel supports. The pressure vessel is filled through the valve body, one of which is shown uncapped in Fig. 4.

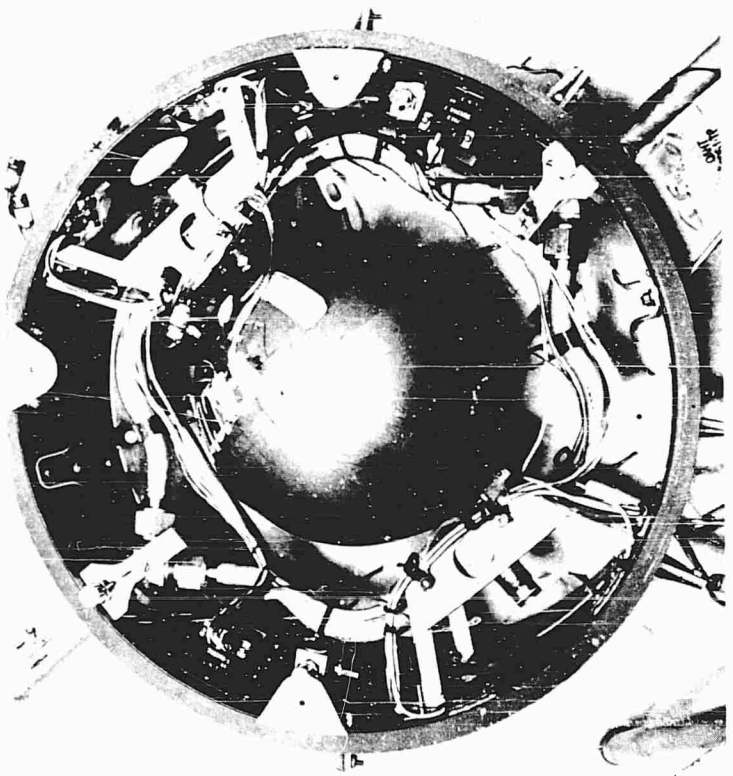

Fig. 4 - Spin interstage

DESCRIPTION OF TESTS

Nose Fairing Separation

Nose fairing separation tests were conducted by Lockheed Missiles and Space Company at the Langley Research Center under simulated altitude conditions, and at Sunnyvale under sea level conditions. These tests were intended to demonstrate nose fairing separation performance under conditions simulating, as nearly as practicable, the physical conditions and operating environment. In addition, these tests provided an opportunity for STL to investigate the effects of nose fairing separation on the tendem NDS spacecraft assembly and interstage.

Three nose fairing separation tests included spacecraft shock measurements. Areas investigated included mechanical shock effects, surface contamination, and fragmentation associated with the explosive nose fairing separation. The first two were performed at Langley Research Center in the 60-foot vacuum chamber. The nose fairing charge configuration for these tests was that shown in Table 1 as "initial." For the final test, under sea level conditions at Sunnyvale, the configuration was that shown in Table 1 as "final."

The lower spacecraft was a structural test model, having structural characteristics virtually identical to a flight spacecraft. The spin interstage and upper spacecraft were sheet metal mockups. Selected electronic assemblies, considered to be possible shock susceptible, were installed on the lower spacecraft and interstage. During the LRC tests, in addition to the flight-type spacecraft assemblies, five sample panels were mounted at various locations on the lower spacecraft and interstage structure. Each of these panels consisted of a small aluminum sheet on which were mounted representative electronic components.

The methods used to determine shock susceptibility were based on the mode of failure which would compromise spacecraft objectives. Generally, the spacecraft subassemblies and component parts are not required to operate during the instant of nose fairing separation. Therefore, with the exception of the Command Distribution Unit and the Stage II Relay Package, no functional monitoring of the test specimens was performed except for a visual examination and performance test before and after the nose fairing separation tests. Since a transient malfunction of the Stage II Relay Package or the Command Distribution Unit could cause premature spacecraft separation, injection rocket ignition, or heat shield ejections, functional monitoring to detect these malfunctions was performed during the nose fairing separation. The Command Distribution Unit and the Stage II Relay Package were set up to monitor relay contact chatter and transfer of 2 milliseconds duration or greater. The individual relay contact positions were monitored on eight-channel Visicorders.

Twelve shock measurements were made during each of the nose fairing separation tests. Measurement locations were chosen to determine the shock levels at selected critical components, and at other locations on the lower spacecraft and interstage structure to determine shock transmissibility. Accelerometer data were recorded on magnetic tape and subsequently transferred to an oscillograph recording to provide a visual time history of the separation shocks. These oscillograph recordings were made at a speed of 240 inches per second; this speed provided good resolution for high frequency components.

The shock levels experienced during the first test generally exceeded the predicted values, and were of sufficient amplitude to cause saturation in 5 of the 12 accelerometer preamplifiers. In addition, three of the accelerometers were separated from their mountings by the shock. Of the 12 measurements, 6 were invalidated by these discrepancies. Based on the experience from the first test, adjustments were made to preclude saturation of the preamplifiers, and the method of accelerometer mounting was improved.

A full complement of shock data was obtained from the second test. The levels for areas of primary interest are shown in Table 2. Tests of all assemblies following the nose fairing separation indicated satisfactory performance. No indications of relay contact chatter or transfer were obtained during the tests for either the Command Distribution Unit or Stage II Relay Package. Examination of the five test panels disclosed that some of the diodes contained loose particles inside the glass envelope which could cause possible shorting. In addition, one of the ceramic transformer spindles mounted on the upper interstage truss sample plate was broken.

As a result of the high shock levels measured during the second test, and because of uncertainties regarding the nature of the observed component fragility, LMSC undertook further development testing. Variations in charge sizes and types, as well as structural isolation modifications, were investigated. The final configuration was tested with spacecraft instrumentation

TABLE 2
Nose Fairing Shock Test Results

Location	Sensitive Axis	Peak (g)	
		LRC #2	Sunnyvale
CDU	Vert	300	150
Detector	Axial	850	60
Cent Cyl (Upper)	Vert	440	375
Cent Cyl (Lower)	Vert	4000	1000
Sta 247 (+Y)	Vert	4000	7000 (Sat.)
Sta 247 (-Z)	Vert	2300	4000 (Sat.)
Stage II Relay	Axial	N/A	5000

similar to that employed for the second test. Shock data for this test are also given in Table 2.

The reduction within the spacecraft due to the improved isolation is clearly evident, even though the input level (as shown by the Station 247 readings) was significantly higher, due to the required use of 10-grain/foot MDF for the entire fairing event. Assembly tests and relay monitoring again indicated no performance degradation or transient malfunctions.

Spacecraft Separation

The flight proof (prototype) spacecraft and spin interstage were used as the primary test articles for these separation shock tests. A weighted structural model spacecraft was installed in the upper spacecraft position. The configuration of the spacecraft separation system was previously briefly described and is illustrated in the separation band installation shown in Fig. 3.

Accelerometer instrumentation similar to that employed in the nose fairing tests was installed on the spacecraft and interstage. All ordnance firing circuits were monitored during the band separation tests. In addition, to provide a qualitative measure of spacecraft susceptibility, system tests were performed on the spacecraft before and after the shock test sequence. These tests were used in a manner very similar to the common pre-environmental and post-environmental unit tests.

The data obtained from the Agena interstage tests are summarized in Table 3. All values shown represent the average of two runs since data repeatability was excellent. A radially oriented accelerometer at the separation flange indicated very high input levels, on the order of ± 4000 g. The configuration of the band and the high compressive loads imposed on the separation flanges readily accounts for this high level when the band load is released. The low vertical shock components evident within the structure, even adjacent to the separation plane, demonstrate the excellent attenuation of this particular structure. Separation of the spin interstage band induced lower shock levels in the spacecraft, due to the lower strain energy and compressive loads associated with the band tension for the upper bands. The results are shown in Table 3, and may be compared directly with those from the lower band separation. Levels adjacent to the timers in the spin

TABLE 3
Separation Shock Test Results

Location	Sensitive Axis	Peak (g)	
		Agena Sep.	Spin Sep.
CDU	Vert	16	10
Detector	Axial	110	10
Cent Cyl (Upper)	Vert	45	200
Cent Cyl (Lower)	Vert	500	190
Spin Int (Timer 1)	Vert	40	230
Spin Int (Timer 2)	Vert	40	200

interstage are higher, because of the proximity to the separation event.

Spin Valve Actuation

Spin system configuration has been described earlier and is illustrated in Fig. 4. Timers and relays controlling upper and lower spacecraft separation from the spin interstage are mounted near the "Y" manifolds. The excellent mechanical coupling between the valve mounting and the interstage ring provided some concern that valve actuation might cause relay transfer and premature separation.

The eight accelerometer locations are indicated in Fig. 4. A triaxial unit was mounted as close as possible to each timer and a single vertical accelerometer was mounted on each manifold.

A functional test was performed on the timer assemblies prior to the valve actuation shock tests. In addition to the direct recording of the accelerometer outputs, the release ordnance circuits were monitored on a system test console. The pressure vessel was filled to flight pressure of 4000 psi and the valves were fired. The shock levels recorded are shown in Table 4.

TABLE 4
Spin Valve Shock Test Results

Location	Sensitive Axis	Peak (g)
Timer 1	Vertical	120
Timer 1	Radial	100
Timer 1	Tangential	45
Timer 2	Vertical	145
Timer 2	Radial	100
Timer 2	Tangential	70
+Y Manifold	Vertical	480
-Y Manifold	Vertical	330

DESIGN EFFECTS

Nose fairing separation, spacecraft separation, and spinup events induce high amplitude, high frequency shocks in the interstage and spacecraft structure. These shock levels are of short duration and represent very small displacements. Experience on similar systems has indicated that failure of load carrying structures does not usually occur under these conditions. No design changes to improve structural strength were instituted as a result of the shock tests.

Shock levels substantially in excess of unit environmental test levels were found to occur at mounting points of some subassemblies and components. As a result, some design changes were incorporated to provide improved isolation and attenuation of these high level shocks. Primary isolation of the nose fairing separation shock was provided by incorporation of tungsten pads between the LMSC nose fairing support ring and the STL interstage truss fittings, and a full tungsten ring between the nose fairing ring and the Agena forward bulkhead. These pads provide a shock path discontinuity, both into the interstage and the Agena.

Additional isolation was provided for the Stage II Relay Package because of its mounting location on a lower truss fitting immediately above the nose fairing support ring. This isolation consisted of the addition of a 3/32-inch-thick epoxy fiberglass pad between the Relay Package base and the truss fitting, and epoxy fiberglass bushings in the mounting bolt holes.

The inherent attenuation characteristics of the spacecraft structure provide excellent reduction of the high shock levels experienced on the interstage. Discontinuities similar to that at the epoxy fiberglass end flange and aluminum interstage ring interface exist throughout the spacecraft structure due to the necessary utilization of a variety of materials for thermal, RF, and other reasons. Materials such as the honeycomb sandwich panel used for the equipment platform also provide high attenuation.

It is evident that care should be exercised in placement of assemblies which might be highly susceptible to transient or permanent shock damage. When system constraints require placement of a particular unit in an undesirable location, such as the relay package on the interstage truss, isolation and internal attenuation should be adequately considered.

While the shock levels experiences for separation and spinup in this system did not provide any design constraint, the problems associated with large explosive charge sizes and extensive use of shaped charges should be considered in the total design. Explosive charge sizing tests are primarily based upon functional performance. If these tests do not account for possible induced shock effects in nearby structure or electronic assemblies, later design compromises may be required.

CONCLUSIONS

Test results have indicated that shocks induced by normal spacecraft separation and

spinup events with relatively low energy, pose no significant design problems. Shock levels associated with higher energy events, such as nose fairing separation, require special attention to the location and mounting of sensitive components. Components and as emblies mounted close to any source of shock input, regardless of level, should be considered potentially susceptible.

Testing, required for development and design verification of electro-explosive actuated systems, should include shock level measurement as a routine parameter. Shock inputs representative of anticipated levels should be included in unit qualification and acceptance testing. Where structural and other considerations permit, maximum use of material discontinuities to provide shock isolation should be employed. Structural design techniques providing high inherent damping, such as honeycomb sandwich panels, also provide a useful mechanism for attenuating induced shock effects.

REFERENCES

1. V. R. Paul, "Mechanical Shock from Frangible Joints," Shock, Vibration and Associated Environments Bulletin No. 33, Part IV (March 1964), pp. 63-71.

2. H. J. Roberge and J. Rybacki, "Shock Environments Generated by Pyrotechnic Devices," Shock, Vibration and Associated Environments Bulletin No. 33, Part IV (March 1964), pp. 73-81.

3. D. E. Hines, "Generation and Propagation of Stage Separation Shocks in Missiles and Space Vehicles," Institute of Environmental Sciences, 1964 Proceedings, pp. 681-689.

* * *

SIMULATION OF THE PYROTECHNIC SHOCK ENVIRONMENT

A. L. Ikola
Lockheed Missiles and Space Company
Sunnyvale, California

The shock environment generated by the detonation of explosive actuated devices (primacord, jet cord, squib valves, pin pullers, pin pushers, explosive nuts, and bolts) has been overlooked as a potentially damaging environment in many equipment specifications. Failure to reeognize this potential equipment hazard has, in many cases, been rationalized on the basis of the short time history of the event and the flexible structure over which the energy must be transmitted to reach equipments. In some speeifications, where the environment was known, unrealistic test criteria were adopted because suitable testing facilities were not available.

Flight and ground test shock measurements made on the Agena vehieles have resulted in a definition of the environment in terms of shock spectrum curves over a 100 to 10,000 cps frequeney range. Once having defined the event, studies were initiated on two separate test systems. These systems generate complex transient vibrations which produce shock spectra curves similar to those obtained from actual vehicle data.

The major portion of the paper will discuss the development of the systems and their application to equipment qualification.

The first system whieh will be discussed consists of a modified drop tester incorporating a specially designed mechanical transfer test table. The transfer table, installed between the drop table and seismic mass, transforms the impulse from the drop table into eomplex vibrations on the transfer table.

The second system discussed is a more direet approach to the simulation of explosive shocks generated during vehicle staging events. The facility consists of a barrel type structure, 5 feet in diameter and 5 feet in length. An explosive separation joint attached to one end of the fixture creates the desired shock input with environmental control being obtained by the selection of the proper explosive content and separation joint material thickness. Unlike the rigid type of installation used for equipment during testing on the mechanical transfer table, equipments tested on the barrel tester have installation frequencies similar to those in an actual launeh vehiele.

INTRODUCTION

The pyrotechnic shock environment has been present in military vehicles since the introduction of armament. Recently, explosive devices have been used in space vehicles to perform such functions as staging, nose fairing ejection, valve operation, antenna erection, satellite separation, and the like. Explosives have been used in primacord, jet cord, pin pullers, pin pushers, and squib operated valves to perform these functions. In general, commercial-type shock isolators would be used to obtain protection from the explosive environment. The extensive use of isolators in space vehicles, however, would be extremely costly in terms of installation area and payload capability. The requirement was, therefore, to guarantee that the equipment package or component would perform satisfactorily, unprotected, in the

pyrotechnic shock environment. Since the nature of the environment presently defies qualification by analysis, the only practical solution was to devise a test to simulate the pyrotechnic environment.

MEASURING PROGRAM

Before a qualification test environment could be specified, it was required that environmental data be obtained from the flight vehicle during the shock event. A measuring program was initiated to obtain shock measurements over the entire Agena structure during a typical staging separation. The two-part program required that an extensive data sample be taken during a ground test program concurrently with specifically duplicated measurements from two vehicles in flight. A correlation study performed on the ground and flight test data showed that the shock environment occuring in near vacuum conditions was duplicated at atmospheric conditions. It was, therefore, established that the shock environment could be realistically simulated at atmospheric conditions. The merits of equipment qualification during the simultaneous application of the space environments and pyrotechnic shock will eventually require an extensive investigation.

Instrumentation used during the ground test program consisted essentially of shock-type piezoelectric accelerometers and an FM magnetic tape recorder. All shock data were recorded at 60 ips. The data reduction to oscillograms was obtained by playing the tape system back at 15 ips into a recording oscillogram containing a 2500-cps galvanometer. The recorder's paper speed was 100 ips rendering vibration data to 10,000 cps. The total instrumentation system capability was 10,000 cps.

DATA ANALYSIS

Having once recorded the shock event, it was necessary to convert the transient structure response into equipment qualification test criteria. The methods of shock spectra analysis were used to show the response of hypothetical single degree of freedom systems to the shock transient. Figure 1 shows a typical composite transient vibration and a shock spectrum of the maximum vehicle shock transient.

ENVIRONMENTAL TEST CRITERIA

Since the environmental data was obtained over the 200- to 10,000-cps test spectrum, it was required that a standard comparison method be established so that data obtained during a qualification test could be compared to establish the qualification requirements. The method selected was similar to the treatment of the acoustic test data in that octave bands were used for the standard bandwidths. Unlike the db vs frequency plots obtained with acoustic test data, the shock data were in the form of acceleration ("g" vs frequency). The data evaluation would then consist of a comparison of the peak g levels over the frequency spectrum and a graphical integration of the area in each octave band. An acceptable qualification test was then considered achieved when the three following requirements were satisfied.

1. The peak accelerations shown at any frequency on the shock spectrum curve would not be exceeded by more than a factor of 2.5 at the same frequency during the qualification test (see Fig. 2).

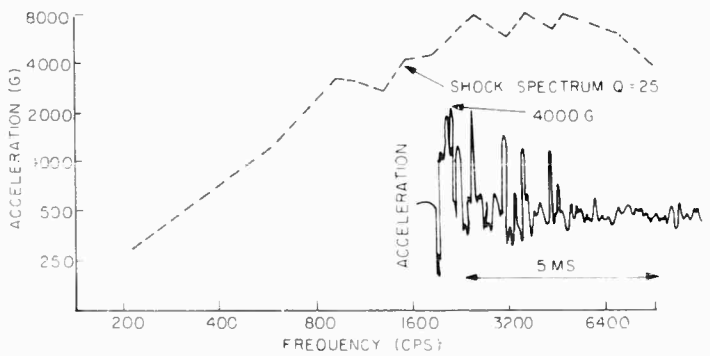

Fig. 1 - Maximum flight environment

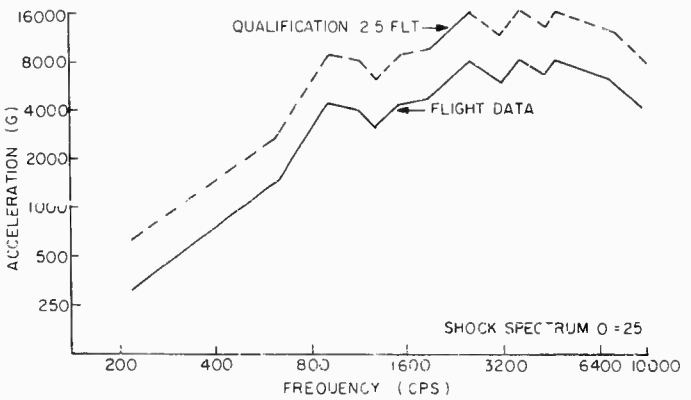

Fig. 2 - Test criteria (peak g)

2. The octave band areas obtained during a test should exceed the same octave band area obtained from the flight data by a factor of 2 (see Fig. 3).

3. The complex vibration peak amplitude and total duration should be similar in shape to the actual vehicle measurements (see Fig. 1).

The conversion of the shock spectrum into shock test criteria was required to establish ground rules for the development of the testing machines.

After establishing the ground rules, it was then possible to consider methods of generating an environment that would fulfill the three prime objectives of the test criteria. It was also felt that if the objectives were met, a realistic simulation for the pyrotechnic shock environment would be available.

Two independent simulation systems; (1) The transfer table, and (2) The barrel tester were proposed with the intention that the system most closely duplicating the requirements of the test criteria be used as the standard tester for qualification of equipments to the pyrotechnic environment.

TRANSFER TABLE

Standard drop testing machines commercially available were unable to satisfy the requirements set forth in the test criteria. The test machines produced excessive over-tests on equipment packages in the low frequencies, and

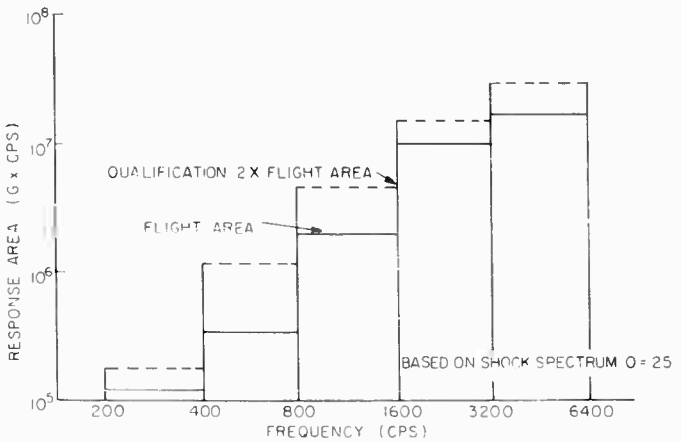

Fig. 3 - Test criteria octave band area

the wave shape consisted of a single pulse as opposed to the complex vibrations shown in Fig. 1. A drop test machine of the standard type was, however, available, so a program was initiated to modify it in an attempt to simulate the shock event.

The nature of the complex vibrations from which the test criteria was evolved suggested that the environment was essentially a local transient response with a decay curve lasting for approximately 10 milliseconds. The complexity of the vibrations also suggested that the excitation did not occur in phase over the entire equipment package attachment interface.

To produce such a complex vibration on a drop tester without excessive low frequency damage to equipments required a modification which inserted a mechanical transfer table between the drop table and seismic mass. The table consisted of a flat aluminum plate ($3 \times 12 \times 16$ inches). Attached along each of the 12-inch sides were support legs $2 \times 10 \times 12$ inches. The legs in turn were fastened to the original seismic mass furnished with the basic drop machine (see Fig. 4).

The design of the transfer table and legs evolved from a requirement that 1000- and 3000-cps frequency components be present in the complex transient vibration shape. The frequencies were required to produce the desired shock spectrum. The transfer table was constructed entirely of aluminum with bolted interfaces between the table legs and seismic mass.

The environment at the table was generated by the drop test machine table striking the transfer table, thereby subjecting it to an impulsive load. The complex shape of the table upon an impulsive type loading then produced a complex transient vibration that visually appeared to be similar in amplitude, frequency content, and duration to the vibration specified in the test criteria. After contacting the transfer table, the original drop table rebounded and was caught, thereby removing it from the dynamics of the transfer table system.

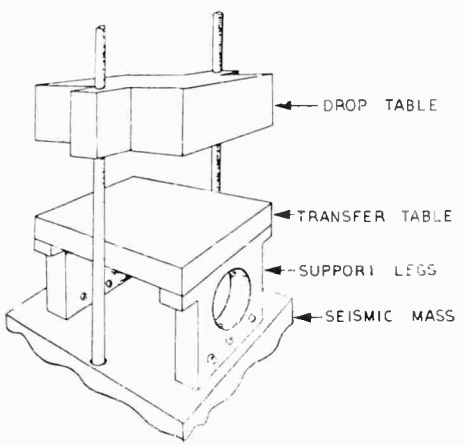

Fig. 4 - Transfer table system

The testing of components was to be accomplished by installing them on suitable brackets to the underside of the transfer table. Figure 4 shows the transfer table and its installation between the drop table and seismic mass.

Data obtained during the development of the transfer table showed the repeatability over the shock spectrum profile to be in the order of 25 percent on a point for point comparison. The repeatability based on the maximum peak amplitude of the transient vibration was approximately 10 percent. Figure 5 shows the comparison of the maximum transfer table environment to the flight data.

The measuring techniques and instrumentation used to obtain the flight data were duplicated during the development of the transfer table. Although the objectives originally specified were reasonably accomplished, there existed several additional secondary considerations which required evaluation before the final selection of a testing facility. They are as follows:

1. The inability of the transfer table to produce an over test of the maximum vehicle environment.

2. The degree of control over the amplitude of the shock environment was limited.

3. The size of the test component was restricted to approximately that of a 10-inch cube.

4. The excitation at the test equipment interface is dependent on the model shape of the table. Small components would, therefore, be less affected than large.

5. The artificial simulation of a pyrotechnic explosive event by a drop table.

BARREL TESTER

Although the results obtained from the transfer table were encouraging, the limitations

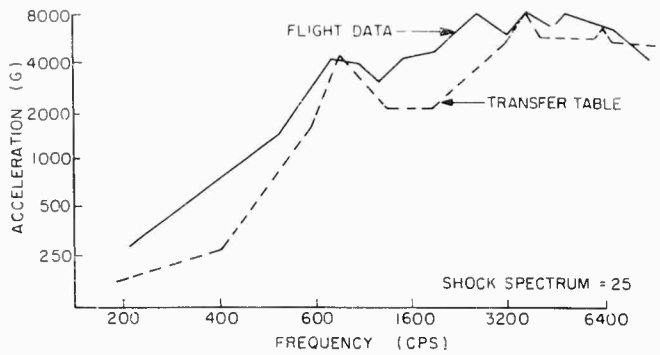

Fig. 5 - Comparison of transfer table to flight data

present suggested that another approach could possibly improve on the environmental simulation. The second approach (the barrel tester) was an attempt to duplicate the environment by similarity. The similarity existed between the diameter and skin thicknesses used on the barrel tester and flight vehicle. The similarity of the flexibility between the two structures would provide for essentially the same path for the pyrotechnic shocks to travel to component packages while the transfer table structure was a relatively rigid plate. Secondly, the mechanism of excitation would be similar to that in the vehicle system in that both would use explosives and fracture a metallic separation joint, while the environment at the transfer table resulted from the impulsive loading by the drop tester table.

Experience gained with explosives on previous programs had shown that the shock event was very repeatable. The problem was therefore, to devise a test system that could control the shock amplitude. A development program was undertaken to investigate three variables known to provide for a limited degree of control over shock environment. The three variables are:

1. Distance from shock source

2. Quantity of explosives used (5, 10, 15, 30 grain)

3. Separation joint thickness (0.05, 0.092, 0.125, 0.190 inches)

BARREL DESIGN

The barrel tester is basically an aluminum cylinder 5 feet in diameter and 5 feet in length. The substructure consists of eight symmetrically located 3 × 1 × 3/8-inch aluminum channel longerons which terminate at either end of the structure in 3 × 3 × 1/2-inch aluminum angle rings. Equally located between the two angle rings are two additional 3 × 3 × 3/8-inch aluminum "T" Section rings. The angle and T-ring sections then separate the barrel in the longitudinal axis into three symmetrical equipment mounting bays. The barrel sub-structure is then circumferentially symmetrical in eight quadrants and three bays. By alternately installing 0.090-inch welded and bolted panel sections in the eight symmetrical quadrants, the barrel was divided into four sections containing removable equipment mounting panels. In each equipment bay there are four panels available for equipment qualification testing. The entire barrel structure is a continuous weldment with exception of the 12 bolted panel sections. Since the barrel structure is identical in each panel location in that equipment bay, the environmental exposure at each panel in each bay is similar. The requirement was, therefore, to calibrate the barrel in terms of explosive content and separation joint thickness so that the shock environment at various vehicle locations could be duplicated in a particular equipment bay on the barrel tester. Figure 6 shows the barrel configuration with a typical component installed in the test bay I.

SHOCK GENERATING JOINT

The use of an explosive joint as the shock generator was the basic requirement for the barrel tester approach. It was also a requirement that the joint structure be useful over a long period without degradation of performance. The two requirements were successfully achieved in the design shown in Fig. 7.

The joint construction consisted of three parts. The first and most difficult part was the

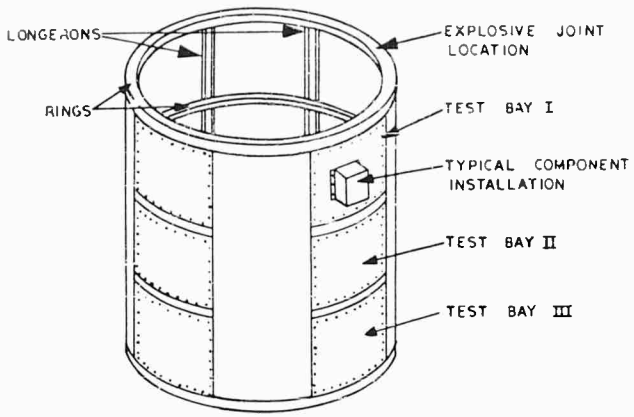

Fig. 6 - Barrel test system

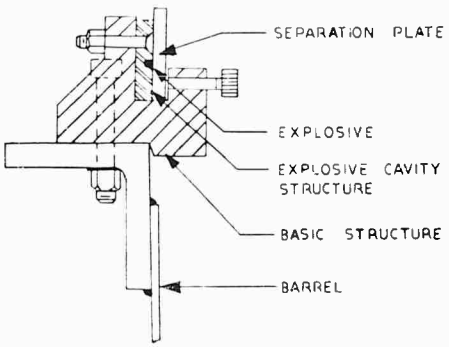

Fig. 7 - Shock generating joint

explosive cavity. The explosive cavity was constructed from a 3/8 × 1-1/4-inch strip of 4130 steel that was heat treated to 190,000 psi. A 0.125-inch groove was machined into the steel to retain the explosive cord. The second part of the joint assembly is the separation plate which covers the steel insert and explosive cord. The third part of the shock generating joint is the basic structure which supports the steel insert and the separation plate. The basic joint structure also couples the shock to the barrel structure.

The operation procedure consists of inserting the explosive cord into the joint cavity and securing the separation plate in the basic joint structure with 32 5/16-inch machine bolts. The ignition of a detonator at one end of the explosive cord starts the explosive propagating (at a speed of approximately 20,000 fps) in the separation joint, around the circumference of the barrel. The detonation then fractures the separation plate, thereby producing both an acoustic shock wave and a bending wave in the barrel structure. The response of the barrel structure was then measured with the same type instrumentation as was used during the flight and transfer table tests.

ENVIRONMENTAL CONTROL

After obtaining a shock generating joint that would function repeatedly without degradation in performance and whose action was similar to the flight vehicle staging joint, it was necessary to evaluate the barrel environment to determine if the requirements specified in the test criteria could be accomplished. It was also necessary to determine if the barrel could improve on the limitations of the transfer table, i.e., the degree of control over the shock amplitude and size of components which could be tested. The barrel had already accomplished the simulation of the shock by explosive.

As previously mentioned, the control over the shock amplitude could be obtained by position along the barrel structure and by the combination of explosives and separation joint thickness. Several tests performed showed that varying the amplitudes did not change the transient vibration shapes. The transient vibrations measured were also shown to be similar to vehicle flight data. Figure 8 shows a comparison of the flight test and barrel test data shock spectrum. The octave band comparison of the barrel environment to the flight environment is shown in Fig. 9.

The control over the spectrum amplitude could be obtained as shown in Fig. 10 by the selection of the following combinations of explosives and separation joint thickness. The data were obtained in quadrant I of equipment bay I. It can also be shown that the attenuation between

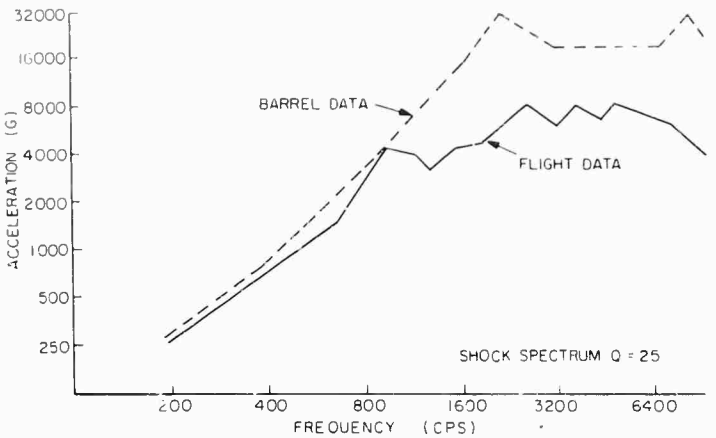

Fig. 8 - Comparison of barrel to flight data

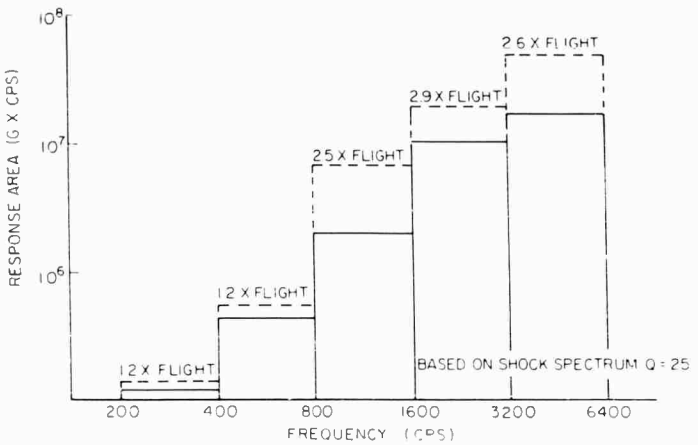

Fig. 9 - Test environment octave band area

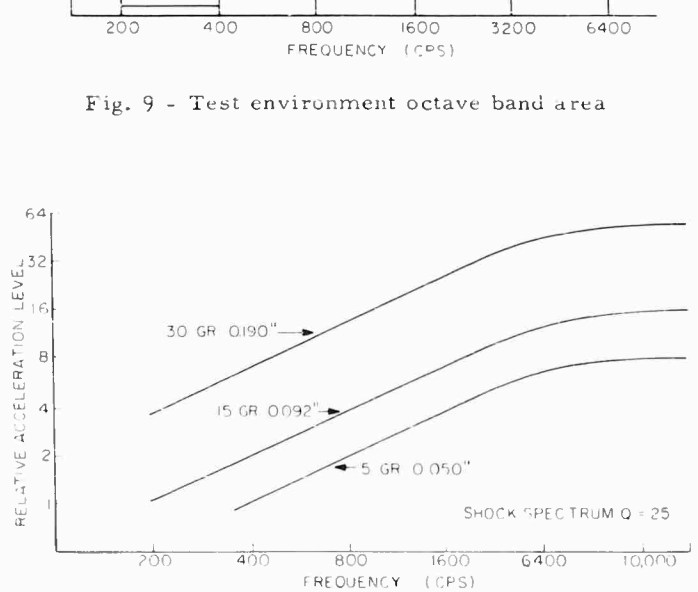

Fig. 10 - Environmental control

the first equipment bay and the second is approximately 2/1.

Although the barrel tester method of pyrotechnic shock simulation was an improvement over the transfer table, it failed to attain the optimum simulation suggested in the test criteria. The limitations are as follows:

1. The peak (g) levels shown in Fig. 8 exceed the 2.5 test criteria factor from approximately 1000 to 10,000 cps.

2. The 200- to 400- and 400- to 800-cps octave band areas shown in Fig. 9 were only 1.2 times the flight level rather than the 2 times factor suggested in the test criteria.

Although limitations presently exist in the barrel tester system, the environmental simulation is considered good; however, future development will be directed to improve the barrel tester shock spectrum.

COMPARISON STUDIES

The environments generated by the barrel tester and transfer table were both reasonable simulations of the flight event, as initially required in the test criteria. The inability to produce an over test for the maximum flight shock, the limited amplitude control and the artificial generation of the explosive shock proved to be the primary deciding factors in the selection of the barrel tester over the transfer table as a standard qualification system for Agena equipments. The transfer table, although not a qualification tool, is presently being used for equipment development testing and correlation studies.

Future studies will eventually determine if qualification of equipments by a simulated flight pyrotechnic event is a requirement for reliable equipment operation in the pyrotechnic environment.

DISCUSSION

Mr. Getline (General Dynamics/Convair): On what basis did you select your test factors above the flight environment?

Mr. Ikola: These are just artificial ground rules that were established. We have no way right now of interpreting shock in terms of failure criteria. We don't know how to take a shock transient of 8000 or 5000 g and convert it to a stress level in a piece of equipment. We only test.

* * *

TEST TECHNIQUES FOR INCREASING THE ACCELERATION AND VELOCITY CAPABILITIES OF AN 18-INCH PNEUMATIC ACTUATOR*

F. H. Mathews
Sandia Corporation
Albuquerque, New Mexico

This report describes four test methods developed for use with an 18-inch pneumatic actuator to obtain shock pulse waveforms beyond the normal capability of the machine. The methods (described below) require no internal modification to the actuator.

The first method—the two-mass impact method—is used to obtain high-amplitude, short-duration, impulsive accelerations. Maximum force levels of 2 million pounds and clean acceleration-time pulses with an amplitude of 15,000 g have been obtained. A method is presented in the report to estimate the maximum acceleration. This technique can be applied to most pneumatic shock machines.

Method number two—the gas spring method—is used to obtain high-amplitude, short-duration shock pulses and to increase actuator velocity change capability. Clean unfiltered accelerations of 55,000 g and 500-ft/sec velocity changes have been obtained on small test items. An analysis is made in the report which permits calculations of peak acceleration from setup parameters. The gas spring may be applied to actuators, air guns, and drop tables.

Method number three—the force limiter method—is used to obtain impulsive acceleration-time pulses that are trapezoidal in shape. The force limiter permits multiple tests using the same spring (honeycomb) and a single spring geometry for all tests within machine capacity. Use of the method results in small spring crush, and less unwanted high-frequency input superimposed on the shock pulse. The force limiter may be used on actuators, drop tables, and air guns.

The fourth method—the double force limiter method—is proposed as a means of extending the force limiter, thus permitting control of the entire acceleration-time history. With this technique, nonsymmetrical pulses (such as the initial peak saw-tooth) may be generated.

INTRODUCTION

There is an increasing demand for weapon components which can withstand high acceleration levels. Developing these components frequently requires repeatable shock tests at acceleration and velocity levels beyond the capability of existing shock-testing machinery. Several methods are described in this paper which can be used to extend the shock-testing capacity of an 18-inch horizontal actuator; these same methods can easily be adapted to other shock-testing machinery.

The horizontal actuator shown in Fig. 1 operates by releasing pressurized air behind a piston. This accelerates a thrust column to stroke forward, delivering an impulsive acceleration to a test item on carriage assembly. A nitrogen cushion in the forward pressure chamber of the

*This work was supported by the United States Atomic Energy Commission.

actuator decelerates the thrust column, thus terminating the acceleration pulse experienced by the carriage. The carriage continues its motion along the track and is arrested by air brakes. Operating in this manner, the actuator can generate 15,000-g acceleration pulses of 14 milliseconds duration and 300-ft/sec velocity changes upon a 200-pound test item.

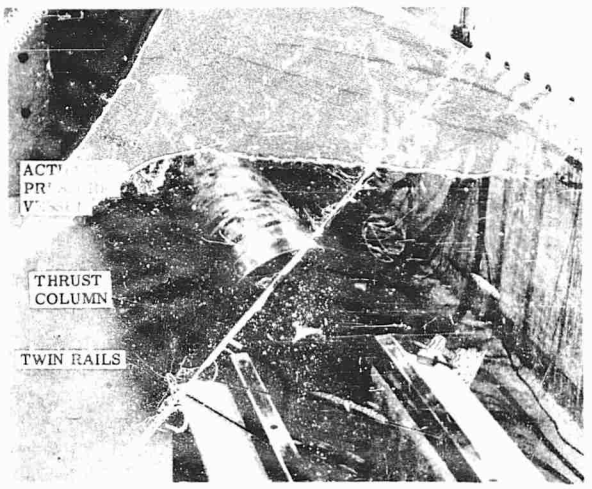

Fig. 1 - Eighteen-inch actuator

THE TWO-MASS IMPACT METHOD

Using the two-mass impact method it is possible to produce high-amplitude, short-duration, impulsive accelerations. In shock testing using this method, acceleration amplitudes several times the basic capability of the actuator have been obtained. A typical setup requiring no modification to the actuator is shown in Fig. 2. Important elements of this two-mass impact system are a 10-pound test assembly on a cushion of Ensolite* material, the actuator thrust column (which acts as the ram mass), and a sawdust-filled catcher for stopping the test item after it has sustained the desired acceleration. When the actuator is fired, the thrust column moves forward, compressing the cushion material. As the cushion is compressed, it transmits a force of increasing amplitude to the test item. Figure 3 shows the unfiltered acceleration records measured on the test item. Identical setups were used to obtain each record. The only change was a progressively increasing actuator pressure corresponding to increasing acceleration amplitude. The 15,000-g acceleration produced an impulsive velocity change of 250 fps.

*Ensolite is a low-density, flexible foam polyvinyl chloride produced in sheet form by the U. S. Rubber Corporation.

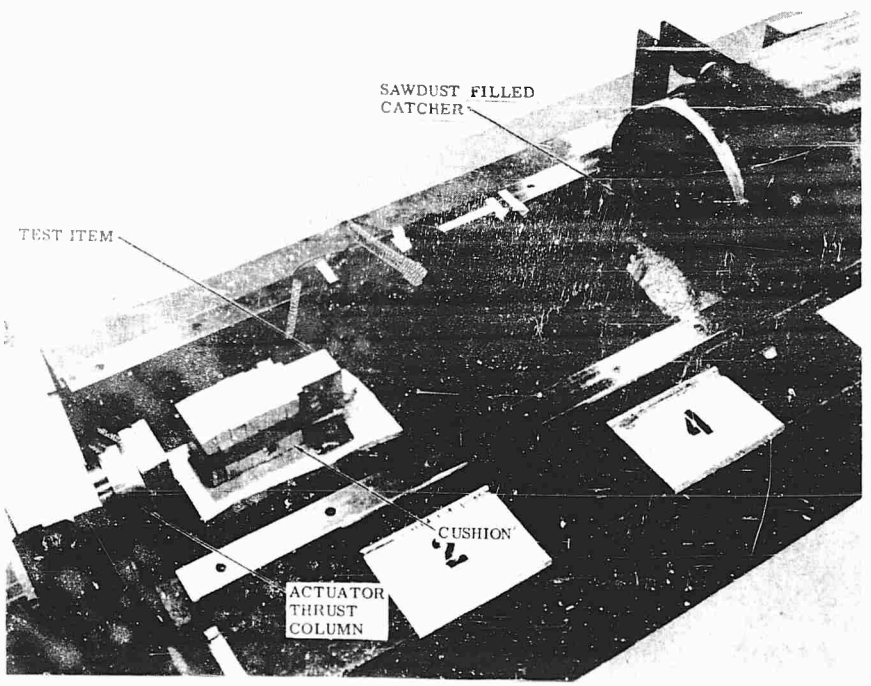

Fig. 2 - Setup for 15,000-g shock on 10-pound assembly

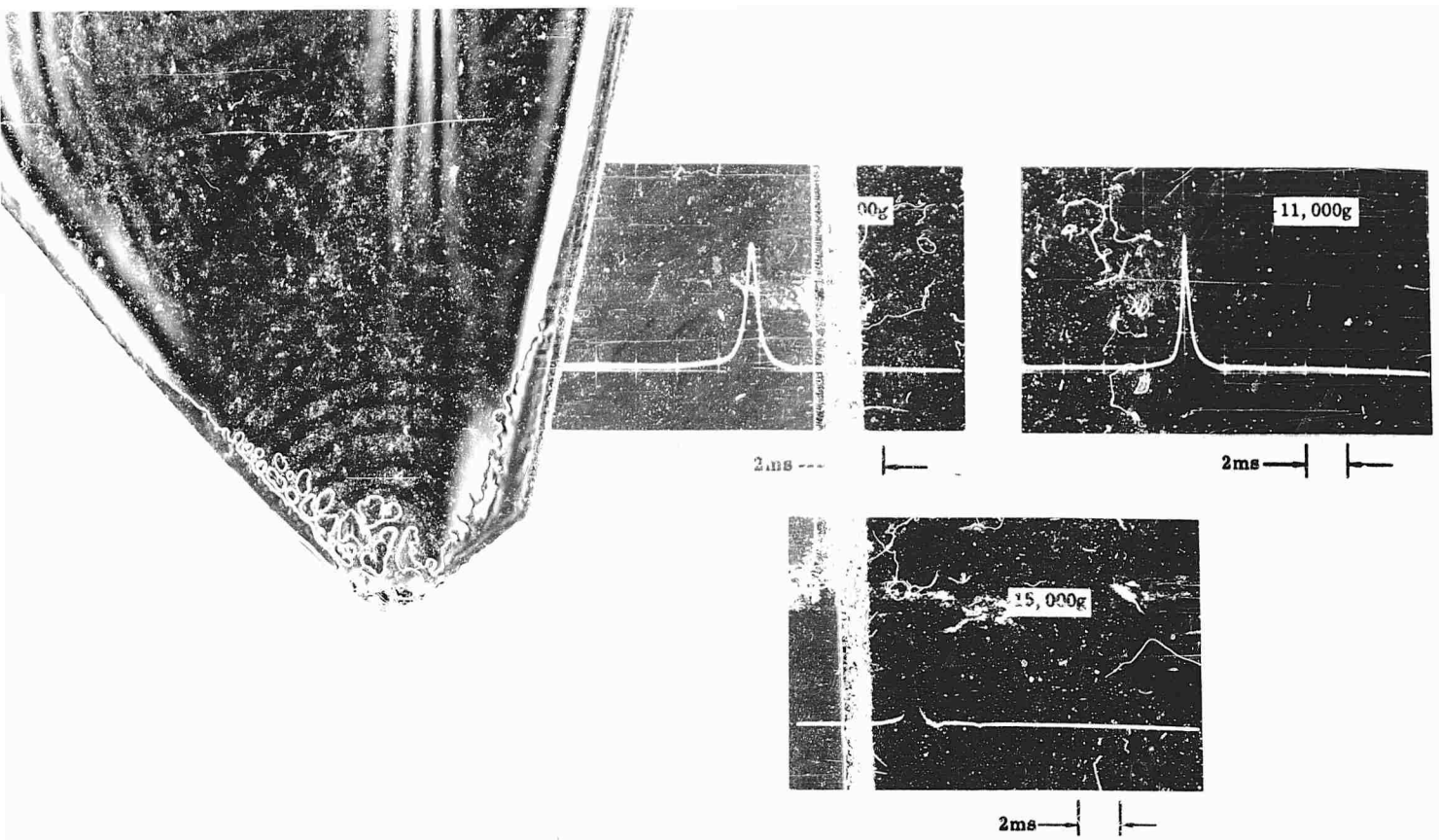

Fig. 3 - Unfil ed records of test item acceleration
r setup shown in Fig. 2

Acceleration pulses of from 3000 9000 g were obtained on heavier assemblies mounting the carriage and test item directly to the twin rails and separating the carriage and test item from an 840-pound ram carriage by an Ensolite cushion (Fig. 4). In the actual test, the ram is accelerated forward by the actuator thrust column compressing the cushion and thus transferring a high-amplitude, short-duration force to the test assembly. Figure 5 shows the acceleration-time history of ram and test carriages during a 5200-g shock of a 330-pound assembly. The ram, driven by the actuator, experienced a long-duration, low-amplitude acceleration as it moved forward and compressed the cushion. The test carriage experienced negligible acceleration until the cushion deformed about 70 percent. The maximum acceleration occurred when ram and test item attained the same velocity. After the acceleration peak, the test item rebounded from the ram and was stopped by a retaining strap wound over the two carriages. The ram was stopped by air brakes.

[illegible] frequently generated on actuators by the impact method, in which a carriage (initially launched by the actuator) impacts against a cushion mounted on a massive reaction block. The two-mass method gives several advantages over the impact method. First, in the two-mass method, the test item is initially at rest and is accelerated to the desired test velocity by the applied shock. Hard-wire instrumentation, therefore, experiences no motion before the shock. In contrast, the impact method requires that signal cables sustain approximately 50 feet of high-velocity motion before the test. This motion frequently produces cable damage with a resultant loss of data. A second advantage of the two-mass method is that it produces cleaner acceleration records than the impact method.

The amount of unwanted high-frequency noise present in the test records is related to the manner in which the cushion is loaded. If the surface of a carriage loads the cushion at a high rate, it initiates strong transient stress waves which excite unwanted high-frequency vibrations in the test item. This situation prevails when the impact method is used, since the carriage, when it initially contacts the cushion, is moving at the maximum test velocity. In the two-mass method, however, soft, nonlinear cushions, such as Ensolite, are used to fill all, or nearly all, of the initial spacing between the ram and the test item carriage. Thus, as indicated in Fig. 4, the ram is accelerated only across the

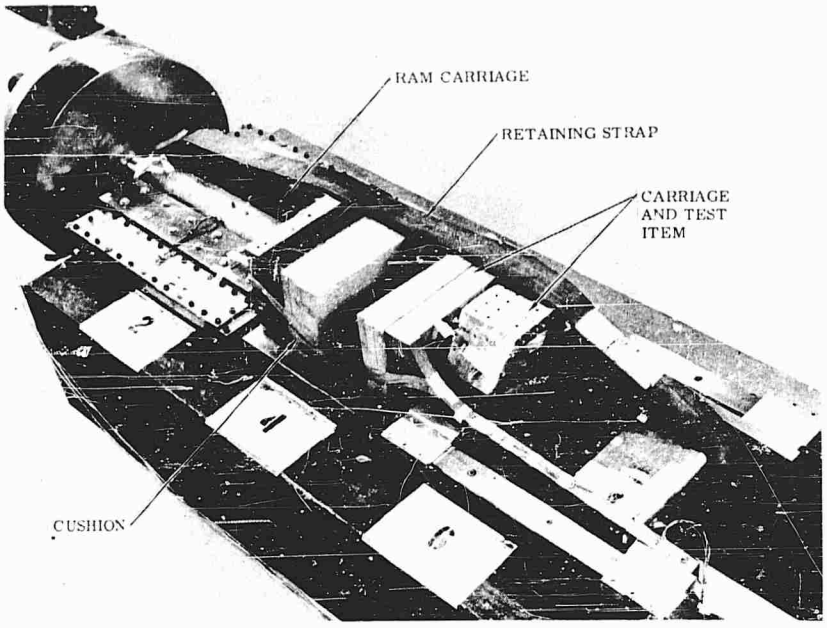

Fig 4 - Two-mass impact test setup

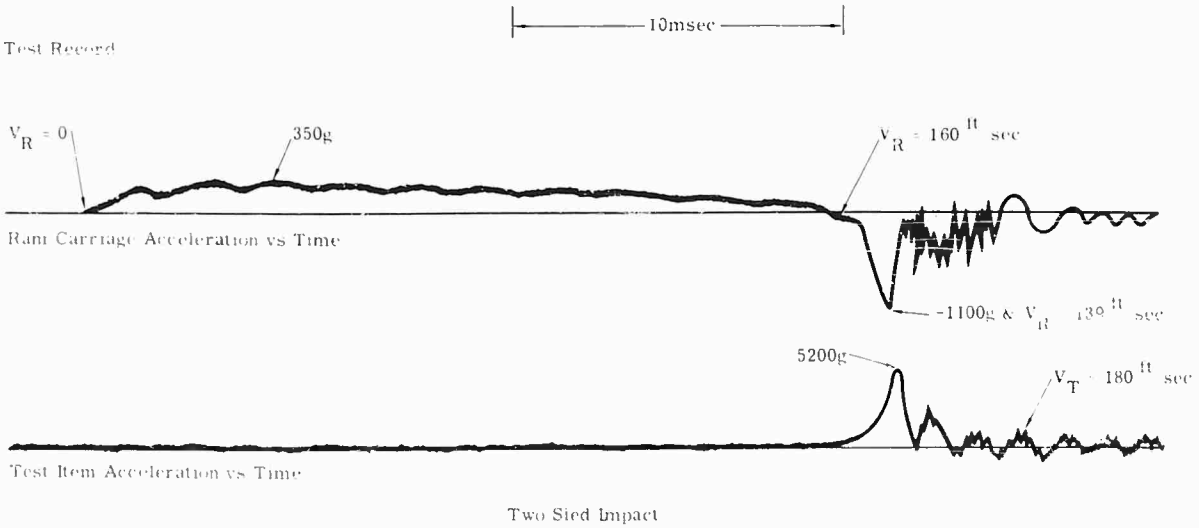

Fig. 5 - Test record from two-mass impact

small gap between the pads initially on the ram and those initially attached to the test item carriage before loading of the cushion is initiated. In the two-mass method, the relative velocity between ram and carriage is thus very low, or perhaps zero, when loading of the pads is initiated, and more uniform compression of the cushion, with desired absence of transient stress waves, may therefore be obtained.

An analytical method has been developed for estimating the peak accelerations which can be attained with the two-mass system using Ensolite No. 266. The data necessary to begin such a calculation are: (1) the geometry of a proposed setup (including the assumed size of the cushion and the assumed initial spacing between the ram carriage and the test carriage); (2) the velocity-displacement performance of the actuator when

loading the ram carriage; (3) dynamic properties of the Ensolite material (such as a restitution factor and stress level which are functions of loading); and (4) the desired level of test item acceleration and velocity change. A detailed explanation of this computation (also curves of material properties) is given in appendix A. A numeric computation for the conditions used to produce the record of Fig. 5 is included. The computed peak acceleration was 5700 g, which compares favorably with a measured value of 5200 g.

THE GAS SPRING METHOD

In the gas spring method, the Ensolite cushion used in the two-mass method is replaced by a spring of compressed gas. An example of such a setup is shown in Fig. 6. The component parts include the 18-inch actuator, a cylindrical barrel open at one end and attached to the actuator thrust column to retain the compressed gas, and a test item piston. For the setup shown, pistons weighing 0.42 to 0.72 pound were used with gas columns (initially at atmospheric pressure) which varied in length from 1/2 to 9-3/4 inches. Pulses up to 55,000 g and 1/2 millisecond duration were obtained with the setup.

Gas spring operation is illustrated schematically in Fig. 7(a), and typical acceleration histories of the piston and thrust column are shown in Fig. 7(b). This record indicates that the barrel followed a low-amplitude acceleration pulse typical of normal actuator operation. During this pulse, the barrel moved forward with increasing velocity as the gap between the barrel's bottom surface and the piston was closed. At the same time, the piston, which was coupled to the barrel only through the trapped air, experienced small forces and remained near its original position. Eventually, the gas, which was forced to occupy a continually diminishing volume, rapidly reached a highly compressed state. The piston then experienced the high-amplitude, short-duration acceleration pulse shown in Fig. 7(b). Maximum acceleration occurred when piston and barrel attained equal velocities. The piston finally left the barrel at a velocity approximately 80 percent greater than the barrel velocity at the instant of maximum piston acceleration.

The test record of Fig. 7 indicates that a barrel velocity of 239 ft/sec (at maximum piston acceleration) produced a 420-ft/sec piston velocity. Maximum piston velocity will be obtained for a particular actuator performance when the maximum projectile acceleration occurs at the instant of maximum barrel velocity, i.e., the instant marked 282 ft/sec in Fig. 7(b). This condition has not been achieved in any tests because the required barrel length of 2-1/2 to 3 feet is inconveniently long.

The unfiltered acceleration records obtained with the gas spring (Fig. 8) illustrate the unusually clean pulses and very large acceleration amplitudes which can be attained with this technique.

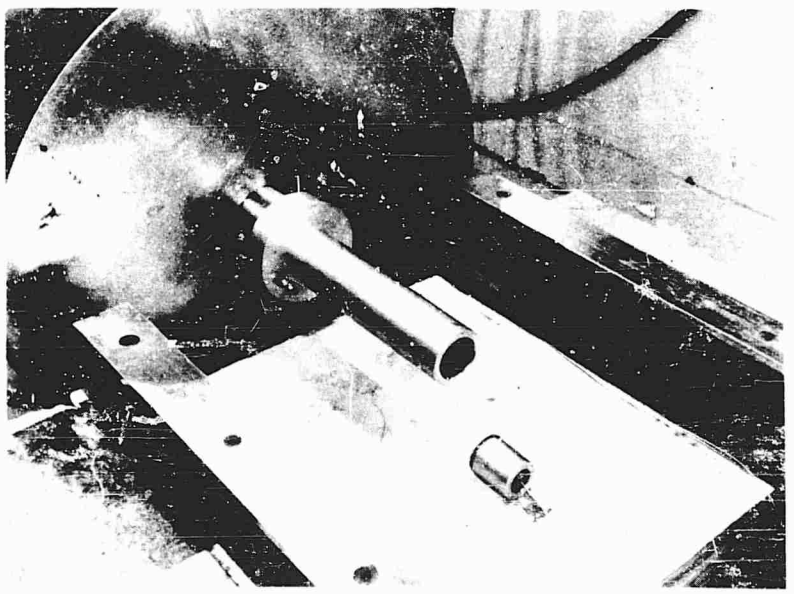

Fig. 6 - Gas-spring setup on actuator

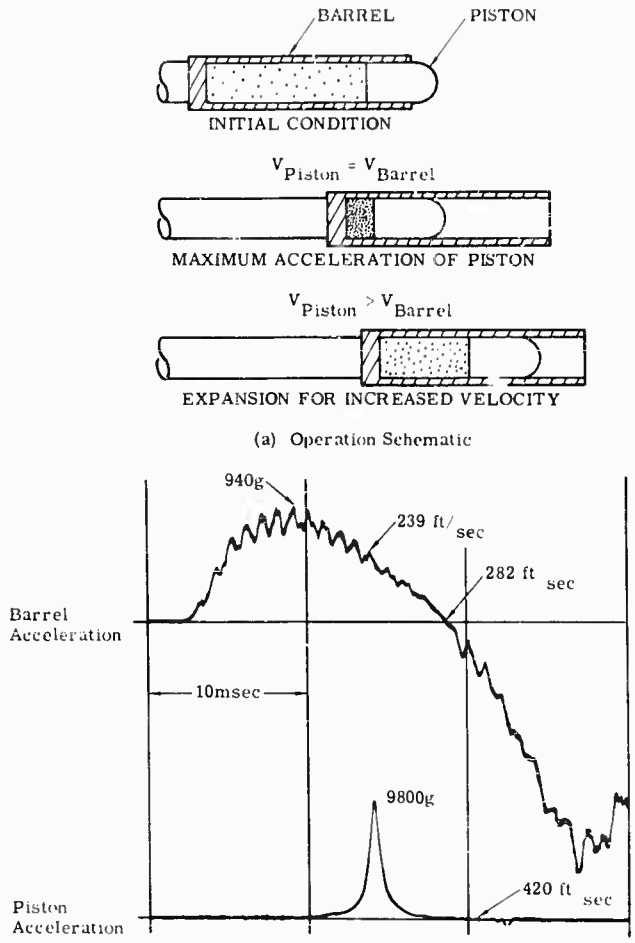

Fig. 7 - Gas-spring operation and typical acceleration record

The 55,000-g acceleration pulse required near-maximum actuator performance; however, the resulting maximum gas pressure (10,000 psi) probably does not represent maximum attainable pressure levels. Presumably, even higher gas pressures could be obtained under proper conditions. The 55,000-g pulse was measured using an Endevco 2225-M2 accelerometer rated at 20,000-g maximum amplitude. While the indicated acceleration was considerably beyond the linear range of the transducer, it closely approached the value predicted theoretically

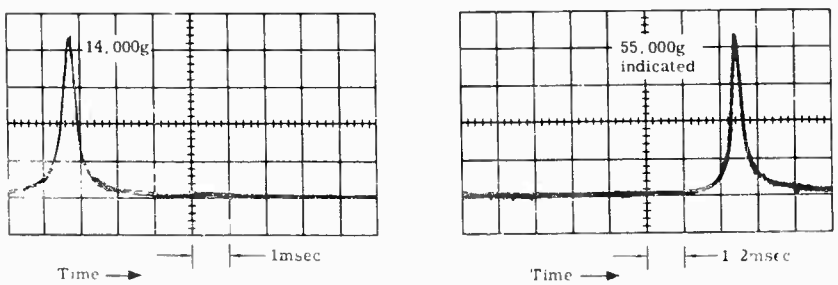

Fig. 8 - Unfiltered acceleration records obtained with gas spring

(51,000 g). The transducer's sensitivity, indicated by post-test calibration, remained unchanged.

The peak acceleration value can be estimated by assuming that the gas undergoes an approximately adiabatic process as it is compressed to maximum pressure. During this process, work delivered to the gas is equal to the change in kinetic energy of the projectile. The predicted maximum pressure is modified by an empirical coefficient which accounts for departures from adiabatic theory. The following equation expresses these conditions:

$$P_{max} = \alpha P_I \left[1 - \frac{W(K-1)}{P_I V} \right]^{K/(K-1)} , \qquad (1)$$

where

P_{max} = maximum pressure,
P_I = initial pressure of the gas in the spring,
α = empirical factor*
W = $-1/2\ M\dot{X}^2$ (work done on gas during compression),
M = mass of the projectile (assuming that the projectile mass is much less than the thrust column and gas-spring mass),
$\dot{X}$ = velocity of the gas spring barrel when the projectile attains the peak value of acceleration,
V = initial volume of gas in the spring, and
K = gas constant.

Since both projectile and barrel velocities are equal at the instant of peak acceleration, either barrel or projectile velocity may be used to estimate the kinetic energy of the projectile at the instant of maximum pressure. A numerical example of this computation for the conditions used in obtaining the test record of Fig. 7 is given in appendix B. The predicted maximum acceleration of 10,000 g is an acceptable agreement to the 9800-g test value.

The maximum-pressure equation can also be used to estimate the effect of various changes in the setup and machine performance. It can be shown that if all other parameters are held constant, the peak acceleration increases as the mass of the piston is increased. Further, the performance of the gas spring is quite sensitive to small variations in the velocity delivered to the gas spring barrel by the actuator; for example, a 5-percent increase in velocity can produce a 25-percent increase in peak acceleration. Gases with different gas constants can be used to replace air, and calculations show that the peak acceleration is sensitive to the type of gas used, with a lower gas constant causing increased values of acceleration.

The gas spring can also be adapted for use with a free-fall shock machine as shown in Fig. 9. Tests were conducted by allowing the drop table to impact against a rubber spring which produced the drop table acceleration pulse of Fig. 10. During this impact, a relative velocity was developed between the piston and gas spring barrel, thereby compressing the air trapped between the piston and the barrel. The resulting piston acceleration (Fig. 10) occurred in two phases. First, a positive acceleration was obtained while forces developed by the compressed gas were dominant. When this phase was completed, a large relative velocity between piston and barrel existed, with the piston moving toward the open end of the barrel. The second phase, a negative piston acceleration, occurred as the friction forces between piston and barrel slowed the piston to the existing barrel velocity. The piston remained in the gas spring barrel during these tests. The whole assembly, drop table, barrel, and piston were finally arrested by drop table brakes. This setup permits a piston velocity change during Phase One which is greater than the drop table velocity change, as indicated by the following equation:

$$\Delta V_T = (1 + e_g)(1 + e_t)\sqrt{2gh} .$$

where

ΔV_T = shock pulse velocity change of the test item,
e_g = gas spring restitution factor (0.6 to 0.8),
e_t = drop table restitution factor (0.5 to 0.9), and
$\sqrt{2gh}$ = drop table impact velocity caused by gravity-driven free fall.

Data applying to Figs. 9 and 10 are: impact velocity = 25.4 ft/sec; e_t = 0.65; e_g = 0.62; and ΔV_T = 68 ft/sec. Note that the piston velocity change obtained from this 10-foot free fall and 4-foot drop table rebound would require a 26-foot free fall using the drop table alone. Another gas spring system, designed to permit 60,000-g shock testing of an 8-pound, 5-inch-diameter assembly, has been fabricated and is currently being tested. Clean 20,000-g accelerations of 450-ft/sec velocity changes have been obtained. The gas spring has also been applied to a 5-1/2

*The empirical factor for the setup of Fig. 6 was 0.30 when $P_{max}/P_I = 100$, and 0.25 when $P_{max}/P_I = 1000$.

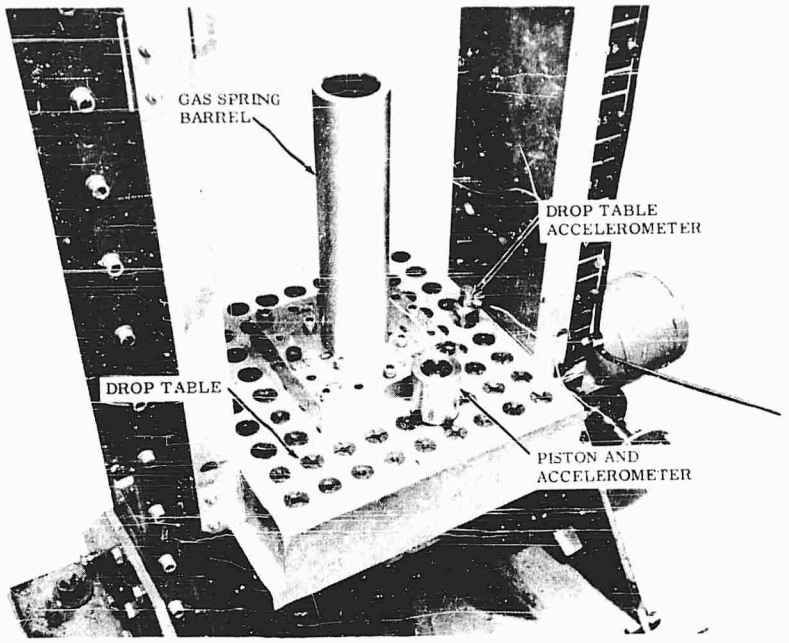

Fig. 9 - Gas spring mounted on drop table

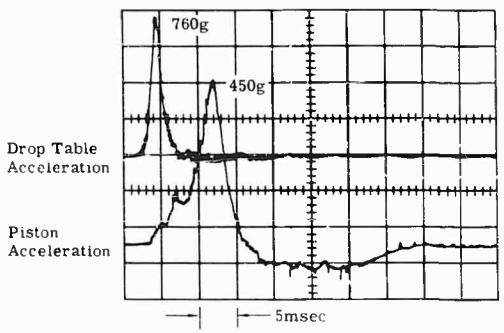

Fig. 10 - Test record using gas spring mounted on drop table

inch air gun in which the gas spring is formed by air trapped between a ram piston and a test item piston. The normal 5000-g acceleration capability of the air gun was increased to 20,000 g. A system in which the gas spring replaces the Ensolite cushion for the largest two-mass impact system is also being studied. The gas spring is expected to provide more repeatable shock pulses and greater velocity changes.

THE FORCE LIMITER METHOD

In a recent test, a shock pulse was required with a 2-millisecond rise to 175 g and a 20-millisecond dwell at that level. The required velocity change was 120 ft/sec. The well-known method of impacting a carriage into a properly shaped honeycomb spring was impractical because (1) the launch acceleration with the 18-inch actuator was more severe than the test value, (2) honeycomb permitting the required crush of 20 inches was not immediately available, and (3) the properties of the honeycomb were unknown for loading at the high rates required. Consequently, an alternate setup using a honeycomb force limiter was designed (Fig. 11) and used to complete a program requiring 30 tests.

Qualifying tests, for which an acceleration record is shown in Fig. 12(a), were conducted using a weighted carriage without the force limiter. These tests established the actuator firing conditions necessary to produce an acceleration rising to 175 g in 2 milliseconds. A total velocity change of 125 ft/sec was obtained. The test setup was completed by placing honeycomb which had a crushing strength equal to the force required to produce a 175-g acceleration on the carriage between a load plate attached to the actuator thrust column and the test carriage. When the actuator was fired, the honeycomb transferred the actuator force during the 2-millisecond rise to 175 g and then began to crush, limiting the acceleration to a constant value of 175 g. After the loading plate and

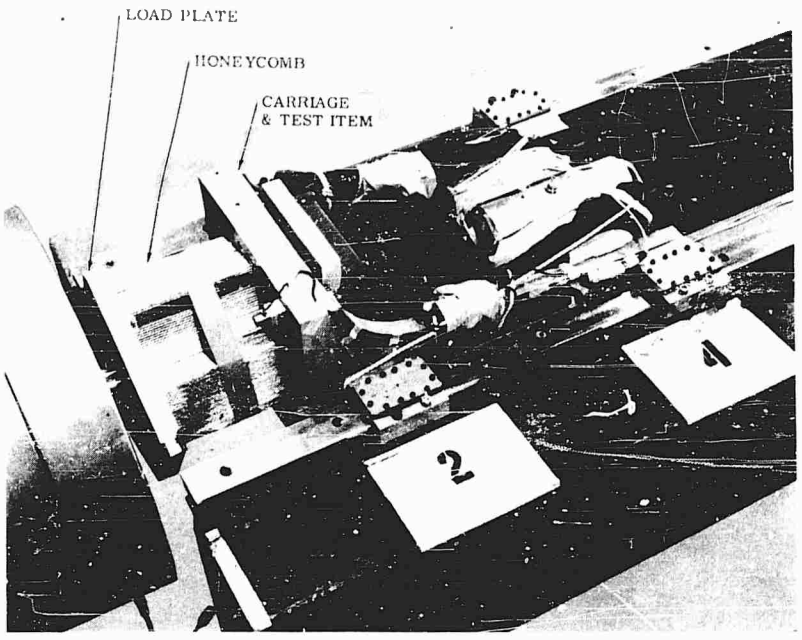

Fig. 11 - Force limiter

carriage attained the same velocity, the carriage separated from the loading plate (which was being decelerated by the actuator), terminating the acceleration pulse. This time is labeled "Equal Velocity" in Figs. 12(b) and 12(c). Figure 12(c) indicates a typical acceleration obtained on the test item. Since the honeycomb was crushed only 3 inches during each test (compared with the 18 inches required for impact shaping of the same pulse, indicated in Fig. 12(d)), two tests were conducted with a single 10-inch-long honeycomb force limiter before the available crush distance of 7 inches was exhausted.

The only problem encountered during the use of the force limiter was in controlling the pulse rise time. During the 30 tests involved in the program, the rise time varied from 1 to 3 milliseconds. This time was apparently quite sensitive to small gaps between the honeycomb and loaded surfaces. The average acceleration value during the 175-g dwell proved highly repeatable. A variation of ±10 g was obtained for the 30 shots.

The use of the force limiter with an actuator provides a number of advantages. The acceleration is impulsive; that is, the test item experiences no preliminary motion. As a result, hard-wire instrumentation must survive only the small displacements associated with the shock. When using a force limiter, both honeycomb and carriage are simultaneously experiencing positive acceleration. The honeycomb crush rate is therefore much lower than that which would occur during impact, and strain rate effects (variable crush strength and increased noise associated with high strain rates) are suppressed. The noise frequently produced during impact is also avoided, since the honeycomb and test item are initially in contact. Finally, the honeycomb may be reused, without modification, until its full capacity is exhausted.

The force limiter may also be used on free-fall shock machine to produce flat-topped acceleration pulses, while maintaining full velocity change capability (impact plus rebound) of the table. Figure 13 shows the setup used in obtaining the acceleration time records of Fig. 14. In this case, the honeycomb was attached to the drop table and test item with double-faced tape. The whole assembly was then dropped as a unit and allowed to impact against the drop table spring. Carriage brakes arrested the assembly after rebound. The acceleration record of Fig. 14 indicates that the test item followed the rising portion of the table acceleration until enough force was generated to begin crushing the honeycomb. The test item acceleration then remained constant at the level corresponding to the honeycomb crush strength until the test item and table approached the same velocity. Because the table acceleration was nearly completed when test item and table reached the same velocity, the

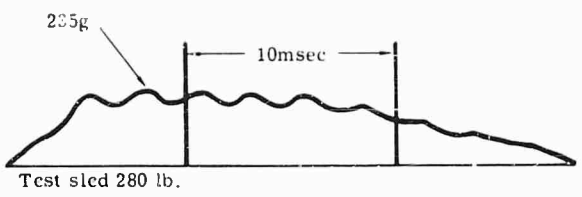

(a) Carriage Acceleration without Force Limiter (Test Record)

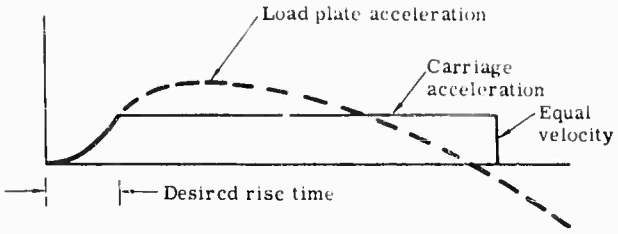

(b) Accelerations of Load Plate and Carriage

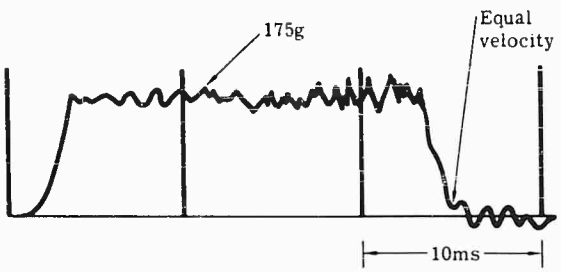

(c) Carriage Acceleration with Force Limiter (Test Record)

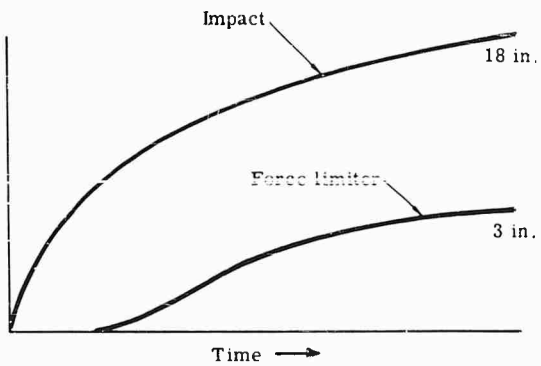

(d) Displacement Time Comparison Between Force Limiter and Impact Tests

Fig. 12 - Force limiter test results

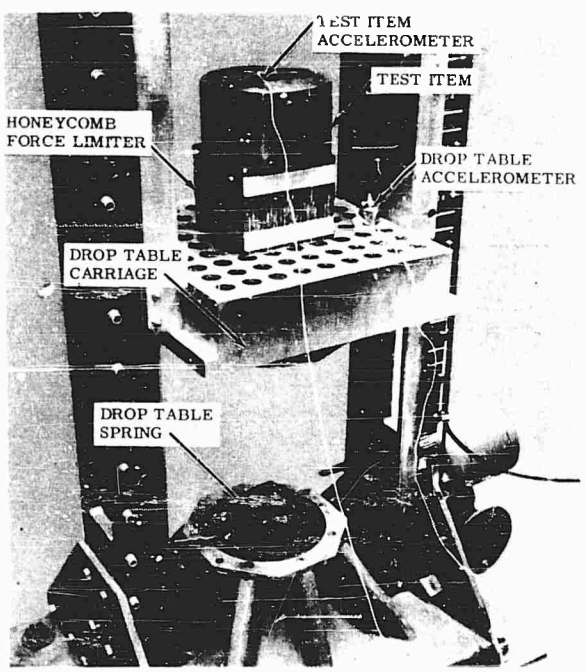

Fig. 13 - Force limiter mounted on drop table

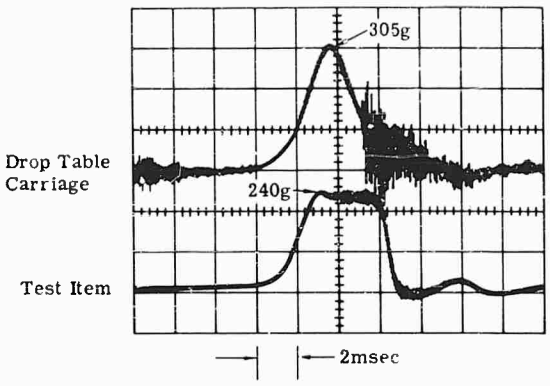

Fig. 14 - Acceleration record from the drop table force limiter

test item acceleration rapidly fell to zero. If the table acceleration was not completed, the test item acceleration would be expected to fall to the existing table acceleration value and then follow the remainder of the table pulse. With this setup, the carriage weight, impact velocity, and drop table spring control the pulse rise time (provided the unbuckled honeycomb is stiff enough to transmit the rising pulse accurately) while the force limiter controls the maximum acceleration.

A similar shock pulse could be obtained without the force limiter by impacting into a properly shaped honeycomb spring. With the force limiter, however, the full velocity change capability of the drop table is used, including that caused by the rebound of the table. The 32-ft/sec shock pulse of Fig. 14 required a 5-foot free-fall machine with force limiter. An equal shock using direct impact on a honeycomb programmer would require a 16-foot free-fall machine.

THE DOUBLE FORCE LIMITER METHOD

The principle of the force limiter can be extended to permit control of the entire acceleration time history. A proposed setup for a double force limiter is shown in Fig. 15. This method requires that a test carriage be placed between the actuator thrust column and a resisting mass. A honeycomb spring mounted on the thrust column would load the test item, causing the positive portion of the force-time curve in Fig. 15. After completing the rising portion of the shock pulse, the test item would contact a resisting spring. The force supplied by the resisting spring would be subtracted from the constant force supplied by the thrust column

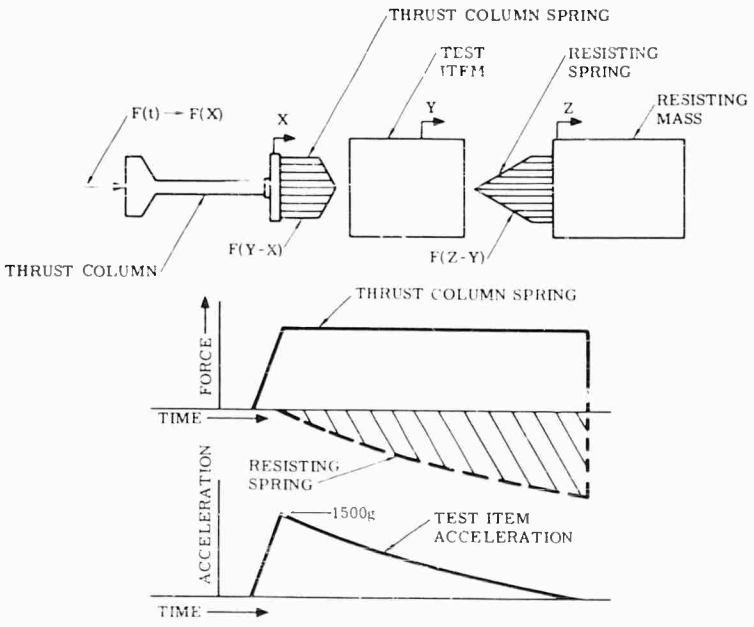

Fig. 15 - Double force limiter

spring. The entire acceleration pulse could thus be controlled by properly shaping the honeycomb springs.

CONCLUSIONS

By way of conclusion, it seems prudent to summarize briefly the capabilities of the four methods described in this report. These methods were used to obtain shock pulse waveforms beyond the normal capacities of the 18-inch pneumatic actuator, and they required no modification to the actuator.

The Two-Mass Impact Method

This method can be used to obtain high-amplitude, short-duration, impulsive accelerations. Maximum force levels of 2-million pounds and clean acceleration-time pulses with an amplitude of 15,000 g have been obtained. This technique can be applied to most pneumatic shock machines.

The Gas Spring Method

This method can be used to obtain high-amplitude, short-duration shock pulses and to increase actuator velocity change capability. Clean, unfiltered accelerations of 55,000-g and 500-ft/sec velocity changes have been obtained by this method on small test items. The gas spring may be applied to actuators, air guns, and drop tables.

The Force Limiter Method

This method can be used to obtain impulsive acceleration-time pulses that are trapezoidal in shape. The force limiter method permits multiple tests using the same spring (honeycomb) and a single-spring geometry for all tests within machine capacity. Use of the method results in small spring crush and in less unwanted high-frequency input superimposed on the shock pulse. The force limiter may be used on actuators, drop tables, and air guns.

The Double Force Limiter Method

This method is proposed as a means of extending the force limiter, thus permitting control of the entire acceleration-time history. With this technique, non-symmetrical pulses (such as the initial peak saw-tooth) can be generated.

Appendix A

ESTIMATING THE PEAK ACCELERATION FOR TWO-MASS IMPACT

It is possible to estimate the peak acceleration of a two-mass impact by using a calculation modeled after the simple case of a falling weight and attached spring impacting against a fixed surface. For this case, the peak acceleration can be calculated from knowledge of the impact energy of the falling mass and the stress energy properties of the cushioning materials. The cushion properties are determined by conducting a series of tests using various cushion volumes and cross sections at different impact velocities. First, a curve of maximum cushion stress is derived as a function of the impact energy of the falling weight. Once this curve is available, the peak acceleration for any test can be computed from impact velocity, weight, cushion area, and cushion volume.

The falling weight calculation is extended to the case of a ram mass impacting against a test item mass by observing that the ram and test item motions occur in three segments. The first segment, the impulse phase, involves the impulsive acceleration of the ram mass under the driving force of the actuator. During this phase, the ram mass develops the energy which it will later transfer through the cushion into the test carriage. The ram mass may be compressing the cushion during any part or all of this phase, but the resulting force on the ram is low and offers negligible resistance to ram motion. When the cushion becomes highly compressed, however, cushion forces become appreciable and begin to affect the ram and test item motions. This starts the impact phase. In this phase, the cushion forces dominate, causing the ram carriage to decelerate and the test item carriage to experience the rising portions of the shock pulse. Eventually, when peak acceleration is achieved, the ram and test item attain the same velocity. Finally, the rebound phase occurs as ram and test item separate, providing the decreasing portion of the test item acceleration.

The processes occurring on the test item during the impact and rebound phases are similar to those occurring on the falling weight during its impact. The major difference is that the ram which replaces the fixed surface is moving and has a finite mass allowing its velocity to be changed during the impact. The velocity change of the test item at the instant of peak acceleration is similar to the shock induced velocity change of the freely falling mass taken at the instant of peak acceleration. Therefore, the peak acceleration for a two-mass impact can be estimated using a technique similar to that applied to the falling weight, provided proper account is taken of the finite mass of the ram.

The scheme employed in this computation is to assume a particular setup condition including initial spacing between ram and test item, volume of Ensolite cushion, and loaded surface. Since the desired values of maximum test item acceleration and total test item velocity change are known, the calculation is continued by establishing the required ram carriage velocity (and therefore the required actuator performance) and then predicting the peak acceleration resulting from these conditions. Finally, the predicted acceleration is compared with the desired value and a new setup condition assumed. A new acceleration is then predicted and compared with the desired value and the calculation is repeated until predicted and assumed values agree.

An example of this computation follows. The numerical values, including the assumed setup geometry (loaded area, initial spacing, and cushion volume) are those actually used in obtaining the test results presented in Fig. 5. The following illustration, therefore, serves the dual purpose of describing the method and comparing the predicted value with an experimental result obtained using the assumed setup.

The computations below involve a situation in which it is necessary to produce a 5200-g pulse of 180-ft/sec velocity change upon a 330-pound test item. The initial spacing between the test item and the 1100-pound ram (including the weight of the thrust column and ram) is assumed to be 23 inches. This space is completely filled with a cushion of Ensolite No. 266 having a loaded area 17 inches square. The problem is to compute the ram velocity required to produce the above shock pulse. The required average stress may be computed from the acceleration, loaded area, and test mass:

$$\sigma = \frac{M_T \ddot{X}_T}{A} = \frac{(330)(5200)A_g}{A_g\,(17)(17)} = 5950 \text{ lb/in.}^2,$$

where

σ = average stress in the cushion at the instant of peak acceleration,
M_T = mass of test assembly (including carriage),
$\ddot{X}_T$ = desired peak acceleration, and
A_g = gravitational constant 32.2 ft/sec^2.

The required ram carriage velocity at the beginning of the impulse phase may be computed from the equations of impact between two bodies:

$$V_r = V_T \frac{M_R + M_T}{M_R\,(1+e)} = 180\,\frac{(330+1100)A_g}{1100\,(1+.35)A_g}$$

$$= 173 \text{ ft/sec},$$

where

V_r = required ram carriage velocity at impact,
V_T = velocity change of test item,
M_R = mass of ram,
M_T = mass of test assembly, and
e = restitution coefficient.

A curve of restitution as a function of stress for Ensolite No. 266 is given in Fig. A1. This data was obtained from a series of two-mass impact tests. The final velocity of the ram is expressed by the following impact equation:

$$\bar{V}_R = \frac{(M_R - eM_T)\,V_r}{M_R + M_T} = \frac{[1100 - 0.35(330)]A_g[173]}{[1100+300]A_g}$$

$$= 119 \text{ ft/sec}.$$

After reaching this stage, the energy loading of the cushion can be computed by assuming that maximum loading occurs when the ram carriage attains its mean velocity, as given by

$$\bar{V}_R = \frac{V_r + V_R}{2} = \frac{119 + 173}{2} = 146 \text{ ft/sec}.$$

and since the test item also has a velocity equal to V_R at this instant, the total kinetic energy of the test assembly (M_T) is

$$KE = \frac{1}{2} M_T \bar{V}_R^2.$$

Since M_T was loaded only by the Ensolite cushion in attaining this velocity, the above value is also the potential energy stored in the Ensolite spring at the instant of maximum acceleration. Therefore,

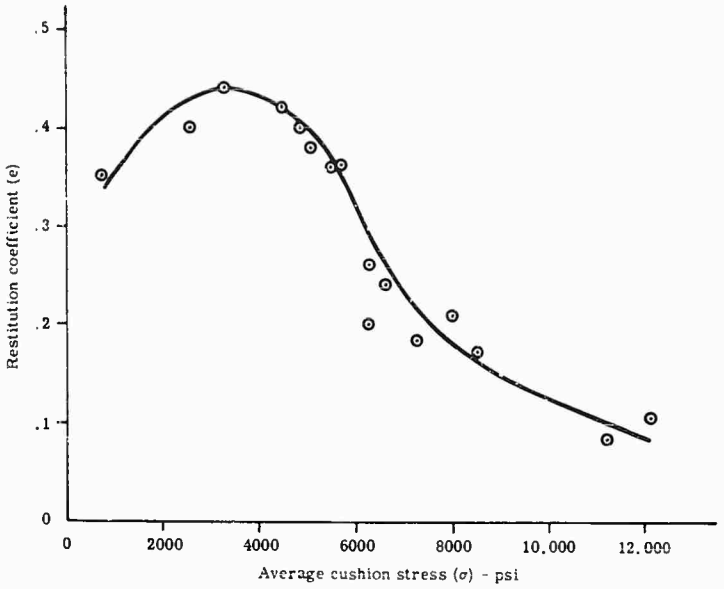

Fig. A1 - Restitution coefficient as a function of average cushion stress for Ensolite No. 266

$$E_{sp} = \frac{\frac{1}{2} M_T \bar{V}_R^2}{A\ell} = \frac{1}{2}\left(\frac{330}{32.2}\right)\frac{146^2}{17(17)}\ \frac{(1728)}{(23)}$$
$$= 27{,}500 \text{ ft lb/ft}^3 ,$$

where

ℓ = length of cushion, and
E_{sp} = specific energy.

The curve of mean stress level as a function of specific energy (Fig. A2) is then entered using the calculated value of specific energy. A mean stress level is obtained (6500 psi) and the expected peak acceleration computed from:

$$\ddot{X}_T = \frac{\sigma A}{M_T} = \frac{(6500)(17)(17)}{330} = 5700 \text{ g} .$$

The predicted acceleration of 5700 g is an acceptable estimate of the 5200-g test value.

The data presented in Fig. A2 was obtained from a series of tests using the setups of Figs. 2 and 4. The test information was obtained through hand integration of test records similar to Fig. 5. The scatter of data around the curve applying to the setup for Fig. 4 is typical of this calculation, which must be considered only an estimate of peak acceleration.

The only remaining unknowns are the initial actuator pressures required to perform the test. This idealized calculation, which neglects the fact that the ram carriage is under actuator impulse during the shock, requires that the ram carriage attain a velocity of 146 ft/sec at the instant of peak acceleration. If the same test were conducted using an impact in which a ram carriage weighing 1100 pounds and moving at 173 ft/sec (and completely free of any thrust by the actuator) impacted into a test item, exactly the same velocity—146 ft/sec—would be obtained on the ram at the instant of peak acceleration. In the two-mass impact, the actuator must deliver exactly the same energy as that required in the free impact. The energy, however, is developed both by the impact velocity of the ram and the impulse added by the actuator during the impact phase of the test. The ram carriage, therefore, never actually attains this velocity, but instead reaches a velocity of 160 ft/sec (Fig. 5). The actuator energy requirement is known, therefore (173 ft/sec, 1100 pounds), and only an estimate is required of the position along the actuator stroke at which the energy must be developed. High-speed motion pictures taken during tests indicate that the cushion typically compresses to 5 percent of its original thickness. The test item carriage moves a negligible amount (about 1 inch) during the impact phase of the shock. The full impact energy, therefore, must be developed when the ram has been displaced a distance, approximately equal to the initial space between carriages, including the space filled by cushion. With this information, and experimental curve describing actuator energy as a function of pressure and position is used to determine the required actuator setup pressures.

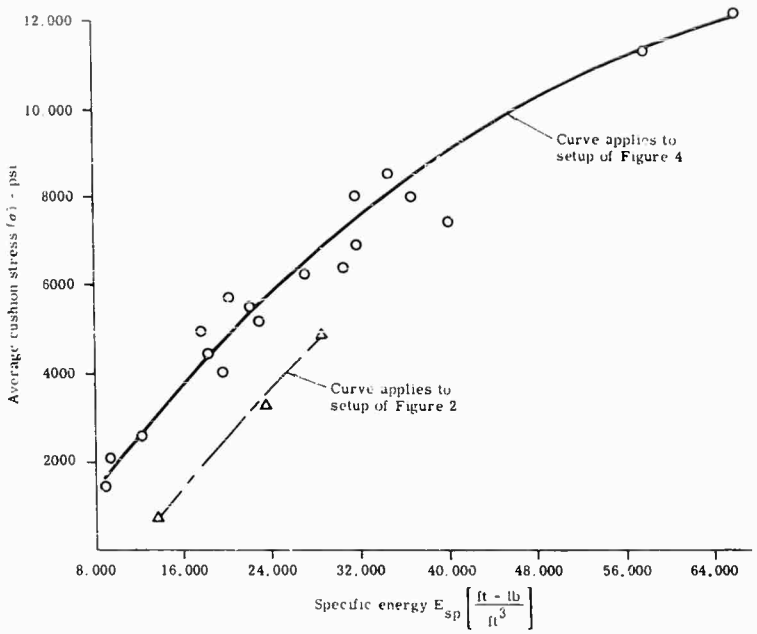

Fig. A2 - Stress as a function of specific energy for Ensolite No. 266

Appendix B

EXAMPLE COMPUTATION FOR GAS SPRING

The test record of Fig. 7 was obtained using the following setup: a 2.125-inch-diameter projectile weighing 0.42 pound was placed 9-3/4 inches from the bottom of a gas spring containing air at 12.3 psia. The actuator drove the gas spring barrel to a velocity of 239 ft/sec at the instant of maximum projectile acceleration. The ratio of maximum pressure to initial pressure is estimated to be 100, indicating that the factor α should take the value of 0.30 (see footnote, page 281.

With these values, and the nomenclature defined on page 281, the various terms for use in Eq. 1 are:

$$W = -\frac{1}{2}M\dot{X}^2 = -\frac{1}{2}\,\frac{0.42}{32.2}\,(239)^2 = -372 \text{ ft/lb},$$

and

$$V = 0.785d^2\ell = \frac{0.785(2.125)^2(9.75)}{1728} = 0.0200 \text{ ft}^3.$$

With these values, Eq. 1 (page 281) becomes:

$$P_{max} = \alpha P_I \left[1 - \frac{W(K-1)}{P_I V}\right]\frac{K}{K-1}$$

$$= 0.30(12.3 \text{ psi})\left[1 - \frac{-372(1.4-1)}{12.3(144)(0.0200)}\right]\frac{1.4}{1.4-1}$$

$$= 1180 \text{ psi},$$

and

$$\ddot{X} = \frac{P_{max}A}{M} = \frac{(1180)(0.785)(2.125)^2}{(0.42)} = 10{,}000 \text{ g}.$$

The calculated value of 10,000 g is in good agreement with the measured value of 9800 g shown in Fig. 7. The predicted acceleration for the 55,000-g pulse of Fig. 8 was 51,000 g, which is also an acceptable agreement.

Mr. Arnold (ACE): I noticed in the film that the instrumentation cables, evidently from the attached accelerometers, were whipping quite rapidly along the course of the travel. Did you have any difficulties in instrumentation recordings?

Mr. Mathews: Of course, this is the point of the impulsive acceleration. The test item carriage in all these cases was initially at rest. The other carriages, particularly in the case of the two mass impact, required some motion. We didn't have difficulties in this case because the velocities were relatively low, but this is the point of producing the impulsive accelerations on the test item.

Mr. Getline (General Dynamics Convair): On what basis did you select those sections of honeycomb?

Mr. Mathews: The desired motion of the middle carriage was known. The desired acceleration pulse, the impact velocities, the energy levels of the ram carriage, and the amount of resisting mass could be calculated. Then numerically you calculate the displacement time histories of all of the carriages. In addition you calculate the force time histories and cut the honeycomb to the proper shape. This was done by hand for this case. A computer program is in process.

* * *

FIVE-MILLION POUND SHOCK TESTING FACILITY

R. M. Phelan
Cornell University
and
Lawrence Radiation Laboratory
Livermore, California

This paper describes one approach for upgrading a shock testing facility from 250,000 to 5,000,000 lb when acceleration pulses are desired with levels up to 10,000 g and rise times measured in tenths of a millisecond. The system uses the transfer of momentum between a carriage and a reaction device, or pulse shaper, to provide a degree of control over the shape of the shock signature. Basic design philosophy and practical limitations are presented. Modifications in operating theory and procedure that have resulted from experience with the system at levels up to 3,300,000 lb and 8300 g are discussed.

INTRODUCTION

For some time it has been evident that future programs would place greater emphasis on shock testing components and assemblies, particularly with respect to high-level short-duration pulses. Although programmatical requirements could not be specified with any degree of exactitude, there was general agreement that the peak accelerations should be several thousand g with objects weighing several hundred pounds and the rise times should be measured in tenths of a millisecond.

The facility on hand that appeared to be best suited for use in meeting the new requirements was an 18-in. Hyge actuator and track complex, shown schematically in Fig. 1. It was immediately apparent, however, that the Hyge could not be used as a direct push device in this application, because the thrust force of the 18-in. Hyge under dynamic conditions is limited to about 250,000 lb, and the acceleration signature is characterized by rise times and durations exceeding 5 and 20 milliseconds, respectively.

The first method considered for, and used in, extending the capabilities of the 18-in. Hyge was to combine impact and direct push by leaving an initial gap between the thrust foot of the Hyge and the contact surface of the specimen. As with all schemes involving impact, it was necessary to insert a crushable pad between the impacting surfaces to control the rate at which the acceleration increases during the rise-time part of pulse. This phase of the development was carried out by Mr. K. W. Volkman of UCLRL at Livermore. The thrust column of the Hyge was replaced with a stronger one and antimonial lead (95 percent Pb and 5 percent Sb) pads with triangular-shaped grooves were used. The maximum force capacity was increased to 1.5×10^6 lb and the rise-times were decreased to the desired tenths of milliseconds.

A number of tests were run using the initial gap scheme and useful information was obtained. At the time, the following limitations became apparent:

1. The capacity could not readily be increased beyond 1.5×10^6 lb and the need for greater force capability was at hand.

2. The crushing of the impact pad controlled only the rise-time part of the pulse and the decay was almost instantaneous. This resulted in an acceleration-time curve that was approximately saw-tooth in shape, as desired, but it was just backwards in comparison with the desired rapid rise and relatively slow decay.

3. Air brakes on the carriage were the only means of stopping the carriage, and thus the specimen, after impact. The brake operation had been found to be notably inconsistent and there was no way to predict accurately where the carriage would stop. In fact, if the carriage were damaged during impact or if the air pressure were lost by any means, such as a failure of a

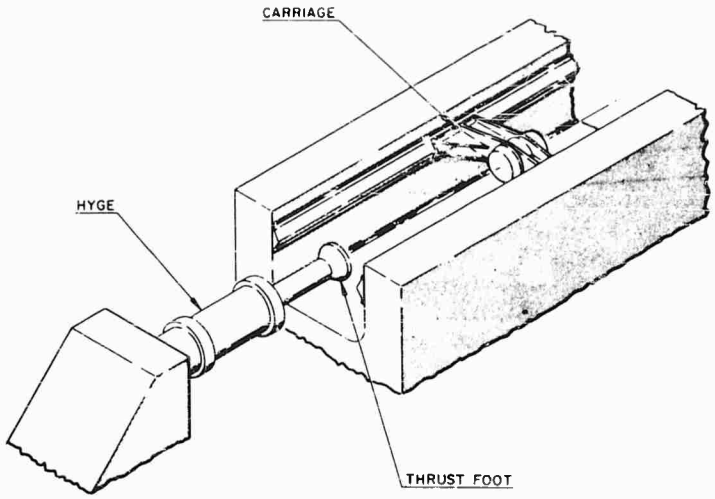

Fig. 1 - Original system with braking carriage

quick-disconnect coupling, the carriage would run off the end of the track and come to rest in the adjacent field.

4. The impact (acceleration) force was concentrated near the center of the carriage and the elastic action of the system was such that the carriage would vibrate as a free-free beam. This resulted in an oscillating variation in the acceleration-time curve and in successive impacts as a gap opened and closed between the Hyge pusher foot and the carriage. The secondary impacts were particularly serious because each new impact occurs on a pad that is already crushed and therefore much stiffer than for the previous impact.

Although some of the limitations and operational problems could be alleviated by redesign of the carriage and braking system, the gain in performance would not be sufficient to meet the new requirements.

SYSTEM DESIGN CONCEPTS

Since impact is primarily a problem in momentum exchange between two bodies, it is obvious that, when only one body can have an initial velocity, the maximum effect will be obtained if the second body is held fixed in place. This observation led to considering use of the energy-releasing, rather than the acceleration-producing, characteristics of the Hyge in converting the system into the horizontal equivalent of a drop tower. Further consideration of this scheme pointed out several definite advantages over the conventional drop tower and led to its adoption as a basis for design. The advantages are:

1. The Hyge can deliver about 200,000 ft-lb of energy in a distance of about 30 in. This is the equivalent of a drop tower 1000 ft high when the specimen and carriage weigh 200 lb, and 400 ft high when the weight is 500 lb.

2. The travel of the carriage must exceed the total stroke of the Hyge pusher, about 4 ft, but otherwise it can be as short as one wishes. This greatly simplified the overall operation, particularly with respect to instrumenting the specimen.

3. The horizontal direction of travel and the accurate guidance of the carriage on the fixed rail system would make it relatively simple to achieve better control over the acceleration-time characteristics by introducing some shock-absorbing device that would eliminate rebound and provide more control during the decay-time period of the pulse than is possible with crushable materials only.

At the time the design was begun, a force capability of 3×10^6 lb was considered to be adequate, but this was quickly changed to 5×10^6 lb when preliminary calculations showed that the greater capacity was feasible within the space limitation imposed by the existing track width of about 30 in.

The major components that had to be designed and built are: (1) the device that controls the acceleration-time characteristics of the shock, hereafter called the "pulse shaper,"

and (2) the carriage. These will be considered in turn.

Pulse Shaper

The acceleration signature requirements were relatively loose at first in that almost any decay curve would be acceptable as long as the rise time could be as short as 0.5 ms. In the interest of providing flexibility in operation, it was decided to try to provide an acceleration-time curve that would be made up of three sections. As shown in Fig. 2, the accelerations are negative and the sections are (1) rise, (2) constant acceleration, and (3) decay. Mechanisms for providing each of the sections were then considered.

The only method that seemed at all feasible for controlling the rise period ? , that using crushable materials. A number of materials

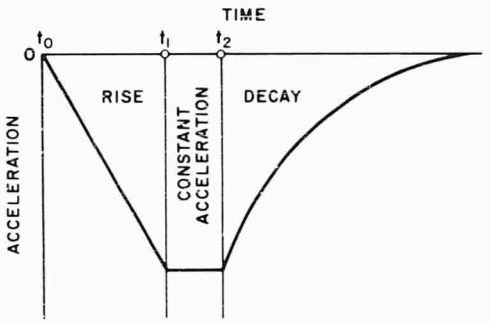

Fig. 2 - Idealized shock signature

could be used, but the requirements of a material that (a) could be readily formed, (b) would have a high crushing strength, and (c) would be inelastic indicated that lead or a lead alloy would probably be most satisfactory.

The simplest form of impact pad is one with circular rings that have a saw-tooth cross section. Previous tests have shown that the pad crushes, as shown in Fig. 3(a), and that the force-displacement curve is almost a straight line, as shown in Fig. 3(b). Since this force-distance characteristic is exactly the same as that of a linear spring, the acceleration-time curve for a mass crushing the pad against a fixed base will be a quarter-sine curve, as shown in Fig. 4. Therefore, the cross section of the pads would have to be made up of curved, rather than straight lines, if the rise period is to consist of a straight line acceleration-time

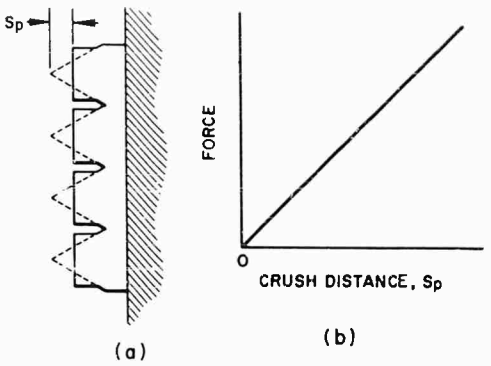

Fig. 3 - Antimonial lead impact pad: (a) crushing configuration; (b) variation of force with crush distance

curve. Although this requires a different profile for each set of test parameters, the problem was not felt to be too serious, and subsequent design calculations were based on the straight-line acceleration-time curve during the rise period.

The constant acceleration can again be provided most readily by inelastic deformation, but the part should have a constant cross section area. The best possibilities appeared to be the crushing of a cellular material, such as Hexcel, the elastic-plastic deformation of tension members, or shearing of metal by use of cutting tools. It soon became evident that it would be extremely difficult to achieve the 5×10^6-lb capacity in the space available with all except the stretching of tension members, or bolts.

The necessity for adding the force from the bolts at the right time to give a smooth transition from the rise to the constant acceleration part of

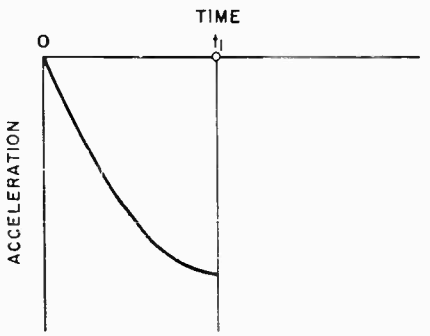

Fig. 4 - Acceleration-time curve for inelastic impact against a fixed pad having a linear force-crush distance curve

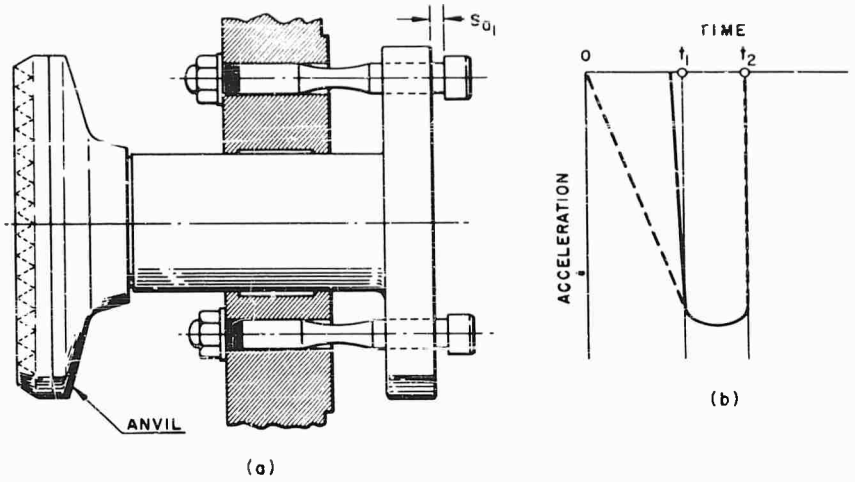

Fig. 5 - Tension member energy absorber: (a) schematic drawing; (b) theoretical contribution to the acceleration-time characteristics of the shock

the curve was apparent. The general scheme is illustrated in Fig. 5(a) where the gap S_{a_1} is the distance the anvil travels during the time interval 0 to t_1, while the pad is being crushed before the bolts begin to stretch. The contribution of the bolts is shown in Fig. 5(b) where the effect of the elastic deformation is exaggerated relative to the plastic deformation. It should be noted that the anvil (actually includes all parts that move with the anvil) and the carriage will be moving at the same velocity at time t_1 when the pad crushing is completed. Thus, the bolt force must be greater than the pad crush force because it must decelerate both the carriage and the anvil.

The decay part of the acceleration-time curve requires a force that decreases as time and distance increase or as velocity decreases. The latter corresponds to the action of a liquid being forced through an orifice. The scheme adopted is illustrated in Fig. 6(a) where h is the initial air space necessary to permit piston travel without appreciable fluid forces during the time interval to 0 to t_2 while the pad is crushing and the bolts are breaking. Some

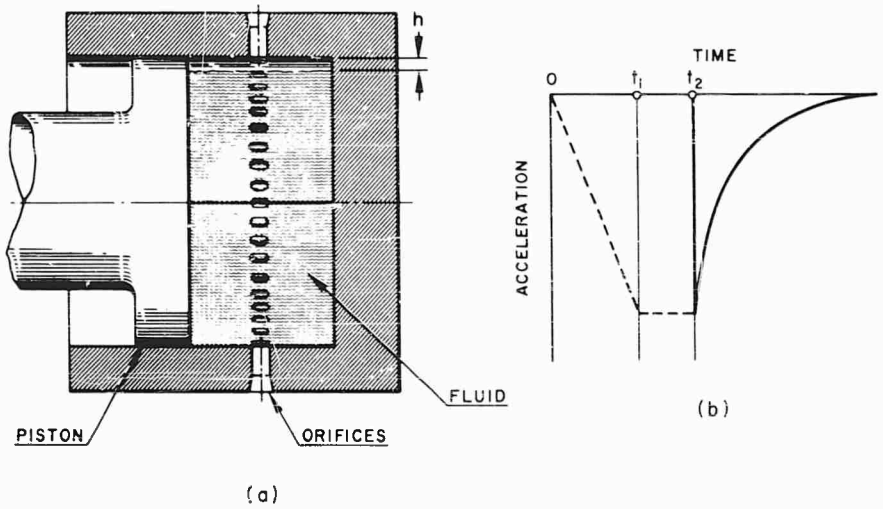

Fig. 6 - Fluid energy absorber: (a) schematic drawing; (b) theoretical contribution to the acceleration-time characteristics of the shock

control of the magnitude of the fluid force as a function of travel could be gained by locating the orifices in such a manner that the orifice area decreases as the piston moves

The remaining major area, as far as general concepts were concerned, was arriving at a method for supporting all of the parts that would maintain alignment under repeated shock loads of several million pounds. Previous experience had shown that it would be difficult, if not impossible, to accomplish this by using a typical mass of concrete sunk into the earth. It was decided to not even try to hold the parts fixed relative to the earth but to attach them to a large mass that can slide on tracks in the direction of the force. Since conservation of momentum would apply, the final velocity will be small if the ratio of the masses is large. The kinetic energy of the total mass moving at the final velocity will be dissipated in friction between the shoes and the rail. The only force, other than dead weight, transmitted to the rails will be that due to friction between the shoes and the rails. This force will be the coefficient of friction times the weight and, thus, a very small fraction of the several million pounds that would otherwise have to be handled.

The concept of using a large difference in mass to effect a favorable exchange of momentum was also applied to the Hyge mounting itself. The Hyge had been mounted on a large concrete mass in the ground in a more or less conventional manner. However, after a relatively few shots it was observed that the axis of the Hyge had shifted in relation to that of the track and that small chunks of concrete were breaking off at a joint. The shock, particularly when stopping the Hyge thrust column, was so severe that it broke a 1-in, diameter steel reinforcing rod.

There appeared to be no way to correct the situation without breaking out the original massive foundation and replacing it except to apply the sliding reaction block scheme as devised for the pulse shaper. The features of a relatively simple installation and potentially trouble-free operation outweighed the disadvantages, and another sliding reaction block (described below) was ordered and installed, as shown in Fig. 7(a), with

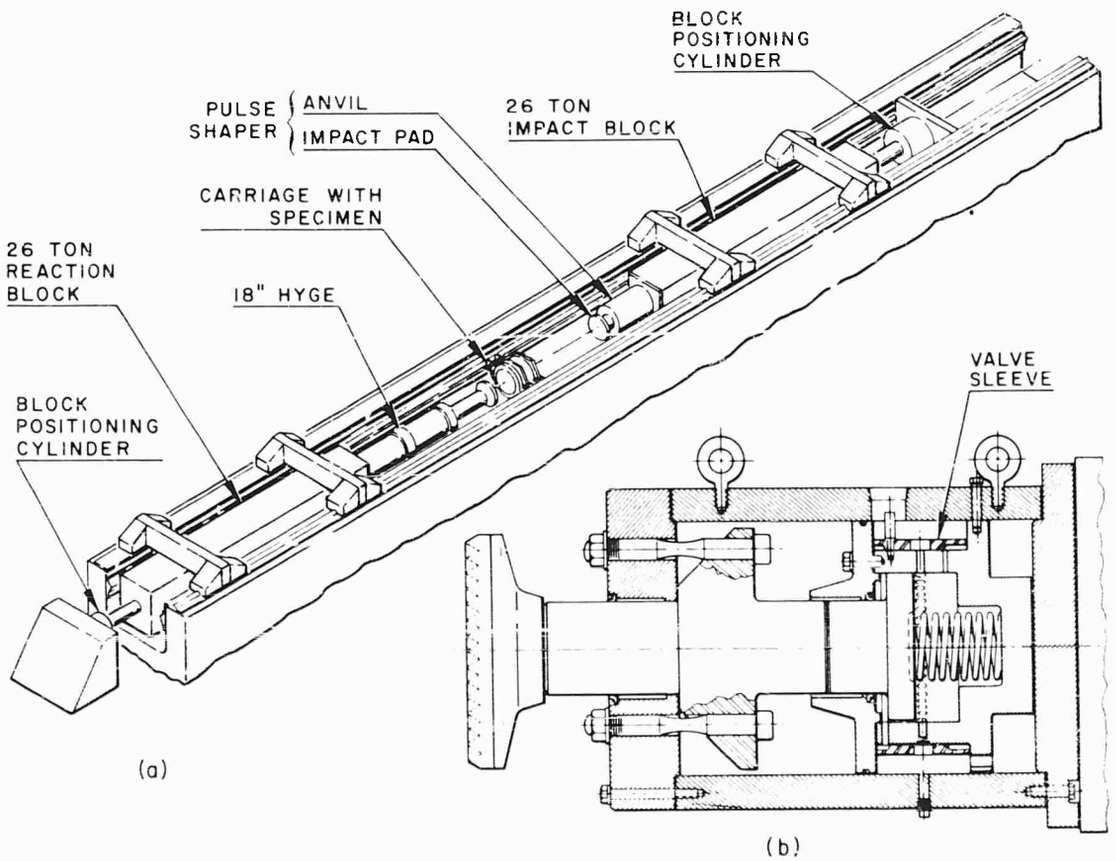

Fig. 7 - Five-million pound shock testing facility: (a) schematic drawing; (b) pulse shaper

the Hyge mounted on one end and an air cylinder pushing against the other end. The cylinder is always energized at a pressure just high enough to overcome the friction between the shoes and the rails and automatically repositions the unit after each shot.

Rated Capacities, Design Limitations

The major limitation on force magnitudes was that imposed by the necessity of fitting the system within the 30-in. width and 18-in. depth of the existing rail system. The system, as designed and constructed, is shown in Fig. 7(a), and a section through the pulse shaper is shown in Fig. 7(b).

The reaction blocks are steel ingots 29 in. wide, 32 in. deep, and 16-1/2 ft long and weigh about 52,000 lb. The total impact reaction mass becomes about 59,000 lb. If friction between the shoes and the rails is ignored during the shock period, from conservation of momentum we can write

$$V_c V_0 = (W_c + W_r)\, V_f \qquad (1)$$

from which

$$V_f = \frac{W_c}{W_c + W_r} \cdot V_0 \qquad (2)$$

where

W_c = weight of the carriage, including specimen,

V_0 = velocity of carriage at instant of impact,

W_r = weight of total reaction mass, and

V_f = final velocity with carriage and reaction mass moving as one unit.

If, for example, the carriage weighs 1000 lb, $V_f = V_0/60$.

The distance the block slides before coming to rest is a function of V_f and the coefficient of friction between the cast-iron shoes and the steel rails. Even though the overhead cranes can be used to reposition the reaction block after each test, or after a series of tests, it was decided that, as for the Hyge reaction block, this could be done more conveniently by an air cylinder that is pressurized at all times. The pressure is again adjusted so that the air cylinder force just exceeds the friction force. Thus, the two forces add in opposing motion during impact and the difference is available for automatic repositioning the unit after each test. Under extreme operating conditions with zero air pressure, the maximum travel should not exceed 4 in., and the air cylinder stroke is 10 in.

The number, diameter, and material selection and treatment of the bolts would have to be specified for each test. As designed, the maximum force of 6×10^6 lb is to be achieved by using 16 bolts with reduced section diameters of 1.432 in. when the dynamic mechanical properties of the bolt material corresponds to SAE 4340 steel, oil-quenched from 1550°F, and tempered for 1 hour at 850°F [1].

The most serious force limitation is that for the fluid. Both space and strength limitations are critical and the most reasonable compromise resulted in a maximum fluid force of 3.5×10^6 lb, which requires a fluid pressure of over 26,000 psi on the 13-in. diameter piston.

The bolt-and-fluid force limitations of 6.0×10^6 and 3.5×10^6 lb, respectively, are serious with respect to the 5.0×10^6-lb capacity of the anvil itself—assuming that a material can be found with properties necessary to provide this force in a diameter of 20 in. For example, if we let

W_c = weight of carriage + specimen + pad (if attached to the carriage),

W_a = weight of anvil + piston + pad (if attached to anvil), and

$$\mu = \frac{W_c}{W_a},$$

the maximum accelerations during the several time intervals are (a) from 0 to t_1

$$A_{max} = \frac{5\times 10^6}{W_c} = \frac{5\times 10^6}{\mu W_a}\ g, \qquad (3)$$

(b) from t_1 to t_2

$$A_{max} = \frac{6\times 10^6}{W_a + W_c} = \frac{6\times 10^6}{W_a(1+\mu)}\ g, \qquad (4)$$

and (c) for $t > t_2$

$$A_{max} = \frac{3.5\times 10^6}{W_a(1+\mu)}\ g. \qquad (5)$$

In all cases, it is apparent that the lightest possible anvil is best. It also appears that a low value of μ is desirable, but such is not the case.

NOTE: Reference appears on page 310.

The crushing of the pad is completed at $t = t_1$, from which time on the carriage and anvil are decelerated as a unit. Since the change in velocity during the time intervals will equal the area under the acceleration-time curve, it is evident that for a curve such as in Fig. 2 the decrease in velocity of the carriage in the time interval from 0 to t_1 should be small relative to the velocity at t_1. From conservation of momentum

$$V_1 = \frac{W_c}{W_a + W_c} V_0 = \frac{\mu}{1 + \mu} V_0 . \qquad (6)$$

Thus,

$$V_0 - V_1 = \frac{1}{1 + \mu} V_0 \qquad (7)$$

and

$$\frac{V_0 - V_1}{V_1} = \frac{1}{\mu} . \qquad (8)$$

From the discussion above and Eq. (8), it can be seen that μ should be as large as possible. Therefore, for a given specimen and carriage, the maximum acceleration and longest decay period will be given when W_a is a minimum.

Since the flange and piston must withstand forces of 6×10^6 and 3.5×10^6 lb, it was obvious that these parts were not going to be particularly light. In discussions with program people, it also became evident that the decay period was going to be more important than the constant acceleration period and that test requirements could generally be met without using the bolts. Under these conditions operation would be greatly simplified because it would not be necessary to disassemble the front end to replace the bolts for each test. When used without the bolts, the flange, and thus several hundred pounds of anvil, would be superfluous. Additional parts were designed and made for this case and the weight of the anvil was reduced from 975 to 600 lb. The system with the lighter anvil, shown in Fig. 8, is called the lightweight model. It is the version with which all tests have been made to date and all subsequent discussion will refer to it.

Carriage

The major requirements for the carriage are that it must (1) support the specimen, (2) transmit the accelerating (push) and decelerating (impact) forces to the specimen with a minimum of ringing, (3) accommodate specimens with a wide range of size, shape, and weight, and (4) have a reasonable service life. The major constraint was that the carriage must fit the existing rail system.

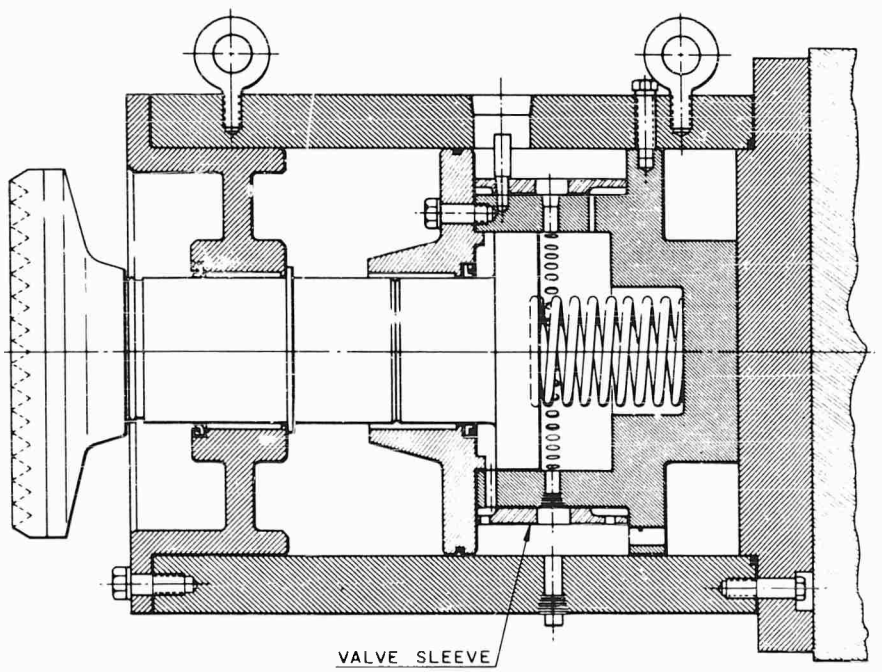

Fig. 8 - Lightweight model pulse shaper

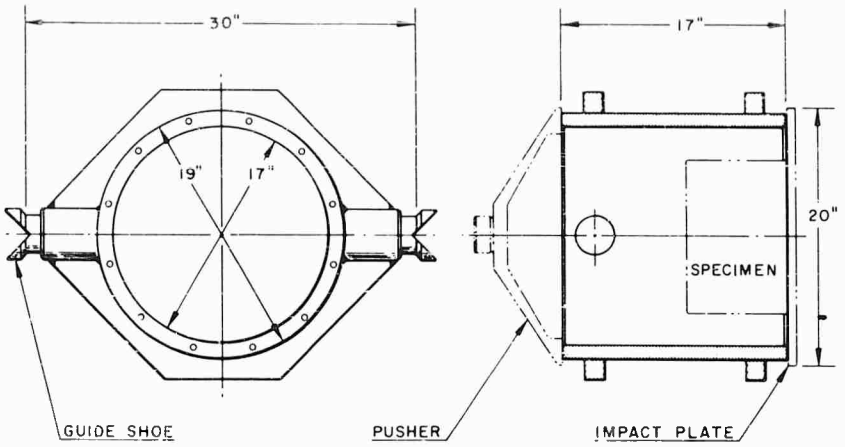

Fig. 9 - 10,000-g carriage

Since the carriage must withstand and transmit to the specimen large forces in both directions, it became obvious that the simplest and most convenient scheme would be to contain the specimen completely within the carriage body. A hollow cylinder was chosen and the complete carriage is shown in Fig. 9.

Since the carriage mass must be decelerated by the pulse shaper, weight was a critical factor and 6061-T6 aluminum was chosen as the material to give reasonable balance between cost and weight. As shown, the specimen can be mounted directly behind the impact plate. Originally it was planned to use an impact plate with sufficient strength to distribute the load during contact with the impact pad in such a manner that the carriage load during deceleration would be due solely to its own mass. During acceleration (push by the Hyge) the force acting on the carriage is due to the mass of the impact plate and specimen as well as the carriage. Considering a weight of carriage plus specimen, and all, of 500 lb as a reasonable value for operation at maximum deceleration, we find that the 5×10^6-lb decelerating force capability would give an acceleration of 10,000 g. The carriage was designed for this level and has a total weight with aluminum guide shoes (not including the impact plate) of 150 lb.

The guide shoes must move to accommodate minor variations in track width. Previous carriages had to be inserted at the end of the track system. This was no longer satisfactory because it would require raising the 59,000-lb reaction block and pulse shaper each time a carriage was to be installed or removed. The new design permits the shoes to be withdrawn so that the carriage can be installed and removed vertically at any point along the track. During a test, the guide shoes on one side of the carriage are located by retaining rings, and the shoes on the other side are forced outward by air pressure. The primary functions of the air pressure are to provide sufficient lateral force to support the weight on the 45° angle of the rails and to keep the guide shoes in contact with the rails as the width changes. Braking action is incidental, in fact undesirable because it dissipates energy, thereby degrading the capability of the system.

DEVELOPMENT

Setup Calculations

Since reliable data were not available in many areas of importance, a number of assumptions and rough estimates were required in making the original design calculations. In many respects, the design could be considered a feasibility study or an order of magnitude design with the exact operating procedures and performance capability being determined by actual use of the system. The major areas of insufficient information were (1) the behavior of crushable materials under test conditions, (2) the magnitude of pressure developed when a fluid is forced through a noncircular orifice at flow rates up to 1500 ft/sec, (3) the effect of elasticity of parts on ringing, and (4) how to set up the Hyge to give the desired velocity and energy to the carriage.

For simplicity, calculations for determining test parameters have been made assuming

that the acceleration during the rise-time interval is a linear function of time. A typical shock signature is shown in Fig. 10 and, as shown, it is completely characterized by only two parameters, the rise time t_1, sec, and maximum acceleration A_1, g, which occurs at time t_1. Relatively early in the design stage, it became apparent that the slight control possible by selectively plugging orifices was not worth the effort involved and a valve sleeve, as shown in Figs. 7(b) and 8, was added. The valve sleeve can be rotated through 44 fixed increments and all 45 orifices are open to the same degree. Thus, only the magnitude at t_1 on the acceleration-time curve during decay interval is actually controlled. Within the above limitations the calculations required for setting up the system were determined to be as follows:

Impact Pad

The impact pad crushes as the carriage is decelerated and the anvil is accelerated to bring the parts to the same speed. As discussed above, the force exerted by a saw-toothed impact pad made from antimonial lead varies almost linearly with crushed distance. Thus, the required crush distance S_p is

$$S_p = 128.8\ (1+\mu)\ A_1\ t_1^2\ ,\ \text{in.}, \qquad (9)$$

where A_1 is in g and t_1 in sec. To avoid "bottoming," and the resulting rapid uncontrolled increase in acceleration level, a pad, such as shown in Fig. 11, must be chosen with $h_c \geq 2S_p$.

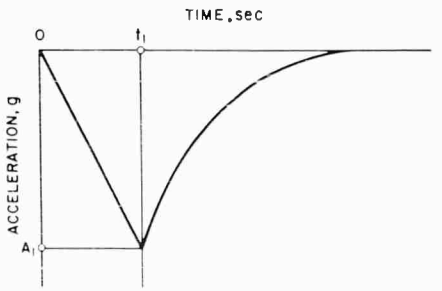

Fig. 10 - Idealized shock signature for calculation of test parameters

The resisting force of the impact pad is a function of the total area in contact at a given time and the dynamic crushing strength of the pad material. For a pad, such as in Fig. 11, the area will be related to the circumference of the triangular rings. Thus

$$C_p = \left(\frac{h_c}{S_p} - 1\right)\frac{W_c\ A_1}{s_b\ h_c}\ ,\ \text{in.}, \qquad (10)$$

where

C_p = total circumference required, and

s_b = crushing strength of pad material.

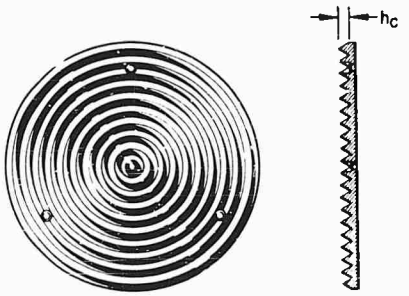

Fig. 11 - Impact pad

As a matter of convenience, full-diameter pads are kept in stock as cast and the rings not required are machined off.

Fluid Forces

The fluid forces were not to become effective until the pad crushing was completed. Thus, air space must be left in the cylinder so that the piston could travel while coming up to velocity V_1 at t_1. This distance is

$$S_{a_1} = 64.4\ \mu A_1\ t_1^2,\ \text{in.}, \qquad (11)$$

and the air space required can be read from a graph.

The fluid force was calculated by using simple orifice theory, which results in the force being proportional to the square of the velocity. For the maximum fluid force to provide the acceleration A_1 at $t = t_1+$, the flow area required is

$$A_o = \frac{3140\ \mu\sqrt{A_1\ t_1}}{\sqrt{(1+\mu)\ W_a}}\ ,\ \text{in.}^2, \qquad (12)$$

and the valve sleeve position giving a total orifice area closest to this can be read from another graph. A problem can arise at this point because

the combination of W_a and μ and the desired acceleration A_i may require a force greater than the 3.5×10^6-lb design capacity of the system. To limit the fluid force to 3.5×10^6 lb requires that

$$A_o \geq 1.672\,\mu A_1 t_1, \text{ in.}^2 \qquad (13)$$

Therefore, the greater value from Eq. (12) or (13) must be used in selecting the valve sleeve position.

Hyge Settings

The combination of fire, set, and cushion pressures required to give the carriage the kinetic energy required for the carriage to have the correct value of velocity V_0 at the instant of impact depends upon the friction losses in the system, the mass of the carriage, the mass of the moving parts of the Hyge (the ram), as well as μ, A_1, and t_1. The velocity at impact should be

$$V_0 = 16.1\,(1+\mu)\,A_1 t_1, \text{ ft/sec.} \qquad (14)$$

The kinetic energy that must be delivered by the fire pressure air will be

$$E_k = \frac{W_c}{2g} V_0^2 + E_f + \frac{W_R}{2g} V_R^2, \qquad (15)$$

where

E_f = energy dissipated in friction as the carriage travels between the Hyge and the pulse shaper, primarily due to friction between the guide shoes and the rails,

W_R = weight of the ram and connected parts of the Hyge, and

V_R = maximum velocity of the ram during the push stroke.

First Tests

The first tests were made using a 2-1/4-in. thick heat-treated steel impact plate on the carriage. It was hoped that the impact plate would be sufficiently rigid and strong so that the correct circumference of impact pad could be obtained by using a band saw to remove the outer unwanted rings. The specimen used in the first tests could not be bolted directly to the back of the impact plate as shown in Fig. 9, and a special Z-ring was used to clamp the specimen against the plate.

Figure 12 shows unfiltered and filtered oscilloscope records, reproduced from tape, for the second test run of the system. Endevco Model 2225 accelerometers were used and the test parameters were calculated to give a rise-time of 0.67 ms and a peak acceleration of 1300 g. The obvious comments about the records in Fig. 12 are that the unfiltered signal contains pronounced high-frequency noise and the 5-kc filtered signal contains a pronounced vibration or ringing at about 2000 cps. The low-frequency vibration was traced to the natural frequency of the impact plate which was being impacted in the center area only. Since the tape recorder attenuates frequencies above 20 kc, the "unfiltered" signal in Fig. 12(a) is not truly representative of the actual signal recorded. Visual examination of directly recorded accelerations indicate that the high frequency is between 25 and 30 kc. At this point, there was no obvious answer for the high frequency except to blame it on impacts resulting from vibrating parts separated by small clearances.

The first thought was to minimize the vibration of the impact plate by distributing the pad rings over the surface in such a manner as to eliminate diaphragming when the impact is concentrated near the center of the plate. Doing this, however, eliminates the only good feature of the heavy impact plate, which was that the diameter of the pad could be simply decreased to give the required circumference of the rings.

In view of this, the logical step appeared to be to use the thinnest possible plate and distribute the pad so that, in effect, the carriage and the specimen would be stopped separately with a minimum of crosstalk when either or both has a residual vibration. The plate must be strong enough to accelerate the specimen and thick enough to permit counterbored holes for socket head cap screws to fasten the plate to the carriage. The lightweight plate is 3/4-in. thick and is made out of 6061-T6 aluminum.

Figure 13 shows the unfiltered and filtered acceleration records for a test using the same specimen and Z-ring as above. The desired peak acceleration was again 1300 g, but the desired rise time had been increased to 1.0 ms. It should be observed that the unfiltered record is cleaner, with some fairly high frequency vibrations in the early part of the pulse and a pronounced burst of high-level, high-frequency signal later on. The 5-kc filtered signal is relatively clean, but an additional peak of acceleration can now be seen to occur about 1.6 ms after the first. The second pulse was both unexpected and unwanted. Although its rise time was slower than

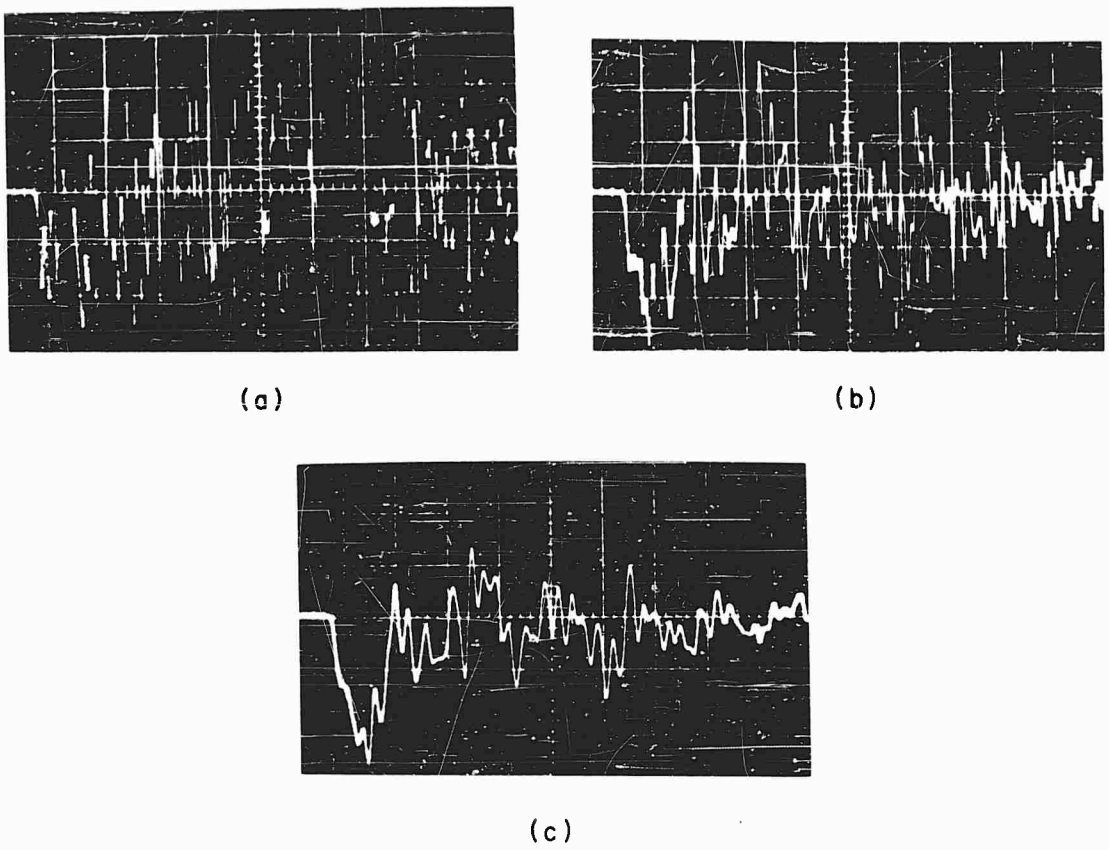

Fig. 12 - Acceleration records from tape playback. Calibration: 500 g/vertical division and 0.5 ms/horizontal division. (a) unfiltered; (b) 10-kc filter; (c) 5-kc filter.

anticipated, the peak level and the velocity change (the area under the acceleration-time curve) were close to the values that would be expected from the fluid forces. Additional evidence to support the belief that the second pulse was the dash-pot effect can be obtained by noting that the burst of high-frequency acceleration occurs at the same time as the second peak. In fact, the latter leads to the conclusion that the high-level, high-frequency signals are largely acoustic, or in other words plumbing noise generated by the high velocity flow through the orifices. The low-level, high-frequency noise noted at the beginning of the pulse is attributed to the use of the Z-ring to hold the specimen in place against the back of the impact plate.

Figure 14 is similar to Fig. 13, except that the shock level was about 5600 g instead of 900 g and the specimen was bolted directly to the impact plate. It should be noted that eliminating the Z-ring has resulted in a cleaner initial pulse and that high-frequency noise is again most severe in the region of the secondary pulse.

The obvious reasons for a delay in the appearance of the fluid force were (1) an incorrect setting of the fluid level in the cylinder, (2) compressibility effects due to entrapped air in the fluid, and (3) compressibility of the fluid itself.

Only few measurements were required to eliminate the possibility of an error in setting the fluid level being responsible for the delay in the fluid action. Entrapped air such as bubbles, and so forth, was also quickly ruled out when a calculation showed that about 25 cubic inches of air would be required, and this seemed unreasonably large. Thus, compressibility of the fluid itself was the remaining factor to be considered.

Although the lack of information about the bulk modulus of the hydraulic oil being used and its variation with pressure, as well as lack of data relative to the actual pressures involved, precluded precise calculations, a rough calculation indicated that under static conditions the displacement due to the compressibility of the

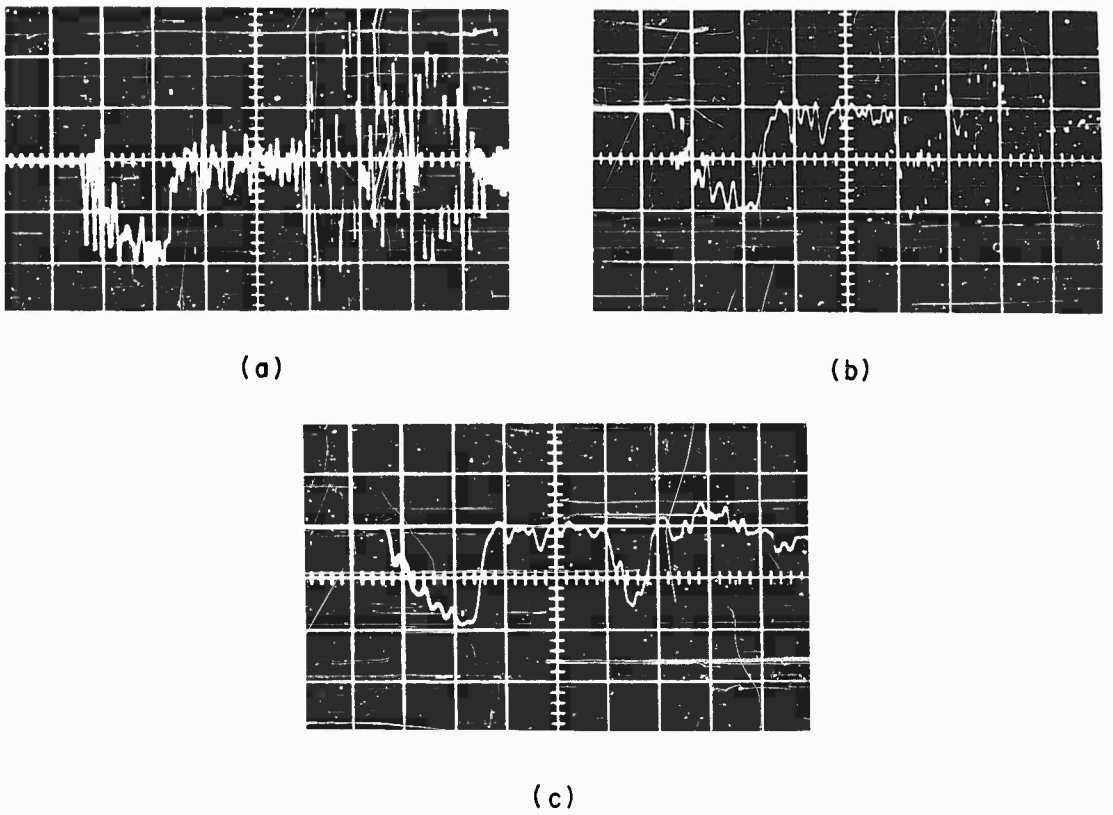

Fig. 13 - Acceleration records from tape playback. Calibration: 500 g/vertical division and 0.5 ms/horizontal division. (a) unfiltered; (b) 10-kc filter; (c) 5-kc filter.

oil under the pressure required to give the recorded acceleration would be in the same order of magnitude as the distance corresponding to the apparent time lag. Consequently, an investigation of methods for minimizing the effect of compressibility was undertaken.

In the meantime the need for the facility was so pressing that, as a matter of expediency, the secondary pulse was reduced to a negligible level by positioning the valve sleeve to give a much greater area for flow. The extra travel resulting from the greater time for stopping at the decreased level of acceleration resulted in the volume of oil displaced by the piston being greater than the space provided for it. This gave rise to some unexpected events, such as blowing out sight glasses, blowing a loosely installed 4-in. pipe plug through the roof, and a continuous need for adding fluid to replace that forced out through the shaft seal. All such problems ceased when a stand pipe was attached to the outer cylinder to accommodate the overflow.

To date, there has been no opportunity for testing the system at its rated capacity of 5×10^6 lb and/or 10,000 g, but it has performed satisfactorily at levels up to 3.3×10^6 lb and 8300 g.

Equipment Modification

For a given force, the travel of the piston resulting from compressibility is a function of the bulk modulus of the fluid and the volume of fluid under compression. A check in handbooks indicated that water and glycerine were the two best choices to replace the hydraulic fluid. The bulk moduli of water and glycerine are about one and one-half and three times, respectively, of that of the oil. Water was selected for use first because it had a lower viscosity and would be simpler to use.

In the original design, the cylinder length had been made much longer than absolutely necessary to provide space for possible overshooting and to avoid placing undesirable restrictions on future uses of the pulse shaper. Calculations had indicated that a piston travel of 0.5 in. would be more than adequate for

foreseeable operating conditions. Since the distance through which the piston would have to move before cutting off the orifices was greater than 1.5 in., no harm could be seen in filling up the space beyond the orifices with solid blocks of steel. This was done and the volume of fluid under compression was reduced to 36.2 percent of the original volume.

Switching to water and reducing the volume should decrease the piston travel resulting from compressibility to less than 25 percent of that for the original system. Since this was now about the distance the piston travels while the anvil comes up to its maximum velocity, it seemed probable that if the cylinder were initially full of water, the fluid force would reach its maximum value about the same time as the impact pad was crushed to its maximum value.

Programmatical needs made it impossible to find time for a thorough experimental investigation at this point, but two runs, under less than ideal conditions, did show that the secondary pulse would disappear when the reduced cylinder volume was full of water at the beginning of the test. Since this mode of operation would be drastically different from that originally planned and since the equipment was not going to be available for extensive experimental investigations, an analytical study was undertaken.

The problem appeared to involve, simultaneously, inelastic impact and the transient flow of a compressible fluid through orifices. The differential equations of the dynamics of such a system are highly nonlinear and numerical methods were required to get answers.

In the process of setting up models for the mathematical solution, study of the acceleration pulses in Figs. 13 and 14 brought to light the previously ignored fact that as far as the specimen was concerned, the crushing of the pad was not a completely inelastic phenomenon. For example, if we assume negligible fluid forces at this time and if the impact had been completely inelastic, the slope of the curve at t_1^+ (immediately after the rise has been completed) would have been infinite. Actually, this was not really

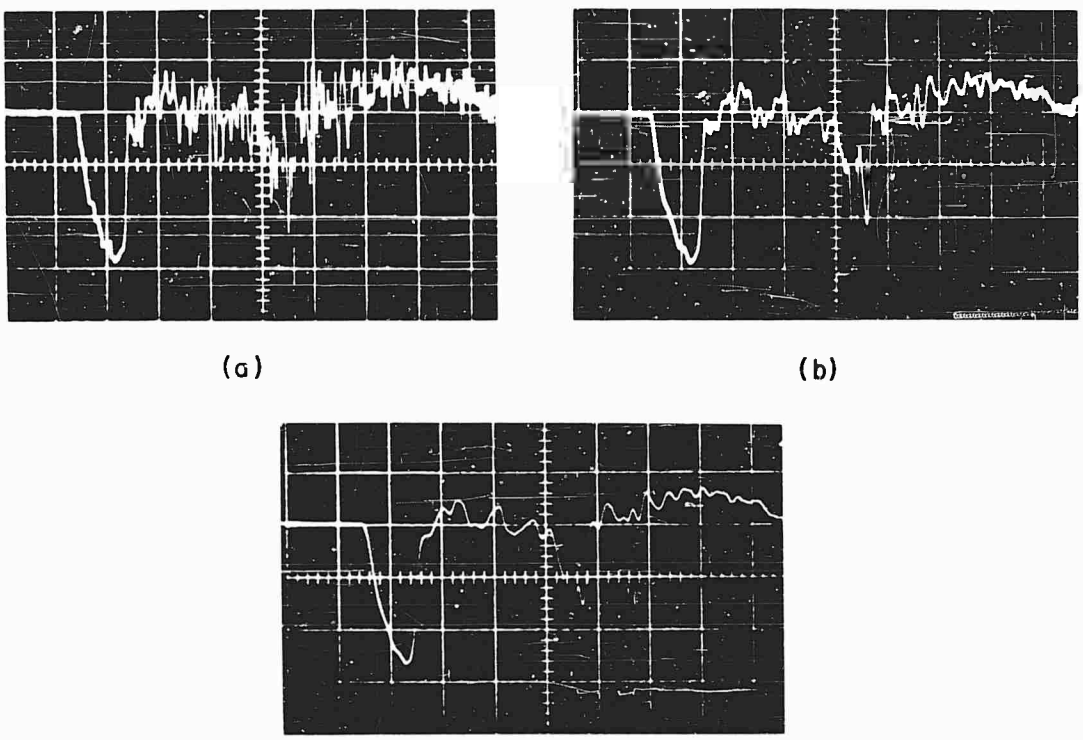

Fig. 14 - Acceleration records from tape playback. Calibration: 2000 g/vertical division and 0.5 ms/horizontal division. (a) unfiltered; (b) 10-kc filter; (c) 5-kc filter.

something new, the carriage, anvil, and the like were known to be elastic and were expected to deform under the loads being applied, but the magnitude of the effect had been underestimated.

Including the elasticity of the impact and the compressibility of the fluid, the pulse period requires one model, Fig. 15(a), for the interval in which the pad is crushing and another model, Fig. 15(b), for the remainder of the pulse. c_i represents the inelastic crushing of the pad, k_i the impact elasticity, k_f the compressibility of the fluid, and c_f the damping force from the fluid flow through the orifices. It should be noted that c_i and c_f are definitely nonlinear and that k_i and k_f can exert forces only when compressed. The impact spring k_i was assumed to be linear

in Fig. 16(b). Similarly, Figs. 17(a) and (b) show the velocities of the carriages and anvils, respectively.

Two observations are particularly worth noting. (1) Although the conditions are quite different, the curve for the delayed fluid force in Fig. 16(a) is quite similar to Figs. 13(c) and 14(c), and (2) although much lower for the case with the cylinder full of fluid, both cases show a secondary peak of acceleration.

The first observation is important because it indicates that the model chosen is at least qualitatively correct. Thus, an understanding of the behavior of the model can be applied to the real system.

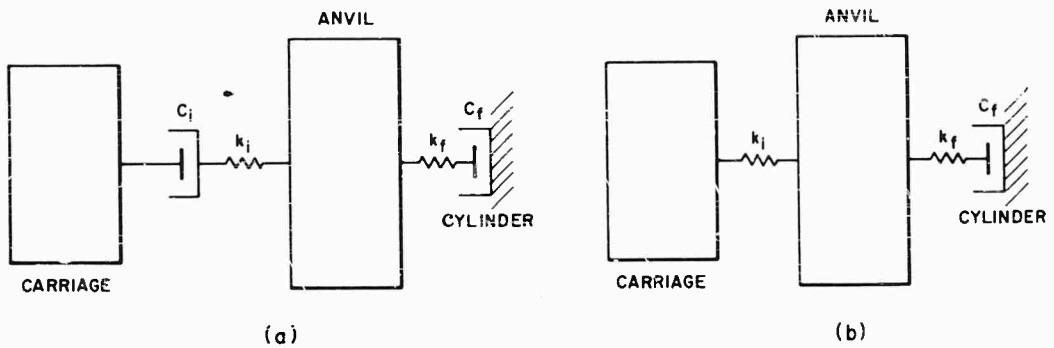

Fig. 15 - Models for numerical solution: (a) during crushing of impact pad; (b) after crushing of impact pad is completed

and calculations, based upon the energy associated with the velocity change given by the fall-off portion of the impact pulse for a typical situation, gave a spring rate of 65×10^6 lb/in.

Using the equations based on the early theory of operation, Eqs. (9) - (15), dimensions, velocities, energies, and valve position were calculated for two hypothetical cases in which a 3000-g peak acceleration was to be reached in 0.80 ms when the mass ratio μ was 0.667. In case 1, the cylinder was full of fluid so that the fluid force would begin to act the instant the piston started moving. In case 2, the level of the fluid in the cylinder was set such that no significant force would be developed until the piston had traveled a distance corresponding to the time at which the fall-off part of the initial pulse would reach zero g.

The calculated accelerations of the carriages for both cases are shown in Fig. 16(a) and the calculated accelerations of both anvils are shown

The second observation points out that fluid compressibility cannot be the sole reason for the presence of the secondary peak. Comparison of Fig. 17(b) with Fig. 17(a) shows that in both cases the anvil velocity becomes greater than that of the carriage. In fact, as shown by the carriage acceleration going to zero in Fig. 16(a), the anvil breaks contact with the carriage and the secondary peak occurs when contact is made again after sufficient time has elapsed for the carriage to catch up with the anvil, which is being decelerated by the fluid force. If the analysis were to be continued further, additional peaks, each lower than the previous one, would be found. This type of separation is associated with impact with a nonzero coefficient of restitution and, therefore, the elasticity of the system is now the major reason for the secondary peaks.

Elasticity was undoubtedly a factor in causing the secondary peaks in earlier tests with the larger volume of oil in the cylinder; but

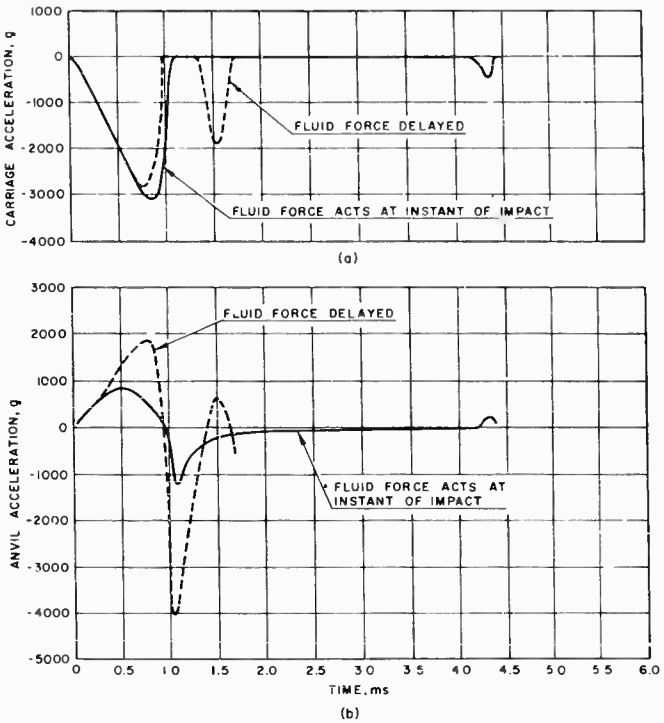

	(a)		(b)	
t ms	SOLID g	DOTTED g	SOLID g	DOTTED g
.05	-140	↑	93	93
.10	-290	|	195	192
.15	-455	|	300	302
.20	-638	|	413	423
.25	-828	|	522	552
.30	-1,038	|	628	691
.35	-1,261	SAME AS SOLID	721	837
.40	-1,478	|	792	987
.45	-1,703	|	832	1,142
.50	1,922	|	869	1,302
.55	-2,140	|	850	1,455
.60	-2,360	↓	798	1,582
.65	-2,540	-2,530	738	1,688
.70	-2,720	-2,680	662	1,787
.75	-2,855	-2,780	533	1,852
.80	-2,950	-2,810	403	1,870
.85	-3,010	-2,475	288	1,654
.89	-3,030		231	—
.90	3,010	-1,529	180	1,020
.95	-2,670	-431	-32	287
.97		0		0
1.00	-1,930	↓	-291	-2,970
1.05	-992	|	833	-4,050
1.10	-2	|	-1,200	-3,070
1.15	0	|	-1,046	-2,060
1.20	↓	|	-783	-1,360
1.25		|	-600	—
1.30		↑	472	-680
1.35		0		-517
1.38		-178		-340
1.40		520	322	-63
1.45		1,300		465
1.50		-1,778	-235	664
1.53		-1,865		660
1.55		-1,852		578
1.60		-1,572		292
1.65		-1,010		118
1.70		315	-142	-546
1.72				
1.90			-95	
2.10			-68	
2.30		|	-49	
2.50		|	-41	
2.80		|	-29	
3.20		|	-21	
3.80	↑	|	-13	
4.15	0	|	-11	
4.20	52	|	18	
4.25	-207	|	122	
4.30	395	|	244	
4.35	-430	|	257	
4.40	-195		136	

Fig. 16 - Results of numerical solution: (a) acceleration time curves for the carriage; (b) acceleration time curves for the anvil

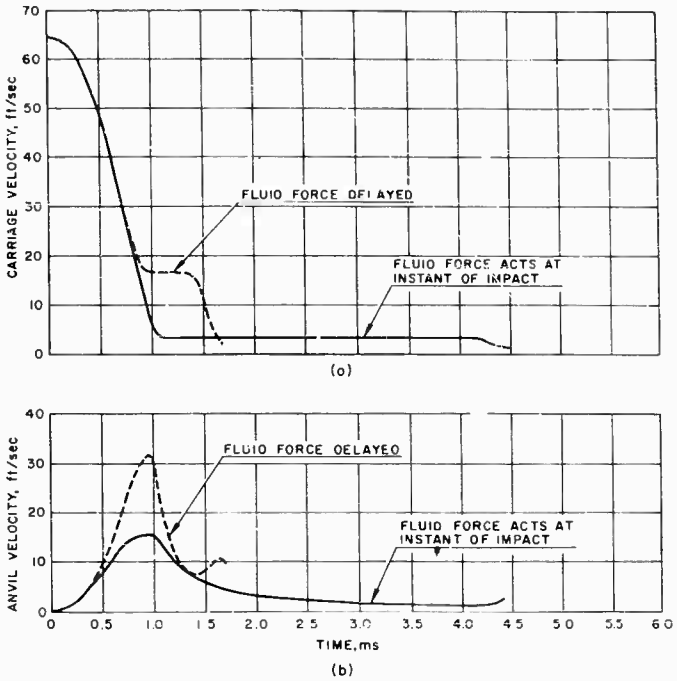

	(a)		(b)	
t ms	SOLID ft/sec	OOTTED ft/sec	SOLID ft/sec	OOTTED ft/sec
0	64.3	64.3	0	0
.05	64.2	↑	.07	↑
.10	64.0	|	.22	|
.15	63.4	|	.62	SAME AS SOLID
.20	62.5	|	1.2	|
.25	61.3	|	2.0	|
.30	59.8	|	3.0	↓
.35	58.0	|	4.0	4.2
.40	55.8	|	5.3	5.7
.45	53.1	|	6.6	7.5
.50	50.5	|	7.9	9.2
.55	46.5	|	9.3	11.9
.60	42.8	↓	10.6	14.3
.65	38.3	38.9	11.9	16.9
.70	33.3	34.7	13.0	19.7
.75	28.8	30.3	14.0	22.7
.80	24.1	25.8	14.7	25.7
.85	19.4	21.5	15.3	28.5
.89	15.5	—	15.5	—
.90	14.5	18.3	15.6	30.7
.95	10.0	16.6	15.7	31.7
.97	—	16.5	—	31.8
1.00	6.3	↑	15.4	30.4
1.05	4.0	|	14.5	24.7
1.10	3.15	|	12.9	19.0
1.15	↑	|	11.1	14.87
1.20	|	|	9.6	12.1
1.25	|	↓	8.5	—
1.30	|	16.5	7.6	8.8
1.35	|	16.4	—	7.9
1.38	|	16.2	—	7.4
1.40	|	14.7	6.4	7.3
1.45	|	11.2	—	7.6
1.50	|	9.5	5.5	8.5
1.53	|	8.3	—	9.1
1.55	|	3.6	—	9.5
1.60	|	3.5	—	10.2
1.65	|	2.5	—	10.4
1.70	|		4.3	9.9
1.72	|		—	—
1.90	|		3.5	—
2.10	|		3.0	—
2.30	|		2.6	—
2.50	|		2.3	—
2.80	|		2.0	—
3.20	|		1.6	—
3.80	↓		1.3	—
4.15	3.15		1.2	—
4.20	3.1		1.2	—
4.25	2.9		1.3	—
4.30	2.5		1.6	—
4.35	1.7		2.0	—
4.40	1.2		2.3	—

Fig. 17 - Results of numerical solution: (a) velocity time curves for the carriage; (b) velocity time curves for the anvil

compressibility was also significant because filling the cylinder with oil only slightly reduced the relative level of the secondary peak, while it materially decreased the interval of time between peaks.

The beneficial effects of filling the cylinder are twofold.

1. The fluid force increases with the square of the anvil velocity. This results in an increased rate of crushing of the pad and increases the level of the force available for decelerating the carriage, thereby increasing the peak acceleration. As shown in Fig. 16(a), the acceleration becomes slightly higher instead of lower than the desired value.

2. The fluid force acts to dissipate additional kinetic energy while the pad is crushing. This gives a carriage velocity at separation of less than one-fifth of that when there is no fluid force acting as the pad crushes, and results in negligible levels of acceleration at the secondary and subsequent impacts.

Several experiments were run to provide a check on the quantitative value of the numerical solution and to determine better values for coefficients in the equations for calculating parameters for setting up the pulse shaper and Hyge. Unfortunately, time was still a critical factor and when the Hyge came available, it was not possible to duplicate the exact conditions of $\mu = 0.667$, $A_1 = 3000$ g and $t_1 = 0.80$ ms used in the numerical solution. The values used were $\mu = 0.484$, $A_1 = 3140$ g, and $t_1 = 0.85$ ms; the oscilloscope traces are shown in Fig. 18. It should be noted that it is no longer necessary to filter below 10 kc.

As can be seen, the peak acceleration is about 3200 g, the rise time is about 0.63 ms, and it is impossible to locate a secondary peak in the residual vibration. Thus, the agreement between observed and desired results is reasonably good. In fact, so good that, in view of the possible variations in pad properties and Hyge operation, one is tempted to say that it is due to chance or coincidence. Five more tests were run that same day with the same specifications of μ, A_1, and t_1, but with different combinations of valve-sleeve position and fluid level. There was also a considerable variation in the hardness of the antimonial lead impact pads. The accelerations observed varied between 3000 and 3500 g and the rise times ranged between 0.53 and 0.63 ms. The main effect of increasing or decreasing the valve-sleeve position by the amount to change the flow area by 25 percent was to introduce a small, but perceptible, secondary peak.

Probably the most surprising observation was that the results were almost identical when using a pad with a hardness of about 16 as when using a pad so soft it gave no reading when measured by use of a Barcol GYZJ 934-1 Impressor. Whether this is due to the presence of fluid forces from the instant of impact or to some other factor is not known at this time.

Therefore, if frequencies appreciably higher than 10,000 cps (the plumbing noise) can be neglected, it can be concluded that the system will operate most satisfactorily if the cylinder is full and that the test parameters can be obtained with reasonable accuracy by use of the equations derived on the basis of the original assumptions, even though the actual mechanism of operation is quite different than was envisioned.

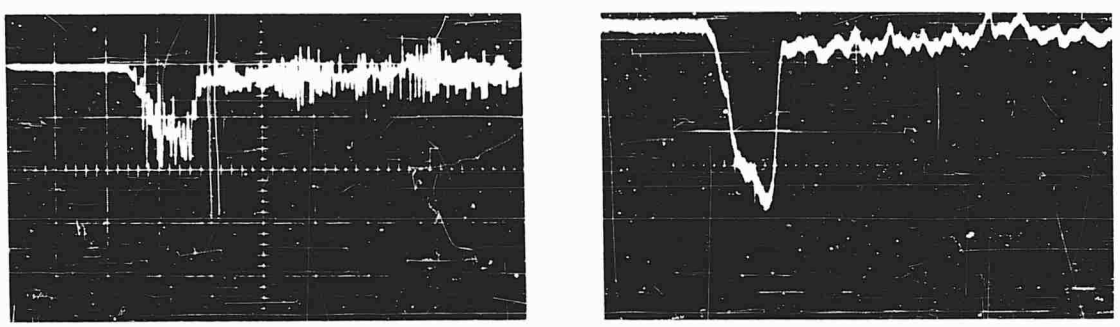

(a) (b)

Fig. 18 - Acceleration records from tape playback: (a) unfiltered. Calibration: 2500 g/vertical division and 0.5 ms/horizontal division; (b) 10-kc filter. Calibration: 1000 g/vertical division and 0.5 ms/horizontal division.

FUTURE DEVELOPMENTS

The major limitation of the present design of pulse shaper is that the mass of the anvil is so great that most of the change of velocity of the carriage takes place while the anvil is being accelerated to a velocity equal to that of the carriage. As discussed above, this results in a decay period that is shorter than the rise time, which is just opposite to the type of pulse desired in some programs.

The main reason for the large mass is that the system was originally designed to support tension members (bolts) that can absorb energy and provide essentially constant accelerations as they stretch plastically. Since it now appears that most tests can be performed better without the bolts, the extra volume and extra strength required can be eliminated. At the same time, it appears that a rating of 4×10^6 lb will be adequate for most foreseeable tests. Thus a considerably smaller and lighter pulse shaper is possible. In fact, two quite different models are currently being designed.

The first model is quite similar in principle to the existing lightweight version, i.e., no bolts, but it will have a rated capacity of 4×10^6 lb for decelerating the carriage and 7.1×10^6 lb for decelerating the carriage and the anvil. Although the new anvil will weigh only two-thirds as much as the original one, it will be considerably shorter and stiffer. The decreased weight will increase values of μ by 50 percent and the greater values of μ in combination with the increased fluid force capacity should provide a better shaped pulse (longer decay periods) with heavier specimens at higher accelerations.

The second model being designed is called the zero mass pulse shaper because it has no anvil and uses no impact pad. As shown schematically in Fig. 19(a), the carriage becomes a piston and the cylinder is extended to become the track. The carriage will move only a few inches beyond the maximum travel of the Hyge pusher foot before the leading edge of the carriage passes the air exit port and traps some air and the liquid in the orifice region of the cylinder. The compressibility of the trapped air and liquid will prevent an instantaneous build-up of fluid force on the carriage, but the rise will be extremely rapid. As a matter of interest, the compressibility of the liquid limited the rate at which the fluid force built up in the numerical solution above to 149×10^9 lb/sec for the case where the fluid began to act at the instant the pad crushing was completed.

Since only the fluid acts to remove energy, the decay period will be much, much greater than the rise time and the resulting pulse will look something like that in Fig. 19(b). The force capacity of this unit is to be 5×10^6 lb.

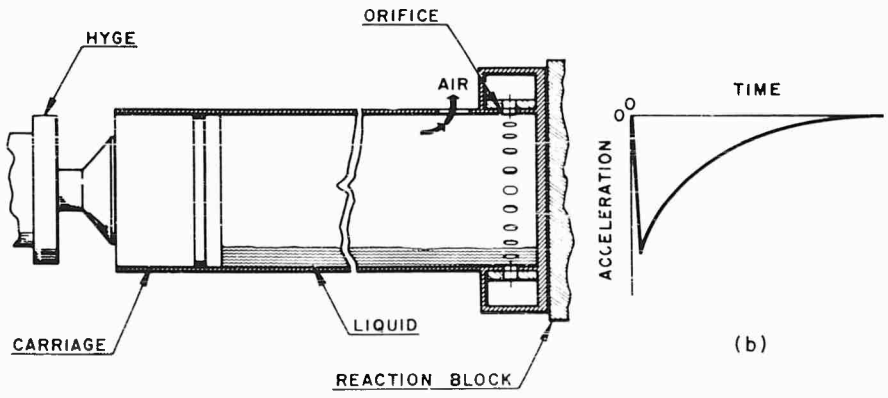

Fig. 19 - Zero-mass pulse shaper: (a) Schematic drawing; (b) idealized acceleration-time curve for shock

ACKNOWLEDGMENTS

Although it is impossible to acknowledge everyone who contributed ideas during the design and development phases of the project, the author would like to acknowledge major contributions from Messrs. L. A. Eastment, P. I. Evans, W. S. Inouye, B. I. Iverson, H. O. Sundberg, K. W. Volkman, R. L. Waldron, and to express his gratitude to all of the staff at the Lawrence Radiation Laboratory, Livermore, California.

REFERENCE

1. R. C. Smith, T. E. Pardue, and I. Vigness, "The Mechanical Properties of Certain Steels as Indicated by Axial Dynamic Load Tests," Proc. SESA, Vol XIII, No. 2 (1956) pp. 183-197.

* * *

SHOCK TESTING WITH EXPLOSIVE GASES

W. M. Sigmon, Jr.
Sandia Corporation
Albuquerque, New Mexico

The mechanical shock pulse resulting from a blast pressure loading often consists of a fractional millisecond rise to an acceleration peak of several hundred to several thousand g followed by an exponential decay of several milliseconds duration. These pulses are difficult to simulate by conventional mechanical shock test procedures. Therefore, a number of experiments have been performed to investigate gas detonation and to develop practical shock test methods using explosive gases.

Preliminary investigations revealed three characteristics of gas detonations to be of particular interest with regard to shock testing. First, the detonation pressure is a known function of initial mixture pressure, providing a convenient and repeatable means of control of peak pressures and accelerations. Second, the detonation generates a high velocity shock wave, and impingement of this wave on a test item results in a pressure (and acceleration) pulse of very short rise time. Third, the pressure pulse decay rate can be controlled by the volume of the detonation chamber and features such as wave traps and frangible diaphragms.

Hydrogen and oxygen mixtures have been used exclusively. The mixtures are controlled by flowmeters, and detonations are initiated by an electric spark or match. The hydrogen-oxygen detonation produces a static pressure approximately 20 times the initial mixture pressure, with a detonation wave velocity of about 10,000 feet per second.

Tests have been performed with four different facilities: (1) a 7-inch-diameter tube, which may be used as a projectile launching gun, a detonation drive shock tube, or a closed explosion test chamber; (2) a 14-inch-diameter vertical projectile launcher; (3) a 16-inch-diameter tube designed to operate without recoil; and (4) the Sandia Corporation 26-inch air gun facility modified for explosive gas use.

Test results have been generally encouraging and have tended to confirm predictions. Shock pressure pulses of the desired shape have been obtained with amplitudes ranging from 300 to 8000 psi. A continuing program is underway to improve present procedures and to develop new methods of shock testing with explosive gases.

INTRODUCTION

Interest in the use of explosive gases as a means of producing mechanical shock pulses has arisen from recent test requests for simulation of blast load conditions. The mechanical shock pulse resulting from a blast pressure loading usually consists of a fractional millisecond rise to an acceleration peak of several hundred to several thousand g followed by an exponential decay of several milliseconds duration. These pulses are difficult to achieve by conventional shock test procedures, particularly in cases where a uniform external pressure on the test item must be maintained during the acceleration pulse.

Preliminary investigations revealed that detonations of explosive gas mixtures exhibited certain characteristics which might fulfill the desired acceleration and loading conditions. Therefore, a number of experiments have been

performed to investigate gas detonations and to develop practical shock test methods using explosive gases. The experimental work, moreover, has not been limited to reproduction of blast load conditions, but rather has been conducted with the object of developing procedures and equipment applicable to other types of mechanical shock testing as well.

GAS DETONATION THEORY

The theory of gas detonation has received a great deal of attention in the literature of recent years [1-6]. Therefore, no detailed account of theory will be included here; instead, the discussion will be limited to a general description of the characteristics of gas detonations, with emphasis given to those characteristics which will be shown later to be of particular importance in mechanical shock testing applications.

Ignition of an unconfined combustible gas mixture produces a flame front which propagates through the mixture at a relatively low velocity. Flame propagation velocities rarely exceed 40 feet per second and may be as low as 1 or 2 feet per second. If, however, the gas mixture is confined in a long tube, and if the composition falls within certain limits, the flame front will quickly accelerate to a very high velocity, and the accompanying release of energy will become extremely rapid and explosive in nature. This phenomenon is known as detonation, and the high velocity reaction front has been given the name "detonation wave." For the more common explosive gas mixtures, the detonation wave velocity is of the order of 10,000 feet per second.

The detonation wave is generally considered to consist of two parts: (1) a high intensity shock front, very closely followed by (2) a combustion zone. The shock front heats the unburned gas mixture to a temperature above the spontaneous ignition temperature, and the resulting combustion supplies energy which maintains the shock front. A detonation, once established, is a stable, self-sustaining condition, and the detonation wave propagates at a velocity which remains constant regardless of the length of the tube.

The detonation wave velocity is determined by the nature of the gases present and the percentage composition of the mixture, and is virtually independent of such factors as initial temperature and pressure, method of ignition, conditions to the rear of the wave, and tube dimensions (except for very small tubes). The velocity at which a detonation propagates may therefore be considered a physical constant of a particular gas mixture. Once the composition of an explosive gas mixture is known the detonation velocity may be determined within fairly close limits, regardless of the values of any other variables.

A detonation is also characterized by a large, practically instantaneous pressure change across the wave front, with the pressure in the burned gases immediately behind the front being some 15 to 20 times higher than the unburned gas pressure. For most practical purposes the ratio of detonation pressure to initial pressure may also be considered a physical constant of a particular gas mixture, determined by the types and relative amounts of gases present, and independent of initial temperature and pressure, method of ignition, conditions to the rear of the wave, and tube dimensions. Therefore, just as in the case of the detonation velocity, the detonation pressure ratio may be determined within fairly close limits once the composition of an explosive gas mixture is known.

The most widely accepted theory of gas detonation was developed independently by D. L. Chapman in 1899 and E. Jouguet in 1905, and hence is known as the Chapman-Jouguet (C-J) theory of detonation. A brief derivation of the theory is given in appendix A. Equations are developed which permit calculation of the detonation velocity, pressure, temperature, and density, given the initial gas conditions and the composition and specific heats at constant pressure and volume of the detonation products.

At first glance, C-J equations appear rather simple, but their actual use is often tedious. The main difficulty is in the fact that real gas specific heats are not constants, but are functions of temperature. Therefore, the usual approach is a trial and error solution in which a temperature of the detonation products is assumed, and the specific heats for that temperature are found from gas tables or other data. The C-J equations are then solved for detonation temperature using these values of specific heat. In general, the calculated temperature will not agree with the assumed temperature, and the procedure must be repeated with other assumed temperatures until agreement is obtained. With the values of temperature and specific heats thus determined, the other detonation conditions may be calculated.

NOTE: References appear on page 327.

A number of researchers have compared computed values of detonation velocity, pressure, and temperature with values observed experimentally for most gas mixtures of interest. The agreement has been excellent in nearly every case. The small discrepancies which have occurred can be at least partially explained as the results of inadequate knowledge of gas specific heats at elevated temperatures or of limitations in test instrumentation. The close agreement between theoretical and experimental results is considered by many as adequate proof of the validity of the C-J equations.

Assuming that a detonation wave consists of a shock wave closely followed by a reaction zone, it is possible to make several deductions concerning the pressure distribution in the wave. It is well known from shock wave theory that a pure shock wave (one not accompanied by a detonation or combustion), traveling at the same velocity as a detonation wave in the same gas mixture, would produce considerably greater increases in pressure and density than those predicted by the C-J equations for the detonation wave. This led to the conclusion that a narrow region of high pressure and density must exist at the front of the detonation wave. This region is usually referred to as the "von Neumann spike." Expansion of the gases in the combustion zone immediately following the spike then produces the lower pressure and density values given by the C-J equations [4].

Until very recently, the existence of the von Neumann spike was difficult to confirm experimentally because of frequency response limitations of available pressure transducers. In 1959, however, Edwards, Williams, and Breeze [7] published the results of an extensive series of detonation pressure measurements made with a transducer capable of microsecond response. Their results clearly show the von Neumann spike. A typical pressure record is reproduced in Fig. 1, along with the calculated C-J pressure for comparison purposes. While the observed peak pressure is about 50 percent higher than the average or C-J pressure, the spike duration is only about 5 microseconds. Because of its relatively short duration the pressure spike normally contributes less than 1 percent to the total impulse from the detonation; therefore, its effect upon most test results will be negligible [6].

The detonation pressure has been defined as the pressure change across the wave front. This would be the pressure measured by a transducer mounted with its sensitive axis normal to the direction of propagation of the wave, such as in the sidewall of the tube, and is also known as the static pressure or overpressure. Another pressure of considerable interest is that produced by the reflection of a detonation wave from a rigid, normal surface. This, for example, would be the pressure recorded by a transducer facing directly into an oncoming detonation wave, and is known as the reflected pressure or total pressure.

As might be expected, the reflected pressure is higher than the static pressure. In order to satisfy the boundary condition of zero particle velocity at the reflection surface the burned gases flowing behind the detonation front must undergo a change in momentum which produces a pressure on the surface in addition

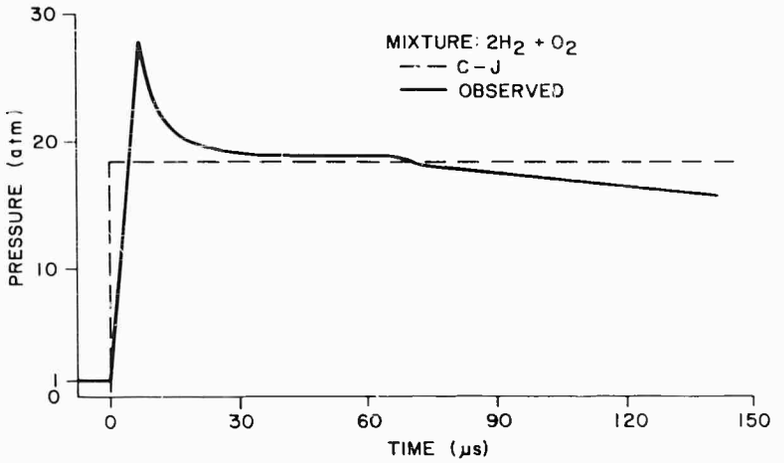

Fig. 1 - Static detonation pressure (from Edwards, Williams, and Breeze)

to the static pressure. For most detonations the reflected pressure will be about 2.5 times greater than the static pressure, or over 40 times higher than the initial pressure [8]. The reflection pressures may be computed from theory, but the process is considerably more complicated than the static pressure computations and will not be discussed here. The work of Edwards, et al [7], includes a comparison of computed reflection pressures to experimental results, and the agreement is reasonably good.

A von Neumann spike is expected in the initial portion of the reflected pressure-time history just as in the static pressure-time history. Reliable experimental data indicate, however, that there is not one but two sharp, high amplitude spikes in the reflected pressure. The second spike is approximately the same amplitude and duration as the von Neumann spike, and occurs about 10 to 20 microseconds later [7]. This is illustrated in Fig. 2. One explanation given for the two spikes is that the second spike may be the von Neumann spike re-reflected from the combustion zone. As in the case of the static pressure, the high amplitude spikes may usually be ignored because the durations are so short that the contribution to the total impulse is negligible.

The gases immediately behind a detonation front are flowing with a relatively high velocity in the direction of the detonation front, or away from the ignition end of the tube. This flow cannot continue, for to do so would eventually produce a void at the ignition end. There is therefore a rarefaction wave behind the detonation wave, and the pressure distribution shows a smooth, exponential decay from just behind the detonation wave back to the ignition point. It is known as a "centered" rarefaction wave because the pressures at the ends (ignition point and detonation wave) remain the same, regardless of how far the detonation wave has traveled. The slope of the pressure decay curve must then become more gradual as the detonation wave travels farther down the tube. This immediately suggests that the duration of the pressure at a given point may be extended by increasing the length of the detonation tube.

A typical detonation tube pressure profile, from Doering and Burkhardt [9], is shown in Fig. 3. This is a plot of pressure versus distance along the detonation tube, but since detonation wave velocity is a constant, a change of scale in the abscissa would convert the same curve to one of pressure versus time at a given observation point. The rate of pressure decay with distance or time is apparently a function of a number of variables and is difficult to calculate. Very little has appeared in the literature on this aspect of detonation. The curve of Fig. 3, based upon an assumption of idealized, lossless conditions, states that pressure decays to 35 percent of its peak value at a point midway between the ignition point and the detonation front. While this appears to be a reasonable value, it should at best be considered only as an estimate until experimental evidence is available.

One additional characteristic of interest concerns the transition of a flame front into a

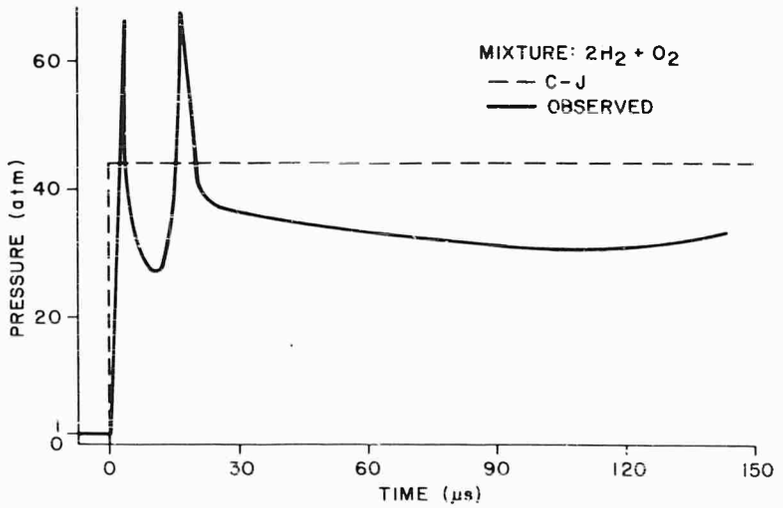

Fig. 2 - Reflected detonation pressure (from Edwards, Williams, and Breeze)

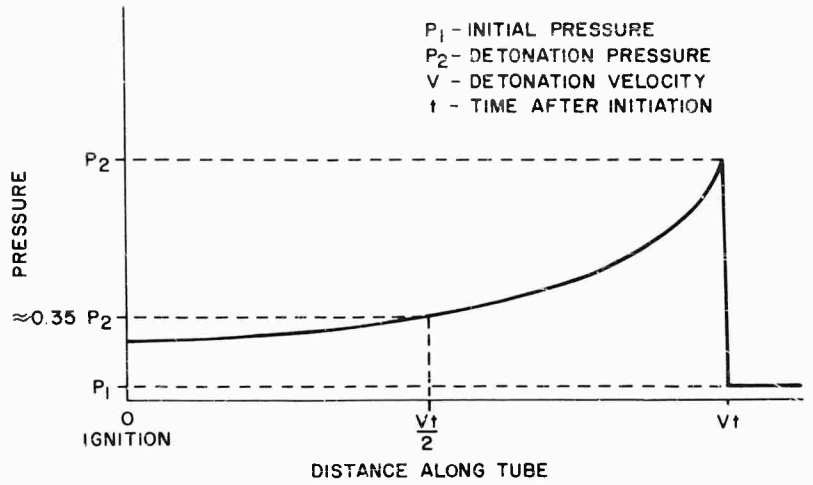

Fig. 3 - Idealized detonation tube static pressure-distance profile

detonation front. Generally it is assumed that the flame front, confined in a tube, behaves somewhat like an accelerating piston, causing a weak shock wave to travel ahead of it in the gas. The shock compresses and heats the gas, and as the flame progresses through the heated gases its velocity increases. This further strengthens the shock and finally the point is reached where the temperature is high enough to cause spontaneous ignition and the establishment of stable detonation conditions.

The distance over which the flame burns until detonation occurs is known as the "run-up" distance. Run-up distance is influenced by many factors, including tube dimensions, tube wall roughness, ignition method, initial temperature and pressure, and gas mixture composition. Initial pressure and mixture composition appear to be the most important factors. Because of the many variables involved, any calculation of run-up distance is virtually impossible. Its value, if required, must be determined experimentally for each detonation test setup. Fortunately in most cases the run-up distance will be negligible. Only in tests at low pressures or with borderline combustible mixtures will run-up become a primary design consideration.

Run-up distance may be eliminated entirely by use of shock initiation. As the name suggests, shock initiation is the initiation of a detonation by means of a strong shock wave introduced from an external source, such as an explosive detonator or a shock tube. Since the shock wave has already been supplied to the gas mixture it does not have to form from a flame front, and run-up is eliminated. Shock initiation is therefore sometimes desirable for this reason. Shock initiation, however, may also produce an overdriven detonation, i.e., a detonation in which the velocity and/or pressure are higher than predicted by the C-J theory, and this might sometimes be undesirable.

SHOCK TESTING APPLICATIONS OF GAS DETONATION

As mentioned in the Introduction our primary reason for investigation of gas detonations is the development of a simple, reliable method of laboratory reproduction of blast load conditions. Figure 4 is a typical idealized acceleration-time pulse produced by a blast loading. Actual values of amplitude and duration will vary with different loading situations, but the general pulse shape will remain the same.

It was proposed that gas detonations be used to produce the desired acceleration pulses. The test setup would consist of a detonation tube in which the test item would be mounted in a manner leaving it free to accelerate down the tube. The tube would be filled with an explosive gas mixture, and the mixture would be ignited so as to produce a detonation wave traveling toward the test item. The high velocity detonation wave would subject the test item to a pressure, and therefore an acceleration, of short rise time. The pressure (and acceleration) peak would then be followed by a relatively long exponential decay determined by the type of expansion or flow permitted in the tube.

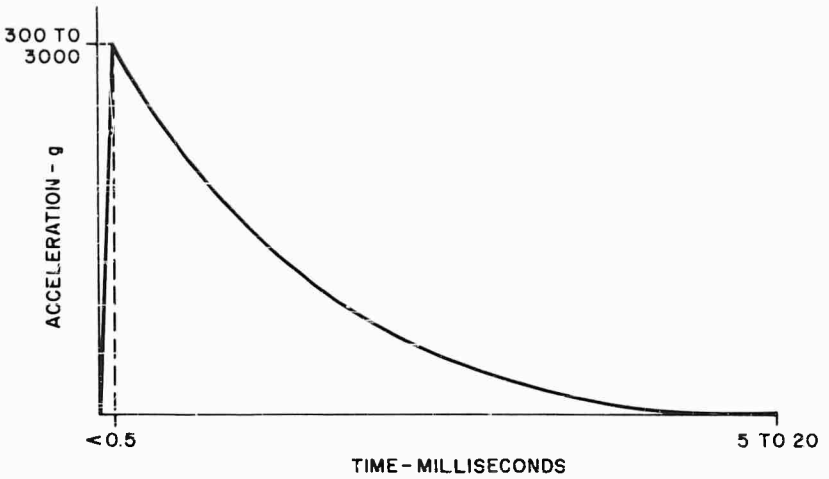

Fig. 4 - Idealized blast loading acceleration-time pulse

Three types of test setups have been considered. The first type is a gun in which the test item is mounted in a piston or projectile sliding in a tube with one end closed (breech) and the other end open (muzzle). The breech volume is filled with the explosive gas mixture. The pressure pulse resulting from detonation accelerates the test item and piston down the tube and out of the muzzle end. Pressure decay as a function of piston displacement may be determined from the well-known gas equations relating pressure and volume. Adiabatic expansion appears to be a reasonable assumption for the short time periods involved. The pulse duration thus depends upon the physical movement of a piston; therefore this type of test setup performs best for longer pulse durations, i.e., 10 milliseconds or more.

The second type of setup considered is similar to a shock tube in form. A detonation tube like that for the gun setup is used, but the test item, instead of being mounted in a piston, is loosely suspended in the tube and breaks free when loaded by the detonation wave. There is space between the test item and tube walls to permit gas flow past the test item after passage of the detonation wave. With this type of setup the pulse duration and rate of decay is a function of tube length as described earlier in the discussion of detonation theory. Therefore, this setup is best suited for short pulse durations, impulse loadings, and tests where the restricting or reinforcing effects of a mounting piston are undesirable.

Finally, a type of setup was considered in which the test item is rigidly mounted on the tube wall or end and is not free to move at all. This is useful in tests where only the shock pressure effects are to be studied and accelerations are either unnecessary or undesired. This setup eliminates the need for a means of test item recovery after a test, and permits better protection of transducers and instrumentation cables. In fact, this type of setup appears ideal for studies of transducer response to shock pressures.

It is evident that for any type of setup the most important characteristics of gas detonations with regard to shock test applications are detonation pressure and detonation wave velocity. The force or acceleration experienced by the test item is directly proportional to the imposed detonation pressure. As discussed previously, the ratio of detonation pressure to initial mixture pressure is essentially a constant for a given gas mixture. This is most fortunate, for it provides a simple, convenient, and repeatable means of varying test pressures to meet specified load or acceleration conditions. Once the required pressure is known and a suitable explosive gas mixture has been chosen, the initial pressure is given by the pressure ratio constant for the gas mixture.

Detonation wave velocity determines the test item pulse rise time. Since the rise time will be the time required for the pressure change to envelop the affected area of the test item, it will be determined by test item dimensions and detonation wave velocity. The size and shape of the test item may possibly alter the detonation velocity slightly, but a close approximation of rise time may be computed by measuring the length of the test item along the direction of detonation propagation and dividing

by the velocity. For example, a flat plate facing directly into the detonation wave will experience a pressure pulse rise time of about a microsecond; for a test item several feet long the rise time will be of the order of hundreds of microseconds.

EXPERIMENTAL PROCEDURES AND EQUIPMENT

In order to study the behavior of gas detonations experimentally, and to develop practical shock test methods and facilities using gas detonations, a number of tests have been performed. The procedures common to all tests will be discussed first, followed by descriptions of each test setup.

It was decided early in the test series to use only hydrogen-oxygen mixtures for the initial experiments. Hydrogen-oxygen detonations produce the highest pressures of any explosive gas except acetylene-oxygen. Acetylene, however, becomes unstable at pressures much higher than 15 psig and also produces free carbon as a detonation product. Hydrogen-oxygen mixtures remain stable over initial pressure ranges of several thousand psi, and produce only pure water as a detonation product. In addition, hydrogen and oxygen are nontoxic, readily available, relatively low in cost, and require no special handling procedures other than those required for any flammable gas.

The detonation characteristics of several hydrogen-oxygen mixtures are given in Table 1. The important fact to note from Table 1 is that wide variations in mixture composition have little effect upon detonation pressures. Mixtures containing 50- to 80-percent hydrogen produce static detonation pressures about 18 times the initial pressure and reflected pressures about 43 times the initial pressures. Therefore, the use of elaborate equipment and procedures to maintain an exact mixture composition is seen to be unnecessary from the pressure standpoint. This, of course, does not hold true if detonation velocity is the prime concern, since Table 1 indicates that velocity is highly dependent upon mixture composition.

The stoichiometric hydrogen-oxygen mixture, consisting of two-thirds hydrogen and one-third oxygen by volume, has been used in most of our tests. Detonation characteristics of the stoichiometric mixture are listed again in Table 2, along with values observed experimentally. Good agreement between theoretical and observed values is seen, especially for the static pressure.

TABLE 1
Detonation Characteristics of Selected Hydrogen-Oxygen Mixtures[a]

Mixture Composition	C-J Static Pressure Ratio	C-J Reflected Pressure Ratio	Detonation Wave Velocity (fps)
$4H_2 + O_2$	17.79	42.22	11,240
$3H_2 + O_2$	18.44	43.79	10,490
$2H_2 + O_2$	18.59	44.18	9360
$H_2 + O_2$	17.63	41.83	7650
$H_2 + 2O_2$	15.79	37.29	6370

[a]From Edwards, Williams, and Breeze.

The hydrogen and oxygen gases used in our tests were drawn from commercial cylinders. A simplified schematic of the gas metering arrangement is shown in Fig. 5. The usual method of obtaining the desired mixture was to adjust the volume flow rates to the desired proportions using a pair of flowmeters. The flowing gases were mixed at a tee connection and fed into the test fixture. The upstream or metering pressures were held to at least twice the desired initial pressure in the test fixture so that the flow rates would not change as the test fixture filled.

Any air initially present in the test fixture must be removed prior to testing; otherwise its presence may degrade the detonation pressures and velocity. The air may be evacuated by a vacuum pump, displaced by a moving piston, or flushed out by repeated filling and emptying with the explosive gas mixture. All these methods have been employed at various times, with the choice determined by which is most convenient for the particular test setup.

Detonations were initiated by either an electric spark or an electric match. Spark ignition was accomplished by triggering a charged capacitor to send a 7000-volt, 7.5-joule pulse to a pair of electrodes spaced about 1/16 inch apart in the test fixture. The electric matches consisted of 40 milligrams of ammonium perchlorate-LMNR ignited by a resistance wire bridge. Both ignition methods work equally well. The electric matches, being low voltage devices, are preferred in tests where the high voltage spark discharge would create instrumentation noise problems.

TABLE 2
Detonation Characteristics of the Stoichiometric Hydrogen-Oxygen Mixture[a]

Composition: $2H_2 + O_2$ by volume

Combustion Equation: $2H_2 + O_2 \rightarrow 2H_2O$

	C-J Theoretical	Observed
Static Pressure Ratio	18.59	18.6
Reflected Pressure Ratio	44.18	62.5 peak 33.8 average[b]
Detonation Wave Velocity (fps)	9360	9100

[a]From Edwards, Williams, and Breeze.
[b]For first 100 microseconds of pulse.

Tests have been performed with four different facilities: (1) a 7-inch-diameter tube, adaptable for use as a projectile launching gun, a detonation driven shock tube, or a closed explosion test chamber; (2) a 14-inch-diameter projectile launcher; (3) a 16-inch-diameter tube designed as a recoilless projectile launcher or shock tube; and (4) the Sandia Corporation 26-inch-diameter air gun facility converted to explosive gas operation.

The 7-inch-diameter tube was the first facility constructed for gas detonation tests. It consists of a 10-foot length of stock seamless mild steel tube, having an inside diameter of 7-inches and a wall thickness of 0.5 inch. Flanges are welded to each end of the tube to accept closure plates or diaphragms. The closure plate on one end contains the gas inlet fitting and feed-through electrodes for the spark gap or electric matches. Several drilled and tapped holes along the tube length provide transducer mounting ports. Figure 6 shows the 7-inch tube mounted in a surplus rocket test stand.

To date, nearly 100 test shots have been fired in the 7-inch tube. Approximately half have been gun-type, or projectile-launching, tests. The firing sequence for a gun-type test is shown in Fig. 7. The projectile containing the test item is inserted into the muzzle and is held in position in the tube by a small plastic shear pin. A hydrogen-oxygen mixture is

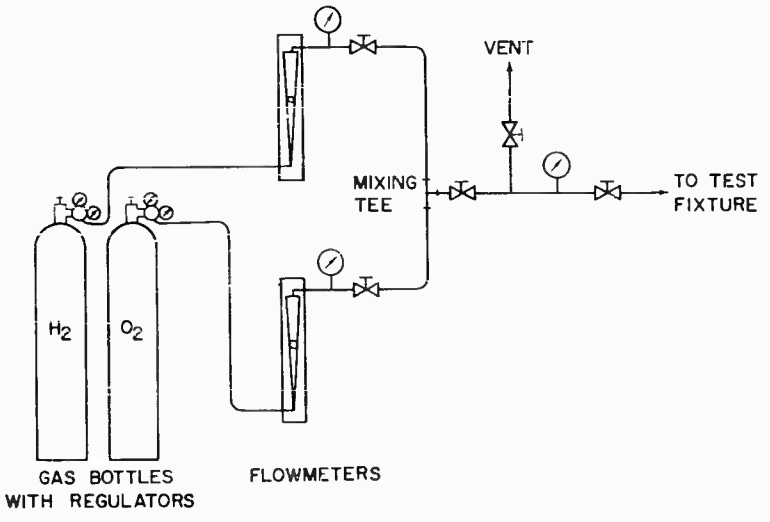

Fig. 5 - Schematic of explosive gas metering equipment

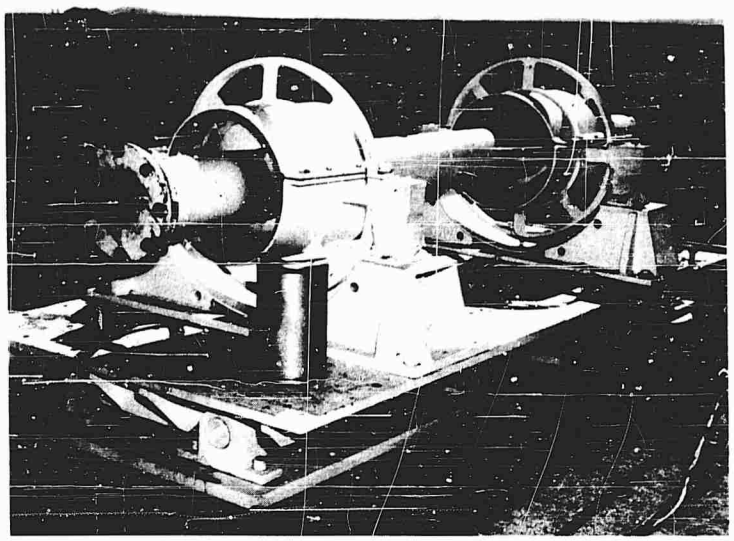

Fig. 6 - Seven-inch-diameter gas detonation tube

introduced into the breech volume and ignited. When the resulting detonation wave strikes the projectile the shear pin breaks, allowing the projectile to accelerate down and out of the tube.

Most other tests in the 7-inch tube have been closed chamber shots for instrumentation research. For these tests both ends of the tube are closed by solid plates. Ports are drilled and tapped in the end plate for mounting items to be subjected to reflected pressures.

The need for a means of testing larger and heavier items than could be accommodated in the 7-inch tube led to the design and construction of a second explosive gas facility, known as the 14-inch vertical projectile launcher, shown in Fig. 8. The upper portion of the launcher is a 4-foot length of stock steel pipe, having an inside diameter of 14 inches and 1.0-inch-thick wall, with mounting flanges welded to each end. The lower portion is an aluminum casting in the shape of a hollow cone

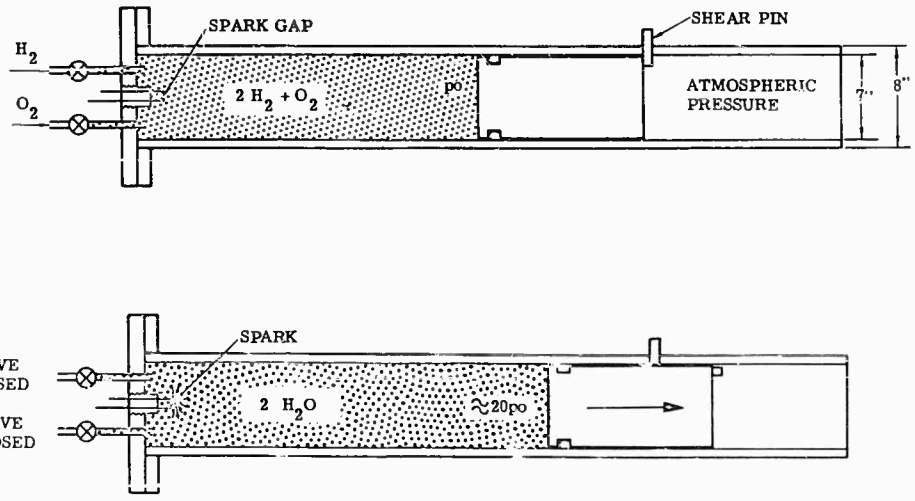

Fig. 7 - Firing sequence for a projectile launching test in the 7-inch gas detonation tube

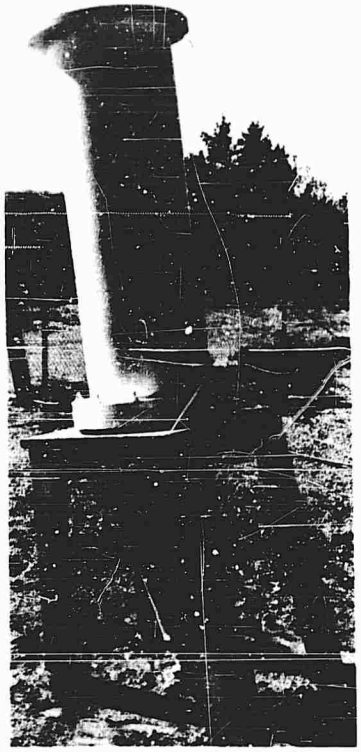

Fig. 8 - Fourteen-inch vertical projectile launcher

about 3 feet long. Spark gap electrodes are located in the apex of the cone, and ports along the side provide transducer mounting locations.

The 14-inch launcher is mounted vertically with the open end pointing upward. The vertical orientation permits use of a relatively simple mounting stand to absorb the heavy recoil forces. The firing sequence is the same as for a gun type test in the 7-inch tube, with the test item held in position initially by a plastic shear ring. After launch the test item continues in a free flight trajectory to impact in the earth. Parachute recovery has been considered to protect more delicate items from impact, but it has not been used on any tests to date.

Early test records from 14-inch launcher shots contained multiple pressure peaks as the result of the shock wave reflecting back and forth between the end of the tube and the test item. To eliminate these peaks a wave trap plate, shown in Fig. 9, was inserted between the two sections of the tube. The wave trap design was based on the fact that a pressure wave reflects from a closed end as an increase in pressure and from an open end as an expansion or decrease in pressure. With a surface that is partly closed and partly open the reflected expansion from the open areas will tend to cancel the reflected pressure increase from the closed areas. It has been determined that a surface with one-third of its area open will bring about complete cancellation of the two effects and will eliminate reflections entirely [10]. Therefore, the wave trap plate in Fig. 9 has approximately one-third of its surface area removed.

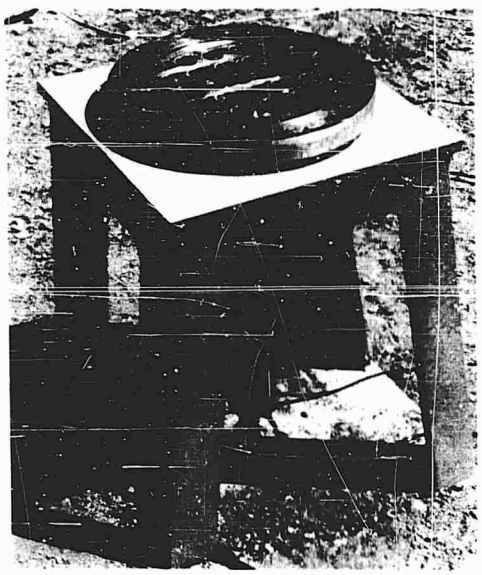

Fig. 9 - Wave trap plate used in 14-inch vertical projectile launcher

A third explosive gas facility, the 16-inch recoilless tube shown in Fig. 10, was constructed to perform tests requiring pressures in the 5000- to 10,000-psi range, well beyond the capabilities of either the 7-inch or 14-inch tubes. This facility is actually the simplest of any now in use; it consists only of a 14-foot length of heavy steel pipe having an inside diameter of 16 inches and a wall thickness of 2 inches. A plate containing the gas inlet fitting and electrodes for the ignition device fits into one end of the pipe, and a piston containing the test item and instrumentation fits into the other end. Both plate and piston are held in place initially by plastic shear rods. The detonation pressure ejects both plate and piston from the tube, leaving the tube with both ends open a few milliseconds after firing. Therefore, no recoil force exists, and no mounting fixture is required for the tube.

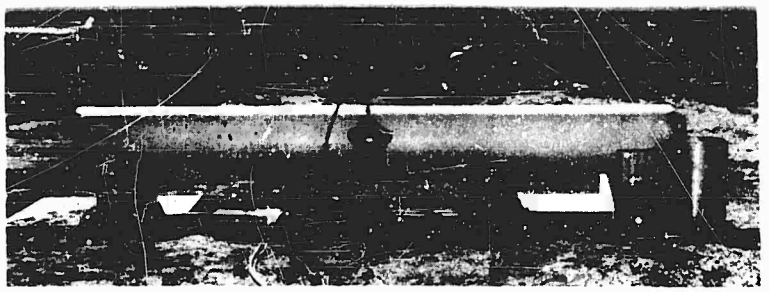

Fig. 10 - Sixteen-inch recoilless gas detonation tube

Explosive gas tests have also been performed in the Sandia Corporation 26-inch air gun facility. The air gun was originally designed to shock test large items (up to 26 inches in diameter and 2000 pounds in weight), by use of compressed air to supply the accelerating force. Since the minimum pulse rise time is about 3 milliseconds in conventional air gun shots, it was necessary to convert the gun to explosive gas operation in order to obtain the shorter rise times required for blast load simulation. Figure 11 is a sketch of the breech portion of the gun, showing a setup for an explosive gas test. The breech plug has been fitted with a gas inlet and igniter electrodes. A volume control plug closes off the unneeded breech air volume. The conical shape of the volume control plug matches the shape of the test item so as to surround the test item with a uniform thickness layer of explosive gas. Friction brake shoes on the test item piston bring the piston to a stop within the gun barrel length after a test firing.

EXPERIMENTAL RESULTS

Figure 12 is an actual static pressure record from a typical projectile launch shot in the 7-inch tube. The record shows a very fast pressure rise time as the detonation wave passes the transducer, followed by a long, exponential decay as the piston moves down the tube. The decay corresponds very closely to an adiabatic expansion for the time period shown. The numerous peaks and dips in the initial portion of the pulse are caused by reflections of the shock wave. These normally damp out in about 5 milliseconds.

In addition to subjecting test items to blast pressures (and accelerations), the 7-inch gun has been used as a velocity generating device for impact testing. Velocities obtained have ranged from 180 feet per second with a 40 pound projectile to 925 feet per second with an 8 pound projectile, all with pressure pulses similar to the one shown in Fig. 12.

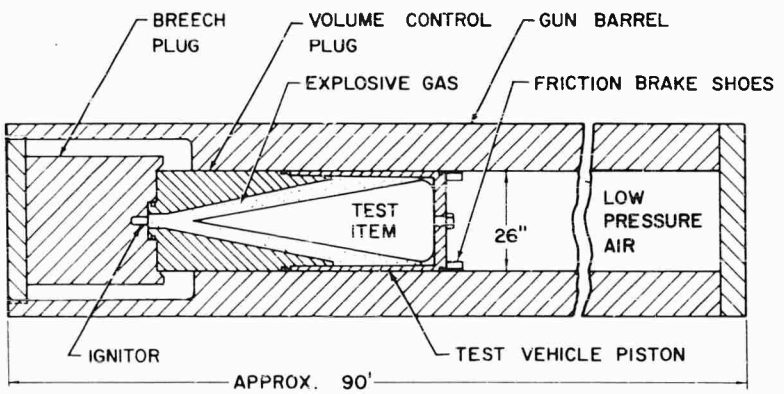

Fig. 11 - Sketch of explosive gas test setup in the Sandia Corporation 26-inch air gun

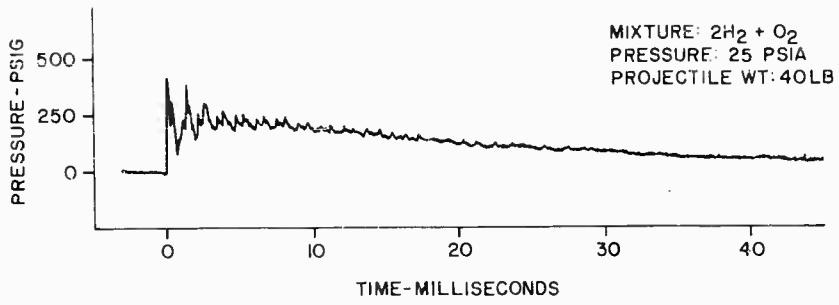

Fig. 12 - Static detonation pressure record from projectile launching shot in 7-inch tube

A comparison of values of static and reflected pressures in a given test shot in the 7-inch tube may be made from Fig. 13. The reflected pressure is seen to be nearly three times the static pressure on this particular test. The expanded time scale in this record further illustrates the extremely fast pressure rise in the detonation wave. The reflected pressure (Fig. 13(b)) was measured with a Hopkinson pressure bar transducer, constructed according to principles set forth by Ripperger [11]. The pressure bar transducer has the capability of measuring pulse rise times much shorter than is normally practical with the usual disphragm type transducers. The static pressure record (Fig. 13(a)) was obtained with a commercially available, fast-response, quartz transducer. Static pressure measurement imposes somewhat less stringent requirements upon the transducer than does reflected pressure measurement, and commercial transducers have been found to be adequate for most static measurements.

Static pressures obtained in the 14-inch vertical launcher are indicated in Figs. 14 and 15. Early tests with the 14-inch facility were plagued by quite severe multiple shock wave reflections, such as are shown in Fig. 14. When the wave trap plate (see Fig. 9) was inserted in the tube, however, the reflections were almost completely eliminated. Figure 15 is a record from a shot made under the very same conditions as the shot of Fig. 14 except with the wave trap plate in place. The impulse, or area under the pressure-time curve, is approximately the same in both shots, but the pulse of Fig. 15 more nearly produces the desired loading on the test item.

The 16-inch recoilless tube was designed for high pressure tests, and Fig. 16 is the

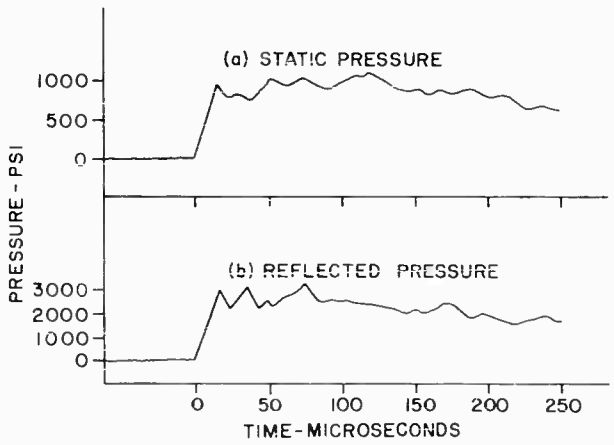

Fig. 13 - Static and reflected detonation pressure records from a typical closed-end test in the 7-inch tube ($2H_2 + O_2$ mixture at 60 psia initial pressure)

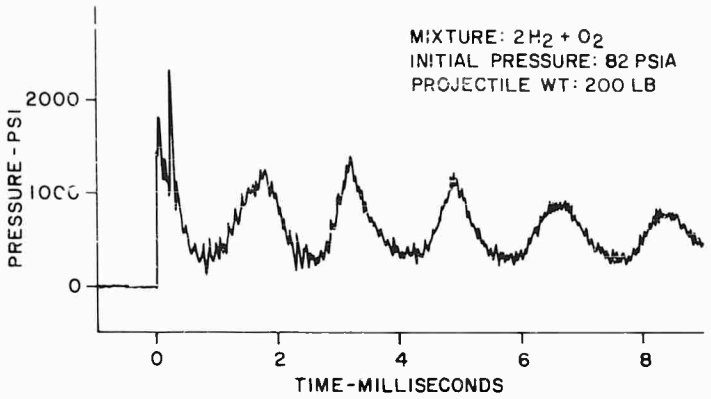

Fig. 14 - Typical static detonation pressure record from a test in the 14-inch vertical projectile launcher without wave trap plate

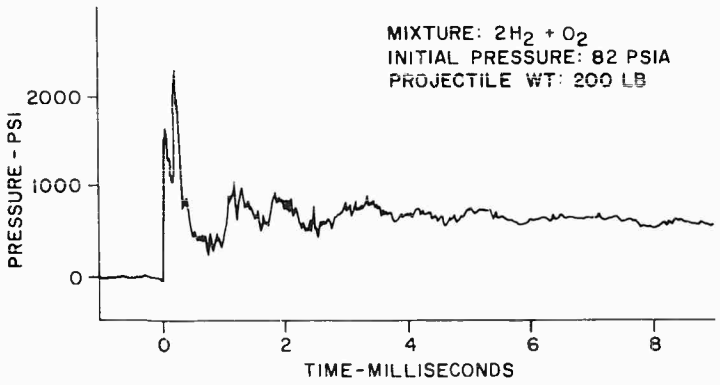

Fig. 15 - Typical static detonation pressure record from a test in the 14-inch vertical projectile launcher with wave trap plate

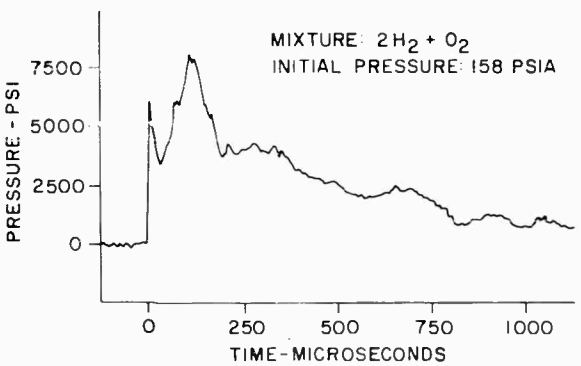

Fig. 16 - Typical reflected detonation pressure record from a test in the 16-inch recoilless tube

record of one such test. A reflected pressure of nearly 8000 psi was imposed on the test item. The recoilless design is so effective that no noticeable movement of the tube occurs during a shot, even though the tube is completely unrestrained in its mounting.

Finally, a static pressure record from an explosive gas test in the 26-inch air gun is shown in Fig. 17. The record is not appreciably different from those of tests in the other facilities, but it is included to illustrate how gas detonations have been successfully applied to tests of relatively large, heavy structures.

CONCLUSIONS

The results of the gas detonation tests have been generally encouraging and have tended to confirm predictions. Shock pressure pulses of the desired shape have been obtained for a wide range of amplitudes and durations. The methods appear to be useful not only for laboratory reproduction of blast conditions but also for other types of shock tests where short acceleration rise times are required. Velocity generation for flight or impact studies is another area in which gas explosions have proved to be useful. The gas gun will perform much the same as a conventional air gun, without requiring expensive and bulky compressors, storage tanks, and high pressure valves.

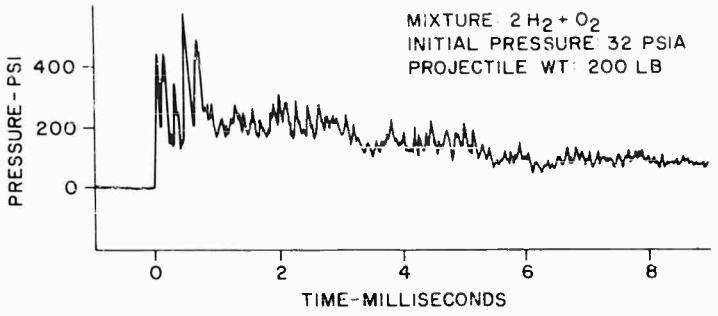

Fig. 17 - Typical static pressure record from an explosive gas test in the Sandia Corporation 26-inch air gun

Test programs are continuing to improve present procedures and equipment and to develop new test methods. Present plans call for investigations of multi-stage detonation tubes, impulse or short duration loadings, pulse shaping with attenuator materials, and shock initiation of detonations. The use of explosive gases has great potential in the field of shock testing, and an increasing number of applications is anticipated in the future.

Appendix A

CHAPMAN-JOUGUET DETONATION EQUATIONS

Derivation of Chapman-Jouguet Detonation Equations

P = Pressure

V = Specific volume

T = Temperature

n = Number of moles per unit mass

R = Universal gas constant

E = Internal energy

S = Entropy

Q = Heat energy

C_v = Specific heat at constant volume

C_p = Specific heat at constant pressure

U = Mass flow velocity

D = Detonation wave velocity

C = Velocity of sound.

Subscripts 1 and 2 refer to before and after detonation, respectively.

The equation of state of a perfect gas is

$$PV = nRT , \tag{1}$$

which in differential form becomes

$$P\,dV + V\,dP = nR\,dT \tag{2}$$

or

$$\frac{dP}{dV} = \frac{nR}{V}\frac{dT}{dV} - \frac{P}{V} .$$

The First Law of Thermodynamics, requiring conservation of energy in any process, may be mathematically stated as

$$dQ = dE + P\,dV , \tag{3}$$

that is, the heat energy absorbed or emitted by a process must equal the sum of the change in internal energy and the external work done.

From the definition of entropy, it may be shown that for a reversible process

$$dQ = T\,dS . \tag{4}$$

By combining (3) and (4),

$$T\,dS = dE + P\,dV \tag{5}$$

for a reversible process.

By following different lines of reasoning, Chapman and Jouguet both came to essentially the same conclusion: a detonation wave may be considered as an isentropic (reversible adiabatic) compression. An isentropic process is one in which the entropy change, dS, is zero; therefore,

$$T\,dS = 0 = (dE)_S + P(dV)_S = \left(\frac{\partial E}{\partial T}\right)_V (dT)_S + \left(\frac{\partial E}{\partial V}\right)_T (dV)_S + P(dV)_S . \tag{6}$$

For a perfect gas

$$\left(\frac{\partial E}{\partial V}\right)_T = 0 \quad \text{and} \quad \left(\frac{\partial E}{\partial T}\right)_V = \overline{C_v} \tag{7}$$

where $\overline{C_v}$ is the mean specific heat in the temperature range of interest.

By combining (6) and (7),

$$0 = \overline{C_v}(dT)_S + P(dV)_S \tag{8}$$

or

$$\left(\frac{dT}{dV}\right)_S = -\frac{P}{\overline{C_v}} .$$

When (8) is substituted into (2),

$$\left(\frac{dP}{dV}\right)_S \quad \frac{nR}{V}\left(\frac{-P}{\overline{C_v}}\right) - \frac{P}{V} = -\frac{P}{V}\left[\frac{nR}{\overline{C_v}} + 1\right] . \tag{9}$$

From specific heat relationships it can be shown that

$$C_p \quad nR + C_v = C_v \gamma , \tag{10}$$

where

$$\gamma \quad \frac{C_p}{C_v} . \tag{11}$$

The substitution of (10) and (11) into (9) gives

$$\left(\frac{dP}{dV}\right)_S \quad -\frac{\gamma P}{V} . \tag{12}$$

The laws of conservation of mass, momentum, and energy must apply to the gases before and after passage of the detonation wave. For the conservation of mass,

$$\frac{U_1}{V_1} = \frac{U_2}{V_2} . \tag{13}$$

For conservation of momentum,

$$\frac{U_1^2}{V_1} + P_1 = \frac{U_2^2}{V_2} + P_2 . \tag{14}$$

For conservation of energy,

$$E_1 + \frac{U_1^2}{2} + P_1 V_1 = E_2 + \frac{U_2^2}{2} + P_2 V_2 . \tag{15}$$

It is convenient to define the coordinate system as being stationary relative to the detonation wave, i.e., the coordinate system moves with a velocity D relative to a stationary observer. Therefore, for a gas initially at rest to a stationary observer,

$$U_1 = D . \tag{16}$$

By combining (13), (14), and (16),

$$D = U_1 = V_1 \sqrt{\frac{P_2 - P_1}{V_1 - V_2}} . \tag{17}$$

For an isentropic process, (17) may be expressed as

$$D = V_1 \sqrt{-\left(\frac{dP_2}{dV_2}\right)_S} . \tag{18}$$

By substituting (12) into (18),

$$D = V_1 \sqrt{\frac{\gamma_2 P_2}{V_2}} = \frac{V_1}{V_2}\sqrt{\gamma_2 P_2 V_2} . \tag{19}$$

By solving (13), (14), and (15) simultaneously and simplifying,

$$E_2 - E_1 \quad \frac{1}{2}(P_1 + P_2)(V_1 - V_2) . \tag{20}$$

The temperature change of the gases is a function of the change in internal energy due to compression and the energy released in combustion,

$$\overline{C}_v(T_2 - T_1) \quad (E_2 - E_1) + \Delta E_C , \qquad (21)$$

where ΔE_C is the chemical energy released by combustion.

When (20) and (21) are combined

$$\overline{C}_v(T_2 - T_1) - \Delta E_C \quad \frac{1}{2}(P_1 + P_2)(V_1 - V_2) . \qquad (22)$$

By substituting (1) into (22) and simplifying,

$$\overline{C}_v(T_2 - T_1) - \Delta E_C - \frac{R}{2}\left(\frac{V_1}{V_2} - 1\right)\left(n_2T_2 + n_1T_1\frac{V_2}{V_1}\right) - 0. \qquad (23)$$

From (17) and (19) it may be shown that

$$U_1 = \frac{V_1}{V_2}\sqrt{\gamma_2 P_2 V_2} . \qquad (24)$$

Similarly,

$$U_2 = \sqrt{\gamma_2 P_2 V_2} . \qquad (25)$$

Substituting (1), (24), and (25) into (14) and simplifying,

$$\frac{V_1^2}{V_2^2} + \frac{n_1T_1}{n_2T_2\gamma_2} - \left[\frac{V_1}{V_2}1 + \frac{1}{\gamma_2}\right] = 0 . \qquad (26)$$

The pressure ratio may be obtained from (1) as

$$\frac{P_1}{P_2} = \frac{V_2 n_1 T_1}{V_1 n_2 T_2} . \qquad (27)$$

Since density is probably a more familiar quantity than specific volume, the equations may be rewritten with

$$\mu = \frac{1}{V} \qquad (28)$$

and the ratio

$$\mu \quad \frac{V_1}{V_2} \quad \frac{\rho_2}{\rho_1} . \qquad (29)$$

Therefore, the pertinent detonation equations may be summarized as follows: from (19),

$$D = \mu\sqrt{\frac{\gamma_2 P_2}{\rho_2}} ; \qquad (30)$$

from (23),

$$\overline{C}_v(T_2 - T_1) - \Delta E_C - \frac{R}{2}(\mu - 1)(n_2T_2 + n_1T_1\mu) \quad 0 ; \qquad (31)$$

from (26),

$$\mu^2 + \frac{n_1T_1}{n_2T_2\gamma_2} - \mu\left(1 + \frac{1}{\gamma_2}\right) = 0 ; \qquad (32)$$

and from (27),

$$\frac{P_1}{P_2} = \frac{n_1T_1}{\mu n_2T_2} . \qquad (33)$$

As a matter of further interest, it may be recalled that the velocity of sound in a gas is given by

$$C^2 = \frac{\gamma P}{\rho} . \qquad (34)$$

Therefore, by substituting (34) into (30),

$$D = \mu C_2 , \qquad (35)$$

the detonation velocity is seen to be equal to the velocity of sound in the burned gases multiplied by the ratio of densities of burned and unburned gases.

The velocity of the burned gas flow relative to a stationary observer is known as the particle velocity, and is given by

$$W = U_1 - U_2 = \sqrt{\gamma_2 P_2 V_2}\left(\frac{V_1}{V_2} - 1\right) = C_2(\mu - 1). \qquad (36)$$

Note that

$$D = W + C_2 . \qquad (37)$$

i.e., the detonation velocity is equal to the sum of the particle and sound velocities in the burned gases.

REFERENCES

1. B. Lewis and G. von Elbe, Combustion, Flames and Explosions of Gases (Academic Press, New York, 1951), pp. 579-612.

2. S. S. Penner and B. P. Mullins, Explosions, Detonations, Flammability and Ignition (Pergamon Press, New York, 1959).

3. W. Jost, Explosion and Combustion Processes in Gases (McGraw-Hill, New York 1946), pp. 160-192.

4. A. G. Gaydon and I. R. Hurle, The Shock Tube in High Temperature Chemical Physics (Reinhold, New York, 1963), pp. 257-282.

5. B. Lewis and J. B. Friauf, J. Chem. Phys., 52:3905 (1930).

6. J. Roth, "Impulses from Detonating Gas Mixtures," Air Force Special Weapons Center Tech. Report No. AFSWC-TDR-62-99 (Nov. 1962) (Unclassified).

7. D. H. Edwards, G. T. Williams, and J. C. Breeze, J. Fluid Mech., 6:497 (1959).

8. R. L. Gealer and S. W. Churchhill, "Detonation of Hydrogen-Oxygen Mixtures at High Initial Pressure," ASTIA Doc. No. AD 202 043 (MICH-5-P-Squid) (Sept. 1958).

9. W. Doering and G. Burkhardt, "Contributions to the Theory of Detonation," Air Material Command Tech. Report No. F-TS-1227-IA (May 1949).

10. R. R. Flagg, "Advances in Shock Tunnel Driving Techniques," Proc. of Third Hypervelocity Techniques Symposium (Mar. 1964), pp. 89-115.

11. E. A. Ripperger, "The Propagation of Pulses in Cylindrical Bars," Tech. Report No. 13, N6-NOR-251, Division of Engr. Mech., Stanford Univ., California (1952).

* * *

HAND-HELD SHOCK TESTER WOX-6A

V. F. DeVost, J. E. Messner, and G. Stathopoulos
U.S. Naval Ordnance Laboratory
White Oak, Silver Spring, Maryland

A 5-lb shock tester the size of a hand tool is described. For items the weight of piezoelectric accelerometers, the tester produces shock-pulses ranging from 400 to 1000 g peak with durations of 1 millisecond and velocity changes up to 15 fps. The principal use of the tester has been the checking of the output of piezoelectric accelerometers through their associated circuitry immediately prior to field trials; the tester has also found wide use in the laboratory. Future modifications will extend its use to checking a wider variety of gages.

INTRODUCTION

The original objective in developing the Hand-Held Shock Tester WOX-6A, Fig. 1, was to devise a simple method for dynamically testing shock transducers in field operations where conventional shock testers were either unavailable or their use was impractical. The new tester not only met this objective, but proved versatile enough to be used extensively in the laboratory as well. In addition, the device possesses enough new and novel features to be patentable [1].

The new tester is not as large as the familiar 16-ounce soft-drink bottle; however it is slightly heavier. It may be held in one hand and operated with the other, or it may be operated from a convenient bench or shelf. Both modes of operation result in the same shock pulse. Two constant-force spring motors propel a 75-gram vehicle (test carriage and payload) into a resilient pad to produce shock pulses whose peak can be varied in four steps from 400 to 1000 g.

Because of the expense in making field recordings of shock and the small number of vehicles or trials allocated for this purpose, it is important that one take every precaution to assure himself that the instrumentation is in A-1 condition. This is complicated by the complexity of the shock recording instrumentation. Because there are many links in the chain of instrumentation, the failure of any one can be very costly from both the monetary standpoint and the delays that it can cause a program. One of the most important links in the instrumentation chain is the accelerometer. Too often the defects of the accelerometer cannot be detected by conventional means. The most meaningful way to check the accelerometers prior to using them

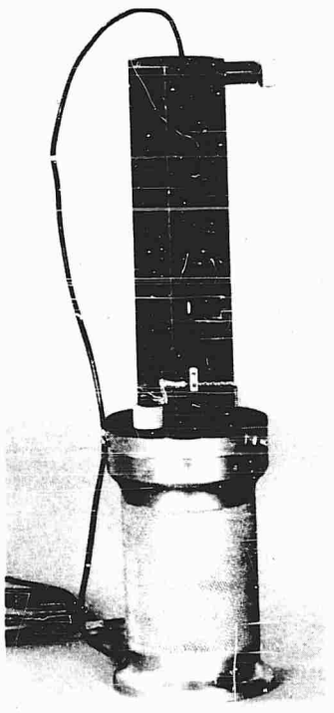

Fig. 1 - Hand-held Shock Tester WOX-6A

NOTE: References appear on page 334.

in a field trial is to subject them to a well defined shock pulse of high enough intensity to screen them for shock induced effects. The Hand-Held Shock Tester WOX-6A is a modest attempt to provide a device for doing this.

While the WOX-6A is designed primarily for field use to test piezoelectric gages, it has the capability for testing larger and heavier shock transducers such as the unbonded strain gage types. Larger payloads have been tested with the device (up to 125 grams) without sacrifice in the quality and repeatability of the shock produced. The shock range for 125 grams can be varied from 200 to 500 g. Among other applications, the accelerometer outputs while undergoing shock with this tester have been recorded to back up step voltage calibrations on tape. Personnel of the Naval Ordnance Laboratory have successfully used this device during several field projects and in many laboratory applications. The present model has an experimental designation since it is expected to undergo several changes before it acquires an official title. Current changes under consideration are (1) the addition of a telescoping test carriage to provide more mounting space for larger transducers, and (2) a small liquid chamber to develop pressure pulses generated as a result of shock. Thus pressure transducers could be tested with the same or a similar device. The current WOX-6A is an operational design, and complete drawings on the device are available for reference or information [2].

PRINCIPLE OF OPERATION

The overall sequence of operation for the WOX-6A is illustrated in Fig. 2. After the test carriage is released, it is propelled toward the shock pad at approximately 5.2 g, or slightly over 0.5 percent of the principal pulse peak. The principal pulse occurs when the carriage strikes the shock pad. For maximum release height, the shock pulse is slightly over 1000 g. When the carriage rebounds, it is resisted with considerable inertia by the backlash in the system. This produces a negative acceleration of about 50 g for the maximum release conditions, or approximately 5 percent of the principal pulse. The carriage rebounds several times until the energy is expended.

Control of payload is essential in maintaining reproducibility. The tester has a small energy output, a carriage mass to reaction mass ratio slightly over one-tenth, and a shock pad whose resisting load varies with impact load. These three factors combine to make a slight change in payload result in significant change (about 1/2 percent per gram) in the peak of the shock produced. For optimum accuracy, payloads should be as close to calibration loads as practicable.

DESCRIPTION

General

The Hand-Held Shock Tester WOX-6A consists of three basic units (see Fig. 3): the base

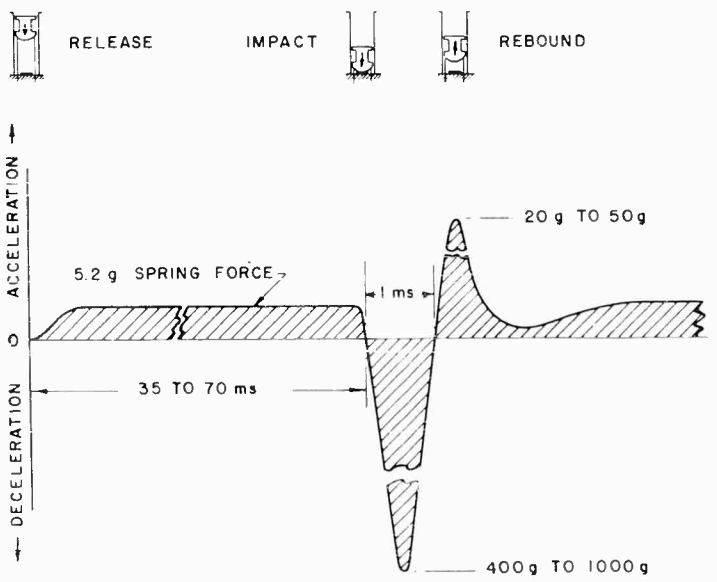

Fig. 2 - Overall shock motion

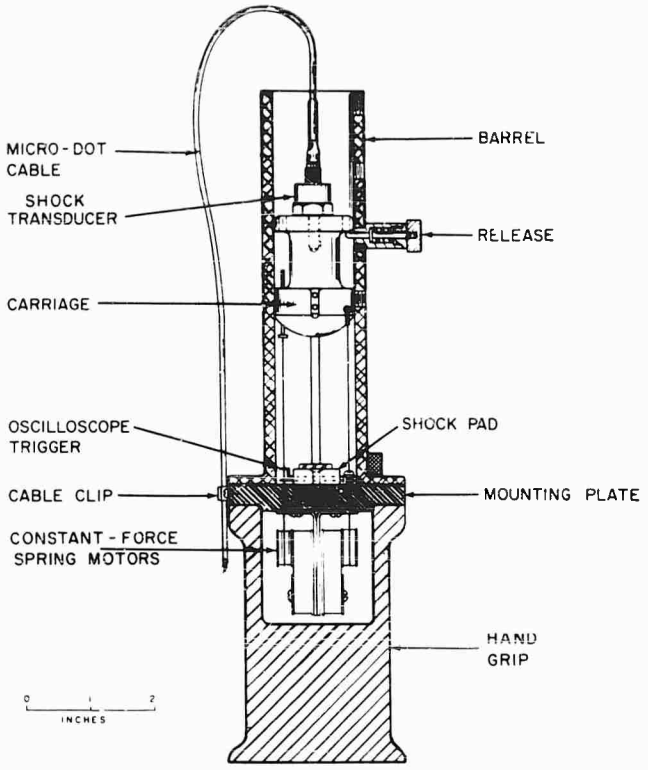

Fig. 3 - WOX-6A components

or handgrip, the barrel, and the shock vehicle assembly. The handgrip serves as a reaction mass, houses the spring motors and supports all other assemblies. The barrel unit guides the test carriage and holds the release mechanism. The shock vehicle assembly includes the moving parts, the test carriage and motors, and the shock pad and trigger. All three units can be disassembled in a matter of seconds.

Handgrip

The bulk of the tester weight (over 80 percent) is concentrated in the base. The brass handgrip provides an impact reaction mass over 10 times the weight of the test carriage plus a test item of 25 grams. The grip is flared at its base to improve its stability when it is used on a bench. The outer surface of the base is knurled to provide a better grip.

Barrel

A lightweight aluminum barrel accurately guides the carriage toward the shock pad and protects delicate parts from damage. The barrel is slotted on two sides to permit fingergrips on the test carriage to protrude through. Thus the carriage may be lifted in the barrel to a point where it engages the release mechanism. The release mechanism is shown inserted at the top of the barrel (Fig. 1). Four holes 1 inch apart are tapped in one side of the barrel to receive the release. Thus the carriage may be propelled for calibrated distances of from 1 inch to 4 inches to vary impact velocity.

Shock Vehicle Assembly

This assembly (see Fig. 4) is the heart of the shock tester. For ease of assembly and maintenance all components are mounted to a common plate. Actually, this unit can be operated independently to perform most of the mechanical functions of the fully assembled tester.

As shown in Fig. 4, the motors fasten to the bottom of the mount, the shock pad and trigger fasten to the top, and the motor tow cables fasten to each side of the test carriage to form a complete assembly. The motors, "Neg'ators" [3] are commercial components. Their rated load is 6 ounces each. Each motor has a durable

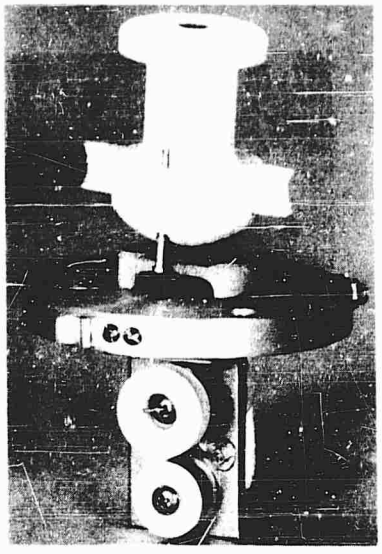

Fig. 4 - Shock vehicle

nylon plastic tow cable stretchable to 3 feet. The cable length for the WOX-6A is reduced to 10 inches to minimize the effects of cable pile-up. The shock pad consists of a small nylon plastic leaf spring on top of which is cemented a 0.070-inch-thick rubber wafer. The test carriage is made of Teflon providing natural lubrication and relatively good damping from a shock standpoint. Fingergrips are attached to each side of the carriage.

SPECIFICATIONS

The mechanical and performance specifications for the tester are listed below.

Mechanical

Total weight (without payload)	5.1 lb
Test carriage tare weight	52.5 gm
Overall height	10.5 in
Maximum diameter	2.25 in.
Barrel inside diameter	1.25 in.
Total motor spring force	12.4 oz.

Performance

Maximum allowable payloand	125 gm
Calibrated payload	25 gm
Energy output	3.8 in-lb
Motor endurance limit	3000 cycles
Maximum shock output (25-gram payload)	1000 g
Minimum shock output (25-gram payload)	400 g
Pulse duration (1000g)	1.0 ms
Pulse duration (400g)	1.2 ms
Maximum impact velocity change	15 fps
Average acceleration (percent of peak)	57%
Reproducibility from drop to drop (same tester)	0.5%
Reproducibility from tester to tester	2%
Shock variation due to temperature (0° F to 100° F)	6%

CALIBRATION

Always a problem with any shock producing device where accuracy is essential is the selection of a standard gage to measure the shock. Reliance on commercial ratings for gage sensitivity and calibration is seldom a good practice. Before calibrating the WOX-6A tester, a careful check was made of the several gages used.

The procedure recommended and adopted at NOL is to check out an unbonded strain gage accelerometer on a suitable centrifuge, then compare several (3 or 4) piezoelectric pickups against this instrument on a calibrated drop tester. Generally, the calibration pulses selected for these tests are long enough in duration to be within the frequency range of the accelerometers in question. When the accuracy of the accelerometer has been verified, the tester is calibrated for shock and the transducer is set aside as a standard for periodic check on the device. For field units the gage becomes part of the tester equipment.

Figure 5 illustrates the character of the principal shock pulses produced by the shock tester. The instrumentation system used to calibrate the tester consisted of the following:

1. An undamped, unfiltered, piezoelectric transducer with a rated natural frequency of 100 kcps.

2. A charge amplifier with a frequency response flat to 35 kcps.

3. An oscilloscope with a frequency response flat to 100 megacycles.

TEST PROCEDURES

To mount transducers or other test items, raise the carriage until it engages the release; the release should be in the top insert. The test items should be finger tight only; it is not necessary to use wrenches. Connect the instrumentation cable to the pickup and lower the carriage. The instrumentation cable should be secured in the cable clip (see Fig. 1) with enough slack allowed so that the cable does not interfere with the carriage travel. The instrumentation cable should be lightweight and flexible in order to keep extraneous forces to a minimum. The fingergrips protrude past the outside diameter of the barrel; therefore, care should be taken to assure their flight path is not obstructed. The oscilloscope trigger contact adjustment screw should be adjusted so that sufficiently long base line is recorded; however, the screw should not extend out too far or it may result in damage to the contacts or shock pulse distortion. When using a continuous recorder instead of an oscilloscope, it is recommended that the screw be backed off so that it clears the contacts.

In order to produce repeatable shock pulses it is necessary that the tester be held firmly, within 5 degrees of vertical, and that the payload weight remain constant (within ±1 gram) from drop to drop. Adapters are used to mount the accelerometers to the carriage and they also serve as mass compensators to maintain the calibration weight (25 grams). In cases where the accelerometer weighs more than 25 grams, calibration at a suitable lower level is used (200 to 500 g).

Before using the tester it is a good procedure to operate the carriage several times to assure that it is sliding in the barrel freely. If the tester does not produce the specified calibrated pulse, the following steps for trouble shooting are suggested:

1. Check tester with the calibration standard to determine if the accelerometer being used is measuring accurately.

2. Check or change instrument cables and recording instruments.

3. Disassemble the tester and inspect the shock vehicle, motors, tow cables, shock pad, and trigger assembly for looseness or damage.

NOVEL FEATURES

Aside from the novelty of having a handy lightweight tester for field use and for simplifying the job of checking transducers in the laboratory, the WOX-6A has several novel components which may find application in other shock test devices:

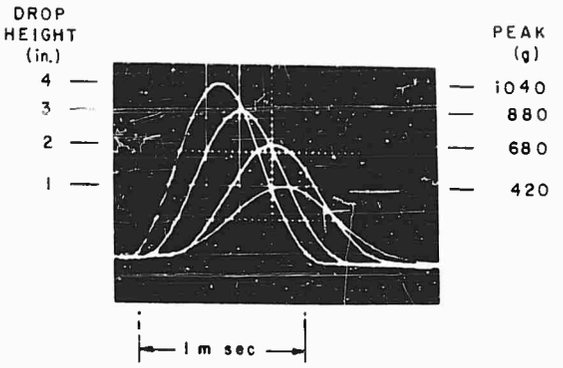

Fig. 5 - Principal pulses

1. The hybrid nylon plastic and rubber shock pad has proved significantly more resilient than most shock pads similarly used.

2. The spring motors are designed to keep accelerating forces to a minimum while providing enough force to get reasonably high velocity.

3. The Teflon used in the test carriage was found to have internal damping four to five times that of aluminum, nylon plastic, phenolic, and even mildly hard woods.

4. The built-in trigger mechanism has proved a great time saver and its micrometer adjustment provides microsecond control for oscilloscope triggering.

5. Combining all critical parts in one assembly (Fig. 4) minimizes manufacturing time and makes maintenance relatively easy.

SUMMARY

A portable, lightweight shock tester has been developed which has been used effectively in both the field and the laboratory to check the output of accelerometers. Shock pulses are produced which can be varied from 400 to 1000 g with durations of approximately 1 millisecond. Future developments will be concerned with increasing tester capacity to check a wide variety of gages and lightweight components.

In the short time the shock tester has been in use, it has run up a high score for screening instrumentation systems for malfunctions and for equipment defects. The following are some

of the more common difficulties discovered directly or indirectly as a result of using the device:

1. Change in transducer sensitivity

2. Intermittent breaks in transducer output

3. Loss of preset in transducer (no negative response)

4. Tape recorder out of balance

5. Oscilloscope out of calibration

6. Charge amplifier or cathode follower out of calibration

7. Open transducer cables

8. Intermittent break at the transducer connectors

9. High noise level in instrumentation systems

10. Attenuation of shock signal through system.

The WOX-6A performs a function not easily duplicated by other means. After the complex job of preparing a vehicle for test has been completed, instrumentation cables have been laid out and recording equipment has been readied, final check through the entire system can be made quickly and with the assurance that input conditions are accurate and not subject to electrical interference.

REFERENCES

1. Navy Case No. 39,045, Invention Disclosure for Hand-Held Shock Tester (Apr. 1964).

2. BUWEPS LD 549400, Parts List and Drawings for Hand-Held Shock Tester WOX-6A (Mar. 1964).

3. F. A. Votta, Jr., "The Theory and Design of Long-Deflection Constant-Force Spring Elements," Transactions of the ASME (May 1952).

* * *

DES'GN AND DEVELOPMENT OF A HYDRAULIC SHOCK TEST MACHINE PROGRAMMER*

J. R. Russell
American Machine & Foundry Company
Santa Barbara, California

The design, development, and test results of a drop-type shock testing machine programmer that can be adjusted to produce half sine, versine, triangle, and trapezoidal pulses in the range of 8 to 100 g at 18 to 240 millisecond durations, are discussed.

Deceleration forces are produced by hydraulic pressure. Hydraulic fluid is emitted through orifices in the wall of a hydraulic cylinder at a rate sufficient to generate a programmed pressure within the cylinder. Programmer versatility is derived from the capability of opening or closing the orifices in the cylinder wall to achieve a required shock pulse. The cylinder stroke can be adjusted to control deceleration displacements ranging from 4 inches to 5 feet. A computer program was developed to compute the open-close status of the orifices for any pulse within the operational limitations of the programmer. Orifice control is adequate to produce a ± 5 percent pulse accuracy.

Design considerations are discussed and the related technical approach is outlined. Design formulae are derived to support the technical discussion. An expression for orifice distribution as a function of cylinder stroke is derived by equating cylinder pressure to the deceleration pulse equation. Curves representing the expressions for various waveforms are given. The feasibility of a reasonable number of programmer orifices is demonstrated in the characteristic negative slope of the orifice area versus stroke curves.

Fluid inertia, encountered at the onset of the programmed pulse, posed the problem of eliminating the resultant deceleration spike. The problem is reduced to the solution of a linear first order differential equation by inserting a spring between the programmer and drop table. A latch mechanism locks the compressed spring. Fluid compressibility introduced the problem of stored energy in the second half of the programmed wave forms. The problem is analytically accounted for by assuming an apparent spring rate for the fluid column and adjusting the orifice distribution expression accordingly. Design considerations are summarized in a general discussion of the computer program developed to direct the orifice control function.

A development test program was successfully conducted. The results of the test are correlated with the design discussion. Photographs of the test setup and test pulse traces are given. The test data demonstrated that the programmer can produce predictable, accurate and repeatable half sine, versine, triangle, and trapezoidal wave forms.

*This paper was not presented at the Symposium.

INTRODUCTION

Drop type shock testing machines develop specified shock pulses by arresting a free falling specimen in accordance with a programmed deceleration-time function. The arresting device is generally called the programmer and assumes various configurations. For example, impact yielding a honeycomb aluminum block will develop a square or trapezoidal shock pulse; a lead extrusion may serve the same shock requirement or in the case of the half sine wave, a coil spring will simply do the job. In all cases, however, existing programmers are limited to an inflexibly narrow operating range. One programmer, in general, can only produce one wave form, i.e., half sine, triangle, versine, or trapezoid. Further, the energy absorption capability of available programmers is limited by the physical size of the specific programmer, and the braking systems employed to prevent rebound are sometimes elaborate and not necessarily reliable.

Clearly, if an extensive range of a laboratory shock testing is to be performed, the need for a more versatile programmer design exists. It is the purpose of this paper to present the design analysis and development test results for a shock programmer capable of producing all the standard shock wave forms in the range of 8 to 100 g and 18 to 240 milliseconds duration. The programmer was developed in response to a customer requirement for testing equipment weighing up to 200 pounds. Purchasing a multitude of single pulse programmers was not acceptable for the prospective test program from the standpoint of cost, space, and inconveniently long set-up times.

DESIGN CONCEPT

The problem was to design a programmer that, with simple adjustment, will produce half sine, versine, trapezoidal, and triangular shock wave pulses, ranging in amplitude from 8 to 100 g at durations extending from 18 to 240 milliseconds. Wave forms must be programmable for any wave shape, "g" amplitude, and duration within the limits of the programmer. Rebound would be eliminated if possible.

Previous experience with hydraulic buffers suggested that the buffer concept could be utilized to design an effective programmer. The frequent engineering task of decelerating a moving mass within tolerable "g" limits and without rebound, is readily solved by employing a suitable hydraulic buffer cylinder. Analogous to the buffer cylinder, a shock programmer also serves as a linear decelerator with the added sophistication of generating a precise shock wave shape. In either case, predictable deceleration of a moving mass is accomplished. Figure 1 diagrammatically shows a conventional, orifice-in-the-wall type buffer cylinder modified to achieve the wave shape generation control adjustment required of a programmer. The modification comprises the addition of valves to the conventional buffer.

To use the hydraulic buffer concept, two parallel design considerations were examined. First, that the allowable programmer cylinder stresses must be capable of handling the pressures associated with the maximum amplitude shock pulse; and secondly, the orifice control valves must be capable of adjusting the programmer to produce the various wave forms

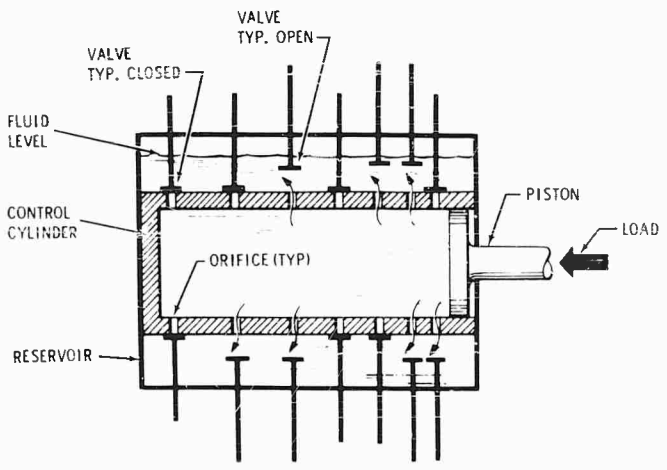

Fig. 1 - Wave shape generator, principle of operation

required. It will be assumed for the purpose of this paper that the mechanical strength of the programmer is designed to handle adequately the loads and accompanying stresses associated with the various shock pulses expected from the programmer. Design discussion shall be focused on the control valve requirement, wherein the fluid dynamic theory of the hydraulic buffer is applied to the design of the programmer valves.

The fluid dynamic theory applicable to the buffer is briefly described to relate how the buffer concept is applied to the programmer requirements. The hydraulic buffer is governed by Bernolli's flow equation, i.e., fluid flow through an orifice is proportional to the square root of the pressure drop across the orifice. An impacted buffer piston will, therefore, incur a reactive pressure from the fluid within the buffer cylinder proportional to the fluid exit velocity through the buffer control orifice. Exit velocity, and subsequently pressure, is controlled by the orifice area not covered by the moving piston at any instant of time. Control of orifice area as a function of piston travel is a basic buffer design consideration. The product of cylinder pressure times piston area will determine the decelerating force produced by the buffer cylinder.

Orifice area control in the programmer is accomplished by opening or closing orifices in the wall of the programmer cylinder in accordance with a computed area versus stroke relationship (see Fig. 1). The orifice in-the-wall approach was selected for its simplicity and adaptability to the programming requirement. Figures 2 and 3 show the orifice valve hardware developed for the concept test model. The sleeve shown in the photographs is installed concentric with the programmer cylinder to retain the valves and to serve as the reservoir indicated in Fig. 1.

PROGRAMMING

Opening the correct orifices to produce a particular shock wave requires that the functional relationship between orifice area and cylinder stroke be known. Arbitrarily selecting the half sine wave shape as an example, the derivation of orifice area (A_o) as a function of cylinder stroke will demonstrate the orifice control computation. Newton's second law is used to equate the buffer reactive force to the desired shock wave deceleration-time function which will be the half sine expression. Therefore,

$$PA_c = m(a_m \sin \omega t + g).$$

Bernolli's flow equation introduces A_o into the analysis.

$$P = \frac{\rho Q^2}{2A_o^2 C_d^2}.$$

By combining the force and pressure relationships, an expression of A_o as a function of time results:

$$A_o(t) = k\frac{(\cos \omega t + 1)}{\sin \omega t + \frac{g}{a_m}},$$

where

$$k = \frac{\rho A_c^3}{2C_d^2 m}.$$

Examination of the $A_o(t)$ expression reveals a problem unique to the buffer hardware concept. At $t = 0$ there would be no cylinder wall since A_o can become quite large. To circumvent this problem, a tolerable initial pressure is selected. In the case of a required five percent maximum deviation from the programmed pulse, the starting point for the shock pulse will be five percent of the peak "g" level programmed for a particular shock test; i.e., a 10,000-psi peak pressure programmed to produce a 100-g shock pulse would begin from a threshold pressure of 500 psi. Building the wave form up to the initial pressure will be subsequently

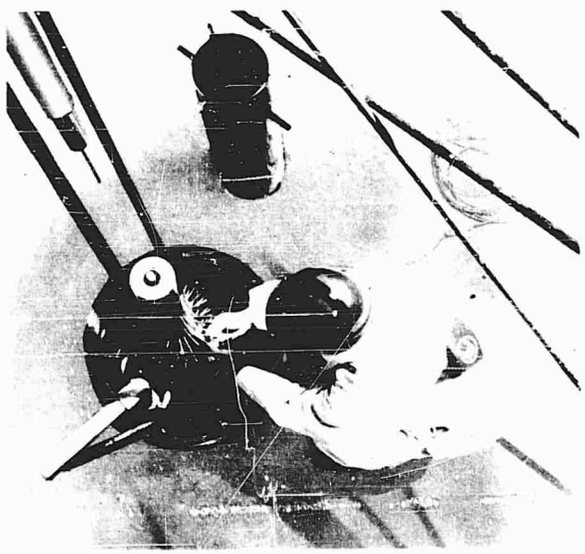

Fig. 2 - Programmer cylinder with valve retaining sleeve removed

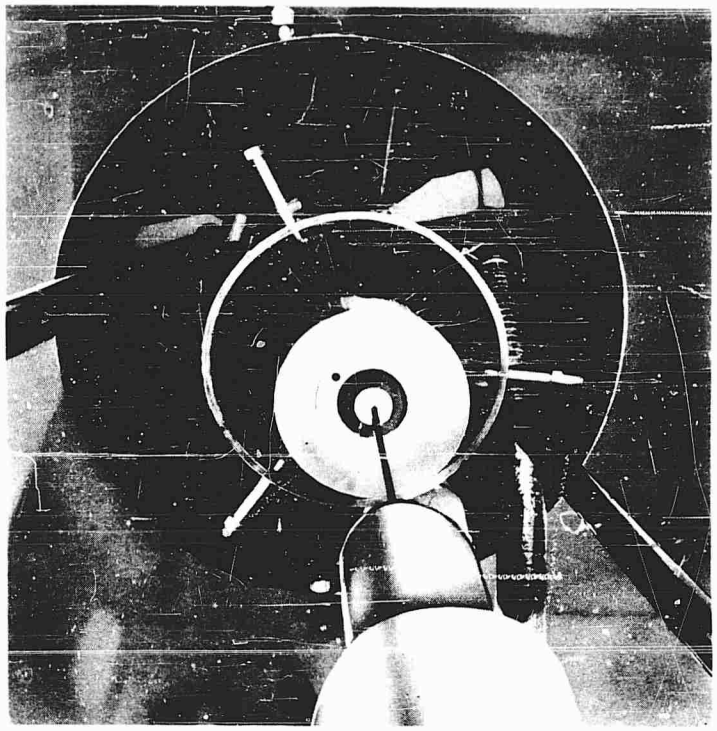

Fig. 3 - Top view of programmer cylinder with valve retaining sleeve installed

discussed as the onset problem. $A_o(x)$ is derived in parametric form from the two functions $A_o(t)$ and $x(t)$, where $x(t)$ is obtained by two integrations of the acceleration function, $a(t)$. For convenience $x(t)$ is expressed as a dimensionless term $\bar{x}(t) = x(t)/x_f$, where x_f is the total stroke. $A_o(\bar{x})$ represents the amount of orifice area remaining open at any position $\bar{x}$. Figure 4 shows a graphical representation of $A_o(\bar{x})$ for the half sine, triangle, and trapezoid wave forms. The initial orifice area is established by the required program accuracy which dictates the starting pressure. Significantly, all of the curves demonstrate a negative slope showing that the required orifice density decreases along the length of the cylinder. To capitalize on the decreasing orifice requirement, all of the programmed shock pulses are started from the top of the programmer cylinder. This reduces the total number of orifice holes needed to produce the desired programmer versatility and actually determines the feasibility of the buffer hardware concept.

Orifice area is translated into open-close orifice valve instructions by differentiating the $A_o(\bar{x})$ relationship. $dA_o(\bar{x})/d\bar{x}$ represents the amount of orifice area to be programmed open in an elemental length of stroke $d\bar{x}$ at position $\bar{x}$.

The half sine orifice expression is given below:

$$\frac{dA_o}{d\bar{x}} = \frac{-k\pi\sqrt{x_f}}{2} \frac{(2 - \cos\omega t)}{(\sin\omega t)^{3/2}} \quad \text{at} \quad 0 \leq \omega t \leq \pi .$$

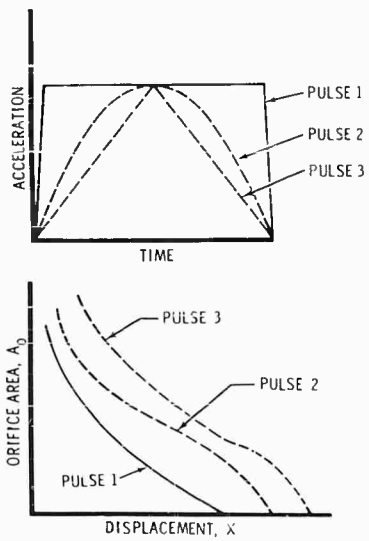

Fig. 4 - Corresponding functions of same shock pulse

The expression theoretically becomes infinite as $\bar{x}$ approaches x_f (i.e., ωt approaches π): however, since $A_o(\bar{x})$ also approaches zero simultaneous to $\bar{x}$ approaching x_f, the relatively small orifice area requirement near the end of the stroke comprises the infinite area rate of change at that point. Subsequently, the orifice programming is cut-off prior to a required area increase due to the $dA_o(\bar{x})/d\bar{x}$ relationship. The programmer cylinder is segregated into control stations, $\bar{x}$ wide, having a discrete number of holes available at each station. Valve status at each station is determined from the orifice area requirement at a particular station.

Valve changing is not as extensive as might be surmized to achieve various shock pulses. The $A_o(t)$ relationship derived earlier includes the ratio of [g] to the programmed "g" level as an additive term. Thus, for a large a_m, A_o is primarily a function of time and total stroke; and, an immediate programming advantage is the capability to achieve various peak "g" and pulse durations for a given wave shape by changing only the programmed drop height. Following one of the constant stroke lines given in Fig. 5 shows the peak "g" and pulse durations that can be achieved for the half sine pulse using a single valve program. The curves shown in Fig. 5 are a plot of the physical relationships of the equations of motion for a half sine deceleration pulse without rebound. The curves are not solely characteristic of the hydraulic programmer. They do, however, conveniently serve to epxress the operational range of the programmer. The shaded area of the curve represents the operational range of the programmer developed for a particular customer requirement that necessitated the development of the hydraulic programmer.

ONSET

To overcome the overly large orifice area problem at the start of a shock pulse, an initial pressure was calculated from the wave shape accuracy requirement. There is still however, the problem of overcoming the inertia of the piston and fluid without perturbing the shock wave. Namely, the programmer piston and fluid must be instantaneously accelerated from rest to a speed synchronous to that of the free falling drop table.

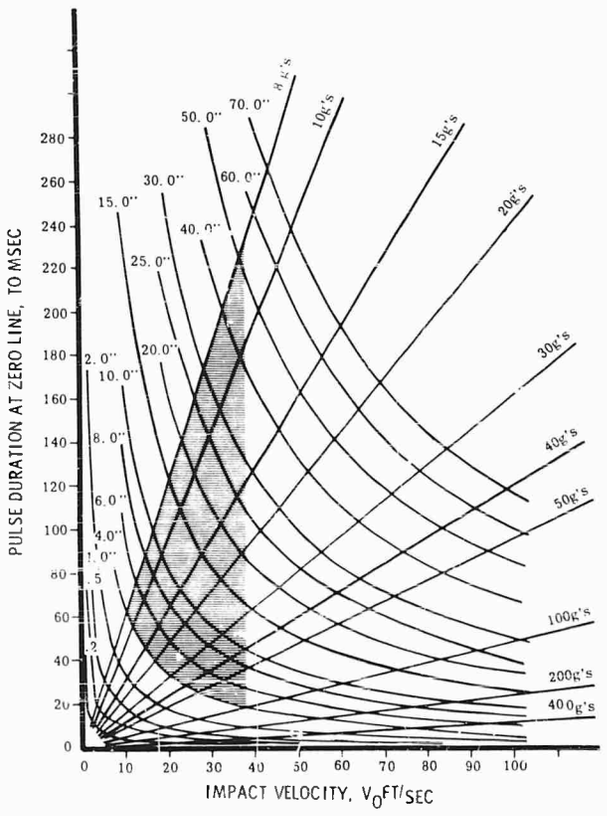

Fig. 5 - Physical relationships for 1/2 sine

Although the mass of the table is large compared to the mass of programmer piston and fluid, an abrupt velocity step can develop an intolerable pressure spike. In fact, testing indicated that the entire shock pulse was annihilated by direct impact between the drop table and programmer piston.

Design considerations relative to the initial pressure and hardware inertia problems occupy opposite ends of a specially controlled pressure region that precedes the programmed shock wave form. This region is referred to as the onset region. Onset control provides a ramp pressure rise from zero pressure to the initial pressure within the onset region of the cylinder. To achieve the desired pressure control, a spring is inserted between the drop table striker and cylinder piston (Fig. 6). In conjunction with the spring, the piston is positioned some distance above the first control orifice to allow full spring compression prior to the piston entering the programmed stroke region of the cylinder. A spring latch prevents spring unloading prior to the completion of the shock wave. Spring rate, spring compression, and piston lead above the control orifices are computed from the solution of a second order differential equation defining the forces acting on the spring-mass system. A single body problem is approximated by assuming that the striker mass is much greater than the combined masses of piston and cylinder fluid. The differential equation of motion for the combined fluid and piston mass, m, is:

$$-m\ddot{y} - c\dot{y} + ky = ky_o - kv_o t ,$$

where y_o and y define the respective initial and instantaneous positions of the piston measured above the first control orifice. In order to maintain a linear solution, the approximate damping term $c\dot{y}$ is used in place of the more exact velocity squared expression. V_o is the impact velocity of the striker and is assumed constant during the entire onset phase. Time, t, is measured from the moment of impact. k and c are spring and damping constants.

A solution of the differential equation must simultaneously satisfy the conditions $\dot{y} = 0$ at $t = 0$, and $y = 0$ at $\dot{y} = V_o$. By further requiring $\ddot{y}$ to be zero at $y = 0$, the relationship between the parameters required a critically damped system. This would require a spring constant and deflection adjustment for each program. The critically damped relationship $c = 2\sqrt{km}$ provides a basic design criterion for determining the onset spring rate. From the solution of the differential equation, programmed spring deflections are expressed by the equation:

$$S_{spring} = 2V_o \sqrt{\frac{m}{k}} .$$

Testing showed that the onset spring requirements for the restraint system shock testing program could be handled with four springs. The test indicated that the programmer was not as sensitive to spring adjustment as might be inferred from analysis. The test however, did demonstrate that the onset analysis was a good approximation and provided the empirical data needed to predict the spring requirement for any shock wave within the capability of the programmer.

DISCHARGE COEFFICIENT

Precision hydraulic pressure control across an orifice infers adherence to predicted flow through the orifice; wherein,

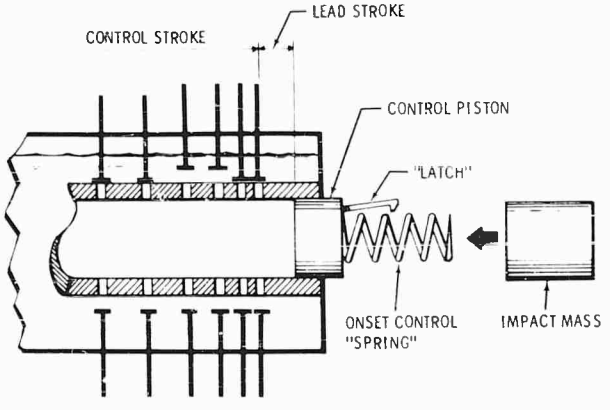

Fig. 6 - ON-SET control

$$Q = A_o C_d \sqrt{\frac{2P}{\rho}} .$$

Orifice area, A_o, is calculated to achieve a desired flow and pressure relationship based on the discharge coefficient, C_d. C_d prominently influences the predictability of the relationship between pressure and flow. It reflects the effects of ambient temperature variations and the geometry of the orifice. It further measures the flow efficiency of an orifice and, subsequently, determines the required orifice density in the programmer. Based on the preceding considerations, C_d is ideally a maximized value to reduce the required number of orifices, and will demonstrate a reluctance to variations caused by temperature changes. The geometry of the orifice governs the desired optimization of C_d.

The programmer orifices, because of the heavy wall cylinder used, are more accurately described as short flow tubes. C_d expresses the net velocity head losses through the orifice by summing entrance, pipe, and exit loss coefficients.

$$C_d = \sqrt{\frac{1}{\epsilon_{in} + \epsilon_{out} + \epsilon_{pipe}}} .$$

The exit loss, ϵ_{out}, approaches unity since the orifice exhausts fluid directly into the reservoir surrounding the programmer cylinder. Entrance loss, ϵ_{in}, varies between 0.05 and 0.50 depending on the degree of rounding possible at the transition between orifice and cylinder wall. Because of a relatively high orifice density at the top of the programmer cylinder, the entrance radii are limited to half the distance between orifice walls, or approximately 0.05 inches using 1/4-inch-diameter orifices. Test showed ϵ_{in} was 0.2 for the 1/4-inch-diameter orifice used in the concept test program.

ϵ_{pipe}, introduces an environmental consideration into the problem. The pipe friction factor used to calculate ϵ_{pipe} is dependent on the Reynolds number. Since the Reynolds number is a function of fluid viscosity and consequently temperature, the effect of a Reynolds number change is considered. With an ambient temperature range of 65 to 85°F assumed, analysis of the fluid viscosity changes shows that the pipe friction factor will vary less than 10 percent. Applying this variation to a nominal ϵ_{pipe} value of 0.174, the net effect of the assumed temperature range produces a C_d variation of less than 1.0 percent. The test results corroborated the C_d analysis and showed that C_d can be assumed constant over a moderate ambient temperature range.

COMPRESSIBILITY

Although hydraulic fluid is normally considered incompressible, Mil 5606 will compress approximately 3.5 percent at 16,000 psi—the peak operating pressure of the programmer. Because all programming is started at the top of the cylinder to take advantage of the maximum hole density in that region, a 100-g, 18-millisecond pulse will use only the top 4 inches of the cylinder. Since the orifice region must be at least 5 feet long to accommodate the low g, long duration shock pulses; the unstroked portion of the cylinder will perform as a fluid spring. To circumvent the problem of computing the effects of a fluid spring in series with the programmer, solid aluminum plugs are lowered into the unstroked portion of the programmer cylinder.

The fluid stroked by the piston cannot be ignored. To analyze the compressibility of the column of fluid stroked by the piston, an apparent spring rate is assumed for the stroked fluid column; and, the spring rate is further assumed to be linearly proportional to the fluid pressure. $A_o(t)$ is then rewritten as a function of time and spring rate. Since the rate of fluid exited from the cylinder is diminished by the volume of fluid compressed, the compressibility analysis showed the need for a harder orifice program (less number of orifices programmed open) than would be computed from the simple assumption that the fluid is incompressible.

TEST RESULTS

A concept feasibility test was conducted with a scale model to verify the design analysis and to obtain the empirical data necessary for full scale hardware design. The hydraulic programmer concept was successfully demonstrated by the test. This conclusion is drawn from the fact that predictable, accurate, and repeatable wave forms were achieved for the half-sine, versine, triangle, and trapezoidal shock pulses.

The test programmer was sized to demonstrate shock pulses in the range of 8 to 100 g acting on a 200-pound free-falling body. Figures 2 and 3 show the test programmer hardware and Fig. 7 shows the 22-foot drop tower installation used for the test program. A 2.6-inch cylinder bore and peak operating pressure of 5000 psi were selected to produce a 100-g pulse.

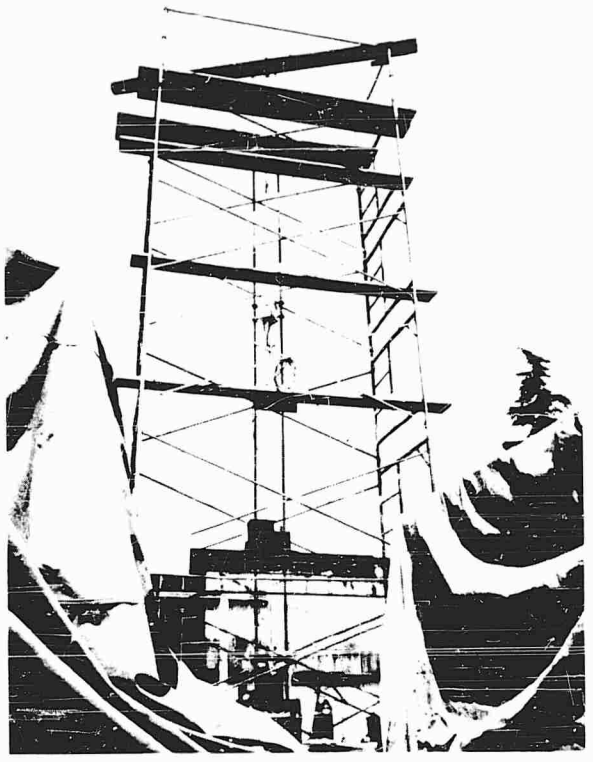

Fig. 7 - Thirty-foot drop tower installation for demonstrating the feasibility of the hydraulic programmer

A 21.0 inch maximum cylinder stroke was chosen to demonstrate the effects of onset on relatively long fluid columns. Combining the available stroke with the "g" range capability of the test hardware, the capacity of the test programmer extended continuously between 100-g at 18 milliseconds and 8-g at 145 milliseconds for the half sine wave. Versine and triangular pulses fall within a few percent of the half sine limitations. Trapezoid waves are limited to a maximum 10,000 g/second rate of force application.

The number and size of control orifices was selected on the basis of planned programming accuracy and hardware economics. A 1/4 inch diameter hole was selected for the orifice size to achieve ± 5 percent programming accuracy. One hundred and thirty seven of the holes were drilled to serve the requirements of the test.

Thirty shock pulses randomly selected from within the operational capability of the test hardware were run to demonstrate the feasibility of the hydraulic programmer. Figures 8-10 show typical traces recorded during the test. The traces were recorded by an instrumentation system sensitive to 250 cycles per second. Theoretical wave shapes are superimposed on the test traces to assist evaluating the test results.

The test did verify the accuracy of the design analysis. All of the test points were either achieved within the expected ± 5 percent accuracy or reasonably close to it. Where deviations from the programmed pulse did occur, the cause of the deviation was analytically identified. For example, test traces showed that the number and size of orifices chosen for the test cylinder did not allow sufficient orifice area control in some cases. Because the available orifice area distribution required averaging the computed orifice areas over an insensitively large region of the cylinder, the break points in the trapezoid and triangle waves could not be accurately programmed. The trapezoid trace (Fig. 10) demonstrates this problem by the rounded trailing slope in the test trace.

The test traces did confirm the accuracy of the onset analysis. Onset control is clearly

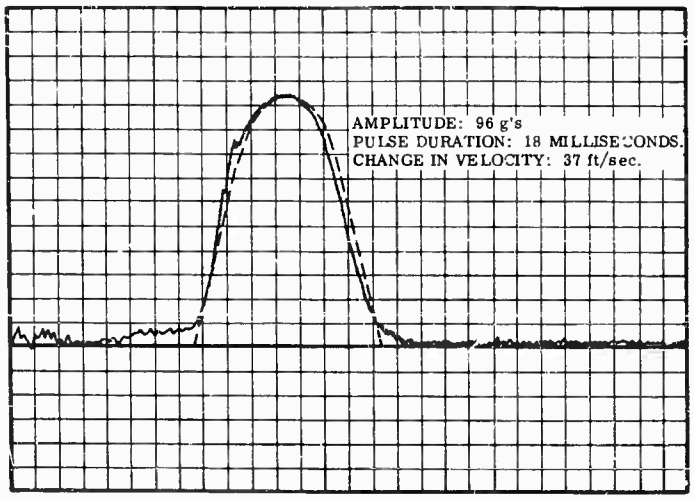

Fig. 8 - Half-sine wave shape (amplitude: 96 g)

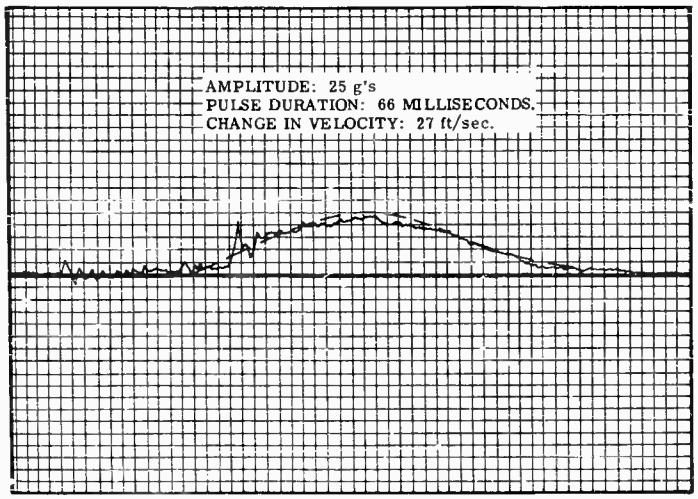

Fig. 9 - Half-sine wave shape (amplitude: 25 g)

shown in Fig. 8 by the ramp "g" rise preceding the programmed pulse.

PROGRAMMING

The problem of computing the open-close status of the orifice valves was programmed into a 704 computer. Computer readout gives the status of each orifice for any particular shock wave. A sequential numbering system identifies the spiral oriented orifices. Orifice coordinates are stored in the computer so that the computer will identify the individual orifices by their respective numbers.

Input information consists of a wave form code, peak "g," and drop height. In the case of the trapezoid, the rate of onset is also fed into the computer. Although drop weight is adjusted to be a constant parameter for the restraint system test program, weight may be programmed as a variable. However, no structural limitations were programmed so that weight variations must be analyzed to determine whether the maximum allowable cylinder pressure would be exceeded.

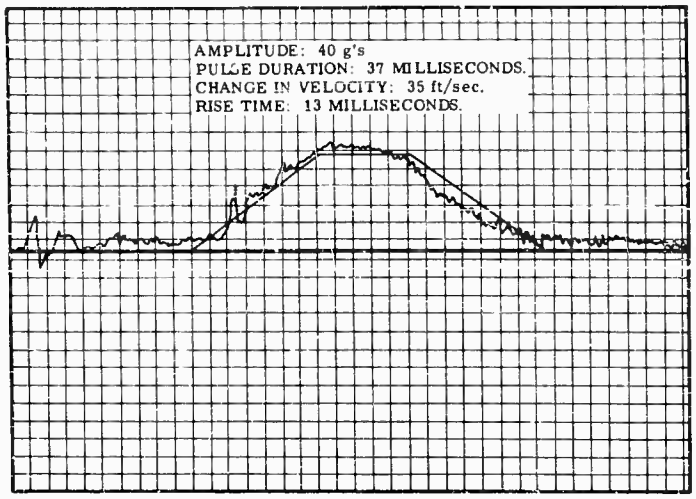

Fig. 10 - Trapezoidal wave shape (amplitude: 40 g)

Appendix A

LIST OF SYMBOLS

A_c = Cross sectional area of cylinder, in^2

A_o = Cross sectional area of orifice, in^2

m = Mass

A_m = Maximum programmed deceleration expressed in g's

g = Gravitational constant

ρ = Fluid mass density

C = Damping coefficient

k = Spring rate

Q = Fluid flow rate

C_d = Orifice discharge coefficient

* * *

SHAPING SHOCK ACCELERATION WAVEFORMS FOR OPTIMUM ELECTRODYNAMIC SHAKER PERFORMANCE*

W. R. Miller
LTV Ling Electronics Division
Anaheim, California

The purpose of this paper is to develop a method by which the KVA requirements of an electrodynamic shaker used to produce a shock pulse can be found. By use of this method it will be shown that by carefully shaping the prepulse waveform, the KVA requirements can be minimized while the main pulse shape remains virtually unchanged.

Shock testing on electrodynamic shakers has become increasingly more popular. Many specifications which require both shock and vibration testing of a specimen can be executed in less time, with the same fixtures, and with a smaller capital outlay by using a shaker for both parts of the test. Several different approaches have been used for shaker shock testing, but the method selected for treatment in this paper depends on the direct shaping of the shock pulse acceleration waveshape.

By carefully shaping the overall shock acceleration waveshape, optimum performance of an existing electrodynamic shaker/amplifier system can be obtained. Conversely, given a specific main pulse waveshape, the shaker/amplifier system required to produce that pulse can be minimized in size.

Typical shock acceleration waveshapes are the half sine pulse, the square pulse, the triangular pulse, and the terminal peak saw-tooth pulse. MIL-STD-810, Method 516, specifies half sine and terminal peak saw-tooth pulses. Several conditions must be met before a specific shock test can be performed with an electrodynamic shaker/amplifier system. These conditions are as follows:

1. The velocity of the shaker table must be zero at the end of the shock pulse.

2. The total displacement imparted by the shock pulse must be within the limitation of the particular shaker used (usually 1.0 inch).

3. The peak acceleration must not exceed the acceleration limit of the shaker used.

In order to meet condition (1) it is necessary to have an acceleration pulse opposite in direction to the main pulse either before or after the main pulse. The total pulse then must meet the condition:

$$\int_0^t a\,dt = 0 .$$

To meet condition (2) it may sometimes be necessary to provide some mechanical biasing system for the shaker table so the full displacement capability can be used. Another method to achieve this end is to use a very long acceleration pulse of low magnitude before the main pulse to "mechanically bias" the table.

*This paper was not presented at the Symposium.

The mobility analog circuit of the electrical and mechanical systems of the electrodynamic shaker is given. By first defining the monitoring point for the acceleration pulse one can solve the analog circuit graphically for any pulse shape. By changing the shape and duration of the prepulse the kva requirements can be altered for a given main pulse shape. For example, having the velocity negative at the positive peak of the main acceleration pulse reduces the overall voltage requirement for that pulse. This can be accomplished by shaping the acceleration prepulse.

The solution is accomplished by using graphical integration starting with the acceleration pulse shape. By use of this method and the definitions presented in the mobility analog, the magnitudes and phases of the various currents and voltages can be plotted directly and summed graphically (algebraically) to obtain the kva requirements. Careful adherence to basic criteria set forth in the body of the paper will allow optimization for the electrodynamic shaker/amplifier system performance.

INTRODUCTION

Shock testing on an electrodynamic shaker offers some very distinct advantages. First, vibration and shock testing may be accomplished on the same shaker system with the same fixtures. There is a very real savings indicated here in both time and capital expenditure. Second, shock pulses of different shapes, magnitudes, and durations may be preprogrammed on tape and fed to the shaker system in rapid succession, without changing the setup or making mechanical changes of the shock machine.

This method of shock testing is being used by many test laboratories throughout the country [1-3]. Several different approaches to this type of testing have been employed; however, this paper will deal only with the method by which the shock acceleration waveshape is synthesized directly. By making use of the shock acceleration waveshape, some basic vibration theory, and the mobility analog circuit of the shaker system to be presented herein, a method of determining the input voltage and current requirements of the shaker will be derived. The shock pulse shape can be altered to yield maximum shaker/amplifier performance by use of this method. Limitations of the method as a function of the type of load and frequency range are cited.

BASIC CRITERIA

Certain basic conditions must be met when shock testing is to be performed on an electrodynamic shaker. These conditions do, in fact, impose real limitations to the shock pulses which may be reproduced on the shaker. The limitations are all due to mechanical design features of the shaker itself, and are as follows:

1. The peak shock acceleration must not exceed the acceleration limit of the shaker, as specified by the manufacturer.

2. The velocity of the shaker armature must be zero at the end of the pulse.

3. The total displacement imparted by the shock pulse must be within the displacement capability of the shaker (usually 1.0 inch for electrodynamic shakers).

The first condition is basically a stress limitation of the armature structure due to differential accelerations throughout the armature structure. Adherence to this limitation insures a satisfactory life span for the armature. The second limitation is due to the fact that there is a definite displacement limitation of the shaker armature. Since displacement is the integral of velocity with respect to time (area under the velocity versus time curve) the velocity must return to zero to yield a definite value of displacement for the shock pulse under consideration. From basic physics it is found that the velocity is the integral with respect to time of the acceleration wave (area under the acceleration versus time curve). This presents a new problem, namely that the total area under the acceleration curve must now be zero for the complete shock pulse. To accomplish this end, it is necessary to add to the main acceleration waveshape an acceleration pulse opposite in sign and have the area under its profile equal to that of the main pulse. It is usually desirable to have the magnitude of the "prepulse" be small relative to the main pulse. MIL-STD-810, Method 516 specifies that the prepulse shall

NOTE: References appear on page 354.

have a maximum magnitude of 20 percent of that of the main pulse. The third limitation is strictly a mechanical one, in that it depends only on the design of the shaker. A 1-inch displacement is usually the maximum stroke for electrodynamic shakers of 1000 pounds force or greater. To use the full displacement capability, since the displacement imparted by the shock pulse is in one direction only, it is necessary to "bias" the shaker armature, either mechanically or electrically. Generally, shock testing with large loads is run at relatively low levels and the armature does not have to be "biased."

There are basic limitations imposed on the performance of the shaker by the power amplifier driving it. The basic limitations are as follows:

1. The armature velocity is limited by the output voltage capability of the driving amplifier.

2. The force capability (and therefore acceleration level) of the shaker is limited by the current capability of the amplifier.

3. The frequency response of the amplifier determines the shaker system capability to reproduce complex input acceleration waveshapes.

4. The design of the high voltage power supply in the amplifier determines maximum time duration available for a shock pulse (a stiff supply yields a long time duration capability).

It is not within the scope of this paper to discuss the above mentioned limitations to any length, rather, given the system limitations, a method will be determined to optimize a shaker/amplifier system.

Some basic relationships to be utilized in the development of this paper are as follows:

1. Given an acceleration waveshape the corresponding velocity waveshape can be found from the relationship,

$$V = \int_{t_o}^{t} A \, dt , \qquad (1)$$

or the velocity at any time, t, is equal to the area under the acceleration versus time curve from t_o to t.

2. Given a velocity waveshape the corresponding displacement waveshape can be found from the relationship,

$$D = \int_{t_o}^{t} V \, dt , \qquad (2)$$

or the displacement at any time, t, is equal to the area under the velocity-versus-time curve from t_o to t.

3. In order to combine the mechanical and electrical systems of the shaker and load, the mobility analog shall be used. In this analogy the relationships given below hold true:

(a) Spring stiffness is inversely proportional to electrical inductance. The exact relationship is as follows:

$$L\,(\text{henrys}) = \frac{0.113\ \mu^2}{K} , \qquad (3)$$

where K is the spring constant in pounds per inch and μ is the force/current ratio in peak pounds per peak ampere.

(b) Damping is inversely proportional to electrical resistance. The exact relationship is as follows:

$$R\,(\text{ohms}) = \frac{0.113\ \mu^2}{D} , \qquad (4)$$

where D is the damping constant in peak pounds per peak inch per second.

(c) Mass is directly proportional to electrical capacitance. The exact relationship is as follows:

$$C\,(\text{farads}) = \frac{2.29 \times 10^{-2}\ W}{\mu^2} , \qquad (5)$$

where W is the weight in pounds.

The various interrelationships in the mobility analog system are given in Table 1.

MECHANICAL SYSTEM

Two basic conditions will be dealt with in this paper. The first condition is the shaker bare table or with a dead mass load at frequencies low enough to be unaffected by resonances in the armature structure. The second condition is the shaker at frequencies unaffected by the armature resonances with a resonant load attached or the shaker bare table or with a dead mass load at frequencies up to the first armature axial resonance. The conditions shall be referred to as Cases (1) and (2), respectively, throughout the remainder of the paper (see Figs. 1 and 2).

TABLE 1

Mobility Analog Interrelationships

Characteristics	Spring-Inductance		Dashpot-Resistance		Mass-Capacitance	
	I	V	I	V	I	V
d (peak in.) =	$\frac{8.85LI}{\mu}$	$\frac{1.41V}{\mu f}$	$\frac{1.41RI}{\mu f}$	$\frac{1.41V}{\mu f}$	$\frac{.224I}{\mu c f^2}$	$\frac{1.41V}{\mu f}$
v (peak in./sec) =	$\frac{55.55LIf}{\mu}$	$\frac{8.85V}{\mu}$	$\frac{8.85RI}{\mu}$	$\frac{8.85V}{\mu}$	$\frac{1.41I}{\mu c f}$	$\frac{8.85V}{\mu}$
a (peak in./sec^2) =	$\frac{349LIf^2}{\mu}$	$\frac{55.55Vf}{\mu}$	$\frac{55.55RIf}{\mu}$	$\frac{55.55Vf}{\mu}$	$\frac{8.85I}{\mu c}$	$\frac{55.55Vf}{\mu}$
g = $\frac{a}{386}$ (peak g) =	$\frac{.904LIf^2}{\mu}$	$\frac{.144Vf}{\mu}$	$\frac{.144RIf}{\mu}$	$\frac{.144Vf}{\mu}$	$\frac{2.29 \times 10^{-2} I}{\mu c}$	$\frac{.144Vf}{\mu}$

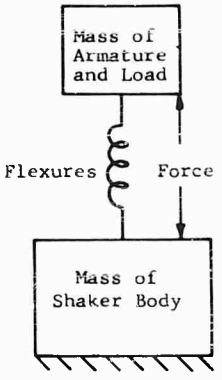

Fig. 1 - Mechanical system for Condition 1

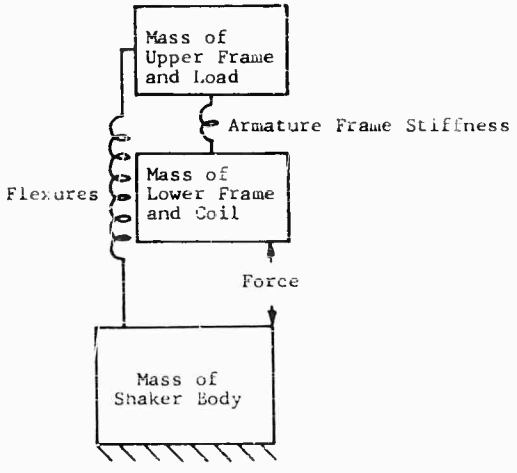

Fig. 2 - Mechanical system for Condition 2

For the sake of simplicity let it be assumed that the body of the shaker is tied to ground; that is, the isolation system is locked out. This assumption allows greater shock acceleration levels with large loads, as the relative displacement of the armature and body is reduced by the addition of an infinite mass to the body.

MOBILITY ANALOG

To complete the electrical analog circuit of the shaker the electrical parameters of the shaker must be known. A valid simplification of the electrical circuit of a shaker reduces to the midband ac resistance of the shaker in series with its total leakage inductance. Using this information the analog circuits for the two conditions were developed and are shown in Figs. 3 and 4. In Fig. 4 the analog of the flexures was left off because displacement at high frequencies is negligible. For very low frequency with the resonant load the equivalent flexure inductance should be added.

In Figs. 3 and 4, the various symbols are as follows:

C_a = Capacitance analogous to total effective weight of armature (farads)

C_c = Capacitance analogous to effective weight of driver coil and lower part of armature frame (farads)

C_ℓ = Capacitance analogous to weight of mass load (farads)

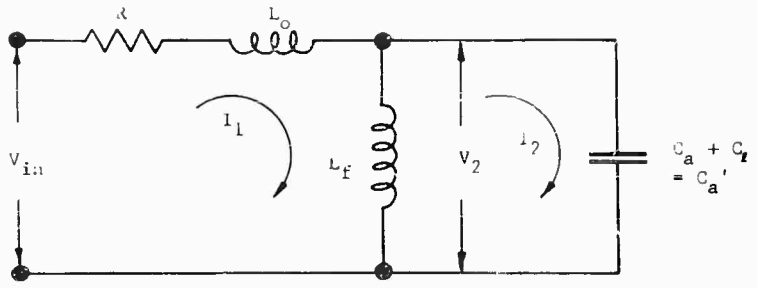

Fig. 3 - Analog circuit for Condition 1

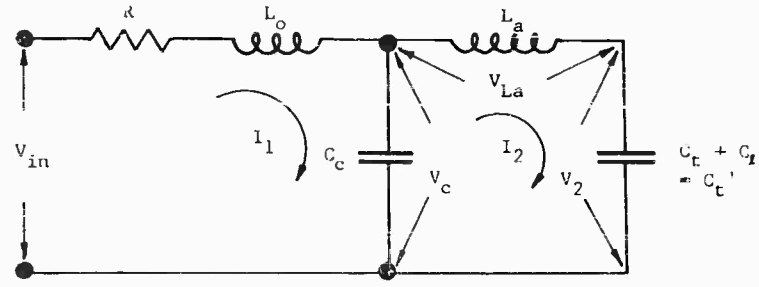

Fig. 4 - Analog circuit for Condition 2

C_t = Capacitance analogous to weight of table and upper part of armature frame (farads)

I_1 = Shaker input current (peak amperes)

I_2 = Current analogous to acceleration (force) applied to load (peak amperes)

L_a = Inductance analogous to armature frame compliance (henrys)

L_f = Inductance analogous to flexure compliance (henrys)

L_o = Total leakage inductance of shaker (henrys)

R = Midband ac resistance of the shaker (ohms)

V_{in} = Shaker input voltage (volts)

SHOCK ACCELERATION WAVESHAPES

Shock acceleration waveshapes vary in shape, magnitude, and duration. The main pulse shapes are generally half-sine, terminal peak saw-tooth, triangular, or square pulses while the prepulses are usually basically sinusoidal. MIL-STD-810, Method 516, requires the main pulse to be either half-sine or terminal peak saw-tooth. Magnitudes and durations are a function of the particular test requirements. Figure 5 shows the limit of accelerations as a function of pulse duration for the various pulse shapes.

The prepulse, so designated because it is placed before the main pulse (there is good reason why it should not follow the main pulse or be distributed before and after it), must now be added to the main pulse.

DERIVATION OF VOLTAGE AND CURRENT REQUIREMENTS

A step by step derivation is given for the shaker voltage and current requirements. By following this procedure it is felt that the requirements can be determined with a minimum of effort.

1. Given the main shock acceleration pulse shape, magnitude, and duration, check to see if it is within the capability of the shaker and system (i.e., acceleration limit and approximate

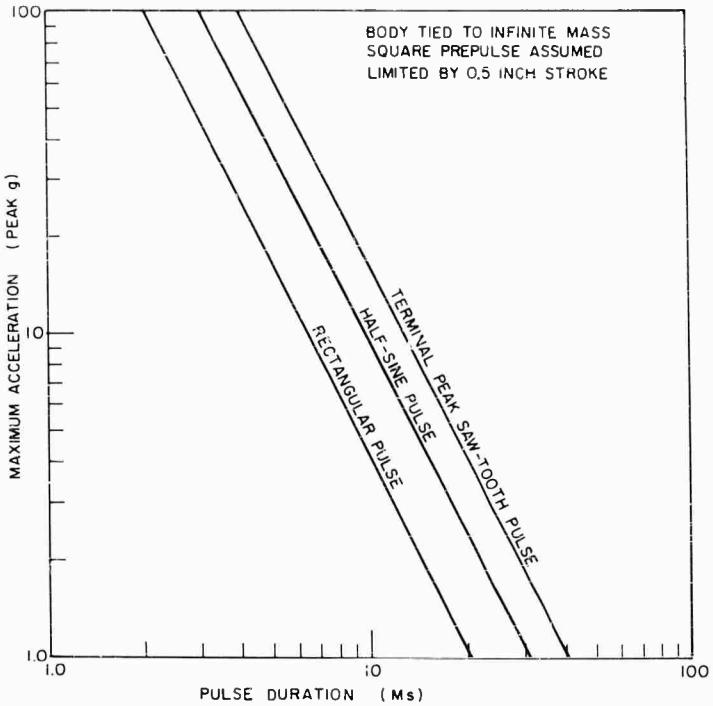

Fig. 5 - Maximum acceleration versus pulse duration

duration limit from Fig. 5). Add the prepulse to the main pulse, while keeping in mind that the area under the prepulse (velocity) must be equal to the area under the main pulse to obtain zero velocity at the termination of the pulse. A prepulse of short duration will yield a lower displacement than one of longer duration for the same magnitude. Keep the magnitude of the prepulse within the limits of the specification. The duration of the prepulse should be carefully determined to avoid undesirable fundamental frequencies (e.g., 60 cps). Plot the complete waveshape as a function of time, as shown in Fig. 6.

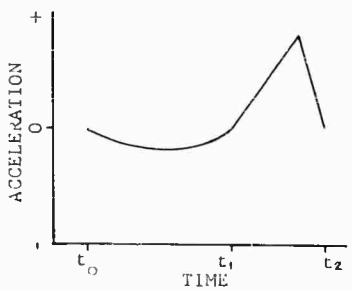

Fig. 6 - Acceleration versus time

2. Plot the velocity waveshape as a function of time by graphically integrating the acceleration versus time curve. The velocity at the end of the complete pulse should be zero, if not the prepulse must be redesigned to comply with this requirement (repeat step 1). Refer to Fig. 7.

Fig. 7 - Velocity versus time

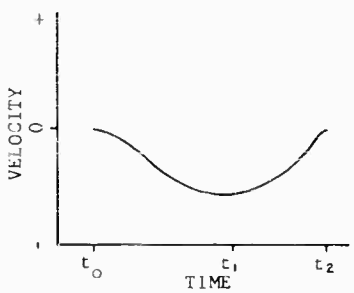

3. Similarly, plot the displacement waveshape as a function of time by graphically integrating the velocity curve, Fig. 8. Make sure that the displacement falls within the capability of the shaker.

4. Calculate the equivalent electrical values for all mechanical circuit elements, such as L_f,

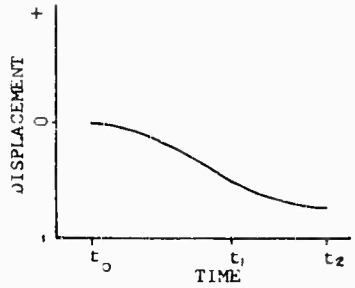

Fig. 8 - Displacement versus time

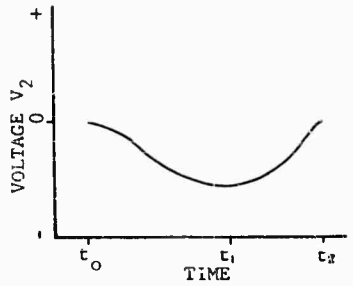

Fig. 10 - Voltage V_2 versus time

L_a, C_c, C_t', and C_a', using the relationships given in Eqs. (3) and (5).

5. Using the force/current ratio given for the shaker and Newton's second law determine and plot the current versus time curve for the capacitance analogous to the armature and load (i.e., C_a' or C_t'). Note here that the acceleration is being monitored on the top of the load or table in both cases. Using the two relationships mentioned above the expression for current is as follows:

$$I = \frac{Wa}{386\ \mu} \text{ amperes}, \qquad (6)$$

where W is the weight in pounds, a is acceleration in inches per second, and μ is the force/current ratio in peak pounds per peak ampere. The current I_2 is now plotted, and it should be the same shape as the acceleration curve (see Fig. 9).

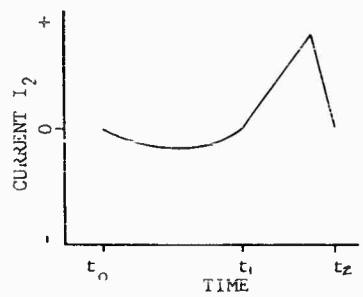

Fig. 9 - Current I_2 versus time

6. Calculate and plot the voltage drop across the capacitor (C_a' or C_t') by using the relationship:

$$V_2 = \frac{1}{C}\int I_2\, dt \text{ volts}, \qquad (7)$$

or the voltage is simply 1/C times the area under the curve of I_2 versus time, Fig. 10. This curve should be identical in shape to the velocity versus time curve shown in Fig. 7.

7. (For Case 2 only, see Fig. 4). Calculate and plot the voltage drop across L_a. Since the current I_2 passes through both L_a and C_t' the voltage drop, V_{La}, can be determined from the following expression:

$$V_{La} = L_a \frac{dI_2}{dt} \text{ volts}, \qquad (8)$$

or the voltage drop is simply L_a times the slope of the curve of I_2 versus time. The shape of the curve in Fig. 11 is identical to the shape of the jerk versus time curve.

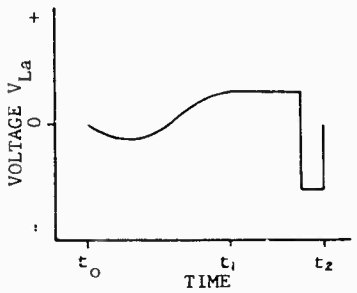

Fig. 11 - Voltage V_{La} versus time

For Case 2 add the V_{La} and V_2 curves to obtain the curve of V_C versus time (see Fig. 12), the voltage drop across the capacitor C_c (the analog of the lower part of the armature frame and the driver coil).

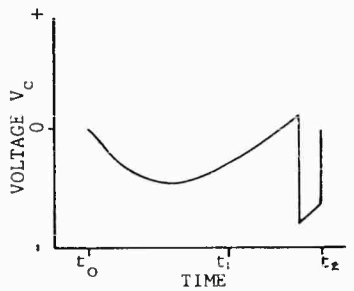

Fig. 12 - Voltage V_c versus time

8. (For Case 1 only, see Fig. 3). Calculate and plot the current through L_f, $I_1 - I_2$. C_a' and L_f are in parallel so the voltage across each element is the same. The current is then:

$$I_1 - I_2 = \frac{1}{L_f}\int V_2 \, dt \text{ amperes}, \qquad (9)$$

or the current is equal to the area under the curve of V_2 versus time (Fig. 10) multiplied by $1/L_f$. This curve, Fig. 13, should have the same shape as the displacement versus time curve, Fig. 8.

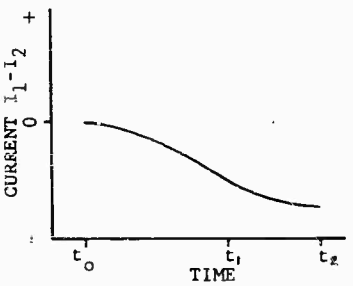

Fig. 13 - Current I_1-I_2 versus time (Case 1)

9. (For Case 2 only, see Fig. 4). Calculate and plot the current through C_c, $I_1 - I_2$. The voltage drop across C_c, V_c, was determined and is shown in Fig. 12. The current is determined as follows:

$$I_1 - I_2 = C_c \frac{dV_c}{dt} \text{ amperes}, \qquad (10)$$

or the current is equal to the slope of the curve of V_c versus time (shown in Fig. 12) multiplied by C_c, and is shown in Fig. 14.

Fig. 14 - Current I_1-I_2 versus time (Case 2)

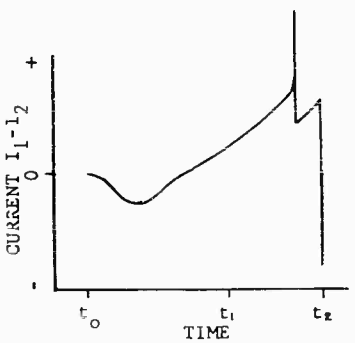

10. The next procedure is to obtain the curve of I_1 versus time. This can be accomplished for both cases by adding the curve of I_2 versus time, Fig. 9, to the respective curve of $I_1 - I_2$, Fig. 13 or 14. (See Figs. 15 and 16.)

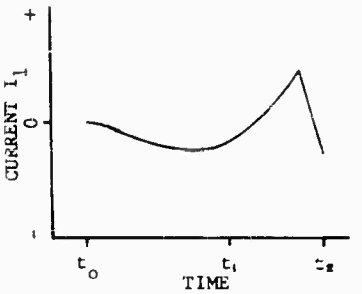

Fig. 15 - Current I_1 versus time (Case 1)

Fig. 16 - Current I_1 versus time (Case 2)

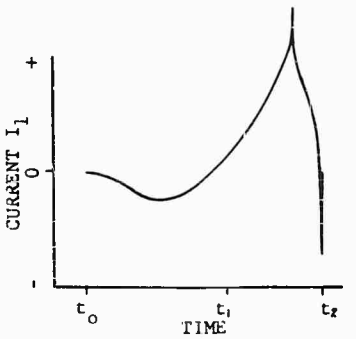

From this point on only Case 1 shall be considered, because the procedures are the same for both cases.

11. Calculate and plot the voltage drop across the midband resistance, R. This is done by multiplying the curve of I_1 versus time by R, that is:

$$V_R = I_1 R. \qquad (11)$$

The curve should have the same shape as Fig. 15, I_1 versus time (see Fig. 17).

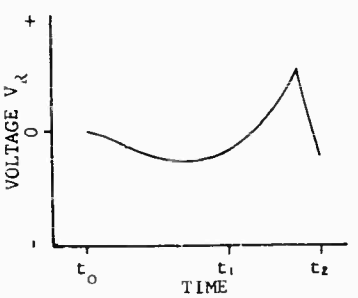

Fig. 17 - Voltage V_R versus time

12. Calculate and plot the voltage drop across the total leakage inductance, L_o. This is accomplished by using the relationship:

$$V_{Lo} = L_o \frac{dI_1}{dt} \text{ volts}, \qquad (12)$$

that is V_{Lo} is equal to slope of the curve of I_1 versus time multiplied by L_o, as in Fig. 18.

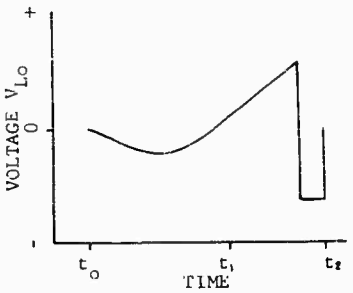

Fig. 18 - Voltage V_{Lo} versus time

13. Calculate and plot the input voltage, V_{in}. By keeping in mind that from Fig. 3 the input voltage, V_{in}, is the vector sum of V_R, V_{Lo}, and V_2 the curves of the three above mentioned voltages versus time can be algebraically summed to yield V_{in}, as shown in Fig. 19.

$$V_{in} = V_R + V_{Lo} + V_2 \text{ (algebraic sum).} \quad (13)$$

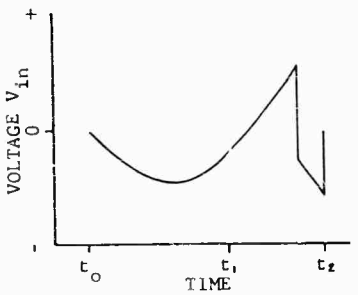

Fig. 19 - Voltage V_{in} versus time

The current requirement, I_1, and the voltage requirement of the shaker, V_{in}, are now determined.

DISCUSSION

Notice first that the velocity voltage, V_2, is opposite in polarity to the main acceleration pulse and therefore reduces the input voltage requirement, V_{in}. If the prepulse had been placed after the main pulse the velocity voltage would have added to the IR drop thereby increasing the voltage requirement of the main pulse. For this reason it is desirable to place the prepulse before the main pulse. The prepulse does not, nor is it designed to, displace the armature in a direction opposite to the displacement imparted by the main shock acceleration pulse. For this reason the displacement limitation must be set at one-half of the shakers displacement limit or about 0.5 inch, if no bias technique is employed. A prepulse sequence could, of course, be synthesized to displace the armature so that the full displacement capability of the shaker could be utilized. Such a pulse could conceivably look like the pulse shown in Fig. 20. Obvious from the figure, the pulse is quite complicated and would involve very sophisticated electronic equipment to synthesize. Since the magnitudes of the prepulses are limited and the zero final velocity condition must still be adhered to, the total pulse length could get out of

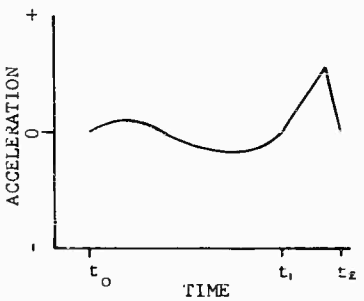

Fig. 20 - Acceleration versus time (pulse designed to allow full shaker stroke capability)

hand. A pulse such as shown in Fig. 20 could be handled in the same manner as the pulse given in Fig. 6. It may be possible to terminate the pulse with some net velocity and rely on the acceleration due to the flexure (spring) force to bring the velocity to zero. The spring force will, in all cases, bring the armature displacement back to the zero position at the natural frequency of the armature and load on the flexures. The method mentioned above could, if incorrectly calculated, allow the armature to hit the overtravel switch and cause the clamper circuit to fire across the armature. The acceleration pulse caused by the clamper may be very undesirable. In some cases, although not recommended, the armature may be allowed to actuate the clamper by design.

The shape of the prepulse is determined by the specific requirements of the test program. For a given peak prepulse magnitude the duration of the prepulse varies with the shape. A rectangular pulse gives the shortest duration for a given acceleration magnitude and velocity requirement, while a triangular pulse gives the longest duration. A half sine pulse gives a duration in between the two mentioned above for the same conditions. It necessarily follows that the square prepulse will yield the lowest displacement at the end of the complete pulse due to the fact that the area under its velocity-versus-time curve is a minimum. This feature makes

the rectangular prepulse desirable, but other disadvantages, such as its steep leading and trailing edges, which cause ringing and its difficult reproduction by large power amplifiers, outweigh this advantage. The lesson to be learned here is to keep the prepulse as much like a rectangle as possible for minimum table excursion. Reducing the displacement will change the input current and voltage requirements as $I_1 - I_2$ will be reduced for the low frequency case, Fig. 3. This reduction in $I_1 - I_2$ tends to increase I_1 which will in turn increase the I_1R drop. This may increase or decrease the V_{in} depending on the particular situation. Keep in mind that the overall voltage peaks should be kept to a minimum.

The valid frequency range for the circuit of Case 1 is up to about one quarter of the first axial resonance of the shaker in point. For most large shakers this is at least 500 cps. Above this frequency the circuit given in Fig. 4 should be used. Should a live load be used in the higher frequency region, an extension of the circuit for Case 2 could be developed. This would make the analysis somewhat more complicated, but still readily accomplished graphically.

By again referring to the analog circuit of Fig. 4, where the mechanical system is assumed to be the low frequency analog of the shaker with a resonant load attached, it should be noted that the location of acceleration monitoring point is very important in the circuit analysis. This paper assumed that the monitor was on the top mass, that is the current through C_t' was used as the starting point of the analysis. Had the shaker table been arbitrarily picked as the monitoring point, the current through C_c would have been used for the analysis (refer to step 5 under Derivation of Voltage and Current Requirements).

By use of the information and procedure given in this paper it is now possible, due to a better basic understanding of the mechanisms involved, to shape the prepulse of a shock acceleration waveform to produce optimum shaker/amplifier performance for a given shock test requirement. Also, given a test requirement, the amplifier power requirements can be easily derived using the method set forth herein.

SUMMARY

This paper has presented a basic outline of the uses of electrodynamic shakers in shock testing applications. The various advantages and limitations of this procedure have been given. Basic criteria, such as acceleration, velocity, and displacement limitations, were discussed at length. Some limitations of the power amplifier were brought out.

A quick review of basic relationships of simple harmonic motion was given as an introduction and review of the mobility analog system. A table of the various interrelationships in this system was presented.

The mechanical shaker and load system was presented for two basic conditions: (1) Shaker at low frequency bare table or with a simple mass load, and (2) Shaker at high frequency bare table or at low frequency with a resonant load. Following the presentation of the mechanical systems the electrical analog circuits, including the electrical parameters of the shaker, were given for the two cases. A discussion of the concept of the prepulse was presented.

A step by step method for graphically determining the power requirement, starting with the acceleration waveshape, constituted the body of the paper. A discussion of pertinent aspects of the prepulse concepts followed in addition to the aspect of optimizing performance of the shaker system.

This paper has presented basic insight into the field of shock testing on electrodynamic shakers. It has presented the concept of prepulsing and has given a method of determining the voltage and current requirements of the shaker for a given shock acceleration waveshape. Srom this information a clear picture of the methods in which the shaker performance can be optimized was presented.

The author wishes to acknowledge the assistance and encouragement rendered by Frank M. Tillou, Jr. and Edward P. Klein.

REFERENCES

1. Edward C. Adams, "Using an Electrodynamic Vibration Machine for Shock Testing" A.C. Spark Plug Report (Mar. 14, 1962).
2. Warren A. Hay and Ralph M. Oliva, "An Improved Method of Shock Testing on Shakers," Proceedings of IES (1963), p. 241.
3. D. J. Dinicola, "A Method of Producing High Intensity Shock with an Electrodynamic Exciter," Proceedings of IES (1964), p. 253.

* * *

SHOCK TESTING WITH VIBRATION SYSTEMS*

F. W. Young
Radiation Incorporated
Melbourne, Florida

Shock tests may be performed on vibration systems by two basic methods. In the first method the desired shock is obtained initially and a gradual force is applied to bring the test item back to rest. In the second method the test item is gradually accelerated to the required velocity and is suddenly brought to rest to produce the desired shock.

It can be shown mathematically that for a given saw-tooth shock, the peak velocity required is the same for both methods. It is significant, however, that with the first method peak velocity is required at the same instant that peak acceleration is obtained, whereas peak velocity occurs at zero acceleration with the second method. Hence, a less powerful amplifier is required with the second method.

Mathematics also show that the distance traveled during a saw-tooth shock of the first method is one-half that of the second method. This difference between the two methods, however, is significant only for long duration shocks.

The main limiting factors of performing shock tests on vibration systems are the structural integrity of the shaker, the output capability of the power amplifier, the velocity limit of the vibration system and the displacement limit of the shaker. Although there are several limiting factors, a wide range of shock tests have been performed on a vibration system by use of a shock pulse generator that provides a signal to (1) displace the shaker armature to almost one limit, (2) drive the armature to the required velocity in the opposite direction, and (3) produce the desired shock as the armature is brought to rest. This is considered to be a very practical and economical way of performing many shock tests.

INTRODUCTION

This paper will delve into the many methods of performing shock tests on vibration systems, discuss some of the limitations imposed by vibration systems, discuss a shock pulse generator, and discuss the wave shapes of some shock tests performed on a vibration system.

METHODS

Shock tests are presently performed by one of two basic methods (or a combination of the two) with present shock machines. The Hyge shock machine utilizes Method 1 — the desired shock is obtained initially and a gradual force is applied to bring the test item back to rest as shown in Fig. 1. The impact-type shock machine utilizes Method 2 — the test item is gradually accelerated to the required velocity and is suddenly brought to rest to produce the desired shock as shown in Fig. 2. Both of these methods can be used to perform shock tests on vibration systems. In Method 1, the shock pulse is applied to the vibration system while the armature is at rest; in Method 2, the shock pulse is applied while the armature is in motion.

*This paper was not presented at the Symposium.

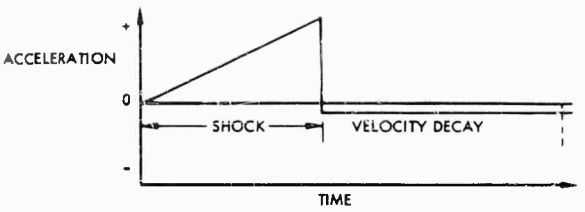

Fig. 1 - "Hyge" type shock

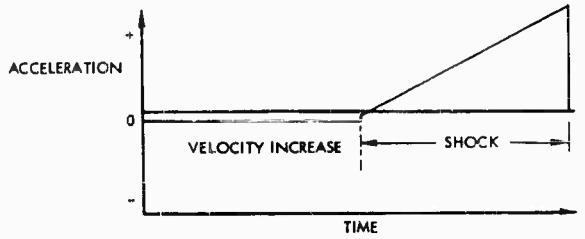

Fig. 2 - Impact type shock

Shock Portion or Cycle (Figs. 1 and 2)

For saw-tooth shocks the equation for acceleration is

$$A = K_1 t . \tag{1}$$

Since velocity is equal to the integral of acceleration we may write

$$V = \int K_1 t \, dt = \frac{K_1 t^2}{2} + C_1 . \tag{2}$$

Since velocity is equal to zero at $t = 0$ for Method 1, $C_1 = 0$ and velocity may be written as

$$V_1 = \frac{K_1 t^2}{2} . \tag{3}$$

Since displacement is the integral of velocity we may write:

$$D_1 = \int \frac{K_1 t^2}{2} dt = \frac{Kt^3}{6} + C_2 . \tag{4}$$

Since the displacement is zero at $t = 0$, $C_2 = 0$ and we may write

$$D_1 = \frac{K_1 t^3}{6} . \tag{5}$$

The acceleration equation for Method 2 is the same as for Method 1 and is given by Eq. (1). The velocity for Method 2 is given by Eq. (2). The constant of integration C_1 may be found if we let the velocity equal zero at the end of the shock pulse. Therefore,

$$V_2 = \frac{K_1 T_1^2}{2} + C_1 = 0 ,$$

or

$$C_1 = -\frac{K_1 T_1^2}{2} ,$$

where T_1 is the shock duration. Therefore,

$$V_2 = \frac{K_1 t^2}{2} - \frac{K_1 T_1^2}{2} . \tag{6}$$

Since displacement is the integral of velocity we have:

$$D_2 = \int \left[\frac{K_1 t^2}{2} - \frac{K_1 T_1^2}{2} \right] dt = \frac{K_1 t^3}{6} - \frac{K_1 T_1^2 t}{2} + C_3 . \tag{7}$$

If we let $D_2 = 0$ at $t = 0$, then $C_3 = 0$ and we may write:

$$D_2 = \frac{K_1 t^3}{6} - \frac{K_1 T_1^2 t}{2} . \tag{8}$$

By comparing Eq. (3) with Eq. (6), we see that in both cases the maximum velocity required for a given shock is

$$V_m = \frac{K_1 T_1^2}{2} , \tag{9}$$

where T_1 is the duration of the shock.

It is significant that the velocity must be a maximum at the end of the shock pulse (maximum acceleration) with Method 1, whereas the velocity is zero at the end of the shock pulse (maximum acceleration) with Method 2.

It is apparent from Eqs. (5) and (8) that with both methods, maximum travel (during shock pulse) will be obtained at the end of the shock ($t = T_1$). Under this condition, Eq. (8) may be rewritten as follows:

$$D_2 = \frac{K_1 T_1^3}{6} - \frac{K_1 T_1^3}{2} = \frac{K_1 T_1^3 - 3K_1 T_1^3}{6}$$

$$= -\frac{2K_1 T_1^3}{6} = -\frac{K_1 T_1^3}{3} . \tag{10}$$

Dividing Eq. (10) by Eq. (5), where $t = T_1$, we get:

$$\frac{D_2}{D_1} = \frac{\frac{-K_1 T_1^3}{3}}{\frac{K_1 T_1^3}{6}} = -2. \qquad (11)$$

We see that travel during the shock pulse of Method 2 is exactly twice that of Method 1. We also see from Eqs. (6) and (10) that the velocity and displacement for Method 2 is opposite to the direction of acceleration.

Velocity Portion (Figs. 1 and 2)

In order to obtain maximum velocity change with minimum acceleration and displacement:

$$A = -K_2. \qquad (12)$$

By integrating Eq. (12), we see that the velocity is given by:

$$V = \int -K_2\, dt = -K_2 t + C_4. \qquad (13)$$

For Method 1, the velocity at the start of the velocity decay period ($t = 0$) is found from Eq. (3) to be:

$$V_o = \frac{K_1 T_1^2}{2}.$$

Therefore,

$$C_4 = \frac{K_1 T_1^2}{2}$$

and

$$V_1 = \frac{K_1 T_1^2}{2} - K_2 t. \qquad (14)$$

By integrating Eq. (14), we see that the displacement is:

$$D_1 = \int \left[\frac{K_1 T_1^2}{2} - K_2 t\right] dt = \frac{K_1 T_1^2 t}{2} - \frac{K_2 t^2}{2} + C_5. \qquad (15)$$

If we set $D_1 = 0$ at $t = 0$, then $C_5 = 0$, and we will have:

$$D_1 = \frac{K_1 T_1^2 t}{2} - \frac{K_2 t^2}{2} \qquad (16)$$

for Method 1.

The velocity at the start of the velocity increase period of Method 2 is zero. Therefore C_4 of Eq. (13) is zero and Eq. (13) reduces to:

$$V_2 = -K_2 t. \qquad (17)$$

By integrating Eq. (17), we see that the displacement is:

$$D_2 = \int -K_2 t\, dt = -\frac{K_2 t^2}{2} + C_6.$$

If we set $D_2 = 0$ at $t = 0$, then

$$D_2 = \frac{-K_2 t^2}{2} \qquad (18)$$

for Method 2.

Since the velocity at the end of the velocity period is zero for Method 2, we can set Eq. (14) equal to zero when $t = T_2$. This gives

$$V_1 = \frac{K_1 T_1^2}{2} - K_2 T_2 = 0.$$

Therefore,

$$T_2 = \frac{K_1 T_1^2}{2K_2}. \qquad (19)$$

From Eq. (6), we see that the velocity is equal to

$$V = -\frac{K_1 T_1^2}{2} \qquad (20)$$

at the end of the velocity period for Method 2. Therefore, we can set Eq. (17) equal to Eq. (20) when $t = T_2$. This gives:

$$V_2 = -K_2 T_2 = -\frac{K_1 T_1^2}{2}.$$

Solving for T_2 gives

$$T_2 = \frac{K_1 T_1^2}{2K_2},$$

which is the same as Eq. (19). This means that the velocity duration would be the same for either method. If we substitute the velocity duration (T_2) for t in Eq. (16) we have:

$$D_1 = \frac{K_1 T_1^2 T_2}{2} - \frac{K_2 T_2^2}{2}.$$

Substituting Eq. (19) for T_2 gives

$$D_1 = \frac{K_1 T_1^2}{2}\left(\frac{K_1 T_1^2}{2K_2}\right) - \frac{K_2}{2}\left(\frac{K_1 T_1^2}{2K_2}\right)^2$$

$$= \frac{K_1^2 T_1^4}{4K_2} - \frac{K_1^2 T_1^4}{8K_2} = \frac{K_1^2 T_1^4}{8K_2} \quad (21)$$

for Method 1.

By substituting the velocity duration (T_2) into Eq. (18) we have

$$D_2 = -\frac{K_2 T_2^2}{2} = -\frac{K_2}{2}\left(\frac{K_1 T_1^2}{2K_2}\right)^2 = -\frac{K_1^2 T_1^4}{8K_2} \quad (22)$$

for Method 2. This shows that the displacement for both methods has the same magnitude but that the displacement for Method 1 is opposite to the direction of applied force.

Tables 1 and 2 give the important equations developed. Table 3 shows actual values for some typical shocks.

LIMITATIONS

Vibration systems provide limitations to shock testing due to their displacement, velocity, and output force capabilities. The amplitude of all shocks are limited by the output force of the vibration system. In many vibration systems the output force is limited by the power

TABLE 1
Equations for Saw-Tooth Shocks

	Method 1	Method 2
Acceleration	$A_1 = K_1 t$ (1)	$A_2 = K_1 t$ (1)
Velocity	$V_1 = \frac{K_1 t^2}{2}$ (3)	$V_2 = \frac{K_1 t^2}{2} - \frac{K_1 T_1^2}{2}$ (6)
Displacement	$D_1 = \frac{K_1 t^3}{6}$ (5)	$D_2 = \frac{K_1 t^3}{6} - \frac{K_1 T_1^2 t}{2}$ (8)

Where T_1 is the shock duration and K_1 is a constant that depends on the acceleration slope.

TABLE 2
Equations for Velocity Portion or Cycle

	Method 1	Method 2
Acceleration	$A_1 = -K_2$ (12)	$A_2 = -K_2$ (12)
Velocity	$V_1 = \frac{K_1 T_1^2}{2} - K_2 t$ (14)	$V_2 = -K_2 t$ (17)
Displacement	$D_1 = \frac{K_1 T_1^2 t}{2} - \frac{K_2 t^2}{2}$ (16)	$D_2 = -\frac{K_2 t^2}{2}$ (18)
Displacement	$D_1 = \frac{K_1^2 T_1^4}{8K_2}$ (21)	$D_2 = -\frac{K_1^2 T_1^4}{8K_2}$ (22)
Duration	$T_2 = \frac{K_1 T_1^2}{2K_2}$ (19)	$T_2 = \frac{K_1 T_1^2}{2K_2}$ (19)

Where T_1 and K_1 are the same as in Table 1, where T_2 is the duration of the velocity portion and K_2 is the acceleration level during the velocity portion.

TABLE 3
Acceleration Velocity and Displacement Levels for Typical Saw-Tooth Shocks on a Shaker System

(Based on 1-inch peak-to-peak armature travel)

Peak Shock Acceleration (Gravity Units)		Eq. (1)	30	60	121	172	30	60	86	30	33	47.1
Peak Shock Acceleration (10^4 in./sec^2)		Eq. (1)	1.16	2.32	4.67	6.64	1.16	2.32	3.32	1.16	1.27	1.81
Shock Duration (ms)			3	3	3	3	6	6	6	11	11	11
K_1 (10^6 in./sec^3)		Eq. (1)	3.86	7.72	15.6	22.2	1.93	3.88	5.55	1.06	1.16	1.66
Method 1	Peak Velocity (in./sec)	Eq. (3)	17.4	34.8	70.0	100	34.7	70	100	58.3	70	100
	Shock Displacement (in.)	Eq. (5)	.017	.035	.070	.100	.070	.140	.200	.234	.257	.367
	Velocity Acceleration (Gravity Units)	Eqs. (12) and (21)	-.397	-1.62	-6.87	-14.3	-1.68	-7.36	-16.2	-7.00	-8.71	-20.9
Method 2	Peak Velocity (in./sec)	Eq. (6)	17.4	34.8	70.0	100	34.7	70	100	58.3	70	100
	Shock Displacement (in.)	Eq. (8)	-.035	-.069	-.140	-.200	-.139	-.280	-.400	-.468	-.514	-.734
	Velocity Acceleration (Gravity Units)	Eqs. (12) and (22)	.405	1.68	7.43	16.1	1.81	8.92	21.6	10.1	13.3	49.7

amplifier rather than the shaker itself. During shock tests, shakers are limited by their structural integrity rather than by a maximum temperature rise. The structural integrity of most shakers is such that they can provide up to three times their vibration rating.

Limitations due to displacement and velocity depends upon the characteristics of the shock. Table 3 shows that the velocity can be a major limiting factor for shock pulses with durations from 3 to about 11 milliseconds. Table 3 also shows that displacement limitations cause the acceleration during the velocity period to be too high for many shocks with durations greater than about 6 milliseconds. As mentioned earlier, Method 1 introduces other limitations on shocks performed with vibration systems. Many vibration systems are not capable of providing maximum output force at the same instant the velocity is a maximum. For this reason, it is recommended that Method 2 be used for most shock tests on vibration systems.

SHOCK PULSE GENERATOR

In order to determine the required characteristics of a shock signal, it is necessary to determine the characteristics of a vibration system.

A vibration system may be represented by the equivalent circuit shown in Fig. 3.

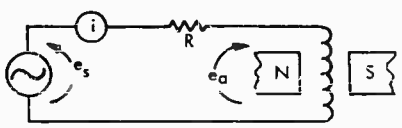

Fig. 3 - Equivalent circuit of shaker system

From the equivalent circuit, we can see that:

$$i = \frac{e_s - e_a}{R}$$

or

$$e_s = iR + e_a . \qquad (23)$$

For a saw-tooth shock, the equation for acceleration is

$$A = \frac{F}{M} = \frac{K_3 i + K_4 D}{W} = K_1 t ,$$

where D is the displacement of the armature from its neutral axis and W is the weight of the moving mass.

From this equation, we see that:

$$i = \frac{K_1 W t}{K_3} - \frac{K_4 D}{K_3} .$$

From Eq. (8), we see that

$$D_2 = \frac{K_1 t^3}{6} + K_5 t$$

where

$$K_5 = \frac{-K_1 T_i^2}{2} .$$

Therefore,

$$i = \frac{K_1 W t}{K_3} - \frac{K_4 K_1 t^3}{6K_3} - \frac{K_4 K_5 t}{K_3} ,$$

by grouping we have

$$i = \frac{(K_1 W - K_4 K_5) t}{K_3} - \frac{K_4 K_1 t^3}{6K_3} . \qquad (24)$$

From Fig. 3, it can be seen that

$$e_a = K_6 V + K_7 \frac{di}{dt} , \qquad (25)$$

where V is the velocity of the armature coil.

From Eq. (2), we see that

$$V = \frac{K_1 t^2}{2} + C_1 .$$

By differentiating Eq. (24) with respect to time, we get:

$$\frac{di}{dt} = \frac{K_1 W - K_4 K_5}{K_3} - \frac{K_4 K_1 t^2}{2K_3} . \qquad (26)$$

By substituting Eqs. (2) and (26) into Eq. (25), we get:

$$e_a = \frac{K_6 K_1 t^2}{2} + K_6 C_1 + K_7 \frac{K_1 W - K_4 K_5}{K_3} - \frac{K_7 K_4 K_1 t^2}{2K_3}$$

$$\left[\frac{K_6 K_1}{2} - \frac{K_7 K_4 K_1}{2K_3}\right] t^2 + K_6 C_1 + K_7 \frac{K_1 W - K_4 K_5}{K_3} . \qquad (27)$$

By substituting Eqs. (24) and (27) into Eq. (23), we have:

$$e_s = R\frac{(K_1W - K_4K_5)t}{K_3} - \frac{RK_4K_1t^3}{6K_3} + \left[\frac{K_6K_1}{2} - \frac{K_7K_4K_1}{2K_3}\right]t^2 + K_6C_1 + K_7\frac{K_1W - K_4K_5}{K_3}. \quad (28)$$

For a given set of conditions we can replace a group of constants with a new constant. This gives

$$e_s = K_8t^3 + K_9t^2 + K_{10}t + K_{11} \quad (29)$$

for saw-tooth shocks.

Equation (29) is only for the shock portion of the shock cycle. It can be shown that

$$e_s = K_{12}t^2 + K_{13}t + K_{14}, \quad (30)$$

for the velocity portion of the cycle shown in Fig. 2. It can also be shown that the input signal should be

$$e_s = K_{15}t + K_{16} \quad (31)$$

for the displacement portion of the cycle.

Figure 4 shows the block diagram of a shock pulse generator that performs the following functions:

1. Displaces the shaker armature to almost one limit of displacement in order that the full peak-to-peak displacement of the shaker be utilized during the velocity and shock portions of the cycle;

2. Drives the armature to the required velocity; and

3. Produces a shock signal that results in a saw-tooth output force.

The polarity of the shock generator signal can be reversed in order to perform shocks in both directions without remounting the test item.

Figure 5 shows the front panel and controls of a shock pulse generator. It can be seen that the displacement signal, velocity signal, shock signal, decay signal, and output level can all be varied for varying shock characteristics. The velocity, shock, and decay signals can be varied in duration as well as in amplitude.

SHOCKS PRODUCED BY A VIBRATION SYSTEM

Figures 6 through 16 show shock pulses produced on a vibration system and input signals. These shock pulse traces were all produced with about a 3-pound load on the shaker armature consisting of a flat magnesium plate. The instrumentation circuit consisted of an accelerometer, an accelerometer amplifier, and a broadband dc oscilloscope. There were no filters in the instrumentation circuit.

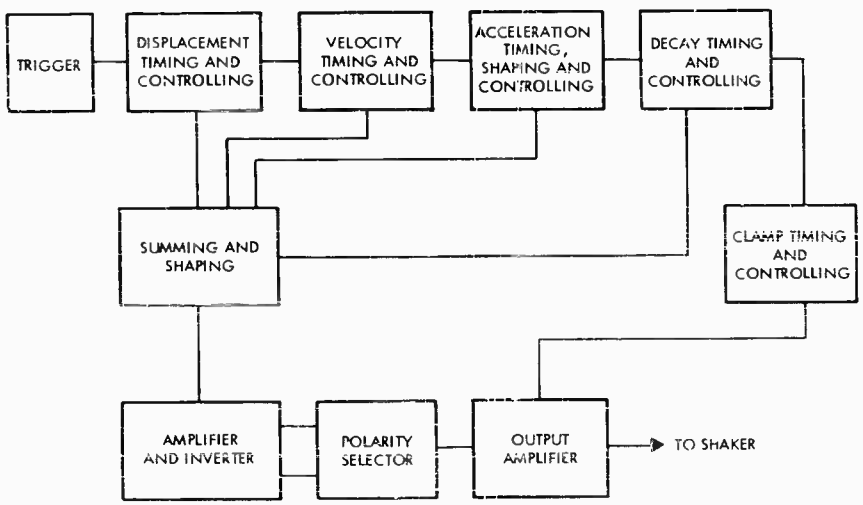

Fig. 4 - Block diagram of pulse generator

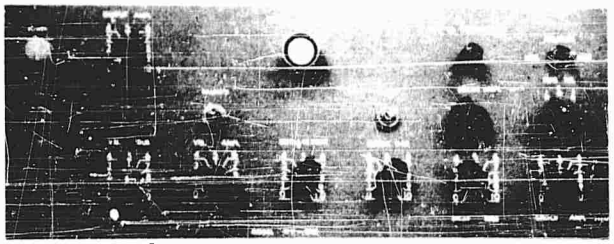

SHOCK PULSE GENERATOR

Fig. 5 - Shock pulse generator

Fig. 6 - Saw-tooth shocks (3 ms)

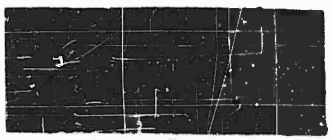

POSITIVE

10 g/cm VERT
0.5 ms/cm HOR

NEGATIVE

POSITIVE

50 g/cm VERT
0.5 ms/cm HOR

NEGATIVE

Fig. 7 - Saw-tooth shocks (3 ms)

Fig. 8 - Saw-tooth shocks (3 ms)

POSITIVE

50 g/cm VERT
0.5 ms/cm HOR

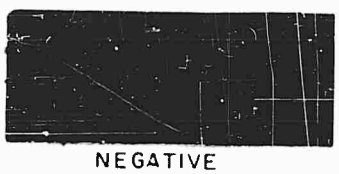

NEGATIVE

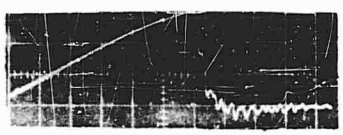

10 g/cm VERT
1 ms/cm HOR

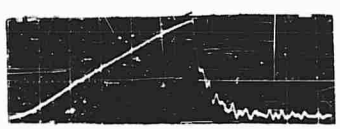

20 g/cm VERT
1 ms/cm HOR

Fig. 9 - Saw-tooth shocks (6 ms)

Fig. 10 - Saw-tooth shock and input signal (3 ms)

ACCELERATION
20 g/cm VERT
0.5 ms/cm HOR

INPUT SIGNAL
0.5 VOLT/cm VERT
0.5 ms/cm HOR

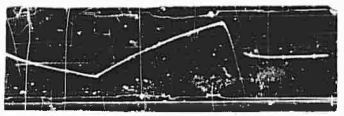

ACCELERATION
20g/cm VERT
5.0ms/cm HOR

(3ms SHOCK)

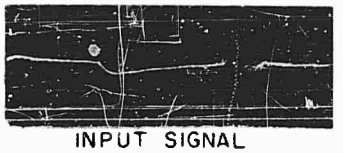

INPUT SIGNAL
0.5 VOLT/cm HOR
5.0 ms/cm HOR

Fig. 11 - Acceleration and input signal during displacement, velocity, and shock portions of shock cycle

50 g/cm VERT
0.5 ms/cm HOR

Fig. 12 - Triangle shock

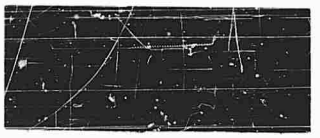

10 g/cm VERT
2ms/cm HOR

Fig. 13 - Square-wave shock

Fig. 14 - Displacement, velocity, and shock portion of shock cycle

ACCELERATION
50 g/cm VERT
5.0 ms/cm HOR

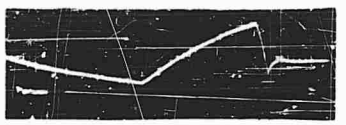

INPUT SIGNAL
0.5 VOLT/cm VERT
5.0 ms/cm HOR

ACCELERATION
20 g/cm VERT
0.5 ms/cm HOR

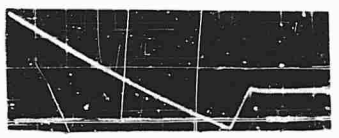

INPUT SIGNAL
0.2 VOLT/cm VERT
0.5 ms/cm HOR

Fig. 15 - Square-wave shock and input signal

Slight variations were made to the shock pulse generator in order to produce the shock pulses shown by Figs. 12 through 16. It can be seen that an acceptable triangle shock pulse can be generated. The figures also indicate that a square wave shock pulse can be generated with slight modifications to the input signal to reduce the rise time of the shock pulse. It is conceivable that half-sine shock pulses could also be produced on a vibration system. No attempt has been made to produce them with this shock pulse generator thus far.

ACCELERATION
20 g/cm VERT
5.0 ms/cm HOR

INPUT SIGNAL
0.2 VOLT/cm VERT
5.0 ms/cm HOR

Fig. 16 - Displacement, velocity, and shock portion of shock cycle

SUMMARY

We have studied two methods of performing shock tests with vibration systems, seen the limitations vibration systems impose on shock tests, investigated the characteristics of input signals for saw-tooth shocks, discussed a shock pulse generator, and reviewed some shock pulses produced on a vibration system. It is concluded that many shock tests can be performed on vibration systems.

* * *

HYGE SHOCK FACILITY IMPROVEMENTS*

R. M. Stuart
Hughes Aircraft Company
Tucson, Arizona

This paper describes improvements made in a Hyge shock facility to provide additional testing capabilities, to decrease the time per test, and to make the entire operation more economical and reliable.

The first of these improvements is the incorporation of timing circuits to control the start of the shock pulse and the recording equipment and to stop the recording equipment. These timing circuits are also used to program the initiation of shock at the proper time during an operational test of a missile or subsystem; a capability which is valuable when testing items that have very short operating times or when shock must occur at a critical time during an operational sequence.

The second improvement provides remote control of the nitrogen bottles used to pressurize the shock actuator. This eliminated a manual task and made the operation faster, less troublesome and more economical.

THE PROBLEM

Several problems are encountered when using conventional Hyge shock machines. Some of these problems are:

1. Coordinating high speed oscillograph recording equipment. Because there is separate manual control of both the shock tower and the recording equipment, as much as 20 feet of paper is run unnecessarily in order to be assured of obtaining data.

2. During operational shock tests on missiles or subsystems, it is necessary to apply the shock at the critical time during the operating sequence of the test specimen. The shock must be applied within a few milliseconds of a critical point during the operational sequence of the test specimen, and it is impossible to accomplish this by manually actuating the shock machine.

3. "One-shot" items with operating times of less than 1 second are occasionally operated without getting data because shock is initiated too soon or too late.

4. The task of individually opening and closing each nitrogen bottle manually while pressurizing the shock machine for a test is very troublesome and time consuming, particularly when several nitrogen bottles must be used.

The improvements described in this paper have been incorporated on a standard 6-inch Hyge shock facility. These improvements have eliminated the problems mentioned.

CONSTRUCTION AND OPERATION

The first three problems mentioned were eliminated by incorporating the control system shown in Fig. 1. The operation is started by either the manual pushbutton switch or a remote switch in some piece of test equipment or programmer. This closes relay K1 which starts the recording equipment and energizes the first time delay circuit which closes relay K2 at a fixed time later. This time delay is determined by the position of switch, S1. Relay K2 provides power to the solenoid valve, V1, which actuates the Hyge shock. Relay K2 also initiates the second time delay to open relay K1 and stop the recording equipment.

The fourth problem was eliminated by installing the Nitrogen Bottle Control System

*This paper was not presented at the Symposium.

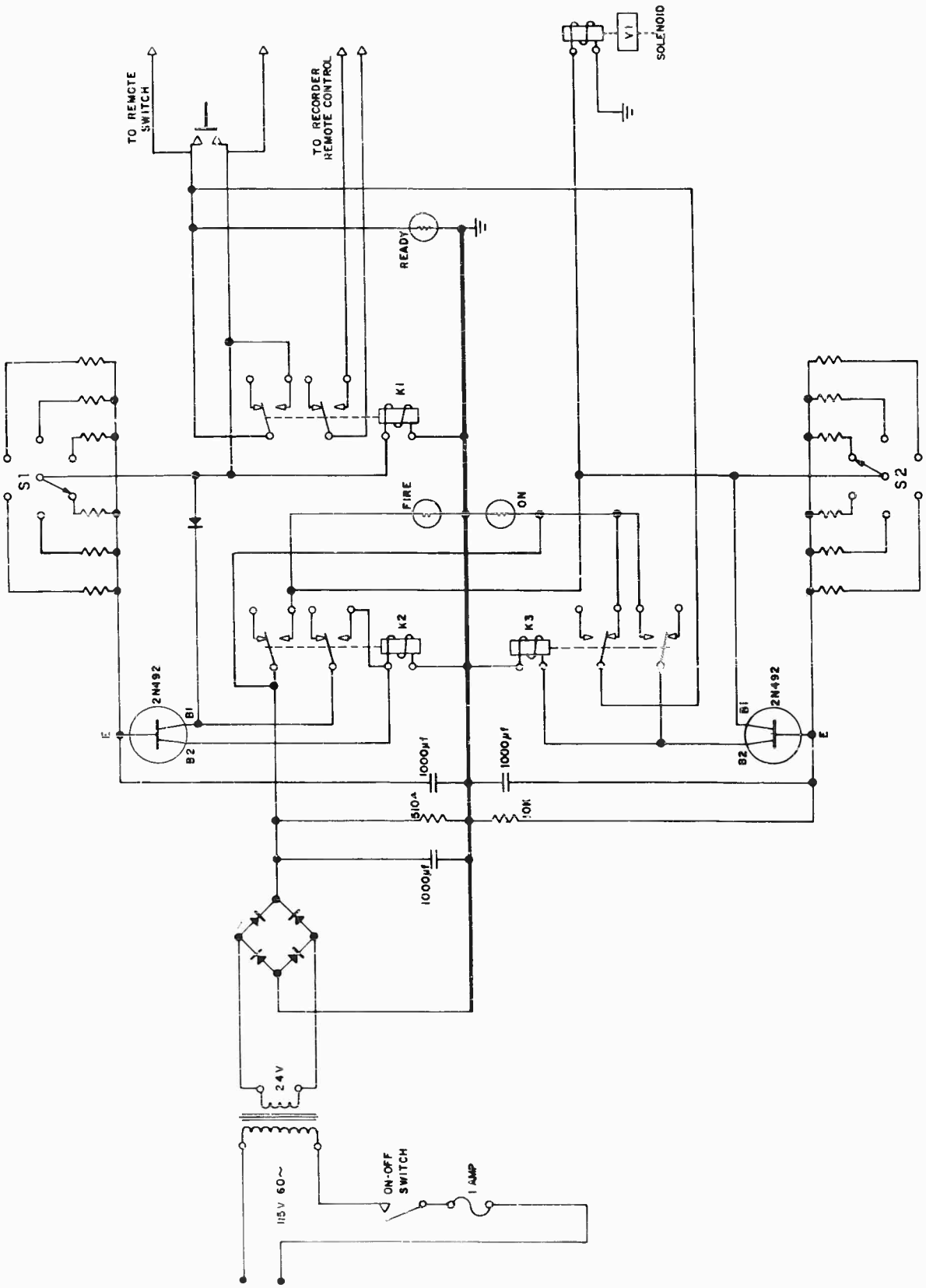

Fig. 1 - Hyge control circuit

shown in Fig. 2. This system allows each bottle to be selected individually by the operator. After the test, the high pressure nitrogen remaining in the Hyge shock machine may be partially returned to the lower pressure bottles. It is necessary to use check valves as shown to prevent leakage back through the solenoid valves.

ADVANTAGES

Many advantages have been derived from these improvements. The time delay circuits may be selected for a wide range of times depending on the test being conducted. The repeatability errors of the time delay circuits are extremely small. These timing circuits may be initiated manually or by other test equipment, as they are during present operational tests of TOW missiles. This allows batteries, gyros, electronics, and other equipment to be operating the precise amount of time that they would be operating before an actual launch. This operation could not be duplicated by manual controls. The control of recorders by these timing circuits ensures that the recorders are running only during the time that data must be obtained. As little as 2 feet of paper is used during a test in which data is desired only during the shock and while running the recorder at 100 inches per second.

"One shot" items with short operating times such as batteries and squib-actuated devices can now be programmed to operate during shock since the application of shock can be controlled within a few milliseconds.

The remote control of the nitrogen bottles has made the task of pressurizing the shock machine less troublesome and faster. By refilling the lower pressure bottles after the shock with the gas remaining in the Hyge's bottom chamber, the bottles can be used for many more shocks. Before installing the solenoid valves, refilling the bottles from the Hyge was found to be too troublesome to accomplish.

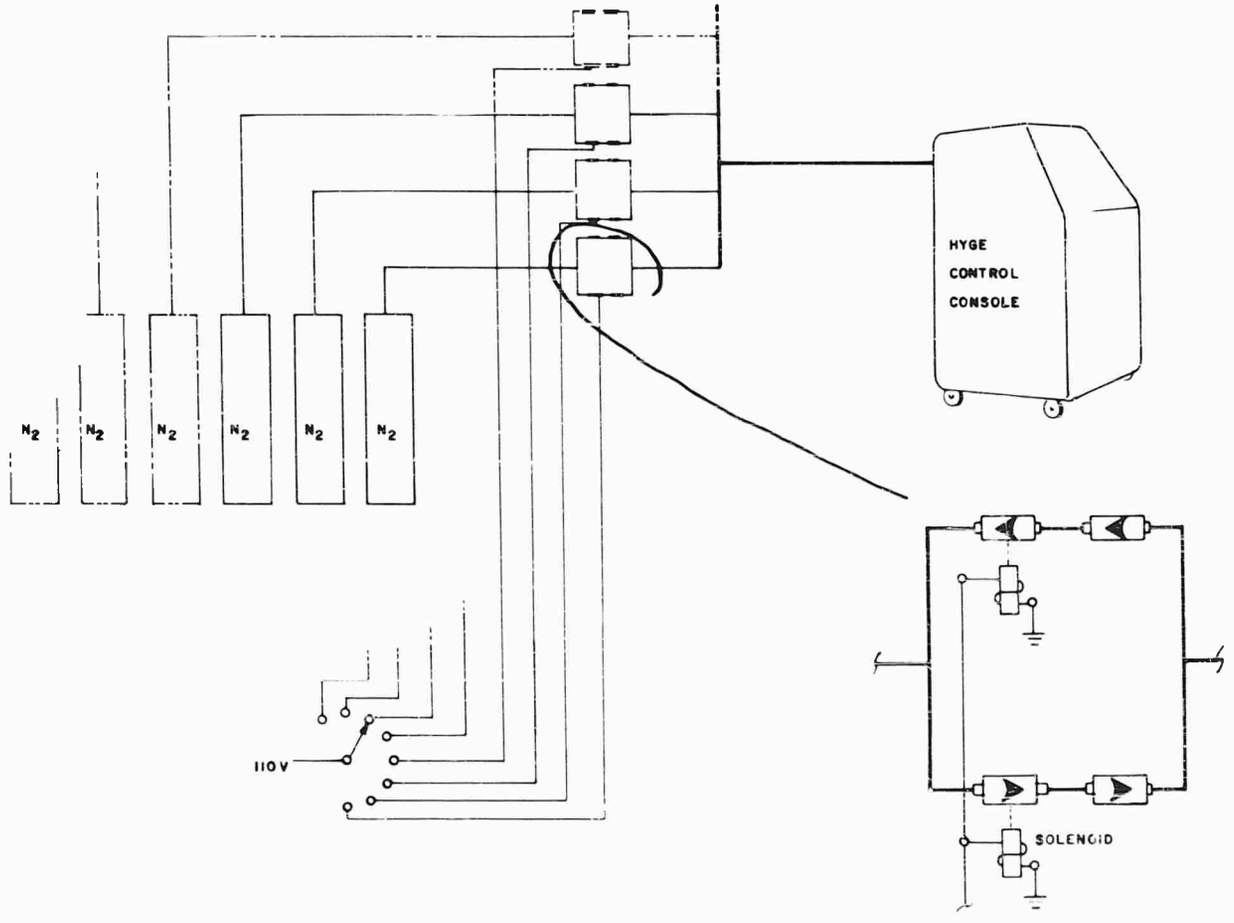

Fig. 2 - Gas supply control system

CONCLUSION

The improvements incorporated in the Hyge shock facility have greatly increased its capabilities and reliability. The operation is more economical since less recorder paper and nitrogen are used and because of the reduction in preparation time.

* * *

DISTRIBUTION

Aberdeen Proving Ground, Md.
- Att: Ballistic Research Lab. 1
- Att: Development & Proof Services 1
- Att: Physical Test Lab. 1

Advisory Group on Electron Tubes, New York
- Att: Secretary 1

Air Defense Command, Ent AFB
- Att: Deputy for Civil Engineering 1
- Att: ADIRP 1

Air Force Packaging Evaluation Agency, Brookley AFB
- Att: MOSPR 1
- Att: MONE 1

Air Proving Ground Center, Eglin AFB
- Att: PGTRI, Technical Library 1

Air Force Headquarters, DC
- Att: Operations Analysis Off., Off. Vice Chief of Staff, Library 2
- Att: AFDRD-GW 1

Air Force Logistics Command, W-PAFB
- Att: G. P. Civille, MCTEP 1

Air Force Missile Development Center, Holloman AFB
- Att: RRRT/Miss R. Porter 1
- Att: MDS/Dr. M. G. Jaenke 1
- Att: MDSGL-2/Mr. H. J. Dunbar 1
- Att: MDSGS/Mr. J. H. Gengelbach 1
- Att: MDSTE/Mr. P. N. Sonnenburg 1

Air Force Missile Test Center, Patrick AFB
- Att: MT LLL-3 (Classified Material) 2
- Att: MU-135, Technical Library (UNCLASSIFIED) 1

Air Force Office of Scientific Research, DC
- Att: Library 1

Air Force Regional Civil Engineer
- Att: North Atlantic Region, AFRCE-NA-A 1
- Att: South Atlantic Region. AFRCE-SA-E 1

Air Force Rocket Propulsion Lab., Calif.
- Att: Mr. A. J. Davies (RPFDE) 1
- Att: Mr. R. A. Silver 1

Air Force Systems Command, Andrews AFB
- Att: Technical Library 2

Air Force Weapons Laboratory, Kirtland AFB
- Att: Development Test Division 1
- Att: Dr. W. E. Fisher, WLRS 1
- Att: SWOI 631-276 1

Army Air Defense Center, Ft. Bliss
- Att: Technical Library 1

Army Chemical Center, Maryland
- Att: Library 1

Army Electronics Materiel Agency, Phila. 1

Army Electronics Materiel Support Agency, Ft. Monmouth 1

Army Electronics R&D Laboratory, Ft. Monmouth
- Att: SELRA/SL-ADT 1
- Att: SELRA/SL-PEE 1
- Att: SELRA/SL-PRT 1
- Att: SELRA/SL-G 1
- Att: SELRA/SL-GTF 1
- Att: Mr. J. J. Oliveri 1

Army Engineer District, New York
- Att: NANGD 1

Army Engineer R&D Laboratories, Ft. Belvoir
- Att: Package Development Branch 1
- Att: Mr. A. Carolla 1
- Att: Director of Research 1
- Att: Chief, Spec. Proj. Branch 4

Army Engineer Waterways Experiment Station, Vicksburg
- Att: Mr. J. M. Strange 1

Army Erie Ordnance Depot, Pt. Clinton
- Att: Chief, Materiel Testing Div. 1

Army Materials Research Agency, Watertown
- Att: Dr. Reinier Beeuwkes, Jr. 2

Army Materiel Command, DC
- Att: AMCRD-RS-CM 1

Army Materiel Command, Redstone Arsenal
- Att: Technical Library 4

Army Missile Command, Redstone Arsenal
- Att: AMSMI-RB 1
- Att: AMSMI-RG 1
- Att: AMSMI-RL 1
- Att: AMSMI-RS 1
- Att: AMSMI-RT 1
- Att: AMSMI-RTR, Mr. J. M. Taylor 1
- Att: AMSMI-RSM, Mr. E. J. Wheelahan 1

Army Mobility Command, Centerline
- Att: Mr. Otto Renius 1

Army, Office Chief of Engineers, DC
- Att: ENGMC-EM 2

Army, Office of Quartermaster General, DC
- Att: Military Planning Division 1

Army, Office Chief of Research & Development, DC
Att: Scientific & Technical Information Division 1

Army, Office Chief Signal Officer, DC
Att: Research & Development Division 1

Army, Office Chief of Transportation DC
Att: Director of Transportation Engineering 1

Army Ordnance Ammunition Command, Joliet
Att: ORDLY-T 1
Att: NNSC/A 1

Army Tank-Automotive Center, Warren
Att: SMOTA-RRS, Tech. Library 1
Att: SMOTA-RCE.3, Mr. D. J. Hackenbruch 1
Att: SMOTA-RRC 1
Att: Mr. D. W. Rees 1

Army Transportation Engineering Agency, Ft. Eustis
Att: Library 1
Att: Mr. L. J. Pursifull 1

Army Transportation Research Command, Ft. Eustis
Att: Dr. R. L. Echols, Physical Sciences Res. Group 1

Arnold Engineering Development Center, Arnold AFS
Att: AEOIM 1

Atomic Energy Commission, Oak Ridge
Att: Office of Technical Information 6

Atomic Energy Commission, DC
Att: Library 1
Att: Tech. Evaluation Branch (Army Reactors) Division of Reactor Development 1

Aviation Supply Office, Philadelphia
Att: Code TEP-1 1

Ballistic Systems Division, USAF, Norton AFB
Att: Technical Data Division 3

Boston Naval Shipyard, Mass.
Att: Library 1

Bureau of Medicine & Surgery, USN, DC
Att: Research Division 1

Bureau of Naval Weapons, USN, DC
Att: DLI-3 2
Att: FWAA, C. H. Barr 1
Att: RREN-5 5
Att: RRMA 1
Att: RAAE-2 1
Att: RM-3 2
Att: RM-2 1
Att: RSSH 2
Att: FWAE 1
Att: RREN-8 1

Bureau of Naval Weapons Rep., E. Hartford 2

Bureau of Naval Weapons Rep., Pomona
Att: Chief Engineer 1
Att: Metrology Dept. Code 60 1

Bureau of Naval Weapons Rep., Sunnyvale 1

Bureau of Ships, USN, DC
Att: Code 423 20

Bureau of Supplies & Accounts, USN, DC
Att: Library 1

Bureau of Yards & Docks, USN, DC
Att: Code D-440 1
Att: Code D-220 1
Att: Code D-220 (UNCLASSIFIED) 6

Coast Guard Headquarters, DC 1

David Taylor Model Basin, UERD, Portsmouth
Att: Code 281A 1
Att: Mr. E. W. Palmer 1

David Taylor Model Basin, DC
Att: Library 3
Att: Mr. Harry Rich 1
Att: Code 591L, Mr. J. A. Luistro 1
Att: Contract Res. Administrator 1

Defense Atomic Support Agency, DC
Att: Technical Director 1
Att: Weapons Development Division 1
Att: Mr. John G. Lewis 1

Defense Atomic Support Agency, Livermore
Att: Administrative Officer 1

Defense Documentation Center, Va. 20

Defense Intelligence Agency, Va.
Att: DIAAP-1K2 1

District Public Works Office, 14th Naval District 1

Electronic Systems Division, AFSC, L. G. Hanscom Field
Att: Library 1

Electronics Supply Office, USN, Great Lakes 1

Federal Aviation Agency, DC
Att: Emergency Readiness Div., Off. Plans & Requirements 2
Att: Chief, Tech, Processing Br., Library Serv. Div. (UNCLASSIFIED) 1

Forest Products Laboratory, Dept. of Agriculture, Madison
Att: Robert Stern (UNCLASSIFIED) 1

Frankford Arsenal, Philadelphia
Att: Library Branch, CC 0270/40 1
Att: Mr. David Askin, CC 1730/230 1

Harry Diamond Laboratories, DC
Att: Chief, Lab. 700 1
Att: Chief, Branch 850 1
Att: Technical Information Officer 2

Inspector of Naval Material, San Francisco 1

Library of Congress, DC (UNCLASSIFIED) 2

Long Beach Naval Shipyard, Calif.
Att: Code 240 1

Los Angeles Air Procurement District, Calif.
Att: Quality Control Division 1

Los Angeles Ordnance District, Pasadena
Att: ORDEV 1

Mare Island Naval Shipyard, Vallejo
Att: Library 1

Marine Corps Equipment Board, Quantico 1

Marine Corps Headquarters, DC
Att: Research & Development Section 1
Att: Code AO4E 1

Maxwell AFB, Air Command & Staff School
Att: Air University Library 1

NASA, Ames Research Center, Moffett Field
Att: Director 1

NASA, Flight Research Center, Edwards
Att: Library 1

NASA, Goddard Space Flight Center, Greenbelt
Att: Code 320, Mr. J. C. New 1
Att: Code 623.3, Mr. G. Hinshelwood 1
Att: Code 321.2, Mr. K. M. Carr 1
Att: Code 321.2, Mr. F. Lindner 1
Att: Dr. Elias Klein 1

NASA, Langley Research Center, Hampton
Att: Library 2
Att: Mr. S. A. Clevenson 1

NASA, Lewis Research Center, Cleveland
Att: Library 2

NASA, Manned Spacecraft Center, Houston
Att: Mr. G. A. Watts 1
Att: Technical Library 1

NASA, Marshall Space Flight Center, Huntsville
Att: Mr. J. H. Farrow, M-P&VE-ST 1
Att: Mr. R. M. Hunt, M-P&VE-S 1
Att: AMSMI-RBLD 1

NASA, Scientific & Technical Info. Facility, Bethesda
Att: NASA Representative 1

National Bureau of Standards, DC
Att: Mr. B. L. Wilson 1
Att: Mr. S. Edelman, Mech. Div. 1

National Security Agency, DC
Att: Engineering 1

Naval Air Development Center, Johnsville
Att: Mr. L. R. Mullen 1
Att: Aeronautical Instrument Lab. 1
Att: NADC Library 2

Naval Air Engineering Center, Philadelphia
Att: Library 1

Naval Air Test Center, Patuxent River
Att: Electronics Test Div. 1
Att: VTOL/STOL Branch 1
Att: Instrumentation Br., Flight Test Division 1

Naval Ammunition Depot, Crane
Att: Code 3540 1
Att: Code 3400 1

Naval Ammunition Depot, Portsmouth
Att: Mr. Jerome Smith, Code QALE 1

Naval Ammunition Depot, Red Bank
Att: Chief Engineer 1

Naval Ammunition Depot (Oahu)
Att: Weapons Technical Library 1

Naval Applied Science Laboratory, Brooklyn
Att: Library 3

Naval Attache, Navy No. 100, NY
Att: Logistics Division 1

Naval Avionics Facility, Indianapolis
Att: MAL-Library 1

Naval Civil Engineering Lab., Pt. Hueneme
Att: Library 2

Naval Construction Battalion Center, Pt. Hueneme
Att: Civil Engineer Corps Officers 1

Naval Medical Field Research Lab., Camp Lejeune 1

Naval Mine Engineering Facility, Yorktown
Att: Library 1

Naval Missile Center, Pt. Mugu
Att: Library, N-03022 1
Att: Env. Div., N314 2

Naval Operations, Office of Chief, DC
Att: Op 31 1
Att: Op 34 1
Att: Op 75 1
Att: Op 07T6, Mr. T. Soo-Hoo 1
Att: Op 725 1

Naval Ordnance Laboratory, Corona
Att: Code 234, Technical Library 1
Att: Code 56, Sys. Eval. Division 1

Naval Ordnance Laboratory, Silver Spring
Att: Technical Director 1
Att: Library 3
Att: Environmental Simulation Div. 6
Att: Mr. George Stathopoulos 1

Naval Ordnance Test Station, China Lake
Att: Technical Library 1
Att: Code 3023 1
Att: Code 3073 1
Att: Code 4062 2
Att: Code 4066 1
Att: Code 5516 1

Naval Ordnance Test Station, Pasadena
Att: P8087 3
Att: P8092 1
Att. P8073 1
Att: P80962 1

Naval Postgraduate School, Monterey
Att: Library 1

Naval Propellant Plant, Indian Head
Att: Library 1

Naval Radiological Defense Lab., San Francisco
Att: Library 3

Naval Research Laboratory, DC
Att: Code 6250 1
Att: Code 6260 1
Att: Code 6201 1
Att: Code 4021 2
Att: Code 2027 2

Naval Security Engineering Facility, DC
Att: R&D Branch 1

Naval Supply R&D Facility, Bayonne
Att: Library 1

Naval Torpedo Station, Keyport
Att: QEL, Technical Library 1

Naval Training Device Center, Pt. Washington
Att: Library Branch 1
Att: Code 4211 1

Naval Underwater Ordnance Station, Newport
Att: Technical Documents Library 1

Naval Underwater Weapons Systems Engrg. Center, Newport
Att: Library 1

Naval Weapons Evaluation Facility, Albuquerque
Att: Library, Code 42 1

Naval Weapons Laboratory, Dahlgren
Att: Technical Library 1

Navy Electronics Laboratory, San Diego
Att: Library 1

Navy Marine Engineering Laboratory, Annapolis
Att: Library 1

Navy Mine Defense Laboratory, Panama City
Att: Library 1

Navy ROTC and Administrative Unit, Cambridge 1

Navy Underwater Sound Laboratory, New London
Att: Technical Director 1
Att: Mr. J. G. Powell, Engrg. & Eval. Div. 1

Navy Underwater Sound Reference Lab., Orlando
Att: Mr. J. M. Taylor, Code 120 1

Norfolk Naval Shipyard, Portsmouth
Att: Design Superintendent 1

Norton AFB, Off. of Inspector General
Att: AFIMS-2-A 1

Office Director of Defense R&E, DC
Att: Technical Library 3
Att: Mr. Melvin Bell 1
Att: Mr. W. M. Carlson 1

Office of Naval Material, DC 1

Office of Naval Research, DC
Att: Code 439 6
Att: Code 104 1

Office of Naval Research Branch Office, Boston 1

Office of Naval Research Branch Office, Pasadena 1

Office of Naval Research Branch Office, San Francisco 1

Ogden Air Materiel Area, Hill AFB
Att: Service Engineering Dept., OONEOO 1

Oklahoma City Air Materiel Area, Tinker AFB
Att: Engineering Division 1

Pearl Harbor Naval Shipyard, FPO
Att: Code 264 1

Philadelphia Naval Shipyard, Pa.
Att: Ship Design Section 1
Att: Naval Boiler & Turbine Lab. 1

Picatinny Arsenal, Dover
Att: Library SMUPA-VA6 1
Att: SMUPA-VP7, R. G. Leonardi 1
Att: SMUPA-T, R. J. Klem 1
Att: SMUPA-D, E. Newstead 1
Att: SMUPA-VP3, A. H. Landrock 1

Portsmouth Naval Shipyard, NH
Att: Code 246 1
Att: Mr. E. C. Taylor 1
Att: Mr. J. E. Smith 1

Puget Sound Naval Shipyard, Bremerton
Att: Code 275 1
Att: Material Laboratories 1
Att: Code 242, Mr. K. G. Johnson 1
Att: Code 281 1

Quartermaster Food & Container Institute, Chicago
Att: Director, Container Lab. 1
Att: Technical Library 1

Quartermaster R&E Airborne Test Activity, Yuma
Att: QMATA 1

Quartermaster R&E Center, Natick
Att: Technical Library 2
Att: Dr. W. B. Brierly 1

Randolph AFB, School of Aviation Medicine, Texas 1

Rome Air Development Center, Griffiss AFB
Att: Mr. Dana Benson, RASSM 1

6511th Test Group (Parachute), USAF, El Centro
Att: Mr. E. C. Myers, Tech. Director 1

6570th Aerospace Medical Research Labs., W-PAFB
Att: MRMAE 1
Att: Mr. R. G. Powell MRBAI 1

San Francisco Naval Shipyard, Calif.
Att: Design Division 1

Savanna Ordnance Depot, Illinois
Att: OASMS 1

Special Projects Office, USN, DC
Att: SP Technical Library 1

Springfield Armory, Mass
Att: Library 2

Strategic Air Command, Offutt AFB
Att: Operations Analysis Office 1

Supervisor of Shipbuilding, USN, Camden
Att: Code 299 2

Tobyhanna Army Depot, Pa.
Att: SMC Packaging and Storage Center 1

Watervliet Arsenal, New York
Att: ORDBF-RR 2

White Sands Missile Range, New Mexico
Att: STEWS-AMTED-T 2

Wright-Patterson AFB, Dayton
Att: AFFDL (FDFE, E. H. Schell) 1
Att: AFFDL (FDFE, C. W. Gerhardt) 1
Att: AFFDL (FDD, H. A. Magrath) 1
Att: AFFDL (FDDS, C. A. Golueke) 1
Att: AFML (MAMD, J. P. Henderson) 1
Att: RTD (SEDSV, R. F. Wilkus) 1